

The Lithotectonic Setting and Paragenetic History of Deposit No.1, Mary River District, North Baffin Island

Sean A. Fulcher

Supervisor

Dr. Norman Duke and Dr. Desmond Moser

The University of Western Ontario

Follow this and additional works at: <http://ir.lib.uwo.ca/etd>

 Part of the [Geology Commons](#)

THE LITHOTECTONIC SETTING AND PARAGENETIC HISTORY OF DEPOSIT
NO.1, MARY RIVER DISTRICT, NORTH BAFFIN ISLAND

Monograph

by

Sean Alexander Fulcher

Department of Earth Sciences
Graduate Program in Geology

A thesis submitted in partial fulfillment
of the requirements for the degree of
Masters of Science

The School of Graduate and Postdoctoral Studies
The University of Western Ontario
London, Ontario, Canada

© Sean Alexander Fulcher 2015

Abstract

Baffinland Iron Mines Corporation is currently extracting the highest grade BIF-hosted direct shipping iron ore in the world from their flagship Deposit No.1 on north Baffin Island. This deposit and several other prospects are hosted within the isoclinally folded Mary River Group, a Neoproterozoic greenstone belt terrane hosting Algoma-type BIF, ultramafics, volcanoclastics and sediment. Mary River Group supracrustals are juxtaposed against Mesoproterozoic basement gneisses due to the Trans-Hudson Orogen overprint, forming a regional dome-keel tectonic framework.

Detail mapping and core logging of Deposit No.1 combined with geochemistry and geochronology reveal the previously interpreted footwall gneisses, volcanics and metasediments to be mylonitized and altered ~2900 Ma monzogranite. The footwall monzogranite has endured three stages of hydrothermal alteration during Paleoproterozoic extension, removing up to 40% SiO₂. Stage 1 is the formation of epidote-carbonate-hornblende veins. Stage 2 involves the breakdown of feldspars and quartz to muscovite forming quartz-augene muscovite schist (QAMS). A low amphibolite facies metamorphic event follows stage 2 alteration, producing large cordierite porphyroblasts. Stage 3 further desilicifies QAMS by biotite alteration forming quartz-augene biotite schist (QABS) and biotite schist. Retrogression of biotite schist forms chlorite schist. Stage 3 schists are overprinted by a second low amphibolite facies metamorphic event, producing andalusite-staurolite-almandine and grunerite-almandine porphyroblastic assemblages. Temperatures and pressure of the second metamorphic event are calculated between 368-481°C at a maximum pressure of 3550 bars. Paragenetic sequencing of silica loss in monzogranite to form chlorite schist is identical to the formation of ore zone chlorite schist and therefore related to the formation of high grade iron ore. U-Pb dating of hydrothermal monazite in footwall QABS and ore zone chlorite schist bracket hydrothermal desilicification between 1873 ± 20 Ma and 1800 ± 12 Ma. Last, the paragenetic alteration-metamorphic history of Deposit No.1 is not fully consistent with previous metamorphic and gneiss dome models. A post-collisional model is presented to account for the paragenetic and metamorphic differences.

Keywords

BIF, Algoma-type, geochronology, monazite, zircon, mass balance, dome and keel.

Acknowledgments

Funding for this study was provided by Baffinland Iron Mines Corporation in conjunction with an Industrial-Postgraduate Scholarship by the Natural Sciences and Engineering Research Council of Canada. The author would like to thank both parties for their contributions, especially BIMC for employment and logistical aid. The supervisors of this thesis added tremendously to the quality and coherence of text. Dr. Norman Duke is further applauded for his in the field contributions and open door approach. Gratitude is extended to Dr. Desmond Moser for awarding the author the necessary tools and ideas to complete a geochronological study.

Table of Contents

Abstract	ii
Acknowledgments.....	iii
Table of Contents	iv
List of Tables	ix
List of Figures	xi
List of Plates	xvii
List of Equations.....	xx
List of Appendices	xxii
Chapter 1 Introduction	1
1 Introduction	1
1.1 Statement of Purpose	1
1.2 Physiography of Study Area	2
1.3 Previous Mineral Exploration & Research	5
1.4 Regional Geology & Tectonic Framework.....	6
1.5 Mary River Area Lithologies	10
1.5.1 Basement Complex	10
1.5.2 MRG Metasediment and Quartzite	13
1.5.3 MRG Iron Formation	14
1.5.4 MRG Volcanics	17
1.5.5 MRG Intrusives (Neoproterozoic).....	18
1.5.6 Tectonostratigraphic Framework of the MRG.....	18
1.6 Regional Geochronology	20
1.7 Regional Metamorphism.....	23
1.8 Iron Formation Enrichment & Deposit No.1 Geology	26
1.9 Summary & Hypothesis	27

Chapter 2 Banded Iron Formations & Iron Ore Genesis	29
2 Introduction	29
2.1 Spatial and Temporal Distribution of BIF	30
2.2 BIF Mineralogy, Texture & Chemistry	33
2.3 Banded Iron Formation Facies	35
2.4 BIF Origins and Genesis	36
2.5 Metamorphism of Banded Iron Formation	43
2.6 Iron Ores	44
2.7 Iron Formation Enrichment and Deposits	45
2.7.1 Structural Controls	46
2.7.2 Syngenetic Enrichment	46
2.7.3 Supergene Enrichment	47
2.7.4 Hypogene Enrichment	50
2.8 Geochronology of Banded Iron Formation and Iron Ore	53
Chapter 3 Methods	55
3 Introduction	55
3.1 Mapping & Sampling Methods	55
3.2 Preparation Techniques	56
3.3 Analytical Techniques and Methods	56
3.3.1 Optical Microscopy	56
3.3.2 Geochemistry	57
3.3.3 Electron Microscopy	61
3.3.4 Electron Micro Probe Analysis	65
3.3.5 U-Pb Geochronology	69
Chapter 4 Mapping, Drill Core Logging & Petrography	76
4 Introduction	76

4.1 Mapping & Drill Core Logging	76
4.1.1 Footwall Units.....	76
4.1.2 Ore Zone Units.....	90
4.1.3 Hangingwall Units	91
4.1.4 Polyphase Deformation.....	93
4.2 Deposit No. 1 Petrography & EMP Analysis	97
4.2.1 Footwall Lithologies	97
4.2.2 Ore Zone Lithologies	131
4.2.3 Hangingwall Lithologies.....	142
4.3 Mineral-Textural Paragenesis	154
4.3.1 Footwall Paragenesis	154
4.3.2 Ore Zone Paragenesis	159
4.3.3 Hangingwall Paragenesis	161
Chapter 5 Geochemistry	163
5 Introduction.....	163
5.1 Deposit No. 1 Footwall Lithogeochemistry.....	163
5.1.1 Footwall Major Element Oxides.....	163
5.1.2 Footwall Trace Elements	167
5.1.3 Footwall Rare Earth Elements	172
5.2 Deposit No.1 Ore Zone Lithogeochemistry.....	177
5.2.1 Ore Zone Major Oxides	177
5.2.2 Ore Zone Trace Elements	179
5.2.3 Ore Zone Rare Earth Elements	182
5.3 Hangingwall Lithogeochemistry.....	184
5.3.1 Hangingwall Major Oxides.....	184
5.3.2 Hangingwall Trace Elements.....	186

5.3.3	Hangingwall Rare Earth Elements	189
5.4	Mass Balance Changes	192
5.4.1	Density and Fv Determination	192
5.4.2	Mass Balance Changes ASG & Footwall Schists.....	194
5.4.3	Mass Balance Changes BIF to Iron Ore	198
5.4.4	Arithmetic Mass Balance Change BIF to Ore	201
Chapter 6	Geochronology	202
6	Introduction	202
6.1	Sample 6078 (QAMS) Description.....	202
6.1.1	6078 BSE-EDS Feature Phase Mapping.....	202
6.1.2	6078 BSE & SE Images of Datable Phases	203
6.2	Sample 6225 (QABS) Description.....	206
6.2.1	6225 BSE-EDS Feature Phase Mapping.....	206
6.2.2	6225 BSE, SE and CL Images of Datable Phases	208
6.2.3	6225 Zircon U-Pb Isotopic Data and Th/U Ratios.....	210
6.2.4	6225 Monazite U-Pb Isotopic Data and Th/U Ratios	214
6.3	Sample 6220A (Ore Zone CS) Description	216
6.3.1	Sample 6220A BSE-EDS Feature Mapping	216
6.3.2	6220A BSE, SE and CL Images of Datable Phases.....	218
6.3.3	6220A Zircon U-Pb Isotopic Data and Th/U Ratios.....	220
6.3.4	6220A Monazite U-Pb Isotopic Data and Th/U Ratios	224
6.4	Sample 716 Description	225
6.4.1	716 BSE-EDS Feature Phase Mapping.....	225
6.4.2	716 SEM Imaging and Element Mapping of Features.....	227
6.5	Sample 709 Description	229
6.5.1	709 BSE-EDS Feature Mapping	230

6.5.2	709 SEM Imaging and Element Mapping of Features.....	230
6.6	Sample 6416 Description.....	234
6.6.1	6416 BSE-EDS Feature Phase Mapping.....	235
6.6.2	6416 SEM Imaging and Element Mapping of Features.....	235
Chapter 7	Discussion	240
7	Introduction.....	240
7.1	Litho-Tectonic Stratigraphy.....	240
7.1.1	Footwall	240
7.1.2	Ore Zone	243
7.1.3	Hangingwall.....	245
7.1.4	Structure.....	245
7.2	Geochronology.....	246
7.2.1	Zircon.....	246
7.2.2	Monazite	249
7.3	Paragenesis & Mass Balance	253
7.3.1	Footwall	253
7.3.2	Ore Zone	257
7.3.3	Hangingwall.....	262
7.4	Metamorphism	263
7.4.1	Assemblages and Facies	263
7.4.2	Isograds.....	268
7.4.3	Thermometry & P-T Zones.....	272
7.5	Tectonic-Paragenetic Model.....	279
Chapter 8	Conclusions	284
8	Introduction.....	284
8.1	Lithotectonic Setting.....	284

8.2 Metamorphism & Paragenesis	285
8.3 Model Validation – Hypothesis Testing	286
8.4 Regional Implications & Final Remarks.....	291
References.....	292
Appendix 1 Samples	311
Appendix 2 EMPA.....	315
Appendix 3 Geochemistry.....	318
Appendix 4 Density	324
Appendix 5 U-Pb Isotope Data	325
Appendix 6 Zircon & Monazite Images	327
Curriculum Vitae	365

List of Tables

Table 1-1 MRG iron formation types.	14
Table 1-2 Grade and tonnage of historic Deposits No.1-3	15
Table 1-3 Regional geochronological data f.....	23
Table 1-4 Metamorphic mineral assemblages from Mary River metasediments.	24
Table 2-1 Common BIF mineralogy.....	34
Table 2-2 Major global BIF-hosted iron ore districts..	45
Table 3-1 Major elemental oxides analyzed by ICP-AES	58
Table 3-2 Trace and rare earth elements analyzed by ICP-MS.	59
Table 3-3 Immobile elements in geologic systems.....	61
Table 3-4 BSE-EDS feature mapping recipe A.	68
Table 3-5 BSE-EDS feature mapping recipe B.	69

Table 3-6 Radiogenic parent nuclides and daughter products.	70
Table 4-1 Subdivisions of QAMBS unit.....	77
Table 4-2 Mineral abundance chart of footwall granitoids.....	100
Table 5-1 Average major elemental oxide composition of footwall lithologies including carbon and sulphur. Maximum and minimum values are listed in adjacent columns.	165
Table 5-2 Trace element values for footwall intrusives.....	169
Table 5-3 Trace element values for footwall quartz-augen schists and ASG units	170
Table 5-4 Trace element values for footwall biotite and chlorite schist units.....	171
Table 5-5 Rare earth element values for footwall intrusives, quartz-augen schists and ASG units.....	174
Table 5-6 Elemental oxide values for BIF, HGIF and ore zone chlorite schist.....	178
Table 5-7 Trace element values for BIF, HGIF and ore zone chlorite schist.	180
Table 5-8 Rare earth element values for BIF, HGIF and ore zone chlorite schist.....	183
Table 5-9 Elemental oxide values for hangingwall lithologies	185
Table 5-10 Trace element a values for hangingwall lithologies.....	187
Table 5-11 Rare earth element values for hangingwall lithologies.	190
Table 5-12 List of footwall and ore zone unit densities and volume factors.	194

List of Figures

Figure 1-1 Regional map of Nunavut.	3
Figure 1-2 Physiographic map of northern Baffin Island.	4
Figure 1-3 Regional tectonic map of the Churchill Province and domains.	8
Figure 1-4 Map of Baffin Island tectonic domains.	9
Figure 1-5 Legend for regional geology map.	11
Figure 1-6 Regional geology map of Deposits No.1-5.	12
Figure 1-7 Geology map of Deposits No.1-3.	16
Figure 1-8 Deposit No.1 stratigraphic columns.	20
Figure 1-9 Regional map of isotopic ages.	22
Figure 1-10 Regional metamorphic facies map of the Mary River Group.	25
Figure 2-1 Frequency timeline of banded iron formation deposition worldwide.	31
Figure 2-2 World map showing BIFS hosted within cratonic blocks.	32
Figure 2-3 pH - Eh chemical stability diagram.	38
Figure 2-4 Depositional environments of banded iron formations.	39
Figure 2-5 $\delta^{30}\text{Si}$ isotopic ratios ($^0/_{00}$) from Archean banded iron formations and sea floor precipitates.	41
Figure 2-6 Illustration of syngenetic BIF hosted iron ore formation.	47
Figure 2-7 Illustration of supergene processes.	49
Figure 2-8 Illustration of iron formation enrichment type stratigraphy.	52

Figure 3-1 Scanning electron microscope diagram	62
Figure 3-2 Illustrated diagram of Everhart-Thornely detector.	64
Figure 4-1 Map legend for Figure 4-2.	78
Figure 4-2 Geological map of Deposit No.1.....	79
Figure 4-3 Legend for cross-sections.....	80
Figure 4-4 Cross-section A-B across the southern limb.....	81
Figure 4-5 Cross-section C-D across the northern limb	82
Figure 4-6 Lithologic log of hole MR1-12-226.....	89
Figure 4-7 Structural deformation model of Deposit No.1 footwall..	94
Figure 4-8 Contoured equal-area stereonet of lineations in footwall units.	96
Figure 4-9 Photographs of oriented sample 6534.....	97
Figure 4-10 QAP diagram of Deposit No.1 footwall granitoids.....	100
Figure 4-11 Feldspar ternary diagram of footwall granitoids.....	102
Figure 4-12 Amphibole determination plot of ECH veining amphiboles.....	102
Figure 4-13 Biotite composition diagram.....	108
Figure 4-14 EDS phase scan of QAMS sample 6078.....	115
Figure 4-15 EDS phase scan of QABS of drill core sample 6225.....	116
Figure 4-16 Garnet composition plot from biotite schists.	125
Figure 4-17 Amphibole discrimination plot of footwall chlorite schist amphiboles.	130
Figure 4-18 Garnet composition plot of garnets from footwall chlorite schists.....	131

Figure 4-19	Structural and texture domains in magnetite-hematite ore.	137
Figure 4-20	Chlorite speciation plot chlorite.	140
Figure 4-21	EDS phase scan of ore zone chlorite schist.....	141
Figure 4-22	Garnet composition plot of garnets from ore zone chlorite schists.....	142
Figure 4-23	Amphibole discrimination plot of in ultramafic-amphibolite amphiboles.....	148
Figure 4-24	EDS spectrum of carbonates in ultramafics.	148
Figure 4-25	Mineral-textural paragenesis of footwall schist units.	155
Figure 4-26	Paragenetic mineral timeline for footwall granitoids.....	158
Figure 4-27	Paragenetic mineral timeline for BIF transitioning into high grade ore.	160
Figure 4-28	Paragenetic mineral timeline for ore zone biotite schist into garnet-amphibole chlorite schist.	160
Figure 4-29	Paragenetic mineral timeline for ultramafics changing into ultramafic-amphibolite.	162
Figure 5-1	Bar graphs of major elemental oxides in footwall lithologies	166
Figure 5-2	AFM plot of footwall metagabbro.	167
Figure 5-3	Granite discrimination plot of Rb vs Y+Nb.....	168
Figure 5-4	Chondrite normalized footwall trace element plots..	172
Figure 5-5	Chondrite normalized rare earth element plot of footwall intrusives..	175
Figure 5-6	Chondrite normalized rare earth element plot of monzogranite samples.	175
Figure 5-7	Chondrite normalized rare earth element plot of ASG units.....	176
Figure 5-8	Chondrite normalized rare earth element plot of footwall schists, ASG and monzogranites.	176

Figure 5-9 Bar graph of average major elemental oxides in BIF and HGIF.	179
Figure 5-10 Chondrite normalized trace element plot BIF and HGIF.....	181
Figure 5-11 Chondrite normalized rare earth element plot of BIF, and HGIF.....	184
Figure 5-12 Bar graph of major elemental oxides in hangingwall lithologies.	186
Figure 5-13 Chondrite normalized trace element plot of average hangingwall units.....	188
Figure 5-14 Chondrite normalized rare earth element plot of hangingwall units.....	191
Figure 5-15 Chondrite normalized rare earth element plot of footwall, ore zone and hangingwall chlorite schist units.....	191
Figure 5-16 Mass balance changes of elemental oxides in footwall schist and ASG lithologies.....	195
Figure 5-17 Mass balance changes of elemental oxides (K ₂ O-S) in footwall schist and ASG lithologies.....	196
Figure 5-18 Mass balance changes of rare earth elements (REE) in footwall schist and ASG lithologies.....	196
Figure 5-19 Mass balance changes of transition metal, high field strength and main group elements in footwall schist and ASG lithologies.....	197
Figure 5-20 Mass balance changes of elemental oxides in iron ore types.....	198
Figure 5-21 Mass balance changes of elemental oxides in iron ore types Ca-P.....	199
Figure 5-22 Mass balance changes of large ion lithophile, transition metal, high field strength, rare earth and main group elements in iron ore types.....	200
Figure 6-1 BSE-EDS feature map of sample 6078.....	205
Figure 6-2 BSE-EDS feature map of thin section sample 6225.....	207
Figure 6-3 Concordia plot of all zircon ²⁰⁷ Pb/ ²⁰⁶ Pb values from sample 6225.....	211

Figure 6-4 Concordia plot of zircon $^{207}\text{Pb}/^{206}\text{Pb}$ values from central zircon zones in sample 6225.....	212
Figure 6-5 Concordia plot of zircon $^{207}\text{Pb}/^{206}\text{Pb}$ values from marginal zircon zones in sample 6225.....	212
Figure 6-6 Cathodoluminescence and secondary electron images of zircon 4393 from sample 6225.....	213
Figure 6-7 Sample 6225 zircon Th/U plot of with respect to age.....	213
Figure 6-8 Concordia plot of all $^{207}\text{Pb}/^{206}\text{Pb}$ monazite values from sample 6225.....	214
Figure 6-9 Concordia plot of culled $^{207}\text{Pb}/^{206}\text{Pb}$ monazite values from sample 6225.	215
Figure 6-10 Sample 6225 monazite Th/U plot with respect to $^{207}\text{Pb}/^{206}\text{Pb}$ age.....	215
Figure 6-11 BSE-EDS feature map of sample 6220A.....	217
Figure 6-12 Back scatter electron images of patchy monazite.	218
Figure 6-13 $^{207}\text{Pb}/^{206}\text{Pb}$ counts over time from analyses 3185-S1 and 4431-S1..	221
Figure 6-14 Concordia plot of all $^{207}\text{Pb}/^{206}\text{Pb}$ zircon values from sample 6220A.....	222
Figure 6-15 Concordia plot of culled zircon ages anchored at zero and regressed to a concordant age of 2748+ 11 Ma.	222
Figure 6-16 Concordia plot of concordant cluster $^{207}\text{Pb}/^{206}\text{Pb}$ zircon values from sample 6220A.....	223
Figure 6-17 Th/U values of sample 6220A zircon with respect to $^{207}\text{Pb}/^{206}\text{Pb}$ age.....	223
Figure 6-18 Sample 6220A monazite concordia plot of all $^{207}\text{Pb}/^{206}\text{Pb}$ analyses.....	224
Figure 6-19 Concordia plot of culled $^{207}\text{Pb}/^{206}\text{Pb}$ monazite values from sample 6220A.	225
Figure 6-20 BSE-EDS feature map of polished thin section of sample 716	226

Figure 6-21 BSE-EDS feature map of polished thin section of sample 709..	231
Figure 6-22 BSE-EDS feature map of polished thin section of sample 6416.	236
Figure 6-23 Calcium-thorium scatter plot of EMP analyses from monazites.	239
Figure 7-1 Tectonic stratigraphic column of Mary River Group and basement granitoids.	244
Figure 7-2 Multi-point U-Pb analysis comparison of QABS zircon 4528	248
Figure 7-3 Multi-point U-Pb analysis comparison of QABS monazite 2674.	252
Figure 7-4 Concordia plot illustrating all zircon and monazite ages.	253
Figure 7-5 Interpretation of hangingwall ultramafics altering to chlorite schist.	262
Figure 7-6 AFK diagram of QAMS metamorphic assemblage.	264
Figure 7-7 AFK diagram of footwall biotite schist assemblage.	266
Figure 7-8 AFK diagram of footwall chlorite schist assemblage.	267
Figure 7-9 Compilation AFK diagram showing progression of footwall schist composition.	267
Figure 7-10 Geology map with mineral in isograds	270
Figure 7-11 Tectono-stratigraphic E-F cross-section of Deposit No.1	271
Figure 7-12 Garnet-chlorite P-T diagram and EDS map of Mn zoned ore zone almandine.	276
Figure 7-13 K_D temperature lines of garnet biotite thermometry of core and rim zones from sample 6227	277
Figure 7-14 P-T diagram of garnet-chlorite thermometry with mineral reaction lines.	278
Figure 7-15 P-T diagram of serpentine, talc and anthophyllite stability fields.	279
Figure 7-16 Metallogenic model for high grade iron ore	283

Figure 8-1 Metamorphic cross-section of low pressure-high temperature gneiss dome metamorphism.....	289
---	-----

List of Plates

Plate 4-1 Oriented QAMBS sample 6534.	85
Plate 4-2 Photographs of footwall outcrop contacts..	86
Plate 4-3 Outcrop photos of Deposit No.1 footwall lithologies.....	87
Plate 4-4 Outcrop photographs from the footwall and hangingwall of Deposit No.1.	88
Plate 4-5 Various HGIF contacts and textures at Deposit No.1.	92
Plate 4-6 Outcrop photographs of footwall lineations..	95
Plate 4-7 Structural footwall outcrop photographs..	96
Plate 4-8 Footwall granitoids.	101
Plate 4-9 Textures in footwall granitoids.....	103
Plate 4-10 Photographs of metagabbro..	104
Plate 4-11 Metagabbro textures..	105
Plate 4-12 QAMBS and QABS units.....	109
Plate 4-13 QAMBS textures in polished thin sections.....	110
Plate 4-14 QAMBS accessory minerals and textural features.....	111
Plate 4-15 QAMS drill core.	112
Plate 4-16 QAMS textures in samples 6078 and 6210..	113
Plate 4-17 BSE images of QAMBS accessory phases.....	114
Plate 4-18 Fluid inclusions from QAMBS units.....	114

Plate 4-19	Varieties of altered silicified granitoid.	118
Plate 4-20	ASG mineral textures..	119
Plate 4-21	Mineral textures and features in epidote-carbonate-hornblende (ECH) veining..	120
Plate 4-22	Varieties of footwall biotite schist in drill core..	122
Plate 4-23	Various porphyroblastic growth and reaction textures in biotite schist.	123
Plate 4-24	Various mineral textures in biotite schist	124
Plate 4-25	Varieties of footwall chlorite schist.....	127
Plate 4-26	Garnet porphyroblasts from the PS2 site.....	128
Plate 4-27	Inclusions within garnet porphyroblasts.....	129
Plate 4-28	Mineral textures in footwall chlorite schists.....	130
Plate 4-29	Texture and mineralogy of Deposit No.1 banded iron formation	132
Plate 4-30	Varieties of iron ore	134
Plate 4-31	Various iron ore textures.	135
Plate 4-32	Various hematite alteration textures in iron ore..	136
Plate 4-33	Ore zone chlorite schist minerals and textures	139
Plate 4-34	Hangingwall chlorite schist mineral textures..	143
Plate 4-35	Various mineral and textural features in HW biotite schists.....	145
Plate 4-36	Ultramafic (UM) and ultramafic-amphibolite (UA) drill core.	147
Plate 4-37	Mineral textures in ultramafic units.....	149
Plate 4-38	Mineral textures in ultramafic-amphibolite units.....	150

Plate 4-39 Mineral and textural features in volcanoclastic units.....	152
Plate 4-40 Mineral and textural features in hornblende-amphibolite..	153
Plate 6-1 Representative zircon crystal morphologies from sample 6078.....	203
Plate 6-2 Representative monazite crystal morphologies from sample 6078.....	204
Plate 6-3 Representative zircon crystal morphologies from sample 6225.....	209
Plate 6-4 Representative monazite morphologies from sample 6225.....	210
Plate 6-5 Representative zircon crystal morphologies in sample 6220A.	219
Plate 6-6 Representative monazite morphologies in sample 6220A..	220
Plate 6-7 Datable phase morphologies in sample 716	227
Plate 6-8 Qualitative WDS element maps of monazite grain 217	228
Plate 6-9 Qualitative WDS element maps of xenotime grain 847.	229
Plate 6-10 Datable phase morphologies in sample 709.	232
Plate 6-11 Qualitative WDS element maps of monazite grain 484.	233
Plate 6-12 Qualitative WDS element maps of xenotime grain 1082.	234
Plate 6-13 Datable phase morphologies from sample 6416.....	237
Plate 6-14 Qualitative WDS element mapping of monazite 615.....	238
Plate 6-15 BSE and SE images of zircon in hematite ore sample 6416..	239
Plate 7-1 Comparison of hydrothermal monazite textures..	251

List of Equations

Equation 2-1 Chemical reactions during supergene enrichment.	48
Equation 3-1 Gressen`s equation mass balance equation.	60
Equation 3-2 Half-life equation derived from the Rutherford and Soddy.	70
Equation 3-3 Half-life equation where $T_{1/2}$ is the time for half of the parent isotope.....	70
Equation 3-4 Half-life equations for radiometric decay in a closed system.	71
Equation 4-1 Plagioclase \rightarrow Epidote	156
Equation 4-2 K-feldspar \rightarrow Epidote	156
Equation 4-3 K-feldspar \rightarrow Muscovite.....	156
Equation 4-4 Plagioclase \rightarrow Muscovite.....	156
Equation 4-5 Quartz \rightarrow Muscovite	156
Equation 4-6 Biotite \rightarrow Pycnochlorite.....	156
Equation 4-7 Muscovite + Quartz + Pycnochlorite \rightarrow Cordierite + Biotite	156
Equation 4-8 Cordierite \rightarrow Biotite + Al_2SiO_5 + H_2O	156
Equation 4-9 Quartz \rightarrow Biotite	157
Equation 4-10 Muscovite \rightarrow Biotite	157
Equation 4-11 Biotite \rightarrow Ripidolite.....	157
Equation 4-12 Biotite \rightarrow Andalusite.....	157
Equation 4-13 Biotite + Ripidolite + Cordierite + Al_2SiO_5 \rightarrow Staurolite.....	157
Equation 4-14 Biotite \rightarrow Almandine	157

Equation 4-15 Ripidolite \rightarrow Grunerite.....	157
Equation 4-16 Ripidolite \rightarrow Almandine	157
Equation 4-17 Biotite \rightarrow Ripidolite.....	159
Equation 4-18 Magnetite \rightarrow Hematite	159
Equation 4-19 Ripidolite \rightarrow Almandine	159
Equation 4-20 Ripidolite \rightarrow Almandine	161
Equation 4-21 Serp +3CO ₂ \rightarrow Talc + 3Magnesite +H ₂ O	161
Equation 4-22 Serp \rightarrow Talc + H ₂ O	161
Equation 4-23 Serp + Talc \rightarrow Anthophyllite + H ₂ O + Vapor	161
Equation 4-24 7Talc \rightarrow 3Anthophyllite + 4Quartz +H ₂ O	162
Equation 5-1 Arithmetic derivation of BIF volume ratio to iron ore.....	201
Equation 7-1 Silica increase in ASG calculation.....	256
Equation 7-2 Magnetite to hematite redox reaction by free oxygen.....	258
Equation 7-3 Magnetite to hematite oxidation by aqueous oxygen.....	258
Equation 7-4 Magnetite to hematite oxidation by acid base reaction.....	258
Equation 7-5 Parent BIF volume calculation.....	259
Equation 7-6 Total silica loss calculation from BIF to iron ore..	260
Equation 7-7 Gibbs free energy equation.	272
Equation 7-8 Equilibrium constant equation for garnet-biotite reaction..	273
Equation 7-9 Derived thermodynamic equation for garnet-biotite thermometry.	273

Equation 7-10 Garnet-biotite reaction.	273
Equation 7-11 Garnet-chlorite reaction.	273

List of Appendices

Appendix 1 Samples	311
Appendix 2 EMPA.....	315
Appendix 3 Geochemistry	318
Appendix 4 Density	324
Appendix 5 U-Pb Isotope Data.....	325
Appendix 6 Zircon & Monazite Images	327

Chapter 1 Introduction

1 Introduction

1.1 Statement of Purpose

Direct shipping iron ores (DSOs) are the primary source of iron for steel manufacturing around the world. DSOs are generally defined as having a total iron content exceeding 50% with less than 1.5% deleterious elements. DSOs require less mineral and chemical processing and are directly injected into blast furnaces, thus having a higher economic return than lower grade taconite ores. The Mary River Group (MRG) on northern Baffin Island, Nunavut, Canada is an Archean greenstone belt terrane, hosting the highest grade DSO in the world averaging 66.3% total iron content with grades exceeding 70%. Mineral exploration and development by Baffinland Iron Mines Corporation (BIMC) has revealed 2-5 km long tabular bodies of massive iron oxide within Algoma-type banded iron formation. Host banded iron formation occurs within folded Mary River Group greenstone belts containing mafic-felsic volcanics, ultramafics and sediment. Folded Mary River Group supracrustals lay proximal to gneiss domes with interbedded schists and locally intruding pegmatites. High grade iron ore bodies appear at the boundary zone between the MRG and the basement complex. Iron ore bodies have lost all original silica banding and retain a massive texture.

Investigating boundary conditions is paramount to understanding iron formation enrichment. MacLeod (2012) proposed a gneiss dome model with three stages of iron formation enrichment on the basis of property scale mapping of Deposits No.1-5 with supporting petrography, bulk rock and mineral chemical data.

Further investigation of the dome and keel boundary setting of DSOs is the purpose of this thesis. Detailed outcrop mapping, diamond drill core logging is supplemented with detailed petrography and combined with whole rock geochemistry to define the footwall, ore zone and hangingwall lithologies of Deposit No.1. The paragenetic sequence of banded iron formation to high grade iron ore is characterized as well as the footwall and hangingwall paragenetic sequences. The tectonic history of the

footwall boundary zone is then compared to the enrichment sequence of banded iron formation to high grade iron ore. The elucidated enrichment sequence of banded iron formation to high grade iron ore is further bracketed by geochronology. Comprehending the paragenesis of iron ore and the boundary zone will aid ongoing regional iron ore exploration. Funding for this thesis was provided by BIMC and an NSERC Industrial Postgraduate Scholarship (IPS-1). The database of material is an eclectic library gathered by the author or inherited from previous thesis studies supported by BIMC.

1.2 Physiography of Study Area

The historic Mary River Deposits, No. 1-5, are located in north Baffin Island in the Quikigtani District of Nunavut. Deposits No.1-5 are located between the tide waters of Milne Inlet (85 km NNW) and Steensby (150 km SSE). The Mary River camp lies at the southwest base of Deposit No.1 and is approximately 957 km NNW of Iqaluit, the capital of Nunavut. Inuit communities of Pond Inlet (est. 1,500 population) and Igoolik (est. 800 population) are the closest populated settlements in the region, lying 160 km north and 240 km south respectively (Figure 1.1). Aircraft and sealifts are the only access to the Mary River camp. A 5000 ft gravel airstrip allows turboprop and jet aircraft to service the site while sealifts barge materials seasonally to Milne. The mineralization area is located in a northwest-southeast corridor following the Central Borden Fault Zone (CBFZ)(Figure 1.2) between the Baffin Uplands and the Lancaster Plateau physiographic provinces (Bostock, 1970; Utting et al., 2006). From the Lancaster Plateau to the Baffin Uplands, topography transitions from rolling plains to prominent ridges. Both tundra plains and ridges are covered by thick glacial sediment and boulder fields. The tallest of the ridges is Nuluujaak Mountain, comprising Deposit No. 1 at 710 metres above sea level. Large plateaus continue west and the Baffin Uplands extend eastward into the Davis Region (Bostock, 1970).

Arctic willows, muskeg, labrador tea and other low lying shrubs comprise the only vegetation. Polar bears have been witnessed at the Mary River camp but are rare visitors. Caribou, wolves, foxes and hares form the large land mammal population inhabiting the area. Thousands of snow geese, snowy owls and song birds migrate to nest in the area

during the summer months. Narwhal and beluga whales regularly visit the ports of Milne and Steensby.

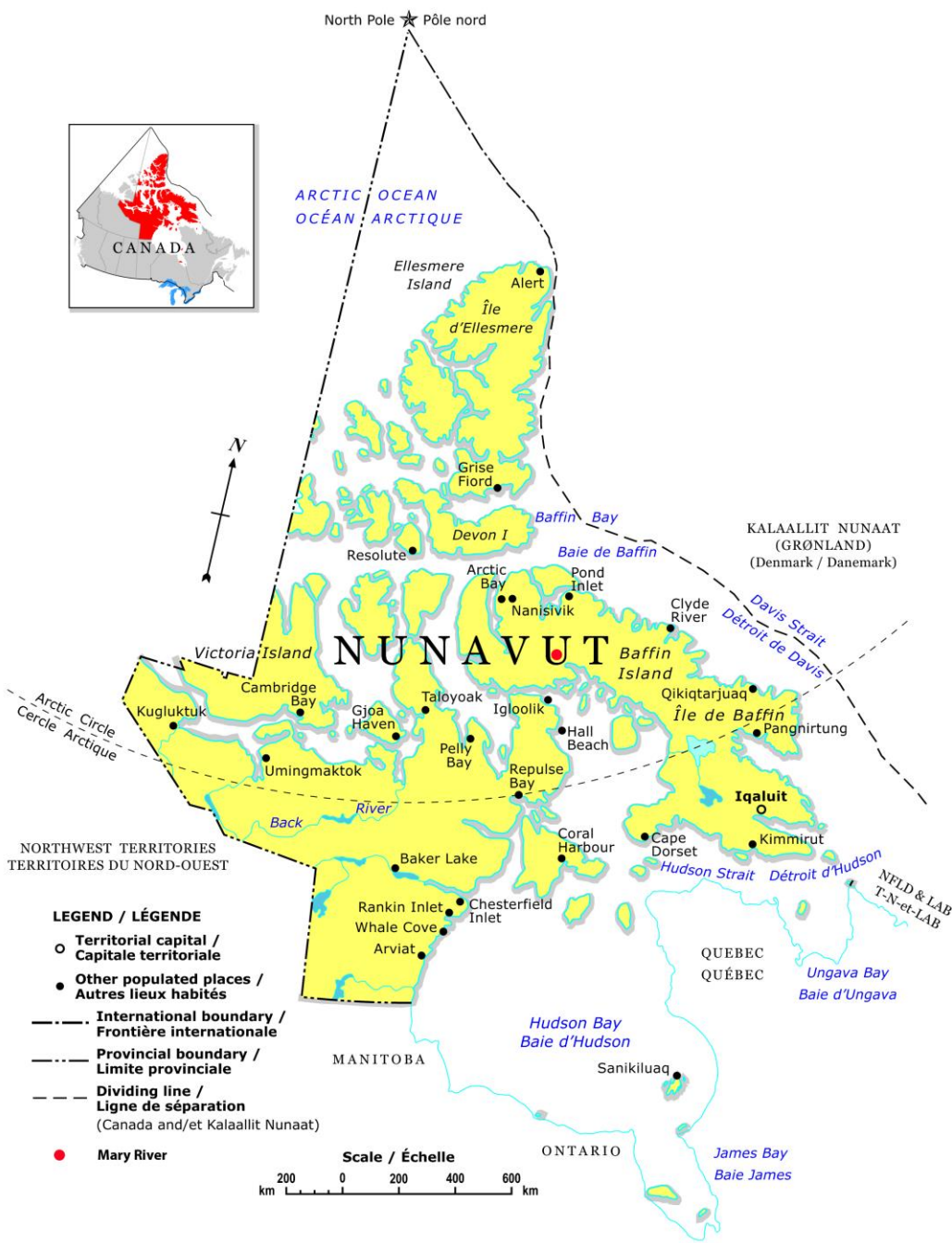


Figure 1-1 Regional map of Nunavut with political borders. Modified from The Atlas of Canada (2006) Red dot indicates Mary River camp.

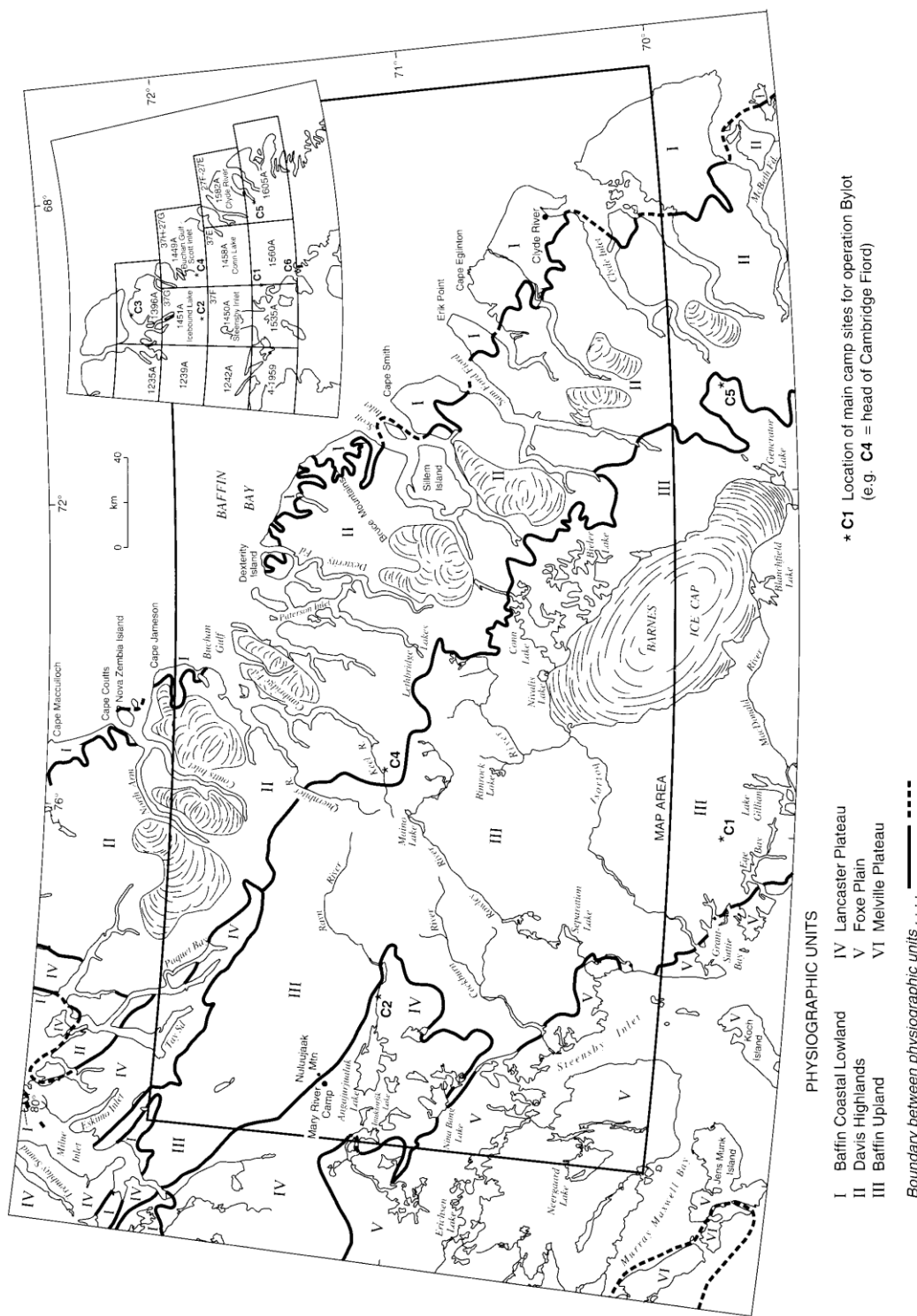


Figure 1-2 Physiographic map of northern Baffin Island. Physiographic provinces are numbered. Map taken from Jackson (2000).

1.3 Previous Mineral Exploration & Research

Banded iron formation on Baffin Island and on the Melville Peninsula has been known for hundreds of years. Magnetite-pyrite ores, mistaken for gold ores, were first noted by Frobisher on southern Baffin Island in 1577 and were shortly mined after in 1578 (Nourse, 1879). Charles Francis Hall revisited these sites in 1863 while looking for survivors of the lost Franklin expedition and found iron ore in Repulse Bay and on South Hampton Island (Nourse, 1879).

Mineral exploration and research on the Mary River Group and its banded iron formation started in the early 1960's and spanned a decade. More than 40 years of quiescence followed after. Initial discovery of historic Deposits No.1-5 are accredited to Murray Watts, then president of British Ungava Explorations Ltd., and pilot Ron Sheardon in 1962 (Jackson, 1966). South African-London based Anglo-American Mining Corporation financed Baffinland Iron Mines Corporation for preliminary exploration work from 1963-1964. Detailed geologic mapping and several diamond drill holes were completed on Deposit No.1. Lowering iron ore prices and mass production from Brazil's Carajás district and Australia's Hamersley Basin made the project uneconomical. As a result, the project was deactivated until 2004 when BIMC was refunded. From 2004 to 2014 BIMC has spent over \$340,000,000 U.S. on exploration and development of Deposits No.1-5 with the primary focus of advancing Deposit No. 1 into an operational mine. Deposit No.1 contains a 416 million tonne (Mt) measured resource grading 66.3% total iron content.

Research has followed the same timeline relative to discovery and economic development. G.D. Jackson of the Geological Survey of Canada completed mapping projects during the summers of 1965 and 1966 producing 1:50,000 scale maps on NTS map sheets 37G/5 and 37G/6 of the area surrounding high grade iron ore bodies, covering a 750 square mile area (Jackson, 1966). During this period G.A. Gross (1966) classified the iron formation as Algoma-type and proposed a metallogenic model for banded iron formation deposition. Regional scale mapping via helicopter reconnaissance of the Clyde-Cockburn area followed in 1969 by Jackson and produced 1:250,000 scale geology maps of north-central Baffin Island. In 1973 a Ph.D thesis was completed by Thomas

Crawford at University of Washington entitled ‘Metamorphic Iron Formations of Ege Bay and Adjacent Parts of Northern Baffin Island’ which included bulk rock chemistry of both silicate and iron-oxide banded iron formation from the Mary River Group.

More recently, the Geological Survey of Canada in a collaboration with Canada-Nunavut Geoscience Office completed a three year (2003-2006) Polar Shelf Project focussing on refining Jackson’s regional maps. This project allowed the revisiting of Deposits No.4 and No.5 by Young et al., (2004) and BIFs hosted in the Committee Bay Belt. To date, BIMC has supported five BSc. theses; MacLeod (2009), Nicpon (2011), Fulcher (2011), Howitt (2012) and Herbranson (2012) and two Master’s theses; MacLeod (2012) and Illiev (2011). Current research projects include the investigation of Rowley River iron ore formation by Jon Hey at the University of Western Ontario. Geophysical studies focussed on directional magnetic fields of iron ore are presently under review by Ilya Inov at Macmaster University.

1.4 Regional Geology & Tectonic Framework

Baffin Island lies entirely within the Churchill Province, an amalgamation of seven Archean crustal blocks during the Paleoproterozoic (1.92-1.82 Ga) cratonization of the proto-continent Laruentia, known as the Trans-Hudson Orogeny (THO) (Hoffman, 1988, 1990; Lewry and Collerson, 1990). Two domains comprise the island; the northerly Rae craton and the southerly Baffin Orogen (Jackson and Berman, 2000) (Figure 1.3). The Rae and Baffin Orogen are separated by the Isortoq thrust fault.

The Rae craton extends from northern Saskatchewan northeast across Nunavut and northern Baffin Island into northern Greenland. The southern Snowbird Line mylonites separate the Rae from the Hearne craton while the northern Thelon tectonic zone and Archean Queen Maud Block split the Rae from the Archean Slave craton (Hoffman, 1990; Lewry and Collerson, 1990). Small outliers of the Rae maybe present on the south eastern side of Baffin Island (Sandborn-Barrie et al., 2014). Over much of the Rae, linear Mesoarchean (2970-2968 Ma) to Neoproterozoic (2740-2710 Ma & 2730-2690 Ma) (Wodicka et al., 2011) greenstone belts are separated by 3300-2800 Ma felsic orthogneisses and felsic granitoids (Hoffman, 1990). Three Archean tectonic episodes are proposed to have formed the Rae craton involving 3.0-2.8 felsic plutonism, 2.76-2.71 Ga

volcanism and later felsic plutonism followed by a cryptic 2.55-2.50 Ga thermal event (Jackson, 2000; Jackson and Berman, 2000).

The Baffin Orogen, comprises of the charnockite-monzogranites of the Cumberland Batholith, (Jackson and Morgan, 1978; Hoffman, 1990) the gneissic-plutonic Meta Incognita terrane (Skipton et al., 2012) and the Sugluk terrane. Piling Group metasediments form the northern margin of the Baffin Orogen. Baffin Island has been further divided into eight tectonic domains with subdomains on the basis of aeromagnetic data, structural features, lithologies and geochronology (Jackson and Berman, 2000)(Figure 1.4).

The MRG is a Neoproterozoic (2759-2718 Ma) granite-greenstone terrane lying within the north eastern zone of the Rae craton (Jackson et al., 1990; Jackson, 2000; Bethune and Scammell, 2003a, b). The MRG group forms up to 65 km long northwest-southeast trending belts that are deformed by kilometer scale folds. The group is composed of Neoproterozoic mafic to felsic volcanics, siliclastic sedimentary units, mafic to felsic intrusives and ultramafic units that unconformably overlie a mixed Mesoproterozoic granitic-gneiss-migmatite basement (Gross, 1966; Jackson, 1966, 1969, 2000). The BIF-wacke-komatiite-quartzite sequence of the MRG is arguably correlative to the Committee Bay Fold Belt, a 300 km long ~15 km wide Neoproterozoic supracrustal belt hosting the Prince Albert Supergroup and Woodburn Lake Group on the Nunavut mainland (Jackson and Taylor, 1972; Jackson, 2000; Johns and Young, 2006; Sandborn-Barrie et al., 2014). The correlation relies principally on the BIF-komatiite-quartzite sequence observed in all three groups. Wodicka et al. (2011) identified 2970-2968 Ma rhyolites within the Prince Albert Hills showing the correlation maybe more complex.

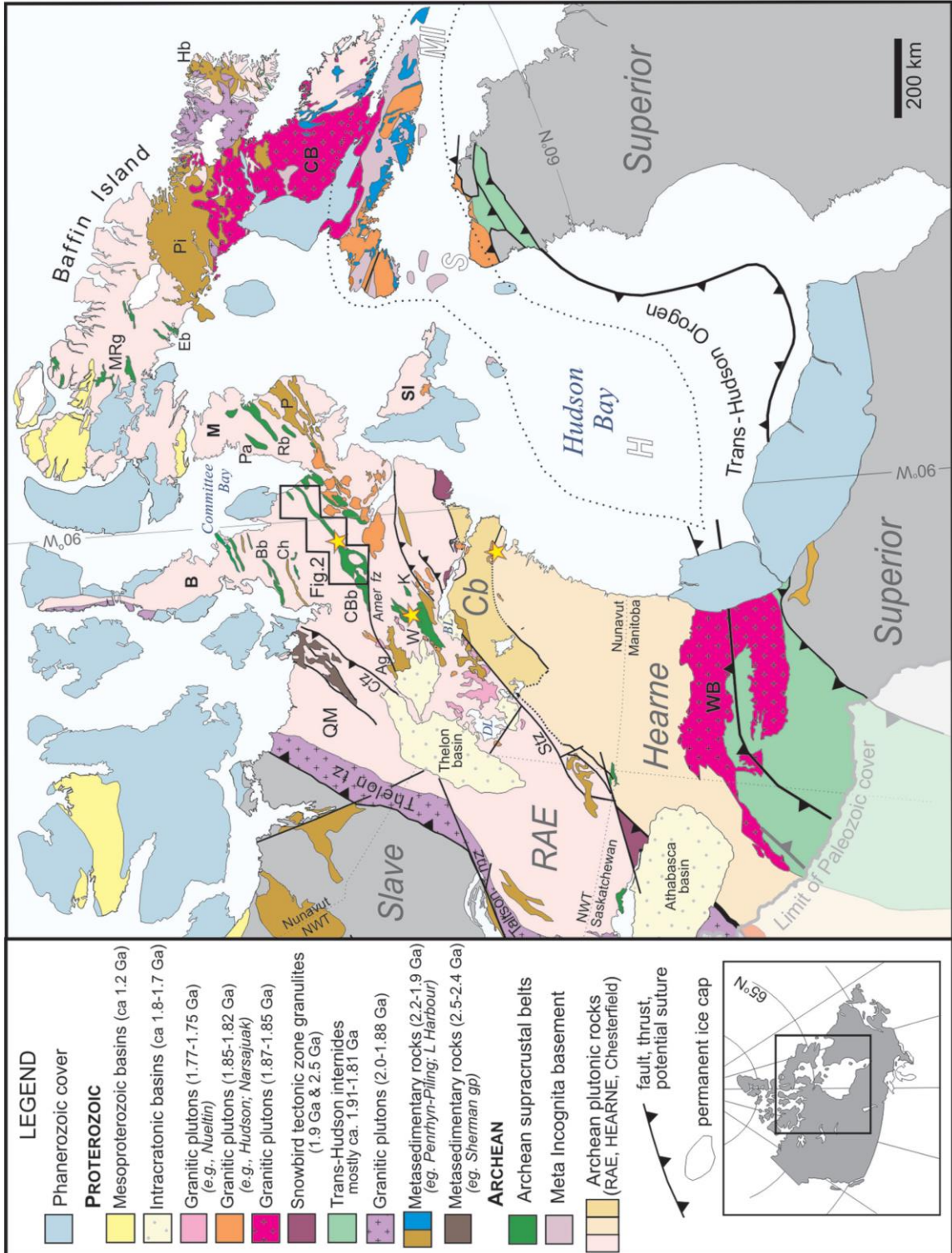


Figure 1-3 Regional tectonic map of the Churchill Province and domains (Sandborn-Barrie et al., 2014).

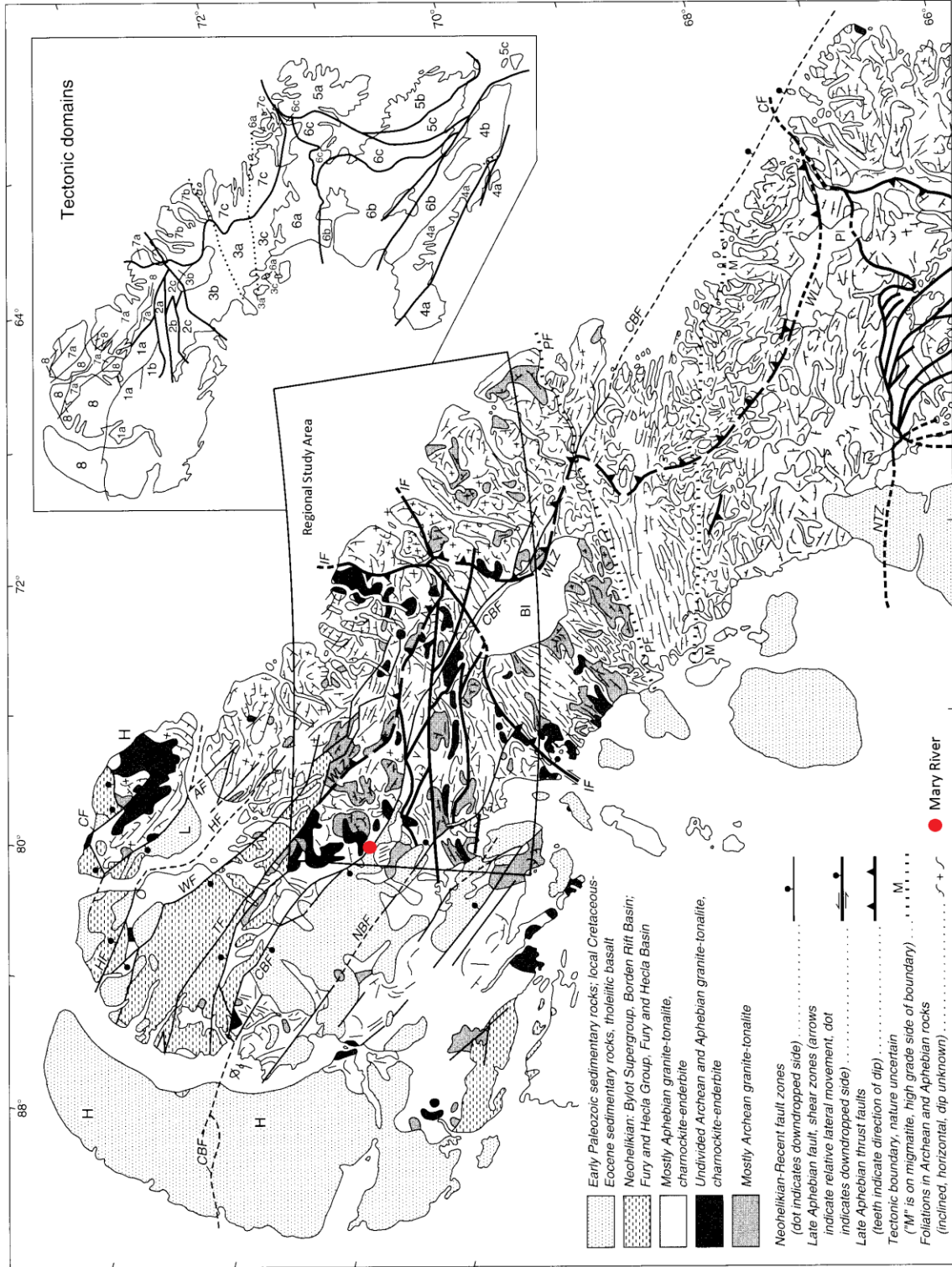


Figure 1-4 Map of Baffin Island tectonic domains (Jackson, 2000). Regional Jackson study area outline with the Mary River property represented by red dot.

1.5 Mary River Area Lithologies

The following subsections provide a description and characterization of major lithologies within the MRG and underlying basement complex. Extent, composition and mineralogy of mapped units are presented at both a regional and property scale from map sheets 37G and Deposits No.1-5. Regional aspects are modified by property scale work of MacLeod (2012). A cropped regional map of the 37G area with legend is provided in Figures 1-5 and 1-6.

1.5.1 Basement Complex

The MRG basement complex contains three defined units, foliated monzogranite and diorite (Agn), nebulitic granite migmatite (Amn) and metamorphosed monzogranite-granodiorite (gr-Agr) (Jackson et al. 1990; Jackson, 1966, 1969, 2000). Foliated monzogranites are mapped on the most western portion of NTS map sheet 37G on the eastern margin of the Central Borden Fault zone (CBFZ) extending into the Clyde-Cockburn area. Agn units are deformed foliated pinkish grey granitic plutons composed of quartz, oligoclase and andesine with minor felsic volcanics and phenocrysts (Jackson, 2000). Nebulitic granite migmatites are concentrated in northern extent of the 37G map sheet and occupy much the Clyde-Cockburn area. Amn rocks are chiefly plagioclase, K-feldspar and lesser quartz-bearing poly-deformed gneisses-granites or migmatites (Jackson, 2000). Units classified as gr-Agr are monzogranites or granodiorites and cover 15% of the 37G map area. Four rock types are distinguished within the gr-Agr; pink syenogranites, pink porphyritic monzogranites, foliated granodiorite and migmatitic (Jackson, 2000). Granodiorite compositions are the dominate type in the 37G area (Jackson, 2000). Mapped basement gneiss and associated intrusive units in the Deposit No.1-5 area were re-classified by fabric and texture into gneiss dome core, dome margins augen-gneiss sheets. This dome and keel framework is later discussed in the tectonic framework section.



Figure 1-5 Legend for regional geology map (Figure 1-6). Edited from Jackson et al. (1978).

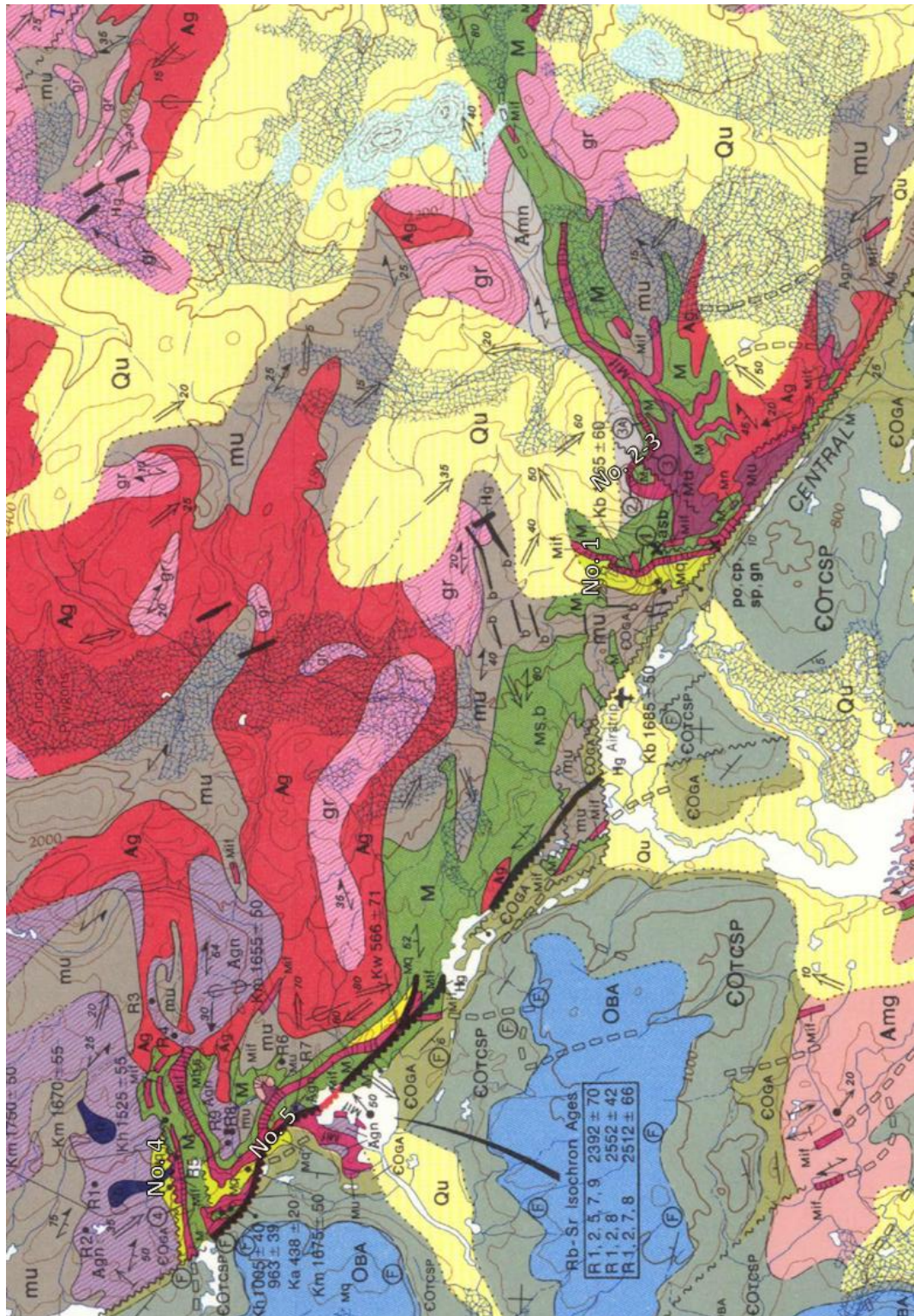


Figure 1-6 Regional geology map of Deposits No.1-5. Edited from Jackson et al. (1978).

1.5.2 MRG Metasediment and Quartzite

Metasediments are the lowest segment of MRG supracrustals and are separated into a lower unit (metapelite-amphibolite) and upper unit (Ms). The lower unit is divided into two members by Jackson (2000); (1) basal metaconglomerates (0-45 m thick) with interbedded metapelites, metamafics and ultramafic volcanics and (2) metapelites with lenses of pebble conglomerate. The basal member is observed at foot of Deposit No.1 containing oligomitic metaconglomerates roughly 10 metres in thickness with mild lineations (Jackson, 2000). Conglomerate lenses exist at the base of Deposit No.4 as well (Jackson, 2000). The upper member is a 0-122 metre thick metapelitic unit consisting of paragneisses, and lit-par-lit migmatite containing porphyroblasts of cordierite, staurolite, andalusite, sillimanite (Jackson, 2000). Upper metasediments (Ms) are gneisses and schists of metasilstone and greywacke composition (Jackson, 2000). Property scale mapping reclassified metasediments as amphibolitic-wacke ranging between psammite to calc-silicate (MacLeod, 2012). Amphibolitic-wacke reported similar minerals to Jackson's metapelite-amphibolite with the exception of sillimanite and andalusite. Aluminous schist and paragneiss containing an andalusite-staurolite-garnet metamorphic mineral assemblage are separated from the upper Ms unit and mapped wrapping around the footwall of Deposit No.1 and pump station 2 site (PS-2) (Nicpon, 2011; MacLeod, 2012; Herbranson, 2013).

Quartzites are regionally identified but most prominent in the Deposit No.4 and No.5 area and differentiated into two members (Jackson, 2000; Young et al., 2004; Johns and Young, 2006). The lower member is composed of rodded quartz-feldspar mica schists up to 460 metres thick and closely associated with iron formation at the base of Deposits No.1-3 (Jackson, 1966, 1969, 2000; MacLeod, 2012). The upper member is a quartz rich (>90%) lithology 0-130 metres thick (Jackson, 2000). The member is massive, lacks sedimentary features and shows strong lineations (Jackson, 2000). Property scale mapping by Jackson (1966) and MacLeod (2012) incorporated both members into a single unit.

1.5.3 MRG Iron Formation

Iron formation is the most diagnostic lithology in the MRG. Four facies are present and were first defined by the works Gross (1966) and Jackson (1966, 2000) and remapped by MacLeod (2012). Several terms exist to describe various iron formation oxide facie states and types; banded iron formation (BIF), enriched banded iron formation (EBIF), magnetite ore (MO), magnetite-hematite ore (MHO) and hematite ore (HO). Banded iron formation is composed of millimetre to centimetre thick bands of alternating silica and magnetite with minor hematite. BIF contains less than 50% total iron content. EBIF is banded iron formation that has undergone physical and chemical changes. These changes are identified texturally as brecciation, iron oxide veining and dissolution of silica bands. Total iron content is between 50% and 60%. Iron ores are defined by having a total iron content of 60% or more and further divided by the principal iron oxide mineral. Magnetite ores contain 75% or more magnetite and have the highest grades (total Fe). Magnetite-hematite ores contain a split amount of magnetite and hematite (26-74%). Hematite ores are composed of more than 75% hematite. The term high grade iron formation (HGIF) is generalization term for mapping and incorporates EBIF and any of the iron ores. This term is useful as all iron ore bodies have lenses of EBIF and various ore types. Table 1-1 lists the various iron formation types and there corresponding mineralogy and total iron content. Table 1.2 displays tonnage and mineralogy of historic Deposits No.1-3.

		Mineral Abundance		
Iron Formation Types		Magnetite	Hematite	Total Fe
HGIF	Banded Iron Formation	50-100%	50-100%	20-49%
	Enriched Banded Iron Formation	50-100%	10-50%	50-60%
	Magnetite Ore	75-100%	0-25%	60-72%
	Magnetite-Hematite Ore	26-74%	26-74%	60-69%
	Hematite Ore	0-25%	26-74%	60-69%

Table 1-1 MRG iron formation types with normalized iron oxide mineral abundance and corresponding iron content.

Deposit	Measured		Indicated		Inferred	
	Grade	Tonnage (Mt)	Grade	Tonnage (Mt)	Grade	Tonnage (Mt)
No.1	66.3	418	-	-	66.9	213
No.2 & 3	-	-	65	26	65.9	336

Table 1-2 Grade and tonnage of historic Deposits No.1-3

The oxide facies are the most dominant and include BIF and HGIF. BIF, regionally and at Deposits No.1-5, is composed of millimetre to centimetre thick laminae-bands of alternating silica and magnetite with minor hematite forming tabular bodies, 50-90 metres thick that strike 1-5 kilometres (Gross, 1966; Jackson, 2000). Deposit No.1 BIF displays centimetre thick bands of magnetite and silica transitioning out of HGIF in the northern limb (Figure 1.7). HGIF formation ranges between 50-150 metre thick tabular bodies with 2-5 km strike lengths. HGIF hosts iron ore is composed of compact granoblastic magnetite-martite to vuggy microplaty hematite with impurities of chlorite, cummingtonite-grunerite and silica (Gross, 1966; Jackson, 2000; MacLeod, 2012). Chlorite-mica schists envelope and interleave iron ore and EBIF. Varieties of porphyroblasts occur in chlorite-mica schists including almandine, staurolite, cummingtonite-grunerite and tourmaline (Fulcher, 2011; Nicpon, 2011; MacLeod, 2012).

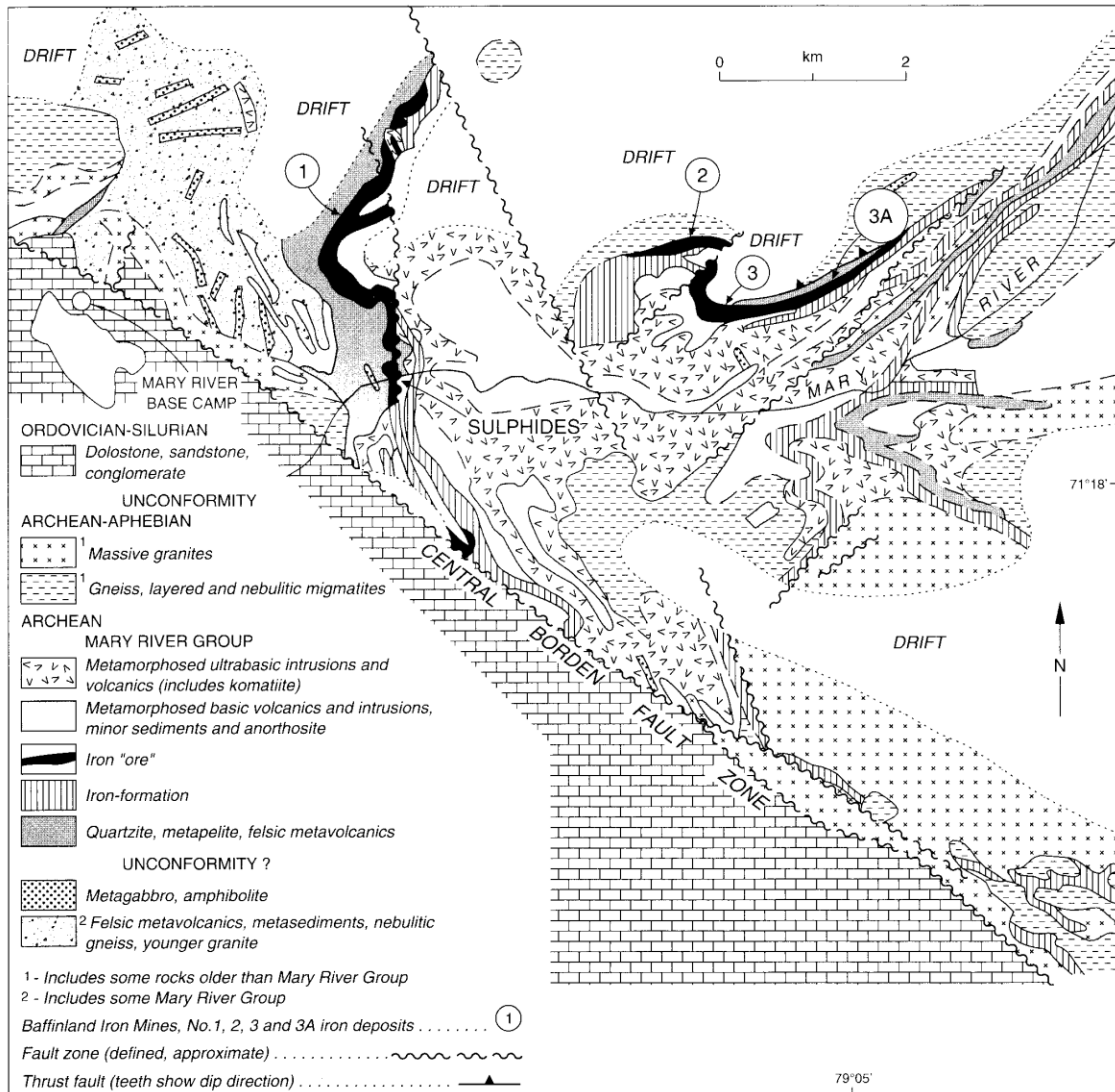


Figure 1-7 Geology map of deposits No.1-3 (Jackson, 2000).

Silicate facies banded iron formation is second to oxide in thickness and distribution. Mapping by Jackson (1966), masks the fact that silicate and oxide facies transition into each other and are virtually impossible to segregate (Deposit No.4). Silicate facies BIF thicknesses ranges from 58-112 metres (Jackson, 2000). Commonly, 1-5 cm straw to white colour grabenschiefer grunerite-cummingtonite overgrow a chloritic matrix hosting millimetre euhedral magnetite porphyroblasts (Jackson, 2000; Fulcher, 2011; MacLeod, 2012).

Aluminous facies occur as a minor stratigraphic unit displaying thin laminations or thin beds hosting a quartz-cordierite-anthophyllite-garnet-biotite assemblage (Jackson, 2000). Sulphide facies are found generally within oxide facies or within silicate or aluminous facies (Jackson, 2000). Sulphide facies form 1.5 metre thick discontinuous beds containing quartz, magnetite, pyrite and or pyrrhotite (Jackson, 2000). Abundant sulphides occur in BIF along the northern limb at Deposit No.1. Carbonate facies is rare and considered the least preserved. Jackson (2000) only identifies two localities southwest of Deposit No.4 of centimetre to 2 meter thick beds containing siderite with magnetite (MacLeod, 2012). Carbonate in these beds is generally replaced by tremolite-actinolite, hornblende and pyroxenes (Jackson, 2000; MacLeod, 2012).

1.5.4 MRG Volcanics

Regionally, the MRG contains felsic to mafic volcanics above and below iron formation with no lateral or spatial correlation to other MRG localities (Jackson, 2000). Felsic volcanics are categorized as rhyolite, quartz latite and dacite (Jackson, 2000). Blastoporphyritic textures and are commonly identified in eastern mapped metavolcanic-intrusives (Jackson, 2000). Dacitic tuff was identified by Young et al. (2004) surrounding the Deposit No.4 and No.5 banded iron formation. BIMC, Fulcher (2011) and MacLeod (2012) have never observed felsic volcanics from mapping or drilling at Deposit No.4 or No.5.

Mafic and ultramafic volcanics are amphibolitized to hornblende and grunerite-cummingtonite species and are classified as amphibolites to amphibolitic-basalts and metakomatiites (MacLeod, 2012). Pillow structures are uncommonly preserved with exceptions of a variolitic pillow sequence at Turner River (Campbell, 2012). Amphibolites (orthoamphibolites) contain clinopyroxene replaced by hornblende with cusped epidote features resembling pillow structures at Deposit No.4 (Fulcher, 2011; MacLeod, 2012). Basal amphibolites and metakomatiites in the Deposit No.1-3 map area are the most abundant and associated with high grade iron formation (Jackson, 2000; MacLeod, 2012). Metakomatiites along the CBFZ and strongly serpentinize and outcrop at the base of Deposit No.1, the PS-2 site and at the quere fold of Deposit No.5

(MacLeod, 2012; Herbranson, 2013). MacLeod (2012) noticed arguable quenched flow tops in metakomatiites.

1.5.5 MRG Intrusives (Neoproterozoic)

Gabbro (Mg, AMb), anorthosite-gabbro (Mn), and porphyritic monzogranite-granodiorite (Agp) are common in the 37G map sheet. Gabbros (Mg) are metamorphosed dikes and sills 300 metres or less in size intruding basement gneisses and quartz monzonites. Gabbros are also observed as 6-10 metre lenses in Deposit No.5 folded (?) meta-sediment and at Deposit No. 3. Several generations of gabbro may be present as gabbro intrudes upper level intrusives younger than the MRG and as no geochronological data exists (Jackson, 2000). Anorthosite-gabbros are a minor map component in the 37G area occurring as 3-60 metre thick sill-like bodies generally holding lineated plagioclase blastophenocrysts and mafic-hornblende amphibolite margins (Jackson, 2000). Monzogranite-granodiorites mainly occupy a 700 km² northwest area of the 37G map sheet. The intrusions contain quartz, plagioclase and phenocrysts of perthitic microcline and are dated to 2709 ±4/-3 Ma. Monzogranite-granodiorite are interpreted to be late plutonism of the MRG (Jackson, 2000).

1.5.6 Tectonostratigraphic Framework of the MRG

Stratigraphic relationships and correlations are perplexing within the MRG resulting from complete lack of younging directions. The lack of younging directions is due to three to four deformation events culminating into three fold generations as described by Young et al. (2004). These are best preserved at Deposit No.4-5. The first deformational event (D₁) folds S₁ foliations intrafolial to F₁, generally seen as transposed D₁/D₂ (Young et al., 2004). The second stage of deformation (D₂) defines the keels of the MRG as a southeast-dipping and south-plunging reclined folds folding S₁ in the hinge zones of F₂ (Young et al., 2004). D₃ produces the regional structures as F₃ folds such as the McQuat synform at the Deposit No.4-5 area and represent THO overprinting (MacLeod and Duke, 2009b). Structural mapping of Deposit No.1 also confirms this polyphase folding, resulting in an egg crate regional pattern and the anticlinal form of Deposit No.1 (Lindberg, 2010, 2011).

Property scale mapping has invoked a gneiss dome and keel structural framework with three structural zones; dome cores, augen gneiss sheets and dome-keel margins (MacLeod and Duke, 2009 a, b). Dome cores are mixed mafic-felsic gneisses with nebulitic migmatite displaying polydeformed flow folding structures (MacLeod and Duke, 2009 a, b). Flow-folded gneiss transitions into straight gneiss pannels of augen gneisses. Augen gneisses become mylonitic augen schists at MRG keel boundaries (MacLeod and Duke, 2009 a, b) .

Jackson (2000) contains the most complete regional stratigraphic data set. This data set is compiled and illustrated in Figure 1.8 and compared to MacLeod (2012). From the basement up, augen schists, quartzite, paragneiss and metasediment appear in contact. Paragneisses are tectonically emplaced above metasediments and volcanics by both authors. HGIF sharply contacts basal schists and hosts interleaved schist units. A garnetiferous-amphibole-biotite-chlorite schist envelopes HGIF (chloritized lower metasediments). The contact zone to HGIF is marked by a biotite and chlorite overprint with porphyroblasts of almandine, staurolite, cummingtonite-grunerite and lesser tourmaline. Felsic volcanics sandwich iron formation but lack continuity and disappear into metasediments (Jackson, 2000). Amphibolitic basalts and metakomatiites are juxtapose to iron formation and show semigradational contacts.

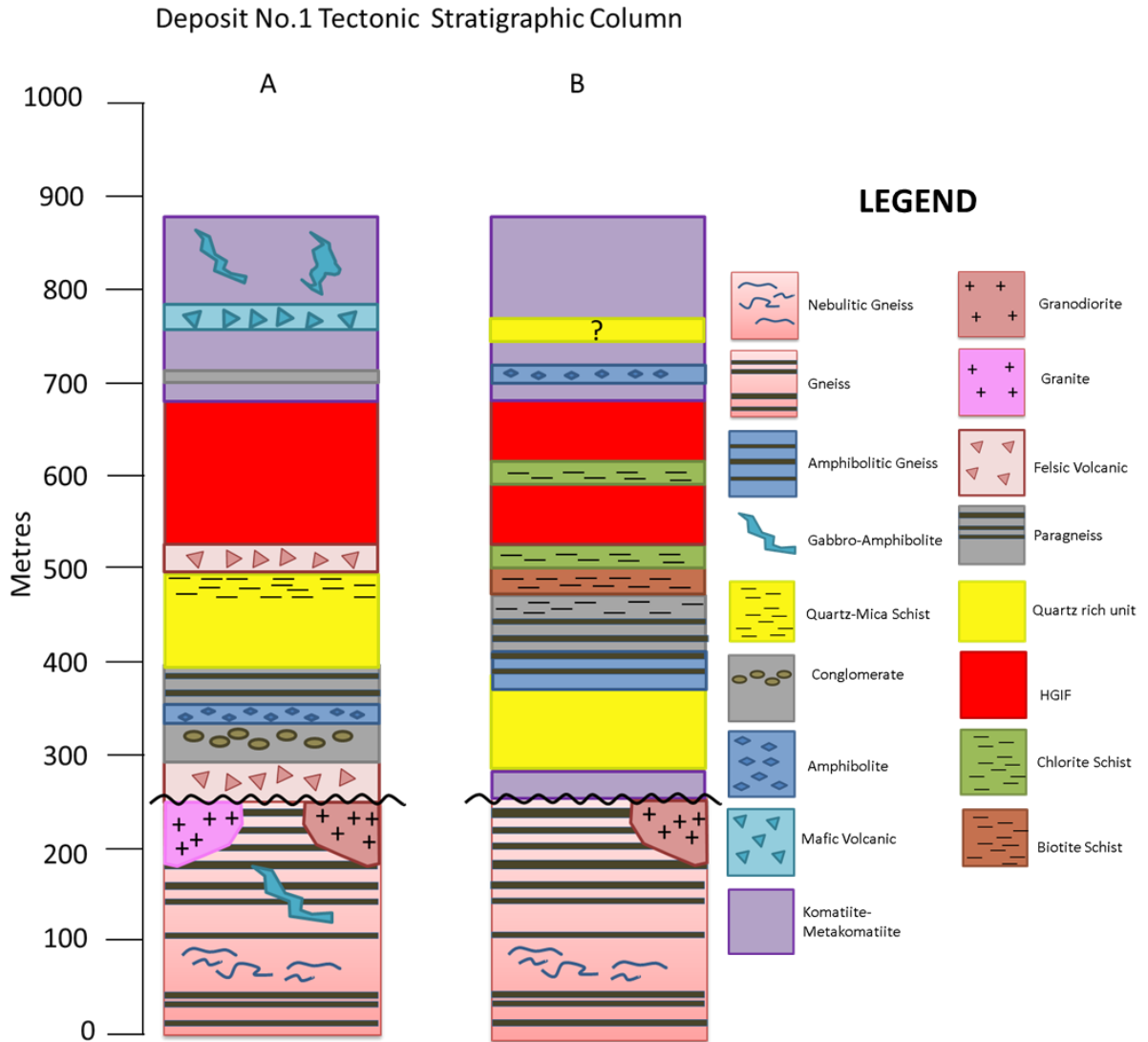


Figure 1-8 Deposit No.1 stratigraphic columns. Column A is depiction units defined by Jackson (1966, 2000). Column B is the MacLeod (2012) interpretation with regionally plotted upper quartzite (?).

1.6 Regional Geochronology

The MRG is geochronologically constrained at a reconnaissance scale at best by U-Pb zircon crystallization ages and few monazite ages from the 37G and Ege Bay area (Figure 1-9). Table 1-3 lists all the discussed ages. Zircons within foliated basement tonalities (gr-Agr) in the 37G map area contained a $^{207}\text{Pb}/^{206}\text{Pb}$ age of $2851 \pm 20 / -17$ Ma and define the upper limit of the MRG basement complex (Jackson et al., 1990). U-Pb ages from small euhedral zircon in dacitic tuff at the Wishbone area (37G) yielded $2718 \pm 5 / -3$ Ma

(Jackson et al., 1990; Jackson, 2000). Other dacites collected by Jackson yielded dates ranging between 2710-2705 Ma (Jackson et al., 1990). Morgan (1982) analyzed zircons from felsic metavolcanics hosting ages of 2752 ± 30 Ma and 2888 ± 35 Ma from outcrops 8 km apart in Ege Bay (Jackson, 2000). The older age is not considered definitive as a 2742 Ma age comprises four points of the two ages and re-analysis from the same sample obtained 2723 ± 1 Ma and 2728 ± 5 Ma values (Bethune and Scammell, 2003b). A more thorough study of the Ege Bay area, completed by Bethune and Scammell (2003b), brackets the area's basement gneiss complex between 3000-2800 Ma with orthogneiss intrusions between 2780-2770 Ma. Intermediate to felsic volcanics in Ege Bay were constrained to 2740-2725 Ma and were terminated by late felsic plutons (Bethune and Scammell, 2003b).

Bulk rock Rb-Sr, Nd-Sm and mineral K-Ar techniques have also been applied regionally within the MRG. Rb-Sr bulk rock analyses from foliated-nebulitic granites produced isochron ages between 2476 ± 72 and 2642 ± 43 Ma from the Deposit No.4 area (Wanless and Loveridge, 1978). Rb-Sr ages of basement gneisses and granites do not retain a Mesoarchean age defined by U-Pb zircon geochronology.

Modeled T Nd/CHUR ages from composite samples by McCulloch and Wasserburg (1978) gave a 2740 ± 50 to 2560 ± 30 Ga age. An older 3670 Ma Nd depleted mantle model age was obtained from nebulitic granite-migmatite, setting the lower age boundary of the basement complex (Hegner and Jackson, 1990; Jackson, 2000). Nd-Sm contrasts Rb-Sr dating by retaining older ages. K-Ar ages, obtained from Archean igneous and sedimentary mica schists, were 1750 Ma from muscovite and 1610 Ma from biotite (Jackson, 1966). K-Ar ages from Deposit No.1 footwall biotite and muscovite yielded 1865 ± 60 and 1685 ± 50 Ma (Jackson et al., 1978). K-Ar also proved unsuccessful at retaining Precambrian ages but shows a prolonged thermal history (Jackson, 2000).

Map Zone	Stratigraphic Unit	Unit	Age (Ma)	System	Mineral	Source
37 G	Basment	Mica schist-granite	1750	K-Ar	Muscovite	Jackson, 1966
37 G	Basment	Mica schist-granite	1610	K-Ar	Biotite	Jackson, 1966
37 G	Basment	Mica schist-granite	1865 ± 60	K-Ar	Biotite	Jackson et al., 1978
37 G	Basment	Mica schist-granite	1685 ± 50	K-Ar	Muscovite	Jackson et al., 1978
37 G	Basment	Nebulitic Granite	2476 ± 72	Rb-Sr	Whole Rock	Jackson, 1978
37 G	Basment	Nebulitic Granite	2642 ± 43	Rb-Sr	Whole Rock	Jackson, 1978
37 G	Basment	Gneiss Nebulite Gra	2740 ± 5	Sm-Nd	Whole Rock	McCulloch & Wasserburg, 1978
37 G	Basment	Gneiss Nebulite Gra	2560 ± 30	Sm-Nd	Whole Rock	McCulloch & Wasserburg, 1978
37 G	Basment	Nebulite Granite	3670	Sm-Nd	Whole Rock	Hegner & Jackson, 1990
37 G	Basment	Foliated Tonalite	2851+20/-17	U-Pb	Zircon	Jackson et al., 1990
37 G	MRG	Dacitic Tuff	2718+5/-3	U-Pb	Zircon	Jackson et al., 1990
37 G	MRG	Trondhjemite-Tonal	2677-2820	U-Pb	Zircon	Jackson et al., 1991
Eque Bay	Basment	Gneiss	3000-2800	U-Pb	Zircon	Bethune & Scammell, 2003b
Eque Bay	MRG	Metavolcanic	2752 ± 30	U-Pb	Zircon	Morgan, (1982)
Eque Bay	MRG	Metavolcanic	2723 ± 1	U-Pb	Zircon	Bethune & Scammell, 2003b
Eque Bay	MRG	Metavolcanic	2728 ± 5	U-Pb	Zircon	Bethune & Scammell, 2003b
Eque Bay	MRG	Int-Felsic volcanics	2740-2725	U-Pb	Zircon	Bethune & Scammell, 2003b

Table 1-3 Table listing all geochronological data from mineral and bulk rock isotopic analyses.

1.7 Regional Metamorphism

The works of Jackson (1966, 2000) and Jackson and Morgan (1978) have proposed metamorphism to be isochemical with the exceptions CO₂ and H₂O (Jackson, 2000). Metamorphic grade for the region ranges from subgreenschist to granulite facies with signs of anatexis at the margins of basement structural breaks to supracrustals (Jackson and Morgan, 1978). Regional metamorphic facies are plotted in Figure 1-10.

Subgreenschist facies form small lenses of a quartz, biotite, muscovite, chlorite, pumpellyite, prehnite +/- sphene (Jackson and Morgan, 1978; Jackson, 2000). Greenschist facies form discontinuous bands predominantly along the CBFZ in the Deposit No.1-5 area and locally in the Milne Inlet Trough. This facies mineral assemblage comprises chlorite, actinolite, clinozoisite and albite (Jackson and Morgan, 1978). Amphibolite facies is segregated into lower and upper zones. Lower amphibolite facies are interleaved with upper amphibolites and granulites as slender lenses. These report a large assortment of mineral assemblages within metapelites, but commonly quartz, oligoclase (An_{>=16}) muscovite, staurolite, cordierite and andalusite are the main constituents (Jackson and Morgan, 1978; Jackson, 2000) (Table 1-4). Upper amphibolite facies covers most of the area as two zones north of the Barnes Ice Cap and southeast

from the Cumberland Peninsula. The distinction from lower amphibolite facies is marked by the presence of garnet, cordierite and K-feldspar with the absence of staurolite (Jackson and Morgan, 1978; Jackson, 2000). Ultramafic rocks garner a phlogopite, cummingtonite and anthophyllite assemblage at upper amphibolite facies. Granulites in the Dexterity Granulite Belt (DGB) envelope the charnockite-enderbite Dexterity Batholith. The lower boundary is marked by orthopyroxene (hypersthene) with a common quartz, clinopyroxene, almandine-pyrope \pm hornblende and/or biotite, plagioclase and K-feldspar assemblage (Jackson and Morgan, 1978; Jackson, 2000). Locally, both sillimanite and cordierite occur. Pressure and temperature calculations from several geothermo barometers; garnet-biotite, feldspar, garnet- Al_4SiO_5 -quartz and CATS-anorthite-quartz calculated regional amphibolite temperatures between 500-550°C and pressures ranging between 3.8-4.3 kbar (Jackson, 2000). Granulites in the Rowley River area are calculated to a pressure range of 5.9-6 kbar and temperatures between 603-650°C (Jackson, 2000).

Mary River Metamorphic Mineral Assemblages (Metapelite & Greywacke)
Quartz-plagioclase-K feldspar-biotite-muscovite-sillimanite +/- (cordierite, or garnet)
Quartz-plagioclase-K feldspar-biotite-muscovite-cordierite-chlorite
Quartz-plagioclase-biotite-hornblende + (diopside, or k feldspar, or muscovite? and epidote)
Quartz-plagioclase-biotite-muscovite + (sillimanite, or calcite)
Quartz-plagioclase-garnet-cordierite-staurolite-sillimanite
Quartz-beryl-muscovite-andalusite
Quartz-biotite-garnet-magnetite + (muscovite, or muscovite and chlorite, or staurolite, or cordierite)
Quartz-anthophyllite-biotite-cordierite + (sillimanite, or plagioclase and magnetite)
Quartz-biotite-muscovite-cordierite-andalusite + (sillimanite and plagioclase, or kyanite, or sillimanite)
Quartz-biotite-garnet-cordierite-andalusite + (staurolite, or sillimanite and magnetite)
Quartz-biotite-cordierite-sillimanite + (garnet and staurolite, or hornblende)
Quartz-biotite-garnet-(hornblende-actinolite + (calcite and chlorite, or muscovite?))
Garnet-staurolite
Garnet-chlorite-anthophyllite

Table 1-4 Table of metamorphic mineral assemblages from Mary River metapelites and greywackes (Jackson and Morgan, 1978).

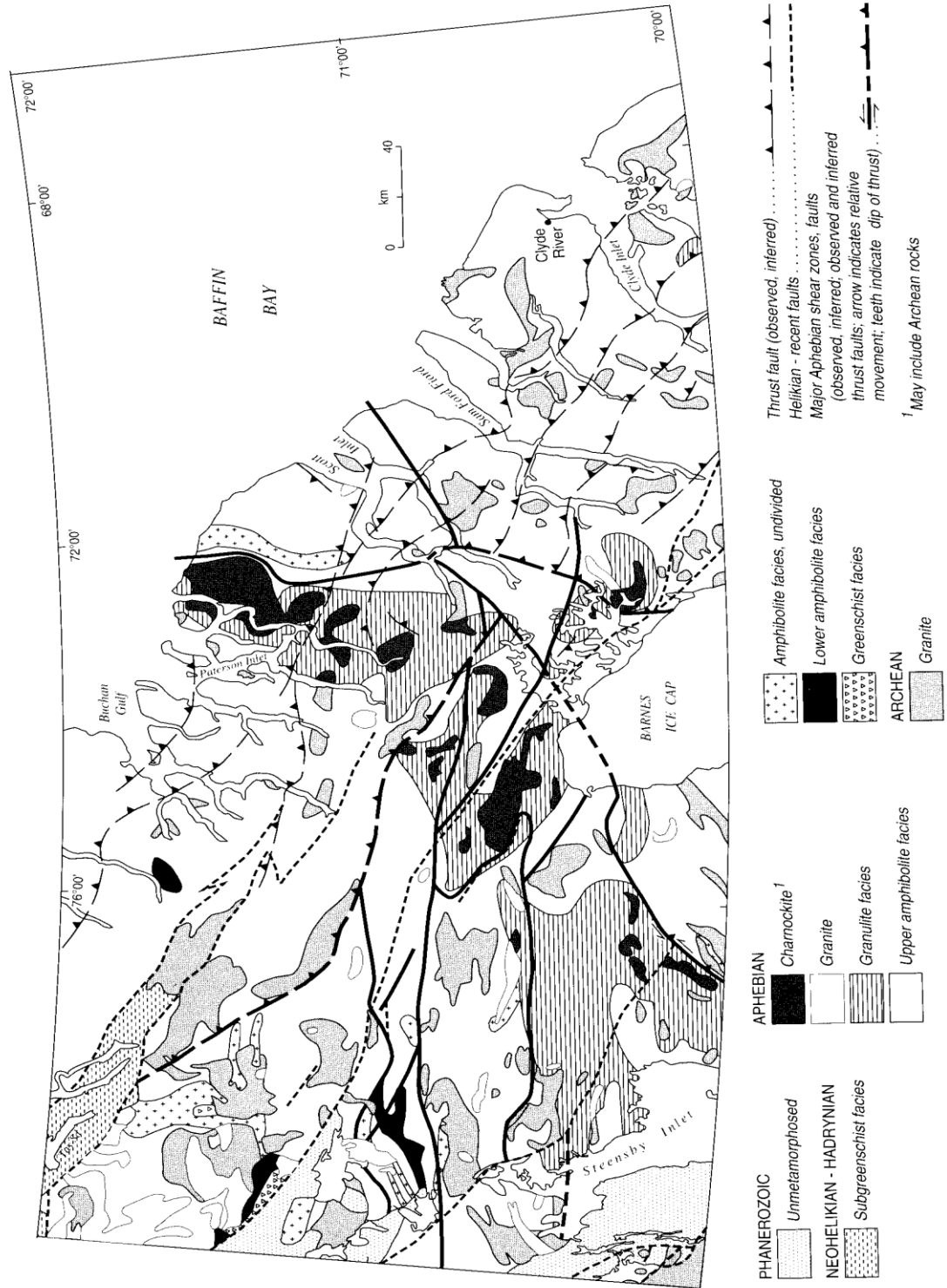


Figure 1-10 Regional metamorphic facies map of the Mary River Group (Jackson, 2000). Metamorphic facies and tectonic divisions depicted.

In the Deposit No.1-5 area, amphibolite, SIF and schist sport a cummingtonite-grunerite, hornblende and ferro-actinolite assemblage with biotite, almandine, clinopyroxene and cordierite; indicating a prograde upper amphibolite facies (MacLeod, 2012). Conversely adjacent orthoamphibolites are overprinted by a lower epidote-amphibolite facies (Fulcher, 2011). Metakomatiites in the Deposit No.4-5 area show wide-spread talc alteration. Aluminous schist at the footwall of Deposit No.1 contains a garnet-cordierite (iolite)-cummingtonite assemblage in a biotite-chlorite matrix. Basal sediments in the same area were observed to have the same assemblage with the additions of kyanite and sillimanite (Jackson, 2000). Interleaved ore zone and bounding schists have prograde garnets overprinting a chloritized biotite schist (Nicpon, 2011).

1.8 Iron Formation Enrichment & Deposit No.1 Geology

Deposit No.1 is the largest and most explored of all the known deposits. HGIF at Deposit No.1 forms a 105-150 metre thick tabular high relief ore body. The Deposit No.1 ore body strikes 2.5 km in length and dips to the east between 68-76°. HGIF is composed of massive magnetite-hematite and localized specularite zones. Brecciated BIF, altered BIF and EBIF lenses and pods occur throughout the iron ore body. Chlorite schist occurs on the footwall boundary with aluminous gneiss-schist and as interleaved units within iron ore. Metasediments, volcanics and ultramafics mapped by Jackson (1966) are designated by Macleod (2012) as greywacke, amphibolite and amphibolitic komatiite extending past the southern limb westward.

The formation of direct shipping ores from BIF has recently been attributed to hydrothermal alteration. Ore textures show granoblastic magnetite overprinted by dendritic veins martite and micro-platy hematite. Specularite veins cross-cutting granoblastic magnetite ore at Deposit No. 4 also support hydrothermal alteration processes (Fulcher, 2011). Other hydrothermal textures observed are magnetite-hematite patches and veins overprinting BIF and pseudobanding in magnetite-hematite ores showing no deformation. In addition, mass chloritization of footwall metasediment-paragneiss followed by prograding Fe-Mg-Mn-Al species is documented and interpreted by Macleod (2012) and Nicpon (2011) as an early hydrothermal alteration episode prior to metamorphism. All of these textures are interpreted as the mobilization of iron and

desilicification of BIF via hydrothermal fluids. A three stage enrichment process proposed by Macleod (2012) entails:

1. Regional Paleoproterozoic Transhudson Orogeny (THO) formed the present dome and keel tectonic architecture dehydrating the colder MRG.
2. Hot silica depleted fluid reaching 400-500 C° ascended and equilibrated with Mg-Fe-Ca proto ore followed by metamorphism and porphyblastic growth of various Fe-Mg (-Ca) amphiboles, spinels and aluminosilicates.
3. A cooling period post thermal peak lowered pH levels and oxidized magnetite to martite and produced the talc, serpentine, sericite and chlorite in iron ore bodies.

1.9 Summary & Hypothesis

Several discrepancies arise from regional and property scale mapping in relation to the MRG's stratigraphy and metamorphic sequence. Some lithologies such as tuffs and conglomerates are disputed. Gneisses are interleaved with lower grade schists and volcanics, encrypting the tectonic-stratigraphy and metamorphic history. As an example, the footwall aluminous schist, supposedly derived from gneiss, is interleaved with HGIF in the southern limb of Deposit No.1, making its association to basement gneiss vague. Stratigraphic positions of corresponding units differ between workers; e.g. the quartzite unit defined as a basal unit to iron formation by Jackson (1966 & 2000) is considered a middle or upper unit by MacLeod (2012). Thrust faults were suggested by MacLeod (2012) to explain the overlapping high grade over low grade stratigraphy, yet no such detachments or textural evidence was presented.

Regional metamorphic boundaries place Deposits No.1-5 within a greenschist facies zone though the mineral assemblages alternatively show amphibolite facies (Fulcher, 2011; MacLeod, 2012). Metamorphic mineral assemblages for metapelites by Jackson and Morgan (1978) provide numerous aluminosilicates that all circle the kyanite-andalusite-sillimanite triple point, yet sillimanite and kyanite are not observed in any drill core logging or previous theses work. The abundances, variance and complexity of metamorphic assemblages within a single unit infers disequilibrium, chemical

heterogeneity or a combination of the three. Multiple P-T paths or the reworking of previously metamorphosed units may be at hand.

The association of garnet-amphibole chlorite and mica schists to HGIF is peculiar, given the complex metamorphic and deformational history of the area. For all HGIFs to have similar footwalls precludes a systematic relationship with the MRG basement complex. Thus, the following hypotheses are proposed for testing at Deposit No.1 in order to review the gneiss dome-keel model previously discussed:

1. Is deformation high strain and extensional at the footwall to HGIF?
2. Does the metamorphic and/or alteration mineral sequence reflect the three different stages proposed?
3. Is the metamorphic mineral paragenesis, if in equilibrium, indicative of similar regional conditions and events?
4. How does geochronology of the footwall units compare to ore zone units?
5. Overall, is direct shipping iron ore a result of chemical and/or physical loss of silica resulting from mass balance changes related to hydrothermal alteration in relation to tectonism?

Chapter 2 Banded Iron Formations & Iron Ore Genesis

2 Introduction

Iron is the fourth most abundant element on earth and has been exploited since the Iron Age around 1100 B.C. Iron deposits over the last three millennia have been mined from ferruginous to Fe-rich chemical sediment known as ironstone and banded iron formation. Iron stones are referred to granular iron formations (GIFs) as they lack banding and contain iron rich sand size grains in a massive to crossbedded texture (Clout and Simonson, 2005). Banded iron formations (BIF), host iron oxides, silicates carbonates and lesser sulphides in alternating compositional segregated laminations or bands. Repetition of these bands gives forth the “banded” texture. James 1954 defined banded iron formation as “chemical sediment typically thin-bedded or laminated, containing 15 percent or more iron of sedimentary origin, commonly but not necessarily containing layers of chert”. Gross (1980) modified the definition to include banding of quartz and carbonate. The definition of banded iron formation adopted in this thesis is modified from Klein’s (2005) definition of banded iron formation as *chemical sediment containing anomalously high iron that is laminated or thinly bedded with silica, lesser carbonate or minor sulphides*.

Banded iron formations are subdivided into Superior-type and Algoma-type, based on age, primary mineralogy and depositional environment (Gross, 1995). These subdivisions have been challenged by Trendall (1968) and Gole and Klein (1981). They advised banded iron formations be classified by age groups; Archean, Proterozoic and Phanerozoic. Defining iron formation solely on age obscures genetic relationships and so the initial Algoma-Superior type classifications are used herein. Also, Algoma and Superior-type iron formations are synonyms for Archean and Proterozoic iron formations.

The following chapter reviews and depicts banded iron formation’s geographic-temporal distribution, chemistry, mineralogy, and origins. Sedimentary facies, metamorphism and the enrichment processes forming direct shipping iron ores are also

reviewed. The focus is on Algoma-type iron formations as Gross (1966) classified the Mary River banded iron formation as such.

2.1 Spatial and Temporal Distribution of BIF

The occurrence of BIF is episodic throughout the geological record, not abiding fully to the law of uniformitarianism, restricted to mainly the Archean and Paleoproterozoic periods (Figure 2-1). The depositional era of banded iron formations is largely constrained between 3.5-1.8 Ga (Klein, 2005) with the oldest being the 3760 ± 70 Ma BIF at Isua, Greenland (Moorbath et al., 1975). New Sm/Nd bulk rock ages from the Nuvvuagittuq greenstone belt suggest banded iron formation maybe deposited as early as 4300 Ma (O'Neil et al., 2012). Iron formation deposition worldwide increased gradually from the Eoarchean into the Mesoarchean. Worldwide deposition peaked at the beginning of the Paleoproterozoic at 2200 Ma and rapidly declined through the late Mesoproterozoic before reappearing in the Neoproterozoic. Late Rapitan-type BIFs occur in the late Neoproterozoic and early Phanerozoic but terminate completely to present day (James, 1983). The idea of terminal BIF deposition is challenged by layered Fe-hydroxide sediment forming alternating compositional bands, similar to Algoma-type BIF, in small brine pools along the Red Sea rift basin (Laurila et al., 2014).

Algoma-type iron formations were deposited within 3800-2650 Ma volcanic sedimentary sequences known as greenstone belts on virtually every continent (Gross, 1965; Moorbath et al., 1973; James, 1983; Klein, 2005) (Figure 2-2). Major Algoma-type banded iron formations occur within the South African Barberton greenstone belt, Michopitcoen area of Ontario, Canada and the Yilgarn block of Western Australia. Superior-type iron formations are Paleoproterozoic in age ranging between 2.5-1.9 Ga (James, 1983) and comprise the largest iron deposits on earth. Major Superior-type districts are the Lake Superior region of North America, the Labrador Trough of Canada, the Minas Gerais of Brazil and the Australian Hamersley Basin (Figure 2-2).

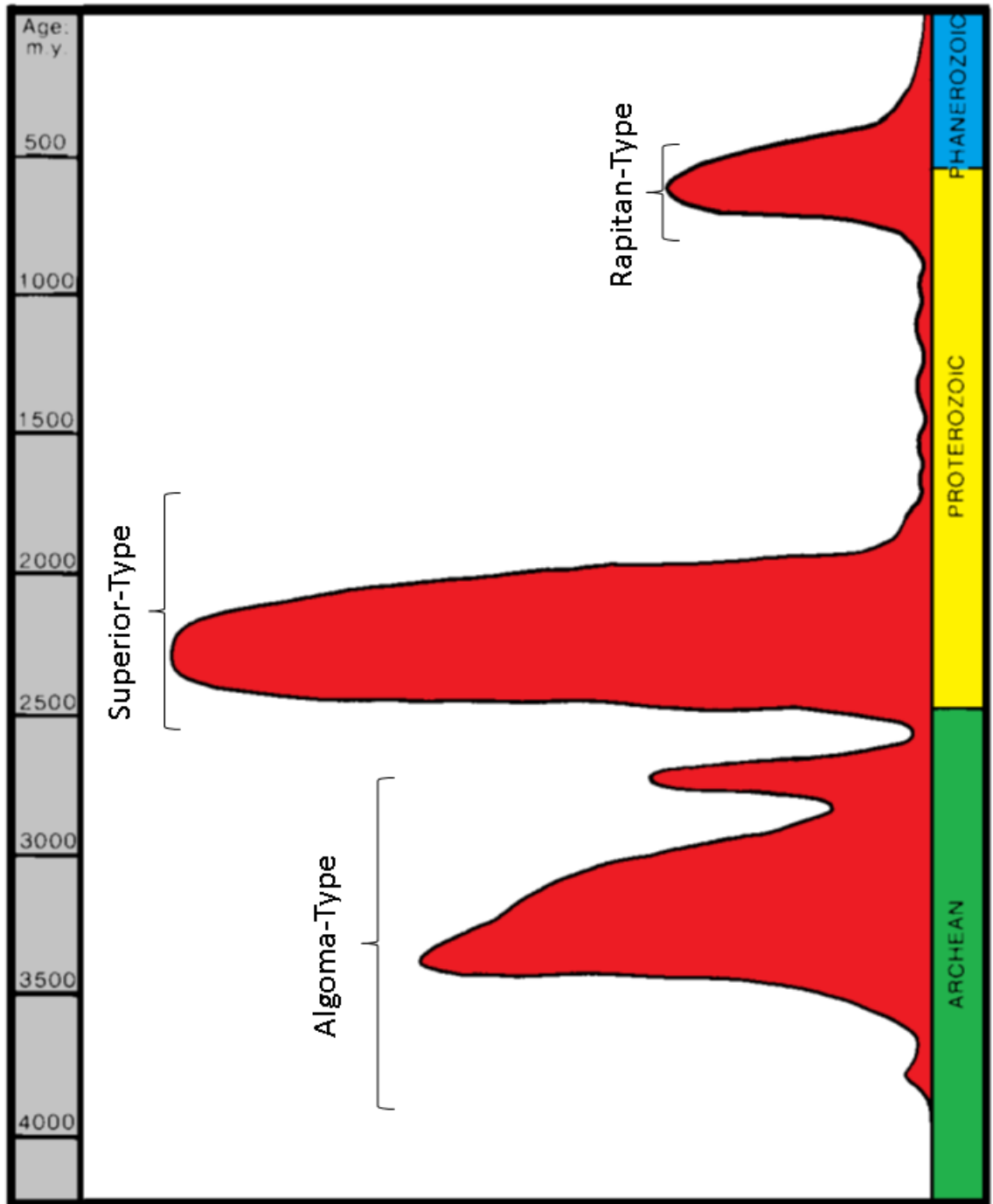


Figure 2-1 Frequency timeline of banded iron formation deposition worldwide with type classes labeled.

Modified from James (1983).

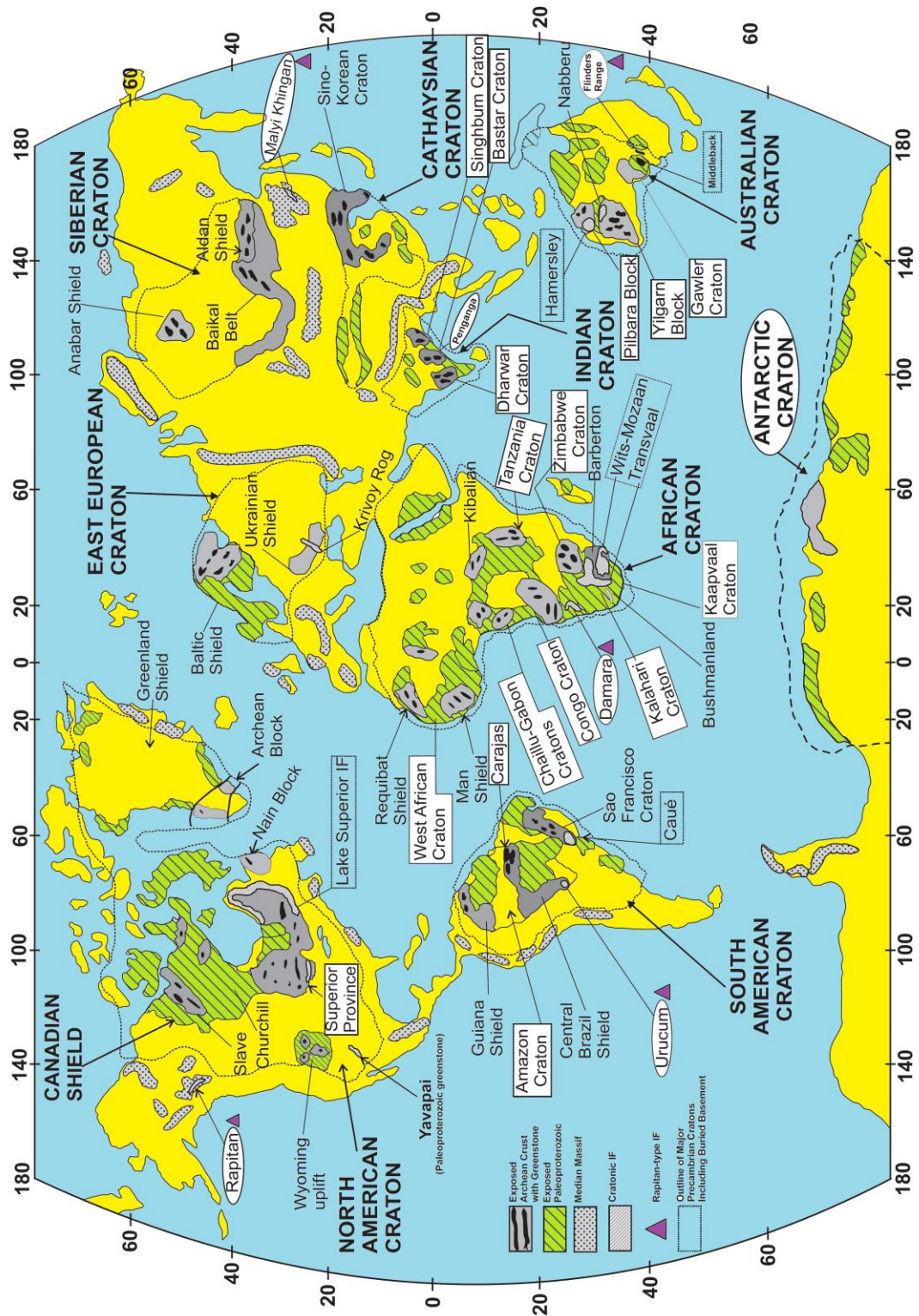


Figure 2-2 World map showing Archean, Proterozoic, and massif cratonic exposures. Iron formations hosted within cratonic blocks are labeled. Modified from Beukes and Gutzmer (2008).

2.2 BIF Mineralogy, Texture & Chemistry

The primary mineralogy of banded iron formations is constrained to iron oxides, hydrous iron-magnesium silicates, iron-magnesium carbonates and pyrite. Chemical formulas with ranges and associated facies are listed in Table 2-1. Unaltered BIF is predominantly fine grained magnetite and hematite (Clout and Simonson, 2005; Klein, 2005). Varieties of hematite may also be present including psuedomorphitic martite after magnetite and platy specularite in altered BIF zones. Hydrous iron-magnesium silicates are the primary-diagenetic minerals deposited alongside iron oxides. Iron-magnesium carbonates are also chemical precipitants. Pyrite and lesser pyrrhotite are the major sulphides observed in BIF.

The characteristic banding texture maybe classified as either micro (.1-1.7 cm), meso (1-2 cm) or macro (>2 cm), modified from Trendall and Blockley (1970). Archean iron formations consist of alternating compositional bands (micro-mesobanding) of iron oxides, chert, lesser carbonate and minor sulphides (Gross, 1965, 1995). Globules, similar to oolites in GIFs, are rare in Algoma-type BIFs. They lack the concentric zoning found in GIFs and are identified to be loadclasts (Gross, 1972). Superior-type iron formations exhibit similar banding but can transition abruptly into oolitic iron stones (Clout and Simonson, 2005). The banding nature of Superior-types ranges from micro to macrobanding, but typically are meso to macro banded (Trendall, 1968; Trendall and Blockley, 1970). Total thicknesses of Algoma-type iron formations span 10 to 100 metres and rarely exceed 100 metres (Gross, 1965). In contrast, Superior type iron formations are known to exceed 700 metres regularly. The lateral extent of each type also differs. Algoma-type BIFs are usually tens of kilometres or less in length while Superior-type BIFs may extend for hundreds of kilometres.

Mineral	Chemical Formula	Compositional Range	Facies
Chert	SiO ₂	None	Oxide/Sulphide/Silicate/Carbonate
Magnetite	Fe ₃ O ₄	None	Oxide
Hematite	Fe ₂ O ₃	None	Oxide
Pyrite	FeS ₂	None	Sulphide
Greenalite	Fe ₆ ²⁺ Si ₄ O ₁₀ (OH) ₈	(Fe _{4.0} Mg _{1.0} to Fe _{5.3} Mg _{0.2})Al _{0.2} Si ₄ O ₁₀ (OH) ₈	Silicate
Stilpnomelane	(Fe, Mg, Al) _{2.7} (Si, Al) ₄ (O, OH) ₁₂ xH ₂ O with traces of K, Na, Ca	(Fe _{1.3} Mg _{1.5} Al _{0.1}) (Si _{3.7} Al _{0.3}) to (Fe _{2.5} Mg _{0.2}) (Si _{3.6} Al _{0.3}) with K 0.1 to 0.2 and Na 0.05 per formula unit	Silicate
Minnesotaite	Fe ₃ ²⁺ Si ₄ O ₁₀ (OH) ₂	Mg _{1.7} Fe _{1.3} to Fe _{2.8} Mg _{0.2} Si ₄ O ₁₀ (OH) ₂	Silicate
Chamosite	(Fe ²⁺ , Al) ₆ (Si, Al) ₄ O ₁₀ (OH) ₈	(Fe _{3.3} Mg _{1.3} Al _{1.3}) (Si _{3.0} Al _{1.0}) to (Fe _{3.8} Mg _{1.3} Al _{0.9}) (Si _{2.8} Al _{1.2})O ₁₀ (OH) ₈	Silicate
Ripidolite	(Fe ₂₊ , Mg, Al) ₁₂ (Si, Al) ₈ O ₂₀ (OH) ₁₆	(Fe _{5.5} Mg _{4.3} Al _{2.3}) (Si _{5.4} Al _{2.6})O ₂₀ (OH) ₁₆	Silicate
Riebeckite	Na ₂ (Fe ²⁺ , Mg) ₃ Fe ₂ ³⁺ Si ₈ O ₂₂ (OH) ₂	Fe ²⁺ /(Fe ²⁺ +Mg) ranges from 0.64 to 0.86	Silicate
Ferri-annite	K ₂ (Mg, Fe) ₆ Fe ₂ ³⁺ Si ₆ O ₂₂ (OH) ₄	Fe ²⁺ /(Fe ²⁺ +Mg) ranges from 0.50 to 0.71	Carbonate
Siderite	FeCO ₃	(Mg _{0.3} Mn _{0.1} Fe _{0.6}) to (Mg _{0.2} Mn _{0.2} Fe _{0.6}) CO ₃	Carbonate
Dolomite-Ankerite	CaMg <-> CaFe(CO ₃) ₂	Ca _{1.0} (Mg _{0.8} Fe _{0.1} Mn _{0.1}) to Ca _{1.0} (Mg _{0.5} Fe _{0.2} Mn _{0.3}) to Ca _{1.0} (Mg _{0.4} Fe _{0.6}) (CO ₃) ₂	Carbonate
Calcite	CaCO ₃	Ca _{0.9} (Fe, Mg, Mn) _{0.1} CO ₃	Carbonate

Table 2-1 List of BIF mineralogy common in all banded iron formation types modified from Klein (2005).

BIF geochemistry is subject to erratic changes due to its banding nature. Finer scale banding, indicating a different depositional facies and chemistry, maybe interleaved with coarser banding (Davy, 1983). Chemical changes of BIF are observed locally on a decimetres scale. As an example, detail examination of drill core samples taken from the same meso band layer, in the Dales Gorge Member of the Hamersley Basin, show small carbonate and silicate lenses within oxide BIF banding (Davy, 1983). Lateral chemical variance (Fe, Mg, Mn) is also common and described in the Mesabi Range (Davy, 1983). However texturally, single bands and lithofacies can be traced for kilometers. BIFs commonly contains 25-45% total iron oxide content (Cloud, 1983). Silica oxide and total iron oxide values can range significantly within a single formation, as much as 35-96% Fe₂O₃ in the Väyrylänkylä area, Finland (Laajoki and Saikkonen, 1977). Regional analyses of the Hamersley Basin banded iron formation is more uniform and less variant with differences of 8.65% SiO₂ and 13.47% Fe₂O₃ content (Davy, 1983). Lower variance of regional analyses supports a more homogenous depositional

environment. Trace element chemistry of iron formations around the world shows low abundances and variation among silicate, oxide and carbonate facies (Davy, 1983; Gross, 1995). Rare earth element concentrations in Archean iron formations are depleted compared to crustal sources and display a mild positive Eu anomaly (Fryer, 1983). Proterozoic iron formations also contain lower abundances of rare earth elements compared to crustal sources and are Ce depleted (Fryer, 1983).

2.3 Banded Iron Formation Facies

Both Superior and Algoma-type BIFs are comprised of marine sedimentary facies defined by James (1954) as carbonate, oxide, sulphide and silicate. BIF facies recognition evolved from the experimental mineral stability work of Krumbein and Garrels (1952) which classified iron-rich marine rocks as chemical sediment belonging to “restricted” marine environments where “physiographic, tectonic, or biologic features impose controls on circulation, oxygenation, or concentration of dissolved salts”. The sedimentary facies therefore represent electric potential (Eh) and alkalinity (pH) environments in ionic sea water solutions where the minerals precipitating are in a stability equilibrium (Krumbein and Garrels, 1952; James, 1954). The final minerals present are a product of precipitation, diagenesis or biologic activity (James, 1954).

Carbonate facies is chiefly comprised bands or laminae of fine grain iron-magnesium carbonate with chert, and can be interlayered or bedded with iron oxides and minor sulphides (Gross, 1965). Carbonate species include siderite, dolomite, and ankerite. The presence of siderite defines a deep calm water depositional environment (Gross, 1965) under strongly reducing conditions. Iron species within carbonate facies are usually in the ferrous state (Gross, 1965). Carbonate facies may grade vertically or laterally into the sulphide or oxide facies as observed in the Michipictoen area (Goodwin, 1962) and Gunflint district of Ontario (Goodwin, 1956). Most carbonate facies are enriched in manganese compared to oxide facies (Gross, 1965).

Oxide facies are dominated by homogeneous millimetre to centimeter magnetite-hematite laminae-layers alternating with silica laminae-layers forming the iconic banded or laminated texture. The homogeneity and lateral continuity of banding in oxide facie

BIF within various districts is distinctive and can be traced for kilometres. Such examples include mesobands within the Dales Gorge Member of the Hamersley Basin. Single mesobands within this member are correlated and traced up to 60,000 km² (Trendall, 1983). Iron oxides and silica comprise the majority of the facies and often segregate into hematite and magnetite types that typically contain under 3% combined Al₂O₃, MgO and CaO (Gross, 1965). Both iron oxides and silica grain sizes are very fine. Algoma-type oxide facies have a strong association to carbonate and sulphide facies compared to Superior-types.

Sulphide facies are considered the least abundant facies (Gross, 1965) and occur as pyritic carbonaceous slates in Superior-type and pyrite-pyrrhotite-siderite masses or beds in Algoma-type banded iron formations (James, 1954; Gross, 1965). Oolitic pyritic beds within the Wabana iron formation, Wabana, Newfoundland have also been noted indicating sulphide precipitation at shallow depths (Gross, 1965). Sulphide grains lack granular texture and tend to have an affinity with siderite facies. Silicate facie BIF is generally composed of greenalite, glauconite, chamosite stilpnomelane and minnesotaite. Silicates facies form laminae or bands of silicates with carbonate, sulphide or iron oxide. This facies is the least understood as the main minerals are bound by layers of silica, carbonate or iron oxide and are susceptible to low grade metamorphism (James, 1954; Gross, 1965).

2.4 BIF Origins and Genesis

The origin of BIFs is a controversial topic in economic geology and metallogeny. Paleo environment, iron-silica sources and mechanism creating the banding texture are the root problems. During the late 1800 and early 1900's, iron formations were interpreted as the depositional product from weathered-leached profiles of terrestrial rocks (Gross, 1991). Van Hise and Leith (1911) questioned the validity of the weathered profile hypothesis as leached terrestrial rocks should underlie banded iron formation sequences. Their work inferred volcanogenic sources of iron and silica and that BIF sediment precipitated from solution. Detailed work by Grout (1919) in the Mesabi range of the Lake Superior region further solidified the depositional environment as shallow marine, classifying iron formation as a chemical or hydrolithic sediment. Krumbein and

Garrels (1952) geochemical work then demonstrated the effects of pH and Eh on precipitation of chemical sediment, further constraining marine environment(s) amenable for iron oxide precipitation (Figure 2-3). James (1954, 1966) used this environmental framework and coupled it with sedimentary features defining four facies (oxide, carbonate, silicate and sulphide) for the Lake Superior region. Goodwin (1956, 1962) later applied stratigraphic relations to volcanic terrains hosting banded iron formation. Gross (1965) then proposed type classifications based on facies, age and depositional environment. The following works of Gross (1966, 1980, 1983, 1991), Trendall (1968, 1983), Trendall and Blockley (1970), and Beukes (1984) provided context on stratigraphy, mineralogy and geochemistry of major iron formations globally.

From this work, banded iron formations were identified as occurring mainly in two distinct marine-tectonic depositional environments; quiet volcanic marine basins or troughs and continental marine shelves (Gross; 1965, 1980, 1983, 1985) (Figure 2-4). Algoma-type iron formations deposition is interpreted to have been in quiet volcanic-marine basins, as they lack storm and wave sedimentary feature and are interbedded felsic-mafic volcanics, ultramafics, turbidites, greywackes, argilites and shales (Gross; 1965, 1980, 1983, 1985, 1995). Algoma-types are associated with sedimentary breaks in stratigraphy. Superior-type iron formations are interpreted to be deposited in a near shore continental shelf environment with neighboring dolomite, quartzites, black shales and minor volcanics (Gross; 1965, 1980, 1983, 1985, 1995).

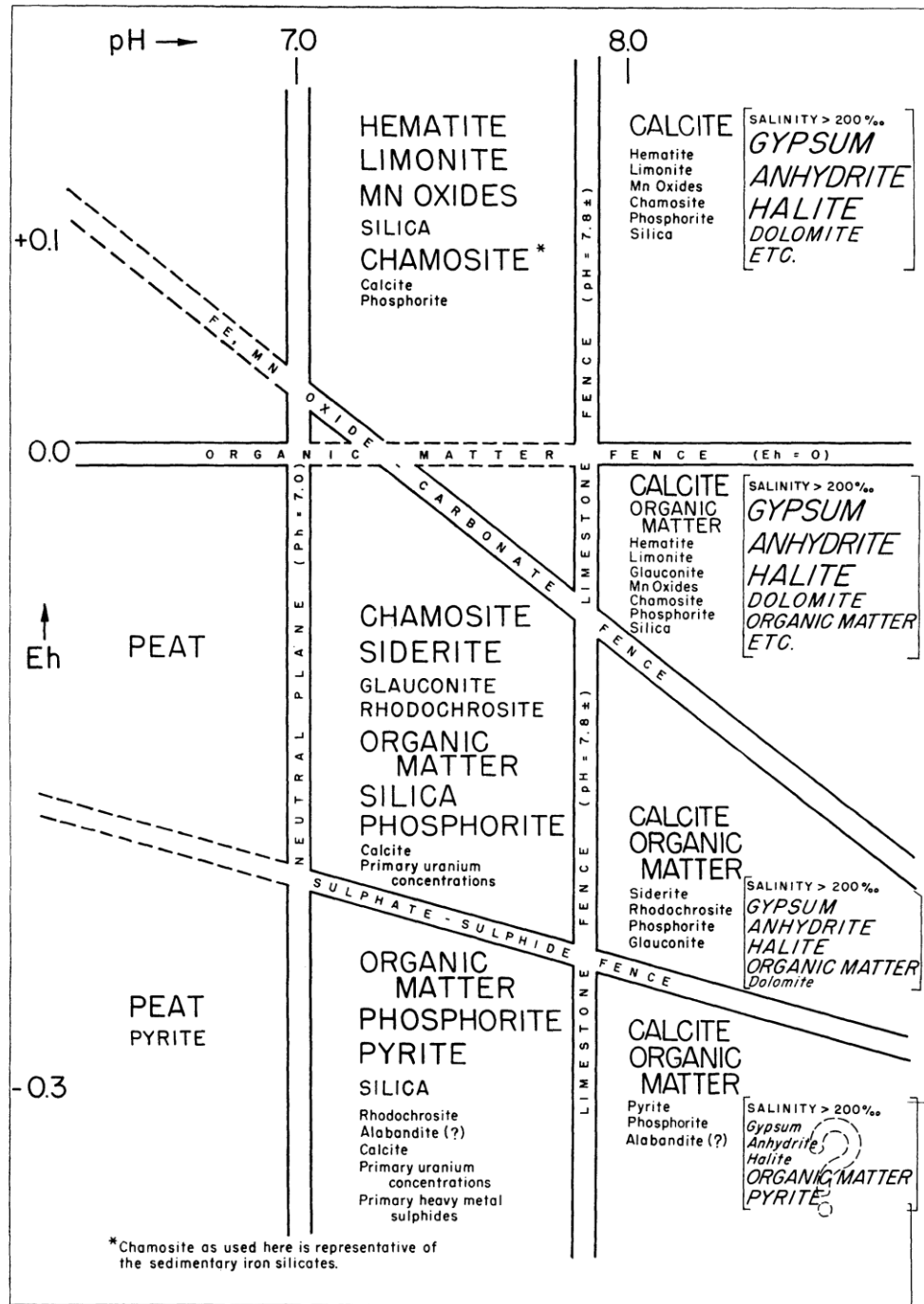


Figure 2-3 Chemical stability diagram illustrating mineral stability environments as a function of pH and Eh. Taken from Krumbein and Garrels (1952).

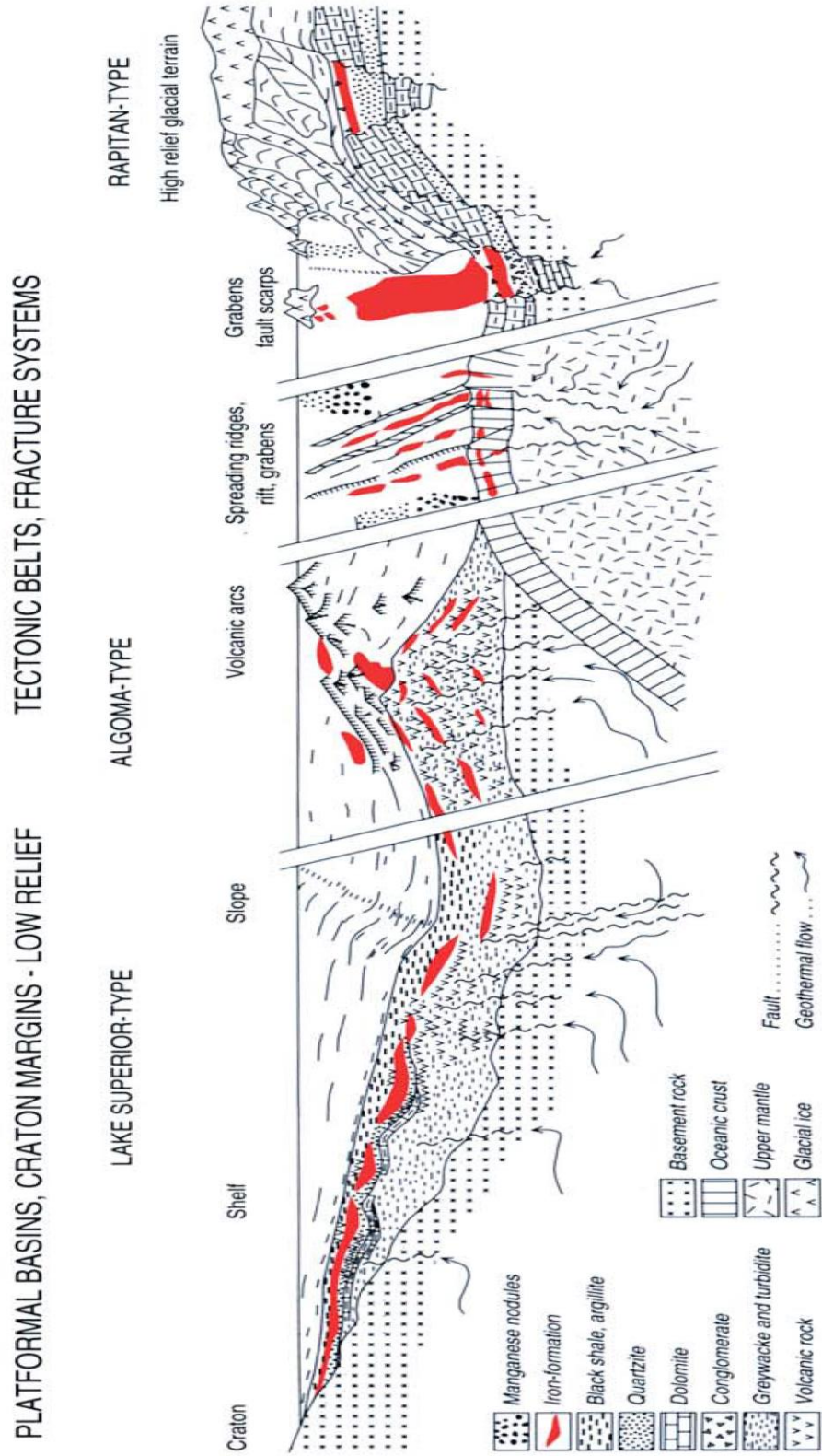


Figure 2-4 Illustration of the depositional environments of Algoma-, Superior- and Rapitan-type banded iron formations. Taken from Gross (1995).

Other issues regarding banded iron formations are the source and transport of iron and silica. Foundations of the discussion are rooted in the physical-chemical controls for dissolution and transport of iron and silica in sea water and the billions of tonnes needed for BIF deposition. Such large iron-silica sources are illustrated by depositional rates calculated within the Hamersley Basin. A single mesoband in the Hamersley Basin was analyzed by Trendall and Blockley (1970) and returned an iron oxide concentration of 22.5 mg/cm^3 . A total of $1 \times 10^{20} \text{ g}$ of iron over 6 million years was calculated given the regional extent. The depositional rate was calculated to be $2 \times 10^{13} \text{ g}$ of iron per year (Trendall and Blockley, 1970)!

The two most common theories with respect to iron sourcing are volcanic and terrestrial. Volcanogenic iron sources are supported by ready dissolution of ferrous iron and large sea floor/mantle reservoirs. Ferrous (Fe^{2+}) iron dissolves willingly into saline solutions producing ferrous hydroxides; FeOH_2 , FeOH^+ and $\text{Fe}(\text{OH})_3^-$. Precipitation of ferrous hydroxides is directly affected by pH and redox conditions (Ewers, 1983). Ferrous iron is stable in a reduce environment with no free oxygen (Mel'nik, 1982). In contrast, Ferric iron is virtually insoluble in current seawater salinities, limited to a pH range of 2.2-4.1 (Mel'nik, 1982). Furthermore, all ferrous colloids automatically precipitate in saline solutions 1/300th of modern seawater (Mel'nik, 1973). Terrestrial sources of iron are supported by the fact that iron precipitation from sea water is likely ferric and rivers such as the Amazon can transport 524,000 tons of iron and silica in solution per day without a significant weathering profile (Gross, 1991).

The other major component, silica, dissolves forming $\text{Si}(\text{OH})_4$. Saturation concentrations are reported up to 120 mg/L at 25 C° (Ewers, 1983). Volcanogenic origins of silica in BIF are supported by lack of aluminum concentrations, inverse to terrestrial sediment concentrations. Also, ^{30}Si isotope values of Precambrian BIF chert layers are similar to seafloor precipitates and hydrothermal products (De La Rocha et al., 2000; van den Boorn et al., 2007; van den Boorn et al., 2010) (Figure 2-5). However, Hamade et al. (2003) points out that Si/Ge ratios from silica and chert mesobands in the Dales Gorge Member are $0.82 \times 10^{-6} \pm 0.16 \times 10^{-6}$ and reflect the same ratio as terrestrial sources.

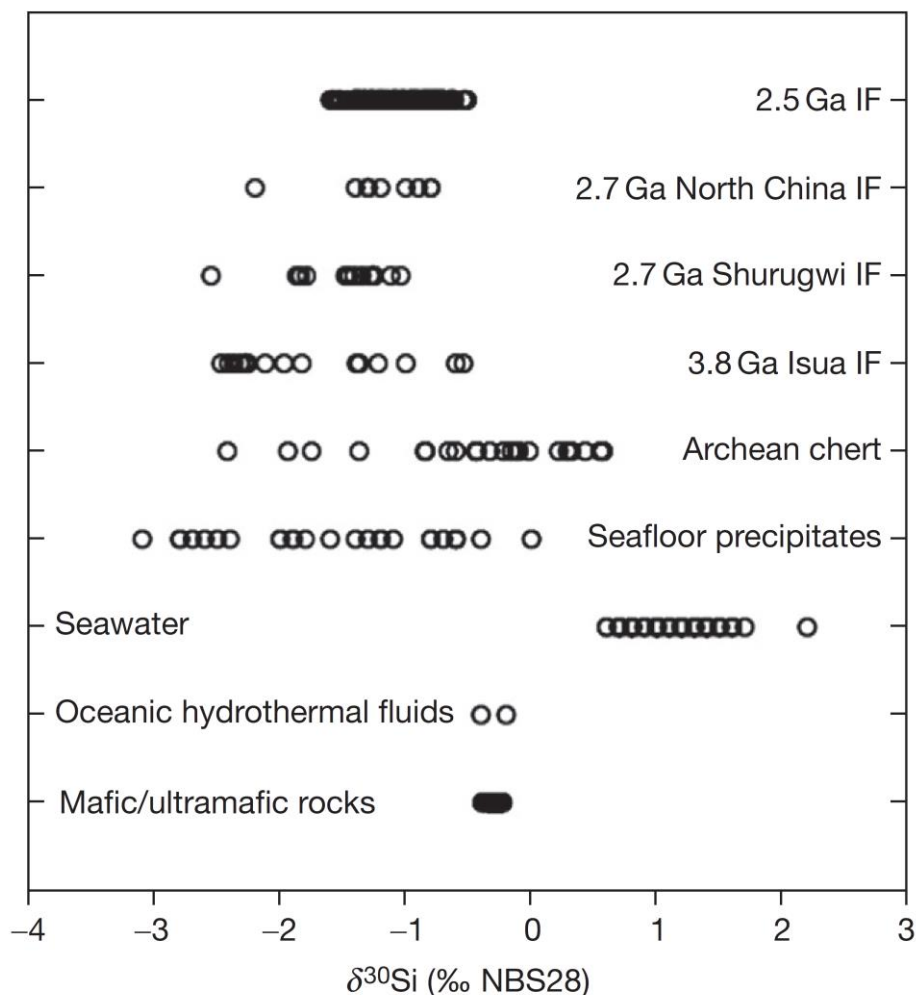


Figure 2-5 Plot of $\delta^{30}\text{Si}$ isotopic ratios (‰) from Archean banded iron formations and sea floor precipitates (Bekker et al., 2014).

The last and most debated topic about banded iron formation is the mechanism creating the characteristic alternating silicate and iron oxide bands. The debate is interconnected to BIF mineralogy, seawater chemistry and atmospheric conditions. Polarized views have unfolded, focussing on either primitive life or volcanogenic-paleotectonics as the driving forces of formation. Primary mineralogy from the Dales Gorge member Australia shows BIF deposition was due to amorphous silica, greenalite, ferrihydrite and siderite (Pecoits et al., 2009). These precipitants are likely to be in colloidal solutions. Similar colloidal gel-like solutions are recognized as exhalative derived solutions in brine pools along the Red Sea rift (Miller et al., 1966; Laurila et al.,

2014). Laboratory experimentation, recreating iron oxide and silica, banding date back to Moore and Maynard's (1929) work that proposed differential settling of dissolved silica and iron. Recent experiments dissolving basalt into acidic meteoric water by Zhu et al. (2014) precipitated alternating bands of ferric and amorphous silica by alternating pH.

Other workers investigating BIF deposition mechanisms have inferred atmospheric and biologic influences. Several workers cite an oxygen poor Archean atmosphere changing to a modern oxygen rich atmosphere around ~2400 Ma (Cloud, 1972, 1973; Garrels et al., 1973; Canfield, 2005). Paleo-redox proxies demonstrating a reduce Archean atmosphere include Archean BIF (Fe^{2+} transport and deposition), (Kump and Holland, 1992) and Archean fluvial pyritic, uranite and siderite deposition in the Witwatersrand basin of South Africa (Rasmussen and Buick, 1999). Oxygenating atmospheric conditions would allow oxidization of ferrous iron, precipitating ferric iron in seawater. Atmospheric oxygenation also coincides with the first photosynthetic organisms. Photosynthetic algae identified in the 2100 Ma Negaunee and 1900 Ma Gunflint banded iron formation of North America suggests ferrous oxygenation precipitation reactions by photosynthetic planktonic and cyanobacteria (Cloud, 1965, 1973; Han and Runnegar, 1992). Other biologic evidence are the controversial 3500 Ma microbial mats in the Dresser Formation of the Pilbara craton, associated with jasperite beds (Van Kranendonk et al., 2008). More recent studies propose ferrous oxidation through metabolic oxidation involving microaerophilic, anoxygenic photosynthetic and nitrate dependent reactions. (Bekker et al., 2014). These physio-chemical reactions allow bacteria to use Fe^{2+} as electron donor.

Even with the enormous body of work from countless researchers dating back over 100 years, a unified and consistent model of banded iron formation deposition does not exist. New focuses on biologic precipitation does not explain Eoarchean BIF deposition and neither do volcanogenic models for Proterozoic BIFs. More research and compilation data is needed but will likely lead to multiple theories.

2.5 Metamorphism of Banded Iron Formation

Metamorphism of banded iron formation is considered isochemical with exceptions of H₂O and CO₂. Chemical distribution of CaO, FeO and MgO from metamorphosed and unmetamorphosed iron formations are similar, inferring the same limited compositional range (Klein, 1978). Bulk rock analyses compiled by Gole and Klein (1981a) from low grade metamorphosed regions of the Labrador Trough illustrate marginal composition differences too. Still, the heterogeneity of primary BIF combined with metamorphic recrystallization can obscure metamorphic effects with respect to mass balance changes (Klein, 1983). Almost all known banded iron formations have undergone at least greenschist facies metamorphism e.g. the Hamersley Basin (Trendall and Blockley, 1970), the Labrador Trough (Klein, 1978), and the iron formations of the Yilgarn of Western Australia (Gole and Klein, 1981b).

Arguably magnetite, hematite, calcite, dolomite-ankerite, siderite and quartz (chert) are considered low grade diagenetic minerals. The primary precipitants were ferrous, ferric, siliceous and carbonaceous hydrosols and hydroxides from colloidal solutions (Klein, 1983, 2005; Pecoits et al., 2009). No experimental data exists currently to discern late diagenetic mineral assemblages (180 C°) (Winkler, 1979) from lower greenschist assemblages (300 C°) (Klein, 1983). Greenschist facies minerals are greenalite, minnesotaite, ripidolite, ferroan talc and stilpnomelane. Chemically, greenalite can be compared to antigorite while minnesotaite's endmember can be compared to talc (Mel'nik, 1982), though not structurally identical for either (Klein, 1983). Estimated pressure-temperature conditions for greenalite assemblages by French (1973) are 100-200 C° at 1-2 kbar pressure. Textural relationships show stilpnomelane overprinting greenalite, indicating stilpnomelane to be a true low grade metamorphic mineral (Klein, 1974, 1983).

Amphibolite facies banded iron formation is characterized by Mg-Fe-Ca amphiboles (Klein, 1983). Minor occurrences of hedenbergite are observed in grunerite assemblages of the northern Gunflint iron formation (Floran and Papike, 1978). Iron rich carbonates are noted occurring with Fe-Mg-Ca amphiboles in the Labrador Trough (Klein, 1978). Stabilities of cummingtonite-grunerite coincide with the metapelitic

biotite zone upwards into the kyanite-staurolite zone (Klein, 1983). Cummingtonite-grunerite amphiboles are the result of metamorphic reactions from hydrous silicates (minnesotaite and greenalite) and iron-magnesium carbonates (Mel'nik, 1982; Klein, 1983). Amphibolite metamorphism of banded oxide facies develops medium to coarse recrystallized quartz and iron oxides. Magnetite-hematite show no signs of alteration during metamorphism (Klein, 1973, 1983) inferring oxygen is buffered during metamorphism. Oxygen buffering maybe due to low reactivity, slow movement or low quantities of free oxygen (Frost, 1979; Mel'nik, 1982; Klein, 1983).

At granulite facies, BIF mineral assemblages change to anhydrous pyroxene and lesser fayalite (Klein, 1983). Both clino and orthopyroxene originate from carbonates reacting with hydrous silicates (Klein, 1983). Garnet and amphibole form minor components of the granulite facies (Klein, 1983). Banded oxide facies iron formation at this metamorphic grade recrystallizes but shows no mineralogical changes (Gole and Klein, 1981b; Klein, 1983). Temperature and pressure calculations of pyroxene assemblages for regional highly metamorphosed banded iron formations in Heany's and Meier's Find of Western Australia are $670 \pm 50 \text{ C}^\circ$ at 3-5 kbar of pressure (Gole and Klein, 1981b). Comparatively, contact metamorphism producing fayalite has temperatures estimated between 780-810 C° and 0.5-2 kbar of pressure in the Duluth Complex aureole on the Biwabik iron formation (French, 1968).

2.6 Iron Ores

Ore is an economic term and influenced by many factors that incorporate demand, price index, logistics and government. Three types of iron ores exist; soft, hard and carbonate. Soft ores are ore composed of friable-slaty iron hydroxides (goethite) and hematite (martite). Hard ores are composed compact and crystalline iron oxides that can be lumped or crushed. A variety of minerals such as magnetite, hematite and goethite can comprise hard ore. Carbonate ores are chiefly composed of siderite and roasted to extract iron. These ore types can be further classified into concentration types as either direct shipping or taconite ores. Direct shipping iron ore (DSO) can be transported directly to smelters after minor crushing and blending. At the moment, the industry benchmark for direct shipping iron ore exports to major Chinese smelters is 62% total Fe

content. Overall, DSOs are elevated with respect to total iron content compared to taconite and generally exceed 50% but can range between 52.4-64.6% as demonstrated by mining operations in the Labrador Trough (Labrador Iron Mines Holdings Limited, 2014). Grades of direct shipping iron ore can also average to extremely high values. The N4E deposit in the Carajás banded iron formation of Brazil averages 66.13% total iron content (Klein and Ladeira, 2002). Taconite ores are banded iron formation with an elevated iron content (>15% total Fe content) requiring crushing and pelletization for smelting. Table 2-2 lists tonnages of major BIF-hosted iron ore districts.

Province Name	Year of discovery	Start of mining	Initial high-grade resource (Bt)	Remaining resource (Bt)	Material mined
Superior (USA)	1844	1848	2.4	<0.1	Taconite (BIF)
Krivoy Rog (Ukraine)	1880	1881		<0.1	BIF
Quadrilatero Ferrifero (Brazil)	1810	1940		2.4	Rich itabirite (BIF) and hematite
Transvaal (South Africa)	1901	1931			Hematite
Orissa (India)	1904	1911			Hematite and hematite-goethite
Hamersley (Australia)	1957	1966	32	<30	Hematite and hematite-goethite
Carajas (Brazil)	1967	1985	18		Hematite
West Africa	1950?	1951	??	??	no present mining

Table 2-2 List of major global banded iron formation hosted ore districts. Date of discovery, start of mining and resource estimates are listed. Taken from Dalstra and Flis (2008).

2.7 Iron Formation Enrichment and Deposits

Iron enrichment is the process(es) removing deleterious components (SiO₂, MgO, CaO, P₂O₄ exct...) from banded and granular iron formations to form various types of iron ores; soft, hard and carbonate. Enrichment processes are categorized into three types; syngenetic, supergene and hypogene. These enrichment processes typically have associated structural controls. Both enrichment processes and structural controls are

described in the subsections below. Major iron ore deposits are often the result of two or more process types. Description and characterization of processes are supported by geochemical and mineral data from deposits and iron formation districts.

2.7.1 Structural Controls

Major BIF hosted iron ore districts such as the Hamersley, Superior, Labrador Trough and Cuadrilátero Ferrífero, show some form of structural deformation pre or syngenetic to iron ore formation. Van Hise and Leith (1911) were first to cite iron ore associations with plunging synclines, fissures and fractures in the Superior province. The Hamersley is folded and overprinted by 3 compressional events (D₂-D₄) producing anticlines, synclines and thrust faults (Dalstra and Rosière, 2008). High-grade hematite deposits of Mount Tom Price, Paraburdoo, and Giles Mini are associated with these deformational events (Dalstra and Rosière, 2008). Iron ore bodies of Cuadrilátero Ferrífero are hosted in hinge zones of complex interference folds and have an association with faults (Rosière and Rios, 2004; Dalstra and Rosière, 2008). Morris (1985) emphasized the importance of structural controls to high grade iron ore as they allow migration and focusing of fluids. Faulted, folded and fractured banded iron formation becomes more porous after initial deformation and acts as an aquifer increasing rock to fluid contact. Normal faults and fold structures are likely the major control for hypogene alteration while upper fractures and faults control supergene fluid flow (Morris, 1985).

2.7.2 Syngenetic Enrichment

Syngenetic enrichment involves sedimentary-diagenetic processes by gravity compaction, pressure solution and dewatering (Lascelles, 2002, 2007) (Figure 2-6). The enrichment model follows five stages: 1) deposition of nontronite and Fe-hydroxides; 2) nontronite breakdown; 3) compaction settling; 4) dewatering; and 5) supergene enrichment (Lascelles, 2002, 2006; Dalstra and Flis, 2008). Ultrafine colloidal solutions of iron hydroxyl-hydroxides, silica, nontronite (Fe³⁺ smectite) and carbonates are precipitated and deposited on an unstable sea floor (Lascelles, 2006). Compaction and disassociation of silicates and iron oxides occur forming a siliceous gelatinous material. Further compaction allows disassociation during diagenesis. At the same time

dewatering and fracturing occur forcing the siliceous gel to escape leaving denser iron oxides behind. Finally, the exposed protore is exposed for supergene enrichment. The five stages are constructed from investigations at the Mt Gibson deposit. Syngenetic interpretations of the Mt Gibson deposit are based on micro-platy hematite clasts and chert free horizons which grade into BIF below the vanadose zone (Lascelles, 2006). The clasts and chert free horizons indicate enrichment pene-contemporaneous to deposition and prior to regional deformation and weathering (Lascelles, 2002).

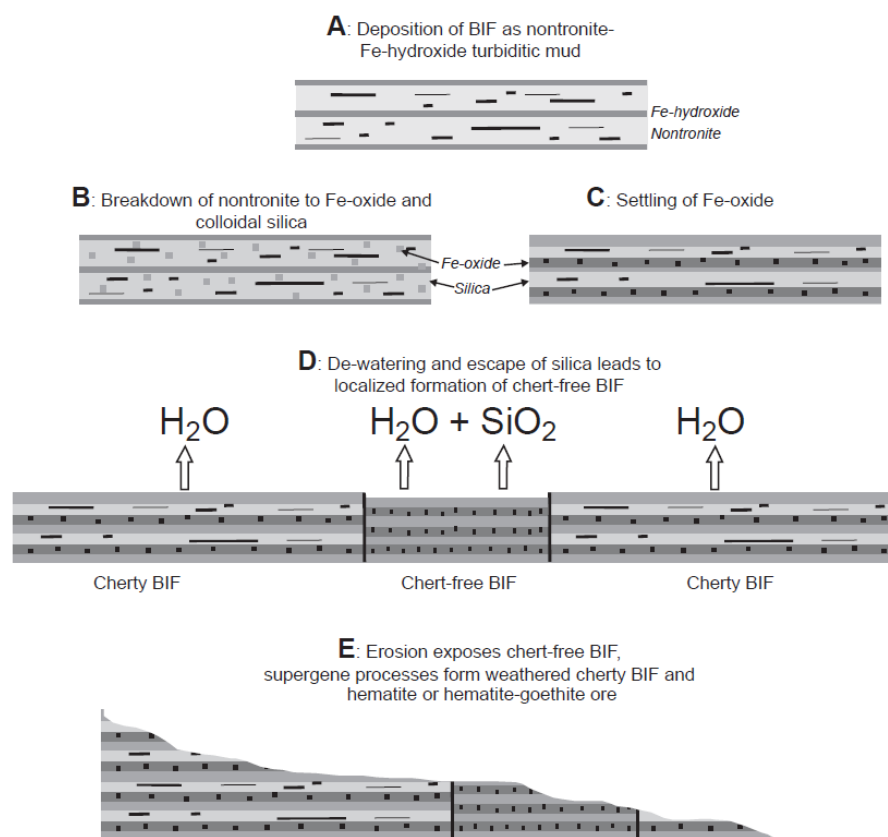


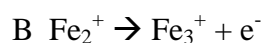
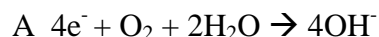
Figure 2-6 Illustration of syngenetic BIF hosted iron ore formation. The five stages are labeled A through E and depict deposition breakdown, settling, dewatering and weathering. Taken from Dalstra and Flis (2008).

2.7.3 Supergene Enrichment

As defined by Martycak et al. (1994), supergene processes are processes “driven by thermodynamic nonequilibrium between ore- and rock-forming minerals and natural waters, gasses, etc.” Supergene enrichment is the metalliferous upgrade by fluid rock interactions at shallow crustal levels. Ionization, hydrolysis and redox are the main

reaction types leaching gangue minerals from BIF while precipitating residual iron oxide (hematite and maghemite) and iron hydroxide (goethite) complexes (Morris, 1985). Meteoric waters percolate into fractures, folds or faults leaching and replacing the primary mineralogy. Infiltrating meteoric waters may descend as far as 2400 m, as reported in Krivoy Rog iron formation (Beletsev, 1973). Supergene processes are further classified into ancient and modern types (MacLeod, 1966). The major difference being ancient supergene derived ores underlie major unconformities (Beukes et al., 2002).

Morris (1980, 1983, 1985) proposes a electrochemical model to explain the dissolution and oxidation of BIF layers (Equation 2-1 and Figure 2-8). Initially, descending ground waters react with magnetite layers creating a cathodic reaction reducing oxygen (Morris, 1985). Ferrous ions enter hydrolysis, later oxidizing and precipitating as iron hydroxyoxides by ferrolysis reactions altering magnetite to martite (Morris, 1985). The result releases more H^+ allowing further reaction with silicates, carbonates and iron oxides (Morris, 1985). The precipitated iron hydroxyoxides and ultimately crystallize as goethite. Laboratory studies indicate an approximate ~ 10 Ma alteration rate for every 100 metres (Morris, 1985).



Equation 2-1 Chemical reactions during supergene enrichment of banded iron formation. Reactions are labeled A through D in order of paragenesis.

Descending migration of meteoric waters is supported by the altered stratigraphic profiles present in the Sishen, Manganore, Beeshoek, Welgevonden and Rooinekke

deposits of the Transvaal Supergroup, South Africa. These deposits show surficial laterites grading downward into hematite ores which terminate at depth into unaltered banded iron formation (Beukes et al., 2002). Mineralogical alterations of upper level primary magnetite and silica to pseudomorphs of hydrous goethite and secondary hematite at the Mt. Whaleback and Paraburdoo deposits also support low temperature alteration and show the same paragenesis outlined in the Sishen deposits (Morris, 1980). Oxygen isotopic ratios of -3‰ to $+3\text{‰}$ from Sishen-type hematite ores infer precipitation from low temperature meteoric water (Beukes et al., 2002). Furthermore, hematite ores show Ce and HREE enrichment implying dissolution of REEs by oxygenated ground waters retaining Ce (Beukes et al., 2002).

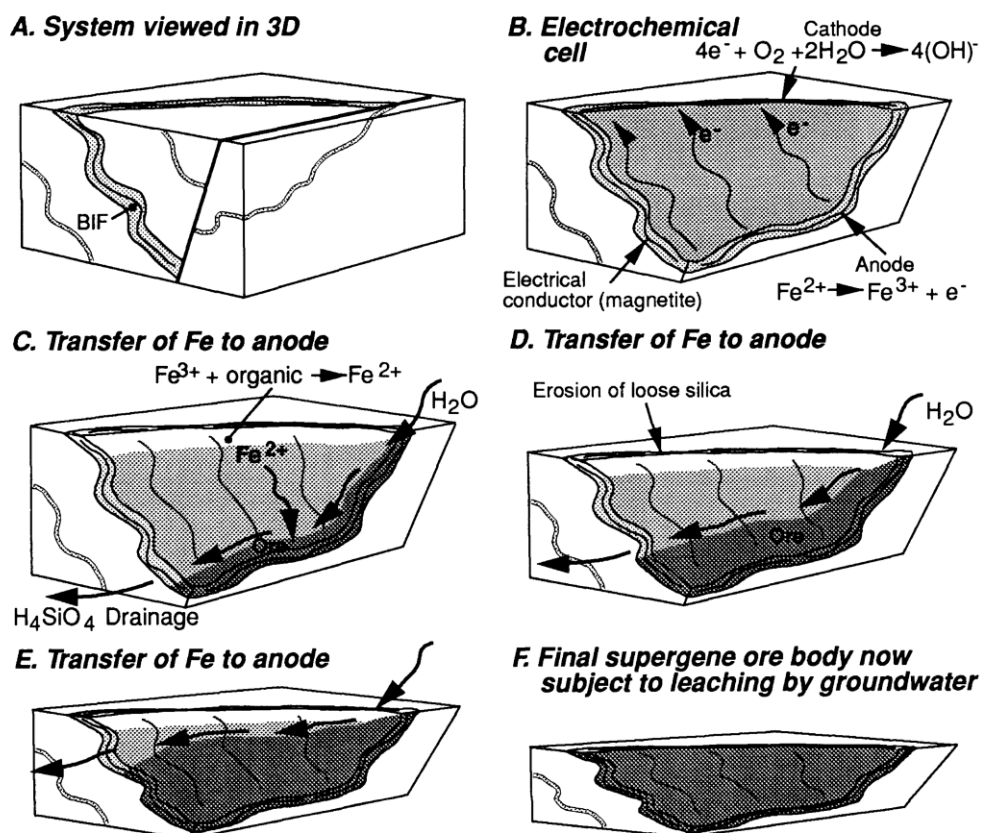


Figure 2-7 Illustration of supergene processes. Cathodal reduction of iron through erosion are depicted in order from A to F.

Supergene enrichment is associated with the creation of soft microplaty hematite saprolitic type iron ores. Supergene enrichment is attributed to the formation of upper

level martite-goethite iron ores in the Hamersley Basin (Morris, 1980; Morris, 1985, 1998), the weathered friable goethite-martite-hematite itabrites of Quadrilátero Ferrífero district Brazil (Dorr II, 1964; Morris, 1985) and the laterite goethite-hematite iron ores of the Noamundi area, India (Beukes et al., 2008). Grades of these deposit types can reach 68.2% total Fe content (Spier et al., 2007) and can form enormous tonnages. Mt. Whaleback in Western Australia contains >1.5 billion tonnes alone.

2.7.4 Hypogene Enrichment

Hypogene enrichment is defined by Jackson and Bates (1997) as *metallogenic upgrading via hot fluid-rock interaction by ascending fluids*. Hypogene iron formation enrichment then involves hot (>100 C°) fluids interacting with BIF bodies leaching gangue minerals. Hypogene enrichment is synonymous with hydrothermal alteration. The composition of hypogene BIF-hosted iron ores is commonly hard hematite (Beukes et al., 2002) or martite-goethite as mined in the Hamersley (Taylor et al., 2001). Major banded iron formation districts including the Kivoy Rog of the Ukraine, the Hamersley Basin of Western Australia and the Carjás region of Brazil, have iron ore bodies that the result of hypogene enrichment.

Evidence to support hydrothermal enrichment of BIF is founded on stratigraphy, structure and mineral replacements textures far below ancient and modern lateritic-weathered profiles. Hypogene iron ores stratigraphically downgrade upward from basal ore contacts upward into unaltered BIF (Beletsev, 1973; Beukes et al., 2002). Eight high grade hematite deposits in the Penge iron formation of the Thabazimbi iron ore district of South Africa show increasing Fe content hundreds of metres below unenriched BIF (Dalstra and Guedes, 2004) (Figure 2-9B). Altered normal fault zones and Fe-Mg metasomatized footwalls, well below lateritic and vandose zones, are systematic with high grade hard hematite bodies of the Hamersley Basin (Taylor et al., 2001; Beukes et al., 2002). The carbonate altered Southern Batter fault in the Brockman iron formation and the basal Fe-Mg metasomatized McRae Shale are such examples (Dalstra and Guedes, 2004; Morris and Kneeshaw, 2011). Cross cutting carbonate (siderite-ankerite-dolomite), magnetite-hematite and quartz veins are observed overprinting BIF oxide facies and replacing silica banding with carbonate in these faults and shales (Lascelles, 2006).

Veining stems from basement assemblages and or faults and extends laterally and upward (Lascelles, 2006). These alterations are considered to form a carbonate proto-ore later leached by supergene processes. Temperature of ankerite-hematite veins from fluid inclusion data by Thorne et al. (2004) of pseudosecondary and secondary inclusions show homogenization of temperatures of $253 \pm 59.9 \text{ C}^\circ$ and $117 \pm 10 \text{ C}^\circ$ at the Mt Tom Price deposit of Western Australia.

Unlike the unified model of supergene enrichment, an integrated hypogene model for BIF enrichment does not exist due to differences in fluid composition, fluid generation, and tectonic paragenesis forming major ore deposits. Comparisons drawn by Dalstra and Guedes (2004) between the Mount Tom Price, N4E, Donkerpoort West and the Krivoy Rog deposits show similarities with respect to hydrothermal alteration. These deposits exhibit Mg-Fe and carbonate metasomatic textures overprinting oxide facie BIF. The Mg-Fe and carbonate mineral replacement textures show overall silica loss. Temperatures of hydrothermal alteration between these deposits vary greatly. The highest alteration temperature is in the Krivoy Rog which produced a magnetite-amphibole-siderite assemblage at temperatures $>400\text{-}500 \text{ C}^\circ$. The Mt Tom Price carbonate-talc-chlorite assemblage have lower estimated temperatures ranging between $150\text{-}320 \text{ C}^\circ$ (Taylor et al., 2001). The lowest temperature is demonstrated by the dolomite-chlorite alteration within the Carjás ($<145 \text{ C}^\circ$) while second fluid phases producing quartz veins and specularite are approximated at 350 C° (Rosière and Rios, 2004).

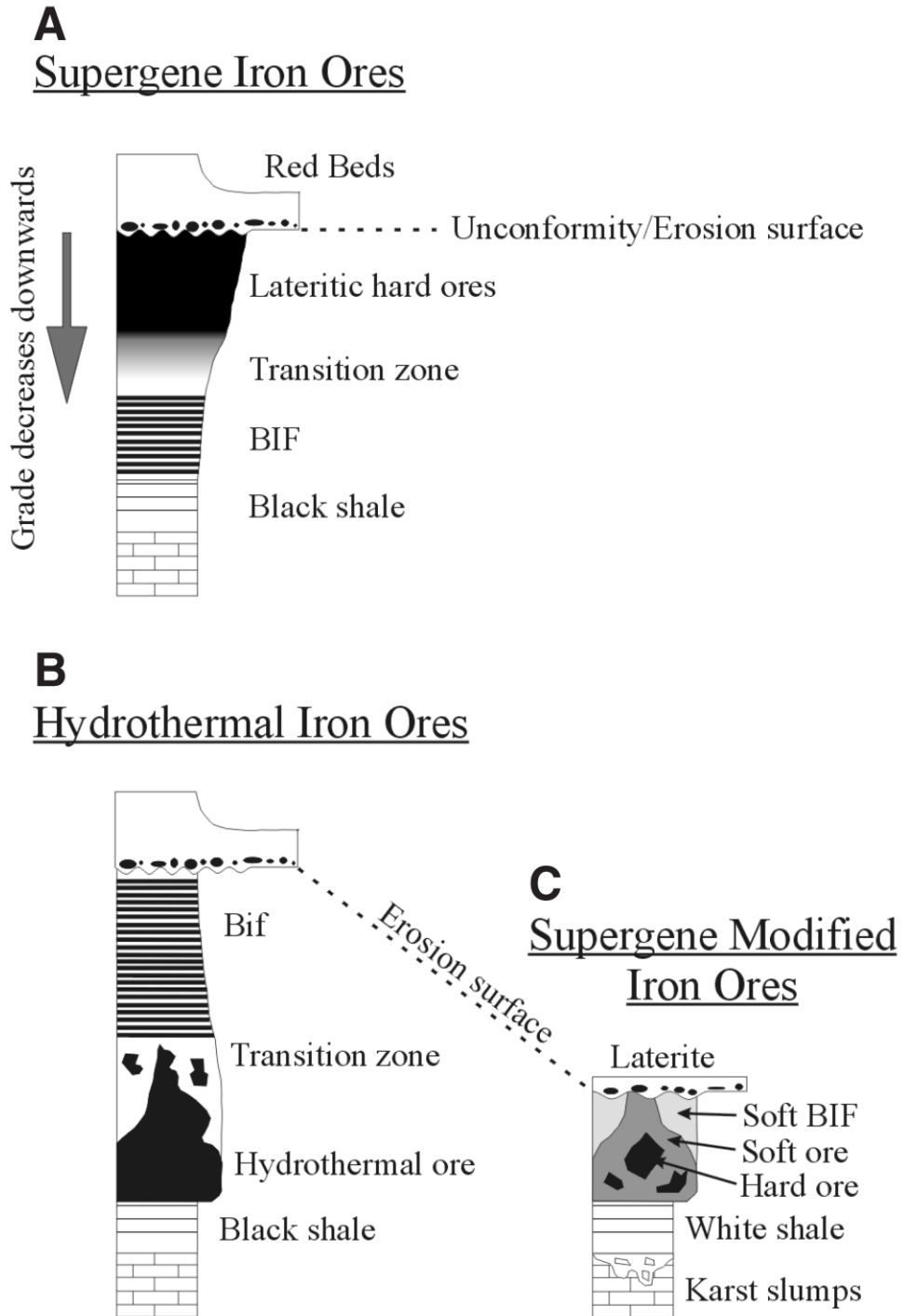


Figure 2-8 Illustration of iron formation enrichment type stratigraphy (Beukes et al., 2002).

2.8 Geochronology of Banded Iron Formation and Iron Ore

Minerals utilized in geo and thermochronology originate from mainly magmatic or metamorphic-hydrothermal processes. As chemical sediment, banded iron formation does not naturally precipitate datable phases such as zircon, baddleyite, monazite, xenotime, apatite, micas or titanite. Apatites are present at trace abundances in some oxide facie BIFs, including the Isua-Akilia in southwestern Greenland (Appel, 1980, 1987; Lepland et al., 2002) and the Dales Gorge member of Western Australia (Pecoits et al., 2009). Phosphorus concentrations from whole rock analysis of oxide facies average 371 ppm in the Isua BIF (Appel, 1980) and 140 ppm in the Dale Gorge member (Pecoits et al., 2009). The textural significance and low concentrations indicates minute detritus impurity or perhaps a biogenic marker (Mojzsis et al., 1996; Lepland et al., 2002) making apatite dating at the current moment unsound.

Geochronology of banded iron formations has been focussed on the surrounding rocks deposited pene-contemporaneously by implementing whole rock and mineral dating techniques using U-Pb, Sm-Nd, Ar-Ar and Sr-Rb systems. Banded iron formation in the Archean Isua greenstone belt of western Greenland is an example of multiple geochronometers testing BIF and surrounding lithologies. Whole rock Rb-Sr analysis was applied to the basement Amîtsoq gneisses producing a lower boundary to greenstone belt formation at 3860 ± 240 Ma (Moorbath et al., 1975). Pb/Pb whole rock analyses from banded iron formation provided ages ranging from 3760 to 3710 Ma (Moorbath et al., 1973). Although the lower and middle zones of the belt seemed constrained several discrepancies were apparent. Whole rock Rb-Sr data from Amîtsoq gneisses was scattered, making the age dependent on modelling. Also, the Pb-Pb whole rock analyses showed significant differences of radiogenic lead between the banded iron formation and the Amîtsoq gneisses. It was not until U-Pb dating of zircons that previous interpretations were anchored. U-Pb analyses of detrital zircons representing crystallization ages from acid volcanic boulders within a conglomerate yielded a single discordant $^{207}\text{Pb}/^{206}\text{Pb}$ age of $3824 +12 -8$ Ma. These zircon and whole rock ages bracket the Archean Isua iron formation between 3860 and 3710 Ma. Recent studies have

extracted detrital igneous zircons with metamorphic overgrowths from the Changyi, banded iron formation in China (Lan et al., 2014).

Geochronologic studies targeting iron formation enrichment have been less frequent due to complexity of iron ore generation and paucity of secondary datable phases related to alteration. Hypogene and supergene ores in the Hamersley Basin and Carjás have recently been investigated using U-Pb and Ar-Ar techniques. Rasmussen et al. (2007) identified monazite and xenotime phases in high grade hematite and martite ores at the Mt Tom Price deposit of Western Australia. U-Pb isotopic measurements of these phosphate minerals showed ages ranging from 2150-850 Ma (Rasmussen et al., 2007). Hypogene iron formation enrichment may have been long lived taking up to 1300 Ma to form direct shipping ores. Supergene goethite ores at the nearby Lynn Peak deposit have also been investigated. Cements from goethite ores located within weathered profiles underwent U-Th/He analysis. Ages ranged from 33 to 14 Ma and some ages were as old as 65 Ma. Cementing Mn oxides were analyzed too via $^{40}\text{Ar}/^{39}\text{Ar}$ methods and produced similarly ages and a lower boundary of 65 Ma. The results indicate supergene enrichment forming goethite ores may have started as early as 65 Ma.

Chapter 3 Methods

3 Introduction

Information pertaining to sampling and analytical techniques is provided and reviewed in this chapter. Several sampling, preparation and analytical techniques were implemented. The primary petrographic and mineral data were obtained through optical and electron microscopy coupled with quantitative and qualitative X-ray spectrometry. Bulk rock chemistry and U-Pb isotopic data was obtained by precision optical and mass spectrometry.

3.1 Mapping & Sampling Methods

Obtaining geochemical and structural data on all MRG lithologies is not possible from surface sampling outcrop at Deposit No.1. Footwall and hangingwall rocks are poorly exposed north of the southern limb due to glacial sediment cover (25-75 metres thick). From the exposed southern limb northward, much of the deposit is inferred from drill core data. Both outcrop and drill core data are combined to portray a more complete picture of the Mary River tectonic-stratigraphy.

Deposit No.1 has been mapped at various scales completed by the GSC, MacLeod (2012) and BIMC. Detailed 1:2000 scale mapping of the Deposit No.1 footwall and hanging wall was completed by the author, Meghan MacLeod and Ian Herbranson during the summer of 2014. A digital Yuma tablet was utilized and synchronized with a global position system. The tablet used integrated MapInfo GIS software to plot geologic features in real time. Orientation of units and features, i.e. strike and trends, via compass measurement could not be completed without the use of a differential global position system (DGPS). High-grade iron formation produces a magnetic field exceeding 300,000 nano-teslas, altering compass readings for over a kilometre orthogonally. Structural measurements were carried out by the author using a Trimble R8 DGPS survey system, achieving an instrument error of 1 degree.

Rock sampling consisted of diamond drill core and grab samples. Drill core samples were taken from holes bored into the footwall, ore zone and hangingwall. Diamond drill core specimens were taken in 15-20 cm intervals from logged-cut core and totaled 104 samples. Grab samples were collected at exposed outcrops following transects throughout the Deposit No.1 area. Grab samples totaled 70. All samples were reviewed, photographed and culled to a 120 sample suite representing distinct lithologies. Several oriented grab samples of footwall schists were also taken from the Deposit No.1 area. Drill core samples 709, 716, 14880 and 2601 were selected from MacLeod MSc. (2012) thesis. Garnetiferous schist sample GCS-016 was also inherited from Nicpon's HBSc. thesis (2011).

3.2 Preparation Techniques

Centimetre thick slabs were cut from hand samples using a rock saw. Slabs were marked for tile cutting, photographed and cut to an approximate size of 27 X 45 mm. Diamond drill core specimens followed the same process with exception of slab cutting. Spectrum Petrographics Inc. in Vancouver, Washington USA made polished thin sections from submitted rock tiles. Polished thin sections were vacuum embedded with an epoxy and synthetic silica forming a rind. Sections were polished to a 45 μm thickness for potential isotopic laser ablation analyses. Other samples not used for geochronology were sectioned by Stephen Wood at the University of Western Ontario to a 30 μm thickness. Scanning of polished thin sections under plane polarized light and cross polarized followed and were completed using an Epson scanner with two sheets of linear polarizing film. Leftover slabs and core were submitted to ALS Global laboratories in Vancouver B.C. for geochemical analysis.

3.3 Analytical Techniques and Methods

3.3.1 Optical Microscopy

Optical microscopy was conducted using a Nikon Eclipse LV100POL polarizing trinocular microscope equipped with a Digital Sight DS-Ri1 camera. The microscope is equipped with 5x, 10x, 20x, 50x and 100x objectives and reflected light capabilities.

NIS-Elements image software with annotation and measurement utilities allowed for accurate mineral measurement and the capture of photo micrographs.

3.3.2 Geochemistry

3.3.2.1 ICP-AES (ICP-OES)

The fabrication of the plasma torch by T.B. Reed in 1962 and the conception of plasma emission source spectroscopy by Greenfield et al., (1964) has led to over 40 years of analytical improvement of inductively coupled plasma atomic (optical) emission spectrometry (ICP-AES or ICP-OES). The method is a form of emission spectrometry measuring the wave length and intensity given off by photons of excited electrons returning to a stable energy state (Dean, 2005). Elemental quantification is allowed because the photon intensity at a given wavelength is proportional to concentration (Dean, 2005). Plasma itself is a neutral ion gas containing equal number of ions and electrons. The plasma energy source is formed by an electrically ignited Argon gas pumped through a magnetic field, induced by radio frequencies between 27.12 to 40.68 MHz (Dean, 2005). Operating temperatures range between 5,000 and 10,000 K° (Hill, 1999). Dissolved aliquot solutions are passed through a nebulizer creating an aerosol. The atomized the solution is injected into the plasma torch. Atoms in the aerosol absorb and emit photons that are focused through a lens into a spectrometer (Hill, 1999). Wave length is measured and processed to identify elemental composition. Intensity is compared to standards to quantify concentration.

ALS Global carried out ICP-AES analysis of 46 drill core samples and 35 grab samples for major elemental oxides listed in Table 3.1. Geochemical sample preparation followed several steps. First 70% of the whole sample was crushed to less than 2 mm in size. A riffle split separated 250 g of crushed sample for pulverization to a consistency of 80% less than 75 microns. Three grams of pulverized sample material was mixed with lithium borate to create a fused bead allowing homogenization of all elemental components from major, trace and refractive minerals. A complete four acid digestion followed. The solution was analyzed using an Agilent 720 ICP-OES. Detection limits are supplied in Table 3-1.

Major Oxides	Detection Range Wt%	Major Oxides	Detection Range Wt%
Al ₂ O ₃	0.01-100	MnO	0.01-100
BaO	0.01-100	Na ₂ O	0.01-100
CaO	0.01-100	P ₂ O ₅	0.01-100
Cr ₂ O ₃	0.01-100	SiO ₂	0.01-100
Fe ₂ O ₃	0.01-100	SrO	0.01-100
K ₂ O	0.01-100	TiO ₂	0.01-100
MgO	0.01-100	LOI	0.01-100

Table 3-1 List of major elemental oxides and their detection ranges analyzed by ICP-AES.

3.3.2.2 ICP-MS

Inductively coupled mass spectrometry uses the same ionization argon plasma source but measures atomic mass (M) to charge (Z) ratios (M/Z) to identify and quantify elemental and isotope concentration. Injected analytes are ionized from the argon plasma and passed through a sample cone and skimmer. Sample ions reach supersonic speeds while passing through the skimmer due to the vacuum change and increased enthalpy from adiabatic expansion (Hill, 1999). Ion lenses emitting a controlled and focused electric field accelerate electrons on to the mass analyzer (Hill, 1999). Several mass analyzers exist but the quadrupole is the most common and the type used for this thesis. A quadrupole mass analyzer contains four rods in which two opposing rods carrying an applied controlled direct current to filter selected elements to an ion detector. The applied direct current forms a hyperbolic electric field filtering out unwanted elemental masses (Hill, 1999). Aliquots used in ICP-AES were also subjected to ICP-MS for trace element analysis. A second aliquot was analyzed for base metals, rare earth metals and rare earth elements via ICP-MS. Detection limits of ICP-MS are listed in Table 3.2.

Element	Detection Range ppm	Element	Detection Range ppm	Element	Detection Range ppm
Ba	0.5-10,000	Hf	0.2-10,000	Sn	1-10,000
Ce	0.5-10,000	Ho	0.01-1,000	Sr	0.1-10,000
Cr	10-10,000	La	0.5-10,000	Ta	0.1-2,500
Cs	0.01-10,000	Lu	0.01-1,000	Tb	0.01-1,000
Dy	0.05-1,000	Nb	0.2-2,500	Th	0.05-1,000
Er	0.03-1,000	Nd	0.1-10,000	Tm	0.01-1,000
Eu	0.03-1,000	Pr	0.03-1,000	U	0.05-1,000
Ga	0.1-1,000	Rb	0.2-10,000	V	5-10,000
Gd	0.05-1,000	Sm	0.03-1,000	W	1-10,000
Y	0.5-10,000	Yb	0.03-1,000	Zr	2-10,000

Table 3-2 List of trace and rare earth elements analyzed by ICP-MS accompanied with their detection limits in ppm.

3.3.2.3 Pycnometer Measurements

Particle density measurements of geochemically analyzed samples were conducted on returned 70 μm pulps in a gas displacement density analyzer known as a pycnometer. The pycnometer measures volume by filling the sample chamber with a non-reactive gas (He). The machine then empties the sample chamber gas into an empty chamber with a known volume and calculates the volume using the difference in pressure. Taking the mass of sample over its volume gives its particle density negating the original bulk porosity. An AccuPyc II 1340 pycnometer was used under the supervision of Ying Zhang at the Spence Engineering building at the University of Western Ontario. Samples were measured three times and averaged with recalibration of the machine after every five samples. Porosity in silicate rocks was absent inferring particle density is equivalent to bulk rock density. Hematite ores contained 5% porosity. Hematite ore density was calculated by measuring the mass and volume of a precision cut tile by scale and micrometer.

3.3.2.4 Mass Balance Calculations

Two main methods of calculation exist for quantification of mass changes in rock and minerals; Gressens' method (1967) and Grant's isocon method (1986). Gressens' method is preferred as it takes into account density and volume changes and illustrated in

Equation 3.1. The variable x_i is the element concentration of either the parent (A) or an altered unit (B) while ρ is the density of the respective unit and Fv is the volume factor. The result is elemental mass change (Δx_i) reported as grams or ppm change of parent sample material.

$$\Delta x_i = Fv \left(\frac{\rho^B}{\rho^A} \right) x_i^B - x_i^A$$

Equation 3-1 Gressen's equation mass balance equation (Gressens, 1967).

All variables in the equation are measured with the exception of Fv . To calculate Fv elements considered immobile are plotted using theoretical Fv values of 0.5 and 2.0 to their respective parent and altered concentrations. This produces two points on a Δx_i versus Fv plot known as a composition-volume (C-V) diagram. The intersection of the line between the two points across the Fv axis is considered the elemental volume change. A grouping of lines (immobile elements) intersecting the same Fv value represents the units volume factor or change in volume. Other criterion needed to aid in the interpretation of mass balance changes are:

1. Supposition of an Fv value can only be determined alongside petrographic evidence.
2. Only component ratio comparisons of parent and altered can show if the component was removed or added.

Elements considered immobile are listed in Table 3.3. Major elements, aluminum and titanium, are generally considered immobile because their low solubility in water and low diffusion coefficients. Rare earth elements, (REEs) and especially heavy rare earth elements (HREEs) are considered immobile because their intermediate ionic potential, odd number valence states and encapsulation in refractory trace minerals such as zircon. All elements considered immobile are plotted on a Fv vs X intercept plot to determine correct volume factors. After an Fv value has been determined for the lithology, it is applied and recalculated for the suite of analyzed elements.

Atomic Number	57	58	59	60	61	62	63	64
Abbreviation	La	Ce	Pr	Nd	Pm	Sm	Eu	Gd
Element	Lanthanum	Cerium	Praseodymium	Neodymium	Promethium	Samarium	Europium	Gadolinium

Atomic Number	39	65	66	67	68	69	70	71
Abbreviation	Y	Tb	Dy	Ho	Er	Tm	Yb	Lu
Element	Yttrium	Terbium	Dysprosium	Holmium	Erbium	Thulium	Ytterbium	Lutetium

Atomic Number	13	22	41	31
Abbreviation	Al	Ti	Nb	Ga
Element	Aluminum	Titanium	Niobium	Gallium

Table 3-3 Tables listing elements considered immobile in geologic systems. Light rare earth elements are in blue and heavy rare earth elements are in green.

3.3.3 Electron Microscopy

3.3.3.1 Background

The scanning electron microscope is an observational instrument that irradiates samples confined in a vacuum chamber with a focused accelerated rastering electron beam. Rastering produces high field of depth micrographs with magnifications typically ranging between 10-10,000x (Goldstein et al., 2003). A general schematic of a SEM is pictured in Figure 3-1. First concepts of field emission optics were brought to light by Knoll (1935) in ‘Aufladepotential und Sekundäremission elektronenbestrahlter Körper’ German for ‘Static potential and secondary emission of bodies under electron irradiation’. Later, von Ardenne (1938) added transmission coils creating the scanning transmission electron microscope (STEM) while Zworykin et al. (1942) discovered the benefits of secondary electron imaging that delivered high topographic contrast. In total six types of electron-photon emissions occur during irradiation of matter in a SEM.

Various technologies, manufacturers and models exist and have different operating voltages and parameters. The following text summarizes common tungsten filament SEM operation, and the instruments used in this thesis are described in the

subsequent sections. SEMs are composed generally of four components; electron gun, lenses, electron collectors and associated image capturing electronics. The electron gun is composed of a filament negatively charged (approximately 0.1-30 kV) in a high pressure vacuum chamber. Temperatures ranging from 2000-2700 K° causing thermionic emission of electrons (Goldstein et al., 2003). Regeneration of filament current is replaced by a resistor and voltage differences force electrons to crossover (Goldstein et al., 2003). Electrons are then accelerated by the lower anode aperture (Goldstein et al., 2003). The surrounding negatively charged Wehnelt cylinder focuses electrons within the electron gun chamber and controls electron emission (Goldstein et al., 2003). Accelerated electrons are directed through demagnifying lenses to the final spot size (~100 nanometres) (Oatley, 1972). Pairs of transmission coils located in the column deflect the focused electron beam in the X-Y plane by altering the frequency and strength of the electromagnetic coils as a function of time (Oatley, 1972; Goldstein et al., 2003). The frequency applied to the transmission coils creates the scanning effect. Diffracted and emitted electrons, resulting from bombarding the sample, are collected by sensors in the sample chamber. Digital processing takes signals obtained from detectors and produces images.

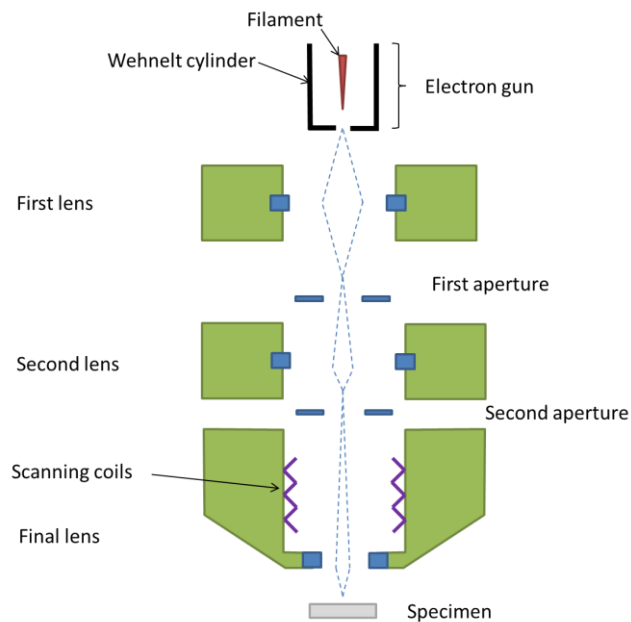


Figure 3-1 Scanning electron microscope diagram illustrating downward focus of electron beam.

3.3.3.2 Hitachi SU6600 SEM

The Hitachi SU6600 SEM is a state of the art field emission variable pressure SEM housing a Schottky electron emission source. The Schottky field emission electron gun differs from traditional tungsten “hairpin” and LaB₆ filaments as it does not rely on high temperatures to cause thermionic emission but precision shape to create high applied electron field at a much higher vacuum allowing electrons to funnel down (Goldstein et al., 2003). Compared to hot filaments the spot size is less than half and a 1000 times brighter (Crewe et al., 1968). The instrument is also furnished with wave-length dispersive spectrometry and energy dispersive spectrometry detectors as well as a Gatan CL image detection system. The instrument is housed in the ZAPLab at the University of Western Ontario under the supervision of Dr. Desmond Moser and operated by Ivan Barker.

3.3.3.3 Secondary Electron Imaging

Secondary electrons (SE) are electrons ejected from in-elastic scattering of the incident electron beam and sample material. In-elastic scattering is due to low energy conductive or valance state electrons interacting with the incident electron beam. SEs are low energy electrons ejected from outer atomic valence states between 5-10 KeV (Goldstein et al., 2003). The SE detector itself is a variation of the Everhart-Thornely detector comprised of a positively charged faraday cup attached to a scintillator (Figure 3-2). As secondary electrons pass into the faraday cup they are accelerated to the scintillator producing light with every bombardment, which is transferred by a light pipe to a photomultiplier. Carbon coated thin and thick sections underwent SE imaging. Higher magnifications were used to identify the morphologies of datable phases.

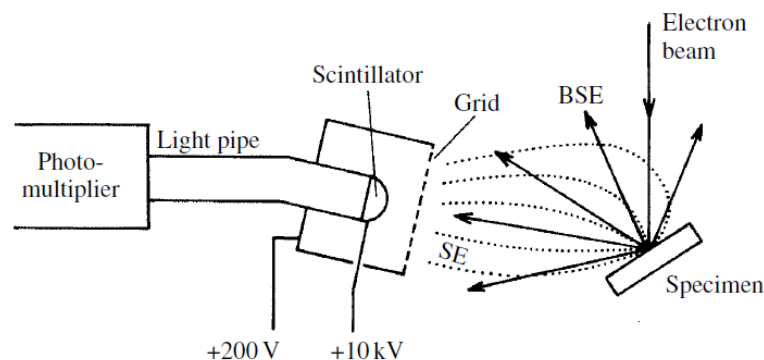


Figure 3-2 Illustrated diagram of Everhart-Thornely detector taken from Reed (2005).

3.3.3.4 Backscatter Electron Imaging

Backscatter electrons are electrons ejected via elastic scattering (deflected) through electron beam interaction with the atom nuclei of the sample material with no loss of kinetic energy. Ejected electrons charge a silicon diode. Through electron-hole principle, the diode lets an electron leave while forming a conduction band while another electron drops back into the valance state (Goldstein et al., 2003). An applied current across the detector surface allows the “hole” and free electrons to move oppositely (Goldstein et al., 2003). The current is measured and is proportional to the number of BSE hitting the detector. Higher atomic number elements produce more BSEs because larger nuclei create a greater effect on the incident electron beam. Carbon coated thin sections containing selected datable phases were imaged using BSE. Brightness controls were dimmed down inversely to contrast levels to identify mineral grain texture and chemical zoning.

3.3.3.5 Cathodoluminescence Imaging

Luminescence is a characteristic of matter defined as the “transition of anion, molecule, or a crystal from an excited electronic state to a ground or other state with lesser energy” by Marfunin (1979). This transition creates electromagnetic photon emission. The emission occurs as two time-based categories: fluorescence ($<10^{-8}$ s) and phosphorescence ($>10^{-8}$ s)(Pagel et al., 2000). The electromagnetic and photon-electron emissions are between ultraviolet and infra-red, within the visible light spectrum, as a result from electrical, mechanical or chemical excitation energy (Marfunin, 1979). Seven

types of excitation energy are classified: photo-, cathode-, thermo-, electro-, chemo-, bio-, tribo-, crystallo-, and X-ray (Gucsik, 2009). Cathodoluminescence develops from the emission of electrons from an accelerated electron beam typically from an SEM or TEM irradiating material 2-8 microns deep (Gucsik, 2009). The long wave length spectrum is influenced by numerous intrinsic and extrinsic variables including; chemical composition, crystal structure, crystal defects, strain and temperature (Edwards et al., 2007). These intrinsic or extrinsic characteristics act as “traps” for electrons returning to the conduction band from the valance band. The energy emitted or lost from the electron leaving the trap is emitted in the 400-700 nm spectrum. Less energy is emitted in the UV and infrared spectrum. CL imaging in relation to minerals’ intrinsic and extrinsic characteristics typically show growth zones. Zircon crystals selected for geochronology analysis were subjected to cathodoluminescence excitation energy and imaged using a simultaneous Gatan ChromaCL detector housed within the Hitachi SU6600 FE-SEM.

3.3.4 Electron Micro Probe Analysis

Electron microprobe analysis (EMPA) is a quantitative spectrographic technique measuring characteristic X-ray emission of elements by either specific energy or wavelength caused by sample irradiation. Electron beam bombardment causes ejection of primary lower energy level electrons creating ionization. Higher level shell electrons drop to fill voids in lower shells and emit a photon by doing so. Electron shells are specific energy states surrounding the nuclei of an atom. Shells are categorized into K, L and M shells, the order representing increasing energy (Goldstein et al., 2003). These shells are subdivided into sub shells (Goldstein et al., 2003). Energy can only be transferred through sub shells of the three major shells forming characteristic X-rays from energy transfers at the boundary of subshells (Goldstein et al., 2003). Specific x-ray energies and wavelengths characterize each element undergoing excitation, defined by Moseley’s Law (Goldstein et al., 2003). As the atomic number of the element analyzed increases, critical ionization energy also increases, leading towards lower spatial resolution.

3.3.4.1 Energy Dispersive Spectrometry

Energy dispersive spectrometry (EDS) is a form of X-ray spectroscopy that identifies-quantifies elements and their abundance by measuring photon energy and converting it to an electrical signal (photoelectric absorption). The conversion is carried out by a lithium silicon solid state EDS detector in a cooled atmospheric chamber. Silicon electrons in the detector are raised into the conduction band while leaving a hole in the valence band by bombarding photons (Goldstein et al., 2003). Both electric signals are captured by electrodes at either end of the detectors silicon plate and are amplified and shaped to form characteristic peaks (Goldstein et al., 2003). Spot analysis of datable phases was carried out by the author under the supervision of Ivan Barker to check mineralogical consistency from feature scans.

3.3.4.2 Wave-length Dispersive Spectrometry

Wavelength dispersive spectrometry (WDS) uses the same photon emission previously described but measures electromagnetic radiation wavelength instead of energy. WDS measures emission wavelength by the use of Bragg's law. Curved crystals, composed homogeneous crystalline material with known d-spacings, are bombarded by X-ray emissions from irradiated samples. Wavelengths sufficing Bragg's law are reflected to a gas proportional counter; a thin tungsten wire in a gas tube (Goldstein et al., 2003). The gas is ionized releasing an electron attracted to a grounded thin wire creating a voltage charge pulse (Goldstein et al., 2003). The pulses are proportional to the original x-ray photon and intensities are counted and compared to standards. In comparison to EDS, WDS offers orders of magnitude higher resolution and can simultaneously measure several elements at the same time, provided several crystals present. Error is derived mainly from overlapping element wavelengths and inappropriate beam current or beam spot size.

WDS analysis was completed by the JEOL JXA-8530F field-emission microprobe housed at the University of Western Ontario. The microprobe contains five wavelength dispersive spectrometers with ten analyzing crystals along with BSE, SE and CL detectors. Spot and elemental mapping of minerals were calibrated accordingly to

relative mineral standards and refractive crystals to avoid wavelength overlap and low count rates. Point and element mapping of monazite and xenotime grains were completed on samples 709, 716 and 6416. Essential metamorphic and alteration minerals were subjected to point analyses too.

3.3.4.3 EDS Phase Mapping

Elemental phase mapping uses simultaneous EDS and BSE imaging to create montaged element maps of sample areas. A grid of image zones is created for a sample area. The SEM acquires an energy spectrum at each pixel in a single image zone with the peak intensities being relative to elemental proportions. Simultaneously captured BSE and EDS images, sized 256 X 192 pixels, are compiled and digitally sewn together in a grid with a 10 pixel overlap creating a BSE image montage. Each grid rectangle in the BSE montage represents a 14 X 10 mm portion of the sample. Processing EDS data through Inca software enabled relative proportions of elements to be displayed geometrically. Selected carbon coated polished thin sections representing distinct lithologies were subjected to EDS phase mapping.

3.3.4.4 BSE-EDS Feature Mapping

Feature mapping is an SEM automation technique utilizing both BSE imaging and EDS to identify features of interest within a sample. Furthermore, details such as morphological measurements and position are recorded for each feature of interest. The technique involves creating a digital grid map of the sample surface. Each grid square acts as a window that the SEM rasters during BSE detection and identifies brighter materials containing higher atomic number elements. The BSE brightness is defined within a grey scale range and scaled to the operator's need. Areas of higher brightness are selected by the routine and analyzed using quantified EDS. The EDS results are compared to a recipe file containing threshold values of acceptable element concentration for categorization. After features contained within the window are analyzed by scanning EDS, the SEM moves the stage slightly to the next window and repeats the process. Window sizes were set to 256 X 192 pixels, approximately 14 x 10 mm with a 10 pixel overlap. Threshold values for datable phases are listed in Tables 3.3 and 3.4. Recipe A

was the initial values used for samples 6225, 6245, and 6220A. After identifying xenotime and baddeleyite during zircon imaging recipe B was implemented. Feature mapping can take hours to few days per sample depending window size, the number of feature categories or the amount of features present. Polished thin section samples underwent feature mapping to identify and locate datable phases (zircon, monazite, xenotime, allanite and baddeleyite). Data processing through ESRI Arc GIS allowed plotting of features on high resolution scanned sample images using the stage coordinates in relation to the sample.

		Recipe A				
		Class				
		Baddeleyite	Zircon	Monazite	Zirconalite	
Elements in Weight %	Si	Min	-0.1	8		
		Max	8	30		
	O	Min	16	20	5	
		Max	60	60.12	100	
	Zr	Min	15	15		15
		Max	82	60		35
	Ti	Min	-0.1			10
		Max	9			25
	Ce	Min			5	
		Max			100	
	P	Min			5	
		Max			100	
	Ca	Min				3.5
		Max				11

Table 3-4 Table listing class recipe A for EDS feature mapping. Elements are listed with maximum and minimum threshold values.

Recipe B		Class				
		Baddeleyite	Zircon	Monazite	Allanite	Xenotime
Si	Min	-0.1	8	-0.5	10	
	Max	8	30	7	35	
O	Min	18	20	15	15	10
	Max	60	60.12	55	70	35
Zr	Min	15	15			
	Max	80	60			
Ti	Min	-0.1				
	Max	7				
Ce	Min			5	1	
	Max			100	50	
P	Min			5	-0.1	
	Max			35	2	
Fe	Min				2	
	Max				30	
Y	Min					10
	Max					35
Ir	Min					30
	Max					60

Table 3-5 Table listing class recipe B for EDS feature mapping. Elements are listed with maximum and minimum threshold values.

3.3.5 U-Pb Geochronology

Geochronology is the temporal study of earthly and planetary materials by absolute or relative dating methods. More importantly, geochronology is concerned with understanding geologic time, when major event(s) occurred and the development and understanding of geochronometers. Absolute dating involves isotopic measurement of parent-daughter ratios of radiogenic isotopes to calculate the age of earth and planetary materials. Isotopes are atoms containing the same number of protons (Z) but different number of neutrons (N) making their atomic mass number (A) lighter or heavier. Radiogenic isotopes decay due to insufficient binding energy in the atom nuclide because of an excess of protons or neutrons. Decaying nuclides emit electromagnetic radiation in the form of three different types; alpha (α), beta (β) and gamma (γ or x-ray). The first observation radioactivity by Becquerel (1896) led to thorium decay experiments by Rutherford and Soddy at McGill University (Rutherford and Soddy, 1902). These

experiments formed the law of radioactive decay based on half-lives and the fundamental half-life equation (Equation 3.2).

$$N = Noe^{-\lambda t}$$

Equation 3-2 Half-life equation derived from the Rutherford and Soddy experiments on thorium decay.

The half-life equation states the concentration of parent atoms (N) is a function of the original concentration (No) to the natural log of the decay constant (λ) multiplied by time of decay (t). The decay constant is the rate of decay of a nuclide to half of its original concentration. The actual half-life ($T_{1/2}$) of the nuclide is represented by Equation 3.3. The half-life is the time it takes for half of the initial unstable isotope to decay. Different radiogenic nuclides have varying decay constants and as a result different half-lives. A list of half-lives for common radiogenic nuclides is listed in Table 3-5.

$$T_{1/2} = \frac{0.693}{\lambda}$$

Equation 3-3 Half-life equation where $T_{1/2}$ is the time for half of the parent isotope to decay to its daughter.

Parent Isotope	Decay Modes	Halflives (10^9 Years)	Daughter Isotope
^{40}K	e, β^+	11.9	^{40}Ar
^{40}K	β^-	1.39	^{40}Ca
^{87}Rb	β^-	48.8	^{87}Sr
^{147}Sm	α	106	^{143}Nd
^{176}Lu	β	36	^{176}Hf
^{187}Re	α, β^-	41	^{187}Os
^{232}Th	α, β^-	14	^{208}Pb
^{235}U	α, β^-	0.704	^{207}Pb
^{238}U	α, β^-	4.47	^{206}Pb

Table 3-6 Table of radiogenic parent nuclides and daughter products compiled by Faure and Mensing (2005).

Symbols α , β and e correspond to alpha, beta and electron capture decay.

Radiometric dating of geologic materials is concentrated around mineral and bulk rock isotopic concentrations. If, the isotope decay system is closed, it represents the accumulation of stable daughter isotopes equal to the number of decayed parent atoms. The half-life equation is reworked to reflect these systematic changes (Equation 3.4) where D is the final number of daughter atoms, D_0 is the initial number of daughter atoms and N is the number of parent nuclides. From this, time (t) can be calculated.

A

$$D = D_0 + N(e^{\lambda t} - 1)$$

B

$$t = \frac{1}{\lambda} \ln \left(\frac{D - D_0}{N} + 1 \right)$$

C

$$t = \frac{1}{\lambda_{238\text{U}}} \ln \left(\frac{^{206}\text{Pb}}{^{238}\text{U}} + 1 \right)$$

Equation 3-4 Half-life equations for radiometric decay of a parent isotope in a closed system (A). Equations B is the same but reformulated to find time (t). Equation C is the application of equation A to U-Pb decay chain of ^{238}U to ^{206}Pb .

Dating geologic materials requires several assumptions outlined by Faure and Mensing (2005):

1. The system is closed and no daughter or parent has been lost.
2. Environmental conditions do not affect the decay constant of the parent nuclide.
3. The initial daughter values are known, or a relative D_0 value can be applied via knowledge of the isotopic reservoir within the hosting material or system.

4. Daughter and parent isotopic measurements are accurate and representative of their respective materials and systems.
5. Secular equilibrium is reached indicating that daughter products measured are the result of the original parent and not an intermittent short lived decay component.

Crystallization, metamorphic and alteration ages are the focus for samples collected within the MRG. Given that the MRG is Archean, the time scale is hundreds of millions of years making the U-Pb decay system applicable. The U-Pb isotope system is unique, having two decay chains resulting from the decay of ^{235}U and ^{238}U to ^{207}Pb and ^{206}Pb . Isotopic data from both systems can be compared and plotted on a concordia plots: this is explained further in the data regression and plotting section. The system also allows for large spectrum of ages to be capture due to half-lives of ^{235}U and ^{238}U being 704 million and 4.47 billion years respectively. In addition, several silicate and phosphate minerals incorporate uranium and lead in to their crystal structure during crystallization. Their low common lead incorporation at the time of crystallization permits several silicate-phosphate mineral species to be used as geochronometers.

3.3.5.1 Datable Phases

3.3.5.1.1 Zircon

Zircon (ZrSiO_4) is a colourless, green, grey, red or brown tetragonal orthosilicate accessory mineral in igneous and metamorphic rocks and occurs as detritus in sedimentary rocks. Zircon has specific gravity of 4.2 and a hardness of 7.5 (Lima-de-Faria, 1994) with 4/m 2/m2/m symmetry. The unit cell is an ATO_4 structure formed by a dodecahedron of one zirconium coordinated by eight oxygen within six SiO_4 tetrahedra (Finch and Hanchar, 2003). The structure forms alternating edge sharing chains at dodecahedron margins parallel to the C axis (Speer, 1982). Theoretical elemental percent values of zirconium, silicon and oxygen are 49.77%, 15.32% and 34.91% respectively, however; the 4^+ cation site generally allows the incorporation of hafnium (~1.71%), REEs (<1.2%) (Speer, 1982), thorium (1-10,000ppm) and uranium (1 -12,000 ppm) (Belousova et al., 2002). These cation substitutions are reflected in the oscillatory crystal

growth of igneous zircon (Speer, 1982) while metamorphic zircons appear as overgrowths. Zircon's solid state stability temperature (1525-1550 C°) (Anseau et al., 1976) and low reactivity make it a robust geochronometer for various geological environments.

3.3.5.1.2 Monazite

Monazite is another accessory mineral primarily observed in igneous and metamorphic rocks. Detrital grains of monazite are identified in sedimentary rocks as well. Like zircon, monazite is a reddish-brown to brown orthophosphate exhibiting a similar APO_4 structure comprised of REEs (Ce, LREE, Th, Y) and phosphate (PO_4) in a monoclinic structure within a space group of $\text{P2}_1/\text{n}$ (Lima-de-Faria, 1994; Boatner, 2002). Monazite exhibits a stubby prismatic habit with a hardness of 5 to 5.5 (Lima-de-Faria, 1994). Unlike zircon, monazite contains an array of rare earth elements and is further classified into varieties based on 10% or more of the REE element in excess. Three varieties exist; Ce, La or Nd (Rosenblum and Fleischer, 1995). The cation slot hosting REEs is coordinated by nine oxygen forming a REEO_9 polyhedra (Ni et al., 1995). This larger nine oxygen coordinated site hosts light rare earth elements from La to Eu (Williams et al., 2007). Monazite's natural melting temperature by experimentation resulted in chemical stabilities up to $2057 \pm 40 \text{ C}^\circ$ (Hikichi and Nomura, 1987). Monazite's uranium concentrations range from 1,000 to 4,000 ppm in granitic rocks or as high as 14% (Kato, 1958). About 1 ppm common lead is incorporated into the monazite structure during crystallization. Monazite's low common lead incorporation coupled with its high temperature stability and low reactivity makes it a robust geochronometer (Parrish, 1990).

3.3.5.1.3 Xenotime

Xenotime ($\text{Y,HREE}\text{PO}_4$) is a yellow, greenish brown to reddish brown stubby to prismatic-pyramidal orthophosphate and accessory mineral in igneous and metamorphic rocks. Like monazite, xenotime hosts a APO_4 structure but is tetragonal and isostructural with zircon, categorized in space group $\text{I4}_1/\text{amd}$ (Ni et al., 1995; Boatner, 2002). Unlike monazite, xenotime has a REO_8 cation site surrounding the PO_4 tetrahedral units and

incorporates heavy rare earth elements with smaller ionic radii into its crystal structure due to lanthanide contraction (Lu-Tb and Y) (Ni et al., 1995). Theoretical xenotime endmembers are generally YPO_4 and HREE-PO_4 and are defined by molar percentages greater than 90%. Uranium concentrations range between 0-1.76% (Bea, 1996) with low common lead. Xenotime also has a high melting temperature of $1896-1995 \pm 20^\circ \text{C}$ reported by Hikichi and Nomura (1987).

3.3.5.2 LA-ICP-MS

Laser ablation inductively coupled mass spectrometry (LA-ICP-MS) is the same analytical technique as described previously with exception of sample introduction to plasma. A laser controlled by the operator vaporizes sample material and introduces the vaporized material to the plasma excitation energy. A Thermo VG PQ EXCELL quadrupole plasma mass spectrometer housed at the University of Toronto and operated by Dr. Don Davis was used in conjunction with an attached Nu-Wave UP-213 laser ablation microscope for U-Pb isotopic analyzes. A Nd:YAG deep UV (213nm) laser beam operating between 5 and 10 Hz ablated zones in zircon and monazite phases with spot sizes ranging between 8 and 12 microns in diameter depending on size and type of phase. Mineral grains subjected to ablation incurred a 10-20 μm square 1 μm deep raster prior to pitting to remove any impurities. Laser ablation pitting commenced after rastering on selected mineral grains of zircon and monazite from polished thin section samples 6225 and 6220A. After three mineral grain analyses, a standard was analyzed and the sequence repeated.

3.3.5.3 Data Regression and Plotting

LA-ICP-MS analysis provided isotopic measurements in counts per second of ^{206}Pb , ^{207}Pb , ^{238}U and ^{232}Th . The counts per second were compared to known age standards of the same mineral type and to a calibration standard prior to ablation. This technique is used to reduce the effects of fractionation during analysis. Ratios of $^{207}\text{Pb}/^{235}\text{U}$ and $^{206}\text{Pb}/^{238}\text{U}$ were calculated by regression software developed by Dr. Davis. Regressed data provided the $^{207}\text{Pb}/^{235}\text{U}$, $^{206}\text{Pb}/^{238}\text{U}$ and Th/U ratios in Excel spreadsheets. An addin Excel program called Isoplot was used to plot U-Pb isotopic ratios on concordia

plots with 2 sigma error ellipses. The program regressed an mean sum weighted deviation (MSWD) as well.

The concordia plots used are a comparison plot of isotopic ratios of $^{206}\text{Pb}/^{238}\text{U}$ to $^{207}\text{Pb}/^{235}\text{U}$. Originally designed by Wetherill (1956), the graph has a concordant line representing equal ages of the two geochronometers. Analyses plotting below the concordant line are discordant and have lead loss while plots above are negatively discordant and have incurred uranium additions or mass fractionation.

Chapter 4 Mapping, Drill Core Logging & Petrography

4 Introduction

This chapter presents and illustrates the results from mapping, drill core logging, petrographic examination and electron microprobe analysis on minerals from; footwall, ore zone and hangingwall lithologies of Deposit No.1. Rock identification and classification is a culmination of outcrop mapping, core logging, and petrography supported by EDS phase scanning and WDS point analysis.

4.1 Mapping & Drill Core Logging

Detail 1:2000 scale mapping of Deposit No.1, was conducted by the author, M.E. MacLeod and I.D. Herbranson during the summer of 2014. Previous ore zone mapping was completed by Paul Lindberg in the summer of 2011. In addition, a total of 15 drill holes penetrating the footwall, ore zone and hangingwall were logged by the author. On the basis of outcrop mapping and drill core logging, seven distinct units were identified in the western footwall of Deposit No.1. These units are quartz-augen muscovite-biotite schist, biotite schist, chlorite schist, altered silicified granitoid, monzogranite, syenogranite and metagabbro. Ore zone units are divided into BIF, enriched BIF (EBIF), magnetite ore, magnetite-hematite ore, hematite ore and chlorite schist. Hanging wall units are classified as volcanoclastic, ultramafic, ultramafic amphibolite, hornblende-amphibolite, mafic volcanic, biotite schist and chlorite schist. The hanging wall, ore zone and footwall units are plotted in Figure 4-2. Units intersected in drill holes are also plotted in plan view. Cross-sections of the southern and northern limbs constitute Figures 4-4 and 4-5. Drill hole MR1-12-226 is the best intersection of HGIF and footwall units and is plotted in Figure 4-6.

4.1.1 Footwall Units

Quartz-augen muscovite-biotite schist (QAMBS) is the dominant unit in the immediate footwall of Deposit No. 1. QAMBS ranges from 10 metre thick zones in the northern limb to 500 metre thick zones in the southern limb. Detailed mapping and drill core demonstrate the schist trends north-south from the northern saddle before wrapping

around the southern limb. QAMBS extends to the south limb extension and terminates at the pump station 2 (PS2-site) iron ore exposure. Contacts are gradational between quartz-augen muscovite, quartz-augen biotite, biotite and chlorite schists in both outcrop and drill core. Contacts with respect to altered-silicified granitoid and monzogranite and syenogranite are sharp to gradational, defined by the appearance of foliated muscovite or biotite. The QAMBS unit sharply contacts banded iron formation on north limb and at the PS2 site.

Nineteen representative samples were selected from drill core and four from exposed outcrop. Twenty-one polished thin sections and two oriented polished thin sections were prepared for petrographic examination. QAMBS is characterized by millimetre to centimetre size quartz augens accounting for 25-40% of the modal abundance. Quartz-augens form penetrative lineations and form a undulating foliation defined by muscovite and biotite (50-75%)(Plate 4-1). Large 1-5 cm porphyroblasts of cordierite, staurolite, andalusite and minor garnet overgrow the foliation.

The QAMBS lithology is subdivided into two end members, quartz-augen muscovite schist (QAMS) and quartz-augen biotite schist (QABS) according to the dominating mica at the 75% margin (Table 4-1). Quartz-augen mica schists whose matrix component lies between 25-75% biotite are deemed QAMBS. QAMBS schist comprises approximately ~75% of the quartz-augen mica schist body.

Unit	Abundance Muscovite	Abundance Biotite	Mica in Matrix
QAMS	≥ 75%	≤ 25%	≥50%
QAMBS	25-75%	25-75%	≥50%
QABS	≤ 25%	≥ 75%	≥50%

Table 4-1 Subdivisions of QAMBS unit based on modal mica concentrations.

QAMS occurs as 1-50 metre thick beige coloured lenses dominated by fine to medium muscovite containing greater than 75% muscovite (mica component) enveloping lineated quartz augens. These units contain large cordierite porphyroblasts that range between 2 and 10 cm in diameter. QAMS units do not contain porphyroblasts of staurolite, garnet or amphibole. Quartz-augen biotite schists have greater than 75% biotite. These units gradationally contact chlorite and biotite schists within proximity (~50 m) of iron ore formation. QABS units contain 1-10 cm porphyroblasts of staurolite, garnet, andalusite, and garbenschiefer cummingtonite-grunerite.

LEGEND



Figure 4-1 Map legend for Figure 4-2.

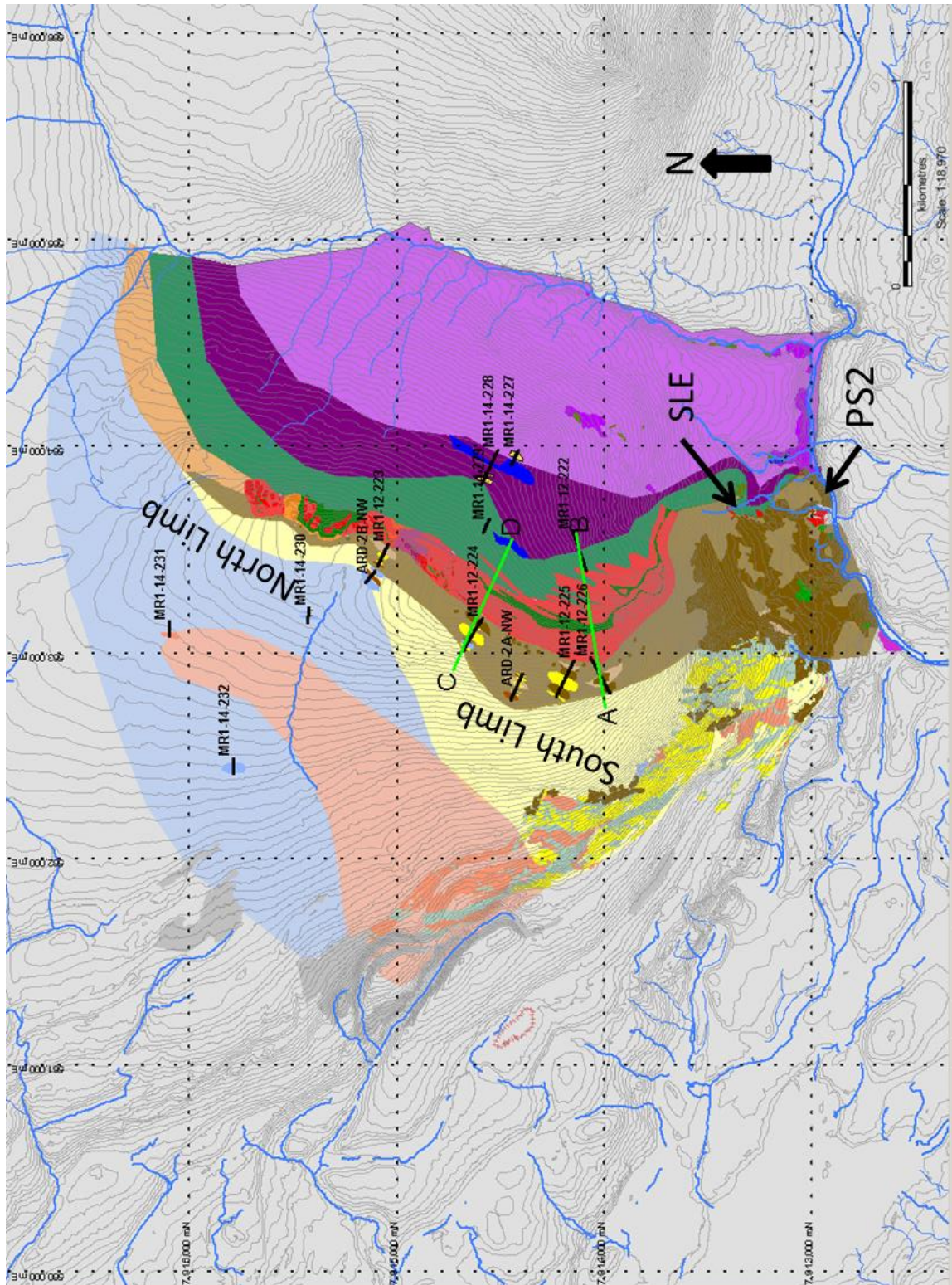


Figure 4-2 Geological map of Deposit No.1 at a 1:2000 scale. Drill hole collars, traces and projected lithology are also plotted. Major geomorphological zones, north limb, south limb, south limb extension (SLE) and Pump Station 2 are labeled. QAMBS unit also include QABS units.

LEGEND

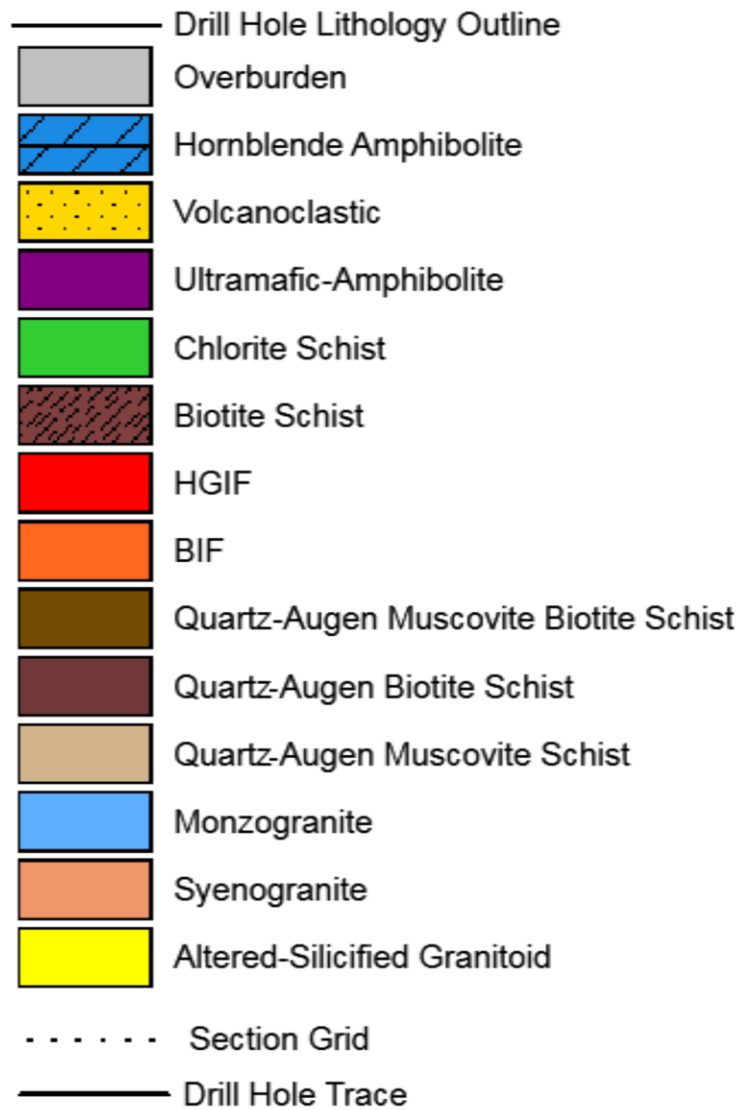


Figure 4-3 Legend for cross-sections in Figures 4-4 and 4-5.

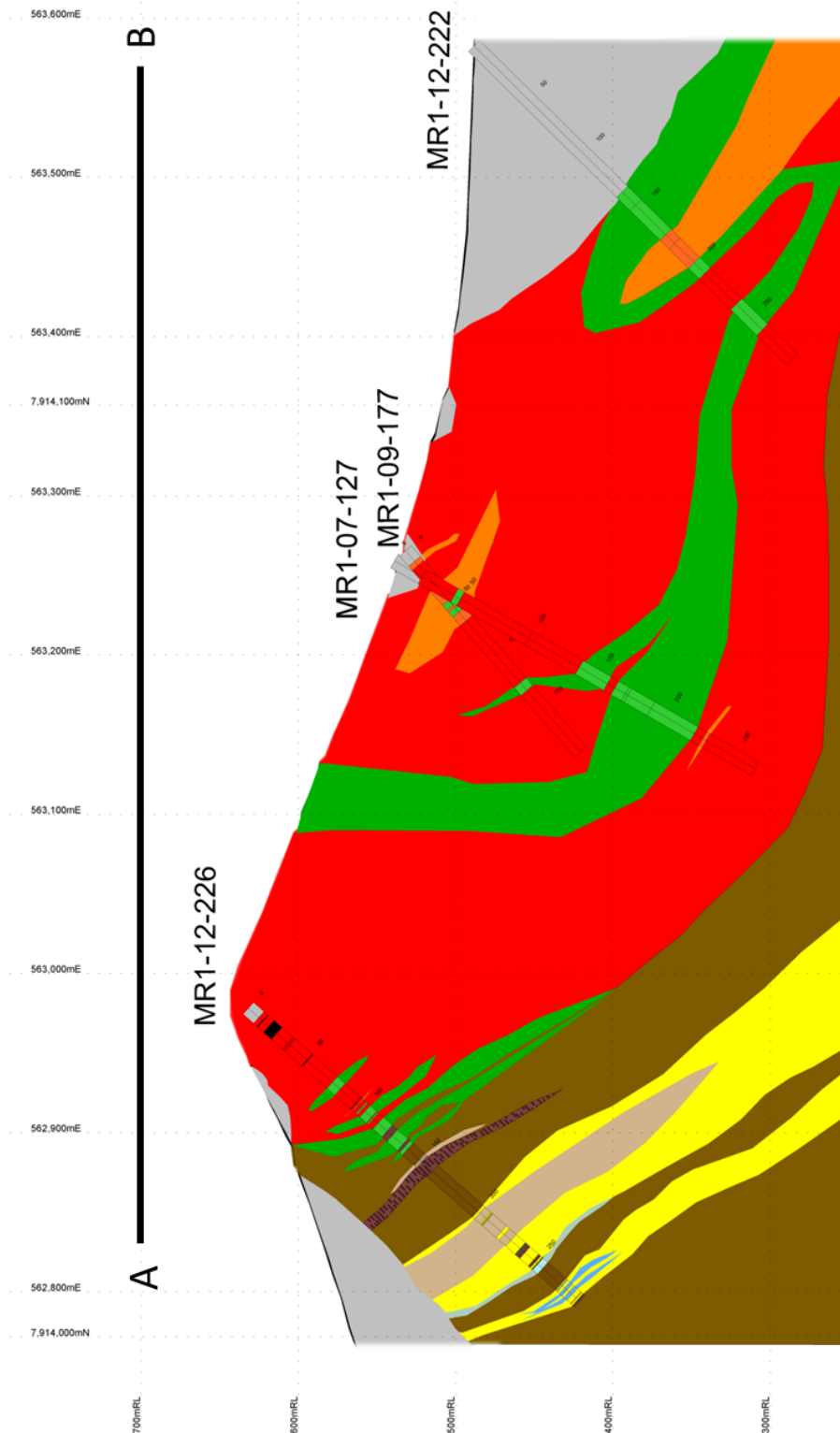


Figure 4-4 Cross-section A-B across the southern limb. Drill holes MR1-07-127 and MR1-09-177 are added from the BIMC database for continuity. Section plan faces 350° and encompasses a 50 metre wide envelope.

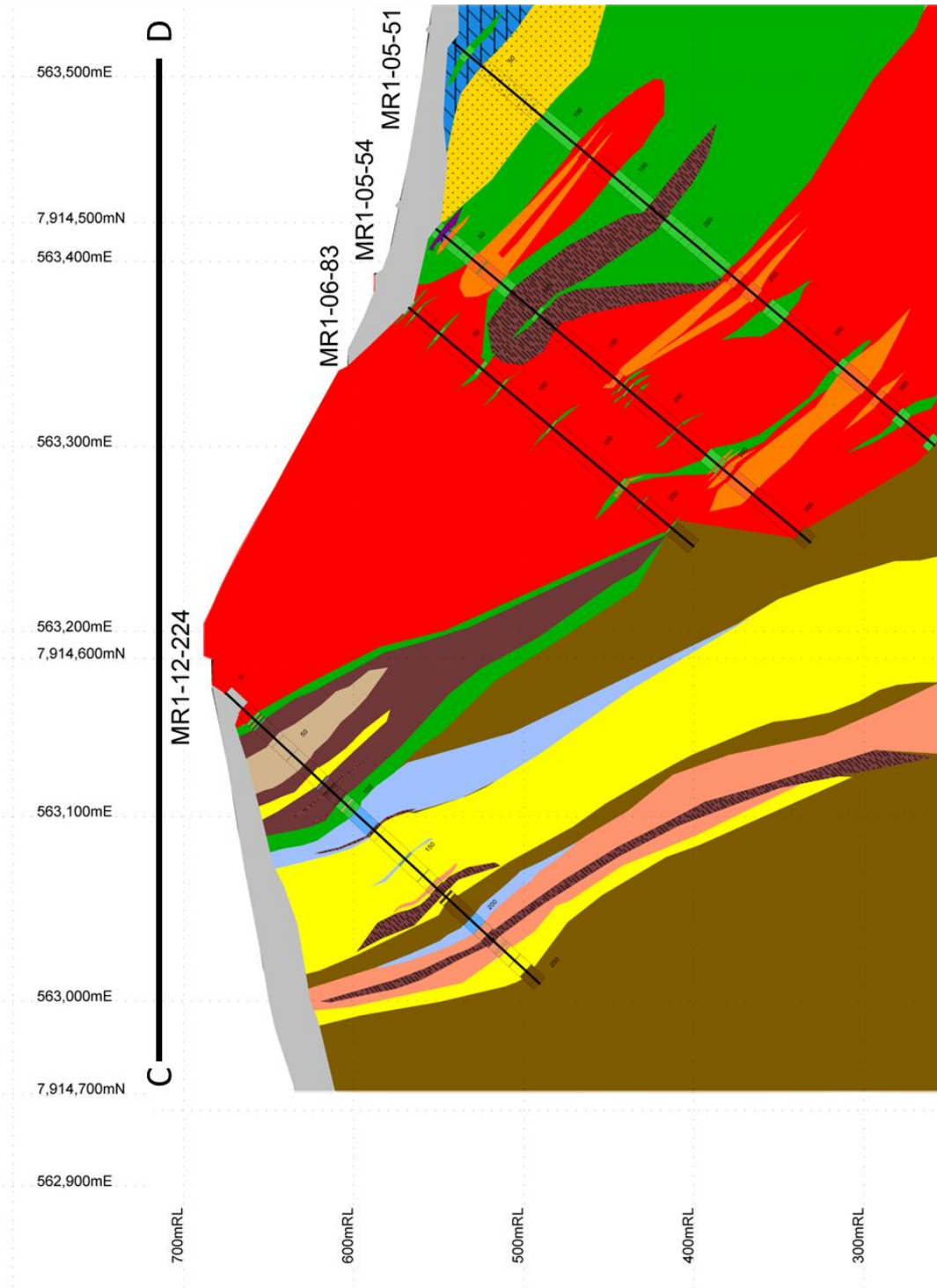


Figure 4-5 Cross-section C-D across the northern limb. Drill holes MR1-06-83 MR1-05-51 and MR1-05-54 are added from the BIMC database for continuity. Section plan faces 025° and encompasses a 50 metre wide envelope.

Altered-silicified granitoid (ASG) is the most prominent unit next to QAMBS. ASG forms massive 12-200 metre thick white-grey to pinkish panels with 1-3 metre interior lenses of syeno to monzogranite. ASGs extend northeastward along the footwall of the southern limb. Lenses of ASG are observed in the QAMBS units south of the southern limb and are also intersected by drill holes MR1-12-22, 224, 225 and ARD-2A-NW and SE. Both ASG outcrops and drill core show gradational contacts to quartz-augen schist and biotite schist (Plate 4-2). Commonly, ASG exhibits millimetre to centimetre quartz and mica lineations. Pink coloured ASG units occur at syenogranite contacts and are sub-classified as ASGr. Five ASG and six ASGr samples were collected from outcrop and drill core. Four polished thin sections were prepared from ASG samples.

Footwall chlorite schists are unique units forming 1-15 metre thick margins to HGIF or as 1-3 metre lenses in biotite and QABS units. In outcrop, chlorite schist sharply contacts HGIF. Drill core also demonstrates distinct well defined contacts to HGIF which grade into biotite and QABS units. Seven samples were collected from outcrop and drill core and six polished thin sections were prepared. Chlorite schists are composed 80-90% green chlorite with large 1-10 centimetre porphyroblasts of staurolite, garnet and cummingtonite-grunerite (Plate 4-3). The coarsest porphyroblastic garnet-amphibole growth occurs at the PS2 site along the southern limb extension where garnets reach 20 cm in diameter.

Footwall biotite schists are honey to dark brown in colour and exhibit coarse porphyroblastic andalusite, staurolite and garnet growth. Biotite schist has no direct contact with HGIF. Biotite schists form 1-5 metre thick zones with gradational contacts to chlorite schist and QAMBS units. Both biotite and chlorite schist have relict quartz-augens. Foliation is lost closer to iron ore creating biotite and chlorite masses. A total of 11 biotite schists were sampled, all from drill core with exception of outcrop sample 15933.

Three intrusives are juxtaposed to footwall schists: monzogranite, syenogranite and metagabbro. Monzogranites are medium quartz-K-feldspar-plagioclase crystalline with lesser biotite and minor actinolite-hornblende. Monzogranites occur as unaltered 1-5

metre pods within the eastern ASG units and in drill core contacting ASG and QAMBS units. Infrequently, 1-5 cm wide epidote-carbonate-hornblende veining cross cuts this unit (sample 6519). Condemnation drill hole MR1-14-232 intersects the western most extent of known monzogranite.

Syenogranites vary textually from medium to coarse grained and from red-pink to white in colour. Red units are almost entirely composed of K-feldspar and classified as alkali-feldspar granite. Pink to white coloured syenogranite contains appreciable amounts of quartz. The two are mapped as one unit because they occur together and are impossible to segregate at a 1:2000 scale (Plate 4-3). The name syeno for the group is adopted because the syeno-type composes over 80% of the abundance. Syenogranite occurs as 1-5 metre pods within ASGr units 500 metres west of the QAMBS contact. A few outcrops show sharp contacts crosscutting monzogranite. Syenogranite shows gradational contacts up to ASGr units. Their extent continues westward changing from pods to massifs. Five monzo and syenogranite samples were collected from outcrop and drill core, five thin sections were prepared.

Metagabbro exists southwest of the southern limb and trends northwest into syenogranite. The unit grades west from lineated hornblende-amphibolite with biotite margins to plagioclase-amphibole-pyroxene gabbro. Pods of 1-2 m coarse gabbro are identified in central portions of the unit. The metagabbro is denoted as an intrusive because of its cross cutting contacts to both monzo and syenogranite (Plate 4-2B). Thirteen samples were collected, 11 from outcrop and two from drill core.

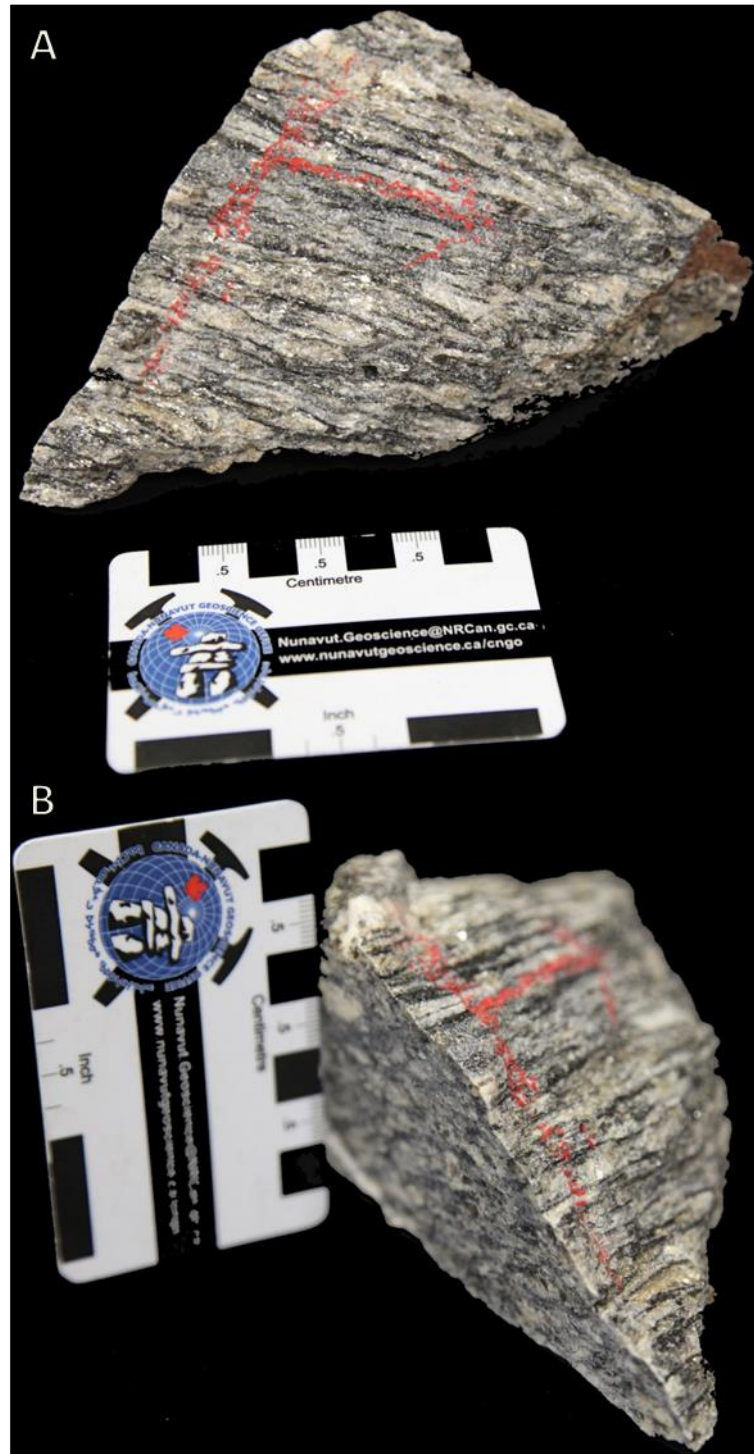


Plate 4-1 Photographs of oriented QAMBS sample 6534. Photograph A shows parallel orientation to strong biotite, muscovite foliation and lineated quartz-augens. B is perpendicular to lineation and illustrates rodded texture.

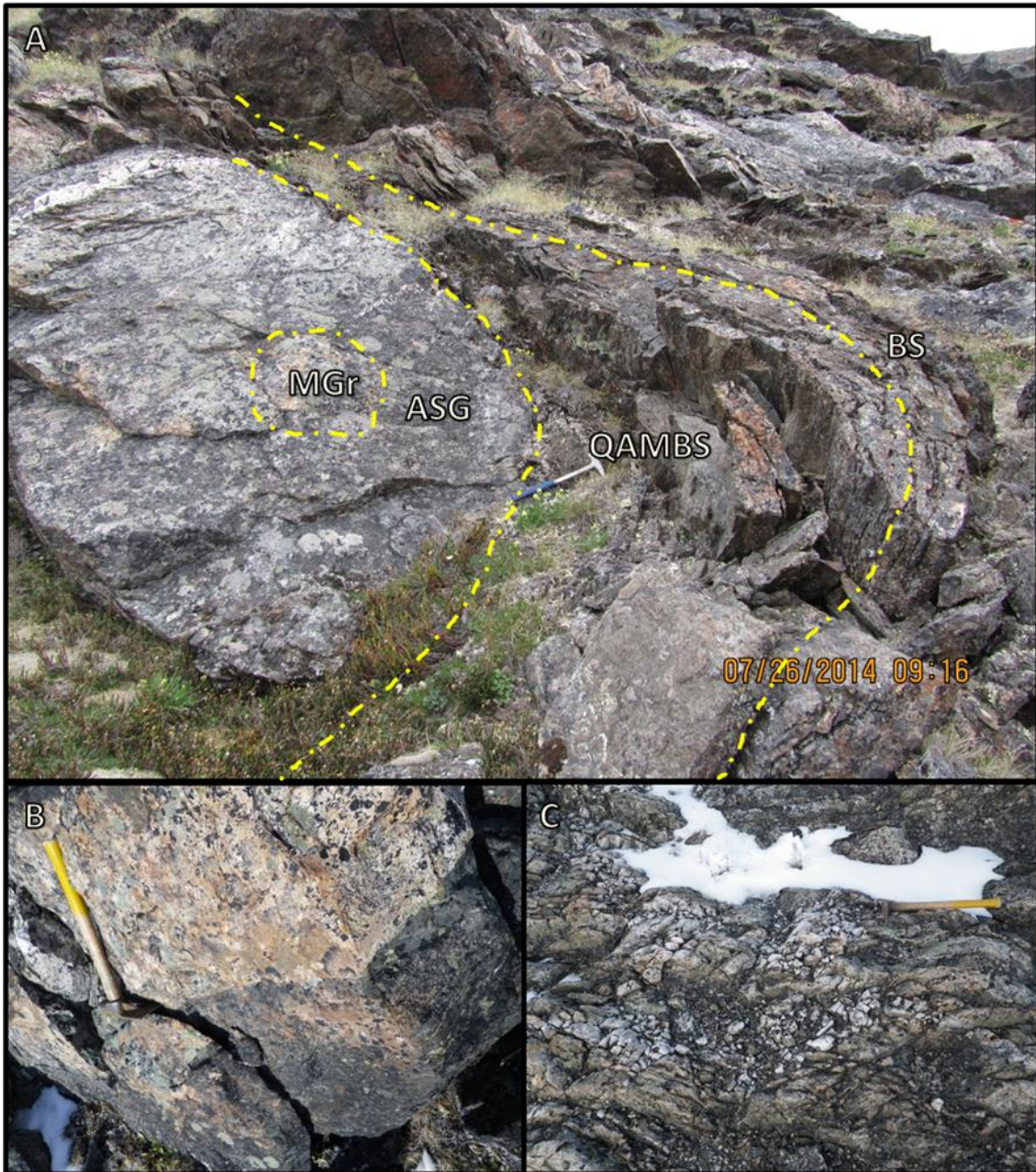


Plate 4-2 Photographs of footwall outcrop contacts. A is an annotated outcrop showing a central pod of monzogranite (MGr) in an altered-silicified granitoid (ASG) contacting quartz-augen muscovite-biotite schist (QAMBS) which contacts biotite schist (BS). Contacts marked by yellow dashed line are gradational. Photograph B shows hard contact of mafic intrusive to syenogranite. Photograph C shows pods of monzogranite in ASG outcrop.



Plate 4-3 Outcrop photos of Deposit No.1 footwall lithologies. Photograph A is example of the fresh unweathered surface of QAMBS. Photographs B and C illustrate a fresh face of alter-silicified granitoid sample and weathered syenogranite outcrop. Garnetiferous chlorite schist is depicted in photograph D while E is an example of the mafic intrusive with cm size hornblendes. Photograph F shows acicular grabenschiefer grunerite in chlorite schist near south limb extension (hammer used for scale).



Plate 4-4 Plate of outcrop photographs from the footwall and hangingwall of Deposit No.1. A is an photograph of lined hangingwall mafic volcanics. QAMS outcrop with cordierite porphyroblasts is pictured in B. I.D. Herbranson measures dip of fold limb, photograph is facing west. Photographs D and E show the only known conglomerate outcrop. The outcrops shows muscovite and biotite schist with giant cordierite porphyroblasts and chlorite-amphibole pods. Silica flooding into monzogranite pictured in F.

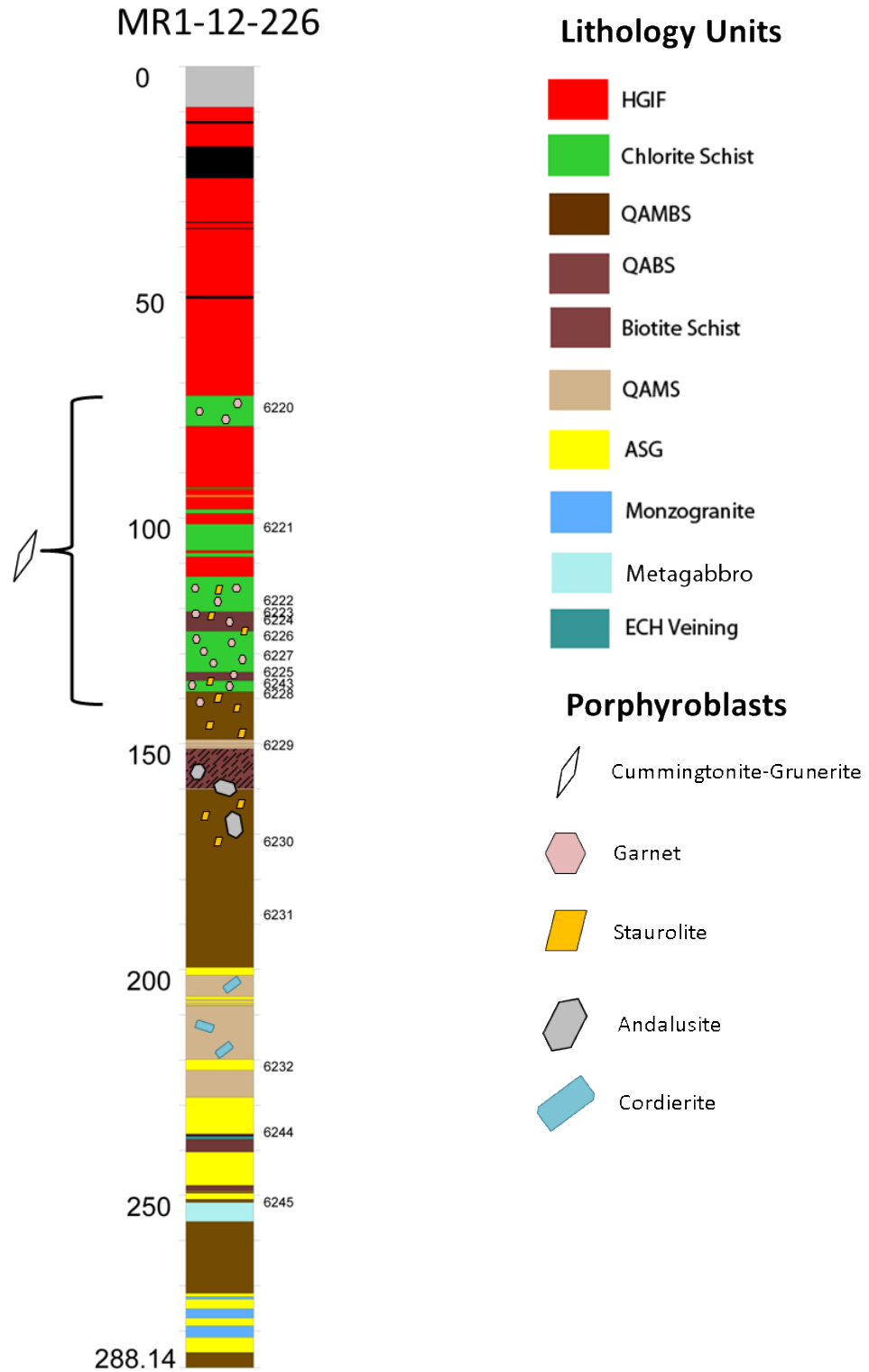


Figure 4-6 Lithologic log of hole MR1-12-226. Drill hole represents ideal footwall example as it was the only hole to fully contact HGIF and footwall units. Lithologies and metamorphic porphyroblasts are depicted. Samples are labeled on the right side of the column at their corresponding depth.

4.1.2 Ore Zone Units

The ore zone is defined by the extent of massive high grade iron formation and its intercalated lithologies. High grade iron ore is defined as iron formation upgraded from banded iron formation to a total Fe content exceeding 50%. Enriched banded iron formation (EBIF) and the three iron ore types: magnetite ore (MO) magnetite-hematite ore (MHO) and hematite ore (HO), comprise HGIF. Iron ore comprises 80-90% of the Deposit No.1 ore zone. Intercalated lenses of BIF, enriched banded iron formation and chlorite schists form the remaining ore zone units. Deposit No.1 HGIF forms folded tabular bodies averaging 327 metres thick in the southern limb to 236 metres thick in the northern limb. Tabular HGIF bodies dip 54° degrees in the southern limb and 65°-70° in the northern limb. Deposit No.1 has a strike length of 2.2 km oriented north-northeast.

Chlorite schists make up the main secondary ore zone unit forming 1-10 metre lenses sharply contacting iron ore, EBIF and BIF. Chlorite schist contacts are coplanar to relict BIF banding. A large chlorite schist zone exists in the central portion of the deposit, averaging 50 metres thick. Green chlorite and lesser cummingtonite-grunerite lathes make up the matrix. Garnet porphyroblasts (1-5 cm) overgrow the chlorite matrix.

Three ore types are classified based on mineral abundance and type, not total iron content as this is a reflection of iron oxide mineral abundances. Ore types identified by drill core logging and mapping are magnetite (MO), magnetite-hematite (MHO) and hematite ore (HO). The three iron ore types transition seamlessly into one another. Iron ore textures are massive with lenses of brecciated and relict BIF. Magnetite ores are composed of granoblastic magnetite. Magnetite-hematite ores are composed of granoblastic magnetite with interstitial hematite and small pore spaces. Hematite ores are porous with millimetre vugs. The southern limb hosts the most granoblastic hematite ore than any other area of Deposit No. 1. The northern limb shows a gradational shift of HGIF to BIF. Specularite ore is a fourth ore type and is isolated to the saddle zone. Specularite ore is not observed anywhere else at Deposit No.1 and is not considered a major component. Four surface grab samples of hematite ore were collected from the collar area of drill hole MR1-14-226. All other iron ore samples are selected from MacLeod (2012).

4.1.3 Hangingwall Units

Hanging wall units are poorly exposed and mainly interpreted from drill core. Outcrops of ultramafics are predominant east of Deposit No.1 with five and three occurring south of the deposit. Ultramafics (UM) are completely serpentized and crosscut by carbonate veins and patches. Ultramafics intersected in drill core grade into zones exhibiting patchy talc overprints. Ultramafics sharply contact hornblende-amphibolites and show semi-gradational contacts against ultramafic-amphibolite (UA) units. Ultramafic-amphibolite is composed of 75-90% garnet-schist anthophyllite. UM and UA units also grade into chlorite schist and sharply contact BIF and HGIF in drill holes MR1-05-54 & MR1-14-228.

Mafic volcanics are not observed in drill core but outcrop east of the deposit as fine to medium grain basalts with patchy chlorite overprints and biotite lineations. A hornblende-amphibolite with similar in texture is recognized. Hornblende amphibolites, identified by Jackson (1966; 2000) as gabbro, sharply contact ultramafic and ultramafic-amphibolites and are composed of medium to coarse grained hornblende (60-80%), plagioclase (15%) and biotite (5-10%).

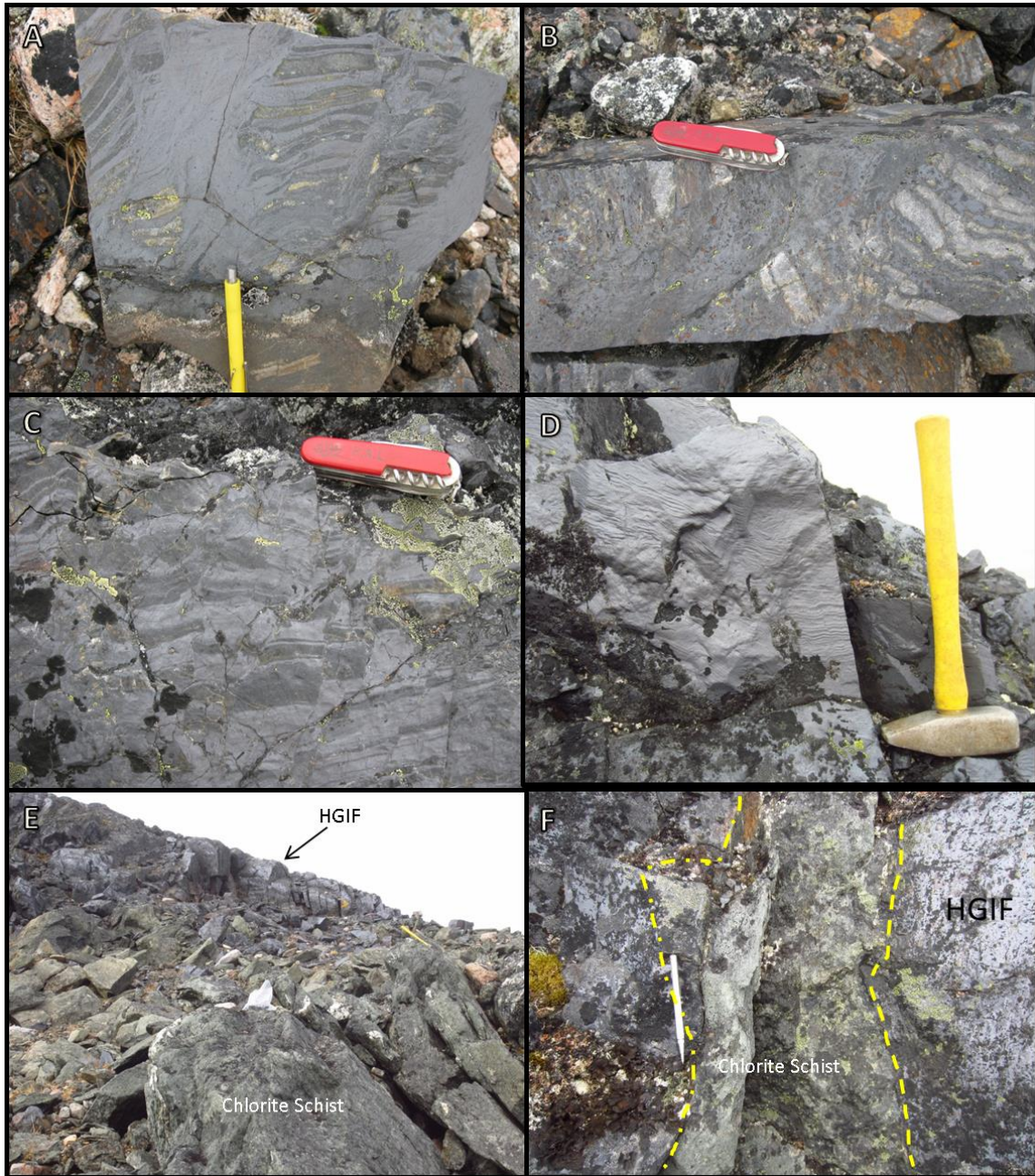


Plate 4-5 Plate of various HGIF contacts and textures at Deposit No.1. Photographs A and B show magnetite veining cross cutting banded iron formation banding. Brecciated and altered BIF is pictured in C. Photograph D is an outcrop of magnetite ore exhibiting relict banding. E and F show outcrop contacts with respect to chlorite schist (hard contact denoted by yellow dashed line). Photos A, B and C are courtesy of Paul Lindberg.

4.1.4 Polyphase Deformation

Polyphase folding is best defined in the southern footwall of Deposit No.1 where it produces an egg-crate pattern of deformation. F_1 - F_2 folds show a WNW-ESE axial plane orientation. Late F_3 fold overprints are dominant and have an axial plane oriented NNE-SSW. Dome-basin pattern outcrops are the result of interference folding between the F_1 - F_2 and F_3 fold generations. Extension on F_3 corrugates contacts of gabbro, granitoids and ASG units (Plate 4-7). The polyphase folding domain transitions to only F_3 -type folds 500 meters west of the QAMBS contact to HGIF. Folding ceases 1 km west of HGIF.

Strong penetrative lineations cross cut both fold axes in all footwall units at a rake of 074° and plunge of 54° (Figure 4-6). Lineations within the QAMBS unit diverge mildly, most notably in dome shaped outcrops (Plate 4-7A). QAMBS lineations are 0.3-3 cm sigma shaped quartz-augen porphyroclasts or biotite-muscovite patches. Oriented QAMBS samples 6534 and 6535 show bottom up top down sense of extension-shearing from sigma shaped quartz-augen porphyroclasts (Figure 4-7). Altered-silicified granitoids contain 0.1-0.3 mm biotite lineations that transition into 0.2-2 cm quartz-augen lineations (Figure plate 4-6). Meta-gabbro also contains strong hornblende lineations traceable throughout its extent (Plate 4-6).

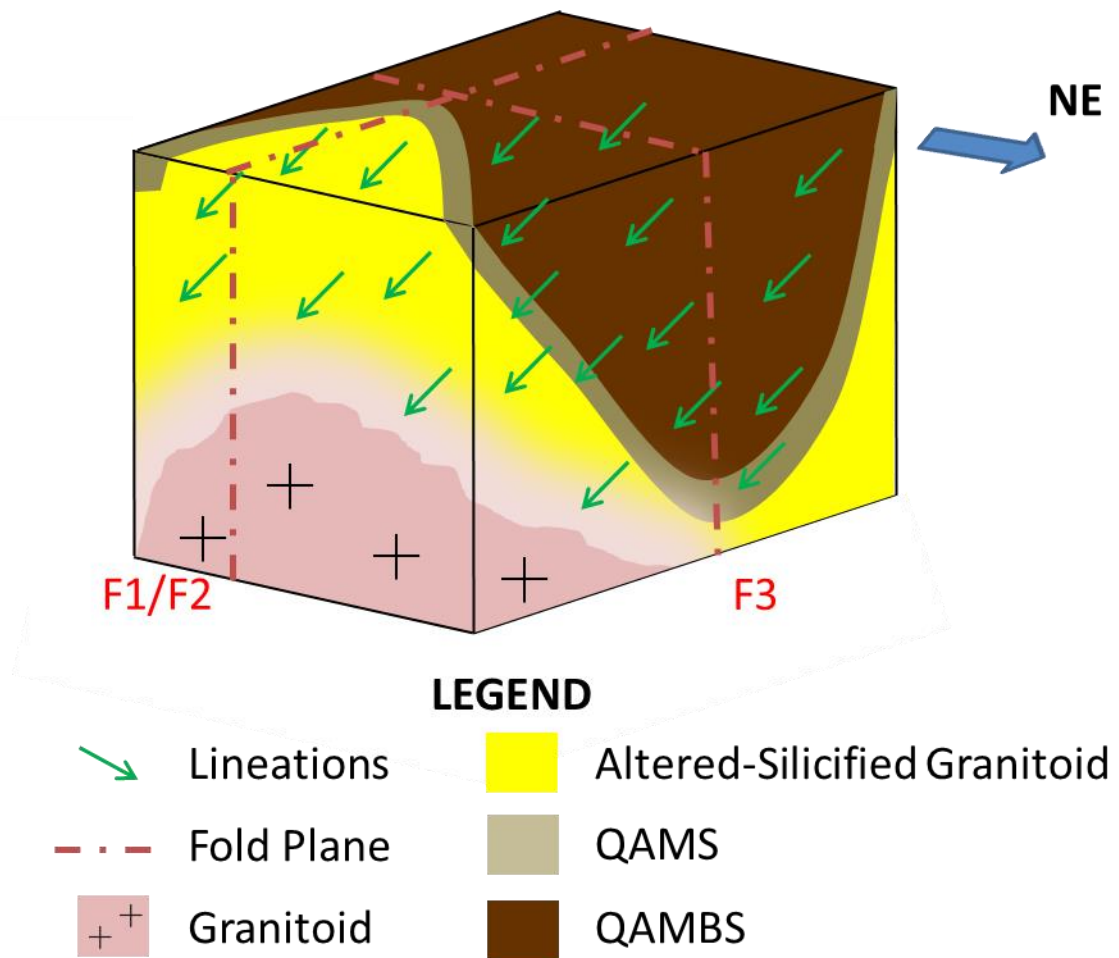


Figure 4-7 Structural deformation model of Deposit No.1 footwall. Fold planes and lineations plotted over volume of granitoid, altered-silicified granitoid (ASG), quartz-augen muscovite schist and quartz-augen muscovite-biotite schist.



Plate 4-6 Footwall outcrop photographs of lineations. Photographs A and B are of lineated ASG units with B showing the development of quartz augens. C and D are lineated quartz-augens and mica in QAMBS units. Biotite lineations in weathered monzogranites are pictured in E. Photograph F is a close-up shot hornblende lineations in a metagabbro outcrop.

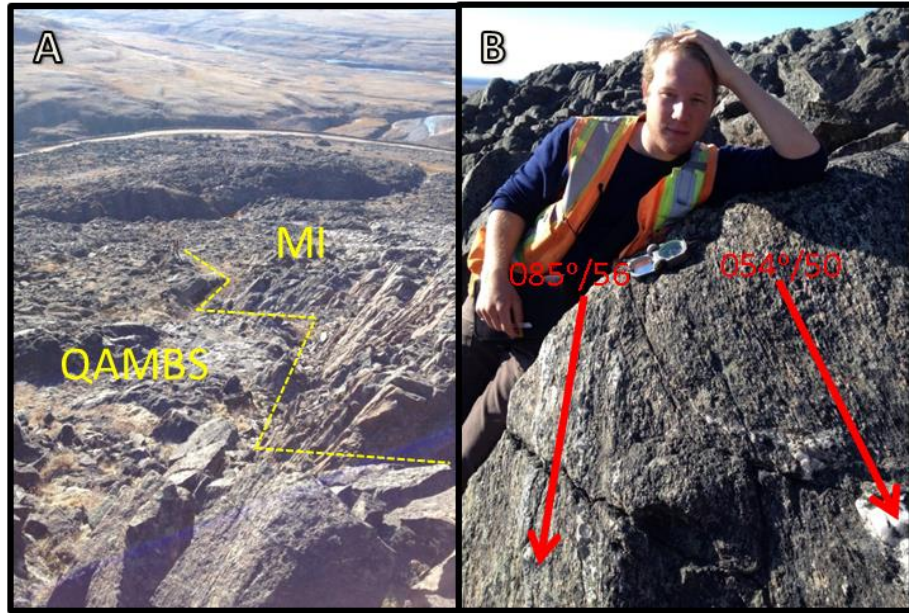


Plate 4-7 Structural footwall outcrop photographs. Yellow dotted line in A shows corrugated contact between quartz-augen muscovite biotite schist (QAMBS) and mafic intrusive. Lineations in red are plotted on domal outcrop of QAMBS.

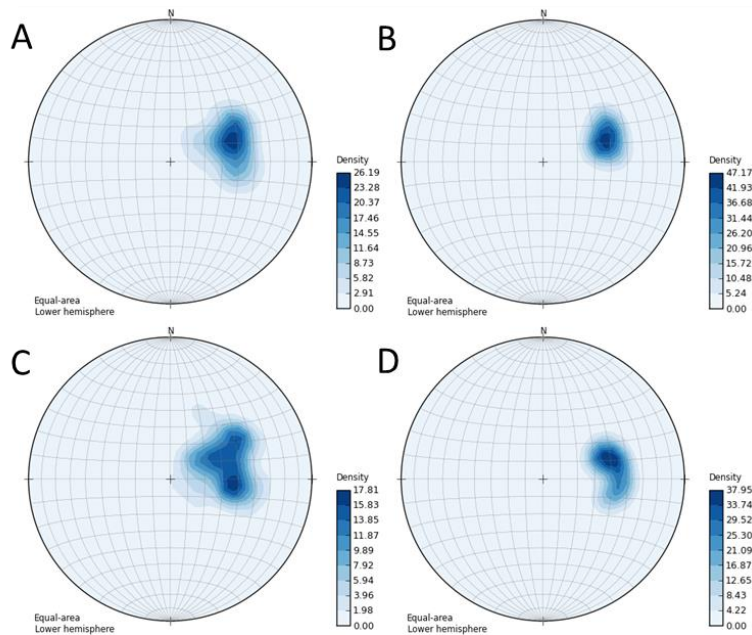


Figure 4-8 Contoured lower hemisphere equal-area stereonet plots of lineations in footwall units measured by DGPS. Lineations are plotted with Openstereo software (Grohmann and Campanha, 2010). Stereonet A is combined plot of all three units totalling 65 measurements. Stereonets B, C and D are of lineations from mafic intrusive, QAMBS and ASG outcrops. Lineaments within all footwall units were measured by a differential global positioning system to negate the high magnetic interference of HGIF.

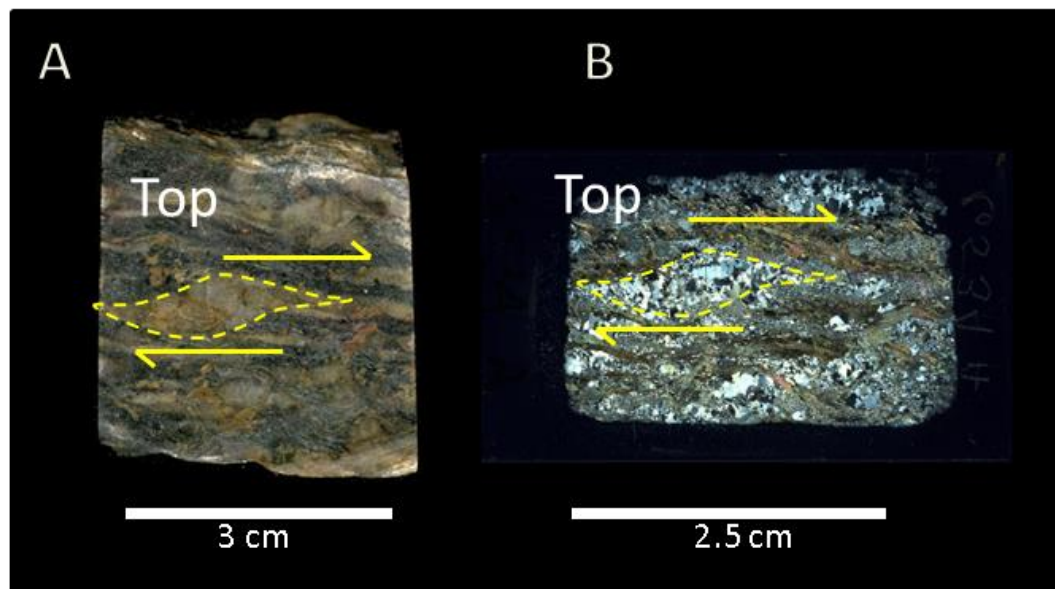


Figure 4-9 Photographs of oriented sample 6534. Left photograph (A) is of a QAMBS quartz augen with a bottom up top down sense of shear. Right photograph (B) is XPL scan of the polished thin with the same sense of shear.

4.2 Deposit No. 1 Petrography & EMP Analysis

Mapped units are described in detail on the basis of microscopic examination using combined transmitted and reflected light techniques. Electron microprobe (EMP) analyses of related mineral grains and their derived chemical formulas are presented for each unit.

4.2.1 Footwall Lithologies

Diamond drill core drilled during the summer field seasons of 2010, 2012 and 2014 was logged and sampled by the author. Drill hole cross-sections are plotted in Figures 4-2 and 4-3. A stratigraphic section is presented in Figure 4-6. Drill core samples were collected from acid rock drainage drill holes (ARD) along the footwall of Deposit No.1 and from condemnation holes west of the Deposit No.1 iron ore body. Grab samples were also collected from footwall outcrops. Oriented samples from two footwall QAMBS outcrops contacting the HGIF were sampled and polished thin sections prepared from them.

4.2.1.1 Monzogranite

Monzogranites (MGr) have an interlocking medium white-grey 0.5-3 mm hypidiomorphic granular texture averaging 42-47% quartz, 25-32% K-feldspar, 15-20% plagioclase, 2-8% biotite, 0-2% magnesiohornblende, and 1% chalcopyrite-pyrite (Plate 4-8 and 4-9). Normalized quartz, plagioclase and alkali feldspar abundances are plotted in Figure 4-10. Representative samples from drill holes MR1-14-230 and MR1-14-232 show fracturing and brecciation. Sample 6073 is the closest discernable monzogranite to high grade iron formation and exhibits mild patchy biotite lineations. Linear 1-5 mm wide epidote-carbonate-hornblende veins with allanite inclusions occur in sampled 6073 and 6519. Fine grain 0.01-1 mm granoblastic quartz occurs interstitially or as inclusions within plagioclase. Fine-medium grain plagioclase are 0.01-1mm subhedral to euhedral oligoclase and labradorite exhibiting moderate to strong polysynthetic twinning. Composition of twinned labradorite and oligoclase was determined by the Michel Levy technique. Anorthosite compositions of plagioclase ranged between 55% and 62% and 15%-26% An (Figure 4-11). K-feldspar forms cloudy 0.1-0.5 mm subhedral blocks with inclusions of biotite and apatite. Microcline comprises the majority of alkali feldspars, averaging 10-15% of the modal composition. Biotite occurs as 0.1-1 mm dark brown lathes with strong basal cleavage. Compositionally, biotite ranges between 15.29% - 17.73% FeO from ten WDS EMP analyses. The average biotite formula was calculated to be $K_{1.94}(Fe_{2.06}Mg_{2.84})(Ti_{0.13}Al_{1.03})[Si_{5.54}Al_{2.0}O_{20}](OH,F_{0.01})$. Hornblendes range between 0.05-1.2 mm in size as subhedral tablets and lathes interlocking with plagioclase quartz and biotite (Plate 4-9B). Hornblende also occurs within veins with carbonate and epidote. Hornblendes compositionally averaged $(Na_{0.22}K_{0.1})Ca_{1.91}(Mg_{2.98}Fe_{1.66})Si_{7.05}Al_{1.35}O_{22}(OH)_2$ on the basis of ten WDS analyses and are classified magnesio-hornblende (Figure 4-12). Actinolite is also observed altering biotite with chlorite. Euhedral 100-200 μ m zircon and titanite are common. Chalcopyrite averages 100 μ m in size and is subhedral to euhedral cubes with pyrite-sphalerite margins.

4.2.1.2 Syeno & Alkali-Feldspar Granite

Alkali granite is subdivided by colour and proportions of alkali feldspar (Figure 4-10 and Plate 4-8). Syenogranite is composed of medium to coarse milky white to pink feldspar with biotite patches. Hypidiomorphic textures are defined by medium interlocking plagioclase (10-15%), orthoclase (30-35%), microcline (20-25%), quartz (30-35%), biotite (2%) and muscovite (2%) (Plate 4-8 and 4-9). Accessory minerals include pyrite (0.5%) and chlorite (0.5%). Plotting normalized quartz, plagioclase and alkali feldspar abundances classifies these white to pink granites as syenogranites (Figure 4-10). K-feldspars are anhedral to subhedral 0.5-2 mm blocks with quartz and muscovite inclusions. Orthoclase exhibits mild exsolution and pericline twinning textures while microcline is moderately tartan twinned. Plagioclase form 0.3-1 mm lathes with moderate to strong polysynthetic twinning and is commonly overprinted and encased by orthoclase. Plagioclase was determined to be oligoclase, averaging $\text{Na}_{0.85}\text{Ca}_{0.14}\text{Al}_{1.16}\text{Si}_{2.85}\text{O}_8$ from four WDS microprobe analyses. Polycrystalline quartz crystals are 0.1-0.8 mm crystals forming 2.5 mm intergranular clusters. Minor biotite and muscovite occur as 0.15-0.8 mm sub-euhedral lathes. Biotite is mildly chloritized.

Red granite is fine to medium grain polygonal texture orthoclase (40-50%), microcline (20%), quartz (29-30%), plagioclase (4-6%), biotite (0.5%) and muscovite (0.5%) (Plate 4-8 and 4-9). Sample 15940 had one 80 μm garnet. Plotting of normalized quartz, plagioclase and alkali feldspar abundances classifies red granite as alkali-feldspar granite (Figure 4-10). Orthoclase and microcline form 0.1-.5 mm anhedral to subhedral blocks and tablets while plagioclase are smaller 0.1-1.5 mm subhedral lathes. K-feldspars are altered by a patchy redish cloudy texture. Four K-feldspar WDS analyses averaged $\text{K}_{0.96}\text{Na}_{0.04}\text{Si}_{2.98}\text{O}_8$. Polycrystalline quartz ranges between 50-250 μm . Biotite forms 100-200 μm dark brown mottled lathes and tablets.

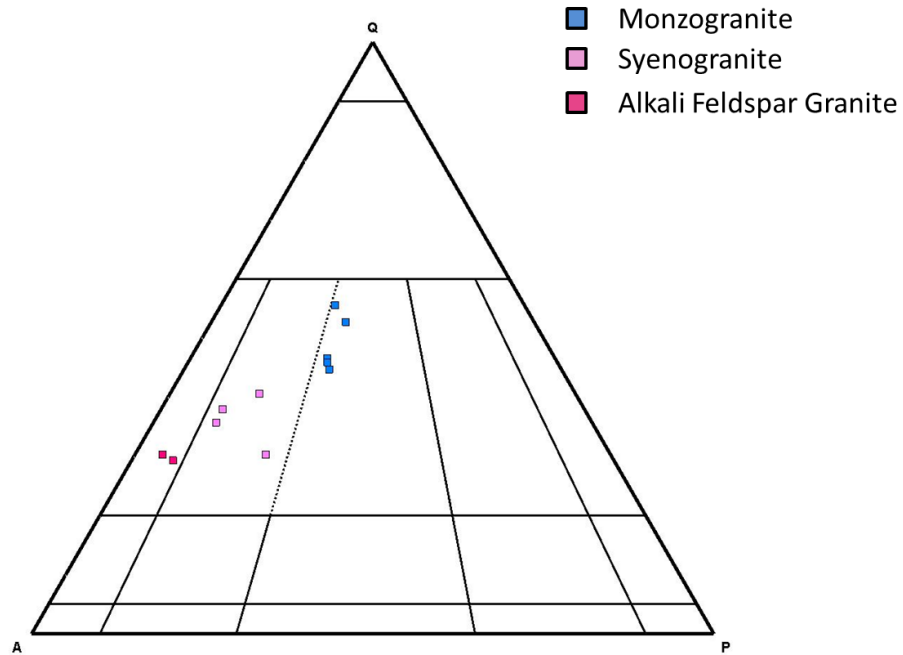


Figure 4-10 QAP diagram of Deposit No.1 footwall granitoids. Types are distinguished by colour.

Mineral Abundance Percentage							
Rock Type	Sample	Type	Quartz	Alkali Feldspar	Plagioclase	Mafics	Total
Monzogranite	6509	Core	42	32	20	6	100
Monzogranite	6518	Core	42	28	20	10	100
Monzogranite	6073	Core	45	33	20	2	100
Monzogranite	15920	Grab	43	27	20	10	100
Monzogranite	6519	Core	47	25	18	10	100
Syenogranite	6516	Core	30	50	19	1	100
Syenogranite	6517	Core	35	54	9	2	100
Syenogranite	15937	Grab	37	42	12	9	100
Syenogranite	15942	Grab	38	45	9	8	100
Alkali Feldspar Granite	15935	Grab	30	65	4	1	100
Alkali Feldspar Granite	15940	Grab	29	64	6	1	100

Table 4-2 Mineral abundance chart of footwall granitoids. Sample descriptions 15935, 15940, 6518-19 and 6073 were derived from thin section.

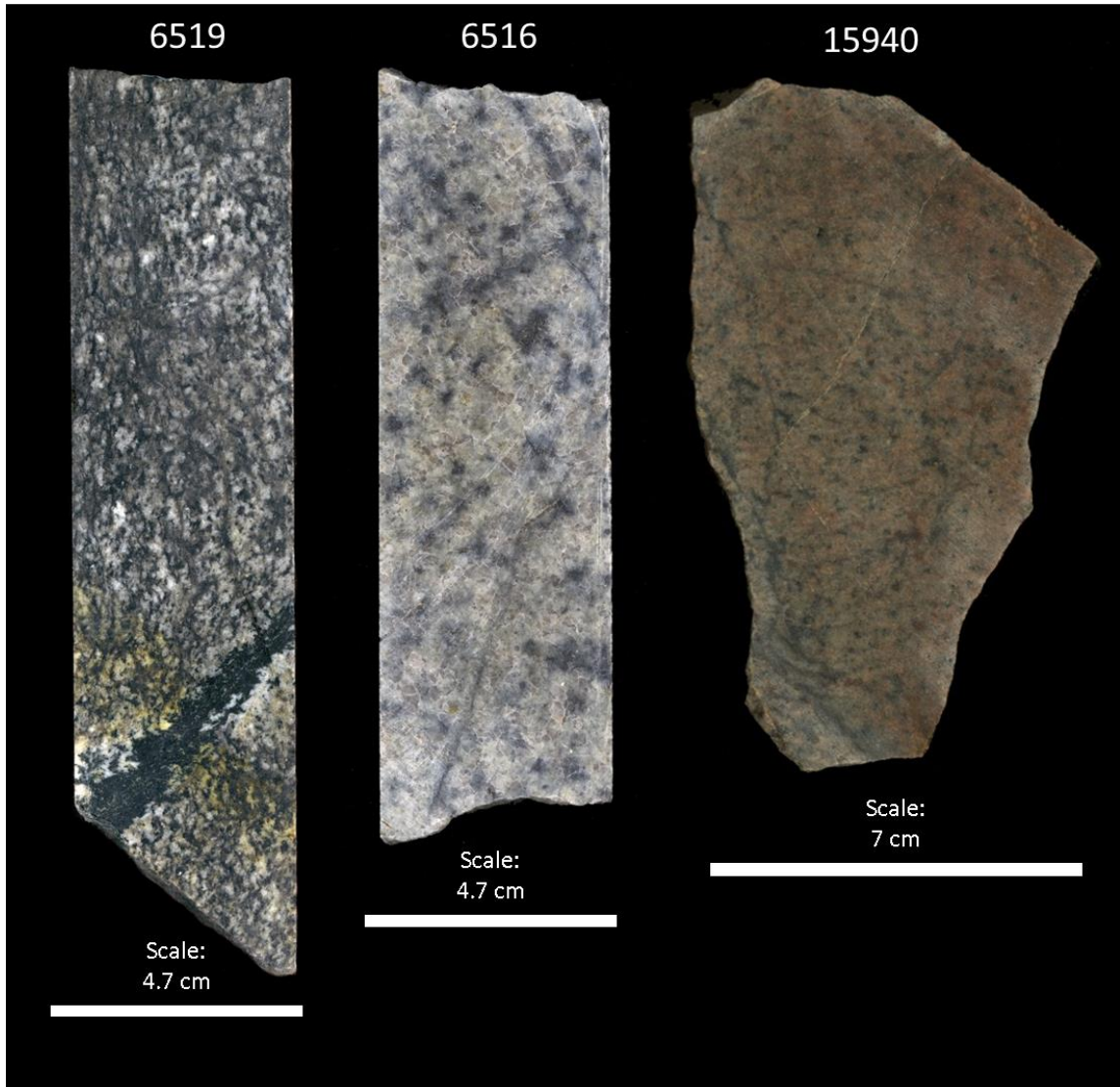


Plate 4-8 Plate of Deposit No.1 footwall granitoids. Sample 6519 is a drill core sample of monzogranite with epidote-carbonate-hornblende (ECH) veining. Sample 6516 is a drill core sample of syenogranite. Sample 15940 is grab sample of alkali-feldspar granite from the western portion of the footwall.

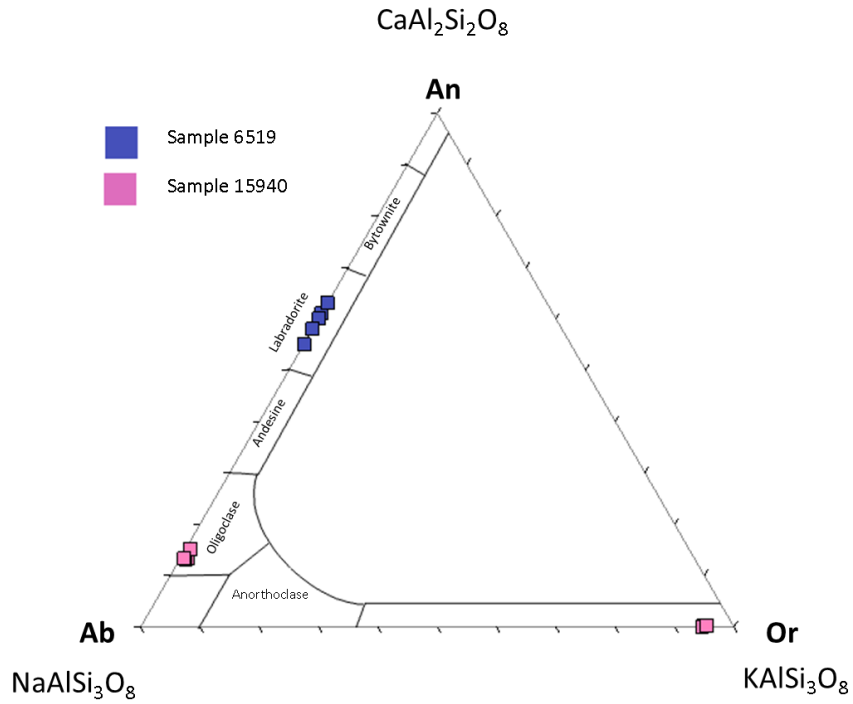


Figure 4-11 Feldspar ternary diagram of footwall granitoids. Labradorite was determined by the Michel-Levy technique using angles of poly-synthetic twinning.

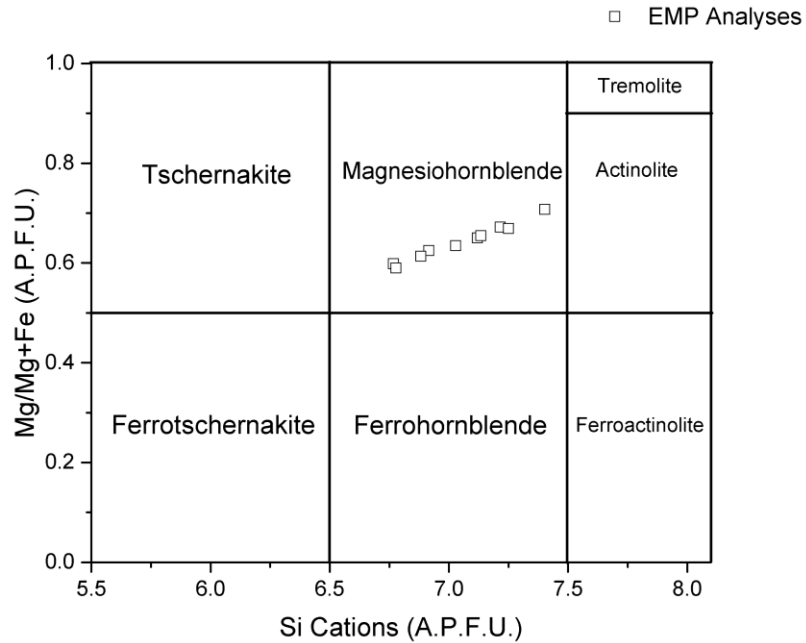


Figure 4-12 Amphibole determination plot of ECH veining amphiboles. Hornblendes plot in the magnesian sector.

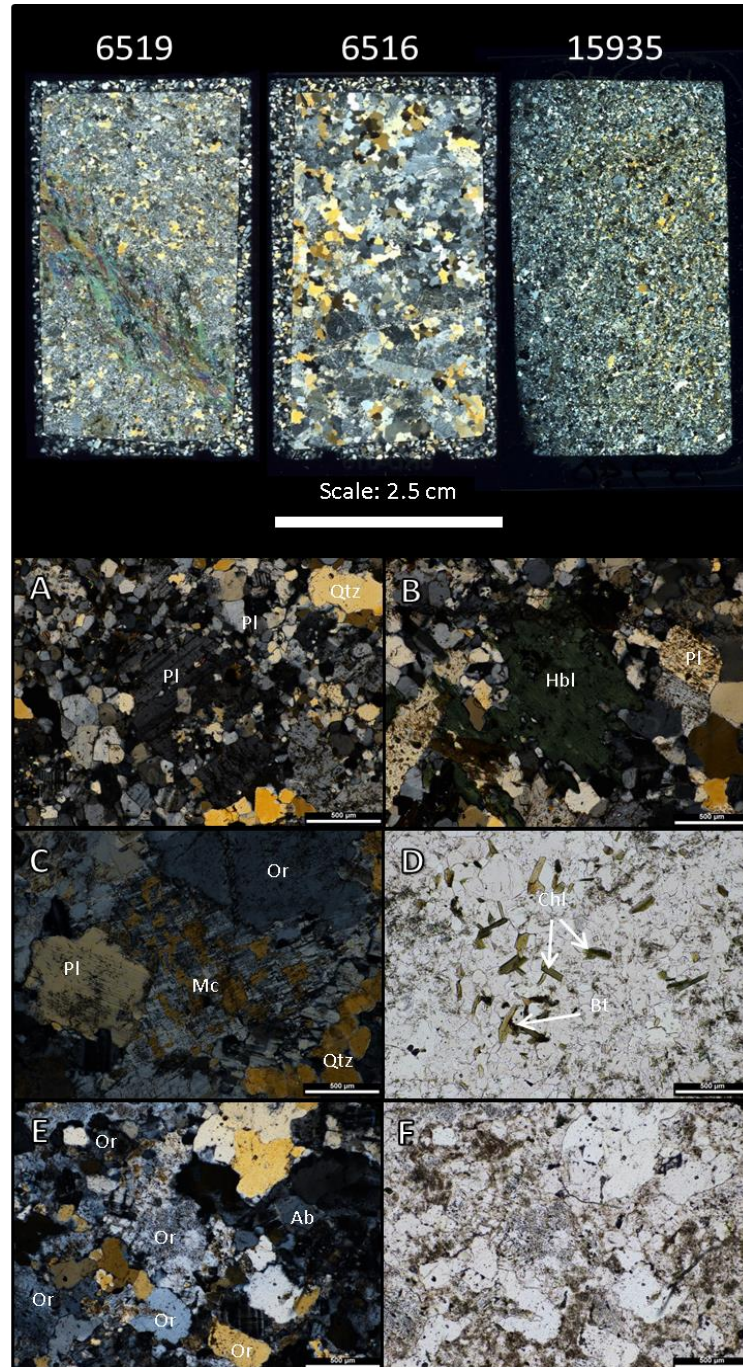


Plate 4-9 Plate of footwall granitoids mineral textures. XPL scans of polished thin sections are in the top row with sample numbers. Sample 6519 is a monzogranite with ECH vein and composed of interlocking plagioclase, orthoclase and hornblende. Sample 6519 textures are illustrated in XPL micrographs A and B showing interlocking plagioclase (Pl), orthoclase (Or) and quartz (qtz). Sample 6516 is a syenogranite. Corresponding micrographs are C in XPL and D in transmitted light (TL). Micrograph C shows coarse interlocking plagioclase, microcline (Mc) and orthoclase compared with D depicting chloritized biotite (Bt). Sample 15935 is alkali-feldspar granite and depicted in micrographs E and F. Fine to medium albite (Ab) and orthoclase are shown in E but show redish cloudy alteration in F.

4.2.1.3 Metagabbro

Metagabbro is composed of 65-85% hornblende, 10-25% plagioclase, 5-25% biotite and 1% quartz. Trace pyrite, pyrrhotite, chalcopyrite and magnetite are approximated at 0.5% each. The lithology is massive with a strong interlocking hypidiomorphic to alpanidiomorphic texture. Margins of mapped units are lineated by elongate and aligned hornblende and biotite. Hornblende forms 0.1-2 mm euhedral lathes and tablets with 60/120 cleavage. Hornblende overprints biotite, chlorite, plagioclase and quartz. Plagioclase and quartz are intergranular to hornblendes, as 30-200 μm anhedral to subhedral blocks, lathes and polycrystalline. Plagioclase grains locally exhibit distorted polysynthetic twinning. Biotite forms 300 μm subhedral to euhedral lathes and tablets. Sample 6515 is from the biotitized margin and shows pleochroic halos and irregular biotite tablets overprinting chlorite. Sulphides occur as 50-200 μm disseminated blebs. Pyrrhotite encompasses blebs of pyrite with margins of chalcopyrite. Magnetite forms 50-200 μm blebs to subhedral octahedron.



Plate 4-10 Photographs of metagabbro. 6514 is a drill core sample of the hornblende amphibolite variety. Sample 6515 is the biotitized and lineated metagabbro type. Outcrop samples 15924 and 15941 show the variance of primary gabbroic texture.

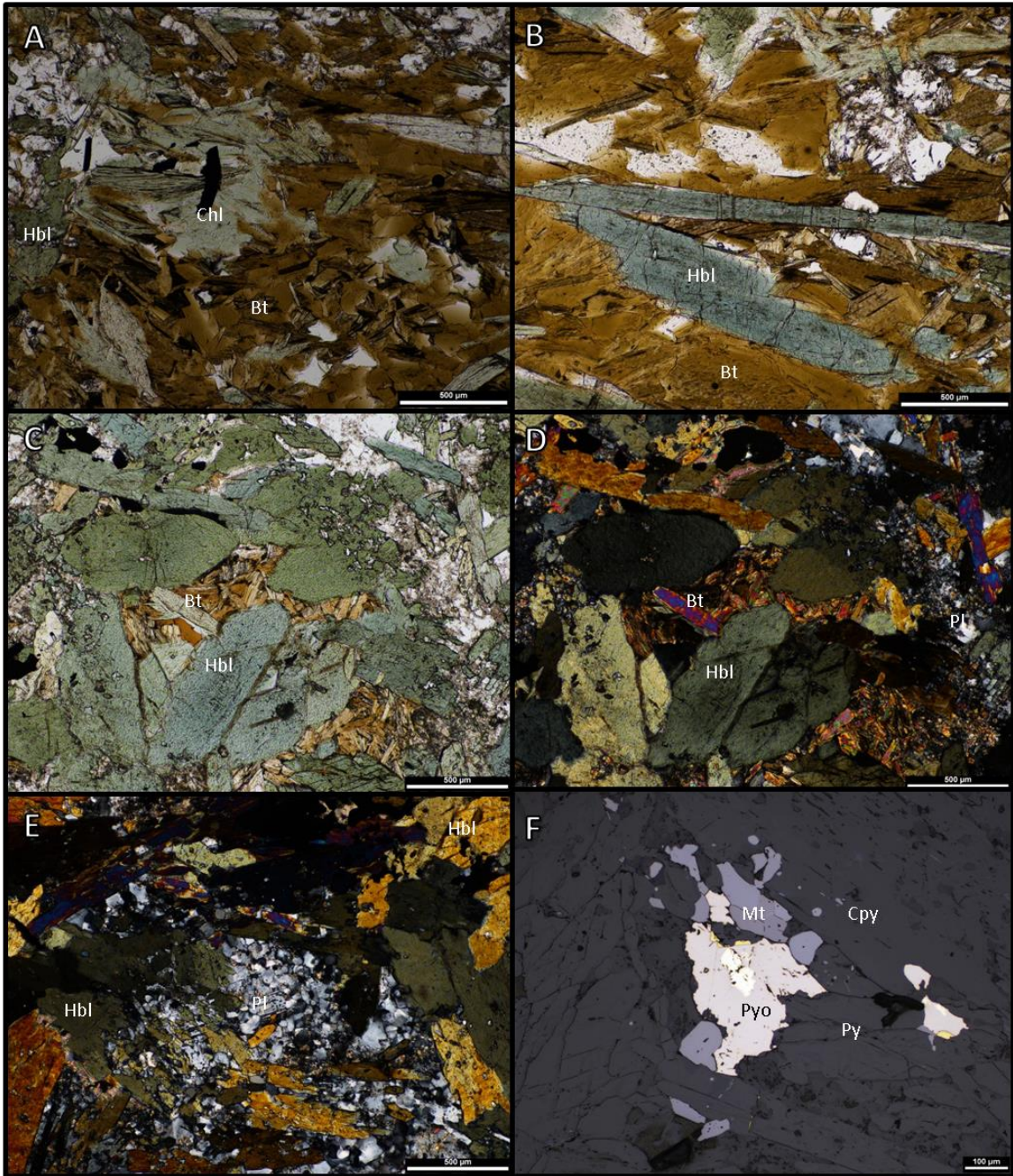


Plate 4-11 Micrographs of metagabbro textures. Micrograph A illustrates biotite overprints by chlorite and hornblende. Micrographs B, C and D (XPL) depicts coarse hornblende overprinting biotite with pleochroic halos. E shows interstitial plagioclase. Pyrrhotite belbs with inclusions of pyrite and margins of chalcopyrite are shown in E with magnetite belbs.

4.2.1.4 Quartz-Augen Muscovite-Biotite Schist (QAMS-QABS)

Modal mineral abundances vary considerably in quartz-augen muscovite biotite schist (QAMBS): 25-45% quartz, 25-45% muscovite and 25-45% biotite, 1-5% cordierite and 1-5% staurolite. Accessory minerals include feldspar (1%), apatite (0.5-1%), rutile-ilmenite (0.25-1%), monazite (0.05-0.1%) and zircon (0.25-0.5%). Quartz-augens are sigma shape porphyroclasts composed of 0.8-1.5 mm sutured quartz with serrated and abraded margins displaying undulose extinction. Quartz-augens are partially enveloped by finer 25-60 μm mosaic quartz and feldspar that extend (tails) forming linear mylonitic shear bands (Plate 4-12). Mylonitic shear bands and quartz-augens define lineations in all quartz-augen mica schists. An undulating foliation is defined by 25-100 μm size muscovite and biotite wrapping around quartz-augens and mosaic quartz envelopes (Plate 4-13). Muscovite and biotite foliation is bounded and defined by the overall mylonitic fabric. Margins of quartz-augens are often impinged and overprinted by muscovite and biotite lathes and tablets with faint dissolution textures. Secondary biotite differs from primary foliated biotite by forming anhedral 50-300 μm patches, lathes, tablets and blebs. Second generation biotite contains 25-100 μm wide pleochroic halos, weak basal cleavage and is rich in fluid inclusions. Composition of secondary biotite is plotted in Figure 4-13. Muscovite overprints quartz and plagioclase and also contains pleochroic halos and fluid inclusions. Secondary biotite also overprints foliated muscovite.

Staurolite and cordierite form 1-10 mm subidioblastic barrel to hexagonal shaped poikiloblasts overprinting secondary biotite and foliated muscovite (Plate 4-13). Cordierite and muscovite exhibit overprinting by anhedral honey brown blobby biotite hosting 5-20 μm wide pleochroic halos. Cordierite in all QAMBS samples is relict, exhibiting vermiform textures with muscovite-pinnite fracture infills and altered margins. Plagioclase and K-feldspar are small 200 μm subhedral blocks at the margins of quartz-augens altered to quartz and biotite. Zircons form 50-300 μm euhedral and prismatic crystals showing brecciation and micro fracturing (Plate 4-14). Monazites occur as 10-50 μm disseminations or clusters in biotite and muscovite. Rutile and ilmenite form 5-20 μm anhedral blebs oriented parallel to foliation.

Modal abundances of quartz-augen muscovite schists (QAMS) range from 20-35% quartz, 50-70% muscovite, 10-35% cordierite and 5-10% biotite. Apatite, zircon, monazite and ilmenite are present in trace 0.25-1%, 0.25-0.75%, 0.5% and 0.25-1% abundances respectively. Quartz-augens are on average smaller than in QAMBS, ranging between 0.1-10 mm in size and are spaced closer together (Plate 4-15 sample 6210). Quartz-augen abrasion and mylonitic shear bands are strongly defined and contain the same undulating foliation defined by 10-400 μm foliated to decussate muscovite lathes. Muscovite composition averages

$\text{K}_{1.72}\text{Na}_{0.11}\text{Al}_{3.39}\text{Fe}_{0.25}\text{Mg}_{0.25}\text{Ti}_{0.09}(\text{Si}_{6.13}\text{Al}_2\text{O}_{22})(\text{OH},\text{F}_{0.01})_4$ based on ten WDS EMP analyses. Flour-apatites, $\text{Ca}_{4.95}(\text{PO}_4)_{3.08}(\text{OH}_{0.29},\text{F}_{0.70},\text{Cl}_{0.01})$, form 50-60 μm blocks. Apatite grains are located within all minerals show monazite margins, monazite fracture infills and monazite inclusions. Flour-apatites are also microboudinage and contain abundant fluid inclusions (Plate 4-17- and 4-18). Giant 20-90 mm cordierites poikiloblasts are common containing inclusions of muscovite biotite, chlorite and apatite. Cordierite poikiloblasts overprint foliated-decussate muscovite and show aligned inclusions parallel to foliation. Cordierite poikiloblasts retrograde to a dark grey pinnite and chlorite producing a spotted macro texture against the light matrix. Previously, this large spotted texture has been identified as dalmationite in drill core (Plate 4-15). Elemental phase mapping did not identify chemical zoning within cordierite poikiloblasts or the foliated matrix (Figure 4-17).

Quartz-augen biotite schists (QABS) contain 60-75% biotite, 10-30% quartz, 1-5% cordierite, 1-5% staurolite, 1% apatite and 0-1% garnet. Accessory minerals are ilmenite, zircon and monazite in concentrations ranging between 0.5-1%. Mylonitic quartz-feldspar shear bands are less preserved and overprinted by biotite (Plate 4-12). Biotite forms 130-900 μm lathes and anhedral tablets that define a foliated to decussate texture. Coarse 10-50 μm wide pleochroic halos within biotite are characteristic (samples 6224 & 6225). Nine WDS microprobe analyses of biotite gave an average composition of $\text{K}_{1.75}\text{Na}_{0.08}(\text{Fe}_{2.42}\text{Mg}_{2.28})(\text{Al}_{0.5}\text{Ti}_{0.16})(\text{Si}_{6.14}\text{Al}_{3.0}\text{O}_{20})(\text{OH},\text{F}_{0.0025})_4$. Coarse almandine porphyroblasts commonly overprint foliated biotite and include ilmenite and chlorite. Chemical zoning is not identified by electron microprobe analysis or phase mapping (Figure 4-15). Five WDS EMP analyses of almandine show a compositional average of

$\text{Fe}_{2.38}\text{Mg}_{0.33}\text{Mn}_{0.21}\text{Al}_{2.05}\text{Si}_{2.96}\text{O}_{12}$. Staurolites also overprint foliated biotite as 5 millimetre poikiloblasts containing inclusions of aligned ilmenite and biotite. Staurolite composition, on the basis of six WDS analyses, shows iron and silica rich speciation, averaging $(\text{Fe}_{1.68}\text{Mg}_{0.38})(\text{Al}_{8.57}\text{Ti}_{0.06}\text{Mn}_{0.02})\text{O}_6[\text{Si}_{3.87}\text{Al}_{0.12}\text{O}_8](\text{O},\text{OH})_2$. Ilmenite occurs as 0.01-0.25 mm blades that corona rutile (Plate 4-17). Apatite forms 50-200 μm blocks texturally stable with biotite and quartz. Apatite overprints fractured and brecciated zircon (Plate 4-17). Four WDS EMP analyses defined apatite speciation to be flour-apatite with an average composition of $\text{Ca}_{4.95}(\text{PO}_4)_{3.06}(\text{OH}_{0.24},\text{F}_{0.75}\text{Cl}_{0.01})$.

All minerals, with the exception of staurolite and garnet, within QAMS, QAMBS and QABS are rich in fluid inclusions (Plate 4-18). Fluid inclusions occur as 1-5 μm vapor and liquid filled blebs. Fluid inclusions form linear patterns in quartz and along biotite-muscovite cleavage planes. Comparisons of fluid inclusion trends through quartz and neighboring micas show several generations are present.

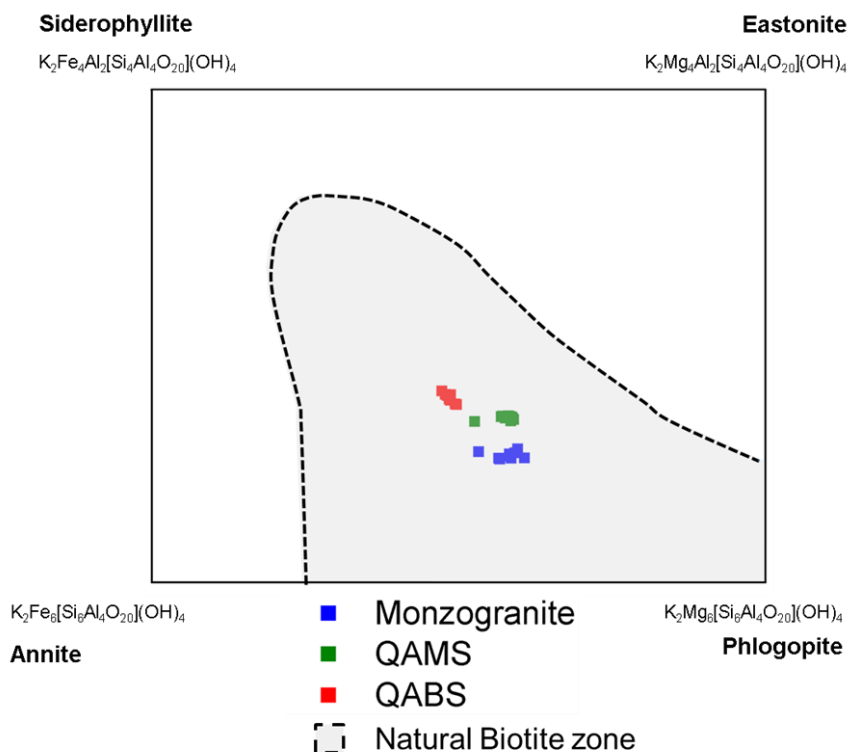


Figure 4-13 Composition diagram of biotite analyzed by EMP from monzogranites, QAMS and QABS units.

EMP analyses biotites totaled 10 from monzogranite and QABS samples 6519 and 6225. A total of 11 biotites were analyzed from QAMS sample 6078.

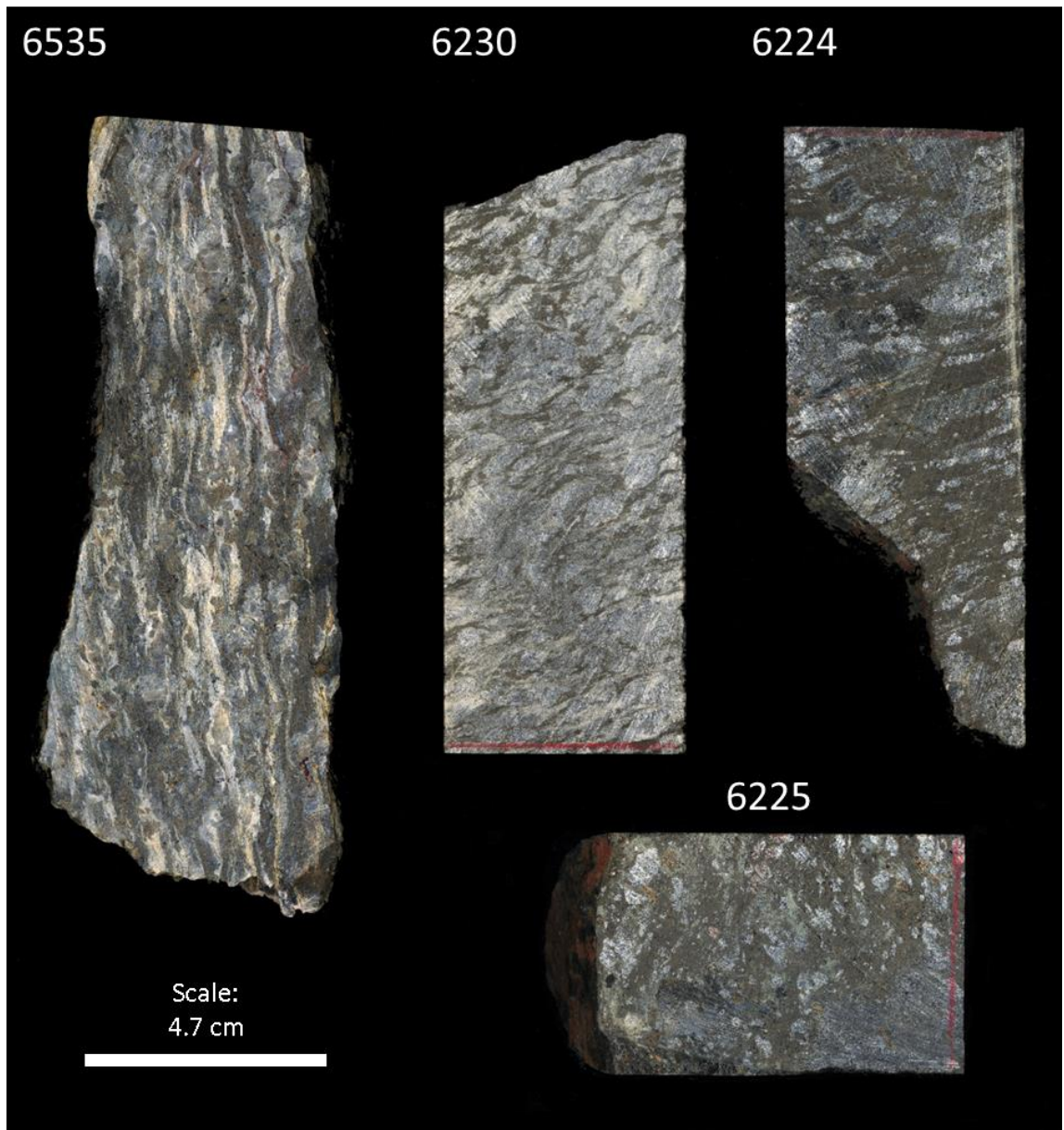


Plate 4-12 Plate of QAMBS and QABS units. Samples 6230 and 6535 are QAMBS drill core and grab samples with cm size quartz augens. Staurolite porphyroblasts are present in sample 6535. Samples 6224 and 6225 are QABS from drill core containing patchy chlorite and staurolite and almandine porphyroblasts.

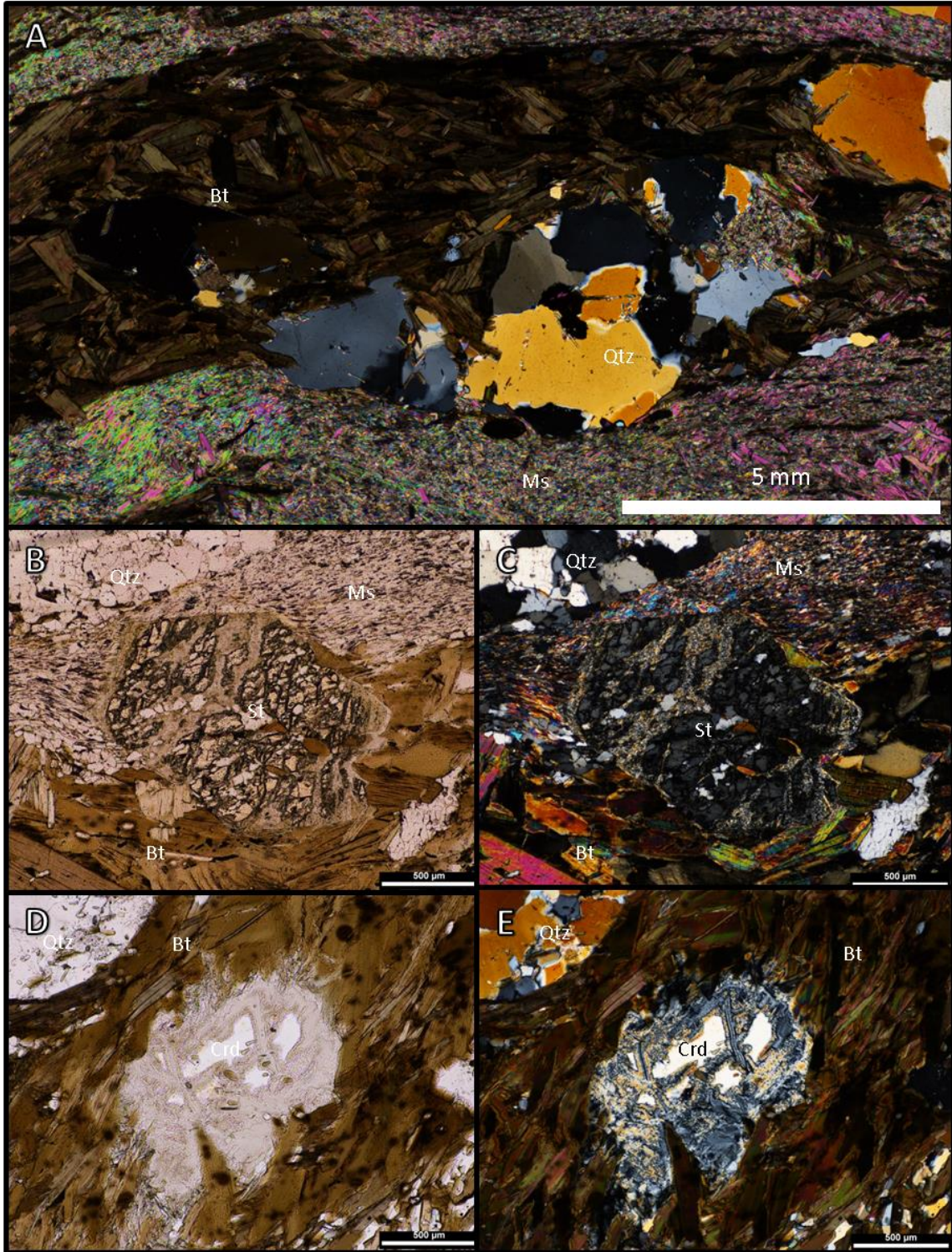


Plate 4-13 Micrographs of QAMBS textures in polished thin sections. A shows a quartz-augen (Qtz) being overprinted by biotite and muscovite (Ms). Micrographs B and C are comparative PPL and XPL of a staurolite (St) porphyroblast with reaction rim. Micrographs D and E are also comparative illustrations of retrograded-pinnitized cordierite (Crd) in PPL and XPL impinged by biotite with pleochroic halos.

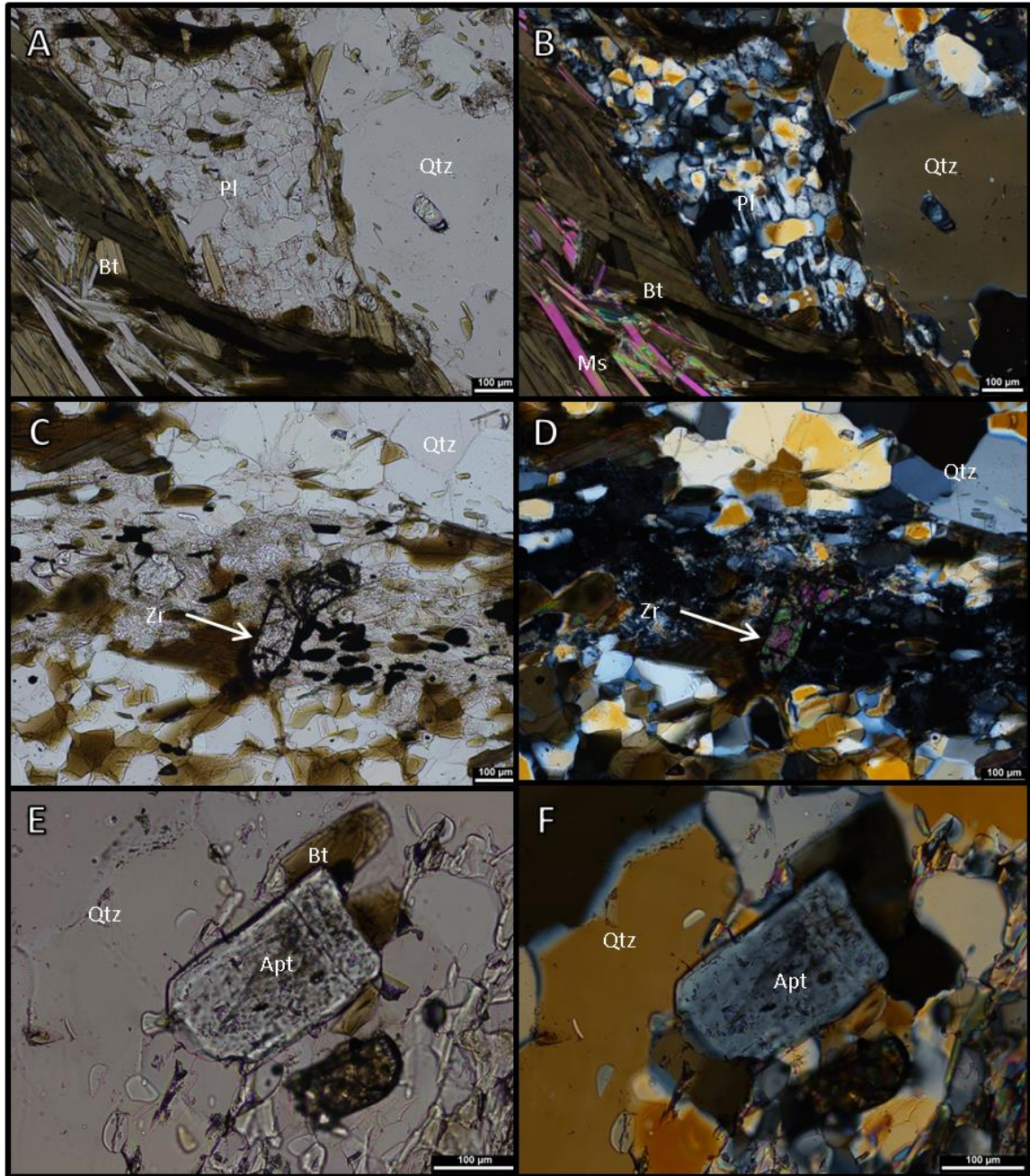


Plate 4-14 Plate of QAMBS accessory minerals and textural features. Micrographs A and B are PPL and XPL images of relict altered plagioclase (Pl) by biotite (Bt) and quartz (Qtz). C and D show a large euhedral zircon (Zr) broken in half in PPL and XPL. Micrographs E and F are of a fluid inclusion filled blocky apatite (Apt) in PPL and XPL.

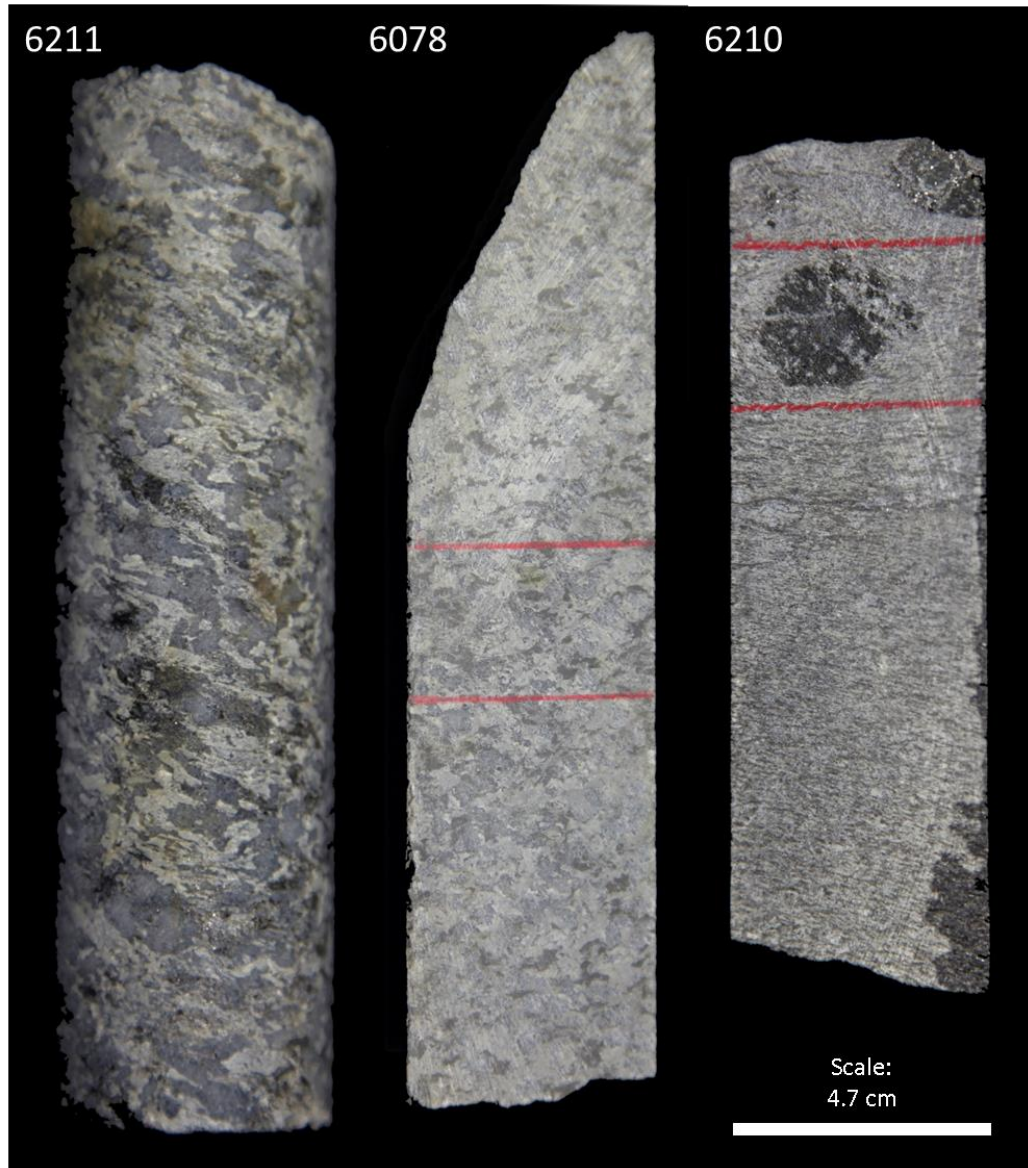


Plate 4-15 Plate of QAMS drill core samples, red outline zone indicates thin sectioned area. Samples 6078 and 6211 illustrate coarse rodded texture defined by lineated quartz-augens. Sample 6210 is an example of finer quartz-augen with a large retrograde cordierite porphyroblast.

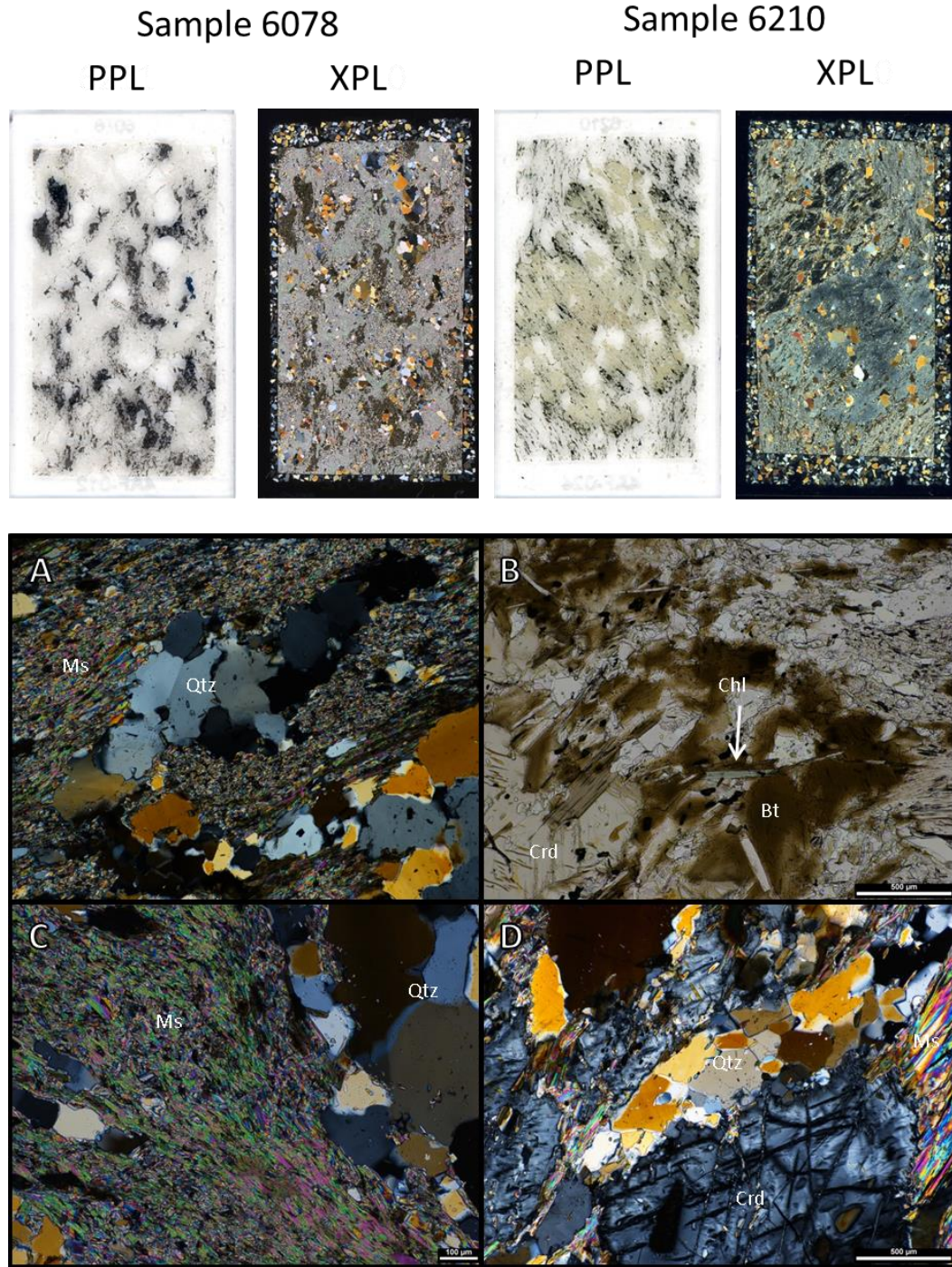


Plate 4-16 Micrographs of QAMS textures in samples 6078 and 6210. The top row are PPL and XPL scanned images of polished thin section samples 6078 and 6210. Micrograph A is a quartz-augen (Qtz) in fine muscovite (Ms) matrix showing abraded and impinged margins. B shows the margins of a cordierite (Crd) porphyroblast altered by patchy biotite (Bt) with chlorite (Chl) and monazite. Micrograph C shows fine muscovite matrix adjacent to quartz-augen in XPL. Veriform texture cordierite in XPL with quartz-augen and muscovite inclusions depicted in D.

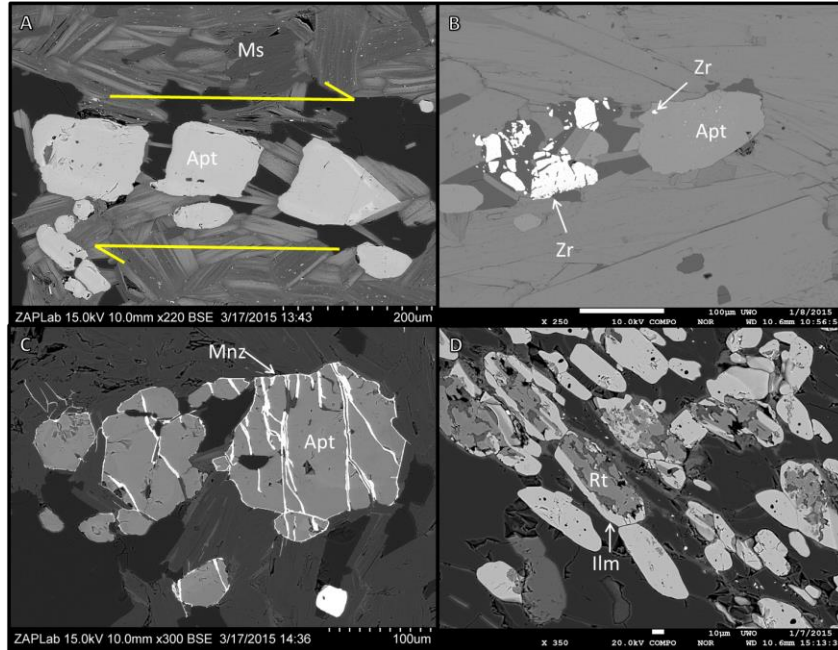


Plate 4-17 BSE images of QAMBS accessory phases. A shows boudinage flour-apatite with shear sense indicators. Micrograph B illustrate apatite with brecciated zircon inclusion. Micrograph C shows fractured flour-apatites infilled with monazite. Rutile grains in micrograph D are overprinted by ilmenite.

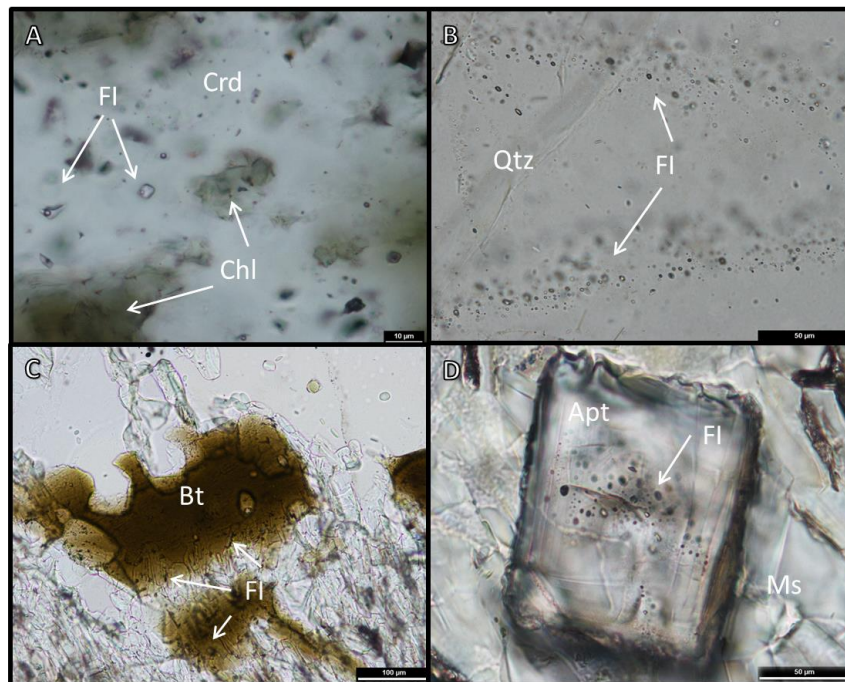


Plate 4-18 Micrographs of fluid inclusions from QAMBS units. A shows liquid-vapor fluid inclusion (FI) in cordierite (Crd). Linear oriented fluid inclusions in quartz (Qtz) are illustrated in micrograph B. Micrographs C and D show fluid inclusions in secondary amorphous biotite (Bt) and in blocky apatite (Apt).

Sample 6078 Phase Map

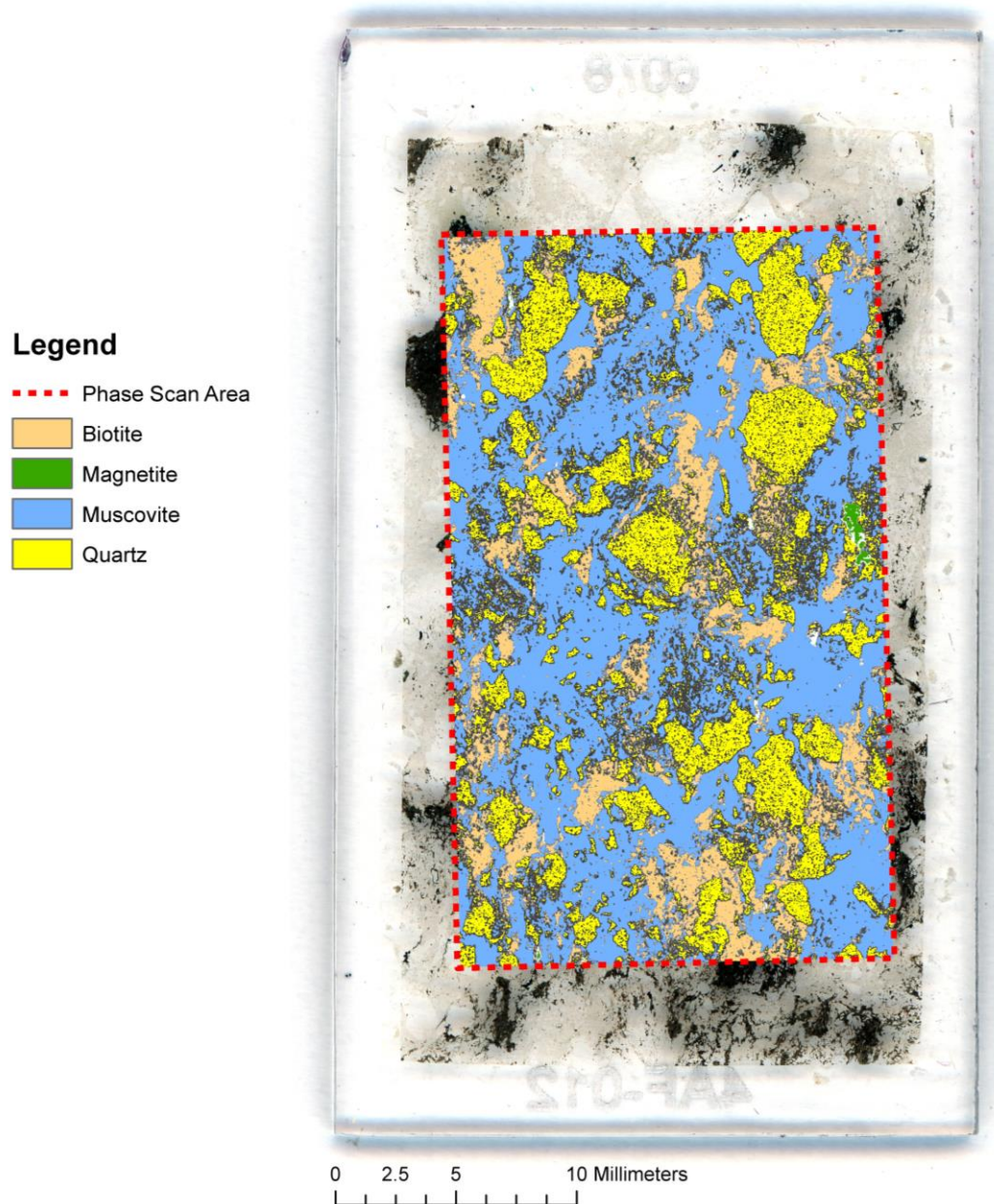


Figure 4-14 EDS phase scan of QAMS sample 6078. Minerals are shown by different colours within the outlined scan area.

Sample 6225 Phase Map

Legend

- - - Phase Scan Area
- Staurolite
- Quartz
- Illmenite-Rutile
- Garnet
- Cordierite
- Biotite

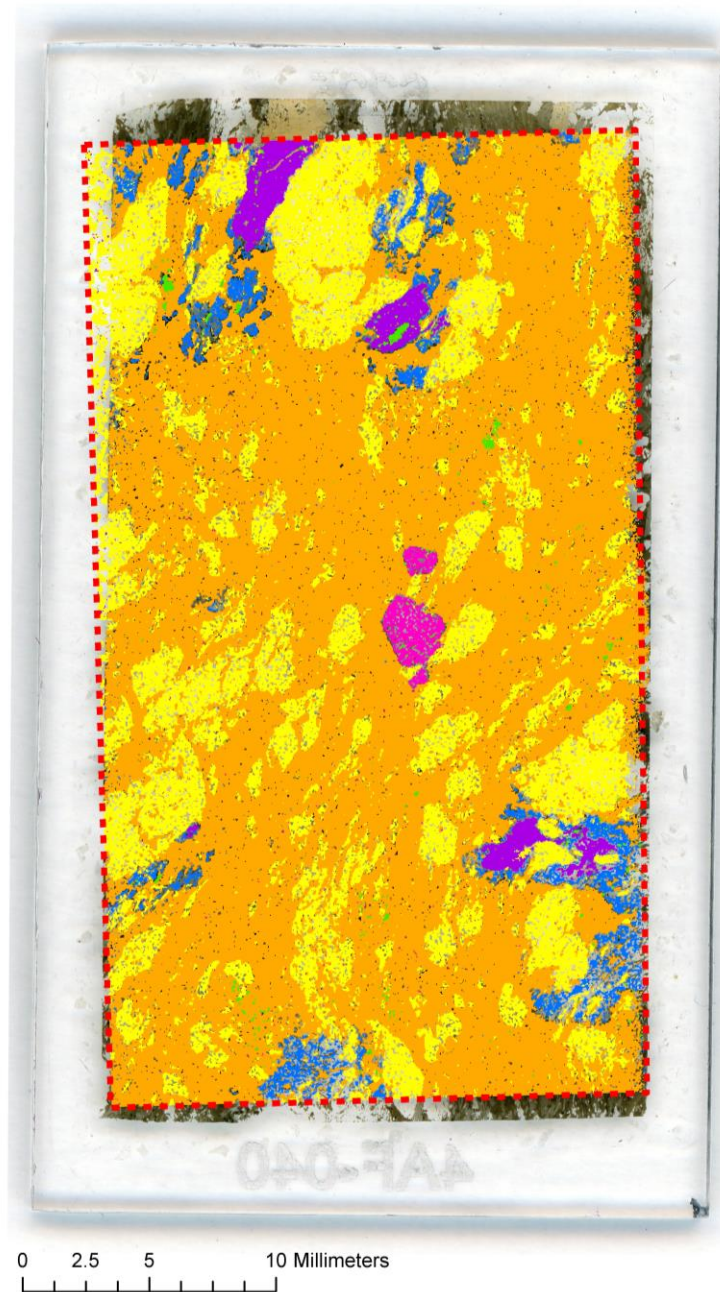


Figure 4-15 EDS phase scan of QABS of drill core sample 6225. Minerals are represented by colour with scan area outlined by red dashed line. Staurolites appear to be encased by cordierite but actually overprint retrograded cordierite and pinnite.

4.2.1.5 Altered Silicified Granitoid

ASGs are massive textured exhibiting hypidiomorphic quartz, plagioclase and K-feldspar. Mild to moderate 1.5 mm wide lineations of quartz and patchy biotite are identified throughout (sample 6066A Plate 4-19). The unit exhibits two distinct fresh surface colours, light grey and pink. Grey colour rocks host relict monzogranite and are identified in the immediate QAMBS footwall to HGIF (samples 6066, 6253 and 6257 Plate 4-19). Pink rocks host relict syenogranite and make up the western lithology and sub classified as ASGr (sample 6404A Plate 4-19). ASG is silica rich, containing 55-75% quartz, 10-20% microcline, 5-10% orthoclase, 5-10% labradorite, 3-10% biotite, 1-5% muscovite and 1% apatite. Trace minerals are titanite (0.5%) and zircon (0.5%). Quartz augens define 1-5 mm quartz lineations. Microcline and orthoclase crystals (50-850 μm) exhibit moderate tartan and exsolution twinning. Microcline are impinged and overprinted by quartz and mottled by muscovite-sericite alteration. Plagioclase forms 25-1000 μm lathes and blocks and is almost completely replaced by fine quartz (samples 6062-6066, 6250, 6253 Plate 4-20). Dark brown biotite occurs as 25-100 μm lathes in a mild foliation or as 1.5 mm decussate patches define lineations.

Linear epidote-carbonate-hornblende (ECH) veins, 5-25 mm thick, crosscut the defined quartz-feldspar matrix in drill core samples 6062 and 6063. Lamellar 1 mm hornblende comprises most of the vein, with inclusions of 100-200 μm euhedral epidotes with allanite cores (Plate 4-21). Epidote also occurs at the margins of veins with carbonate. ECH vein margins are composed of cloudy 50-100 μm interlocking carbonate blocks. Coarse 300-500 μm subhedral-euhedral titanite in ECH veining overgrows primary twinned titanite (samples 6062-6063). Plagioclase in ECH veins is not silicified but alters to blockey epidote hosting allanite cores (6062-6063). Vein epidote and hornblende are overprinted by late anhedral blotchey biotite characterized by large pleochroic halos (Plate 4-21D). Epidotes in sample 6068 are overprinted by quartz then by biotite with pleochroic halos.



Plate 4-19 Plate showing varieties of altered silicified granitoid. Drill core sample 6066 shows patchy biotite lineations. Samples 6253 and 6257 are drill core showing mild and moderate silicification textures. 6404A is an example of ASGr or “pinkish quartzite” in contact with syenogranite.

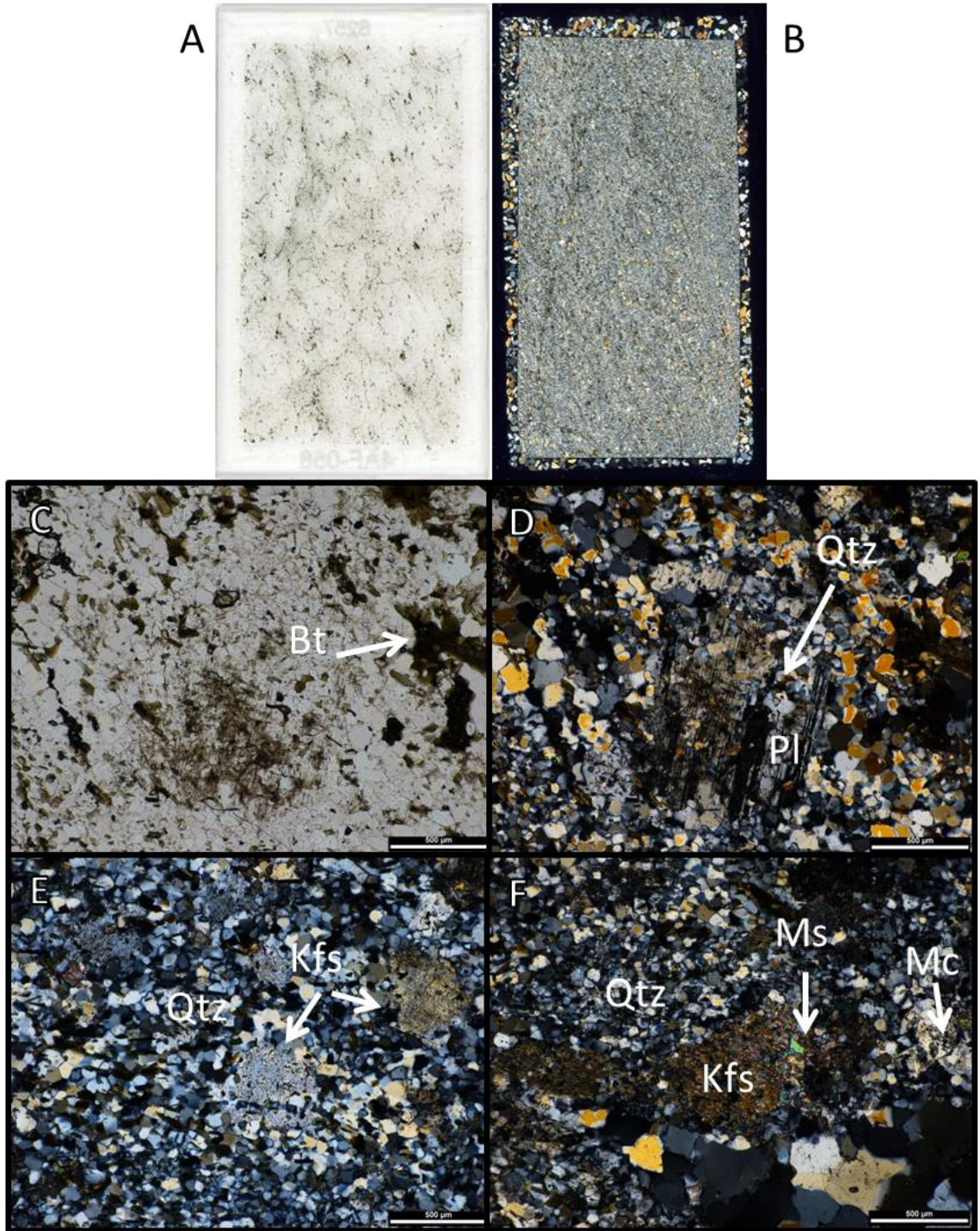


Plate 4-20 Plate of ASG mineral textures. Photographs A and B are PPL and XPL scans of a polished thin section from sample 6257. Micrographs C and D are comparative PPL and XLP images of plagioclase (Pl) replaced by quartz (Qtz) with minor biotite (Bt) overprints over quartz (sample 6062). Micrographs E and F show mottled K-feldspar (Kfs) and microcline (Mc) altered to quartz and muscovite (Ms) (sample 6527).

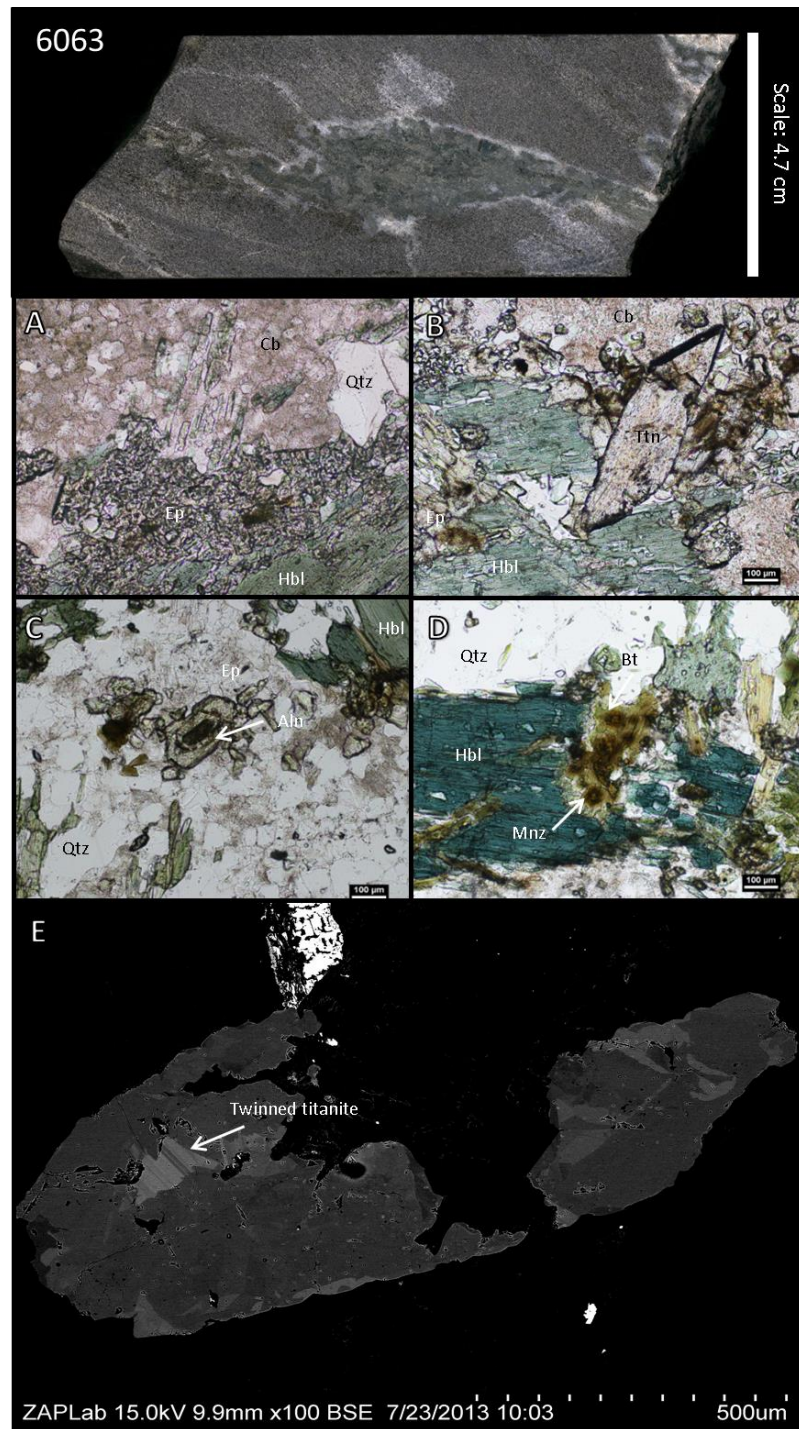


Plate 4-21 Plate of mineral textures and features in epidote-carbonate-hornblende (ECH) veining. Top photograph of drill core sample 6063 shows ECH veining with hornblende-epidote interior and carbonate margins. Micrographs A and B show ECH vein margins containing blocky carbonate (Cb), epidote (Ep) and lamellar hornblende (Hbl) with euhedral secondary titanites (Tnt) in sample 6062. Epidotes with allanite cores are depicted in micrograph C. Biotite with pleochroic halos overprints ECH veining hornblende in D (sample 6063). Back scatter electron image of titanite is pictured in micrograph E illustrating central twinned titanite encompassed by untwinned titanite (sample 6245).

4.2.1.6 Biotite Schists (BS)

Biotite schist (BS) is quite homogenous in nature, essentially composed of 0.1-1 mm brown to honey brown biotite lathes averaging 85-95% modal abundance. Muscovite (1-5%), quartz (0.5-2%), chlorite (1-10%), andalusite (1-4%), cordierite (1-10%), staurolite (0-10%) and almandine (0-10%) attribute to rest of the major minerals. Accessory minerals zircon, monazite and ilmenite occur in 0.1-0.5%, 0.1-1% and 0.1-0.25% abundances respectively. Biotite lathes define a foliated to completely decussate “thatched” texture and completely overprint a previous muscovite matrix (Plate 4-24). Biotite hosts 10-25 μm monazite with 25-50 μm wide pleochroic halos. Lathes of biotite exhibit mild to moderate chlorite alteration. The unit favours porphyroblastic growth of 1-10 mm size staurolite, almandine and andalusite poikiloblasts (Plate 4-22). Several samples have relict pinnitized 0.1-4 mm porphyroblasts of cordierite engulfed by biotite and staurolite (6202, 6215, 6218 & 6223). Cordierite is not texturally stable with staurolite, garnet or andalusite. Porphyroblasts of 5 mm barrel to kite shaped staurolite overgrow biotite and chlorite. Staurolite porphyroblasts contain inclusions of chlorite, apatite, biotite and cordierite (Plate 4-24). Staurolites were iron rich averaging, 15.1 % FeO from three WDS EMP analyses. The average calculated staurolite formula is $(\text{Fe}_{1.79}\text{Mg}_{0.34})\text{Al}_{8.75}\text{Si}_{3.81}\text{O}_{20}(\text{O},\text{OH})_4$.

Idioblastic almandine overgrows biotite, chlorite and relict cordierite. Almandine porphyroblasts also incorporate staurolite porphyroblasts as inclusions forming a poikiloblastic texture (Plate 4-23). The average almandine formula is $\text{Fe}_{2.57}\text{Mg}_{0.32}\text{Mn}_{0.08}\text{Al}_{2.03}\text{Si}_{2.96}\text{O}_{12}$ on the basis of six WDS EMP analyses. Almandine porphyroblasts are chemically zoned. Rims of almandine are Mn depleted, containing 0.63% Mn, compared to core concentrations with 1.63% Mn (Figure 4-16).

Large andalusites in sample 6205 have prograde reaction rims overprinting biotite while andalusites in sample 6215 do not. Andalusite is poikiloblastic, having an abundance of biotite inclusions. Compositions of andalusites show iron impurities of 0.653-0.924 % from 5 WDS EMP analyses. Apatites are 100 μm subhedral cloudy blocks sharply contacting biotite and chlorite. Apatites are also inclusions in andalusite, staurolite and garnet. Zircons are 50-250 μm fracture and brecciated euhedral crystals.



Plate 4-22 Plate showing varieties of footwall biotite schist in drill core. Sample 6216 is biotite schist without porphyroblastic growth. Relict cordierite porphyroblasts are shown in sample 6218. Samples 6203 and 6227 show staurolite growth while 6227 also contains almandine porphyroblasts.

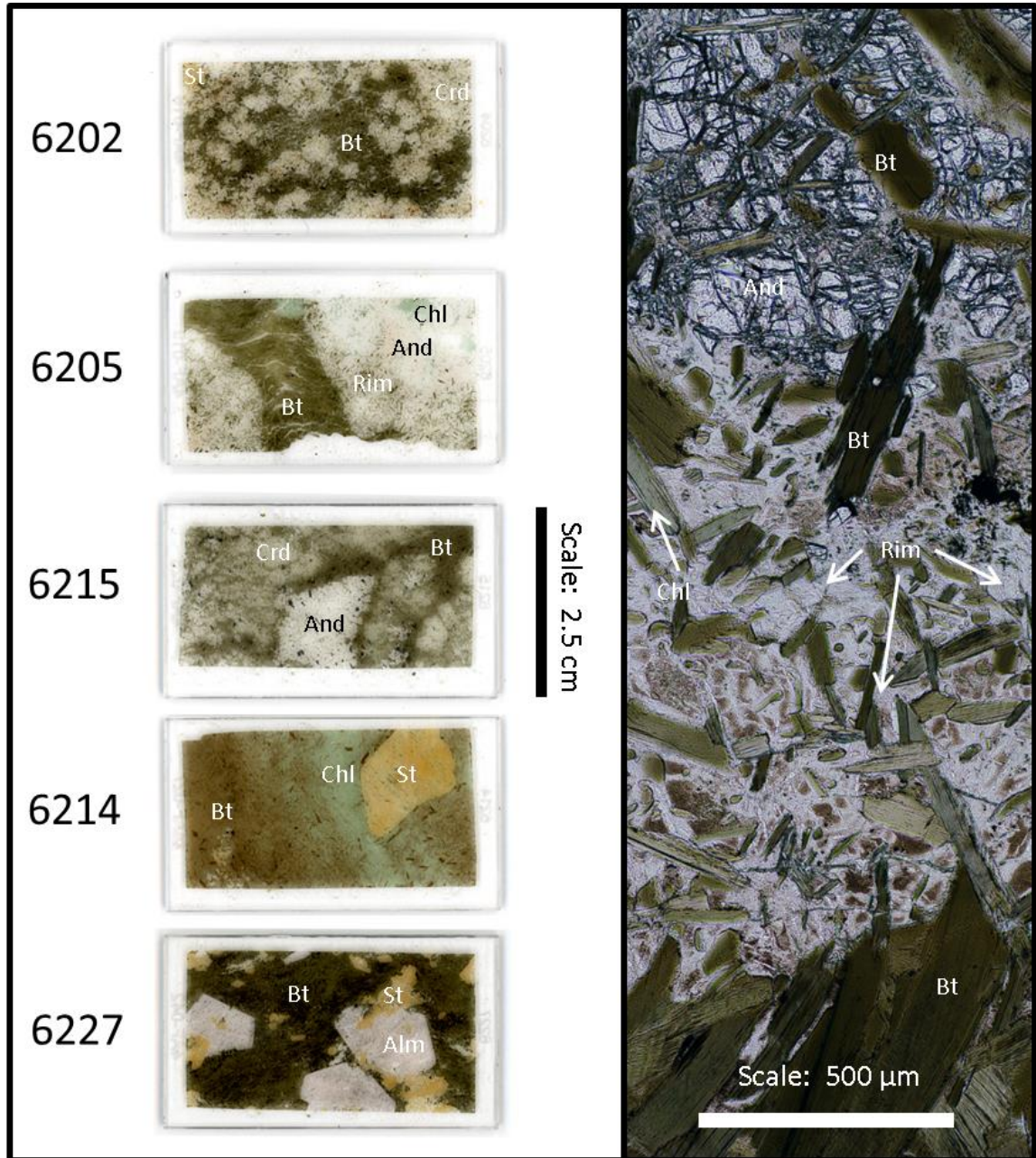


Plate 4-23 Plate illustrating various porphyroblastic growth and reaction textures in biotite schist. Sample 6202 contains relict pinitized cordierite (Crd) overprinted by staurolite (St). Large andalusite (And) porphyroblasts are depicted in samples 6205 and 6215 overprinting biotite (Bt) and chlorite (Chl). Staurolite in sample 6214 grows in chloritized biotite matrix. Almandine (Alm) porphyroblasts encompass staurolite in sample 6227. Right micrograph shows prograde reaction rim of andalusite porphyroblast to biotite in sample 6205.

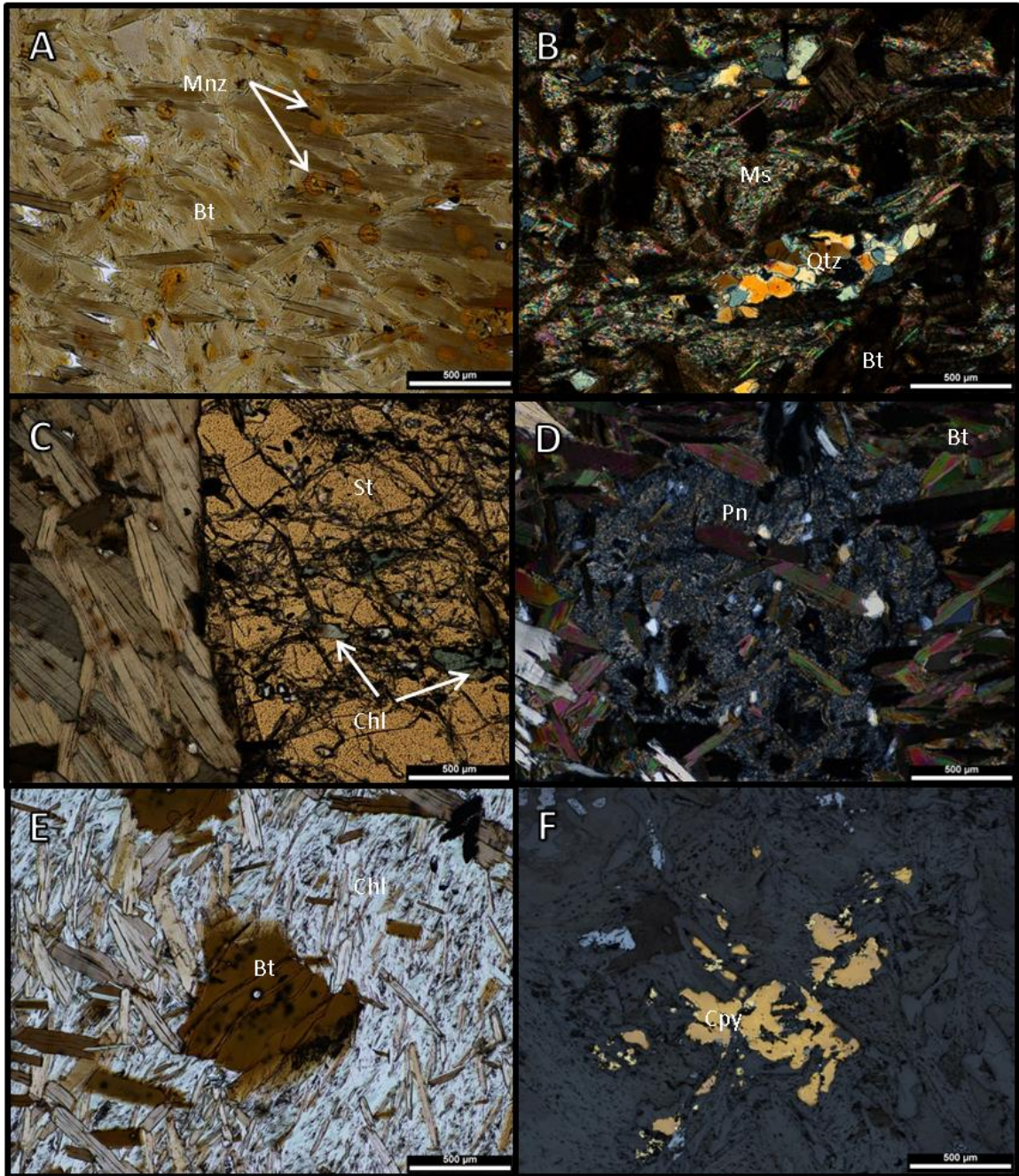


Plate 4-24 Plate of various mineral textures in biotite schist. Micrograph A shows foliated biotite (Bt) in PPL with pleochroic halos host monazite (Mnz). Relict quartz-augens (Qtz) and muscovite (Ms) are overprinted by biotite (XPL) in micrograph B. Staurolite (St) porphyroblast with chlorite (Chl) inclusions growing over coarse foliated biotite is depicted in micrograph C. Micrograph D shows pinitized cordierite (Crd) impinged by biotite. Coarse biotite tablets and lathes overprinting chlorite are depicted in micrograph E. Chalcopyrite (Cpy) blebs in reflected light are shown in F.

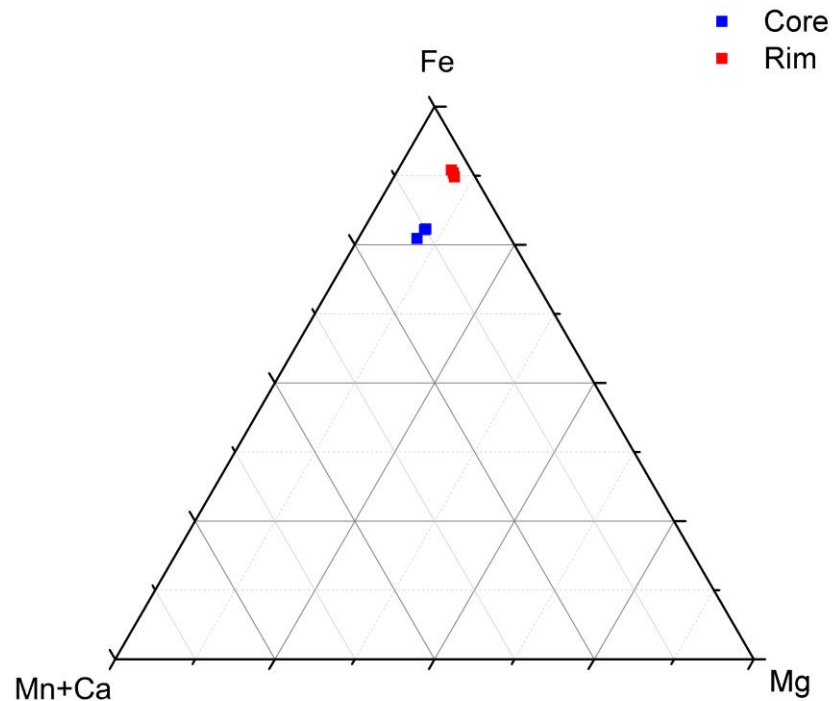


Figure 4-16 Ternary garnet composition plot of garnet porphyroblasts from biotite schists. EMP point analyses of porphyroblastic garnets are plotted as normalized components by area of analyse.

4.2.1.7 Chlorite Schists (OZCS)

Chlorite schist (CS) is dominantly composed of ripidolite (75-95%) with local porphyroblasts of grunerite (0-20%) and almandine (1-20%). The unit also has biotite-muscovite (1-5%), quartz (0.5-2%) and martite (0.5-5%) as minor constituents. Accessory minerals include zircon (0.25-0.5%), monazite (0.25-0.5%), apatite (0.5-1%) and ilmenite (0.5-1%). Chlorite schist is foliated to massive-decussate and hosts the largest grunerite and almandine porphyroblasts (Plate 4-25 and 4-26). Trace 1-3 mm quartz-augens and 20-150 μm anhedral quartz blebs are present in sample 6222 and 6476 (Plate 4-27). Biotite forms 0.01-3mm lathes and tablets altered to chlorite. Muscovite forms 50-250 μm lathes also altered to chlorite. The chlorite replacement of biotite and muscovite produces relict lathes with preserved basal cleavage. Chlorite tablets form feathery and mottled blobs. Chlorite lathes and tablets range between 100-500 μm in length. Secondary tabular biotite overprints chlorite in sample 6243 is then overgrown by almandine. Apatites are small subhedral 50-200 μm blocks and ovoids with cloudy centers in sharp contact to all matrix minerals. Zircons are 50-200 μm euhedral crystals

scattered throughout the matrix. Monazites 10-50 μm in sizes and are scattered throughout the matrix. Ilmenites are blades oriented length wise parallel to S_1 .

Acicular 80-600 μm grunerite overgrows biotite, muscovite and chlorite. Grunerite blades also form radiating 1-5 cm bowties crosscutting biotite, muscovite, chlorite and quartz (sample 6222 and GCS-016). The atomic formula of grunerite averaged $\text{Mg}_{3.30}\text{Fe}_{3.66}\text{Si}_{7.80}\text{O}_{22}(\text{OH})_2$ from 20 WDS EMP analyses. Grunerite composition is borderline with respect to cummingtonite (Figure 4-17). Two analyses identified cummingtonite with 3.65 Mg cation values.

Idioblastic almandine poikiloblasts hold inclusions of chlorite, biotite, muscovite, acicular grunerite and relict quartz-augens (Plate 4-27). Almandine poikiloblasts vary extremely in size from 200 μm to 10 cm in diameter. Chemical zoning was not detected from 20 WDS EMP transect point analyses averaging $\text{Fe}_{2.53}\text{Mg}_{0.33}\text{Mn}_{0.03}\text{Al}_{2.04}\text{Si}_{2.98}\text{O}_{12}$ (Figure 4-18).

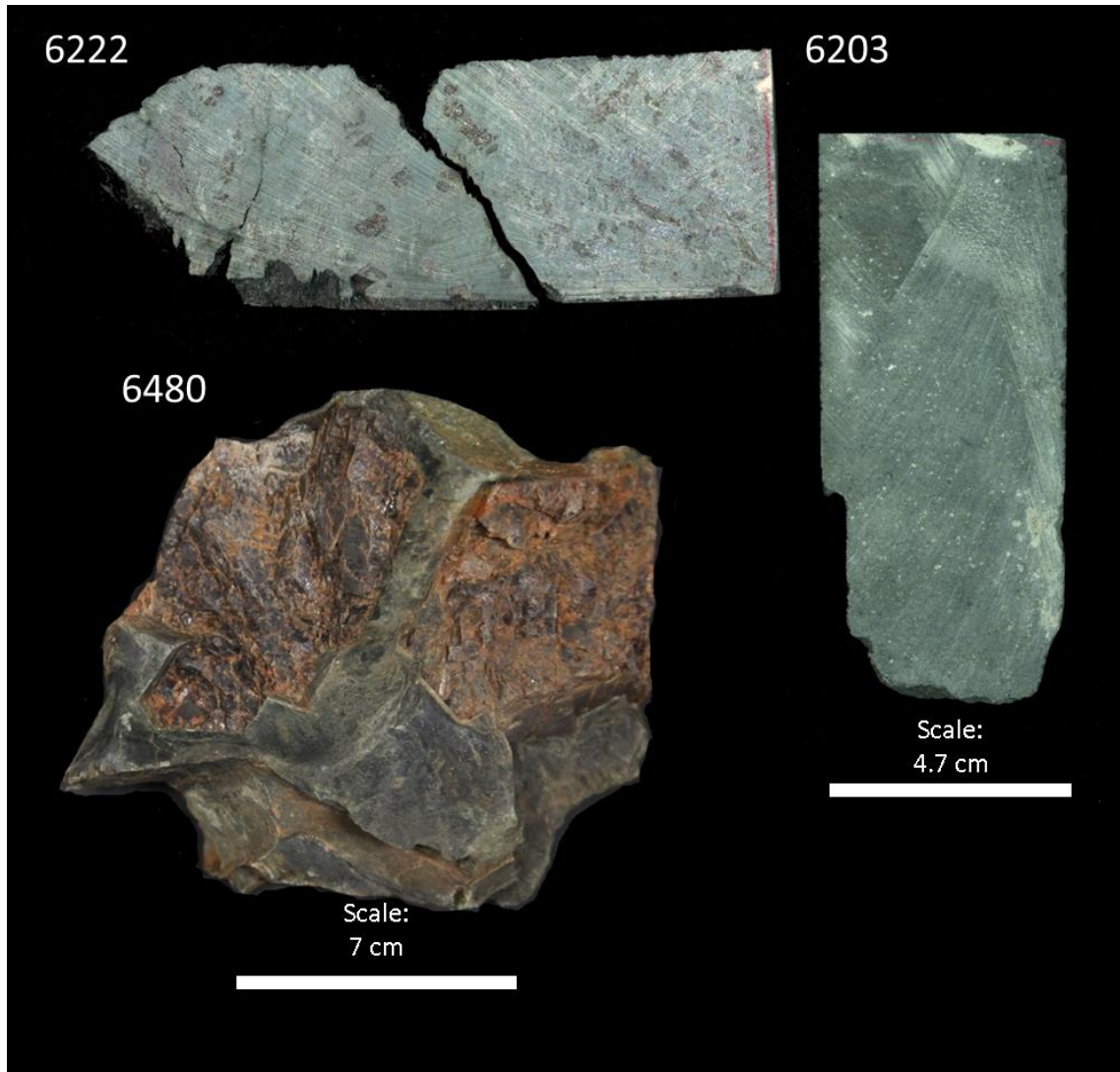


Plate 4-25 Plate showing varieties of footwall chlorite schist. Drill core sample 6222 shows relict quartz-augens, radiating grunerites and 10 mm garnets. Chlorite with relict quartz-augens in sample 6203. Grab sample 6480 is an example of giant almandine garnets from the PS2 site.

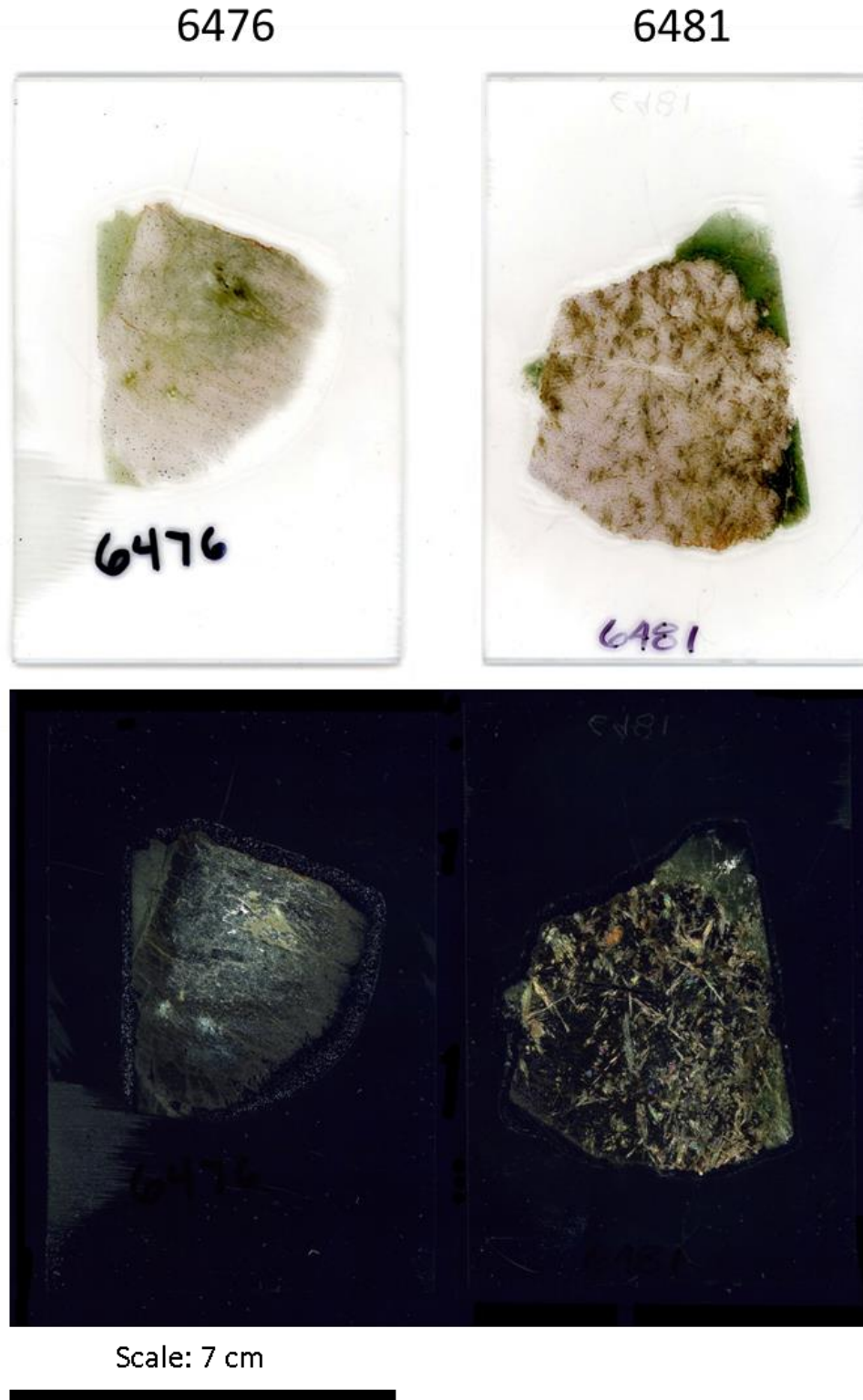


Plate 4-26 PPL and XPL scans of polished thin sections containing large garnet porphyroblasts from the PS2 zone at Deposit No.1. Sample 6476 shows chlorite and relict quartz-augens as inclusions. Contrastingly, sample 6481 contains large bladed and twinned grunerite amphiboles.

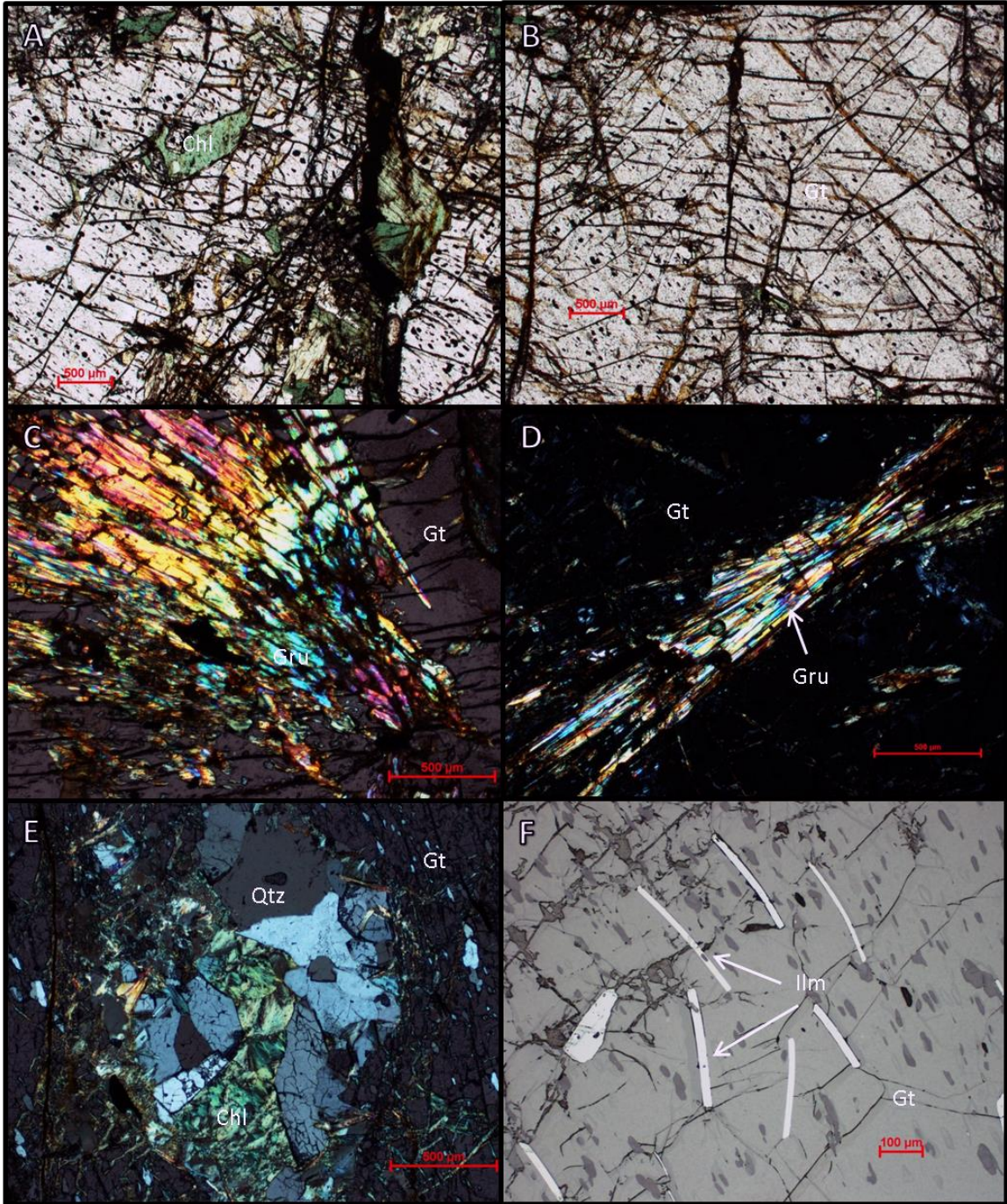


Plate 4-27 Micrographs of inclusions within garnet porphyroblasts in footwall chlorite schist samples from the PS2 site. Micrographs A and B show chlorite (Chl) inclusions in cracked garnet (Gt). C and D are XPL micrographs of radiating and acicular grunerite (Gru) crystals in garnet. Micrograph E shows quartz-augen (Qtz) inclusion while F depicts aligned ilmenite (Ilm) lathes.

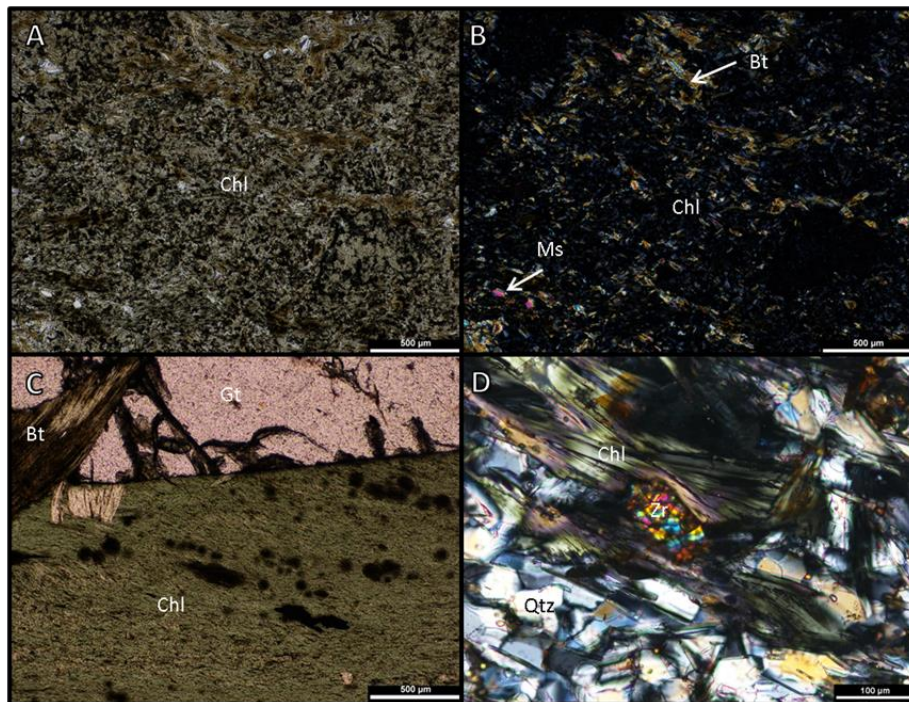


Plate 4-28 Micrographs of mineral textures in footwall chlorite schists from drill core samples. Micrographs A and B are PPL and XPL comparisons of chlorite matrix showing the replacement of biotite (Bt) and muscovite (Ms) by chlorite (Chl). A large porphyroblast of garnet overprints biotite and chlorite containing pleochroic halos in micrograph C. Euhedral zircon (Zr) is pictured in micrograph D with quartz (Qtz).

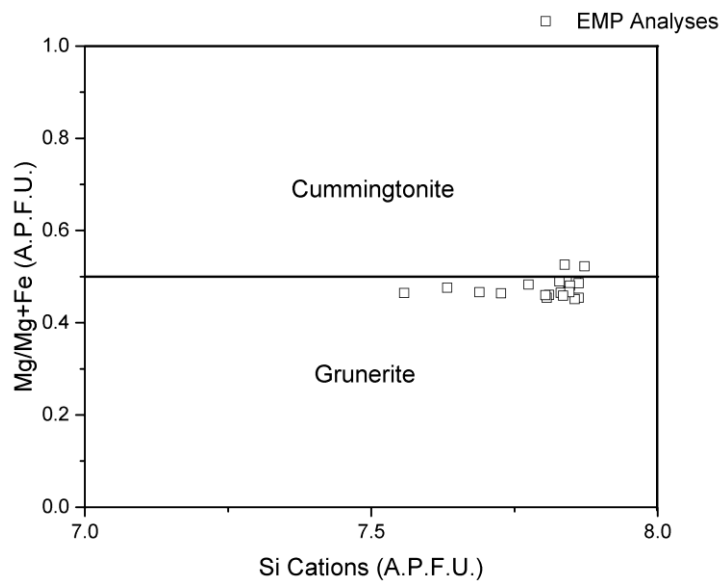


Figure 4-17 Mg/Fe-Si cation plot of EMP analyses of amphiboles in footwall chlorite schist. Total number of analyses totaled 20 and atoms per formula unit (A.P.F.U) calculated on 22 oxygens.

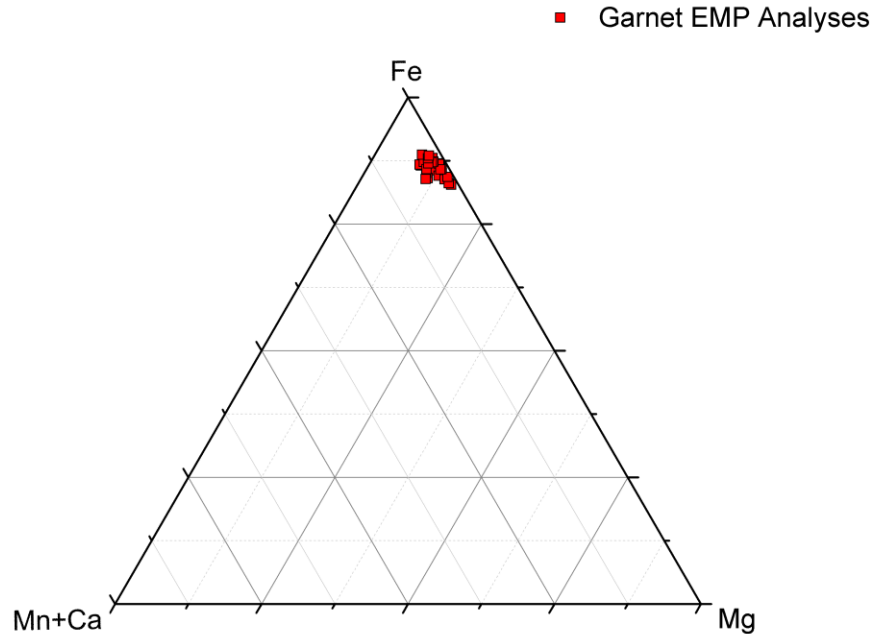


Figure 4-18 Ternary garnet composition plot of garnet porphyroblasts from footwall chlorite schists. EMP point analyses of porphyroblastic garnets are plotted as normalized components.

4.2.2 Ore Zone Lithologies

4.2.2.1 Banded Iron Formation and Enriched Banded Iron Formation

Banded iron formation consists of 1-2 cm thick bands of alternating silica and fine magnetite (minor hematite). BIF textures are illustrated in Plate 4-29. Banding thickness ranges from 5 mm to 2.5 cm. Amphibole commonly forms 50-100 μm size lathes at the contacts between oxide and silica bands. EBIF contains elevated total iron content ranging between 45-60% and has been noted to contain bands of carbonate (MacLeod, 2012). Banded iron formation lenses in high grade ore zones are brecciated and veined by iron oxide (Plate 4-29). As an example, veinlets of 10-25 μm martite-magnetite crosscut linear and brecciated quartz banding (sample 716).

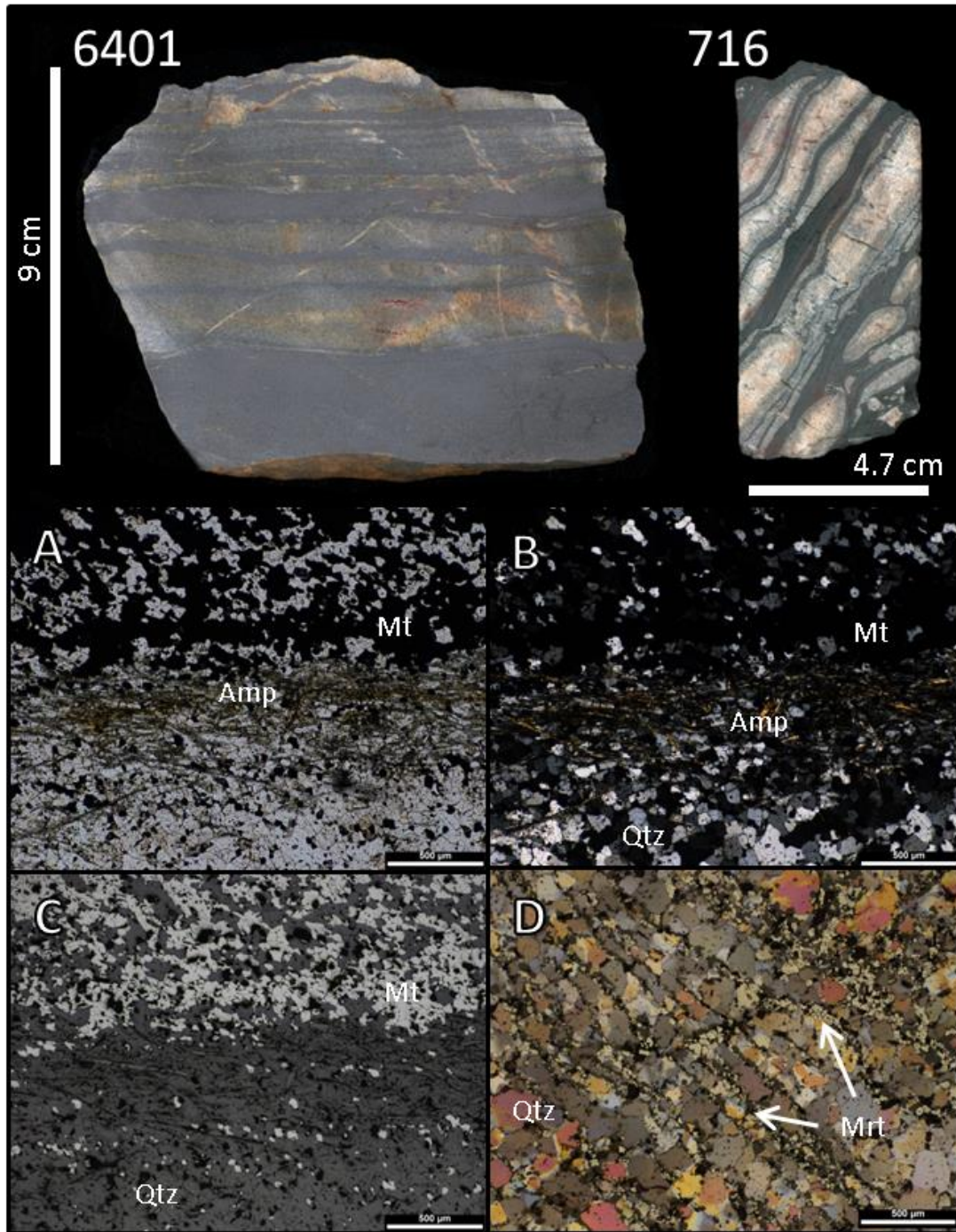


Plate 4-29 Plate illustrating texture and mineralogy of Deposit No.1 banded iron formation. BIF grab sample 6401 shows cm thick banded BIF. Drill core sample 716 is an example of BIF showing brecciation and mild iron oxide veining. Micrographs A and B are comparisons of sample 6401 in PPL and XPL. Magnetite (Mt) and quartz (Qtz) form alternating recrystallized texture with minor amphibole blades at margins. Micrograph C is a reflected light image of A and B. Cross cutting martite veinlets are depicted in micrograph D from altered BIF sample 716.

4.2.2.2 High Grade Iron Formation & Iron Ore Types

Magnetite ore is composed of 75% or more magnetite and 25% or less hematite. Magnetite ores form massive granoblastic mosaics with trace carbonate (0-1%) silicate (0-1%) and sulphide (0-0.5%). Magnetite grains vary widely in size as 50-300 μm octahedra forming a granoblastic-polygonal texture. Granoblastic textures transition into weak breccia textures with increasing porosity (Plate 4-31). Local zones show 1-5 mm pore spaces infilled by carbonate, chlorite and cummingtonite-grunerite. The infilled pore spaces are overgrown by recrystallized granoblastic magnetite. Trace sulphides occur as 0.1-1 mm pyrite cubes and chalcopyrite blebs. All ore types are depicted in Plate 4-30.

Hematite-magnetite iron ore hosts 26-74% magnetite or hematite. The ore shows moderate magnetism and mild to moderate porosity. Granoblastic magnetite textures are overprinted by 5-25 μm veins of hematite forming a network along octahedral magnetite grain boundaries (Plate 4-33). Hematite overprints also occur as cross-hatch patterns replacing magnetite at margins inward. Small folds observed in sample 709 are truncated by a supported breccia texture (Plate 4-33). Pore spaces are 20-200 μm in size, located between subangular magnetite-hematite grains.

Hematite ore contains more than 75% hematite, and generally above 90%. The ore is highly porous from 1-5 mm vugs forming coliform and spongy network textures (sample 6417). Porosity is estimated between 2% and 7%. Magnetism is absent to very weak. In thin section, granoblastic textures are completely overprinted by micro-platy hematite or by martite pseudomorphs; most noticeably in the southern limb (sample 6416).

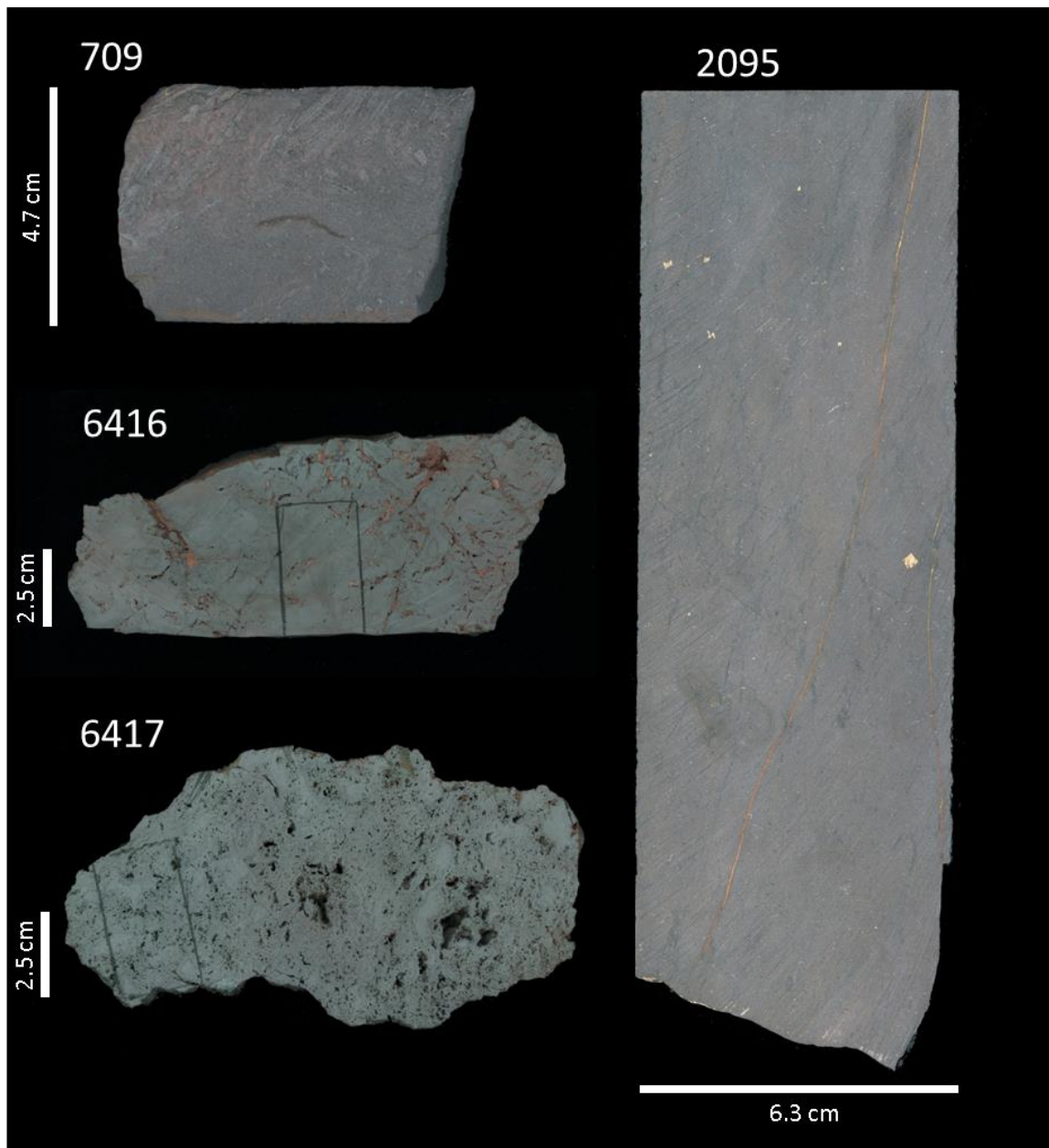


Plate 4-30 Plate of iron ore varieties illustrated by drill core and surface grab samples. Drill core sample 2095 is an example of massive magnetite ore. Hematite-magneite ore is demonstrated by drill core sample 709. Grab samples 6416 and 6417 illustrate martite-hematite and vuggy hematite ores.

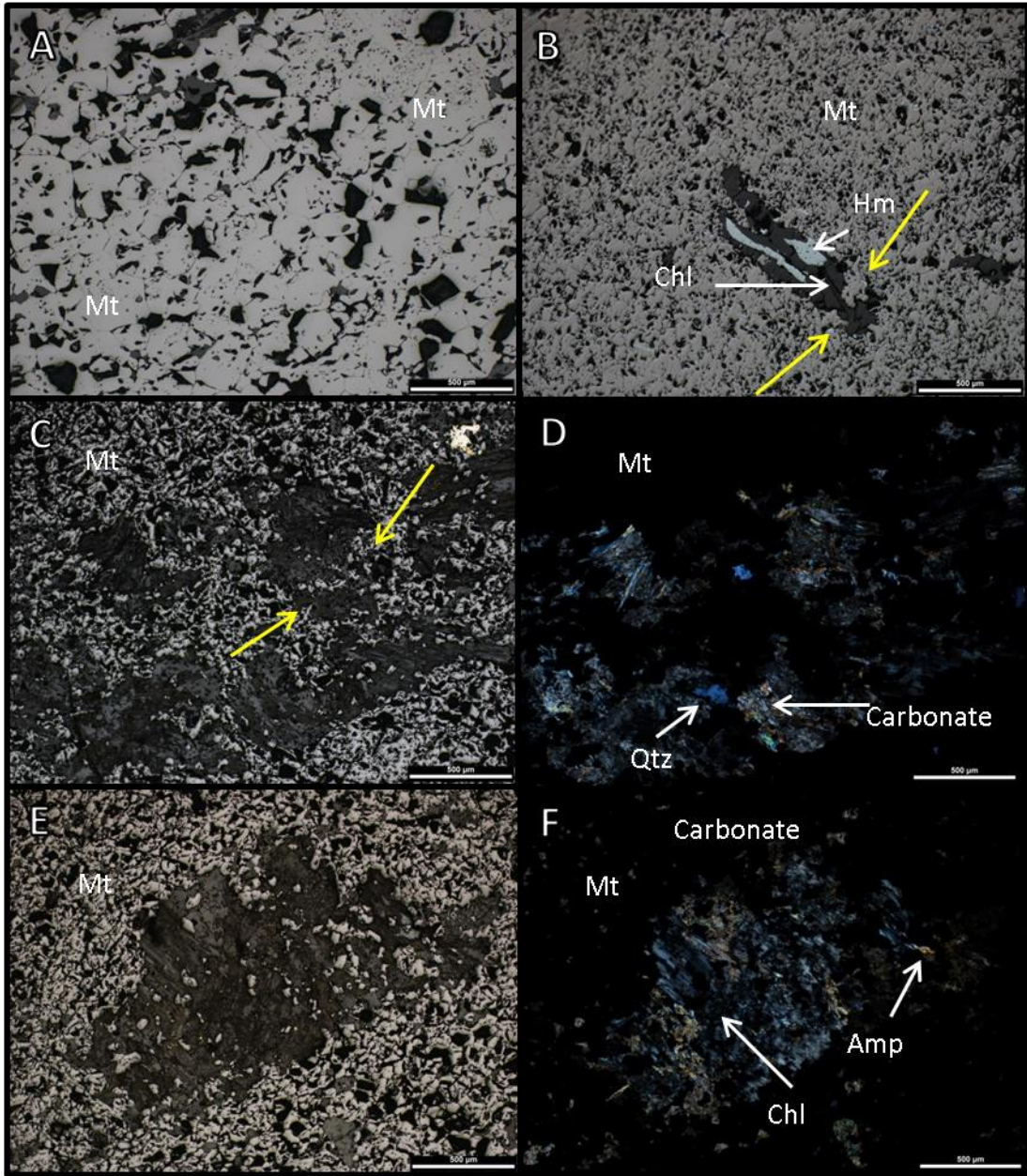


Plate 4-31 Micrographs of various iron ore textures in reflected (RL) and cross polar transmitted light (XPL).

Micrographs A (RL) granoblastic polygonal magnetite (Mt). B (RL) shows finer polygonal magnetite with silicate-hematite infilled pore space impinged by magnetite (yellow arrows). Micrographs C and D are comparative RL and XPL images of pore spaces hosting carbonate (Cb) and quartz (Qtz). Microbreccia textures are overprinted by recrystallized magnetite. E and F show RL and XPL of infilled pore spaces with chlorite (Chl), amphibole (Amp) and carbonate.

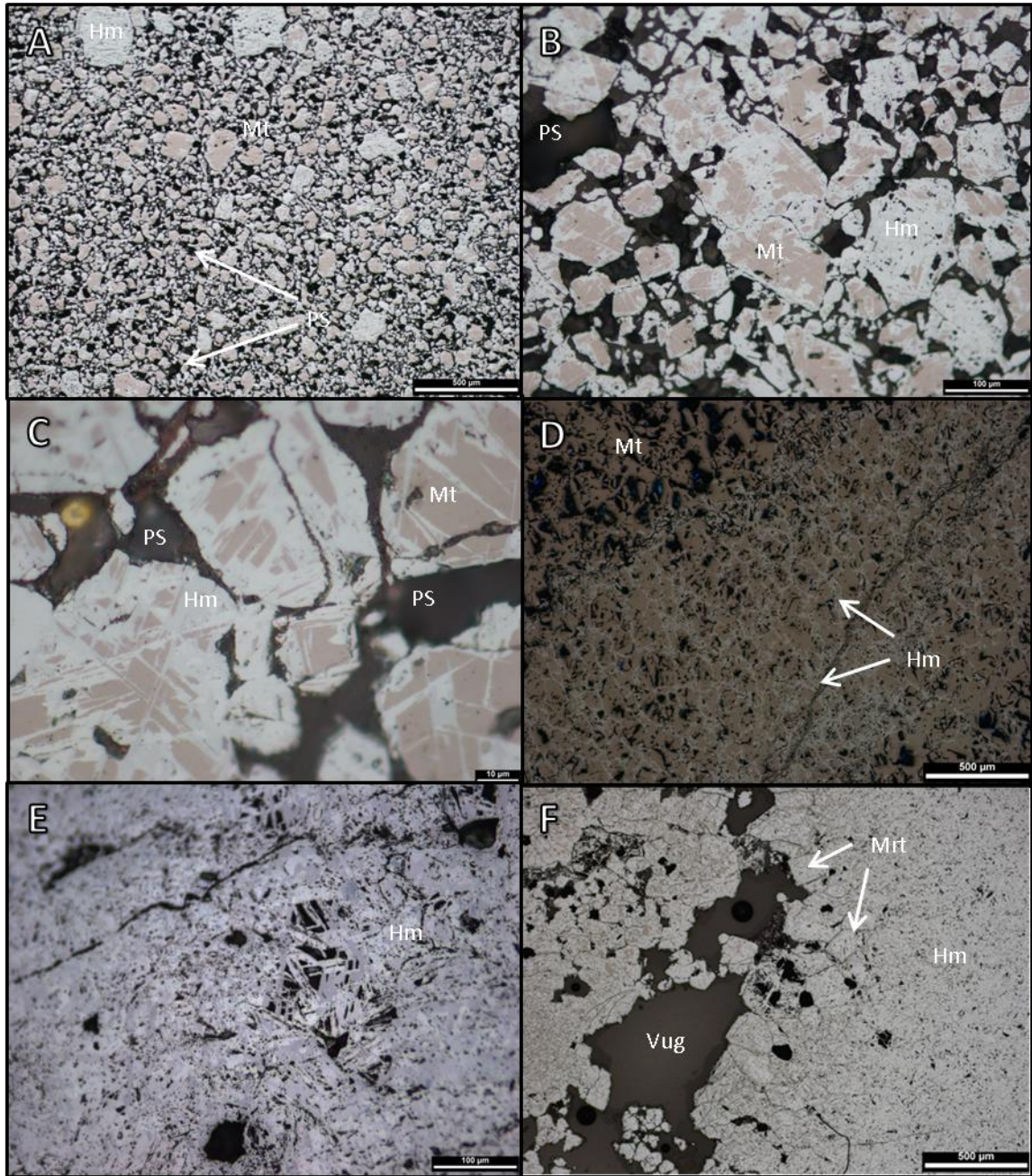


Plate 4-32 Micrographs of various hematite alteration textures in iron ore. Micrographs A, B and C illustrate fine magnetite breccia texture with interstitial pore spaces (PS) and cross-hatched hematized clasts (sample 709). Hematite (Hm) veining is exhibited in micrograph D following polygonal magnetite boundaries. Micrograph E is of microplaty hematite and vugs from sample 6417. Martite (Mrt) pseudomorphs and hematite are displayed in micrograph F with vug space (sample 6416).

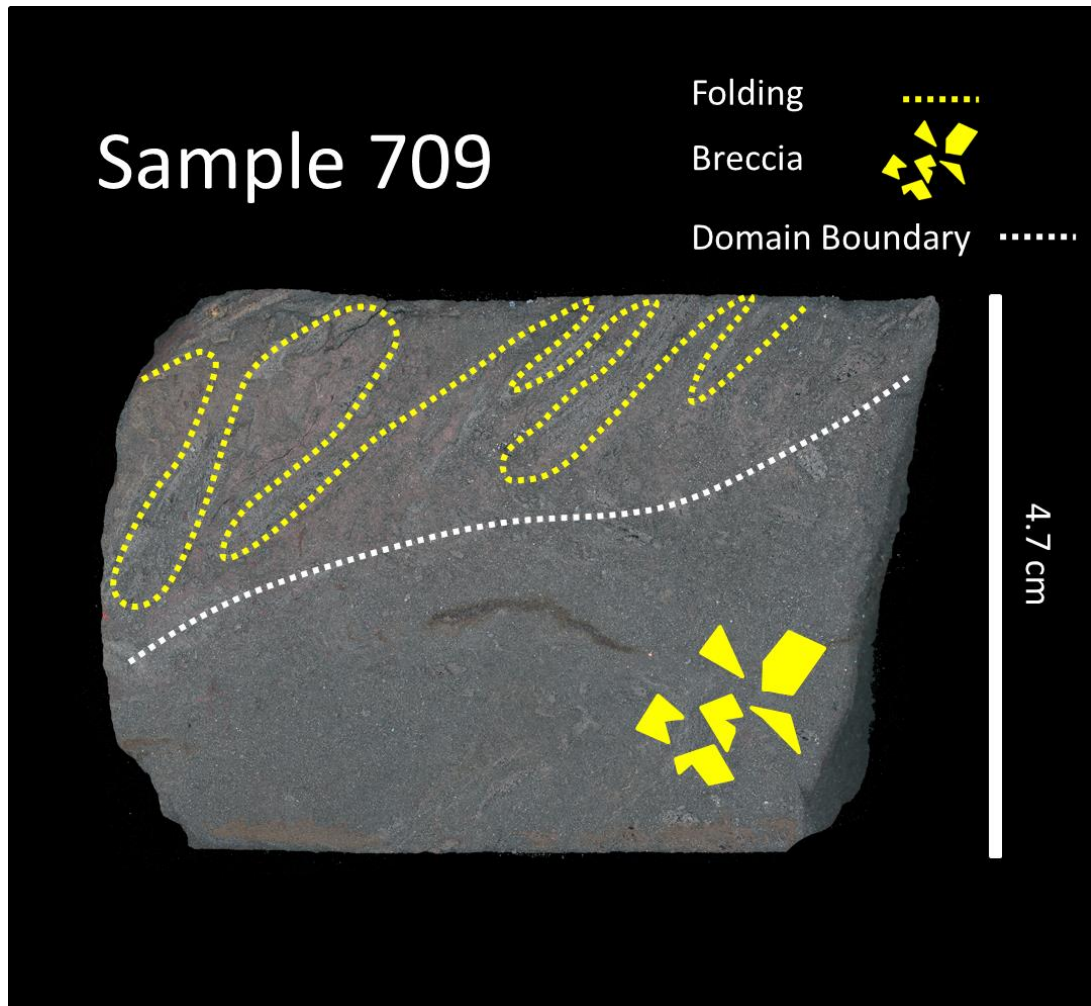


Figure 4-19 Image of magnetite-hematite drill core ore sample 709 with defined structural and texture domains.

4.2.2.3 Ore Zone Chlorite Schists

Chlorite schist is composed of 75-95% ripidolite, 0-20% almandine, 0-10% grunerite, 1-2% martite-hematite and 1% biotite. Trace zircon (0.25%) monazite (0.25-0.5%) and ilmenite (0.5-1%) are also present. Chlorite is the pseudomorphic replacement of biotite as they contain biotite zones and relict basal cleavage. An undulating foliation is present composed of chloritized biotite. Relict crenulation in sample 6220A is overprinted by tabular chloritized biotite at the tapered end of the sample. Chlorite lathes are 25-100 μm in length. Ten WDS EMP analyses of chlorite identify the species to be ripidolite. Chlorite speciation from ore zone chlorite schist and footwall schists is plotted in Figure 4-20. Overgrowing grunerite ranges from 0.1-1mm

size as acicular to rhombic crystals showing minor twinning. Drill core sample 6221 shows acicular to twinned grunerite overprinting chlorite (Plate 4-33). Almandine porphyroblasts are 1-5 cm in size and overprint and contain inclusions of chlorite, grunerite and vuggy martite (sample 6220A). EDS phase mapping and WDS point analyses have identified and quantified manganese enriched cores and rims in almandine (Figure 4-21 and 4-22). Fe rich intermediate zones averaged to 36.06% FeO from eight analyses, forming the equation $\text{Fe}_{2.47}\text{Mg}_{0.32}\text{Mn}_{0.15}\text{Al}_{2.05}\text{Si}_{2.96}\text{O}_{12}$. Manganese rich zones average 7.5% MnO compared to 2.1% from Fe rich zones on the basis of 10 WDS EMP analyses. The Mn rich species was calculated to be $\text{Fe}_{2.12}\text{Mn}_{0.53}\text{Mg}_{0.3}\text{Al}_{2.04}\text{Si}_{2.96}\text{O}_{12}$. Martite-hematite clasts are vuggy 0.5-3 mm subhedral octahedra and subangular clasts with mottled microplaty hematite interiors showing pore spaces (Plate 4-33). Zircons are 10-50 μm blocky euhedral grains within chlorite. Monazites form 200-500 μm patches and clusters comprising of smaller 25 μm anhedral cryptocrystalline monazite grains.

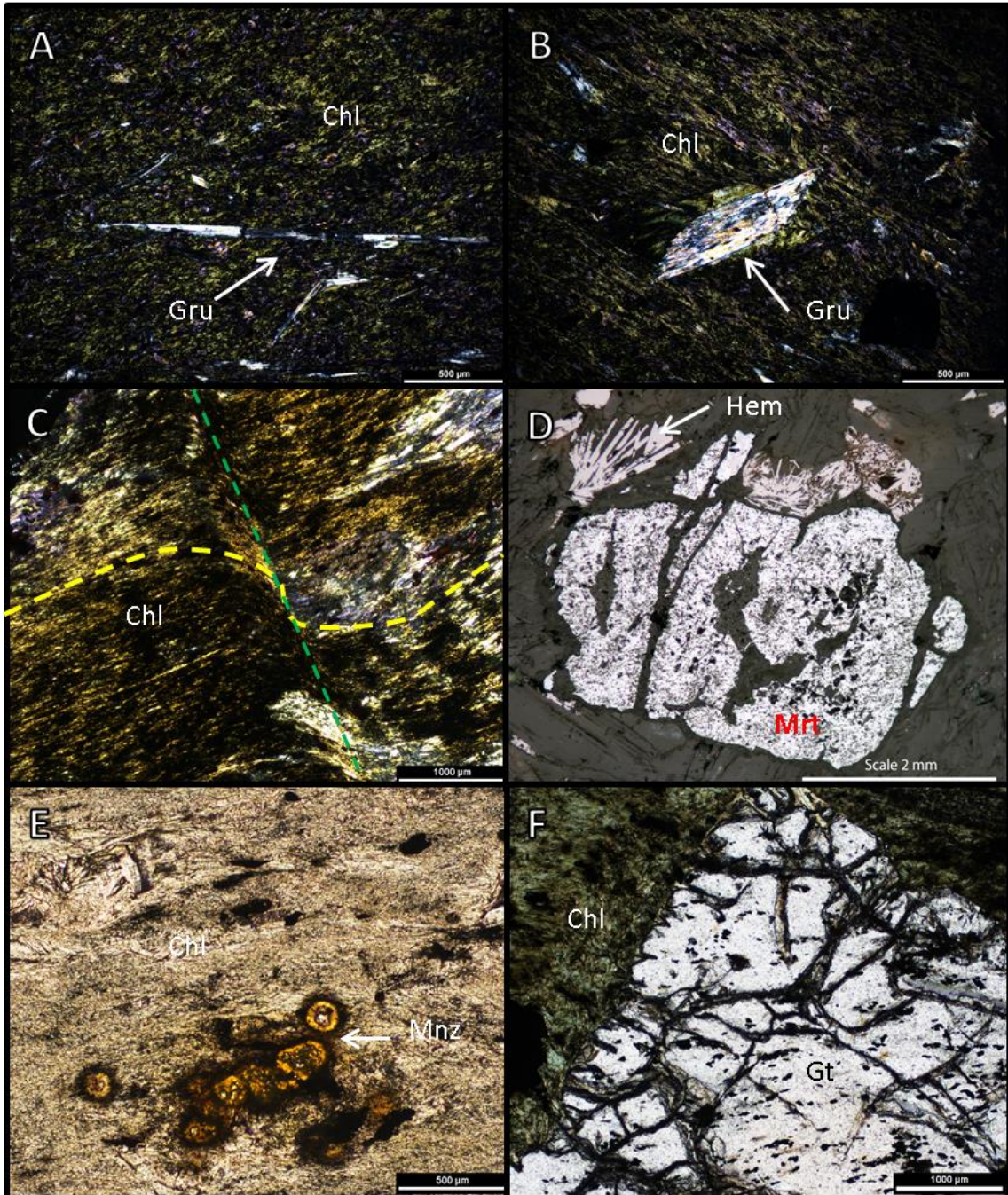


Plate 4-33 Micrographs of ore zone chlorite schist minerals and textures. Micrographs A and B show acicular and rhomb shaped grunerite (Gru) porphyroblasts overprinting chlorite (Chl) in XPL. Crenulation and foliation cleavage depicted in C. Green dashed line indicates crenulation cleavage and the yellow line traces foliation. D shows fractured martite (Mrt) porphyroblast/clast with bladed and microplatey hematite (Hem) and pore spaces. Patchy monazites (Mnz) are depicted in E with pleochroic halos. F shows garnet porphyroblast overprinting chlorite.

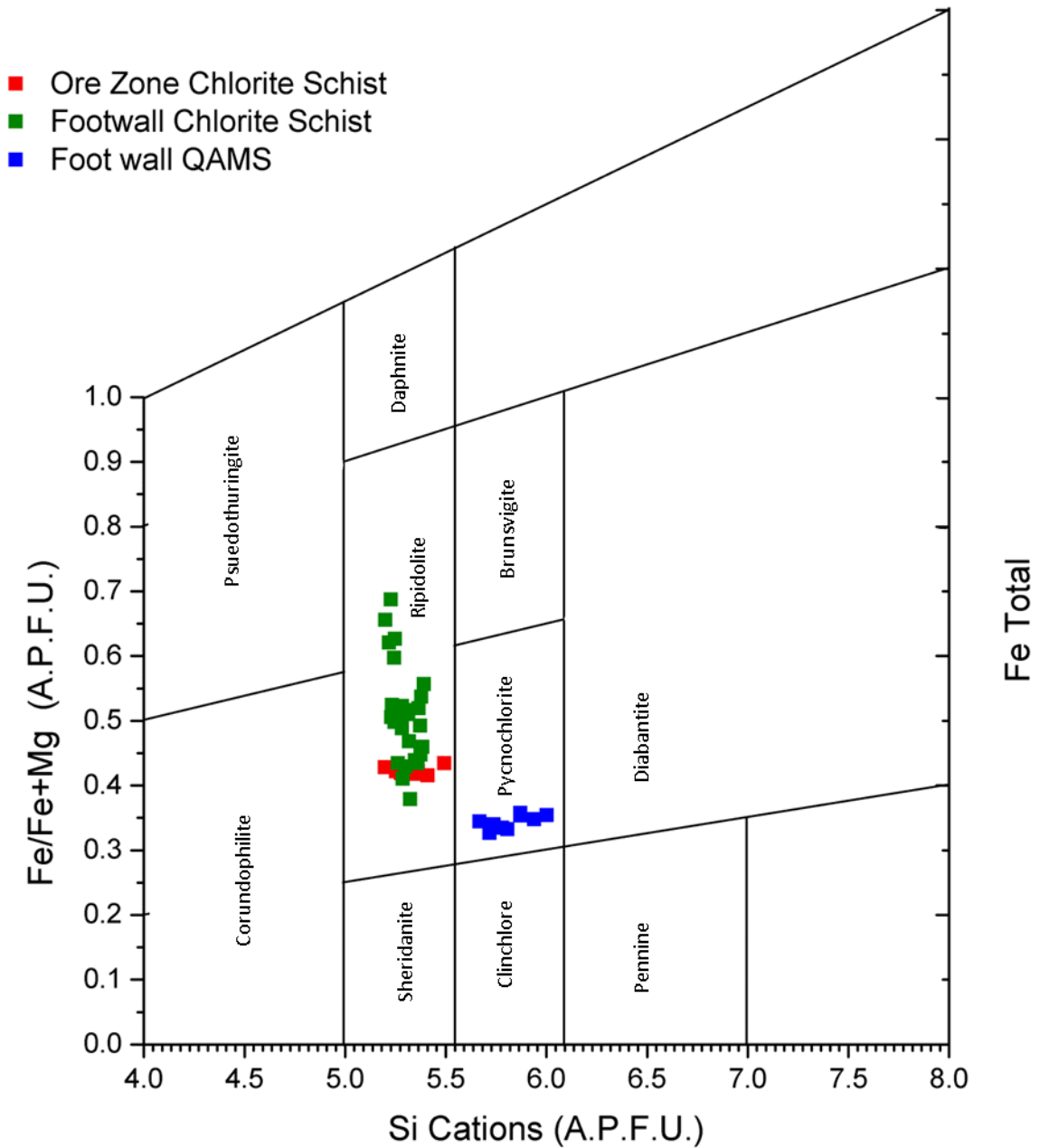


Figure 4-20 Chlorite cation plot discriminating chlorite speciation from footwall QAMS, chlorite schist and ore zone chlorite schist. Calculated atoms per unit formula (A.P.F.U. or cations) from EMP analyses are plotted. Analyses totaled 9 from QAMS, 27 from footwall chlorite schist and 10 from ore zone chlorite schist.

Sample 6220A Phase Map

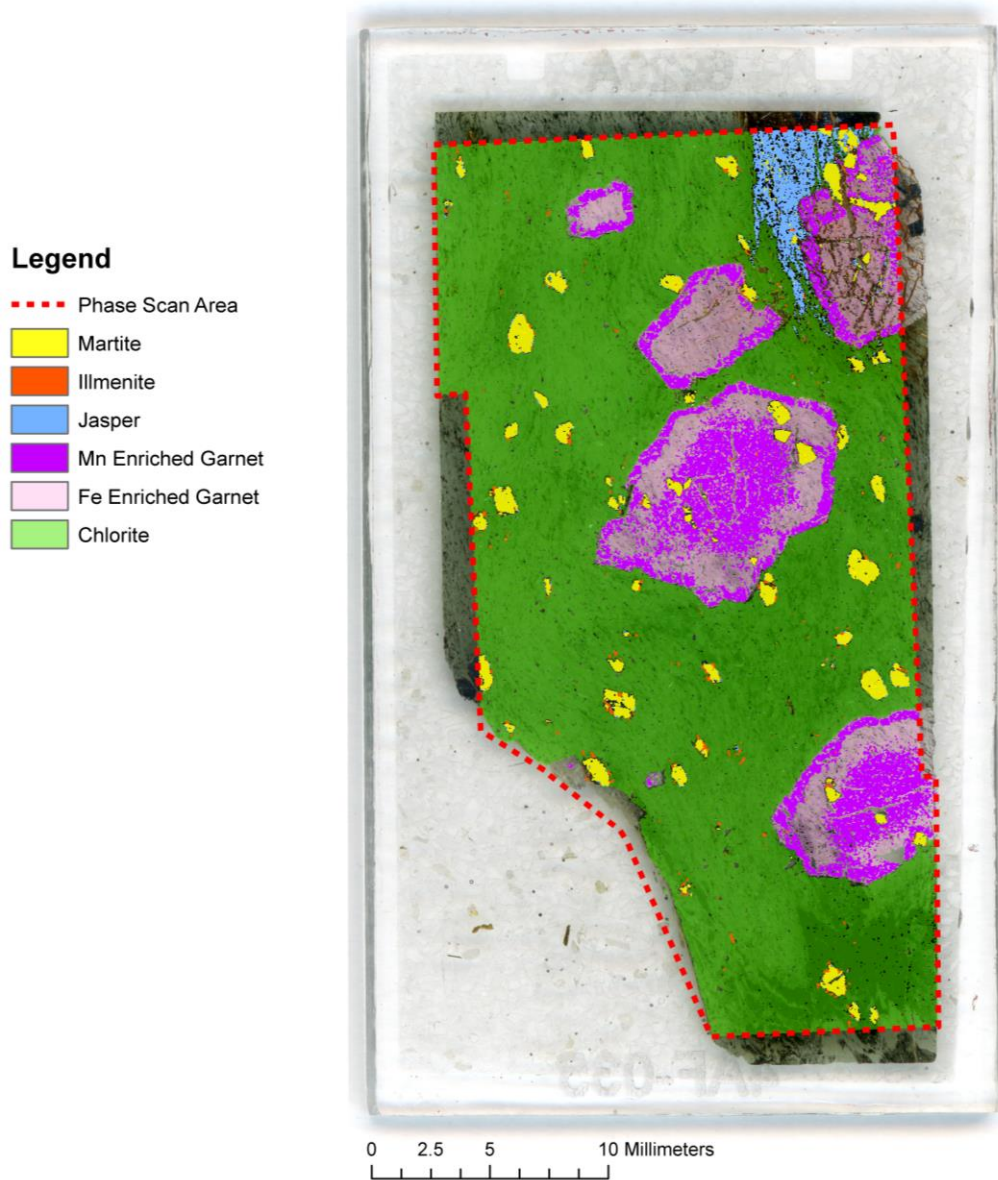


Figure 4-21 EDS phase scan of garnetiferous chlorite ore zone schist. Mn-Fe zone distinguishable in garnets. EDS phase scan area outline by red dash line.

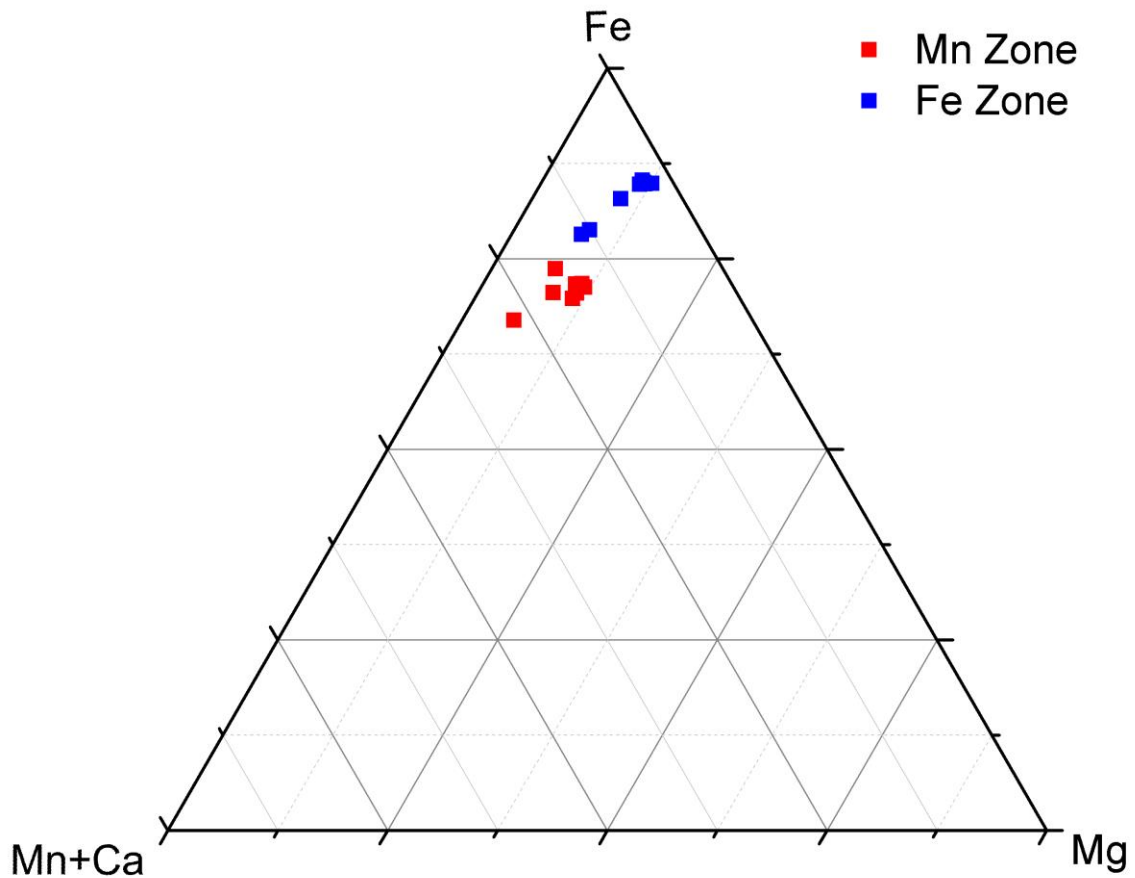


Figure 4-22 Ternary garnet composition plot of garnet porphyroblasts from ore zone chlorite schists. EMP point analyses of porphyroblastic garnets are plotted as normalized components based on area of garnet analyzed with respect to EDS phase mapping.

4.2.3 Hangingwall Lithologies

4.2.3.1 Chlorite Schists (HWCS)

Hangingwall chlorite schists contain 50-75% chlorite, 2-10% biotite, 5-25% garnet, 5-10% cordierite, 2-5% quartz. Accessory minerals are ilmenite, zircon and monazite occurring in 0.5-1%, 0.1% and 0.1% abundances. The matrix consists of 250 μm chlorite lathes and tablets in a foliated to decussate texture with abundant pleochroic halos. Chlorite schist foliation is spaced and undulating, defined by 100-500 μm thick microlithons of 10 μm polygonal quartz. Garnets are 5-10 mm poikiloblasts containing biotite, quartz and chlorite inclusions. Garnets also overgrow 100-500 μm radial-twinned

cordierite. The planar fabric is rotated within garnets by 30 degrees with respect to the foliation plane. The chlorite-quartz matrix wraps around garnet forming small pressure shadows (Plate 4-34). Ilmenites are 80 μm blades predominantly aligned and parallel with foliation. Zircons range between 25-50 μm and are euhedral.

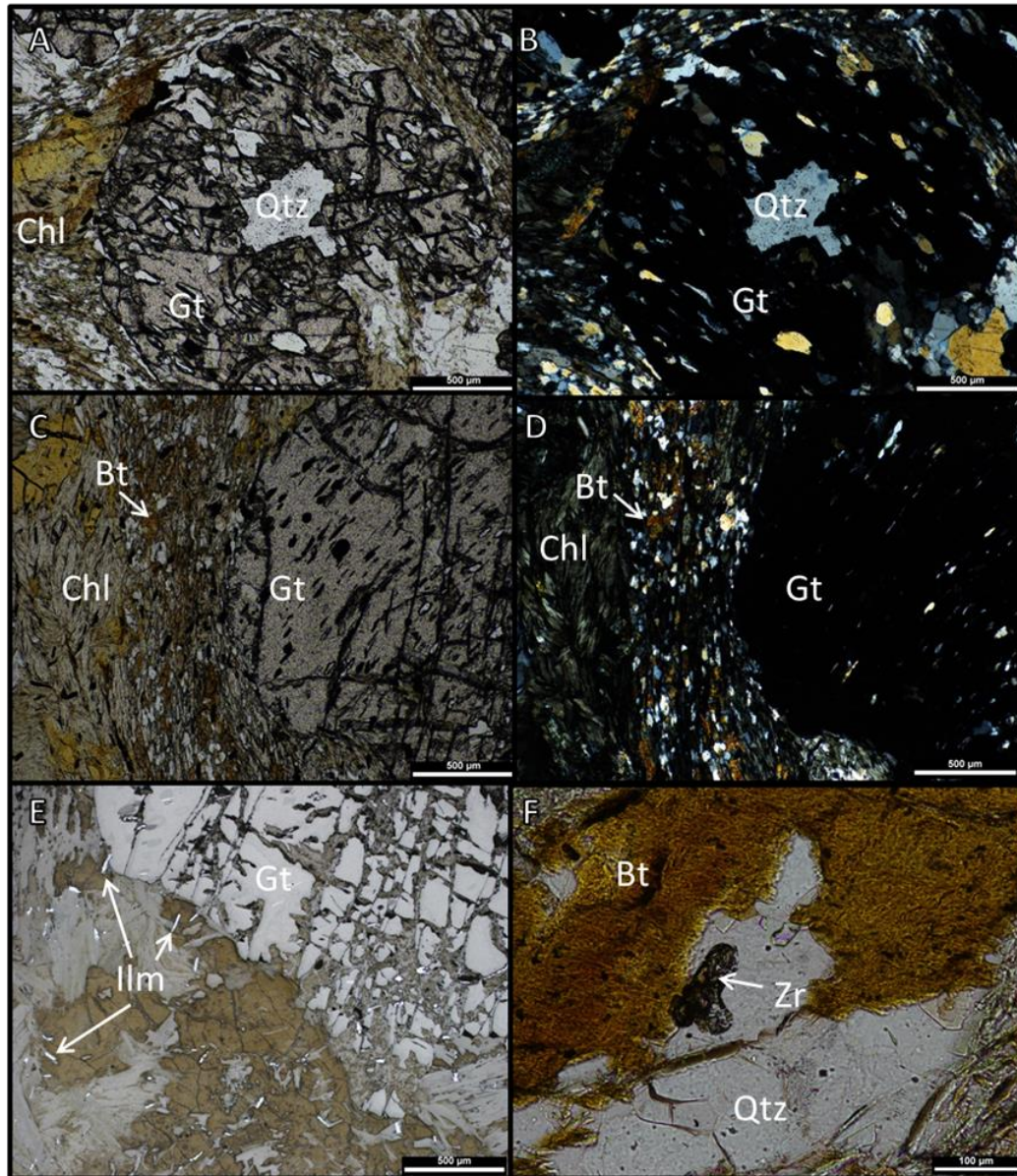


Plate 4-34 Plate of hangingwall chlorite schist mineral textures. A and B are PPL and XPL images of a rotated garnet (Gt) porphyroblast containing quartz (Qtz) inclusions. Micrographs C and D are also PPL and XPL of a rotated garnet porphyroblast but show microlithon of fine quartz. Bladed ilmenite (Ilm) in RL is depicted in E as inclusions in garnet and in the chlorite (Chl) matrix. Micrograph F shows a euhedral zircon (Zr) with quartz, biotite (Bt) and chlorite.

4.2.3.2 Biotite Schist (HWBS)

Chlorite schists grade away from the HGIF contact into biotite schists with porphyroblasts of staurolite, cordierite and garnet. Modal abundances range from 45-55% biotite, 15-25% quartz, 10-25% staurolite, 20% cordierite and 5-15% garnet. Biotites are coarse 1-3 mm euhedral tablets and lathes with strong basal cleavage aligned in a spaced foliation defined by 100 μm thick polygonal quartz. Late anhedral 100-500 μm biotite is present and characterized by numerous pleochroic halos. Staurolites form 3-5 mm barrel shape poikiloblasts hosting inclusions of quartz, cordierite and biotite (Plate 4-5). Cordierites are 0.1-3 mm xenoblastic to idioblastic poikiloblasts hosting inclusions of biotite and quartz. Cordierite shows mild to internal cloudy alteration and radial twinning in sample 6506. Garnets form 5-7 mm subhedral porphyroblasts in 1-50 cm thick zones. Garnets contain inclusions of staurolite biotite quartz and cordierite. Ilmenites are 10-50 μm blades aligned with foliation and identified within all porphyroblasts.

Biotite schist transitions into brittle deformation textures near the contact to volcanoclastics. Oblong clasts of quartzo-feldspathic material are distributed in biotite schists (Plate 4-35 sample 6505). The clasts are, tentatively, fractured and altered pieces of volcanoclastic units surrounded by biotite schist. Biotite veins, up to 5 cm thick, emanate from biotite schist into adjacent fractured volcanoclastic units.

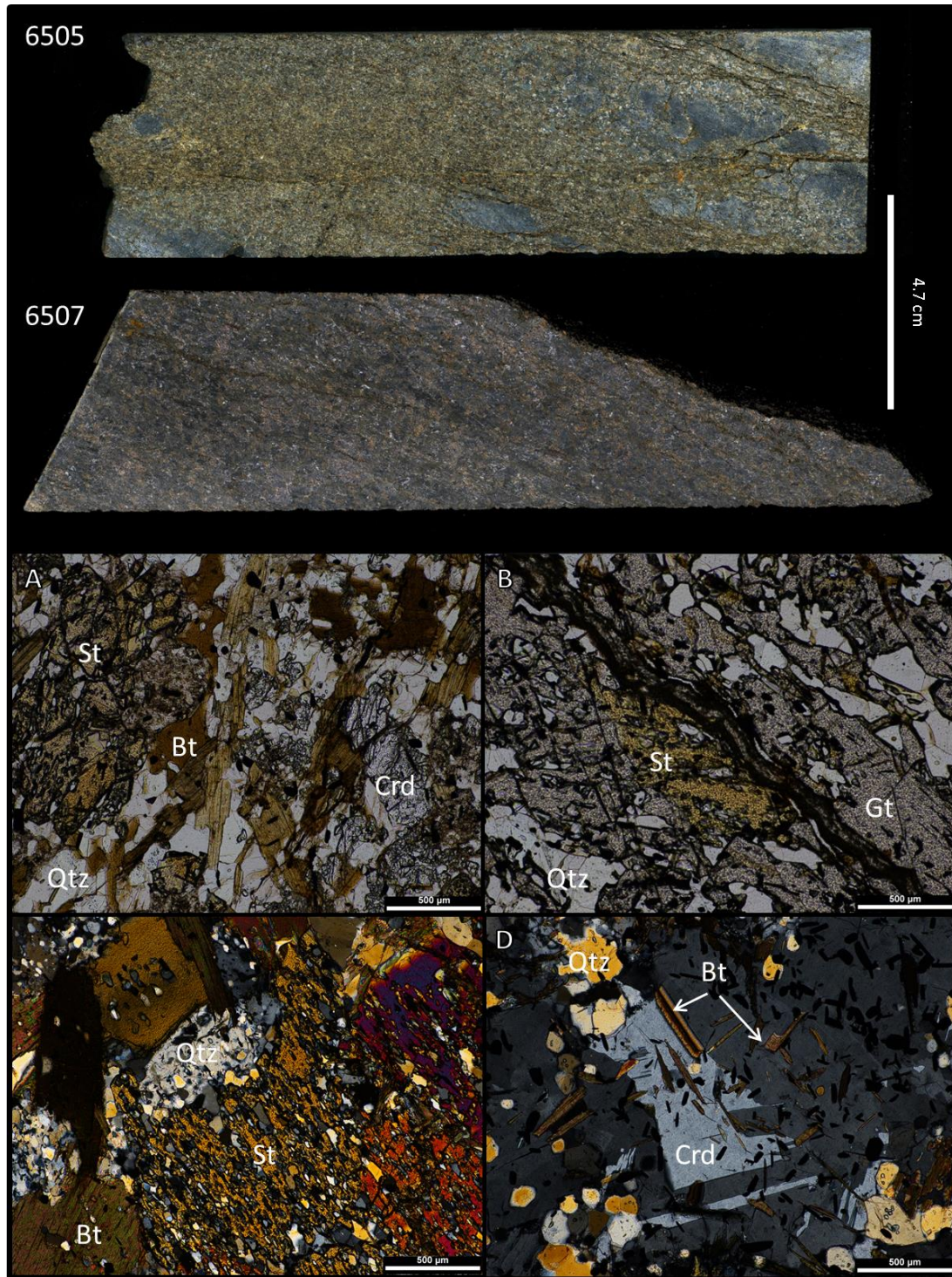


Plate 4-35 Plate of various mineral and textural features in HW biotite schists. Sample 6505 illustrates quartz-felspathic clasts in biotite schist oriented parallel to foliation. Drill core sample 6507 is a garnet bearing biotite schist with microlithons. Micrographs A show staurolite (St), cordierite (Crd), biotite (Bt) and quartz in mildly foliated texture. B shows poikioblastic garnet (Gt) with staurolite inclusion. C shows staurolite poikioblast with quartz (Qtz) inclusions and coarse biotite. D displays radial twinned cordierite with quartz inclusions.

4.2.3.3 Ultramafic

Ultramafic units are greasy, strongly serpentinized rocks. Ultramafics are subdivided into two categories; ultramafic (UM) and ultramafic-amphibolites (UA) (Plate 4-36). UM is composed of serpentine (85-95%), carbonate (5-15%) magnetite-spinel (1%) and traces of pyrite (0.5%). Serpentine forms low birefringent mottled masses. Grey-pink carbonates form 2-8 mm oblong patches and 0.2-0.5 mm wide linear veins. Carbonate veins crosscutting serpentine are composed of 80-300 μm anhedral to subhedral rhombs showing high birefringence and 60/120 cleavage. EDS spot analysis indicates magnesite and dolomite species (Figure 4-24). Disseminated magnetite are light grey (transmitted light) 30-100 μm anhedral to subhedral octahedra. WDS EMP analyses of magnetite shows Cr_2O_3 concentrations range between 1.53 % to 17.49 %, indicating a chromite component. Pyrites are fine 10-25 μm disseminated blebs.

UA units contain variable anthophyllite (30-55%), chlorite-serpentine (15-25%), carbonate (5-45%), talc (15-25%) and magnetite (2%). Ultramafic-amphibolites have greater than 55% anthophyllite while samples 6523 and 6524 have 30% but 40-45% carbonate. Talc forms 1-3 cm wide radiating clusters of 200-700 μm wide lathes overprinting serpentine and carbonate (Plate 4-36 sample 6533). Talc crystals host inclusions of carbonate and show retrogression to chlorite. WDS EMP analysis of talc show iron impurities of 3.21%-3.29% FeO. The formula of talc is $\text{Mg}_{5.88}\text{Fe}_{0.12}(\text{Si}_{7.93}\text{O}_{20})(\text{OH})_4$, averaged from three analyses. Anthophyllites are 0.25-1 mm acicular grains forming 1-2 cm bowties overgrowing retrograded talc, serpentine and carbonate (Plate 4-38). Anthophyllites also contain an iron component averaging 1.95% FeO on the basis of five WDS EMP analyses. The resulting chemical formula for anthophyllite is $\text{Mg}_{2.76}\text{Fe}_{0.10}(\text{Si}_{8.05}\text{O}_5)(\text{OH})_4$ (Figure 4-23). Carbonates are 130-250 μm subhedral blocks in a weak polygonal texture overprinted by both talc and anthophyllite. Magnetite occurs as subhedral 100-200 μm octahedral scattered throughout the matrix.

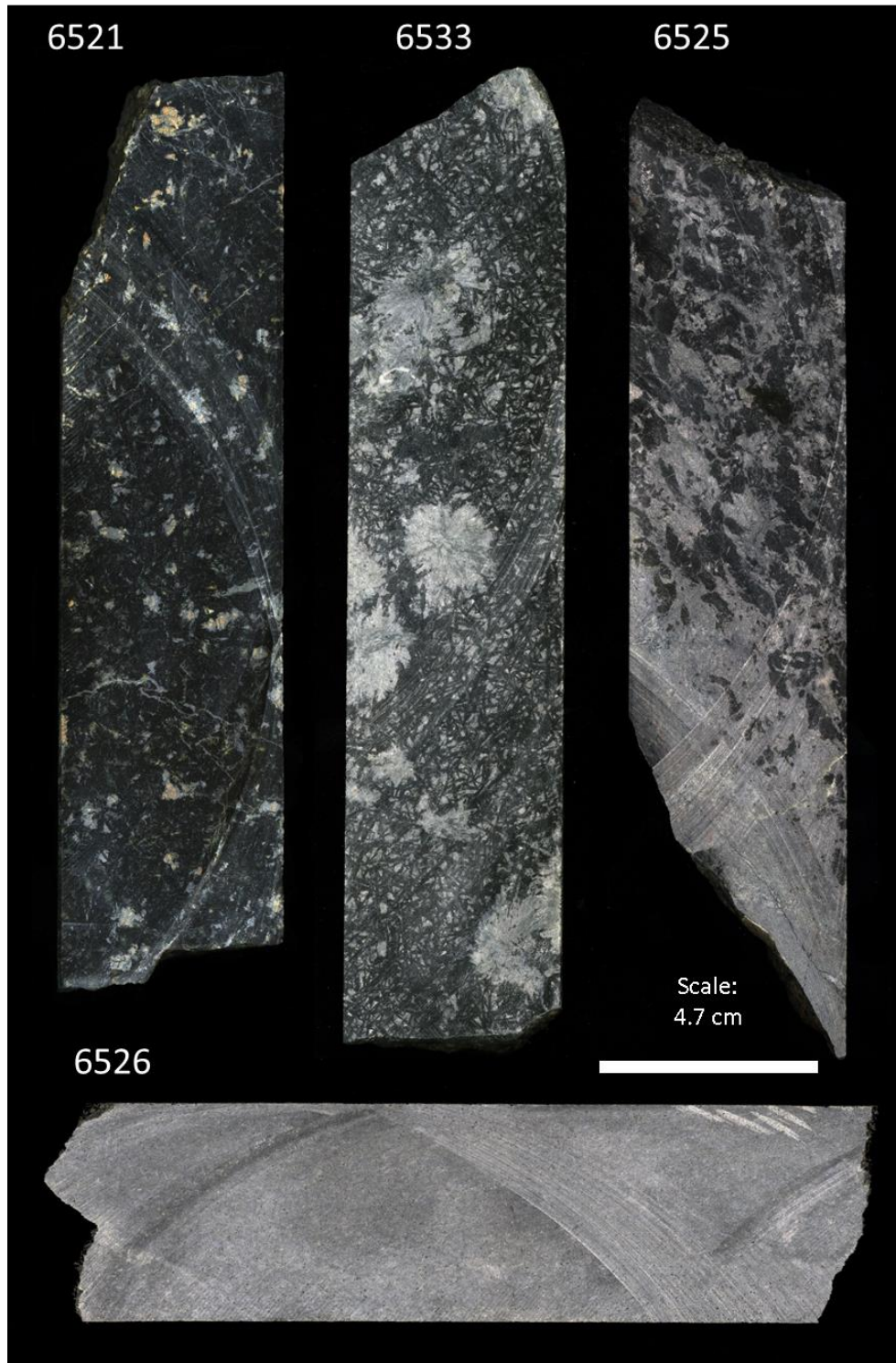


Plate 4-36 Photographs of ultramafic (UM) and ultramafic-amphibolite (UA) drill core. Sample 6521 is an ultramafic sample displaying serpentine with carbonate veins and pink dolomite patches. Sample 6533 is an ultramafic over printed by radiating talc. The contact between UM and UA units is demonstrated by lower portion of sample 6525. Ultramafic amphibolite is represented by sample 6526.

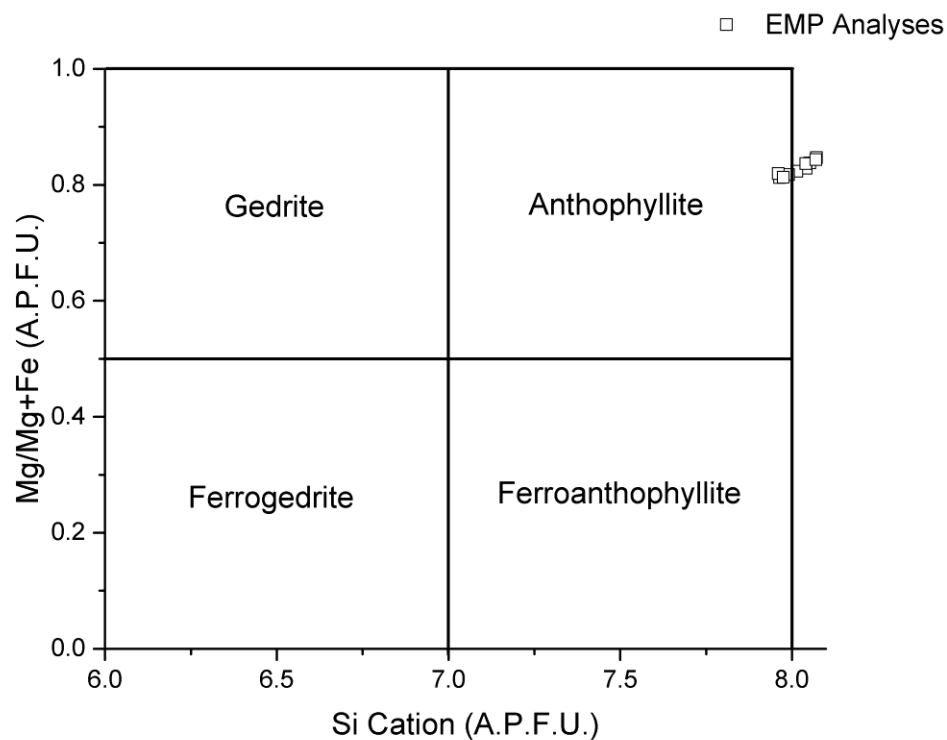


Figure 4-23 Mg/Fe-Si cation plot of EMP analyses of amphiboles in ultramafic-amphibolite units. The number of analyses totaled 10 and atomic units were calculated on 22 oxygens.

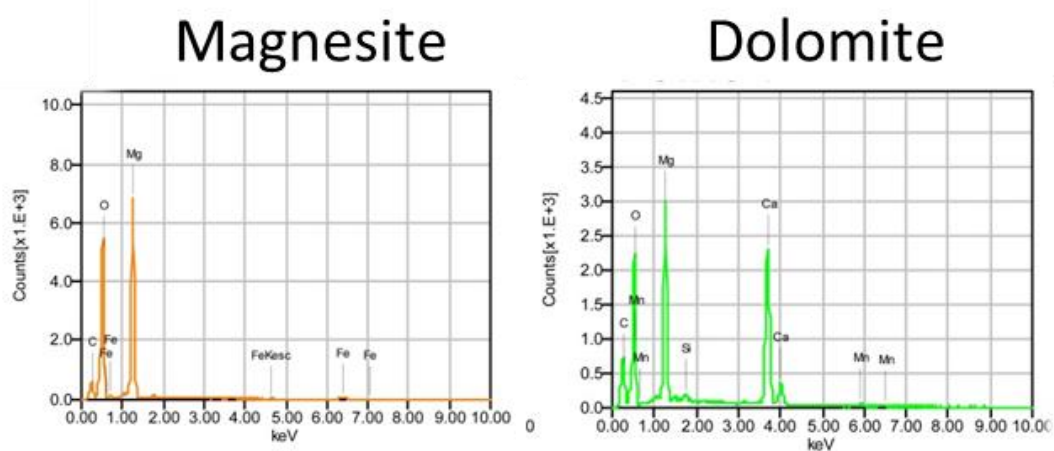


Figure 4-24 EDS spectrum of carbonates in ultramafic sample 6521.

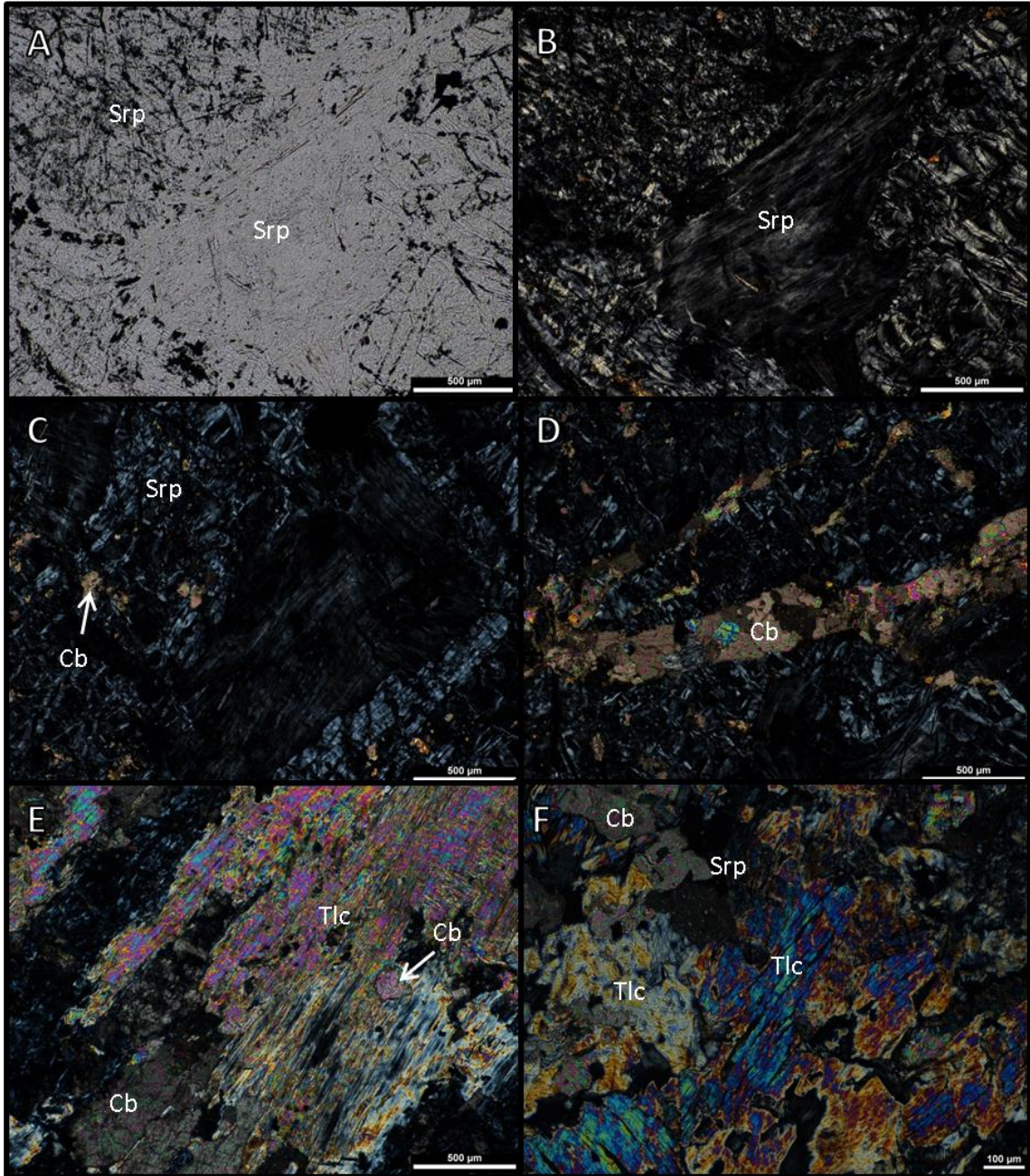


Plate 4-37 Micrographs of mineral textures in ultramafic units. Micrographs A and B are PPI and XPL images of serpentine (Srp). Disseminated blebs of carbonate (Cb) and veins of carbonate shown in C and D. Micrographs E and F show talc (Tlc) overprinting carbonate and serpentine.

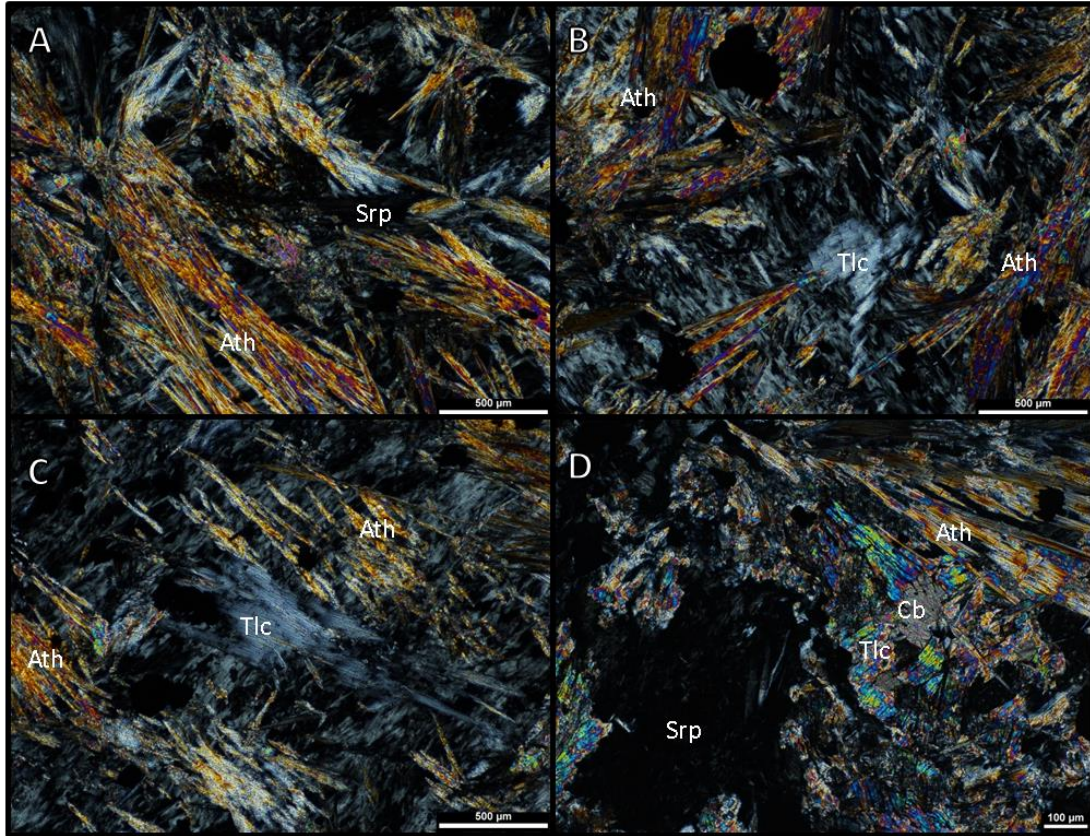


Plate 4-38 Micrographs of mineral textures in ultramafic-amphibolite units. Micrographs A, B and C are anthophyllite (Ath) overgrowing serpentine (Srp) and retrograde talc (Tlc). Anthophyllite also overprints carbonate (Cb), talc and serpentine in micrograph D.

4.2.3.4 Volcaniclastic

The volcaniclastic unit ranges texturally from cryptocrystalline to medium grain polygonal. Cryptocrystalline and recrystallized polygonal textures are described separately.

Cryptocrystalline type samples (6527-6528) are composed of cryptocrystalline (55-60%), quartz (10-15%), carbonate (5-10%) and chlorite (10-20%) forming a finely laminated matrix (Plate 4-39). Pyrite and sphalerite are accessory minerals and form 50 - 200 μm blebs, accounting for 0.5% each. Fine grain angular quartz crystals are between 20-100 μm. Carbonates are cross twinned 40-200 μm blocky grains. Patchy berline blue chlorite (XPL) overprints higher relief cryptocrystalline. Trace 20 μm zircons are disseminated throughout the matrix.

Recrystallized volcanoclastics are composed of fine to medium grain quartz (50%), andesine (5%) hornblende (40%), biotite (3%) and chlorite (1%) (Plate 4-39). Accessory minerals are pyrite (0.5-1%) and chalcopyrite (0.5-1%). Quartz grains are angular 10-100 μm crystals set in a polygonal texture. Quartz grains also form dispersed 0.2-3 mm amalgamated patches (sample 6531). Hornblendes form 100-600 μm subhedral green needles to lathes that host 10 μm size pleochroic halos. Biotite replaces hornblende at margins (sample 6532).

4.2.3.5 Hornblende Amphibolite

Hornblende amphibolite (Hbl-A) is not exposed at surface. Drill core samples show the unit is massive composed of medium to coarse interlocking hornblende (65%), plagioclase (33%) and quartz (1-2%) (Plate 4-40). Trace (0.5%) 50 μm chalcopyrite and sphalerite blebs and lathes occur interstitially. Hornblendes are 0.1-2 mm green subhedral to euhedral tablets and lathes with 60/120 cleavage. Plagioclase lathes (0.5-1 mm) exhibit polysynthetic and carlsbad twinning. Hbl-A units have sharp contacts with ultramafic, ultramafic-amphibolites and volcanoclastic units in drill holes MR1-14-227 and 228. Drill hole MR1-05-54 shows direct contact with BIF.

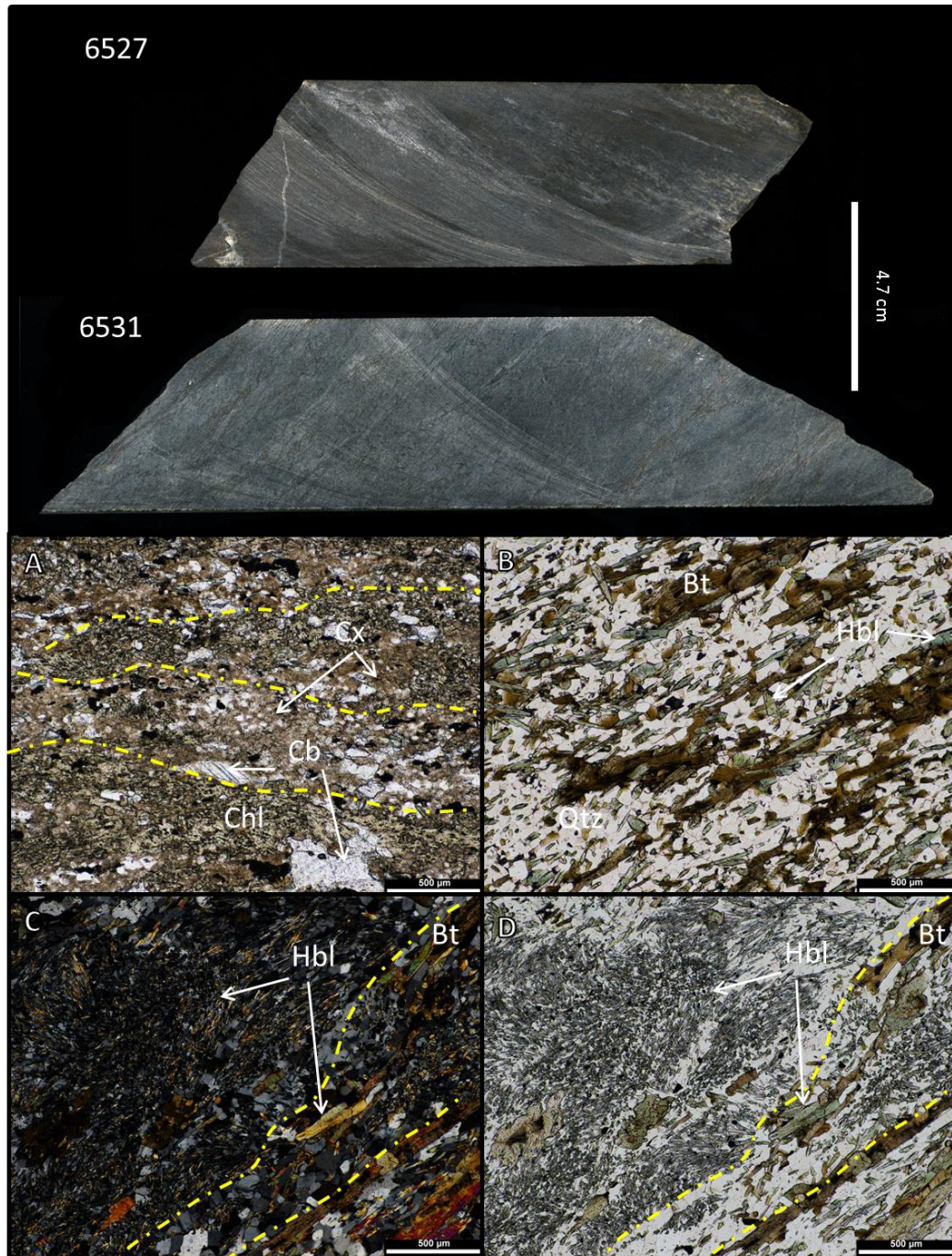


Plate 4-39 Photographs and micrographs of mineral and textural features in volcanoclastic units. Drill core samples 6527 and 6531 represent cryptocrystalline and polycrystalline texture. Micrograph A depicts finely laminated cryptocrystalline matrix (Cx) with chlorite (Chl) and carbonate (Cb). Lamination domains are marked by a yellow dash line. Micrograph B shows honblende (Hbl) lathes mildly overprinted by biotite in polycrystalline sample. Micrographs C and D are comparative XPL and PPL images of polycrystalline laminated volcanoclastic with quartz, biotite (Bt) and acicular hornblende.

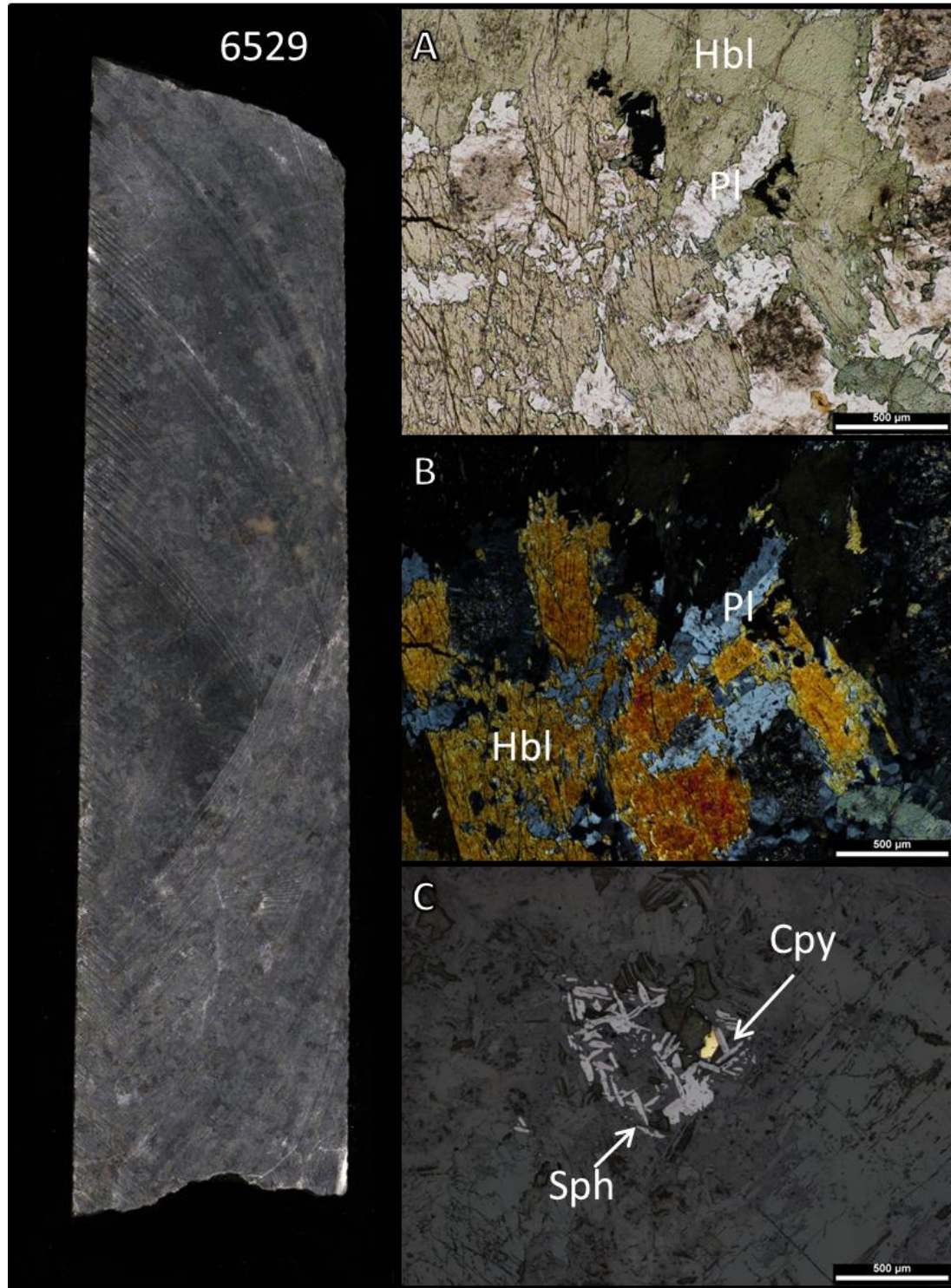


Plate 4-40 Photograph and micrographs of mineral and textural features in hornblende-amphibolite. Sample 6529 is a hornblende amphibolite showing medium grain massive texture. Micrographs A and B are PPL and XPL images of interlocking hornblende (Hbl) and plagioclase (Pl). Chalcopyrite (Cpy) bleb and sphalerite (Sph) blades are shown in RL in micrograph C.

4.3 Mineral-Textural Paragenesis

Complex mineral parageneses are observed in all lithologies of Deposit No.1. The following identifies, classifies and orders mineral growth in footwall, ore zone and hangingwall domains.

4.3.1 Footwall Paragenesis

Quartz-augens are observed in every footwall unit. Quartz-augens decrease in abundance from QAMS units into biotite and chlorite schists. Monzogranite clearly transitions into QAMS and QAMBS units by the marked influx of micas. The onset of lineations forming quartz-augens coincides with the influx of mica. Muscovite overprints form from the breakdown of K-feldspar and predate biotite. A small biotite overprint of muscovite does occur in some QAMS samples. Cordierite hosts chloritized relicts of biotite and muscovite, signifying cordierite overgrew a partially chloritized matrix.

A late biotite event overprints cordierite porphyroblasts and foliated muscovite prior to staurolite growth. This overprint obliterates almost all cordierite leaving only vermiform and pinitic relicts. Cordierite relicts are most abundant in QABS and biotite schist. The precursor protolith to QABS and biotite schist was cordierite-muscovite \pm quartz schist. Chlorite inclusions within staurolite and almandine also demonstrate chlorite retrogression of biotite prior to staurolite and garnet growth (Plate 4-23). Staurolite in biotite schists is later encapsulated by garnet. Blokey andalusites locally occur with staurolite and garnet in biotite schists but are not identified in chlorite schists. Andalusite is in equilibrium with respect to staurolite and garnet. Grunerite occurs sparsely in biotite schist outcrops, but commonly within chlorite schists at the margin of HGIF. Garnet porphyroblasts incorporate staurolite, chlorite and grunerite making it the last growth stage. A textural paragenetic time line is displayed in Figure 4-25. The mineral paragenesis is divided into three stages and outlined in Figure 4-26. All major mineral reactions for footwall paragenesis are listed in balanced chemical equations 1-15.

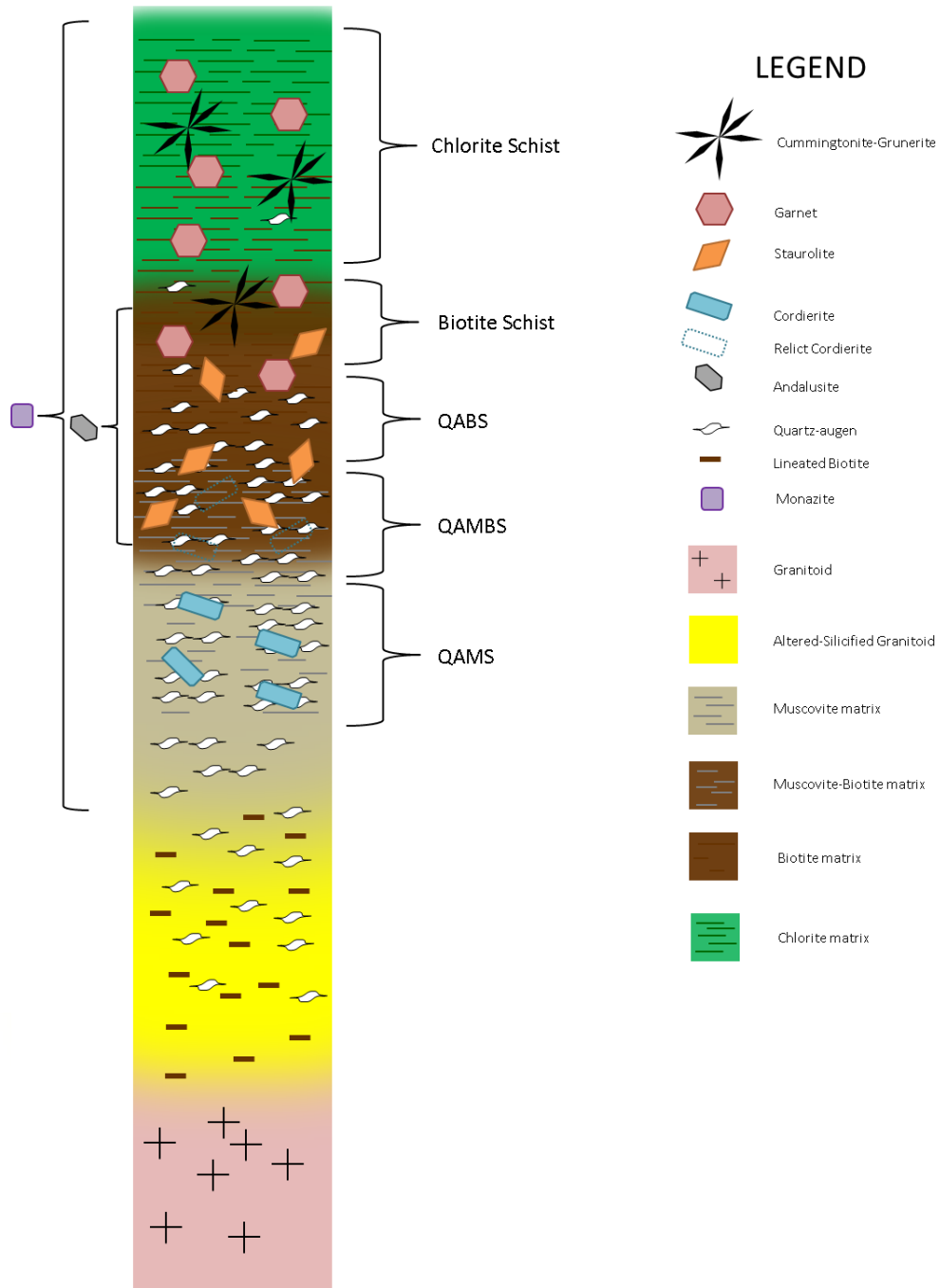


Figure 4-25 Diagram of mineral-textural paragenesis of footwall schist units. Note that the silicified boundary is considered concurrent with the development of micas.

Stage 1 Calc-silicates

Equation 4-1 Plagioclase → Epidote



Equation 4-2 K-feldspar → Epidote

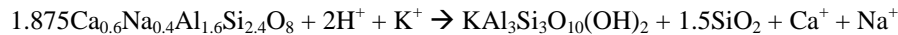


Stage 2 Muscovite Alteration

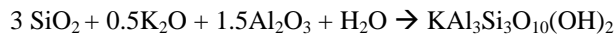
Equation 4-3 K-feldspar → Muscovite



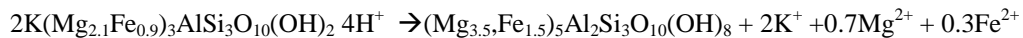
Equation 4-4 Plagioclase → Muscovite



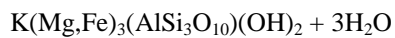
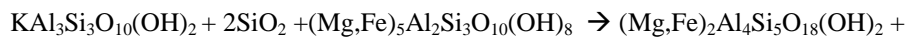
Equation 4-5 Quartz → Muscovite



Equation 4-6 Biotite → Pycnochlorite



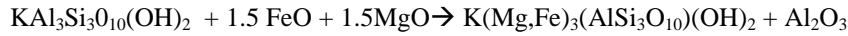
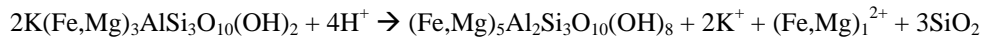
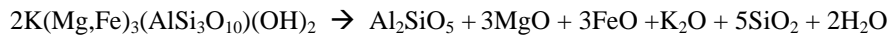
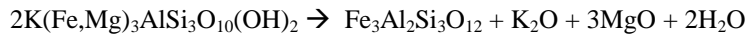
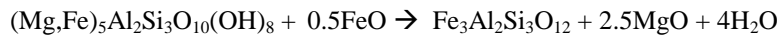
Equation 4-7 Muscovite + Quartz + Pycnochlorite → Cordierite ± Biotite



Stage 3 Biotite Alteration

Equation 4-8 Cordierite → Biotite + Al₂SiO₅ + H₂O



Equation 4-9 Quartz → Biotite**Equation 4-10 Muscovite → Biotite****Equation 4-11 Biotite → Ripidolite****Equation 4-12 Biotite → Andalusite****Equation 4-13 Biotite + Ripidolite + Cordierite + Al₂SiO₅ → Staurolite****Equation 4-14 Biotite → Almandine****Equation 4-15 Ripidolite → Grunerite****Equation 4-16 Ripidolite → Almandine**

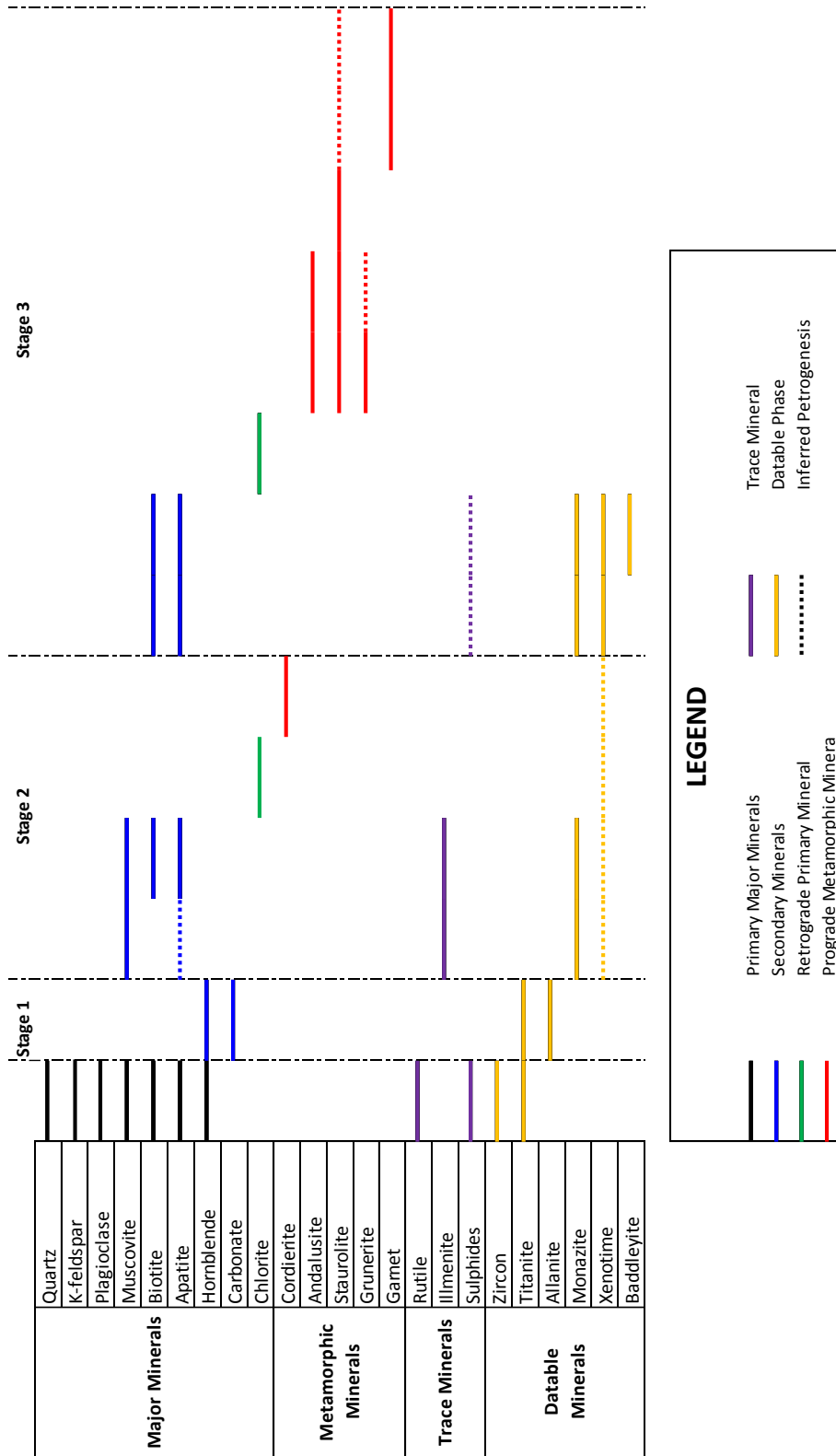


Figure 4-26 Paragenetic timeline of mineral appearance and disappearance for footwall granitoids transitioning into chlorite schist.

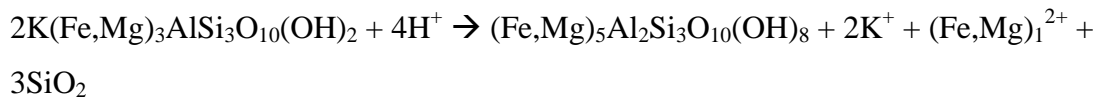
4.3.2 Ore Zone Paragenesis

The parent to iron ore is banded iron formation as demonstrated by the transitional contacts and remnants of BIF in iron ore. Relict BIF is folded and brecciated. Magnetite ores have relict brecciation textures that are recrystallized (samples 14880 & 2061). Pore spaces infilled by silicates and lesser carbonates indicate a fluid influx prior to recrystallization. The absence of silica from the brecciated textures also signifies massive silica loss during this time. Hematization of granoblastic magnetite follows, leaving pseudomorphs of martite, microplaty hematite and increasing pore spaces.

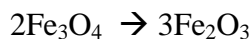
Relict lathes with basal cleavages and internal biotite components illustrate a precursor biotite schist to chlorite schist. Chlorite overprinting obliterated almost all biotite. It is not clear whether the associated martite existed prior to the chlorite overprint. Almandine porphyroblasts hosting porous martite clasts show late microplaty hematization occurred prior. Chlorite is sequentially overprinted by cummingtonite and late Mn zoned almandine.

Ore Zone Mineral Reactions

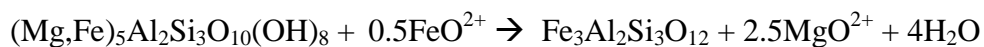
Equation 4-17 Biotite → Ripidolite



Equation 4-18 Magnetite → Hematite



Equation 4-19 Ripidolite → Almandine



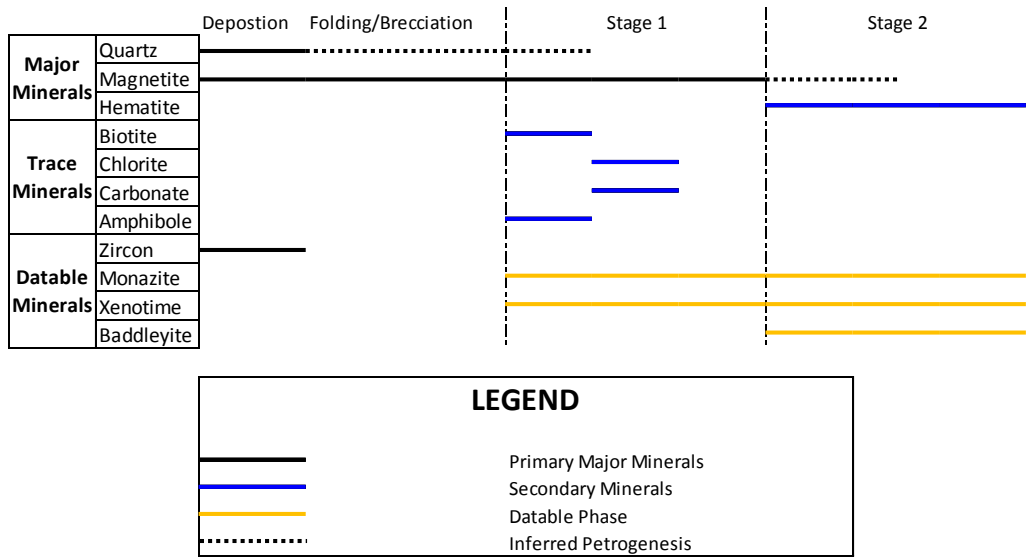


Figure 4-27 Paragenetic timeline of mineral appearance and disappearance for BIF transitioning into high grade hematite ore. Stage 1 represents the formation of magnetite ore and stage 2 represents the transition to hematite ore.

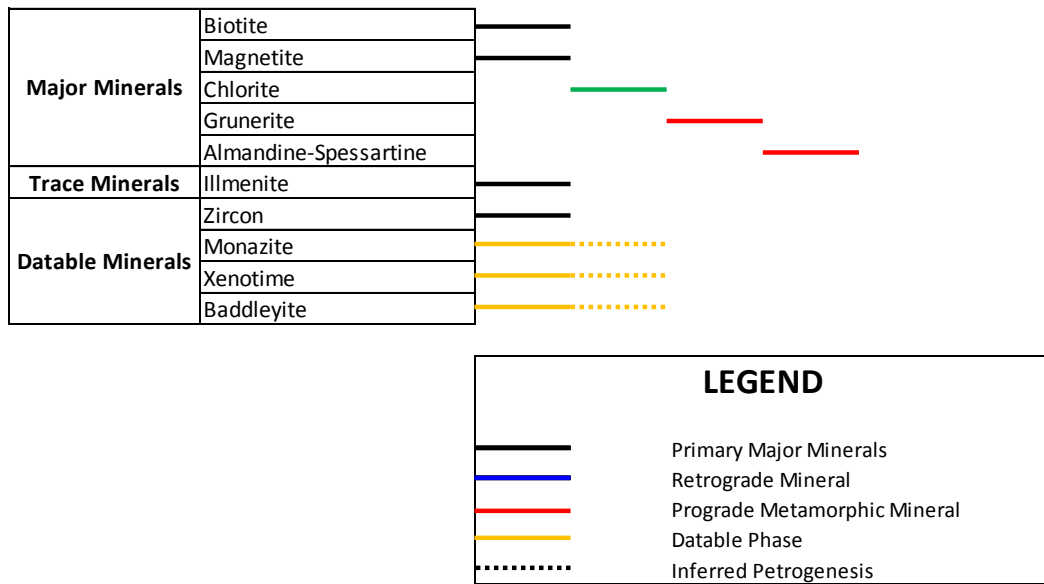


Figure 4-28 Paragenetic timeline of mineral appearance and disappearance for biotite schist into high garnet-amphibole chlorite schist.

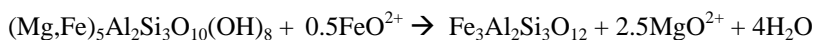
4.3.3 Hangingwall Paragenesis

Chlorite and biotite schists in the hangingwall show nearly the same paragenesis as the footwall schists. Biotite schists contain a cordierite-biotite-staurolite-quartz assemblage that is overprinted by semi-rotated garnets. Chlorite schists show garnet porphyroblasts overprinting ripidolite. Almandine porphyroblasts are thus the last stage of crystallization. Staurolite is an intermediate stage between cordierite and almandine as it host inclusions of cordierite and quartz. Breccia clasts in schists and biotite veining are recrystallized and show porphyroblastic impingement.

Ultramafics are altered by carbonate veining of magnesite, dolomite and rhodochrosite. These units are further encompassed by radiating talc lathes that retrograde to chlorite. Anthophyllite is the final mineral phase and overprints serpentine, retrograded talc and carbonate minerals. Hornblende amphibolites do not contain relict or replacement textures. Cryptocrystalline volcanoclastics are mildly carbonatized but only show metamorphic biotite to hornblende reactions.

Hangingwall Mineral Reactions

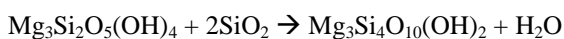
Equation 4-20 Ripidolite → Almandine



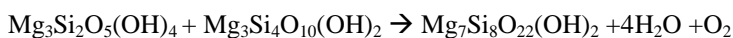
Equation 4-21 Serp + 3CO₂ → Talc + 3Magnesite + H₂O



Equation 4-22 Serp → Talc + H₂O



Equation 4-23 Serp + Talc → Anthophyllite + H₂O + Vapor



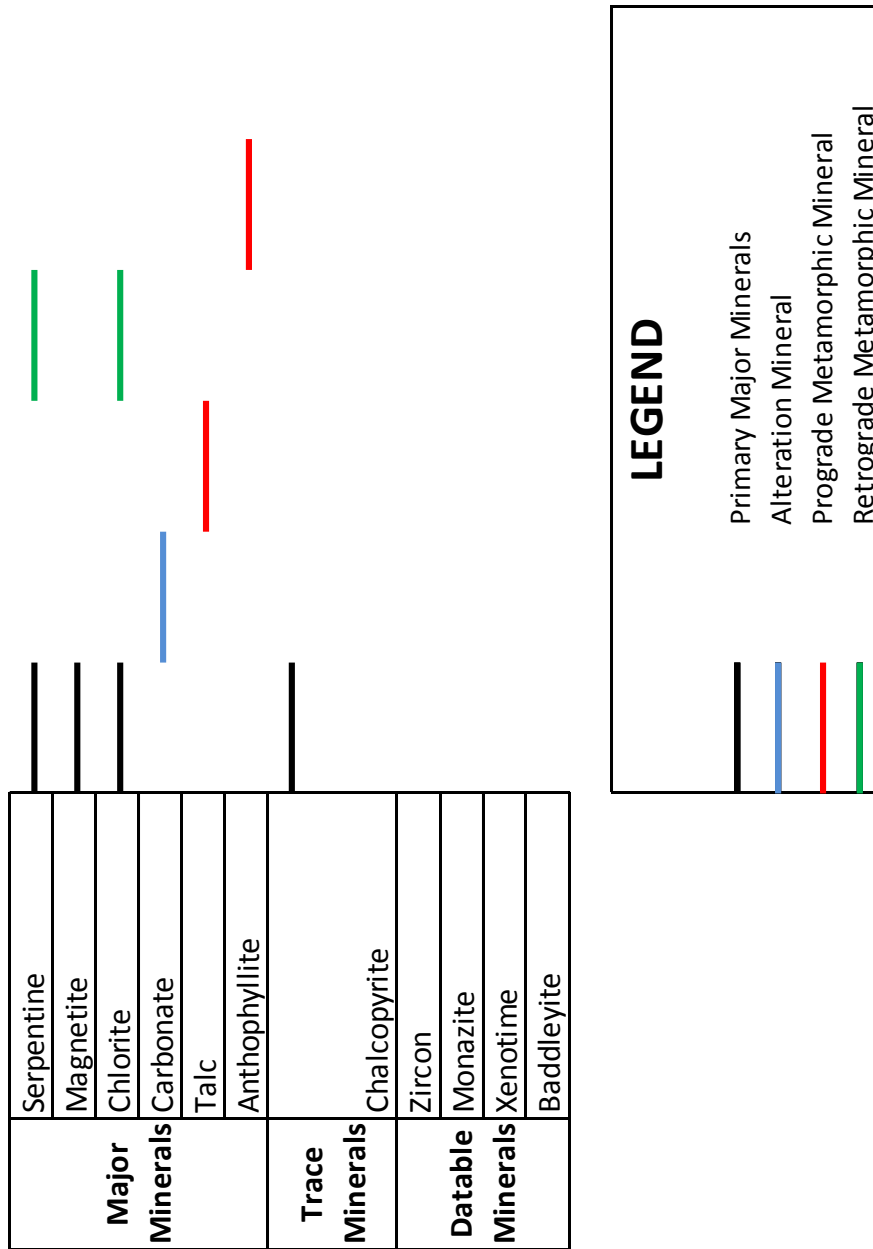


Figure 4-29 Paragenetic timeline of mineral appearance and disappearance for ultramafics into ultramafic-amphibolite.

Chapter 5 Geochemistry

5 Introduction

Surface grab and drill core samples collected by the author and iron formation samples selected from MacLeod (2012) were submitted for bulk rock geochemistry. Analytical procedures and methods, outlined in chapter 3, provided quantitative major, trace and rare earth element compositions of footwall, ore zone and hangingwall units. This chapter presents and compares this data. The concluding section combines whole rock composition with measured bulk rock density and petrographic data to calculate mass balance changes in footwall and ore zone lithologies.

5.1 Deposit No. 1 Footwall Lithogeochemistry

5.1.1 Footwall Major Element Oxides

Major elemental oxide averages for footwall granitoids, altered-silicified granitoids and quartz-augen schists are listed in Table 5-1. Comparative bar charts of elemental oxides are presented in Figure 5-1. SiO₂ averages are above 70% in all granitoids, the most siliceous being the alkali-feldspar granite. Syenogranite shows the largest SiO₂ variation, ranging between 71.8%-77.80% SiO₂. Alkali content (Na₂O + K₂O) is moderately higher in syeno and alkali-feldspar granite compared to monzogranite. Ratios <1 of alkalis over aluminum ($\frac{Na_2O+K_2O+CaO}{Al_2O_3}$) indicate all three granitoids are weakly peraluminous. Fe₂O₃ concentrations are lower by 2.18% and 2.57% in syeno and alkali-feldspar granites compared to monzogranites. Average MgO content is slightly higher in monzogranites (1.62%) than in syeno or alkali-feldspar granites (1.19%). TiO₂, MnO, P₂O₅, C and S are all below 0.1%. P₂O₅ concentrations are higher (0.07%>0.02%>0.01%) in monzogranites than in syeno or alkali-feldspar granites.

Metagabbro is starkly different in composition. SiO₂ averages 48.78% but ranges from 39.70% (ultramafic) to 53.70% (intermediate). Aluminum, iron, magnesium and calcium content are higher than granitoids, averaging 14.94% Al₂O₃, 13.07% Fe₂O₃,

10.24% MgO and 6.28% CaO. TiO₂, MnO, P₂O₅, C and S are less than 1% but elevated compared to syeno and alkali-feldspar granites with the exception of carbon.

Quartz-augen schists show a gradual reduction (QAMS → QAMBS → QABS) in SiO₂ content from 68.47% to 58.8% with an average between 15.08% to 15.11% Al₂O₃. In contrast, ASG units average higher SiO₂ values of 77.43% and average lower Al₂O₃ (12.35%), Fe₂O₃ (1.51%) and MgO (0.68%) concentrations compared to quartz-augen schists. TiO₂, MnO, P₂O₅, C and S are less than 1%. P₂O₅ increases from 0.11% in QAMS units to 0.22% in QABS units. TiO₂ values increase similarly from 0.56% in QAMS units to 0.83% QAMBS.

Biotite and chlorite schist are both ultramafic with respect to SiO₂ content, averaging 35.98% and 32.65% SiO₂ accordingly. Average Al₂O₃ values in biotite and chlorite (23.11% and 22.1%) schist are 1.5X higher than in quartz-augen schists. Biotite schists are elevated in MgO, K₂O, TiO₂ and MnO by 2.80%, 2.07%, 0.51% and 0.41% respectively in relation to QABS units. Chlorite schists are 3.7% higher in MgO and 3.27% lower in K₂O than biotite schists.

	MGr			SGr			AFGr			Metagabbro		
	Average	Min	Max									
SiO ₂	72.90	71.10	75.70	75.64	71.80	77.80	77.55	76.90	78.20	48.78	39.70	53.70
Al ₂ O ₃	12.78	12.00	14.20	12.55	11.90	13.35	12.00	11.95	12.05	14.94	12.75	17.00
Fe ₂ O ₃	2.76	1.75	7.64	1.56	1.17	2.06	1.17	1.06	1.27	13.07	11.15	16.70
CaO	2.00	0.30	3.90	1.22	0.15	3.32	0.29	0.18	0.39	6.28	1.09	10.75
MgO	1.62	0.49	5.11	1.19	0.36	2.68	0.48	0.36	0.60	10.24	6.53	14.70
Na ₂ O	3.19	1.02	3.81	2.82	0.42	4.00	2.97	2.90	3.03	1.52	0.53	3.12
K ₂ O	3.43	1.95	5.93	4.11	2.25	5.17	5.26	4.82	5.69	2.04	0.22	6.93
TiO ₂	0.20	0.13	0.75	0.10	0.04	0.18	0.04	0.03	0.05	0.88	0.68	1.03
MnO	0.06	0.02	0.15	0.04	0.01	0.08	0.04	0.02	0.05	0.22	0.14	0.33
P ₂ O ₅	0.04	0.02	0.17	0.02	0.00	0.04	0.01	0.01	0.01	0.06	0.03	0.12
C	0.06	0.00	0.16	0.06	0.00	0.11	0.02	0.00	0.04	0.06	0.01	0.13
S	0.07	0.01	0.11	0.00	0.00	0.00	0.00	0.00	0.00	0.06	0.00	0.24
LOI	1.37	0.56	2.81	0.74	0.45	1.07	0.64	0.00	0.71	1.68	0.78	2.60
Total	<u>98.66</u>			<u>99.30</u>			<u>99.81</u>			<u>98.15</u>		
Samples	5			5			2			13		

	ASG			QAMS			QAMBS			QABS		
	Average	Min	Max									
SiO ₂	77.43	74.20	81.50	68.47	59.80	73.80	66.62	61.70	71.70	58.80	58.00	59.60
Al ₂ O ₃	12.35	10.50	13.85	15.11	12.05	19.95	15.07	13.15	16.00	15.08	14.60	15.55
Fe ₂ O ₃	1.51	1.06	2.53	4.56	3.35	6.03	6.11	5.02	7.57	11.33	11.05	11.60
CaO	0.92	74.20	2.10	0.36	0.06	1.26	1.17	0.28	2.63	0.32	0.31	0.33
MgO	0.68	0.17	1.54	3.28	2.05	4.74	2.56	1.33	3.68	6.47	5.71	7.23
Na ₂ O	2.87	0.15	4.36	0.44	0.09	1.55	1.95	0.25	3.72	0.11	0.11	0.11
K ₂ O	3.57	1.96	5.89	4.26	2.90	5.66	4.25	3.28	5.08	3.56	3.22	3.90
TiO ₂	0.08	0.02	0.21	0.56	0.16	0.82	0.78	0.45	0.99	0.83	0.82	0.84
MnO	0.04	0.01	0.11	0.04	0.02	0.08	0.07	0.05	0.11	0.07	0.06	0.07
P ₂ O ₅	0.03	0.00	0.06	0.11	0.04	0.20	0.19	0.10	0.23	0.22	0.20	0.23
C	0.08	0.01	0.27	0.03	0.00	0.12	0.04	0.00	0.09	0.03	0.02	0.03
S	0.05	0.00	0.08	0.07	0.00	0.32	0.08	0.00	0.23	0.00	0.00	0.00
LOI	1.09	0.57	2.20	2.93	1.60	4.38	1.81	0.98	2.45	3.20	2.67	3.73
Total	<u>100.67</u>			<u>100.21</u>			<u>100.69</u>			<u>100.00</u>		
Samples	11			9			5			2		

	BS			CS		
	Average	Min	Max	Average	Min	Max
SiO ₂	35.98	32.10	39.80	32.65	29.10	37.20
Al ₂ O ₃	23.11	19.75	25.10	22.10	18.60	26.60
Fe ₂ O ₃	19.96	17.10	23.30	21.14	16.35	31.00
CaO	0.84	0.57	1.48	0.19	0.15	0.24
MgO	9.27	6.05	13.15	12.97	6.94	18.95
Na ₂ O	0.13	0.10	0.15	0.08	0.00	0.13
K ₂ O	5.63	4.89	7.00	2.37	0.38	5.26
TiO ₂	1.34	1.07	1.62	0.71	0.33	1.24
MnO	0.13	0.07	0.18	0.09	0.04	0.21
P ₂ O ₅	0.62	0.43	1.08	0.10	0.04	0.17
C	0.01	0.01	0.02	0.02	0.01	0.03
S	0.23	0.00	0.45	0.17	0.00	0.32
LOI	3.12	0.90	4.47	6.72	2.13	9.50
Total	<u>100.38</u>			<u>99.30</u>		
Samples	4			4		

Table 5-1 Average major elemental oxide composition of footwall lithologies including carbon and sulphur. Maximum and minimum values are listed in adjacent columns.

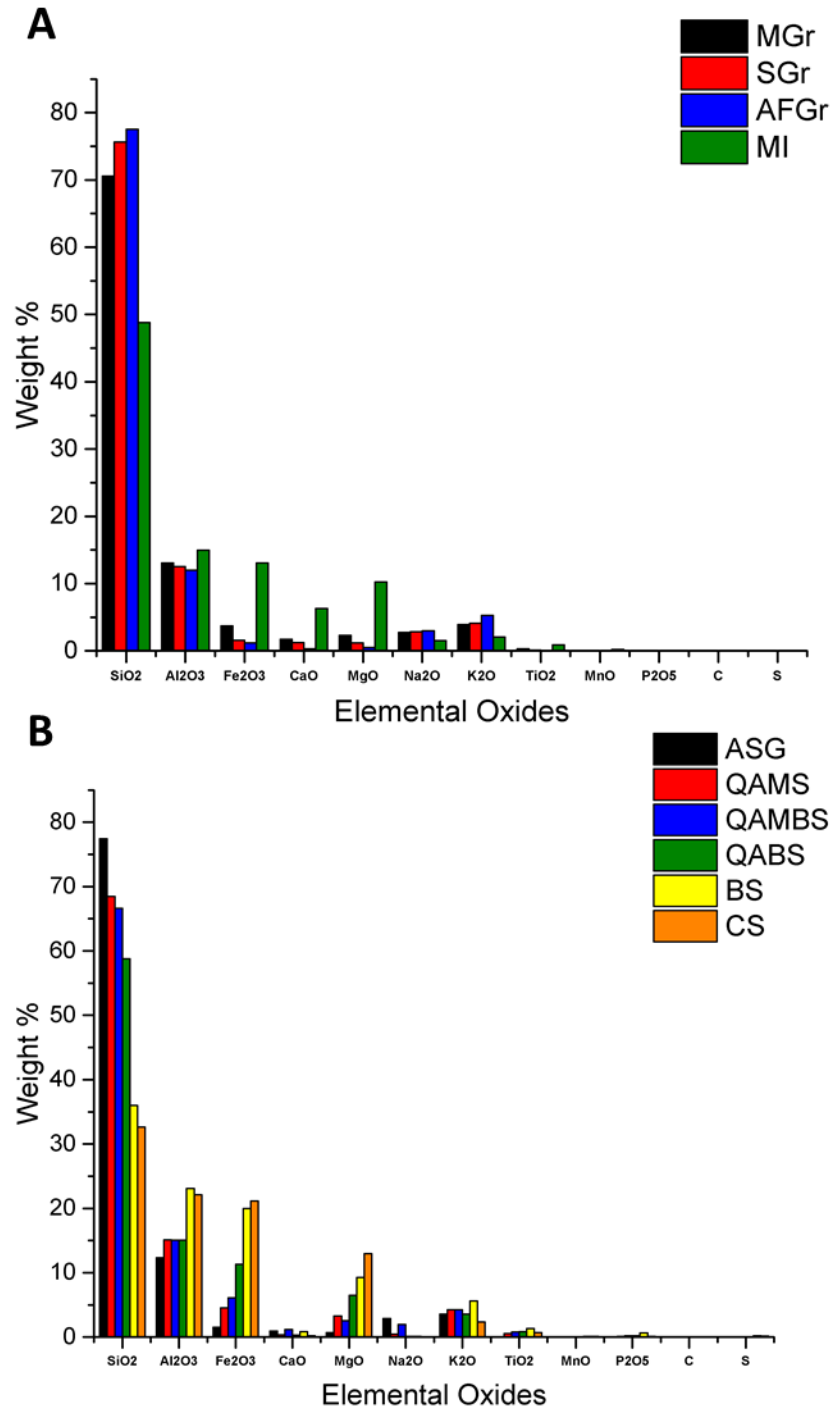


Figure 5-1 Comparative bar graphs of major elemental oxides, carbon and sulphur in footwall lithologies. Granitoids compositions are plotted in graph A and schists with altered-silicified granitoids (ASG) in graph B.

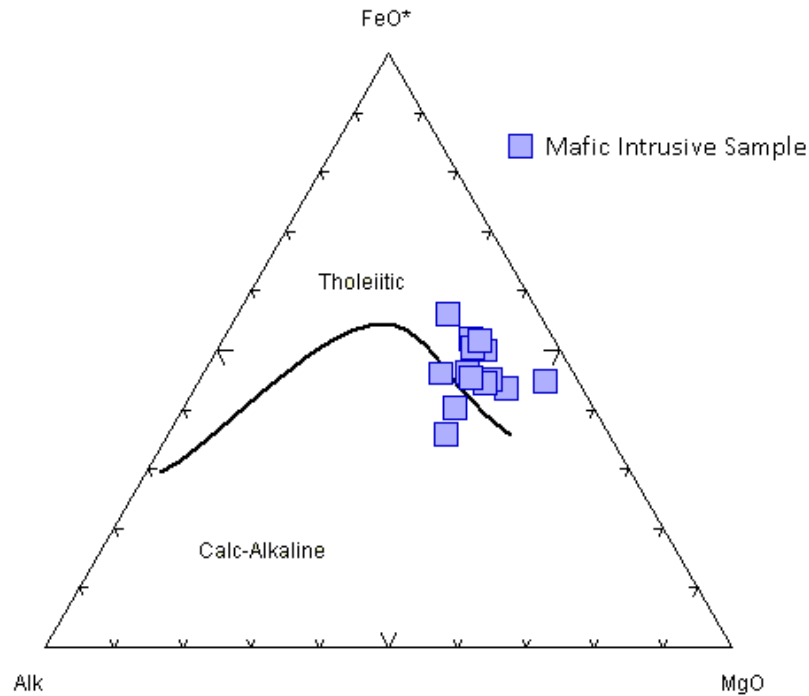


Figure 5-2 AFM plot of footwall metagabbro bulk rock analyses. FeO* is total iron.

5.1.2 Footwall Trace Elements

Trace elements are elements with concentrations under 1%. These include large ion lithophile elements (Li, Ba, Cs, Sr, and Rb), high field strength elements (Zr, Nb, Hf, Ta, Y, W, U and Th) transition metals (Ag, Cr, V, Tl, Sc, Hg, Mo, Cu, Ni, Co, Cd, and Zn) and main group elements (Ga, Sn, Sb, Te, Tl, Pb, Bi, and As). Tables 5-2, 5-3 and 5-4 display average, maximum and minimum values for trace elements from footwall lithologies. Element values are normalized to chondrite and plotted in Figures 5-2 A and B.

Monzogranites are elevated in average Cs (1113 ppm) and Zr (164 ppm) concentrations compared to SGr and AFGr units. Cs shows the largest variation of any trace element with values ranging between 180 to 1696 ppm in granitoid units. Syenogranites have the highest Rb (228 ppm) and Cr (148 ppm) content of the three felsic intrusives. Syenogranites plot as within plate granites in a Rb vs Y+Nb

discrimination plot (Pearce et al., 1984)(Figure 5-3). Mafic intrusives are dissimilar for most trace element concentrations. The largest differences compared to granitoids are transition metals (Cr, V, Cu, Ni, Sc, Co and Zn). The Cr content (463.08 ppm) is more than 10x the MGr content. These variances and differences are illustrated in chondrite normalized comparative plots in Figure 5-2 A.

Quartz-augen schists have elevated cesium values averaging 2028 ppm, 1826 ppm and 1207 ppm in QAMS, QAMBS and QABS correspondingly. Notable increases from QAMS to QABS include Ba, Rb and Zr. Transition metals (Cu, Mo and Ni) show the largest variance in concentration. Average Cu varies by more than 3x in QABS compared to QAMS units. ASG exhibits similar average trace element compositions as quartz-augen schist but contains higher Nb and Ta with lower V, Co and Ni.

Biotite and chlorite schist trace element abundances are similar to quartz-augen schists. Cesium concentrations average to similar values of 1295 ppm and 1380 ppm respectively. Cr and V values are generally low in biotite and chlorite schists, 10-30 ppm Cr and 84-193 ppm V. Cr values in biotite schist sample 6216 are abnormally high at 760 ppm. This schist sample was collected to an adjacent amphibolitized metagabbro. In general, trace metal contents are not as variable compared quartz-augen schists.

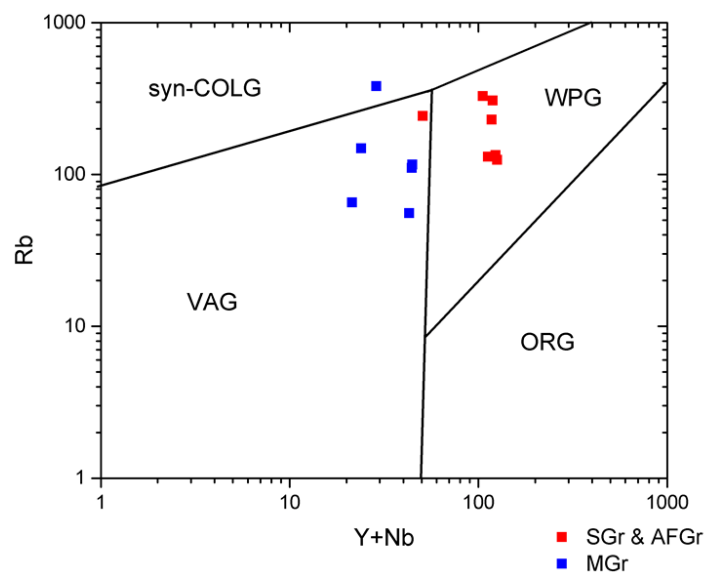


Figure 5-3 Granite discrimination plot of Rb vs Y+Nb. Modeled after Pearce et al. (1984).

Elements	MGr			SGr			AFGr			MI		
	Average	Min	Max	Average	Min	Max	Average	Min	Max	Average	Min	Max
Li	32.50	< 3	80.00	25.00	< 3	50.00	10.00	10.00	10.00	42.31	10.00	140.00
Ba	2.98	0.27	6.12	2.35	1.06	4.77	0.47	0.33	0.61	2.28	0.32	8.55
Cs	1113.60	406.00	1696.00	489.24	170.50	1165.00	264.25	180.00	348.50	358.81	34.20	1127.00
Sr	201.62	24.30	422.00	54.30	18.70	168.20	20.25	17.90	22.60	227.17	13.40	373.50
Rb	146.02	55.60	382.00	228.60	131.00	328.00	177.50	125.00	230.00	163.28	7.00	535.00
Th	23.35	8.78	38.00	29.76	19.10	35.70	34.85	28.90	40.80	1.20	0.26	3.35
U	8.60	2.44	12.50	8.86	4.72	16.30	8.78	7.15	10.40	0.57	0.11	1.84
Y	25.82	15.70	32.20	73.60	34.30	89.20	71.75	70.60	72.90	24.25	14.70	47.50
Zr	164.00	124.00	197.00	120.80	101.00	154.00	128.50	121.00	136.00	57.85	41.00	86.00
Hf	4.84	3.90	5.40	5.64	4.40	6.70	8.80	8.70	8.90	1.68	1.10	2.50
Nb	10.62	5.70	15.40	28.52	16.20	39.20	49.85	44.70	55.00	3.65	1.50	10.80
Ta	1.24	0.70	1.90	3.52	1.50	4.80	6.25	5.80	6.70	0.28	< 0.2	0.60
Ga	17.34	15.20	19.60	20.36	18.50	22.00	21.25	19.90	22.60	17.90	13.10	24.90
Cr	44.00	10.00	150.00	148.00	10.00	670.00	15.00	10.00	20.00	463.08	190.00	1020.00
V	36.80	8.00	113.00	8.80	6.00	15.00	7.00	< 5	7.00	286.23	201.00	396.00
Sn	4.40	2.00	8.00	8.80	7.00	14.00	8.50	5.00	12.00	3.46	1.00	16.00
Tl	1.05	< 0.1	1.60	0.88	< 0.1	1.30	0.60	0.60	0.60	1.64	< 0.1	2.90
W	2.00	1.00	3.00	2.80	2.00	4.00	2.00	2.00	2.00	3.67	< 0.7	25.00
As	0.26	0.20	0.40	0.40	0.10	0.80	0.40	0.40	0.40	0.21	< 5	0.60
Bi	1.46	0.04	6.38	0.08	0.04	0.15	0.52	0.15	0.88	0.32	0.03	2.09
Hg	0.01	< 0.05	0.01	0.01	< 0.05	0.01	< 0.05	< 0.05	< 0.05	0.01	< 0.05	0.01
Sb	0.05	< 2	0.06	0.05	< 2	0.05	0.05	< 2	0.05	0.06	< 2	0.06
Se	0.66	0.50	0.90	1.54	0.40	2.40	2.05	2.00	2.10	0.35	0.20	0.80
Te	0.03	< 6	0.05	< 6	< 6	< 6	0.01	< 6	0.01	0.02	< 6	0.08
Ag	1.20	< 0.5	1.20	< 0.5	< 0.5	< 0.5	< 0.5	< 0.5	< 0.5	0.60	< 0.5	0.60
Cd	0.50	< 2	0.50	< 2	< 2	< 2	< 2	< 2	< 2	0.65	< 2	0.80
Co	7.60	2.00	20.00	1.60	1.00	3.00	1.50	1.00	2.00	49.15	35.00	70.00
Cu	23.60	2.00	37.00	2.25	< 2	4.00	14.50	11.00	18.00	114.69	2.00	283.00
Mo	< 1	< 1	< 1	1.00	< 1	1.00	1.00	1.00	1.00	2.00	< 1	5.00
Ni	12.60	2.00	34.00	1.60	1.00	2.00	2.00	1.00	3.00	97.77	42.00	186.00
Pb	39.40	20.00	74.00	36.60	24.00	48.00	51.00	50.00	52.00	9.11	< 0.8	20.00
Sc	6.00	2.00	16.00	3.00	2.00	4.00	3.00	3.00	3.00	38.38	28.00	52.00
Zn	51.40	14.00	149.00	25.60	8.00	53.00	26.50	16.00	37.00	123.92	80.00	207.00

Table 5-2 Trace element average, minimum and maximum values for footwall intrusives. All values are in parts per million (ppm). Averages do not include values below detection limits. Elements below detection limit are displayed with less than sign and the value of the detection limit in ppm.

Elements	ASG			QAMS			QAMBS			QABS		
	Average	Min	Max	Average	Min	Max	Average	Min	Max	Average	Min	Max
Li	13.00	< 3	30.00	27.78	10.00	100.00	26.00	10.00	50.00	95.00	80.00	110.00
Ba	0.97	0.31	2.71	1.83	0.53	3.09	3.06	1.17	4.74	4.20	4.17	4.22
Cs	703.43	79.20	1840.00	2028.33	600.00	3250.00	1826.80	392.00	4340.00	1207.50	1090.00	1325.00
Sr	50.20	18.40	170.50	41.40	11.50	143.10	106.46	24.10	208.00	13.05	12.10	14.00
Rb	159.25	56.90	379.00	129.99	72.90	163.00	165.88	83.90	339.00	141.25	132.50	150.00
Th	27.18	11.70	35.90	15.13	3.08	37.00	13.28	10.90	19.30	15.45	12.40	18.50
U	8.69	2.90	14.65	4.97	2.59	9.02	3.64	2.20	7.45	5.51	3.24	7.77
Y	42.57	8.40	108.00	16.41	5.40	24.40	23.92	16.70	35.90	24.35	22.20	26.50
Zr	131.09	71.00	231.00	265.89	81.00	521.00	492.60	332.00	746.00	447.00	411.00	483.00
Hf	7.31	2.80	13.10	6.66	2.20	12.30	11.34	8.20	15.50	10.25	9.50	11.00
Nb	31.97	1.70	63.00	9.07	4.60	16.90	12.70	7.90	20.20	12.00	12.00	12.00
Ta	6.18	0.30	16.60	0.78	0.30	1.30	1.14	0.50	2.90	0.80	0.80	0.80
Ga	20.45	13.30	30.80	18.49	15.10	22.20	20.66	17.80	22.60	18.50	18.50	18.50
Cr	13.64	10.00	30.00	22.22	10.00	50.00	16.00	10.00	20.00	30.00	20.00	40.00
V	10.00	< 5	14.00	55.22	11.00	142.00	48.40	30.00	63.00	72.50	68.00	77.00
Sn	9.18	1.00	20.00	3.33	1.00	11.00	5.80	2.00	12.00	2.50	2.00	3.00
Tl	0.80	< 0.1	1.30	0.83	< 0.1	1.20	0.88	< 0.1	1.30	0.65	0.60	0.70
W	2.80	< 0.7	5.00	4.22	2.00	6.00	5.20	1.00	13.00	1.00	1.00	1.00
As	0.24	< 5	0.40	0.83	< 5	2.80	0.20	< 5	0.30	0.80	< 5	0.80
Bi	0.24	0.02	0.82	0.33	0.04	1.60	2.38	0.07	10.05	0.09	0.08	0.09
Hg	0.01	< 0.05	0.01	0.01	< 0.05	0.01	< 0.05	< 0.05	< 0.05	< 0.05	< 0.05	< 0.05
Sb	0.06	< 2	0.06	0.10	< 2	0.10	0.06	< 2	0.06	< 2	< 2	< 2
Se	0.91	< 0.8	1.90	0.33	0.20	0.60	0.64	0.40	0.90	0.35	0.30	0.40
Te	0.01	< 6	0.02	0.02	< 6	0.04	0.14	< 6	0.46	0.01	< 6	0.01
Ag	< 0.5	< 0.5	< 0.5	< 0.5	< 0.5	< 0.5	0.70	< 0.5	< 0.5	< 0.5	< 0.5	< 0.5
Cd	< 2	< 2	< 2	< 2	< 2	< 2	< 2	< 2	< 2	< 2	< 2	< 2
Co	1.78	< 0.2	3.00	12.56	4.00	22.00	10.00	7.00	14.00	12.50	12.00	13.00
Cu	10.91	1.00	50.00	11.13	< 2	53.00	62.00	2.00	154.00	1.50	1.00	2.00
Mo	2.00	< 1	3.00	42.00	< 1	82.00	4.33	< 1	8.00	< 1	< 1	< 1
Ni	3.22	< 10	7.00	18.89	3.00	61.00	6.40	4.00	12.00	13.50	11.00	16.00
Pb	41.00	16.00	62.00	16.78	9.00	30.00	24.20	4.00	65.00	7.50	7.00	8.00
Sc	3.36	1.00	5.00	9.11	3.00	14.00	12.00	9.00	16.00	12.50	12.00	13.00
Zn	27.45	7.00	56.00	43.00	17.00	70.00	113.40	49.00	185.00	55.00	43.00	67.00

Table 5-3 Trace element average, minimum and maximum values for footwall quartz-augen schists and ASG units. All values are in parts per million (ppm). Averages do not include values below detection limits. Elements below detection limit are displayed with less than sign and the value of the detection limit in ppm.

Elements	Biotite Schist			Chlorite Schist		
	Average	Min	Max	Average	Min	Max
<i>Li</i>	35.00	20.00	50.00	32.50	20	50
<i>Ba</i>	1295.75	722.00	2050.00	880.58	63.3	1745
<i>Cs</i>	6.19	5.56	6.97	1.63	0.39	5.03
<i>Sr</i>	16.03	8.00	22.80	11.08	4.2	16.5
<i>Rb</i>	232.25	194.00	312.00	73.13	14.6	191.5
<i>Th</i>	17.89	11.65	23.10	13.35	5.84	23.6
<i>U</i>	9.70	4.14	15.55	5.44	3.46	8.58
<i>Y</i>	32.18	28.90	35.40	21.03	12	30.5
<i>Zr</i>	383.75	135.00	638.00	321.75	137	752
<i>Hf</i>	9.38	3.60	14.70	8.08	3.5	17.7
<i>Nb</i>	15.20	10.60	17.90	12.03	6.9	18.3
<i>Ta</i>	1.08	0.50	1.30	0.95	0.5	1.2
<i>Ga</i>	30.95	22.10	37.20	27.88	20.9	39.2
<i>Cr</i>	263.33	< 30	760.00	25.00	10	60
<i>V</i>	118.75	84.00	193.00	84.25	52	123
<i>Sn</i>	3.50	3.00	4.00	2.50	1	4
<i>Tl</i>	1.25	0.90	1.60	0.80	< 0.1	0.8
<i>W</i>	3.50	1.00	9.00	4.50	3	6
<i>As</i>	1.30	< 5	2.50	1.07	< 5	2.2
<i>Bi</i>	0.13	0.02	0.25	0.56	0.03	1.67
<i>Hg</i>	0.01	< 0.05	0.01	0.01	< 0.05	0.008
<i>Sb</i>	< 2	< 2	< 2	0.13	< 2	0.15
<i>Se</i>	0.60	0.50	0.70	0.40	0.2	0.5
<i>Te</i>	0.03	< 6	0.04	0.03	< 6	0.04
<i>Ag</i>	< 10	< 10	< 10	< 10	< 10	< 10
<i>Cd</i>	0.50	< 2	0.50	< 2	< 2	< 2
<i>Co</i>	26.75	12.00	47.00	26.75	14	39
<i>Cu</i>	3.33	< 2	8.00	8.00	< 2	20
<i>Mo</i>	3.00	< 1	3.00	5.50	< 1	10
<i>Ni</i>	56.00	10.00	179.00	87.25	13	170
<i>Pb</i>	22.25	15.00	33.00	10.00	3	17
<i>Sc</i>	17.00	11.00	21.00	8.75	5	18
<i>Zn</i>	63.00	18.00	143.00	55.50	35	82

Table 5-4 Trace element average, minimum and maximum values for footwall biotite and chlorite schist units. All values are in parts per million (ppm). Averages do not include values below detection limits. Elements below detection limit are displayed with less than sign and the value of the detection limit in ppm.

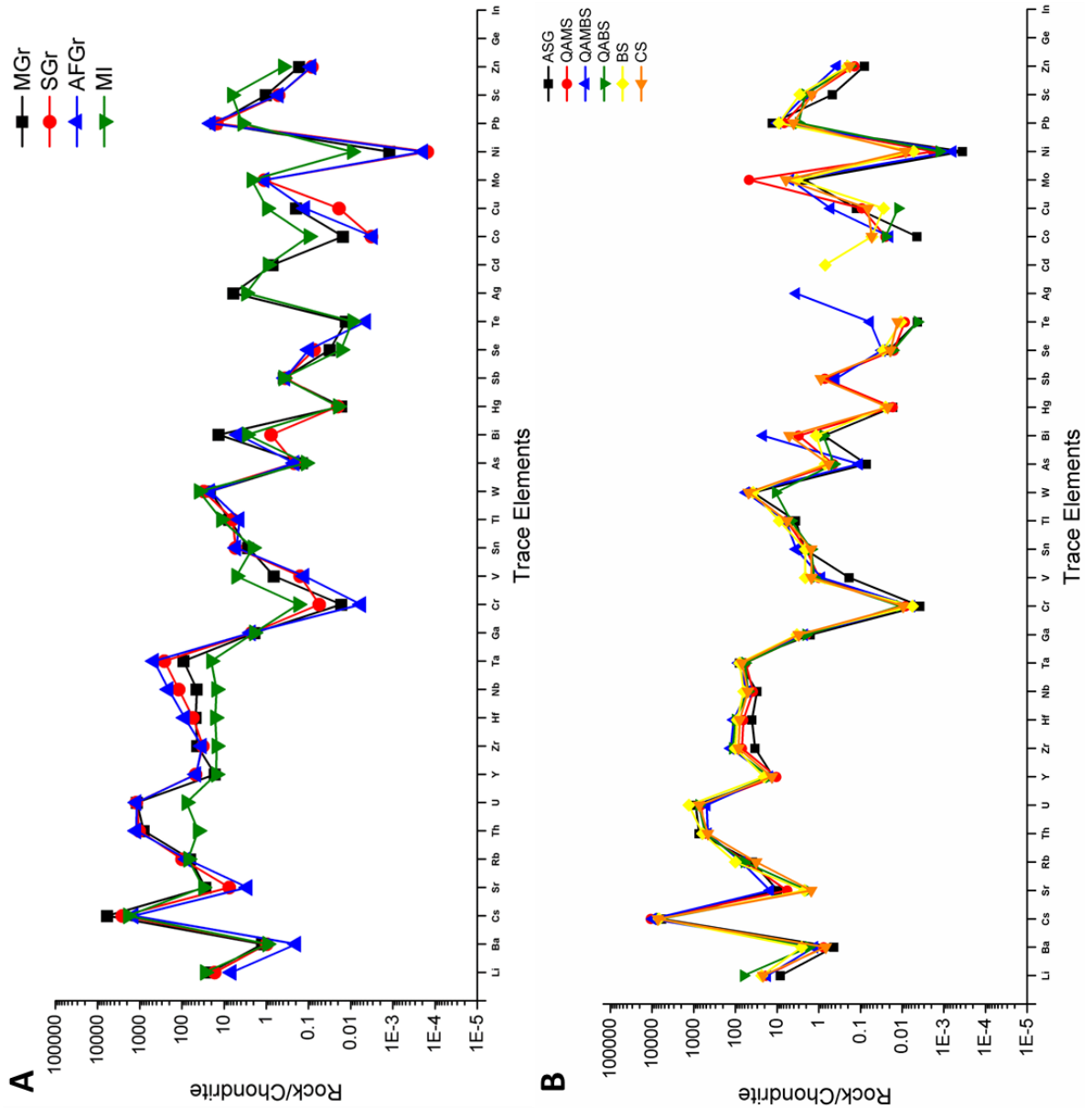


Figure 5-4 Footwall trace element plots normalized to chondrite. A) shows values from footwall intrusives. B) displays footwall schist units and altered-silicified granitoids. Values below detection limit are not plotted.

5.1.3 Footwall Rare Earth Elements

Rare earth element averages are listed in Table 5-5, including minimum and maximum values for footwall lithologies. Average light rare earth elements (La-Sm) in granitoids range between 4.39 ppm to 54.82 ppm. The light rare earth element (LREE) with highest average concentration is Ce. Granitoids contain lower average

concentrations of heavy rare earth elements (Eu-Lu). Values of heavy rare earth elements (HREE) range between 0.42 ppm to 11.75 ppm. The highest average concentration is Dy in AFGr units. Metagabbro averages show markedly lower LREE and HREE abundances (0.36 ppm - 9.62 ppm).

Quartz-augen schists are elevated in LREEs compared to bordering ASG units. La, Ce and Nd hold the highest average concentrations (26.39 ppm - 96.75 ppm) of the LREEs in quartz-augen schists. HREE concentrations in quartz-augen schists are on average an order magnitude lower than LREE concentrations. Average HREE concentrations vary between 0.32 ppm and 4.60 ppm. Dy has the highest and most consistent values within quartz-augen schists. ASG units show higher LREE to HREE values. La, Ce and Nd in ASG units are again the highest, averaging between 17.26 ppm and 39.12 ppm. ASG HREE values are lower except for Gb (4.60 ppm), Dy (6.31 ppm), Er (4.76 ppm) and Yb (6.69 ppm). Biotite and chlorite schist contain elevated LREE values, constituted by La, Ce and Nd. HREE concentrations are sporadic, values range between 0.32 ppm to 9.25 ppm. Gd, Dy, Er and Yb are the most elevated HREE constituents in biotite and chlorite schist.

Normalized averages of the footwall intrusives to chondrite (McDonough and Sun, 1995) are plotted in Figure 5-3. Monzogranites exhibit a negative slope line in LREEs with a moderate low Eu anomaly. HREE within MGr units form a flat line after the Eu anomaly. However, Figure 5-4 shows varying sloped HREE patterns among 6 samples of monzogranite. Syeno and alkali-feldspar granites form a similar gentle negative sloped LREE profile, truncated by a large Eu depletion followed by a positive slope HREE profile. ASG units show two distinct patterns in Figure 5-5. Grey and white ASG units have a negative LREE slope into a moderate negative Eu anomaly and flat HREE pattern. Pinkish to red altered-silified granitoids (ASGr) show a strong negative Eu anomaly but have an elevated LREE profile with mild negative slope and a HREE profile with a positive slope. Quartz-augen schists have the same negative slope LREE pattern as monzogranites and show the same negative Eu anomaly and horizontal HREE profile. The Eu anomaly becomes less intense as the units change from QAMS to QABS.

Elements	MGr			SGr			AFGr			MI		
	Average	Min	Max	Average	Min	Max	Average	Min	Max	Average	Min	Max
La	29.10	18.50	52.00	20.82	14.50	30.10	11.20	10.30	12.10	4.11	2.10	7.60
Ce	54.82	33.90	97.30	47.70	36.30	66.50	37.25	33.40	41.10	9.62	5.30	16.90
Pr	6.25	3.80	10.50	6.08	4.98	7.75	4.65	4.09	5.21	1.40	0.72	2.17
Nd	22.54	13.60	36.70	23.98	20.60	29.10	19.45	17.40	21.50	6.75	3.70	10.20
Sm	4.39	2.36	6.13	6.55	5.32	7.91	6.84	6.59	7.09	2.20	1.37	2.98
Eu	0.64	0.35	1.07	0.22	0.08	0.44	0.11	0.11	0.11	0.84	0.45	1.44
Gd	3.97	2.10	5.80	7.58	5.65	9.61	7.95	7.64	8.25	3.01	2.10	4.40
Tb	0.68	0.40	0.89	1.49	0.96	1.99	1.68	1.67	1.68	0.55	0.39	0.72
Dy	4.31	2.66	5.29	10.02	5.44	13.35	11.75	11.30	12.20	3.75	2.73	5.16
Ho	0.87	0.51	1.08	2.30	1.18	2.90	2.76	2.74	2.78	0.83	0.61	1.18
Er	2.69	1.59	3.52	7.05	3.55	9.35	8.78	8.39	9.16	2.57	1.62	3.98
Tm	0.42	0.25	0.55	1.19	0.59	1.50	1.49	1.46	1.51	0.35	0.27	0.55
Yb	2.89	1.74	4.00	8.41	4.13	10.75	11.03	10.95	11.10	2.52	1.74	4.12
Lu	0.45	0.25	0.65	1.26	0.54	1.70	1.63	1.54	1.71	0.36	0.24	0.55

Elements	ASG			QAMS			QAMBS			QABS		
	Average	Min	Max									
La	17.70	2.50	57.10	31.59	10.60	59.50	47.56	24.50	89.00	49.50	36.90	62.10
Ce	39.12	7.10	106.50	63.98	24.50	103.50	89.56	54.40	154.50	96.75	75.00	118.50
Pr	4.69	0.94	11.35	7.21	2.94	11.05	9.58	5.53	16.70	10.65	8.19	13.10
Nd	17.26	3.40	39.00	26.39	11.70	39.20	34.14	20.80	61.40	39.40	30.20	48.60
Sm	4.45	1.12	7.78	4.77	2.23	6.67	6.32	3.86	11.20	6.97	5.36	8.57
Eu	0.39	< 0.1	1.15	1.10	0.54	1.82	1.60	1.29	2.09	1.69	1.36	2.02
Gd	4.60	1.32	8.62	4.00	1.95	5.86	5.26	3.47	9.02	5.78	4.47	7.09
Tb	0.93	0.20	1.91	0.57	0.27	0.86	0.75	0.49	1.34	0.82	0.64	0.99
Dy	6.31	1.09	14.30	3.16	1.30	4.60	4.44	3.01	7.75	4.60	4.12	5.08
Ho	1.43	0.26	3.29	0.62	0.20	0.90	0.93	0.60	1.50	0.95	0.85	1.04
Er	4.76	0.72	11.15	1.76	0.63	2.71	2.52	1.73	3.94	2.42	2.19	2.65
Tm	0.90	0.13	2.21	0.26	0.10	0.39	0.33	0.25	0.47	0.32	0.30	0.34
Yb	6.69	0.80	17.20	1.71	0.60	2.36	2.37	1.67	3.58	2.13	2.01	2.25
Lu	1.06	0.13	2.82	0.28	0.09	0.39	0.38	0.26	0.64	0.38	0.35	0.40

Elements	BS			CS		
	Average	Min	Max	Average	Min	Max
La	67.40	39.80	93.50	35.30	14.4	56.7
Ce	135.05	82.20	189.50	68.78	31.6	109.5
Pr	15.43	10.00	21.60	7.93	3.53	12.15
Nd	56.43	39.50	76.70	30.23	14.1	49.1
Sm	10.84	9.22	14.10	5.77	3.13	9.04
Eu	2.15	1.40	2.67	1.36	0.65	2.49
Gd	9.25	7.53	11.90	4.88	2.49	8.25
Tb	1.27	1.04	1.49	0.73	0.46	1.15
Dy	6.44	5.52	7.51	4.19	2.6	6.53
Ho	1.27	1.02	1.46	0.80	0.51	1.17
Er	3.19	2.53	3.72	2.29	1.34	3.46
Tm	0.46	0.34	0.54	0.32	0.2	0.45
Yb	2.92	2.40	3.37	2.15	1.31	3.21
Lu	0.45	0.36	0.52	0.33	0.19	0.45

Table 5-5 Rare earth element average, minimum and maximum values for footwall intrusives, quartz-augen schists and ASG units. All values are in parts per million (ppm). Averages do not include values below detection limits.

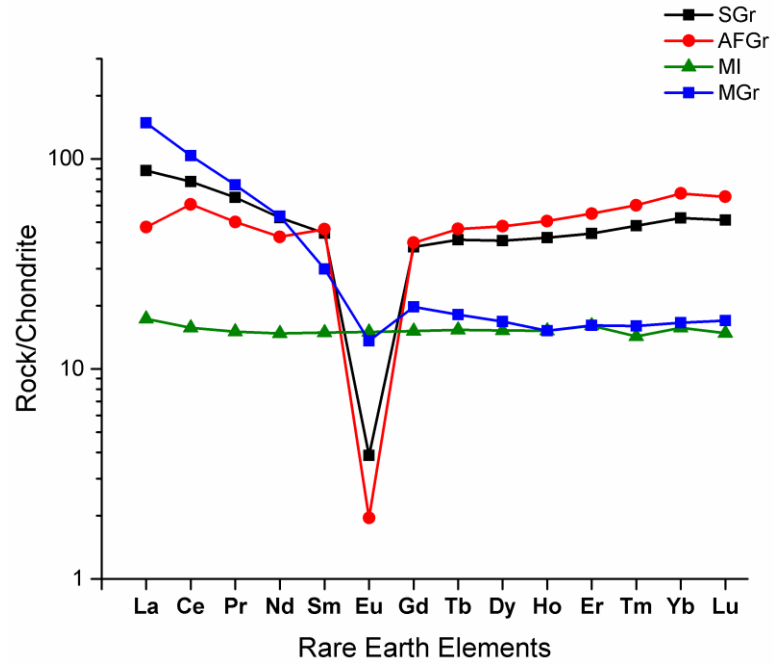


Figure 5-5 Chondrite normalized rare earth element plot of footwall intrusives. Ratios plotted are averages of normalized values.

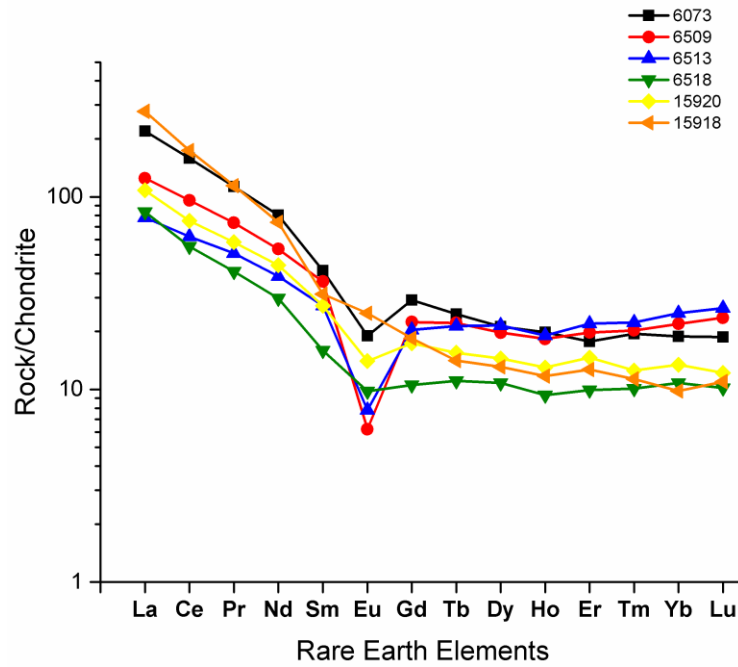


Figure 5-6 Chondrite normalized rare earth element plot of monzogranite samples.

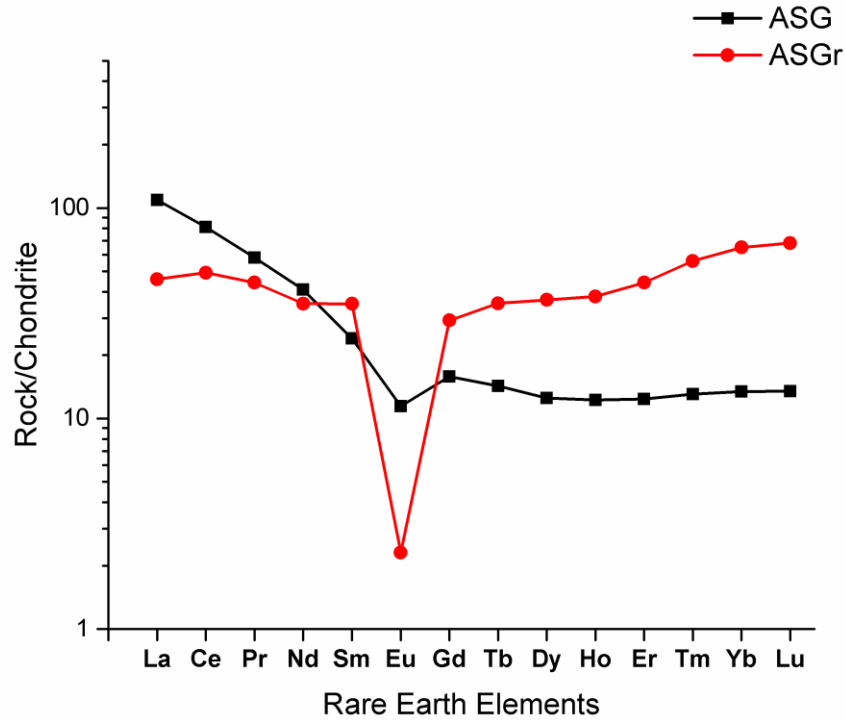


Figure 5-7 Normalized rare earth element plot of altered-silicified granitoids samples to chondrite. Ratios plotted are averages of normalized values.

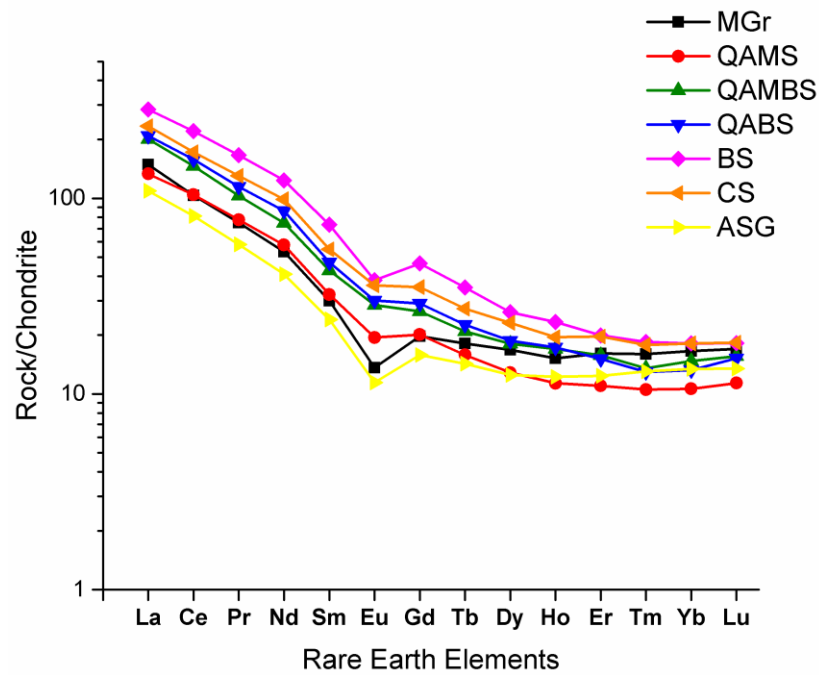


Figure 5-8 Normalized rare earth element plot of footwall schists, altered-silicified granitoids (ASG) and monzogranites (MGr) to chondrite. Ratios plotted are averages of normalized values.

5.2 Deposit No.1 Ore Zone Lithogeochemistry

5.2.1 Ore Zone Major Oxides

Major elemental oxides averages for banded iron formation (BIF), enriched banded iron formation (EBIF), magnetite ore (MO), magnetite-hematite ore (MHO), hematite ore (HO), and chlorite schist are listed in Table 5-6. Comparative bar charts of elemental oxides are presented in Figure 5-9. BIF SiO_2 values average 54.98 but varied from 44.70 % to 65.80%. The BIF Fe_2O_3 content varied by +11.88% and -11.65%. The mean Fe_2O_3 value of BIF is 44.02%. All other major elemental oxides are below 0.5%. EBIF contains a lower SiO_2 average (10.21%) and a markedly higher and less variable Fe_2O_3 content between 64.83%-79.39%, averaging 72.91%. CaO, MgO and MnO content in EBIF have mean values of 3.83%, 3.91% and 1.05% correspondingly. The maximum CaO content of EBIF is 9.31% and its loss of ignition (LOI) is 3.56% more than BIF.

Iron ore's average Fe_2O_3 is 90% and higher. Magnetite ores contain the highest Fe_2O_3 reaching 100%. Sample 14880 with carbonate and silicate impurities has the lowest iron oxide content at 81.23% Fe_2O_3 . Magnetite ore contains less than 0.5% CaO, Na_2O , K_2O , TiO_2 , and MnO. Only sample 14880 contains higher Al_2O_3 (5.32%) and MgO (3.55%). Magnetite-hematite ores range between 94.68% to 98.65% Fe_2O_3 . Deleterious elemental oxides average less than 0.29% each. Hematite ores average lower Fe_2O_3 content (92.19%) and higher SiO_2 content (4.39%). MgO, CaO and P_2O_5 values in hematite ore average 0.68%, 0.78% and 0.58%. Chlorite schist is ultramafic by SiO_2 composition (30.83%) and holds average values of Al_2O_3 and Fe_2O_3 of 16.77% and 29.97% respectively.

	BIF			EBIF			Magnetite Ore		
	Average	Min	Max	Average	Min	Max	Average	Min	Max
SiO ₂	54.98	44.70	65.80	10.21	4.86	23.40	2.25	0.10	7.44
Al ₂ O ₃	0.42	0.23	0.59	2.16	0.61	5.19	1.53	0.05	5.32
Fe ₂ O ₃	44.02	32.37	55.90	72.91	64.83	79.39	95.29	81.23	101.80
CaO	0.10	0.02	0.15	3.83	0.52	9.31	0.30	0.00	0.86
MgO	0.21	0.07	0.43	3.91	2.80	5.27	1.04	0.03	3.55
Na ₂ O	0.09	< 0.01	0.09	0.00	< 0.01	0.01	< 0.01	< 0.01	< 0.01
K ₂ O	0.05	0.01	0.08	0.02	0.01	0.04	0.03	0.02	0.05
TiO ₂	0.02	0.01	0.02	0.11	0.02	0.35	0.10	0.01	0.35
MnO	0.04	0.01	0.09	1.05	0.40	1.67	0.50	0.08	1.54
P ₂ O ₅	0.07	0.00	0.12	0.35	0.21	0.62	0.17	0.01	0.63
C	-	-	-	-	-	-	-	-	-
S	0.24	0.00	0.77	0.35	0.05	0.75	0.04	0.02	0.44
LOI	-0.54	-1.49	0.40	4.10	-1.70	12.90	-1.59	-2.60	0.44
Total	<u>99.70</u>			<u>98.99</u>			<u>99.65</u>		
Samples	5			4			4		

	Magnetite-Hematite Ore			Hematite Ore			Chlorite Schist		
	Average	Min	Max	Average	Min	Max	Average	Min	Max
SiO ₂	0.68	0.40	1.19	4.39	1.89	7.77	30.83	25.00	39.20
Al ₂ O ₃	0.49	0.34	0.65	0.81	0.47	1.20	16.77	12.30	19.95
Fe ₂ O ₃	97.20	94.68	98.65	92.19	90.37	94.50	29.97	28.70	32.10
CaO	0.06	0.01	0.14	0.78	0.06	2.89	0.56	0.11	1.30
MgO	0.29	0.05	0.76	0.68	0.06	1.12	12.87	10.40	14.70
Na ₂ O	< 0.01	< 0.01	< 0.01	0.04	0.00	0.26	0.02	0.01	0.03
K ₂ O	0.01	0.01	0.02	0.05	0.01	0.16	0.07	0.02	0.14
TiO ₂	0.02	0.01	0.02	0.03	0.01	0.05	0.95	0.80	1.05
MnO	0.06	0.04	0.10	0.17	0.04	0.47	0.88	0.12	1.35
P ₂ O ₅	0.05	0.02	0.11	0.58	0.02	2.21	0.34	0.12	0.68
C	-	-	-	-	-	-	0.16	0.01	0.44
S	0.01	< 0.01	0.01	0.76	0.01	2.42	0.19	0.00	0.19
LOI	0.25	-0.40	1.19	-1.11	-2.30	0.32	6.30	2.85	8.07
Total	<u>99.13</u>			<u>99.37</u>			<u>99.90</u>		
Samples	3			6			3		

Table 5-6 Elemental oxide average, minimum and maximum values for BIF, HGIF and ore zone chlorite schist.

All values are in parts per million (ppm). Averages do not include values below detection limits. Elements below detection limit are displayed with less than sign and the value of the detection limit in ppm.

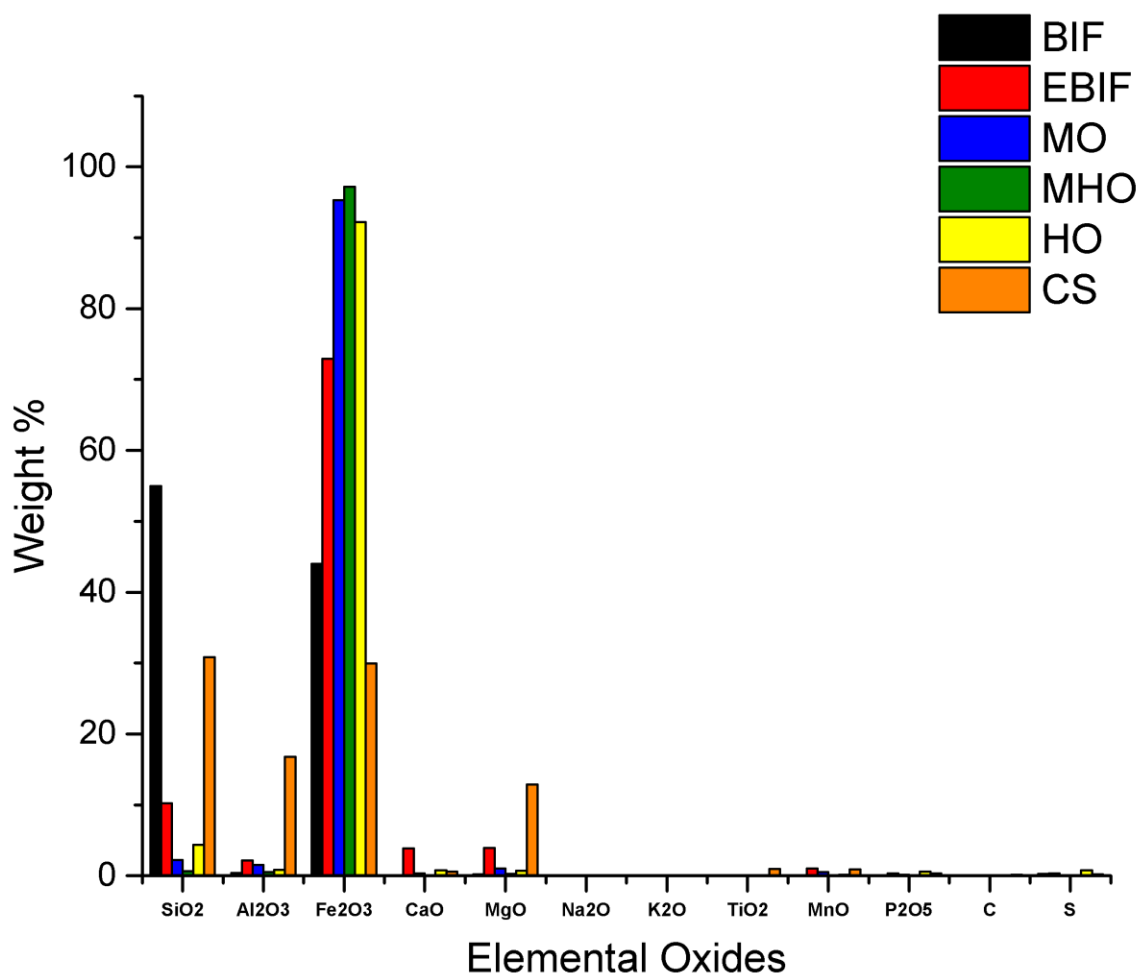


Figure 5-9 Comparative bar graph of average major elemental oxides with carbon and sulphur in BIF, EBIF and iron ore lithologies.

5.2.2 Ore Zone Trace Elements

Lithophile, high field strength and main group elements of ore zone lithologies are listed with transition metals in Table 5-7. The table also displays the average, maximum and minimum values per lithology. Chondrite normalized element values are plotted in Figure 5-10.

Compared to HGIF, banded iron formation holds elevated Ta (7.20 ppm), Sn (13.25 ppm), As (15 ppm), and Sc (1 ppm). Y (6.10 ppm) and Cr (130 ppm) values in BIF are lower than EBIF and iron ores. EBIF contains the highest average Sr (16.75 ppm), V (51.33 ppm), Ag (70ppm), Mo (48.33 ppm), Ni (65 ppm) and Zn (105 ppm).

Magnetite ore has the highest average concentrations of Sn (3.90 ppm), W (34.30 ppm), As (11 ppm), Mo (18 ppm), Ni (36.67 ppm) and Zn (43.33 ppm) with respect magnetite-hematite and hematite ore (figure 5-7). Magnetite-hematite ores average the highest Ag (20 ppm) of the three ore types. Hematite ores contain the highest average Ba (8.05 ppm), Cr (862 ppm), V (28.25 ppm), Co (12.88 ppm) and Cu (69.50 ppm). Chlorite schists are elevated in trace elements with the exception of Cu. Chlorite schists also average 1170 ppm Cr but vary largely (20-2330 ppm).

Elements	BIF			EBIF			Magnetite Ore			MHO			Hematite Ore			Chlorite Schist		
	Average	Min	Max	Average	Min	Max	Average	Min	Max	Average	Min	Max	Average	Min	Max	Average	Min	Max
<i>Li</i>	3.67	< 3	5.00	5.50	< 3	6.00	3.50	< 3	4.00	9.50	< 3	12.00	4.33	< 3	5.00	10.00	< 3	10.00
<i>Ba</i>	4.28	< 3	5.00	3.75	3.00	5.00	4.00	< 3	4.00	5.00	< 3	5.00	8.05	< 3	9.10	34.90	6.10	49.50
<i>Cs</i>	< 0.1	< 0.1	< 0.1	0.10	< 0.1	0.10	< 0.1	< 0.1	< 0.1	< 0.1	< 0.1	< 0.1	0.03	< 0.1	0.03	0.31	0.09	0.67
<i>Sr</i>	6.82	3.10	9.00	16.75	6.00	27.00	9.50	< 3	11.00	9.50	< 3	15.00	11.92	< 3	23.00	11.57	2.10	27.10
<i>Rb</i>	1.10	< 0.4	1.80	0.70	< 0.4	0.70	1.35	< 0.4	2.00	0.50	< 0.4	0.60	1.35	< 0.4	2.00	3.43	1.40	7.10
<i>Th</i>	0.41	0.30	0.50	2.00	0.60	5.10	0.60	0.40	2.00	0.40	0.40	0.40	0.65	0.21	1.40	14.75	10.60	17.65
<i>U</i>	0.30	0.30	0.30	< 0.5	< 0.5	< 0.5	< 0.5	< 0.5	< 0.5	< 0.5	< 0.5	< 0.5	0.56	0.56	0.56	3.50	2.69	4.86
<i>Y</i>	6.10	4.60	7.80	18.08	12.30	22.50	7.45	1.70	14.90	16.53	4.30	31.70	12.52	7.30	19.30	28.23	19.60	45.00
<i>Zr</i>	3.00	3.00	3.00	< 2	< 2	< 2	< 2	< 2	< 2	< 2	< 2	< 2	3.00	3.00	3.00	232.00	155.00	350.00
<i>Hf</i>	< 10	< 10	< 10	< 10	< 10	< 10	< 10	< 10	< 10	< 10	< 10	< 10	< 10	< 10	< 10	5.97	3.60	9.40
<i>Nb</i>	0.82	0.40	2.40	0.40	0.40	0.40	1.68	0.40	5.50	0.40	0.40	0.40	0.40	< 2.4	0.40	10.30	5.50	17.30
<i>Ta</i>	7.20	< 0.2	7.20	3.30	< 0.2	3.30	0.40	< 0.2	0.40	< 0.2	< 0.2	< 0.2	2.60	< 0.2	2.60	0.90	0.50	1.60
<i>Ga</i>	1.36	0.80	1.80	7.55	1.60	20.30	2.48	0.40	5.90	1.50	1.20	1.80	4.15	1.40	9.40	21.20	15.40	24.70
<i>Cr</i>	130.00	< 30	300.00	233.33	< 30	300.00	200.00	< 30	300.00	150.00	< 30	200.00	862.00	< 30	3800.00	1170.00	20.00	2330.00
<i>V</i>	12.00	< 5	14.00	51.33	< 5	111.00	16.00	< 5	16.00	11.50	< 5	15.00	28.25	< 5	48.00	143.67	107.00	204.00
<i>Sn</i>	13.25	< 0.5	24.40	1.55	< 0.5	1.60	3.90	< 0.5	6.20	< 0.5	< 0.5	< 0.5	1.40	< 0.5	1.40	1.00	1.00	1.00
<i>Tl</i>	< 0.1	< 0.1	< 0.1	< 0.1	< 0.1	< 0.1	< 0.1	< 0.1	< 0.1	< 0.1	< 0.1	< 0.1	0.15	< 0.1	0.20	< 0.1	< 0.1	< 0.1
<i>W</i>	4.53	< 0.7	7.10	4.83	< 0.7	8.90	34.30	< 0.7	96.00	2.45	< 0.7	3.50	3.88	< 0.7	10.80	3.00	< 0.7	4.00
<i>As</i>	15.00	< 5	15.00	< 5	< 5	< 5	11.00	< 5	11.00	< 5	< 5	< 5	1.50	< 5	1.50	36.30	1.20	106.50
<i>Bi</i>	0.03	< 2	0.03	< 2	< 2	< 2	10.00	< 2	10.00	< 2	< 2	< 2	0.05	< 2	0.05	0.13	0.02	0.35
<i>Hg</i>	0.01	0.01	0.01	< 0.05	< 0.05	< 0.05	< 0.05	< 0.05	< 0.05	< 0.05	< 0.05	< 0.05	0.01	0.01	0.01	0.01	< 0.05	0.01
<i>Sb</i>	1.56	< 2	3.00	< 2	< 2	< 2	< 2	< 2	< 2	2.00	< 2	2.00	0.34	< 2	0.34	0.13	< 2	0.19
<i>Se</i>	1.10	< 0.8	1.20	1.90	< 0.8	2.40	< 0.8	< 0.8	< 0.8	1.50	< 0.8	1.50	1.50	< 0.8	1.50	0.90	0.20	2.30
<i>Te</i>	0.02	< 6	0.02	< 6	< 6	< 6	< 6	< 6	< 6	< 6	< 6	< 6	0.01	< 6	0.01	0.10	0.01	0.28
<i>Ag</i>	< 10	< 10	< 10	70.00	< 10	70.00	< 10	< 10	< 10	20.00	< 10	20.00	0.60	< 10	0.60	< 10	< 10	< 10
<i>Cd</i>	< 2	< 2	< 2	< 2	< 2	< 2	< 2	< 2	< 2	< 2	< 2	< 2	< 2	< 2	< 2	1.90	< 2	2.30
<i>Co</i>	5.70	< 0.2	7.70	8.75	2.10	24.20	15.78	10.60	25.10	5.60	4.60	6.80	12.88	< 0.2	24.10	49.67	15.00	88.00
<i>Cu</i>	30.00	< 2	54.00	19.00	3.00	42.00	11.75	10.00	13.00	9.00	6.00	13.00	69.50	1.00	239.00	23.33	1.00	55.00
<i>Mo</i>	2.00	< 1	2.00	48.33	< 1	136.00	18.00	< 1	18.00	3.00	< 1	3.00	2.50	< 1	3.00	1.50	< 1	2.00
<i>Ni</i>	13.00	< 10	20.00	65.00	< 10	110.00	36.67	< 10	50.00	20.00	20.00	20.00	28.00	< 10	40.00	482.67	72.00	1080.00
<i>Pb</i>	9.65	< 0.8	15.70	9.43	< 0.8	19.00	9.43	< 0.8	15.00	7.10	< 0.8	8.00	5.88	< 0.8	14.60	16.00	< 0.8	28.00
<i>Sc</i>	1.00	1.00	1.00	< 1	< 1	< 1	< 1	< 1	< 1	< 1	< 1	< 1	< 1	< 1	< 1	13.00	10.00	17.00
<i>Zn</i>	30.00	< 30	30.00	105.00	< 30	120.00	43.33	< 30	50.00	< 30	< 30	< 30	2.00	< 30	2.00	192.00	95.00	350.00
<i>Ge</i>	9.60	< 0.7	10.90	15.45	13.10	17.70	15.05	11.40	17.60	16.27	16.20	16.30	18.78	< 0.7	29.90	< 0.7	< 0.7	< 0.7
<i>In</i>	< 0.2	< 0.2	< 0.2	< 0.2	< 0.2	< 0.2	< 0.2	< 0.2	< 0.2	< 0.2	< 0.2	< 0.2	< 0.2	< 0.2	< 0.2	< 0.2	< 0.2	< 0.2

Table 5-7 Trace element average, minimum and maximum values for BIF, HGIF and ore zone chlorite schist. All values are in parts per million (ppm). Averages do not include values below detection limits. Elements below detection limit are displayed with less than sign and the value of the detection limit in ppm.

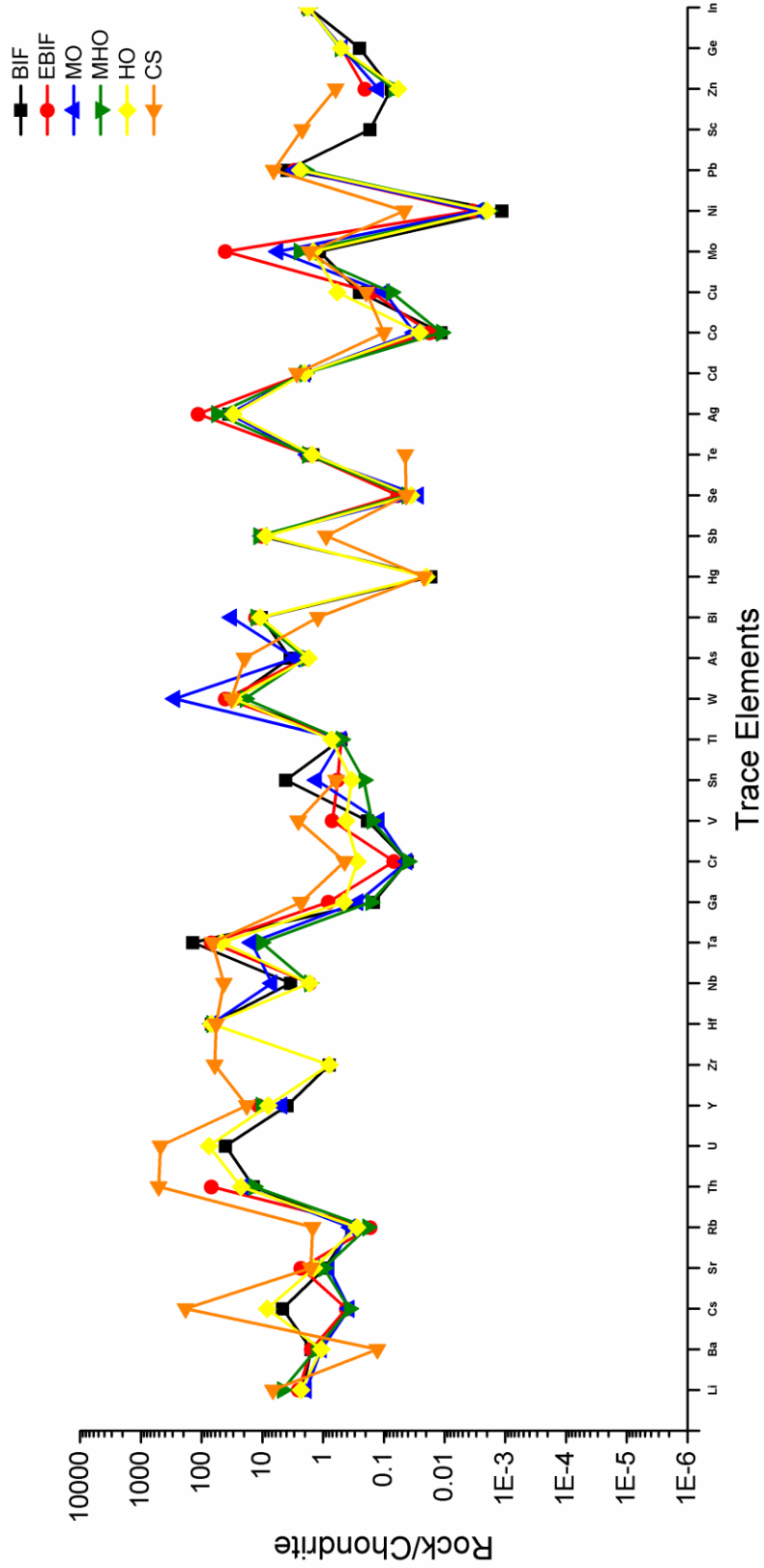


Figure 5-10 Normalized chondrite trace element plot of average BIF, EBIF and iron ore types.

5.2.3 Ore Zone Rare Earth Elements

Rare earth element abundances in banded iron formation and high grade iron formation are low, not exceeding 29.30 ppm. Rare earth element averages from ore zone lithologies are listed in Table 5-8 together with minimum and maximum values.

Banded iron formation contains appreciable amounts of La (3.36 ppm), Ce (6.04 ppm) and Nd (3.84 ppm). Remaining LREE and HREE averages are below 1 ppm. EBIF retains the highest LREE concentrations of La (10.45 ppm), Ce (19.33 ppm) and Nd (9.43 ppm). LREE concentrations of in the three ore types are relatively similar though Ce and La are higher in magnetite-hematite and hematite ores than magnetite ores. HREE concentrations were generally below 1 ppm except Gd, Dy and Yb.

Chondrite normalized values are plotted in Figure 5-11. Both banded iron formation and HGIF units show a remarkably similar negative sloping LREE profile, a positive Eu anomaly and flat to low positive slope HREE trend. All HGIF unit concentrations plot above banded iron formation. EBIF contains the highest REE values and thus the highest normalized chondrite ratios, but retain the same profile as BIF. Magnetite-hematite and hematite ore show virtually identical LREE profiles but diverge after the Eu anomaly with magnetite-hematite ore showing larger HREE ratios.

Elements	BIF			EBIF			Magnetite Ore		
	Average	Min	Max	Average	Min	Max	Average	Min	Max
<i>La</i>	3.36	1.80	5.40	10.45	5.70	15.80	3.48	1.00	7.50
<i>Ce</i>	6.04	3.40	10.90	19.33	10.00	29.30	7.30	1.60	17.90
<i>Pr</i>	0.76	0.40	1.31	2.28	1.30	3.50	0.78	0.10	1.80
<i>Nd</i>	3.84	1.80	7.10	9.43	5.70	14.40	3.45	0.60	8.30
<i>Sm</i>	0.61	0.40	0.97	1.93	1.40	2.90	0.63	0.10	1.30
<i>Eu</i>	0.40	0.20	0.60	1.03	0.80	1.20	0.55	< 0.1	0.60
<i>Gd</i>	0.60	0.50	0.71	1.88	1.50	2.10	0.60	0.10	1.10
<i>Tb</i>	0.10	< 0.1	0.10	0.33	0.30	0.40	0.20	< 0.1	0.20
<i>Dy</i>	0.72	0.60	0.90	2.33	1.80	2.90	1.10	< 0.3	1.70
<i>Ho</i>	0.20	< 0.2	0.21	0.53	0.40	0.70	0.35	< 0.2	0.40
<i>Er</i>	0.54	0.40	0.60	1.55	1.20	2.00	0.63	0.10	1.30
<i>Tm</i>	0.08	< 0.1	0.08	0.23	0.20	0.30	0.15	< 0.1	0.20
<i>Yb</i>	0.53	0.40	0.70	1.68	1.30	2.20	0.63	0.10	1.30
<i>Lu</i>	0.10	0.10	0.10	< 0.01	< 0.01	< 0.01	< 0.01	< 0.01	< 0.01
Elements	MHO			Hematite Ore			Chlorite Schist		
	Average	Min	Max	Average	Min	Max	Average	Min	Max
<i>La</i>	5.13	0.60	12.00	5.37	2.20	8.50	46.17	40.40	54.10
<i>Ce</i>	9.30	1.40	21.10	9.13	4.60	14.10	95.70	82.60	107.00
<i>Pr</i>	1.17	0.20	2.60	1.18	0.56	1.90	11.49	9.97	12.40
<i>Nd</i>	4.63	0.60	10.80	4.68	2.20	7.10	44.67	39.40	47.50
<i>Sm</i>	1.07	0.20	2.30	1.05	0.49	1.40	8.16	7.31	9.64
<i>Eu</i>	0.70	0.10	1.50	0.69	0.36	1.00	2.67	2.15	2.98
<i>Gd</i>	1.43	0.40	3.00	1.15	0.77	1.50	6.81	5.66	8.42
<i>Tb</i>	0.40	< 0.1	0.60	0.22	0.14	0.30	0.93	0.67	1.34
<i>Dy</i>	1.97	0.50	3.90	1.45	0.71	2.00	5.14	3.35	8.37
<i>Ho</i>	0.65	< 0.2	0.90	0.35	0.21	0.50	1.06	0.61	1.82
<i>Er</i>	1.30	0.30	2.50	1.00	0.67	1.40	2.96	1.80	5.22
<i>Tm</i>	0.30	< 0.1	0.40	0.13	0.10	0.20	0.43	0.24	0.77
<i>Yb</i>	1.27	0.40	2.30	0.99	0.70	1.50	2.79	1.63	4.94
<i>Lu</i>	< 0.01	< 0.01	< 0.01	0.10	0.10	0.10	0.42	0.26	0.73

Table 5-8 Rare earth element average, minimum and maximum values for BIF, HGIF and ore zone chlorite schist.

All values are in parts per million (ppm). Averages do not include values below detection limits. Elements below detection limit are displayed with less than sign and the value of the detection limit in ppm.

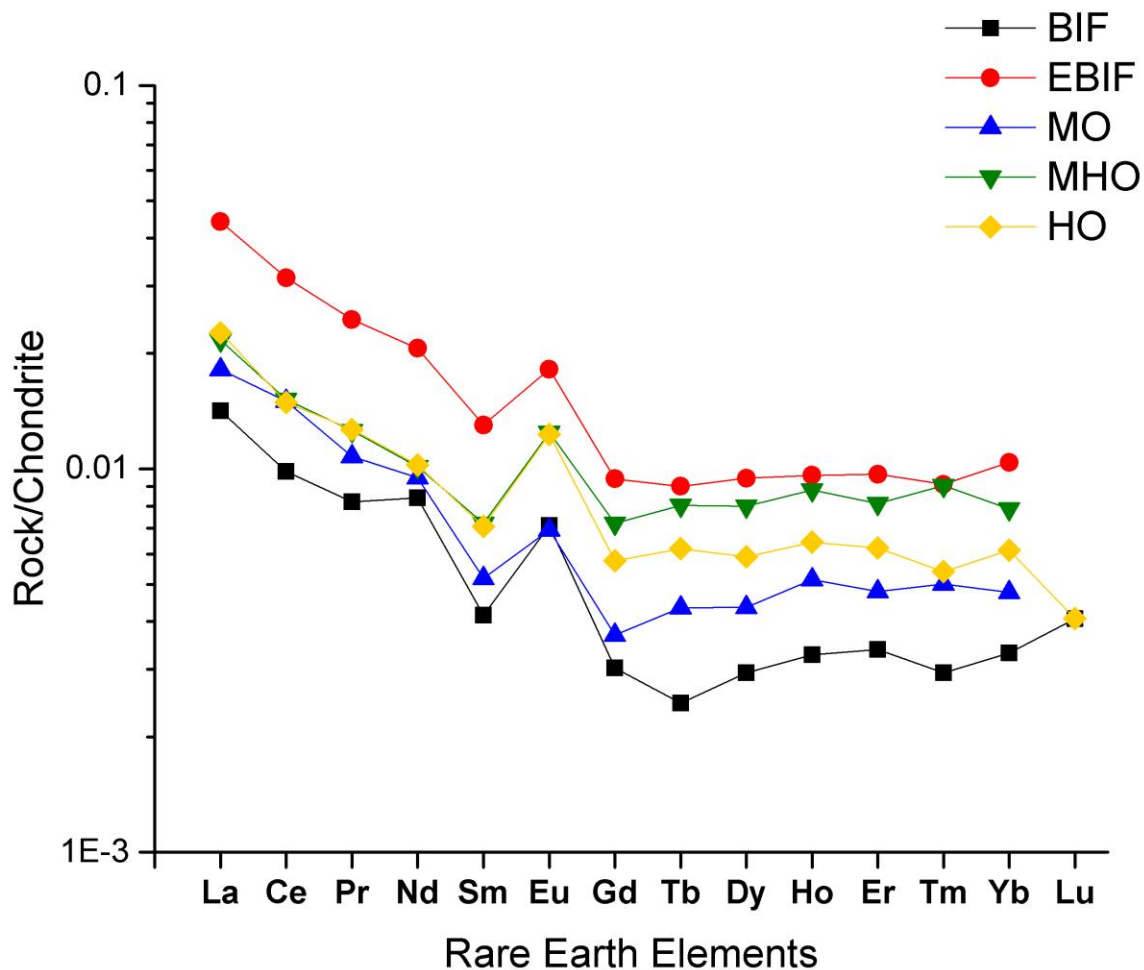


Figure 5-11 Chondrite normalized rare earth element plot of BIF, EBIF and iron ore types. Ratios plotted are averages of normalized values.

5.3 Hangingwall Litho geochemistry

5.3.1 Hangingwall Major Oxides

Major elemental oxides averages for hangingwall chlorite-biotite schists, ultramafics, volcanics and hornblende-amphibolites are listed in Table 5-9. Chlorite schists are ultramafic by average SiO_2 content (37.70 %) and show high concentrations of Al_2O_3 (18.07%), Fe_2O_3 (19.28%) and MgO (12.73%).

Ultramafics average 34.10% SiO_2 , 38.37% MgO and 8.46% Fe_2O_3 . CaO and C values are noticeably higher than chlorite schists averaging 1.72% and 1.68%.

Volcanics are much higher in SiO_2 (54.95%), CaO (5.32%) and Na_2O (4.13%)

content than associated CS and UM units. Al₂O₃ (14.91%), Fe₂O₃ (9.50%), MgO (6.71%) and K₂O (1.19%) are the additional major components in volcanoclastics. The one biotite schist (sample 6503) shows SiO₂ (52%), Al₂O₃ (18.95%), Fe₂O₃ (11.15%), MgO (5.74%) and TiO₂ (1.25%) are its major constituents. Hornblende amphibolite contains similar elemental oxide concentrations compared to volcanoclastics but are higher in MgO (6.71% vs 7.34%) and Fe₂O₃ (9.50% vs 10.90%).

	Chlorite Schist			Ultramafic			Volcanoclastic		
	Average	Min	Max	Average	Min	Max	Average	Min	Max
SiO ₂	37.70	32.80	46.80	34.10	33.30	35.30	54.95	49.80	57.80
Al ₂ O ₃	18.07	16.75	18.90	0.61	33.30	35.30	14.91	14.00	17.00
Fe ₂ O ₃	19.28	16.50	24.60	8.46	33.30	35.30	9.50	8.12	10.30
CaO	0.27	0.20	0.36	1.72	33.30	35.30	5.32	4.62	6.56
MgO	12.73	7.19	17.50	38.37	33.30	35.30	6.71	6.00	7.35
Na ₂ O	0.07	0.03	0.09	0.05	33.30	35.30	4.13	2.49	5.18
K ₂ O	0.87	0.07	1.76	0.03	33.30	35.30	1.19	0.16	2.19
TiO ₂	1.20	1.20	1.21	0.03	33.30	35.30	0.91	0.67	1.58
MnO	0.52	0.12	0.74	0.11	33.30	35.30	0.20	0.13	0.39
P ₂ O ₅	0.07	0.04	0.09	0.01	33.30	35.30	0.09	0.07	0.14
C	0.01	0.00	0.02	1.68	33.30	35.30	0.27	0.02	1.00
S	0.05	0.01	0.10	0.13	33.30	35.30	0.08	0.00	0.16
LOI	8.68	7.58	10.40	16.83	33.30	35.30	2.36	0.47	57.80
Total	<u>99.53</u>			<u>102.12</u>			<u>100.62</u>		
Samples	3			3			4		

	Biotite Schist			Hbl-Amp		
	Average	Min	Max	Average	Min	Max
SiO ₂	52.00	-	-	48.50	-	-
Al ₂ O ₃	18.95	-	-	15.05	-	-
Fe ₂ O ₃	11.15	-	-	10.90	-	-
CaO	0.30	-	-	9.56	-	-
MgO	5.74	-	-	7.34	-	-
Na ₂ O	0.17	-	-	3.37	-	-
K ₂ O	2.84	-	-	0.74	-	-
TiO ₂	1.25	-	-	0.68	-	-
MnO	0.14	-	-	0.18	-	-
P ₂ O ₅	0.14	-	-	0.06	-	-
C	0.01	-	-	0.22	-	-
S	0.01	-	-	0.02	-	-
LOI	7.43	-	-	1.93	-	-
Total	<u>100.13</u>			<u>98.55</u>		
Samples	1			1		

Table 5-9 Elemental oxide average, minimum and maximum values for hangingwall lithologies. All values are in weight %. Averages do not include values below detection limits. Maximum and minimum values do not exist for biotite and hornblende amphibolite (Hbl-Amp) because only sample of each was analyzed.

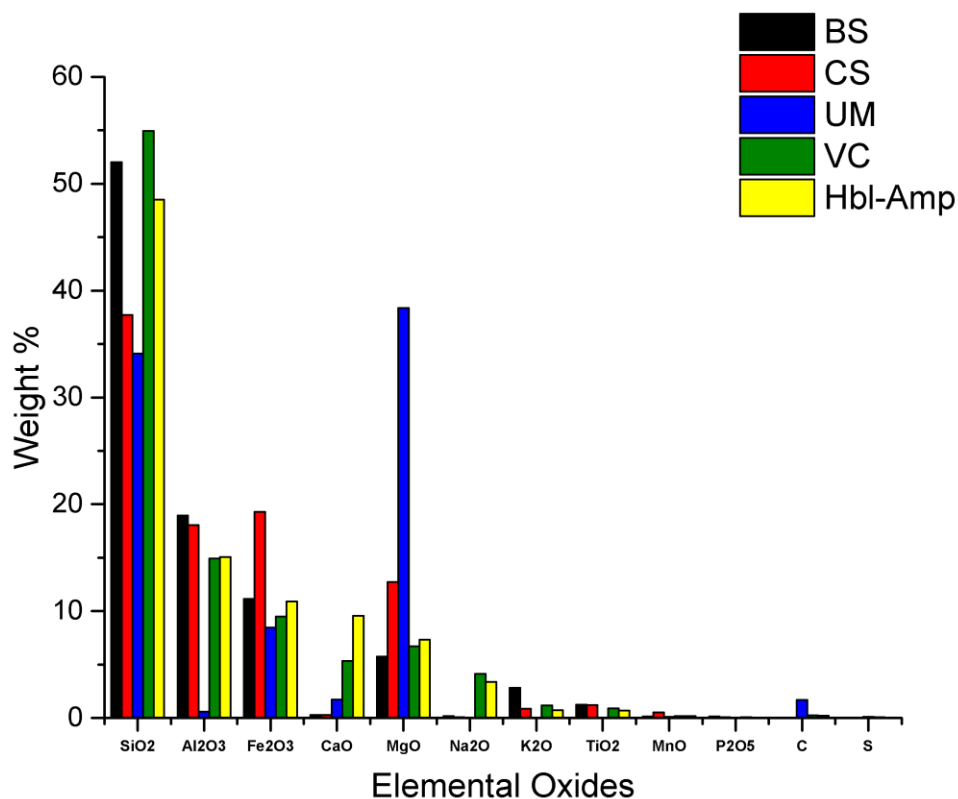


Figure 5-12 Comparative bar graph of average major elemental oxides, carbon and sulphur in hangingwall lithologies.

5.3.2 Hangingwall Trace Elements

Lithophile, high field strength and main group elements are listed with transition metals in Table 5-10 from hangingwall units. The table displays the average, maximum and minimum values per lithology. Chondrite normalized element values are plotted in Figure 5-10.

Ultramafics in comparison to the other lithologies contain the highest average Bi (0.47 ppm), Sb (0.21 ppm), Te (0.16 ppm), Cr (1,803 ppm), Ni (2,810 ppm) and Co (115 ppm) quantities. Ultramafics also contain the lowest Ba, Sr, Th, Y, Zr, Nb, V and Sc. Biotite and chlorite schists show similar trace element concentrations. Average Ba (205.00 ppm), Sr (24 ppm), Rb (79 ppm), Cu (251 ppm) and Cr (400 ppm) are higher in biotite schists than in chlorite schist. However, chlorite schists have higher average Ni

(226 ppm). LILE elements are more concentrated in hornblende-amphibolites and volcanoclastics. Sr in the single hornblende-amphibolite sample is 170.50 ppm.

Elements	Biotite Schist			Chlorite Schist			Hbl-Amp			Ultramafic			Volcanoclastic		
	Average	Min	Max	Average	Min	Max	Average	Min	Max	Average	Min	Max	Average	Min	Max
<i>Li</i>	90.00	-	-	40.00	30	50	20.00	-	-	< 3	< 3	< 3	30.00	10.00	50.00
<i>Ba</i>	205.00	-	-	37.67	10.5	82.7	73.70	-	-	6.37	2.2	9.5	129.43	19.10	259.00
<i>Cs</i>	1.75	-	-	0.82	0.17	1.51	2.40	-	-	0.17	0.14	0.2	11.10	0.26	39.10
<i>Sr</i>	24.00	-	-	5.80	2.4	8	170.50	-	-	10.07	7.9	13	74.85	51.30	91.10
<i>Rb</i>	79.00	-	-	26.97	2	54.3	18.60	-	-	0.27	0.2	0.3	36.93	3.20	96.10
<i>Th</i>	0.30	-	-	0.33	0.28	0.42	0.70	-	-	0.13	< 0.1	0.13	4.79	0.80	6.31
<i>U</i>	0.09	-	-	0.13	0.11	0.15	0.25	-	-	0.22	< 0.5	0.36	1.52	0.29	2.06
<i>Y</i>	22.90	-	-	27.27	21.7	33.4	16.10	-	-	0.73	0.5	0.9	23.63	21.20	29.30
<i>Zr</i>	69.00	-	-	64.33	61	68	44.00	-	-	2.00	< 2	2	103.50	98.00	110.00
<i>Hf</i>	1.80	-	-	1.90	1.8	2	1.30	-	-	< 10	< 10	< 10	3.00	2.90	3.10
<i>Nb</i>	2.80	-	-	2.70	2.7	2.7	1.60	-	-	0.20	< 2.4	0.2	4.68	4.20	4.90
<i>Ta</i>	0.20	-	-	0.17	0.1	0.2	0.10	-	-	< 0.2	< 0.2	< 0.2	0.38	0.30	0.40
<i>Ga</i>	22.90	-	-	22.50	19.7	26	15.00	-	-	0.80	0.6	0.9	18.38	16.30	21.50
<i>Cr</i>	400.00	-	-	293.33	260	310	330.00	-	-	1803.33	1230	2290	230.00	200.00	290.00
<i>V</i>	548.00	-	-	409.67	360	438	260.00	-	-	18.33	17	21	276.50	190.00	515.00
<i>Sn</i>	1.00	-	-	1.00	1	1	1.00	-	-	< 0.5	< 0.5	< 0.5	2.00	1.00	3.00
<i>Tl</i>	< 0.1	-	-	< 0.1	< 0.1	< 0.1	< 0.1	-	-	< 0.1	< 0.1	< 0.1	0.60	< 0.1	0.60
<i>W</i>	1.00	-	-	3.00	2	4	1.00	-	-	3.67	3	5	1.25	1.00	2.00
<i>As</i>	0.20	-	-	0.40	0.1	0.7	0.50	-	-	0.47	0.3	0.7	0.17	< 5	0.30
<i>Bi</i>	0.02	-	-	0.03	0.03	0.04	0.09	-	-	0.47	0.14	0.77	0.08	0.02	0.25
<i>Hg</i>	< 0.05	-	-	0.01	< 0.05	0.005	< 0.05	-	-	0.01	< 0.05	0.005	< 0.05	< 0.05	< 0.05
<i>Sb</i>	< 2	-	-	0.05	< 2	0.05	0.11	-	-	0.21	0.13	0.25	0.10	0.05	0.15
<i>Se</i>	0.40	-	-	0.37	0.3	0.5	0.30	-	-	0.20	< 0.8	0.2	0.43	0.20	1.00
<i>Te</i>	0.03	-	-	0.01	0.01	0.02	0.01	-	-	0.16	0.15	0.17	0.01	< 6	0.01
<i>Ag</i>	< 10	-	-	< 10	< 10	< 10	< 10	-	-	< 10	< 10	< 10	< 10	< 10	< 10
<i>Cd</i>	< 2	-	-	< 2	< 2	< 2	< 2	-	-	< 2	< 2	< 2	< 2	< 2	< 2
<i>Co</i>	59.00	-	-	75.67	61	88	46.00	-	-	115.33	102	125	42.00	38.00	52.00
<i>Cu</i>	251.00	-	-	86.33	39	140	106.00	-	-	26.67	3	41	84.25	33.00	163.00
<i>Mo</i>	< 1	-	-	< 1	< 1	< 1	< 1	-	-	< 1	< 1	< 1	< 1	< 1	< 1
<i>Ni</i>	173.00	-	-	226.33	185	266	101.00	-	-	2810.00	2740	2860	98.75	84.00	131.00
<i>Pb</i>	< 0.8	-	-	< 0.8	< 0.8	< 0.8	16.00	-	-	6.00	3	12	7.25	3.00	11.00
<i>Sc</i>	50.00	-	-	42.67	34	53	41.00	-	-	5.33	5	6	31.75	25.00	46.00
<i>Zn</i>	45.00	-	-	132.67	74	189	90.00	-	-	52.67	21	100	63.75	47.00	81.00

Table 5-10 Trace element average, minimum and maximum values for hangingwall lithologies. All values are in parts per million (ppm). Averages do not include values below detection limits. Elements below detection limit are displayed with less than sign and the value of the detection limit in ppm.

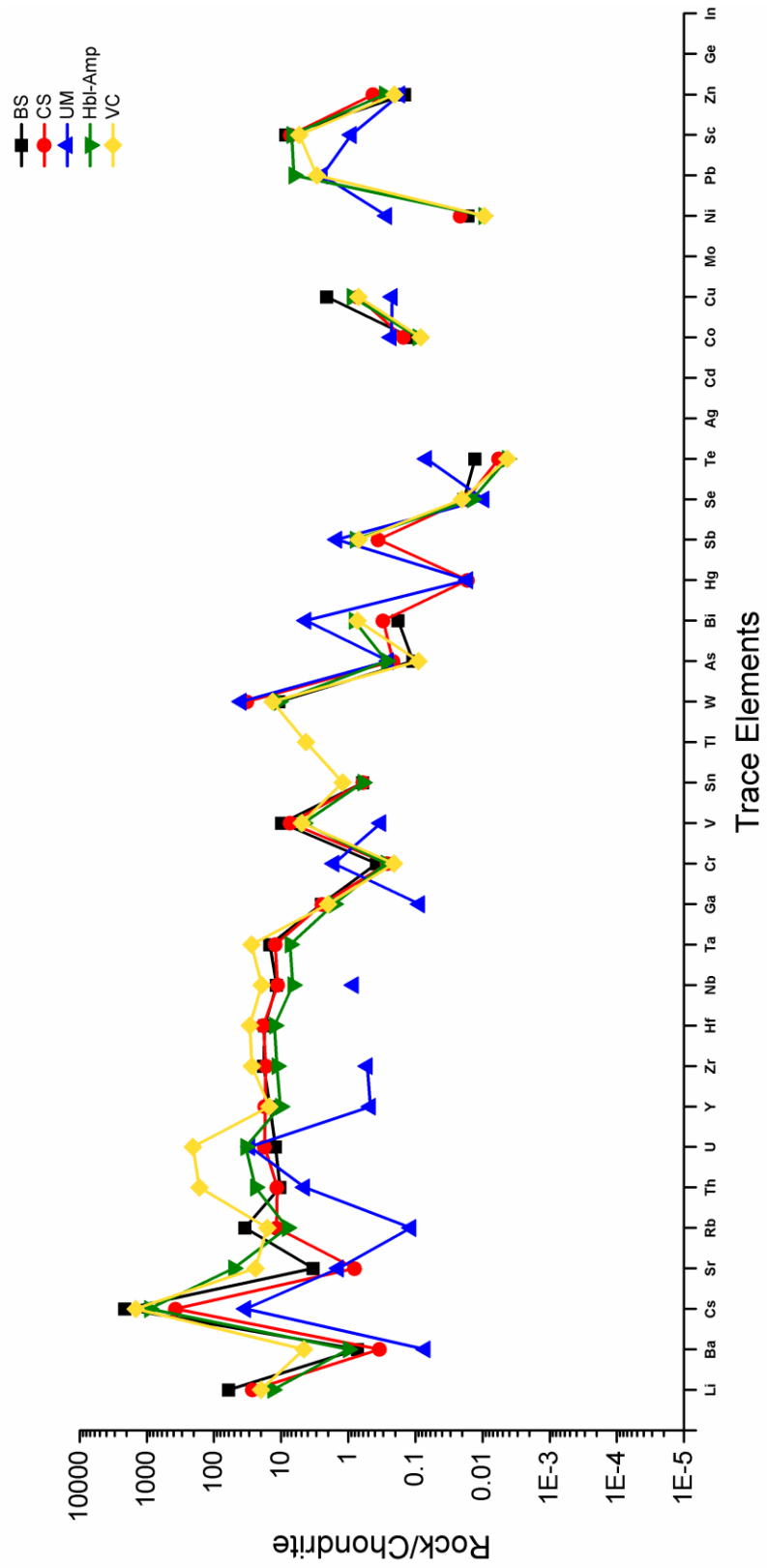


Figure 5-13 Chondrite normalized trace element plot of average hangingwall unit values.

5.3.3 Hangingwall Rare Earth Elements

Rare earth element abundances generally fall under 10 ppm (Table 5-11). Ultramafics contain the lowest values. Only La, Ce and Nd report substantial values while the rest are near the lower limit of detection. Ultramafics show negative Eu anomaly, illustrated in Figure 5-14. Biotite and chlorite schists hold higher LREE values. Dy, Er and Yb are the only HREEs in schists above 1 ppm with exception of Ho at 1.06 ppm in chlorite schist.

Normalize chondrite plots for both biotite and chlorite schists and hornblende-amphibolite are flat with minor perturbations of Eu, Tm and Er (Figure 5-14). The Eu value is only slightly enriched. Volcaniclastics show enrichment of LREEs to chondrite and a gentle negative slope toward Eu. Ultramafics have strong negative slope to a undulating HREE profile. Chlorite schist REE values are plot as flat line between volcaniclastics and hornblende-amphibolite. Figure 5-15 compares normalized REE values of chlorite schist from footwall, ore zone and hanging wall. Hangingwall chlorite schist is depleted in LREEs, Eu and Gd compared to footwall and ore zone chlorite schist.

Elements	Biotite Schist			Chlorite Schist			Hbl-Amp		
	Average	Min	Max	Average	Min	Max	Average	Min	Max
<i>La</i>	5.00	-	-	3.57	2.2	5.3	2.80	-	-
<i>Ce</i>	12.50	-	-	8.73	5.1	12.9	6.80	-	-
<i>Pr</i>	1.97	-	-	1.34	0.83	1.97	0.95	-	-
<i>Nd</i>	10.90	-	-	6.97	4.3	10.2	5.20	-	-
<i>Sm</i>	3.25	-	-	2.63	2.36	3.01	1.66	-	-
<i>Eu</i>	1.42	-	-	0.99	0.92	1.11	0.56	-	-
<i>Gd</i>	3.93	-	-	3.97	3.25	4.97	2.59	-	-
<i>Tb</i>	0.72	-	-	0.76	0.61	1.03	0.43	-	-
<i>Dy</i>	4.57	-	-	4.87	4.03	6.25	2.96	-	-
<i>Ho</i>	0.89	-	-	1.06	0.84	1.24	0.64	-	-
<i>Er</i>	2.79	-	-	3.20	2.54	3.89	1.75	-	-
<i>Tm</i>	0.37	-	-	0.48	0.4	0.56	0.21	-	-
<i>Yb</i>	2.39	-	-	3.14	2.59	3.93	1.68	-	-
<i>Lu</i>	0.39	-	-	0.47	0.37	0.56	0.25	-	-
Elements	Ultramafic			Volcanoclastic					
	Average	Min	Max	Average	Min	Max			
<i>La</i>	1.47	0.35	3.70	11.88	6.10	14.60			
<i>Ce</i>	1.87	0.35	4.90	23.83	14.90	27.70			
<i>Pr</i>	0.17	0.03	0.39	3.08	2.34	3.40			
<i>Nd</i>	0.60	0.20	1.20	12.83	11.60	14.00			
<i>Sm</i>	0.10	0.05	0.16	3.33	3.10	3.70			
<i>Eu</i>	0.02	0.02	0.03	1.09	0.80	1.92			
<i>Gd</i>	0.11	0.06	0.15	3.93	3.46	4.72			
<i>Tb</i>	0.02	0.01	0.03	0.67	0.56	0.82			
<i>Dy</i>	0.11	0.08	0.14	4.27	3.77	5.35			
<i>Ho</i>	0.02	0.01	0.02	0.90	0.76	1.19			
<i>Er</i>	0.07	0.04	0.10	2.83	2.41	3.95			
<i>Tm</i>	0.01	0.01	0.01	0.36	0.29	0.49			
<i>Yb</i>	0.10	0.08	0.12	2.57	2.25	3.45			
<i>Lu</i>	0.01	0.01	0.02	0.39	0.30	0.55			

Table 5-11 Rare earth element average, minimum and maximum values for hangingwall lithologies. All values are in parts per million (ppm). Averages do not include values below detection limits. Elements below detection limit are displayed with less than sign and the value of the detection limit in ppm.

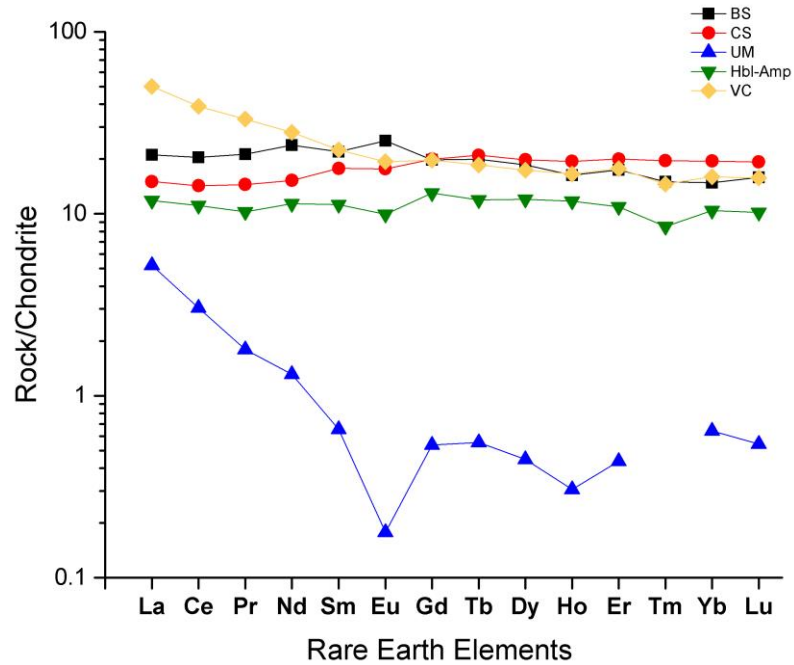


Figure 5-14 Chondrite normalized rare earth element plot of hangingwall unit values. Ratios plotted are averages or normalized values. Elements below the detection limit are not plotted.

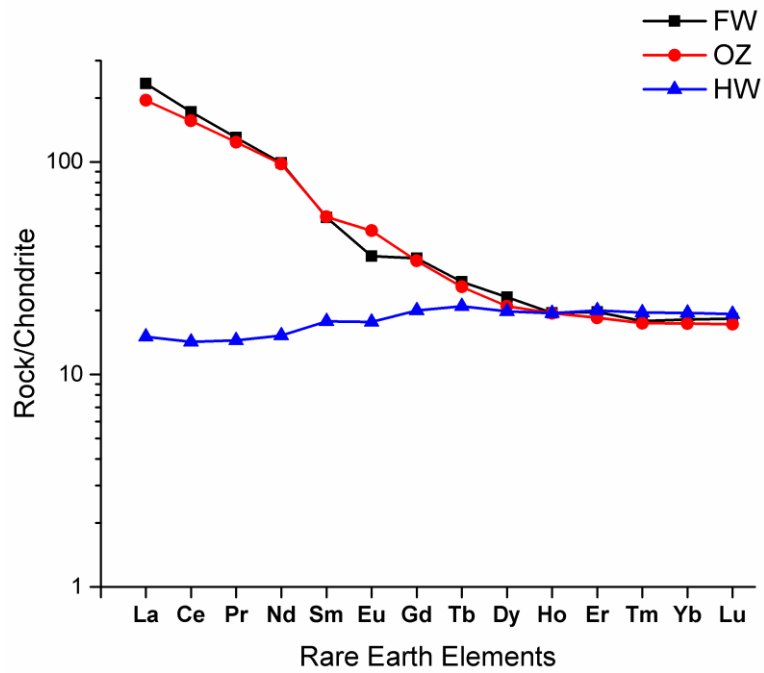


Figure 5-15 Chondrite normalized rare earth element plot of footwall (FW), ore zone (OZ) and hangingwall (HW) chlorite schist unit values. Ratios plotted are averages of normalized values.

5.4 Mass Balance Changes

Mass balance changes are calculated from a known protolith to its altered counterpart. Monzogranite is the protolith of quartz-augen schists and thus also for biotite and chlorite schists in the immediate footwall of Deposit No.1. Strong textural evidence of quartz-augens trending from monzogranites into QAMS, QAMBS and QABS units and gradational contacts defined by the increase of micas support this protolith identification. Altered-silicified granitoids in contact with quartz-augen schist also originated from monzogranite. Banded iron formation is the protolith of enriched BIF and iron ore.

This section presents calculated mass balance changes of footwall schist and altered-silicified granitoids from monzogranites. Mass balance changes are also calculated for iron ores with respect to BIF using Gresens' and arithmetic methods. Major and trace element changes are presented with compositional variance of the parent.

5.4.1 Density and Fv Determination

As discussed in chapter 3, two physical characteristics need to be known for application of Gresens's equation (Gresens, 1967); chemical composition and density of both the parent rock and altered product. Bulk rock densities were derived using a gas pycnometer and balance. Hematite ore density was computed by cutting a symmetrical tile and taking its volume to mass measurements in order to avoid error due to high porosity. All average densities are listed in Table 5-12.

The volume factor (Fv) is crucial for accurate mass balance calculation as this variable represents the volume change caused by alteration of the protolith. Using the methods described by Gresens (1967), theoretical volume factors 0.5 and 2 were inputted into the equation to compute the X-intercept of immobile elements in a composition to volume diagram (C-V diagram). Elements or elemental oxides considered immobile by previous experimentation or chemical nature are plotted in a C-V diagram. Grouping of x-intercepts along the volume axis of the C-V diagram infer that those grouped elements changed in volume symmetrically. X-intercepts of immobile elements Al, LREE, Nb, Ga and Hf were used to calculate Fv. HREEs were not used as concentrations were too low and close to limits of detection. Also HREE varied significantly by proportion in parent

lithologies. Zr was not used because secondary baddeleyite was identified in hematite ore forming at the expense of zircon in Chapter 4, signifying potential zircon mobility. Also TiO_2 intercepts were not utilized because of secondary titanite in ECH veining. Calculated Fv values are listed in Table 5-12. Biotite and chlorite schist show up to 60% volume loss in calculated CV diagrams. Using such low Fv values (0.4-0.55) would virtually deplete the parent composition of SiO_2 . Using these low Fv values also lowers the Fe_2O_3 and MgO values. The result of computing mass balance changes low Fv values (0.4-0.55) for biotite and chlorite schist would create an altered rock that is unlike the current composition the schist units. Fv values of ~.80 for biotite and chlorite schists is favourable because altered bulk rock compositions computed using this value rock are aligned with the units actual composition. Iron ore Fv calculations exploited LREEs for X-intercepts due the extremely low Al, Ti, HFSE and HREE values. Only Ce and Nd were used for MHO because La, Pr and Sm were very low.

It is important to note that none of the calculated Fv values are valid without petrographic and textural inspection. For an increase in volume textural features such as veining, certain mineral replacements and overprints are needed. Fv values lower than 1 mean volume loss. Mineral and textural features thus must indicate potential volume loss.

Volume loss features are identified in quartz-augen, biotite and chlorite schists. Mineral textures of quartz-augen exhibit serrated edges with mosaic quartz indicating grain abrasion. Mineral replacement texture of feldspar to muscovite and biotite also indicate volume loss. However, quartz to mica is a massive volume gain explaining the difference in Fv. Altered-silicified granitoids show volume gain by the replacement of feldspar and mica by larger quartz crystals patches and mild veining. Also at outcrop scale, silica flooding textures are identified. These textures in thin section show filling of mineral grain boundaries. Iron ore shows obvious silica banding loss indicating textural volume loss. Volume factors are listed in Table 5-12.

Lithology	Density Average (g/cm ³)	Fv
MGr	2.73	-
ASG	2.69	1.14
QAMS	2.82	0.9
QAMBS	2.82	0.85
QABS	2.83	0.83
BS	3.11	0.82
CS	3.05	0.8
MO	5.15	0.45
MHO	5.1	0.46
HO	5.02	0.5

Table 5-12 List of footwall and ore zone unit density and volume factors.

5.4.2 Mass Balance Changes ASG & Footwall Schists

Footwall mass balance changes of major elemental oxides are illustrated in Figures 5-16 and 5-17. The baseline represents the average composition of monzogranite. The largest change in footwall units is SiO₂ (-9.30% to -43.77%). Quartz-augen schists show decreasing SiO₂ content from QAMS to QABS. The highest silica depletion occurs in chlorite schists (-43.77%). Na₂O (-1.48 to -3.11 %) and CaO (-0.97% to -1.83%) are mildly depleted below MGr composition variance in quartz-augen schists. Fe₂O₃ (1.48% - 6.98%), MgO (0.62-3.94%) TiO₂ (0.33-0.51%) and P₂O₅ (0.06-0.14%) are enriched above parental composition variance in quartz-augen schists. K₂O is depleted below the average but not below variance in QABS and CS units. K₂O is also enriched in biotite schists by 0.60% above compositional variance. Al₂O₃ lies within compositional variance with exception of chlorite and biotite schists. The increase Al-content is interpreted to element fractionation from porphyroblastic growth of almandine and staurolite. Biotite and chlorite schists that do not contain porphyroblasts average 5-6% lower Al₂O₃. Chlorite schist contains the highest enrichment of Fe₂O₃ (16.10%) and MgO (9.95%). Biotite schist shows the highest P₂O₅ (0.54%) enrichment. ASG units shows the opposite to schists being enriched in SiO₂ by 14.02% and depleted in TiO₂ (-0.11%).

Rare earth elements (REE) gains and losses are plotted in figure 5-18. All REE concentrations are within compositional variance with concession of Sm and Gd. LREEs

trend positively sequentially from QAMS to BS above average but within compositional variance. Chlorite schist, conversely, shows depletion in LREEs.

The remaining trace element gains or losses, including transition metals, LILE, HSFE and main group elements, are plotted in Figure 5-20. Transition metals Cu and Ni are elevated above variance in QAMBS and CS units respectively. Pb is depleted in all lithologies except ASG units. Zirconium shows the highest enrichment in QAMS (50 ppm), QAMBS (234 ppm), and QABS (187 ppm). Large ion lithophile elements (LILE) show little to no enrichment above variance. Cs is enriched in QAMS by 332 ppm above the maximum monzogranite value. Sr is depleted in QABS, BS and CS units below the average monzogranite composition. Rb also shows a depletion in chlorite schist.

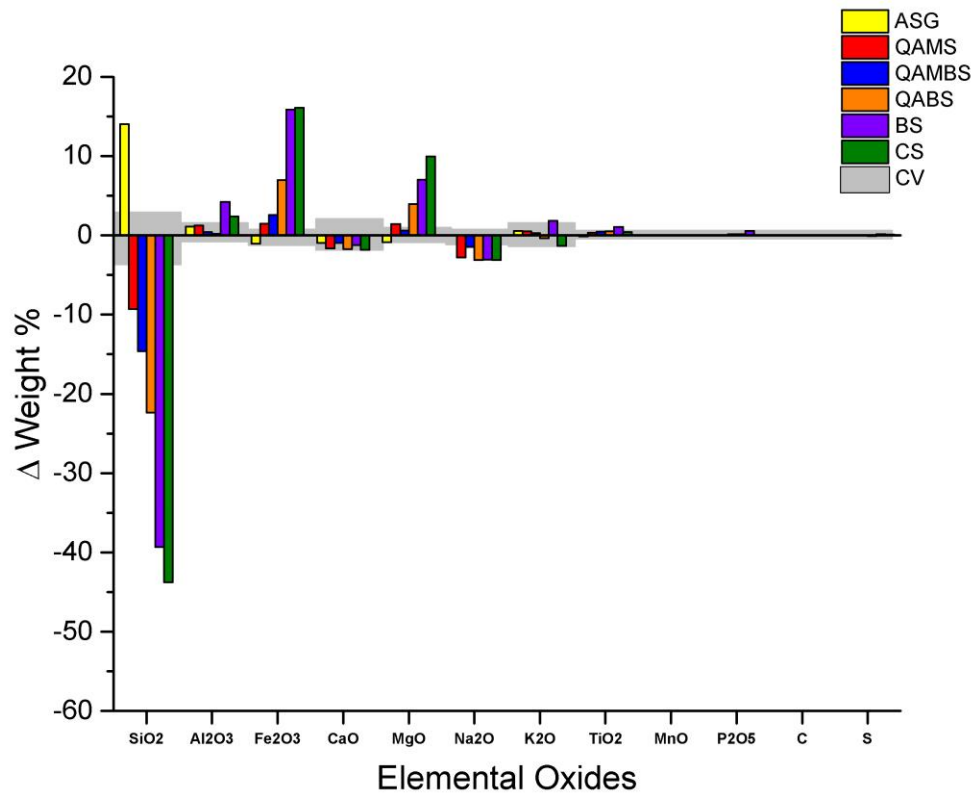


Figure 5-16 Mass balance changes of elemental oxides in footwall schist and ASG lithologies. Comparison is to average unit composition. Protolith compositional variance (CV) is outlined in grey.

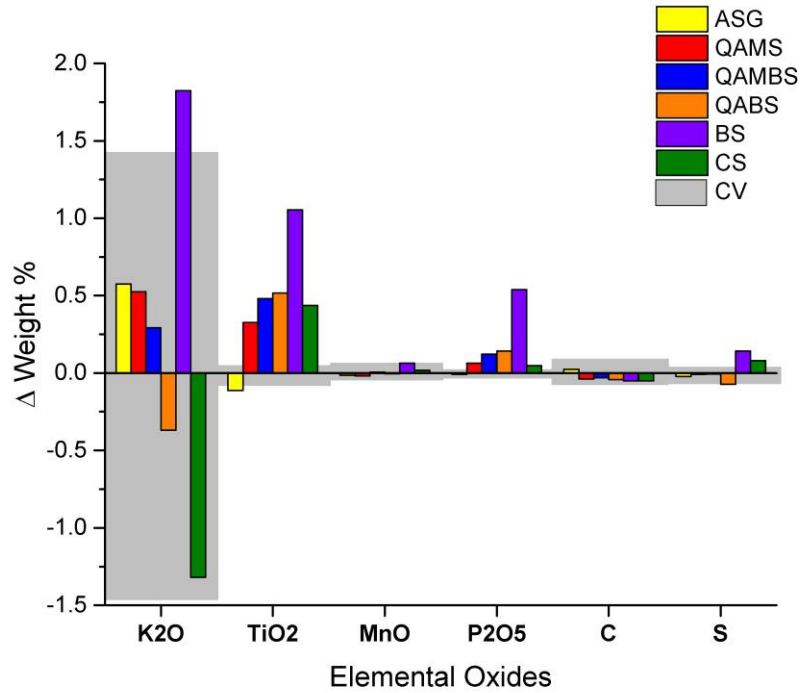


Figure 5-17 Mass balance changes of elemental oxides (K₂O-S) in footwall schist and ASG lithologies. Comparison is to average unit composition. Protolith compositional variance (CV) is outlined in grey.

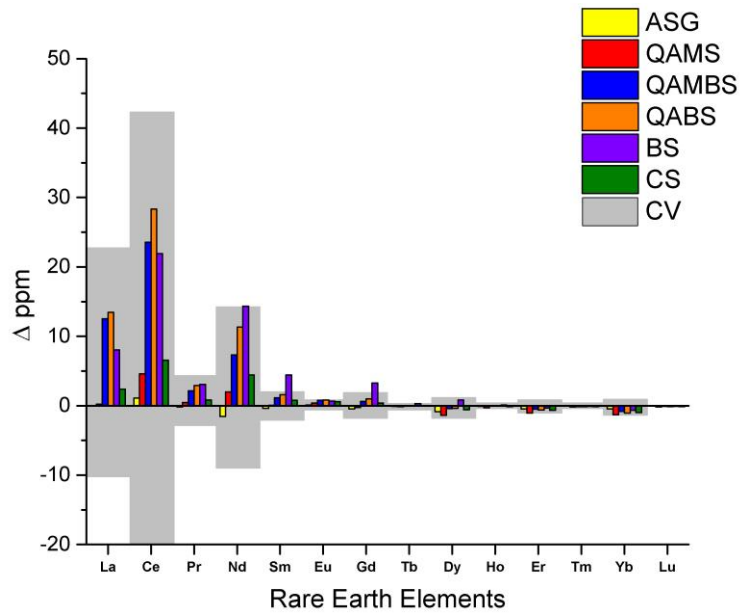


Figure 5-18 Mass balance changes of rare earth elements (REE) in footwall schist and ASG lithologies. Comparison is to average unit composition. Protolith compositional variance (CV) is outlined in grey.

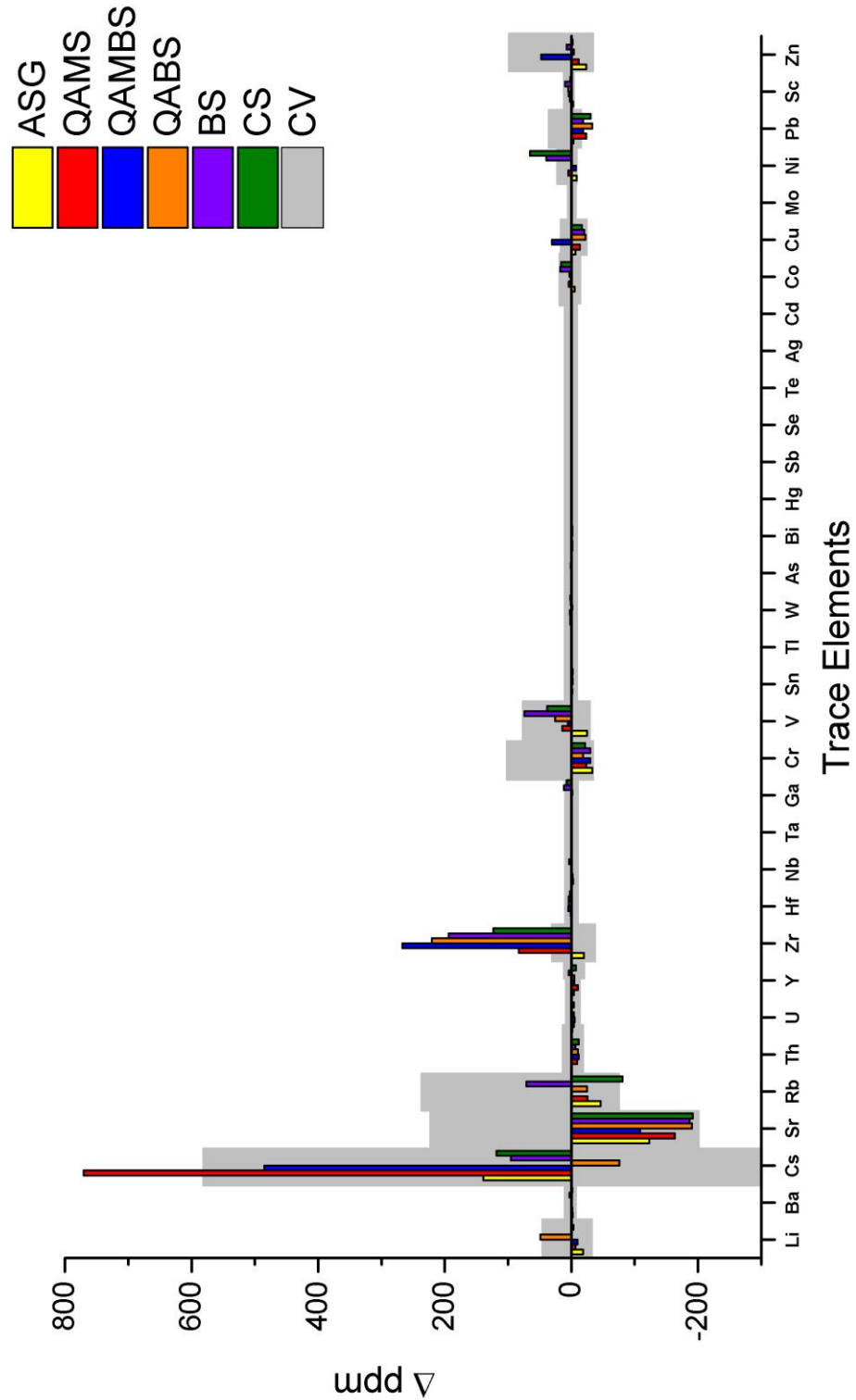


Figure 5-19 Mass balance changes of transition metal, high field strength and main group elements in footwall schist and ASG lithologies. Comparison is to average monzogranite composition. Protolith compositional variance (CV) is outlined in grey.

5.4.3 Mass Balance Changes BIF to Iron Ore

Major elemental oxide changes from BIF to magnetite, magnetite-hematite and hematite ore are illustrated in Figures 5-20 and 5-21. Fe_2O_3 and SiO_2 have the largest depletion and enrichment values. SiO_2 is depleted by 51.97 to 54.53% while Fe_2O_3 is enriched between 17.65% and 20.99%. Magnetite ores show increases in CaO (0.09%), MgO (0.46%), TiO_2 (0.05%) and MnO (0.29%) (Figure 5-21). Hematite ores show an appreciable increase in CaO (0.50%), MgO (0.32%) and P_2O_5 (0.33%).

Trace elements are plotted in Figure 5-22. Cs is the only large ion lithophile element lower than the BIF minimum. The only REE calculated above average and variance is Dy. Magnetite ore (MO) is elevated above average and compositional variance in W, Mo, Co, Zn and Ni. Magnetite-hematite ore is enriched in Y and Ag above average. Hematite ores are moderately enriched in V (7.37 ppm) and less in Co (3.13 ppm). Hematite ores are also mildly enriched in Zn (1.37 ppm).

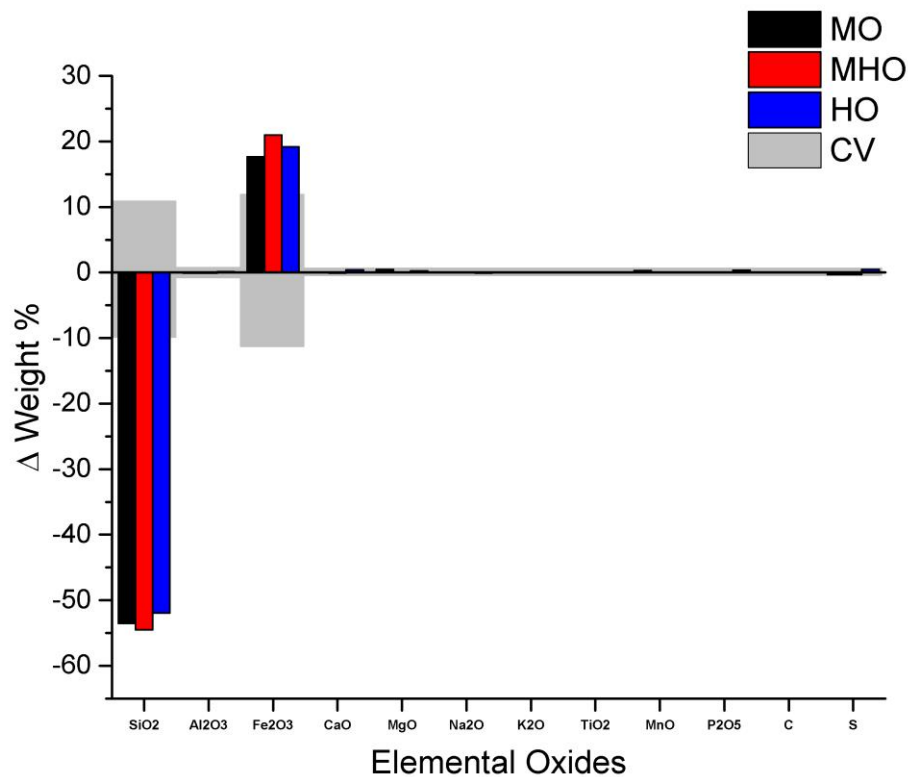


Figure 5-20 Mass balance changes of elemental oxides in iron ore types. Comparison is to average unit composition. Protolith compositional variance (CV) is outlined in grey.

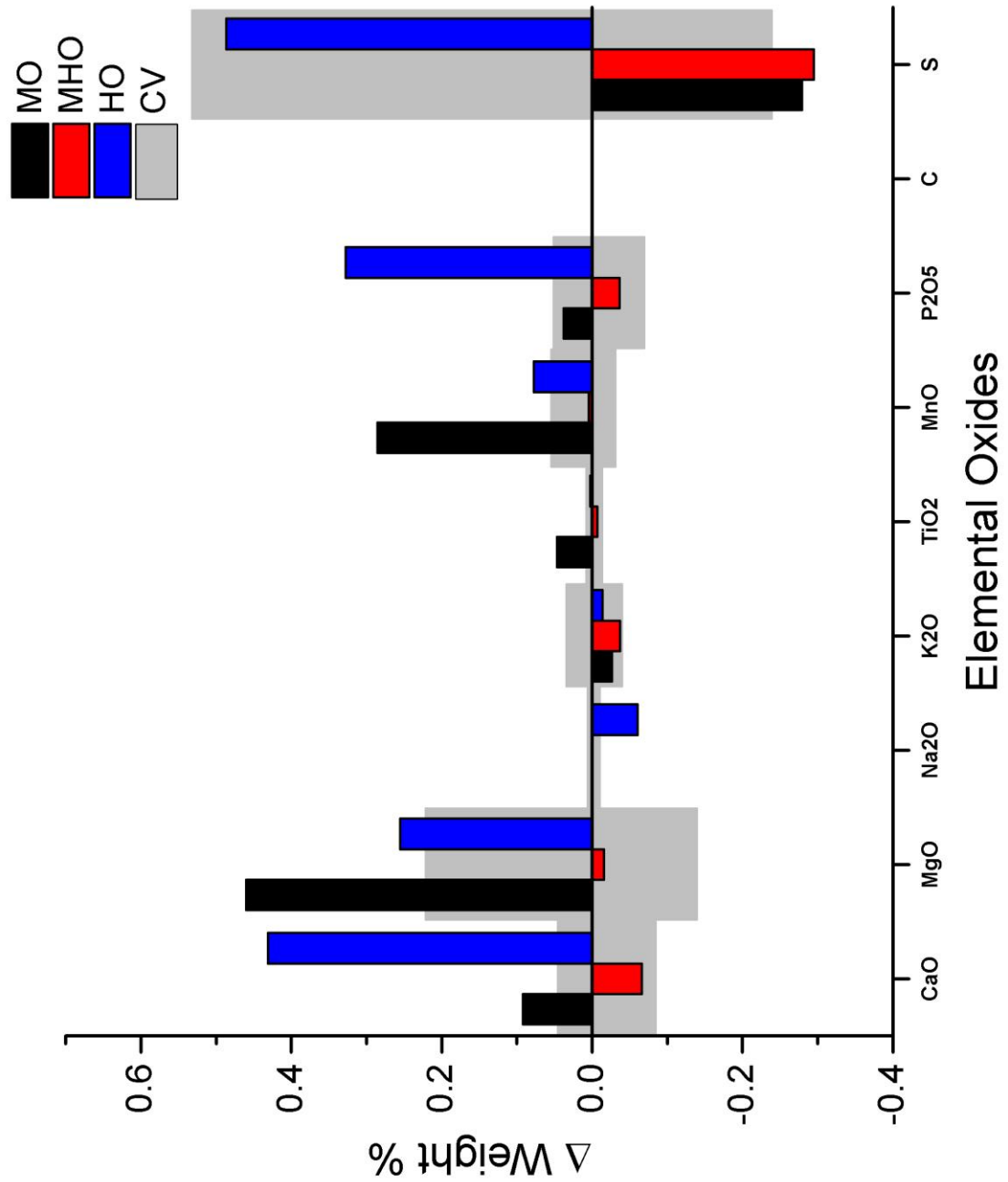


Figure 5-21 Mass balance changes of elemental oxides in iron ore types on a smaller scale. Comparison is to average unit composition. Protolith compositional variance (CV) is outlined in grey.

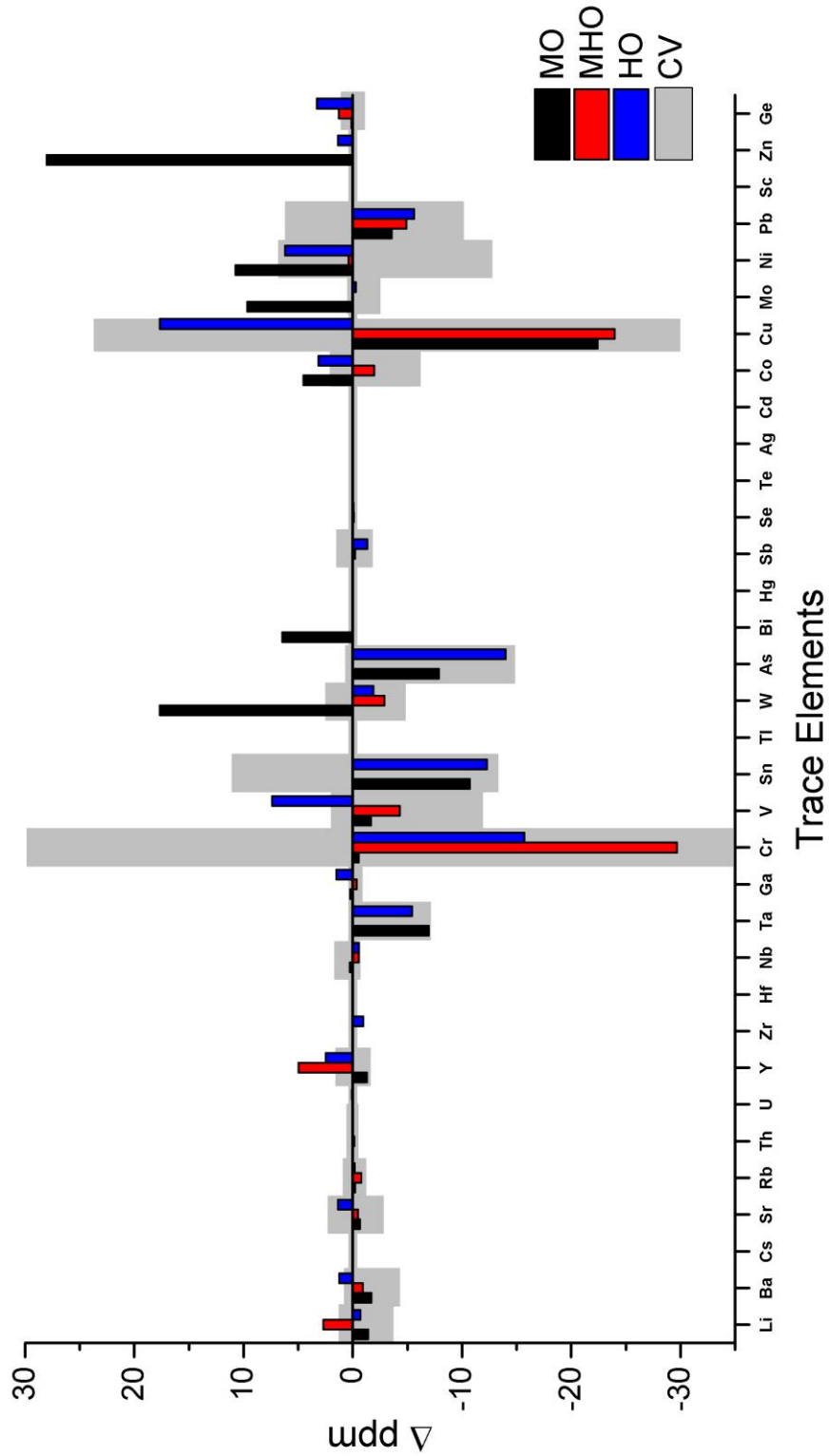


Figure 5-22 Mass balance changes of large ion lithophile, transition metal, high field strength, rare earth and main group elements in iron ore types. Comparison is to average unit composition. Protolith compositional variance (CV) is outlined in grey.

5.4.4 Arithmetic Mass Balance Change BIF to Ore

BIF to high grade iron ore represents a major chemical change. The main chemical components of BIF are SiO_2 and Fe_2O_3 and account for 99.00% of the total composition. Using an arithmetic approach is possible given two conditions: 1) the remaining 1% composition does not account for a substantial portion of the density; and 2) the density and chemical composition of both iron ore and BIF are known. Equation 5-1 shows the derivation for the unknown BIF volume needed to produce 1cm^3 of magnetite-hematite ore. Ratios are set so that the iron oxide content in one cubic centimetre of ore is equated to the amount iron oxide one cubic centimetre of BIF contains. The solution is that 2.25 cm^3 of BIF are needed to produce 1cm^3 of iron ore. The average Fv calculated from Gresens' method for magnetite-hematite ore is 0.46 meaning that 2.17 cm^3 are needed to produce 1cm^3 of ore.

$$\frac{1\text{ cm}^3\text{ BIF}}{2.27\text{ g Fe}_2\text{O}_3} = \frac{X\text{ cm}^3\text{ BIF}}{5.10\text{ g Fe}_2\text{O}_3} = \frac{1\text{ cm}^3\text{ Ore}}{5.10\text{ g Fe}_2\text{O}_3}$$

$$\cancel{2.27\text{ g Fe}_2\text{O}_3} * X\text{ cm}^3\text{ BIF} = \frac{5.10\text{ g Fe}_2\text{O}_3}{\cancel{2.27\text{ g Fe}_2\text{O}_3}}$$

$$X\text{ cm}^3\text{ BIF} = 1\text{ cm}^3\text{ Ore}$$

$$X\text{ cm}^3\text{ BIF} = 2.25$$

Equation 5-1 Arithmetic derivation of BIF volume ratio to iron ore.

Chapter 6 Geochronology

6 Introduction

Selected samples of quartz-augen biotite schist (QABS), garnetiferous ore zone chlorite schist, altered BIF, magnetite-hematite ore and hematite ore were analyzed for datable features by FEG-SEM with EDS scanning. After features were identified and located, targets were selected for geochronological U-Pb isotopic analysis. These targets were imaged using applicable BSE, SE or CL imaging techniques. Chemical zoning identified in features was analyzed during LA-ICP-MS coring or by WDS point analyses. The sections below provide the results of such feature scans, SEM imaging, LA-ICP-MS and WDS analyses by sample.

6.1 Sample 6078 (QAMS) Description

Sample 6078 is a diamond drill core sample collected from QAMS zone in the footwall of Deposit No. 1. The sample was collected from drill hole MR1-12-223 at the 35.56 m to 35.71 m interval. Sample 6078 contains 65% muscovite, 25% quartz and 10% biotite. Rutile, apatite, zircon and monazite occur in trace amounts of 1%, 1%, 0.5% and 0.5% respectively. Quartz-augens are 1-3 millimeter porphyroclasts composed of sutured 10-300 μm quartz crystals with abraded margins showing muscovite overprints at margins. Biotite forms lathes and tablets with strong cleavage that are overprinted by finer secondary muscovite. Rutile occurs as 10-50 μm blebs and blades within muscovite and biotite. Apatites are fine to coarse (10-200 μm) oblong shaped grains located within muscovite and biotite. Coarse apatite exhibits boudinage textures with 5-50 μm gaps. Zircons are coarse and euhedral ranging between 80 to 240 μm in length. Monazites occur as 10-50 μm patches and disseminations with pleochroic halos in muscovite.

6.1.1 6078 BSE-EDS Feature Phase Mapping

The FEG-SEM combined EDS mapping technique described in Chapter 3 obtained microGIS locations and crystallographic data of zircon and monazite (Figure 6-1). A total of 348 zircon grains were identified with areas ranging from 6.30 μm^2 to 10,775 μm^2 with an average of 1141 μm^2 . Spatial association of zircons is scattered,

however; less are identified in quartz-augens (Figure 6-1). A total of 1301 monazites were identified averaging $50.8 \mu\text{m}^2$ and ranging from $6.30 \mu\text{m}^2$ to $2920 \mu\text{m}^2$. Monazite is identified in muscovite, biotite and quartz. The majority of monazite (>95%) are located in the muscovite matrix wrapping around quartz-augens.

6.1.2 6078 BSE & SE Images of Datable Phases

BSE and SE imaging of datable phases was performed on select zircon and monazite grains. All zircon morphologies are plotted in Plate 6-1. Zircon are euhedral to prismatic crystals exhibit concentric oscillatory zoning. Zircons also show fracturing and boudinage textures with infilling quartz and muscovite. All monazite morphologies are illustrated in plate 6-2. SE and BSE imaging of monazites show anhedral to oblong shapes and patches. Fracturing and brecciation is not manifested by monazite grains. Monazites grains tend to cluster and form patches. Monazites also infill apatite fractures and rim boudinage apatite grains.

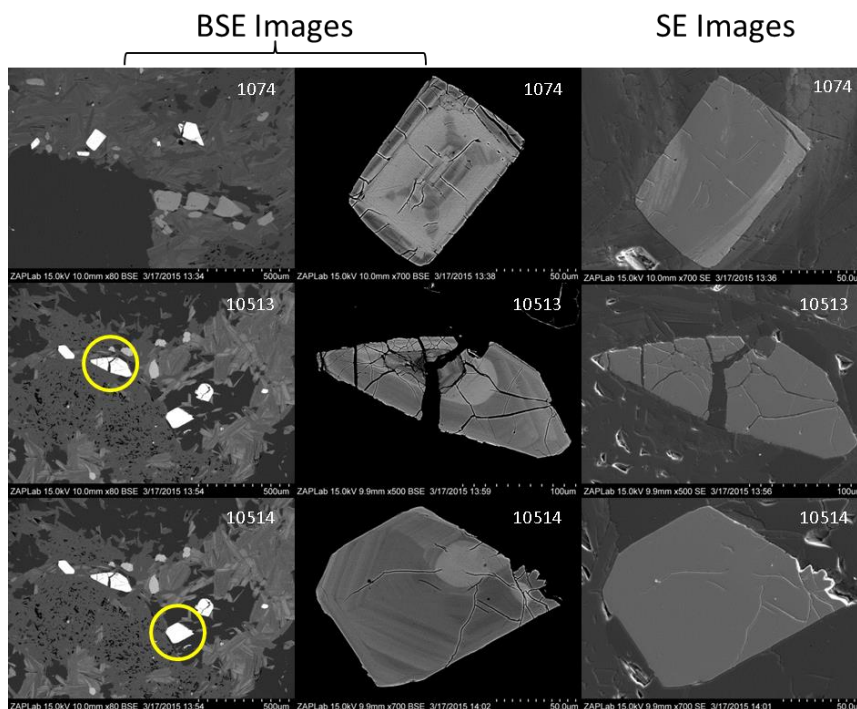


Plate 6-1 Collage of representative zircon crystal morphologies from sample 6078. Micrographs are organized by columns into backscatter electron (BSE) and secondary electron (SE) imaging sources and labeled with their corresponding grain number. Zircon 1074 is an euhedral oscillatory zoned grain. Zircon 10513 exhibits boudinage fractures. Grain 10514 is an example of a zircon fractured in half.

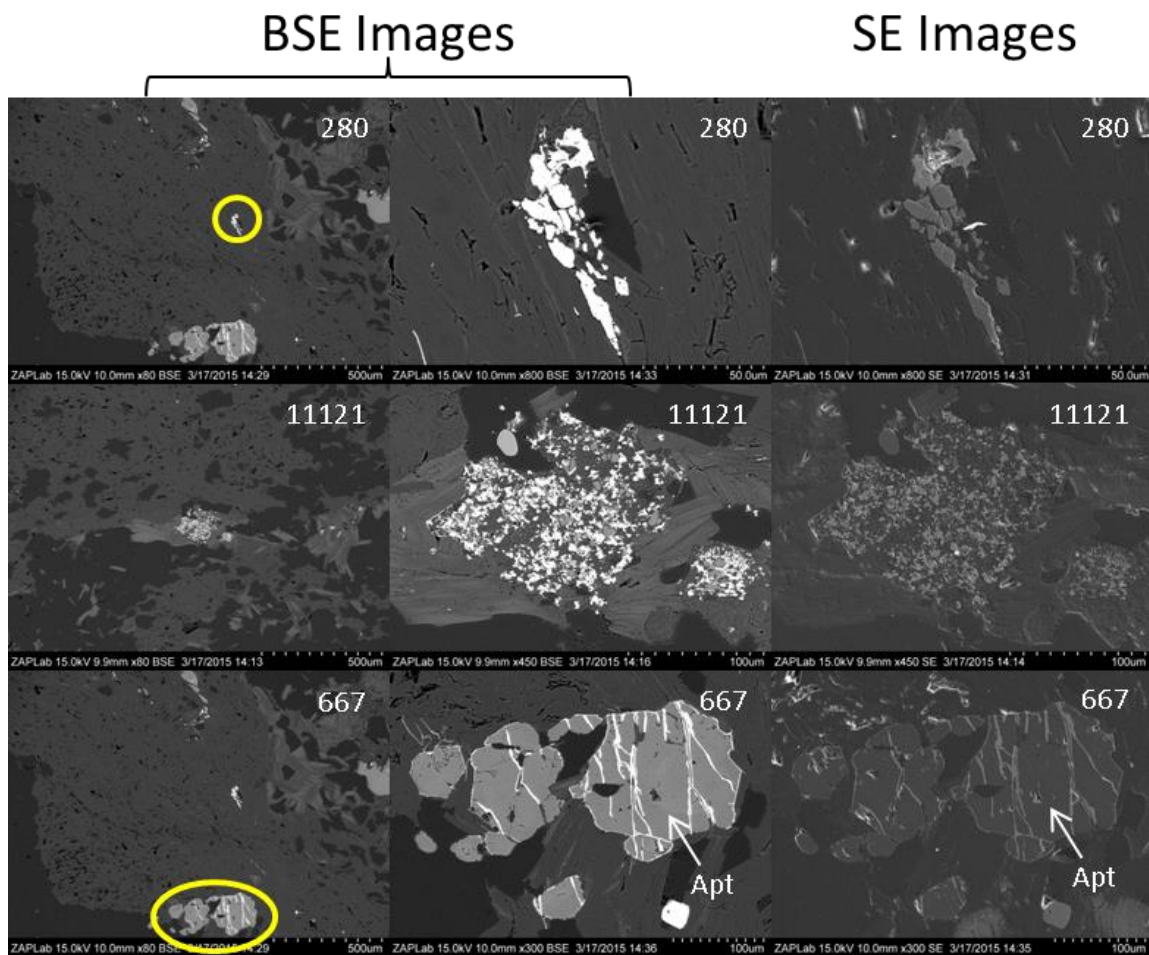


Plate 6-2 Collage of representative monazite crystal morphologies from sample 6078. Micrographs are organized by columns into backscatter electron (BSE) and secondary electron (SE) imaging sources and labeled with their corresponding grain number. Monazite 280 is an example of a cluster. 11121 shows fine interconnected monazite grains forming a patch. Monazite 667 is an example of a monazite infilling fractured apatite.

Sample 6078 Feature Map

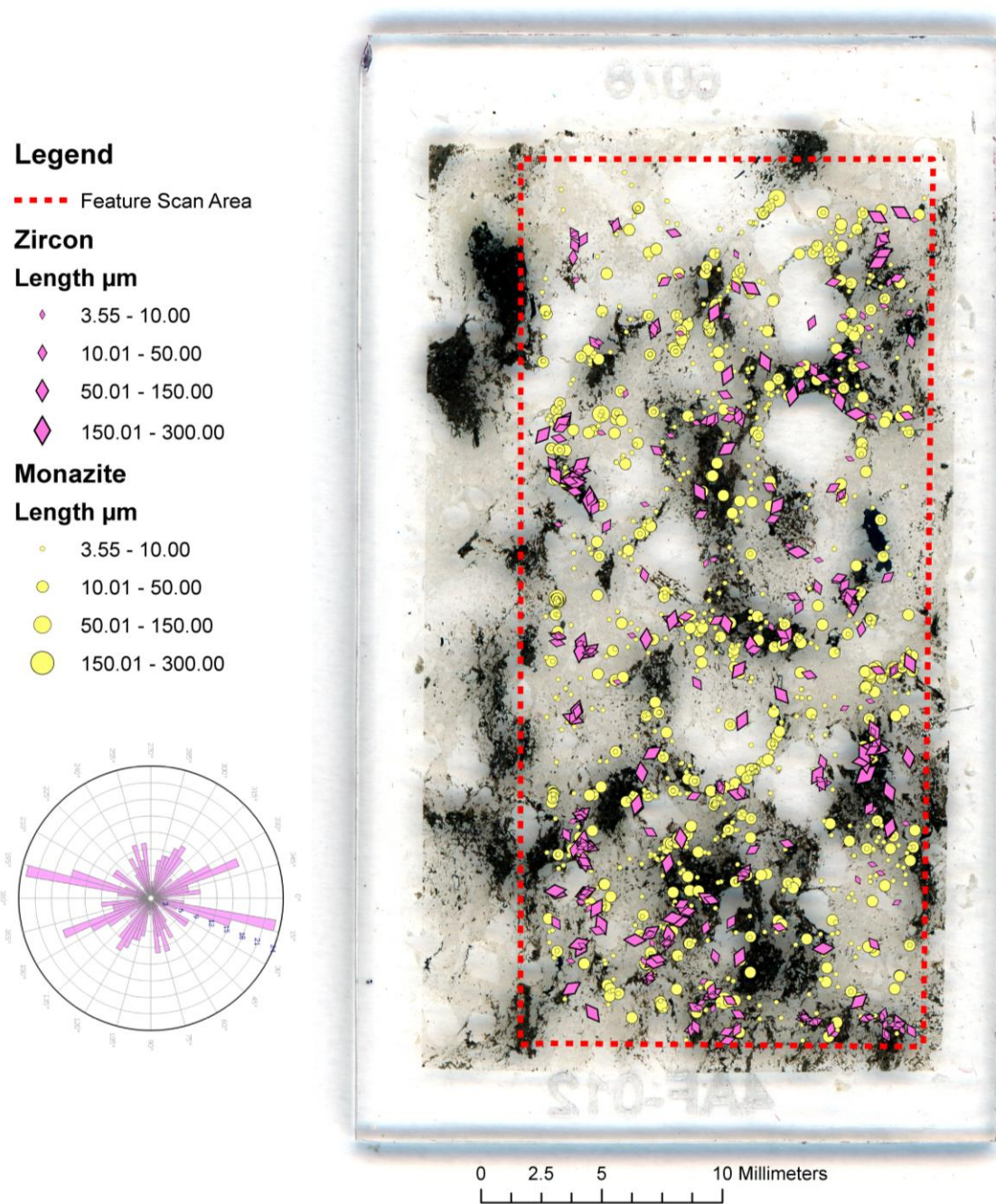


Figure 6-1 BSE-EDS feature map of polished thin section sample 6078. The sample is cut perpendicular to foliation. Zircon and monazite locations are depicted by graduated symbols based on length. Zircon symbols also represent grain orientation. A symmetrical rose diagram depicting orientation of zircons with an aspect ratio of 1.3 and greater is provided. Note the feature scan area is not the full width of the polished thin section.

6.2 Sample 6225 (QABS) Description

Sample 6225 is a diamond drill sample from the chloritized contact between basement and iron ore at Deposit No. 1. The sample was collected from drill hole MR1-12-226 at the 134.11 m to 134.26 m interval. Sample 6225 is classified as a QABS based on modal mineral abundances of biotite (65%) defining a prominent undulating foliation wrapping around quartz augens. Well oriented 0.25-1 mm biotite lathes and tablets form foliation. The 1-2.5 millimeter quartz augens show biotite overprints at margins. Poikiloblastic cordierite and staurolite porphyroblasts are up to 5 millimetre in size and contain inclusions of aligned ilmenite and biotite, accounting each for 5% of the total abundance. Cordierite poikiloblasts are pinitized and overgrown by biotite. Staurolites overgrow biotite and are subidoblastic. Garnet porphyroblasts are idioblastic 1.25-2.5 mm crystals overgrowing foliated and chloritized biotite. Late chlorite alters biotite lathes and tablets but is minor overall at 2% total abundance. Trace ilmenite occurs as 0.01-0.025 mm blebs. Apatite are 0.01-0.5 mm oblong shape grains located within quartz-augens and biotite and account for 1% of the bulk mineral assemblage.

Large 70-80 μm zircons are brecciated or mildly fractured and identified in all porphyroblasts and matrix minerals. Monazites are smaller averaging 25 μm and are observed petrographically in biotite, cordierite and garnet. Sample 6225 represents the last stage of paragenesis as garnet overprints retrograding chloritized biotite.

6.2.1 6225 BSE-EDS Feature Phase Mapping

The FEG-SEM combined EDS mapping technique obtained microGIS locations and crystallographic data of zircon and monazite (Figure 6-2). A total of 1,736 zircon grains were identified with areas ranging from 8.81 μm^2 to 28,510 μm^2 , averaging 317.30 μm^2 . Spatial association of zircons is scattered, however; a linear chain defined by finer zircon grains initiates at the top margin of the sample and trends downward (Figure 6-2). A total of 769 monazites were identified averaging 178.1 μm^2 and ranging from 8.81 μm^2 to 5,952 μm^2 . Monazite is identified in biotite, cordierite, staurolite, quartz and garnet.

Sample 6225 Feature Map

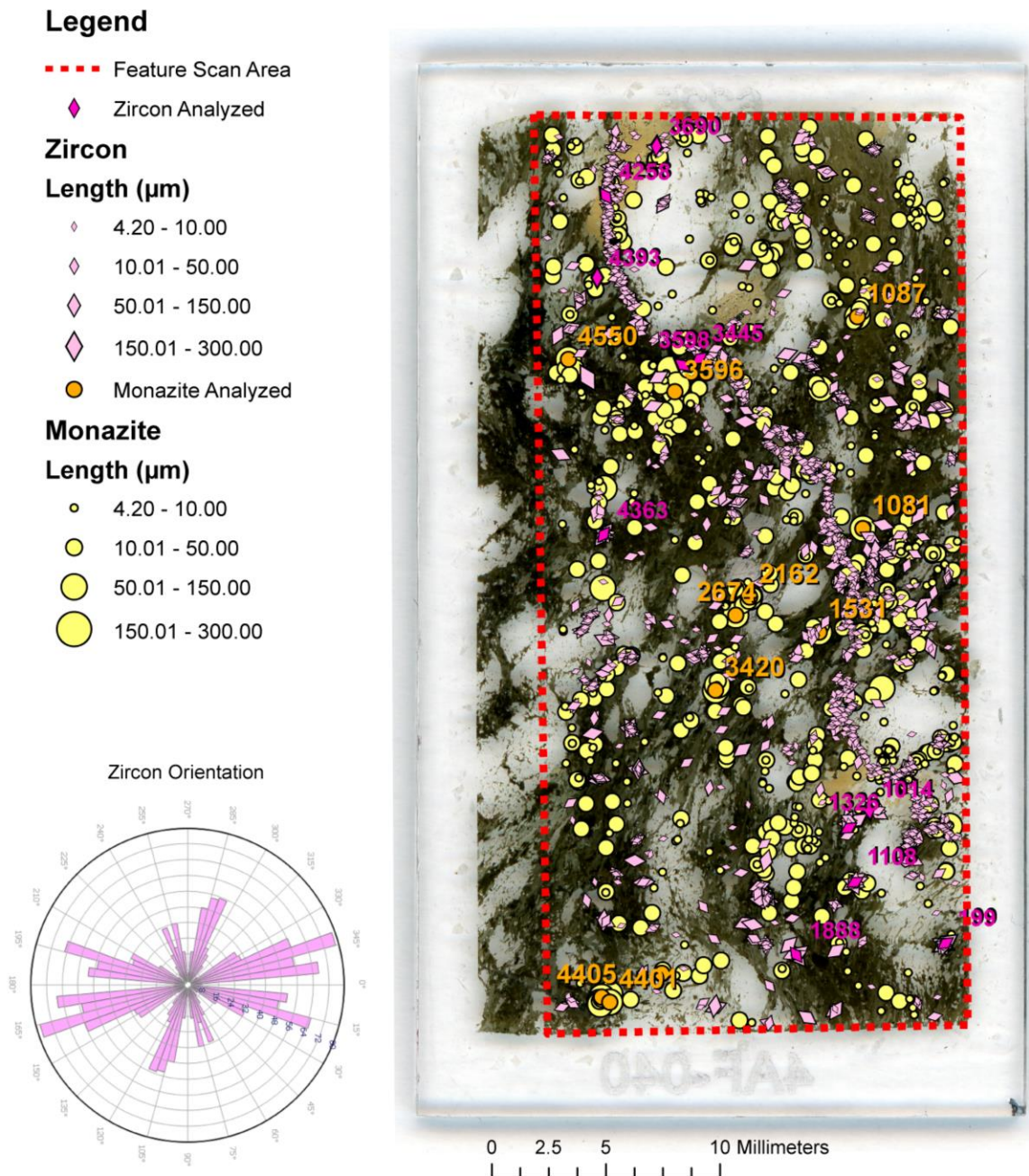


Figure 6-2 BSE-EDS feature map of polished thin section sample 6225. The sample is cut perpendicular to foliation. Zircon and monazite locations are depicted by graduated symbols based on length. Zircon symbols also represent grain orientation. A symmetrical rose diagram depicting orientation of zircons with an aspect ratio of 1.3 and greater is provided. Note the feature scan area is not the full width of the polished thin section.

6.2.2 6225 BSE, SE and CL Images of Datable Phases

BSE, SE and CL imaging of datable phases was performed on select zircon and monazite grains based on size, morphology and spatial relationship to other minerals. All zircon morphologies are plotted in Plate 6-3. Zircon crystals exhibit concentric oscillatory zoning. Few zircons contain metamict domains in cores disrupting regular zoning, indicated by BSE imaging. Zircons also show fracturing and brecciation with infilling quartz. CL imaging and spot EDS analyses reveals quartz and apatite inclusions within zircons as well. Anhedral xenotime and monazite growths are present at the margins of zircons.

All monazite morphologies are illustrated in Plate 6-4. SE and BSE imaging of monazites demonstrate uniform blocky and oblong shapes that commonly contain inclusions of biotite. Faint 3-6 μm thick zones and envelopes were distinguished in monazite grains 2674, 4405 and 4550. Fracturing and brecciation is not manifested by monazite grains. Monazites grains tend to cluster, showing separate grain boundaries (monazites 1087, 2162, 2674 and 3781).

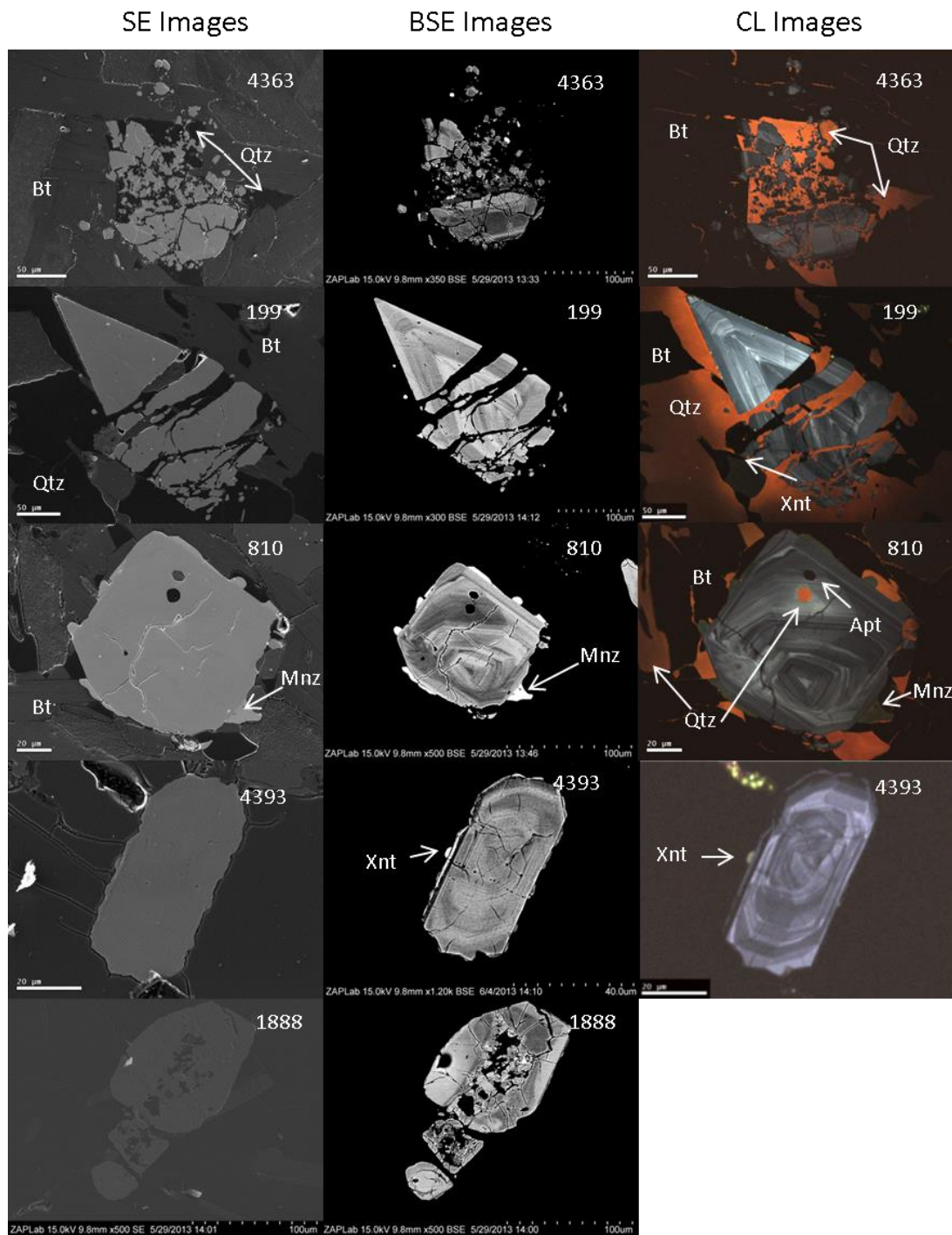


Plate 6-3 Collage of all representative zircon crystal morphologies from sample 6225. Micrographs are organized by columns into backscatter electron (BSE), secondary electron (SE) and cathodoluminescence (CL) imaging sources and labeled with their corresponding grain number. Zircon 4363 is an example of the brecciated type with quartz infills. Grain 199 exhibits deformational fracturing. Zircons 199, 810 and 4393 are concentric growth zircons with xenotime (Xnt) and monazite (Mnz) margins. Apatite (Apt) and quartz (Qtz) are also present in grain 810. Rotted and pitted zircon is illustrated by 1888. Inclusions of quartz and apatite are also depicted within monazite overgrowths.

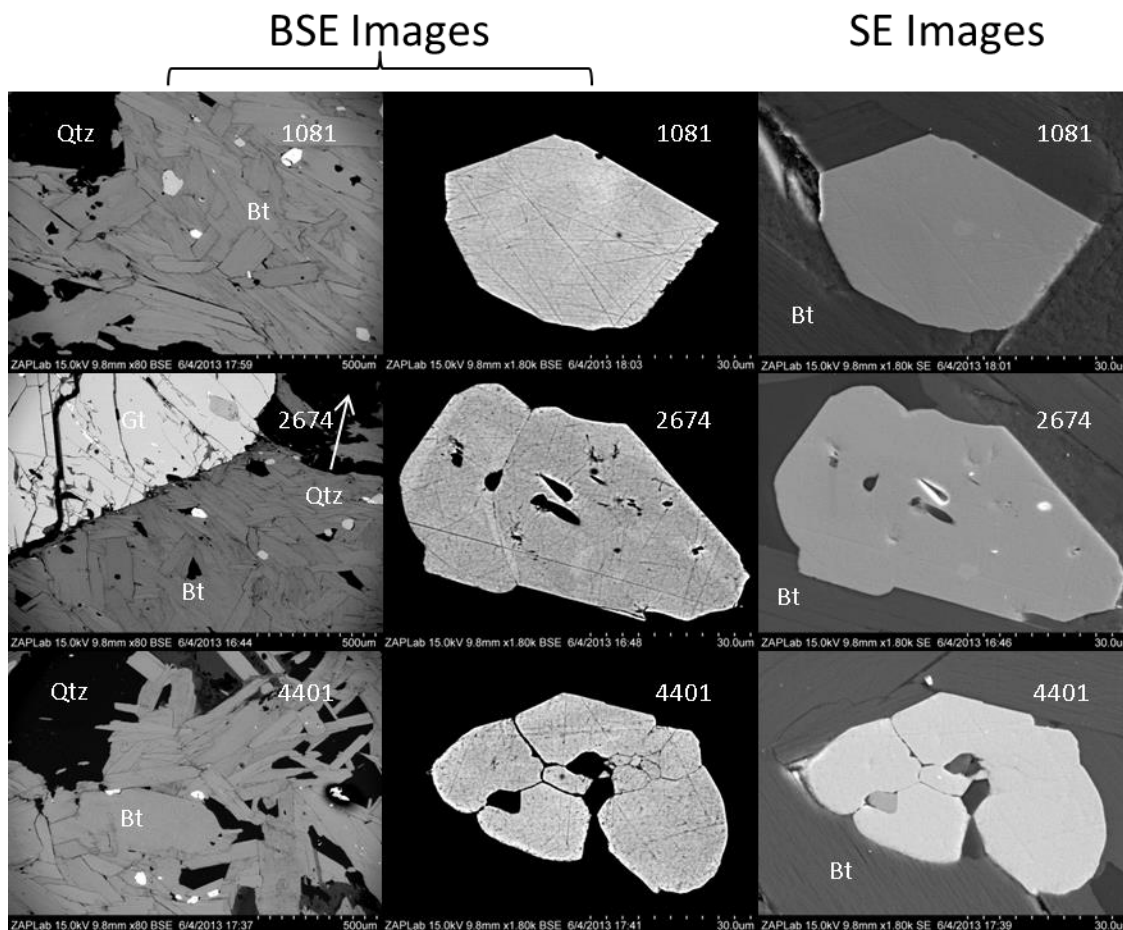


Plate 6-4 A collection of representative monazite morphologies from sample 6225. Micrographs are organized by columns into backscatter electron (BSE) and secondary electron (SE) sources labeled with their corresponding grain number. Images depict single (1081), overgrowth (2674) and cluster (4401) morphologies. Mild zoning is present in monazites 1081 and 2674. Surrounding mineralogy of biotite (Bt), quartz (Qtz) and garnet (Gt) is also annotated.

6.2.3 6225 Zircon U-Pb Isotopic Data and Th/U Ratios

Sample 6225 yielded a range of concordant and discordant $^{207}\text{Pb}/^{206}\text{Pb}$ values ranging from 2910 ± 11 Ma to 2517 ± 17 Ma. All zircon analyses from sample 6225 are plotted on a concordia plot in Figure 6-3. The target zircon grain for analysis 199-S4, was lost during carbon coat removal prior to laser ablation. Analysis 199-S4 is not used further. Analysis 1014-S1 is omitted from further interpretation due to formidable U-Pb fractionation during ablation. Analysis 4393-S1 is also omitted because laser ablation pitting crossed into a metamorphic zone (Figure 6-6). Two zircon age groups are identified. Analyses from central zones form a cluster of $^{207}\text{Pb}/^{206}\text{Pb}$ values centered at

2896.2 ± 8.2 Ma with an MSWD of 1.04 (Figure 6-4). Marginal zircon zones are discordant and plotted in Figure 6-5. Discordant marginal zones of zircon regress to a concordant age of 2943 ± 27 Ma with a lower intercept of 1656 ± 100 Ma. The MSWD of the discordant trend is 1.9. Thorium-Uranium (Th/U) ratios are plotted in Figure 6-6. Core Th/U ratios range from 0.35 to 0.52 and average 0.44 over seven analyses. Marginal and rim zones are generally lower but range between 0.05 and 0.68 averaging 0.33 over eleven analyses.

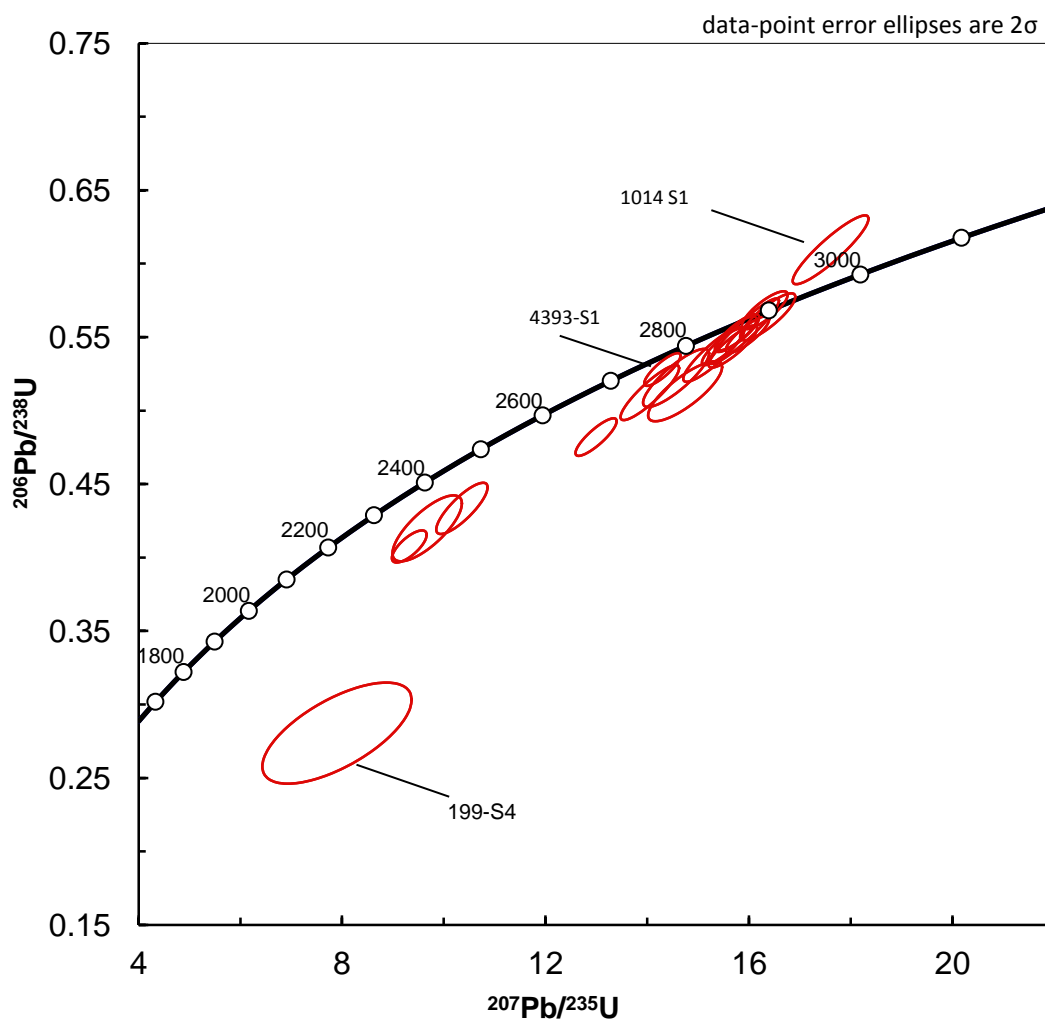


Figure 6-3 Concordia plot of zircon $^{207}\text{Pb}/^{206}\text{Pb}$ values from sample 6225 via LA-ICP-MS. Stricken analyses are labeled.

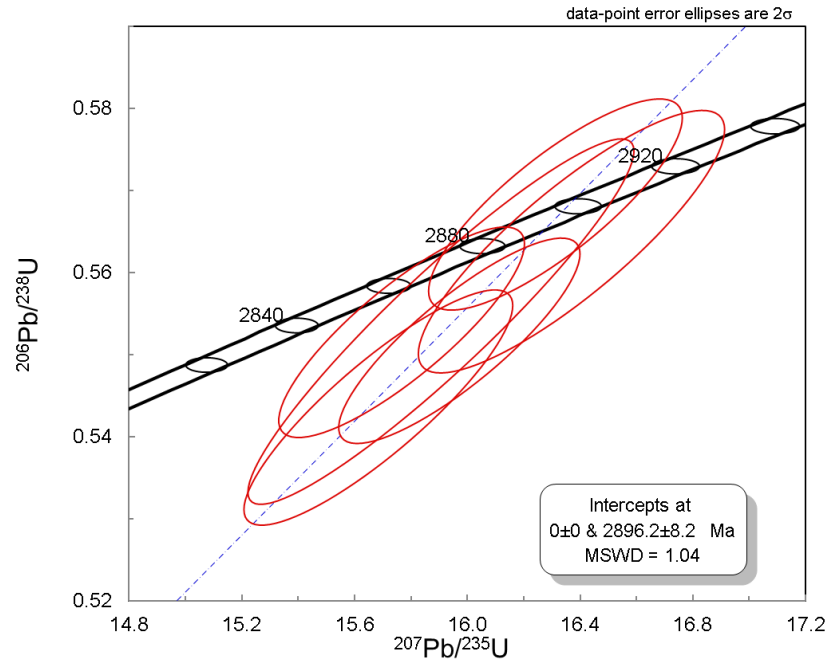


Figure 6-4 Concordia plot of zircon $^{207}\text{Pb}/^{206}\text{Pb}$ values from central zircon zones in sample 6225 via LA-ICP-MS analysis.

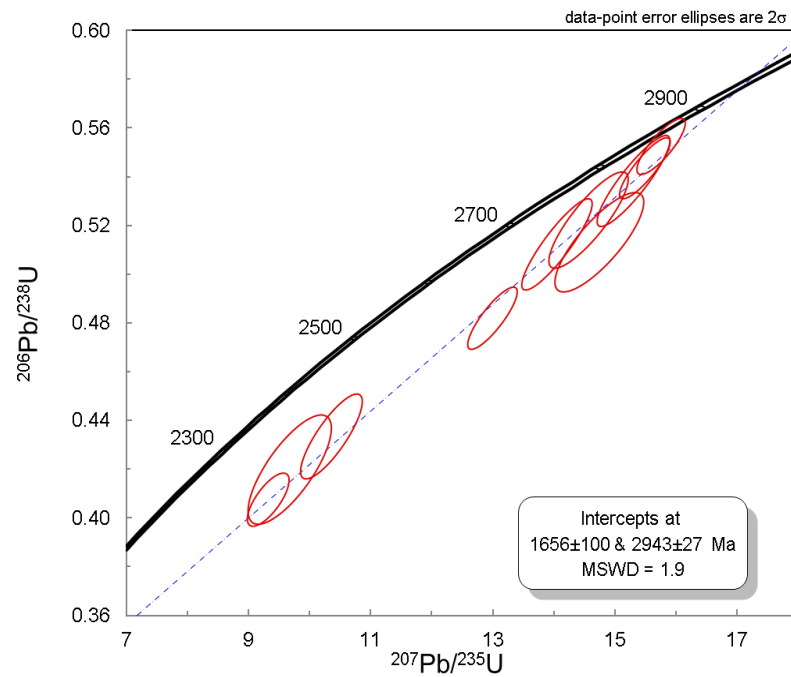


Figure 6-5 Concordia plot of zircon $^{207}\text{Pb}/^{206}\text{Pb}$ values from marginal zircon zones in sample 6225 via LA-ICP-MS.

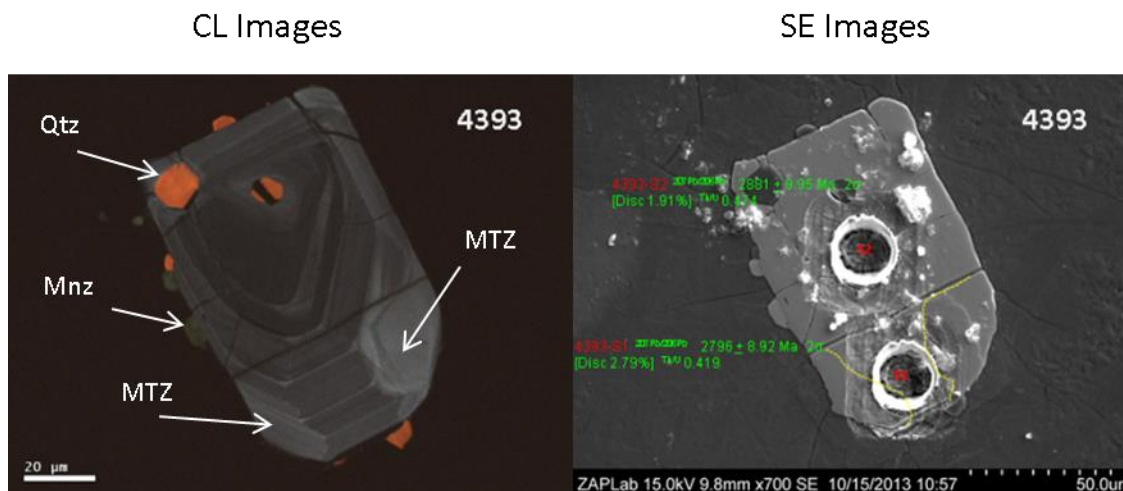


Figure 6-6 Cathodoluminescence and secondary electron images of zircon 4393 from sample 6225. Metamorphic zoning (MTZ), quartz (Qtz) and monazite (Mnz) labeled in CL image. Ablation pits are annotated with $^{207}\text{Pb}/^{206}\text{Pb}$ data while metamorphic zones are outlined by a dashed yellow line.

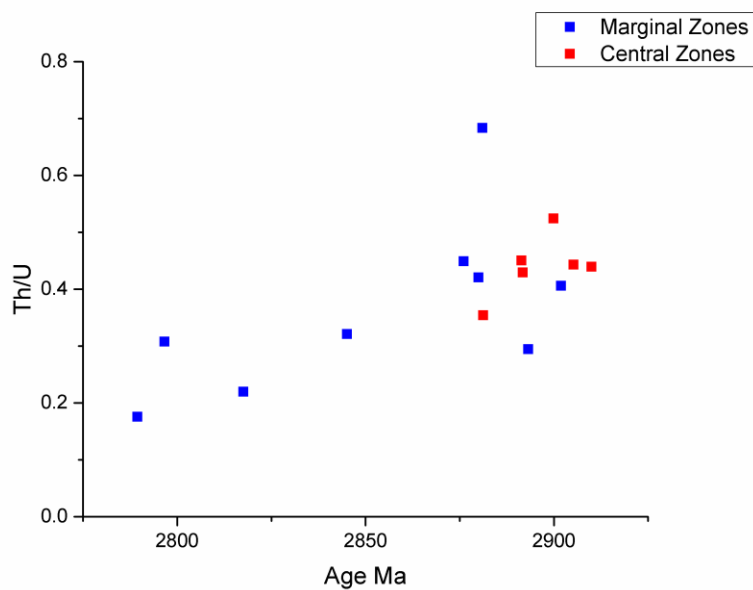


Figure 6-7 Sample 6225 zircon Th/U plot of with respect to age. Central zones are red and clustered while discordant marginal zones are dispersed.

6.2.4 6225 Monazite U-Pb Isotopic Data and Th/U Ratios

Isotopic U-Pb analysis of monazites from sample 6225 produced concordant and negatively discordant $^{207}\text{Pb}/^{206}\text{Pb}$ values ranging from 1855 ± 20 Ma to 1800 ± 12 Ma corresponding to 19 analyses of 12 monazite grains (Figure 6-8). Analyses 3596-S2 and 2162-S2 are excluded because of targeting error during ablation. U-Pb analyses of all monazites from sample 6225 are plotted in Figure 6-8. $^{207}\text{Pb}/^{206}\text{Pb}$ ages are uniform within error; however, a strong negative discordance is visible resulting from analytical sampling error during laser ablation due to fractionating U-Pb ratios. Analyses less than 5% discordance are plotted in Figure 6-9 and show a spread of $^{207}\text{Pb}/^{206}\text{Pb}$ values ranging from 1801 ± 12 Ma to 1854 ± 14 Ma. The excluded negative discordant analyses are not isotopically different reporting $^{207}\text{Pb}/^{206}\text{Pb}$ ages between 1810 ± 11 Ma to 1852 ± 19 Ma and are listed in Appendix 5. Their incorporation into projecting a concordant age may artificially affect the slope, hence not included. The mean $^{207}\text{Pb}/^{206}\text{Pb}$ value for concordant monazite projects to 1819 ± 10 Ma. Th/U ratios of clustered monazite ages are scattered and range from 0.08 to 0.39 (Figure 6-10).

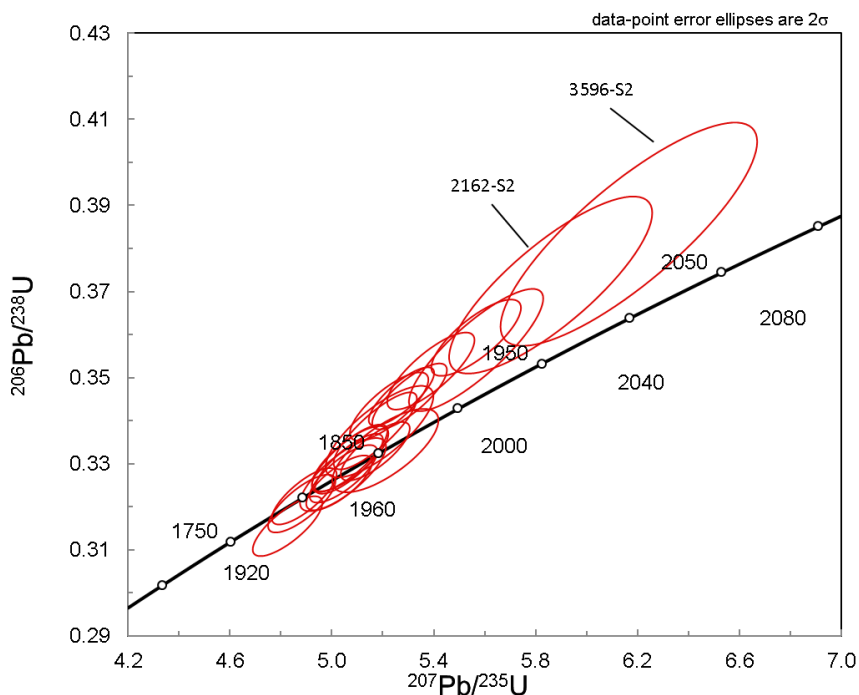


Figure 6-8 Concordia plot of all $^{207}\text{Pb}/^{206}\text{Pb}$ monazite values from sample 6225 via LA-ICP-MS analyses. Analyses with targeting errors are labeled.

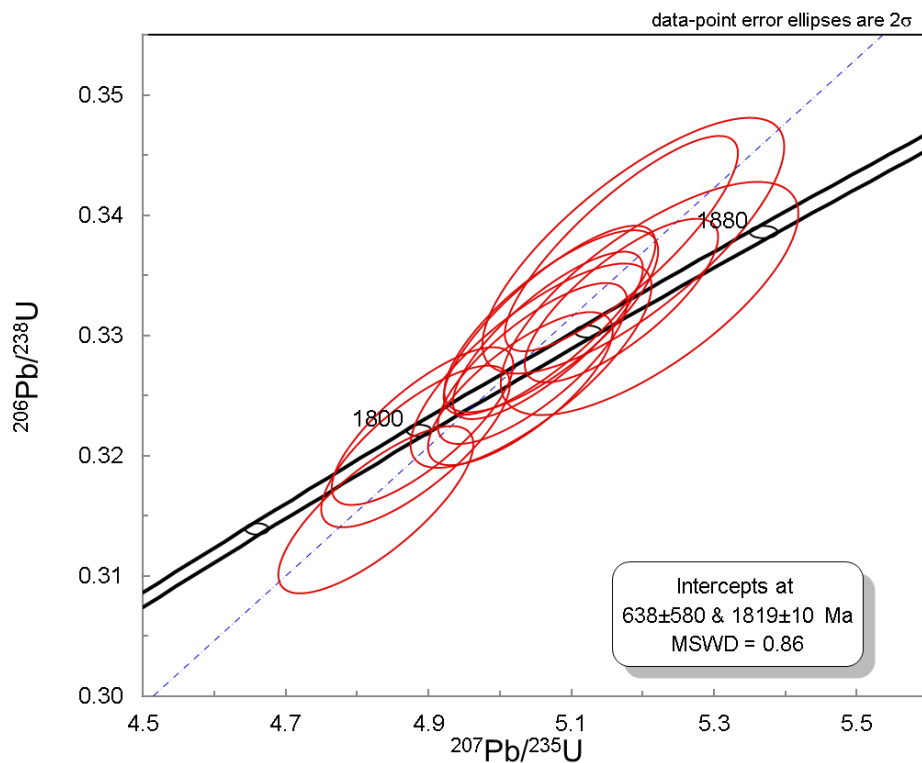


Figure 6-9 Concordia plot of $^{207}\text{Pb}/^{206}\text{Pb}$ monazite values from sample 6225 via LA-ICP-MS analysis. Analyses plotted are less than <5 discordant.

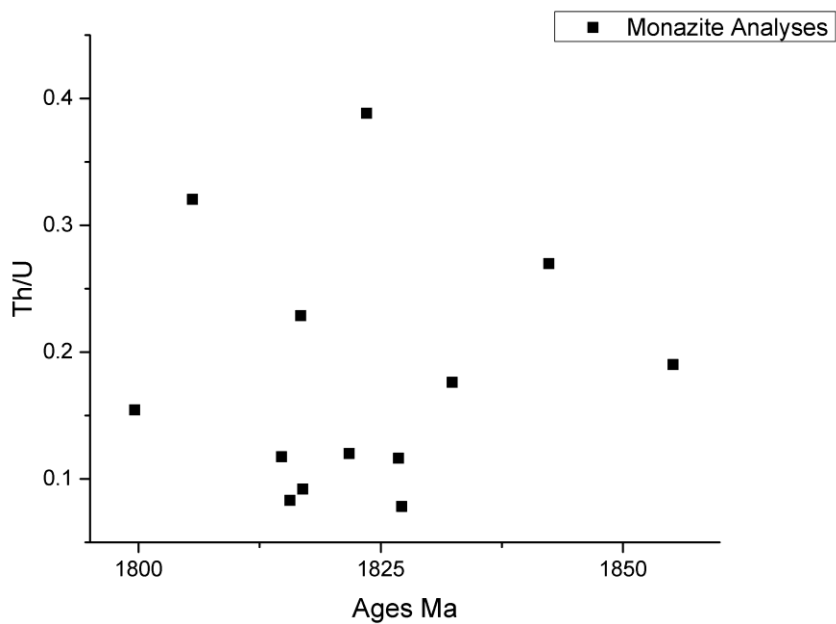


Figure 6-10 Sample 6225 monazite Th/U plot with respect to $^{207}\text{Pb}/^{206}\text{Pb}$ age.

6.3 Sample 6220A (Ore Zone CS) Description

Sample 6220A is a drill core sample of garnetiferous chlorite schist from the high grade iron ore body at Deposit No.1. The sample was collected at the 75.5-75.7 m interval of drill hole MR1-12-226. The unit contains ripidolite (70%), almandine (20%), martite (4%), jasper-hematite (2%), apatite (2%) and ilmenite (1.25%). Monazite and zircon are approximately 0.5% and 0.25% of the total mineral abundance respectively. Chlorite is a pseudomorphic replacement of biotite as chlorite tablets and lathes show well defined basal cleavage and relict biotite margins. Relict S_1/S_2 crenulation is overprinted by chloritized biotite at the tapered end of the sample. Mn-zoned almandine poikiloblasts (2-11 mm) overgrow foliated chlorite and contain inclusions of martite, ilmenite, monazite and zircon. Martite clasts are 250-1600 μm in size in chlorite and almandine. Monazites exhibit a yellow pleochroic envelope and form disseminations or patches within garnet porphyroblasts and chlorite. Zircons are small 20-50 μm grains scattered throughout the chlorite matrix.

6.3.1 Sample 6220A BSE-EDS Feature Mapping

Feature mapping obtained microGIS locations of mineral zircon and monazite grains in sample 6220A. A total of 745 zircon grains were identified with areas ranging from 19.80 μm^2 to 3,550 μm^2 averaging 108.50 μm^2 . Zircons are scattered and identified in almandine and chlorite (Figure 6-10). Monazite features totaled 1,113 averaging 150.56 μm^2 , ranging from 19.80 μm^2 to 2,134 μm^2 . Feature mapping of monazite matched petrographic observations of disseminated, patchy and clustering monazite crystals (Figure 6-11). Monazite patches and clusters are observed and mapped in the chlorite matrix and in almandine porphyroblasts.

Sample 6220A Feature Map

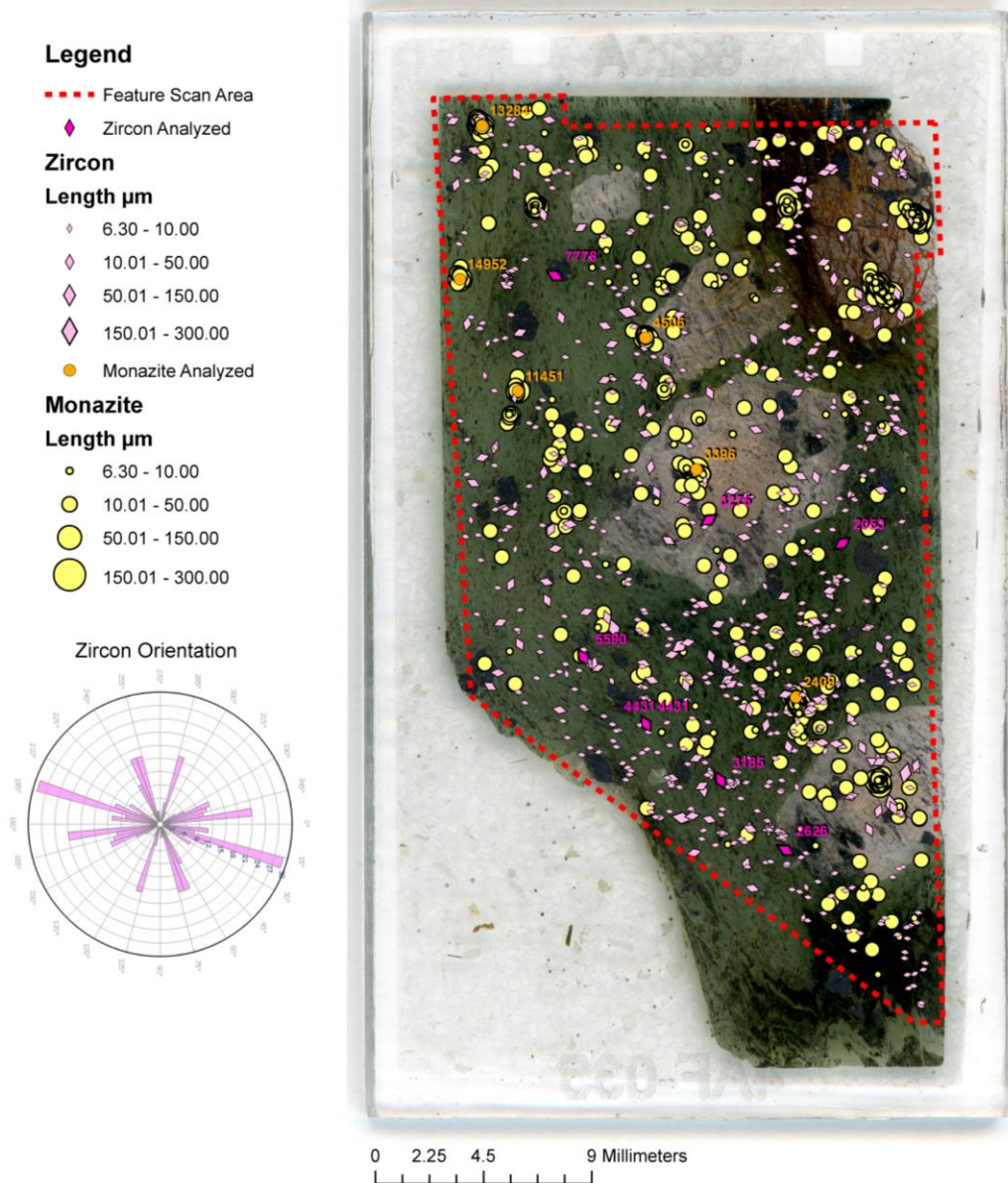


Figure 6-11 BSE-EDS feature map of polished thin section sample 6220A. The sample is cut perpendicular to foliation. Zircon and monazite locations are depicted by graduated symbols based on length. Zircon symbols also represent grain orientation. A symmetrical rose diagram depicting orientation of zircons with an aspect ratio of 1.3 and greater is provided. Note the feature scan area is not the full length of the polished thin section.

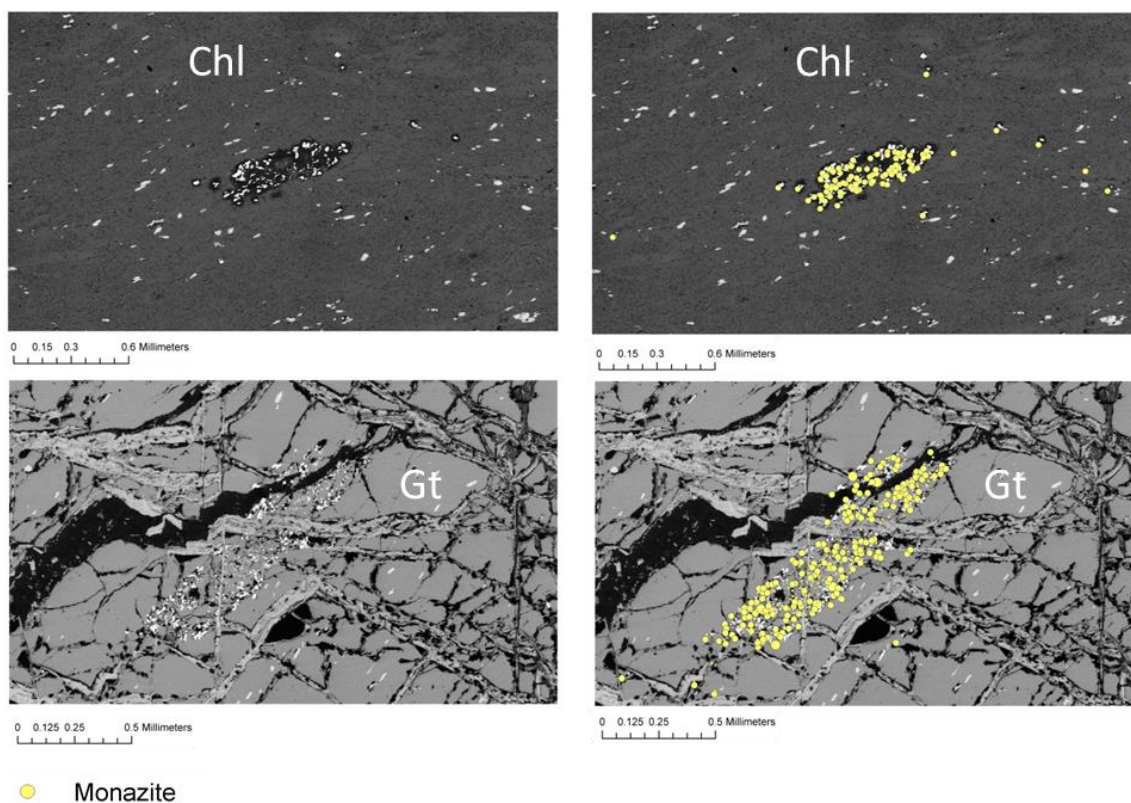


Figure 6-12 Back scatter electron images of patchy monazite compared to BSE-EDS feature scans. Captured monazite grains are represented by yellow dots demonstrating accuracy of feature mapping.

6.3.2 6220A BSE, SE and CL Images of Datable Phases

BSE and CL imaging of zircon crystals reveals concentric zoning with few grains exhibiting metamict cores. Zircon grains also show fracturing initiating from margins inward. CL imaging and spot EDS analyses did not detect inclusions within zircons. Plate 6-5 contains SE, BSE and CL images of all representative zircon morphologies in sample 6220A. SE and BSE imaging of monazites showed uniform anhedral irregular or oblong shapes occurring as individual crystals, clusters and patches. Monazite patches are 0.05-1.1 mm size ovoid shapes with numerous anhedral crystals and enveloped by darker pleochroic material. All monazite morphologies are illustrated in Plate 6-6. Small distinct 5-10 micron size zones and envelopes were distinguished in monazite features 13284 and 14952. Fracturing is not witnessed in monazite features.

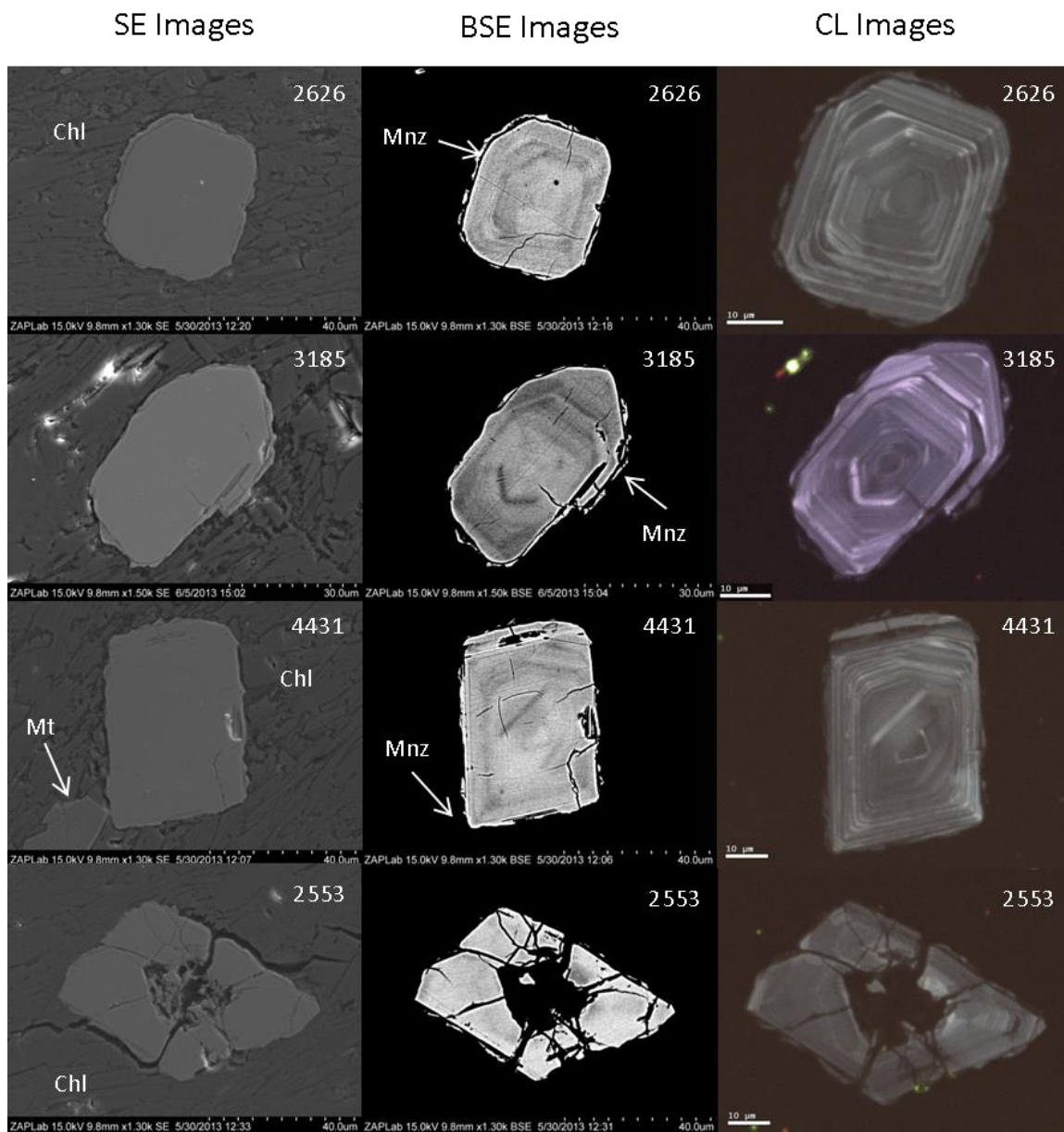


Plate 6-5 Collage of all representative zircon crystal morphologies in sample 6220A. Photomicrographs are organized by column into backscatter electron (BSE), secondary electron (SE) and cathodoluminescence (CL) imaging sources and labeled with their corresponding grain number. Zircons 2626, 3185 and 4431 are examples of the euhedral oscillatory morphology in chlorite (Chl). Zircons 2626, 3185 and 4431 also show overgrowths of monazite (Mnz) at margins and minor cracking. Rotted and pitted zircon is illustrated by 2553.

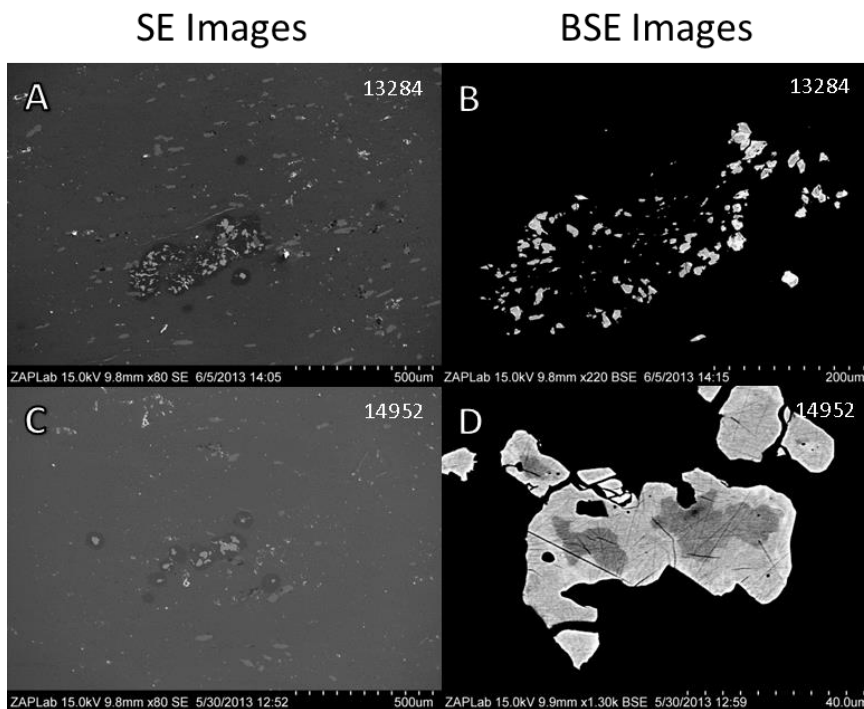


Plate 6-6 Plate of representative monazite morphologies in sample 6220A. Photomicrographs are organized in column by secondary (SE) and backscatter (BSE) electron imaging sources. The patchy texture is demonstrated by micrographs A and B (monazite 13284). Small clusters and disseminated monazite showing internal zoning are exhibited in micrographs C and D (monazite 14952).

6.3.3 6220A Zircon U-Pb Isotopic Data and Th/U Ratios

Sample 6220A yielded zircon $^{207}\text{Pb}/^{206}\text{Pb}$ values ranging from 2769 ± 19 Ma to 2735 ± 20 Ma from eight analyses of seven grains. All zircon analyses are plotted on a concordia plot in Figure 6-14. Analysis 3185-S1 is discounted because a second order magnitude error occurred during ablation, making the $^{207}\text{Pb}/^{206}\text{Pb}$ ratio impractical to decipher (Figure 6-13). Culled zircon analyses from sample 6220 (excluding 3581-S1) are plotted on a concordia plot in Figure 6-15. The culled zircon population shows a $^{207}\text{Pb}/^{206}\text{Pb}$ value of 2748 ± 11 Ma with an MSWD of 1.10, and a lower intercept of 66 ± 40 Ma. Concordant zircon $^{207}\text{Pb}/^{206}\text{Pb}$ values cluster between 2763 ± 12 to 2735 ± 11.5 Ma (Figure 6-16). The average cluster value is calculated to be 2746 ± 11 Ma anchored at zero with an MSWD of 0.79. The MSWD is anchored at zero because the initial lower intercept was -300 ± 1400 Ma. Thorium-uranium (Th/U) ratios are plotted in Figure 6-17. Th/U ratios range from 0.12 to 0.33 and average 0.26 corresponding to eight analyses.

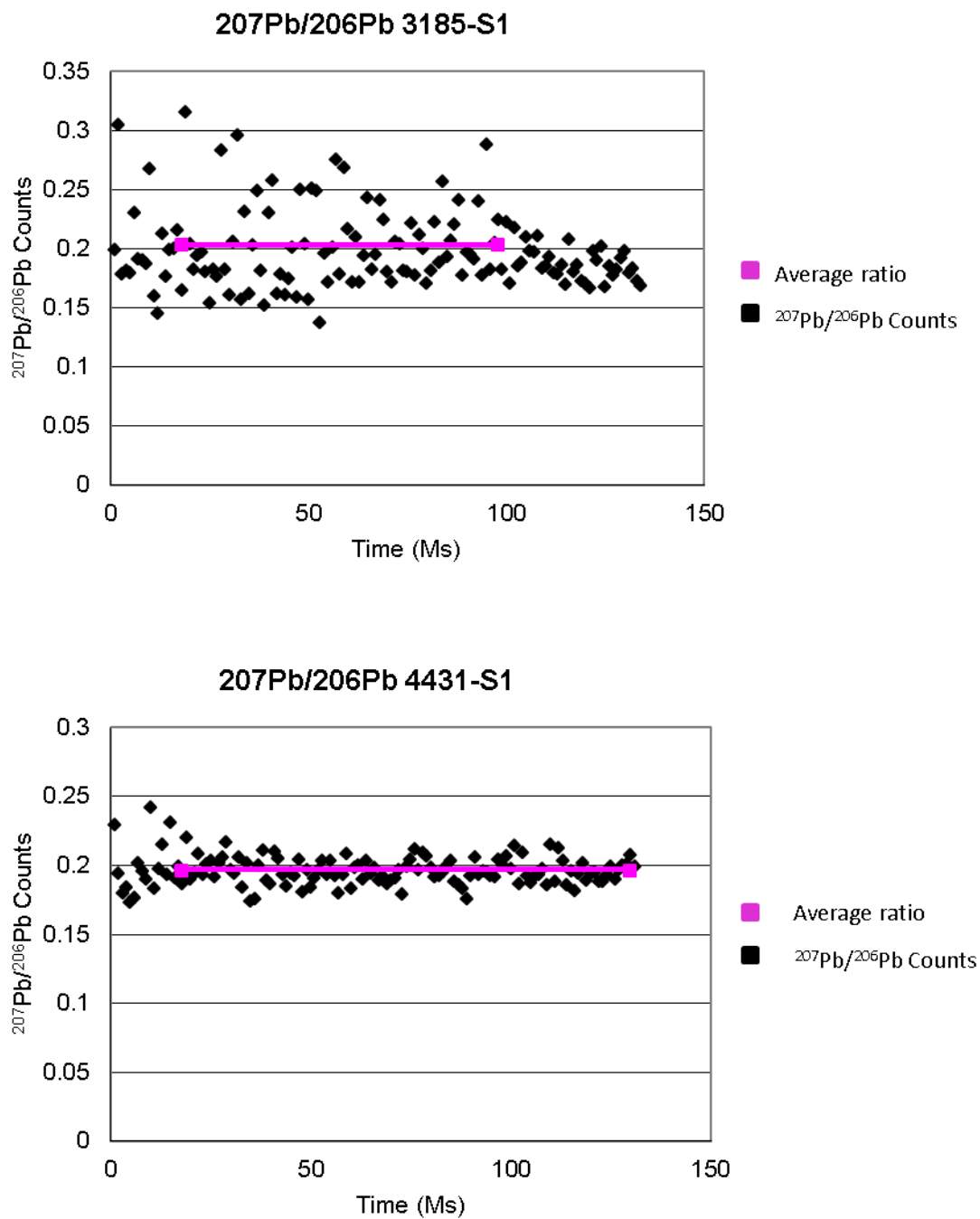


Figure 6-13 Graphs of $^{207}\text{Pb}/^{206}\text{Pb}$ counts over time are presented for LA-ICP-MS pitting from analyses 3185-S1 and 4431-S1. Analysis 3185-S1 is scattered and highly variable compared to 4431-S1 and discounted.

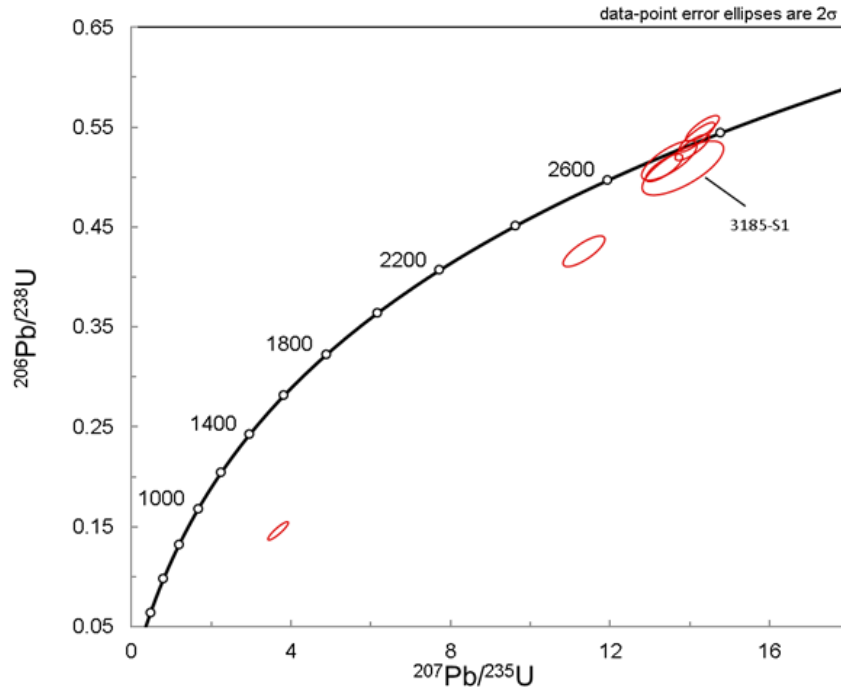


Figure 6-14 Concordia plot of all $^{207}\text{Pb}/^{206}\text{Pb}$ zircon values from sample 6220A via LA-ICPMS. Analysis 3185-S1 is labeled.

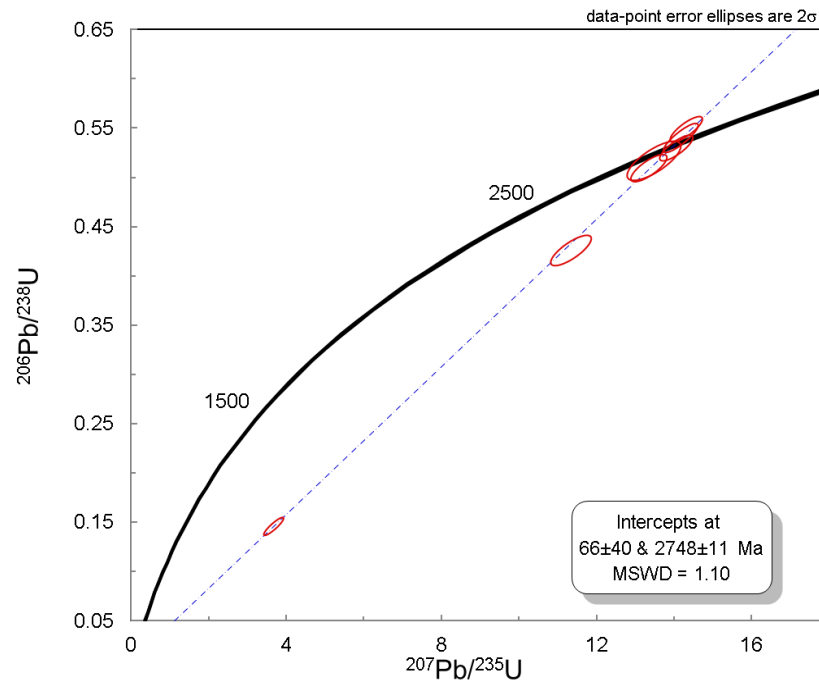


Figure 6-15 Concordia plot of culled zircon values anchored at zero and regressed to a concordant age of 2748 ± 11 Ma.

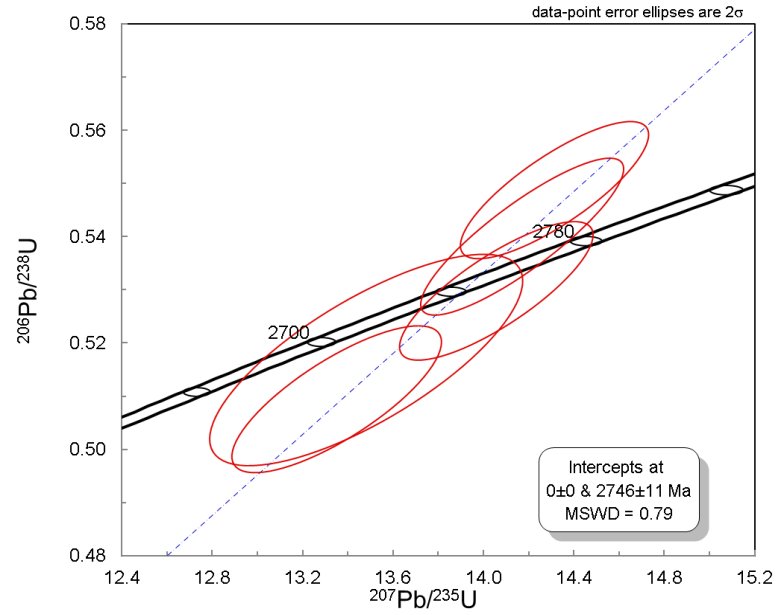


Figure 6-16 Concordia plot of concordant cluster $^{207}\text{Pb}/^{206}\text{Pb}$ zircon values from sample 6220A.

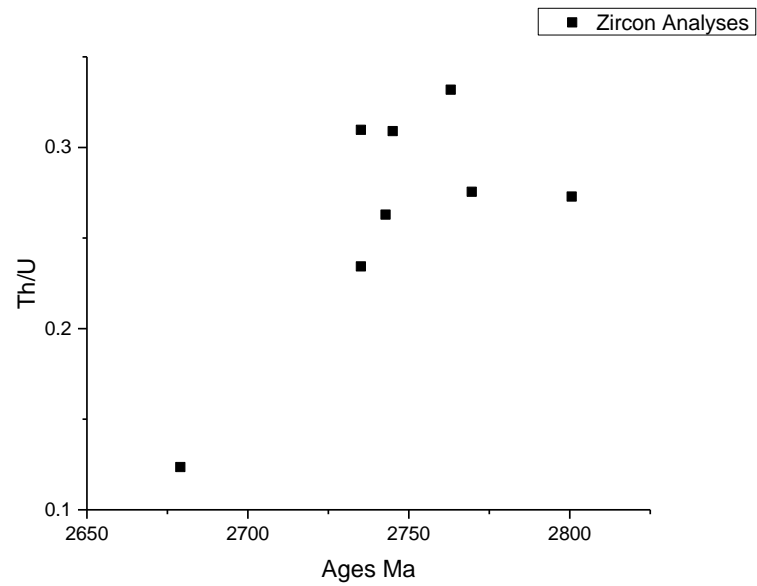


Figure 6-17 Th/U values of sample 6220A zircon with respect to $^{207}\text{Pb}/^{206}\text{Pb}$ age.

6.3.4 6220A Monazite U-Pb Isotopic Data and Th/U Ratios

A total of 18 U-Pb isotopic analyses were completed on 6 monazite crystals; targeting errors during ablation exclude seven. Excluded values are listed in Appendix 5. All 18 U-Pb analyses are plotted in Figure 6-18 while the culled set (11 analyses) is plotted in Figure 6-19. $^{207}\text{Pb}/^{206}\text{Pb}$ values appear continuous within error. Analyses range from -5.5 % to 10.4% discordant. Monazites from sample 6220A produced $^{207}\text{Pb}/^{206}\text{Pb}$ values ranging from 1873 ± 20 Ma to 1810 ± 22 Ma resulting from 11 analyses of 6 monazite crystals. An MSWD of 0.75 anchored at zero projects through the center of the age spread at 1831 ± 13 Ma (Figure 6-19). Th/U ratios were not measured during ablation.

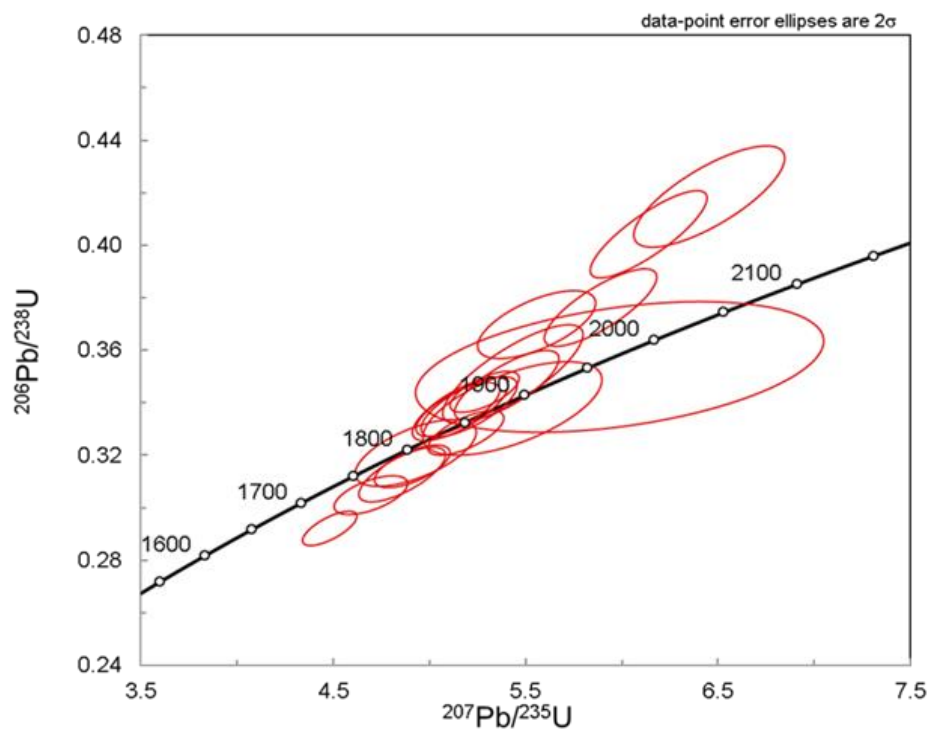


Figure 6-18 Sample 6220A monazite concordia plot of all $^{207}\text{Pb}/^{206}\text{Pb}$ analyses from LA-ICP-MS analysis.

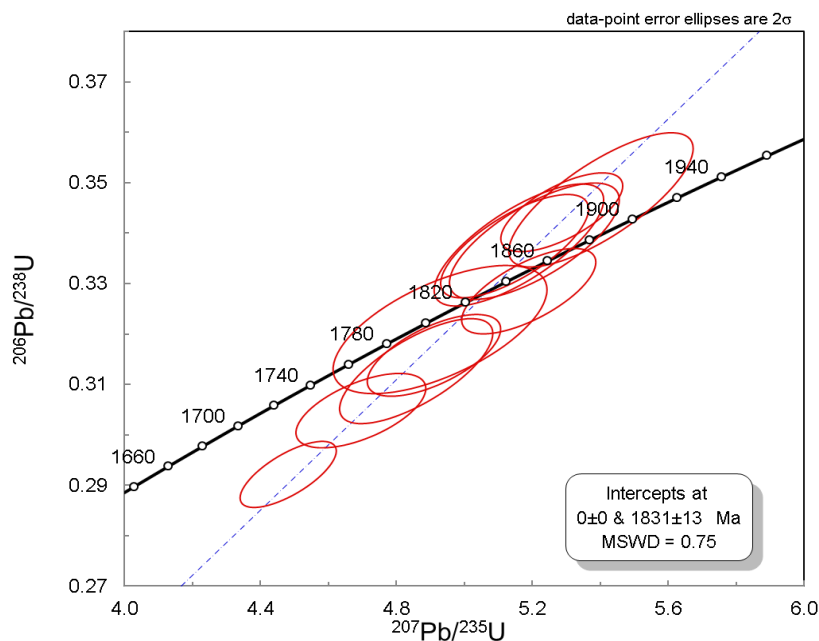


Figure 6-19 Concordia plot of culled $^{207}\text{Pb}/^{206}\text{Pb}$ monazite ages from sample 6220A.

6.4 Sample 716 Description

Sample 716 is brecciated and altered banded iron formation from the deposit No.1 ore zone. The sample was collected from drill hole MR1-08-177 at 37 m. The sample contains quartz (65%) and martite (35%). Primary banding texture is brecciated and disrupted by crosscutting recrystallized veinlets of martite. The silica bands are 0.5-2 millimetres wide. Martite grains are ~20 μm , forming an interlocking granoblastic polygonal texture. Microplaty hematite is visible in some martite grains, forming 5-20 μm wide crosshatch poor spaces.

6.4.1 716 BSE-EDS Feature Phase Mapping

Feature mapping of altered BIF sample 716 identified three U-Pb bearing minerals; zircon, monazite and xenotime. Zircons totaled 39, averaging 14.4 μm^2 and ranging between 8.81 μm^2 to 56.28 μm^2 . Monazites were more abundant, summing to 45 grains ranging between 8.81 μm^2 to 187.82 μm^2 , averaging 32.29 μm^2 . The most prevalent was xenotime totalling 96 grains. Xenotime crystals on were larger averaging 55.61 μm^2 and ranging between 8.81-276.65 μm^2 . All minerals are concentrated in the martite banding, fewer are identified in the recrystallized quartz zones.

Sample 716 Feature Map

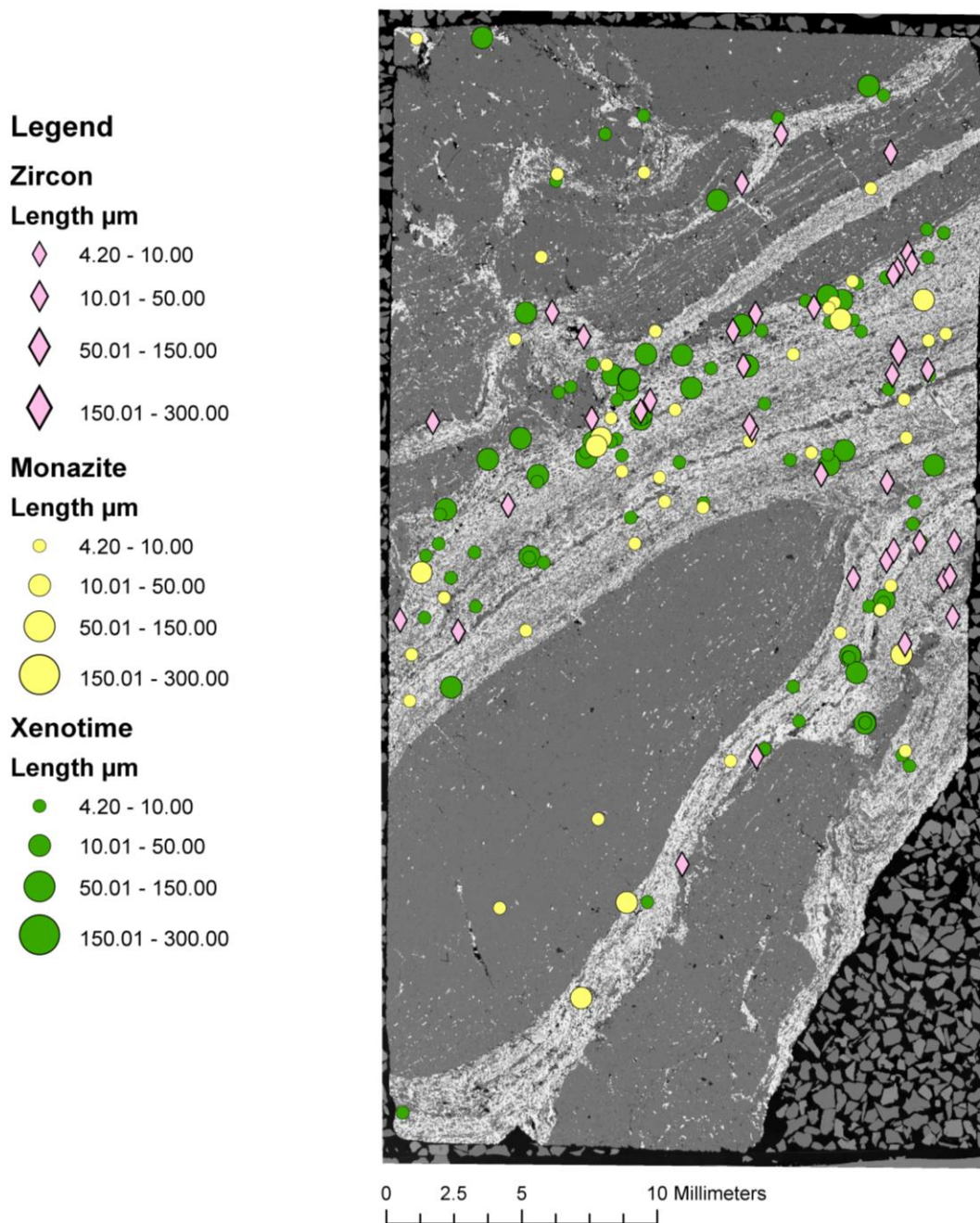


Figure 6-20 BSE-EDS feature map of polished thin section of altered BIF sample 716. Zircons, monazite and xenotime are depicted by graduated circles based on length plotted on BSE montage image of sample 716. The feature scan area is the full width and length of the polished thin section.

6.4.2 716 SEM Imaging and Element Mapping of Features

BSE and SE imaging show irregular and subhedral monazite, xenotime and zircon crystals. Monazite grains are oblong anhedral cryptocrystalline, generally less than 10 μm in length or less. Xenotime grains were ovoid in shape and exhibited minor fracturing. Zircons observed are small anhedral 5-10 μm crystals. The JEOL FEG-SEM with WDS spectrometers qualitatively mapped elements; Ca, Si, Th, U, Pb, P, Y, La, Ce, Nd & Yb, in selected monazite and xenotime phases. Only faint irregular thorium zoning is detected in monazites (Plate 6-8) while mild Th, U and Yb zoning is identified at xenotime margins (Plate 6-9).

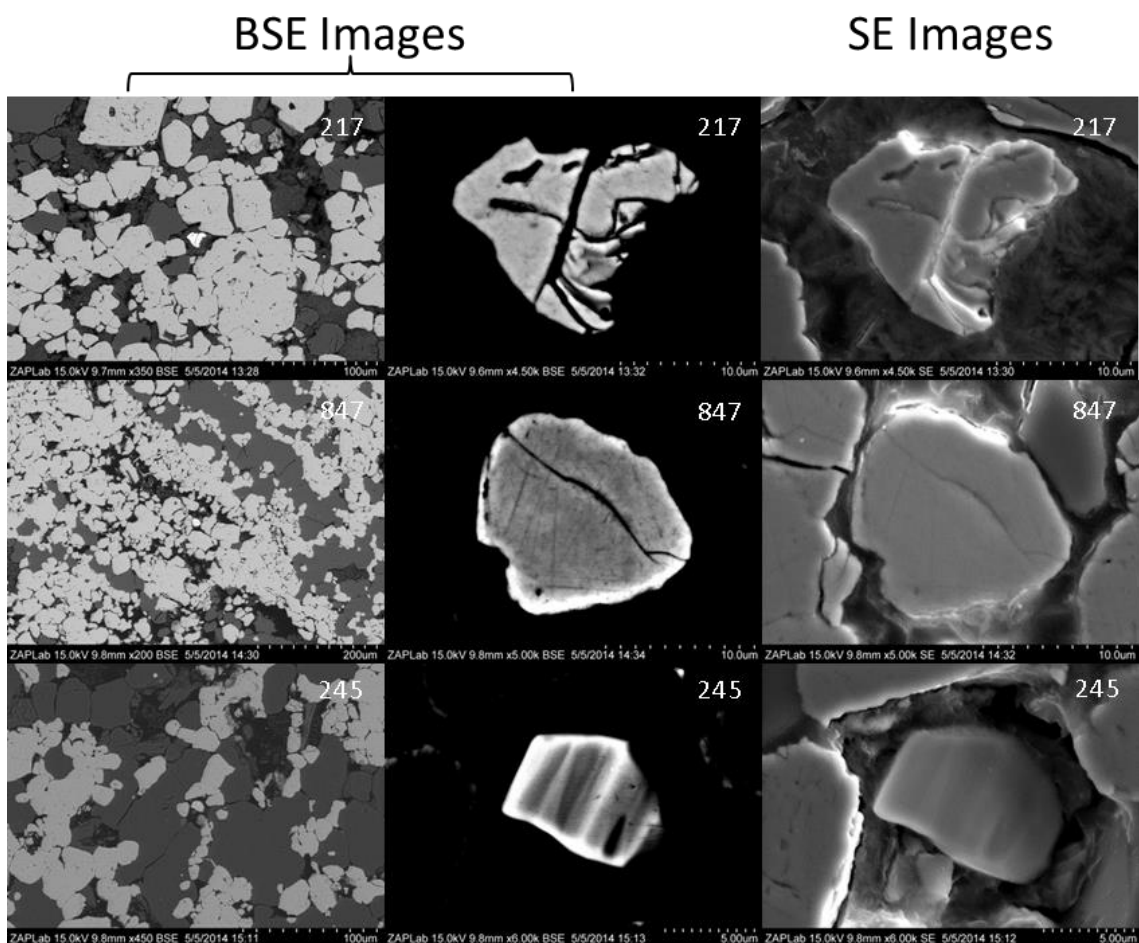


Plate 6-7 Collage of datable phase morphologies in sample 716. Micrographs are arranged in columns by backscatter (BSE) and secondary electron (SE) imaging sources with grain numbers. Grain 217 is irregular shaped monazite in martite-quartz banding. Mildly fracture xenotime is shown by grain 847 while 245 is typical anhedral zircon grain.

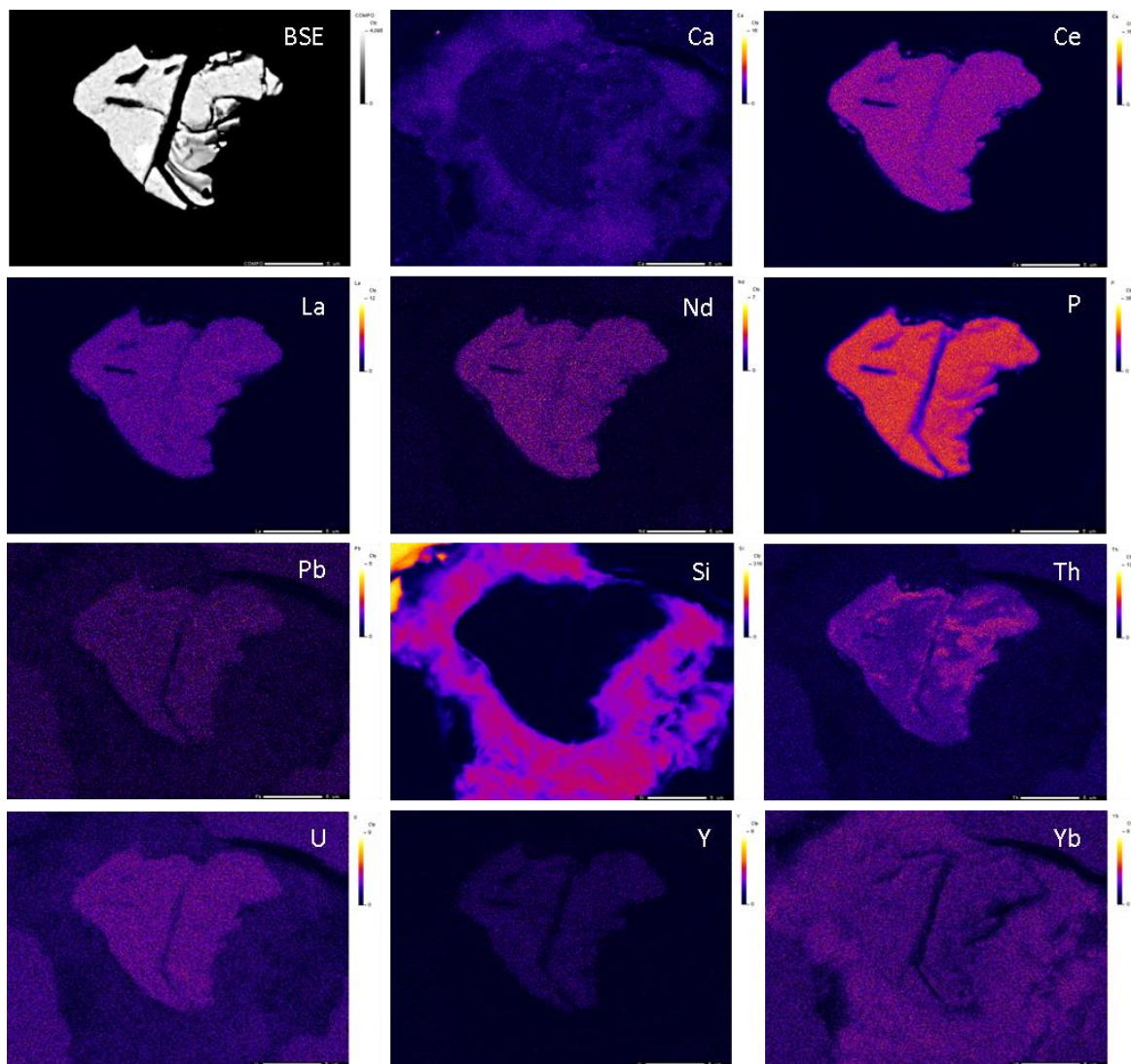


Plate 6-8 Qualitative WDS element maps of monazite grain 217 from sample 716. Each micrograph represents a spectrum intensity from one of twelve elements analyzed. Micrographs are labeled with the corresponding element and graduated scale of counts per second.

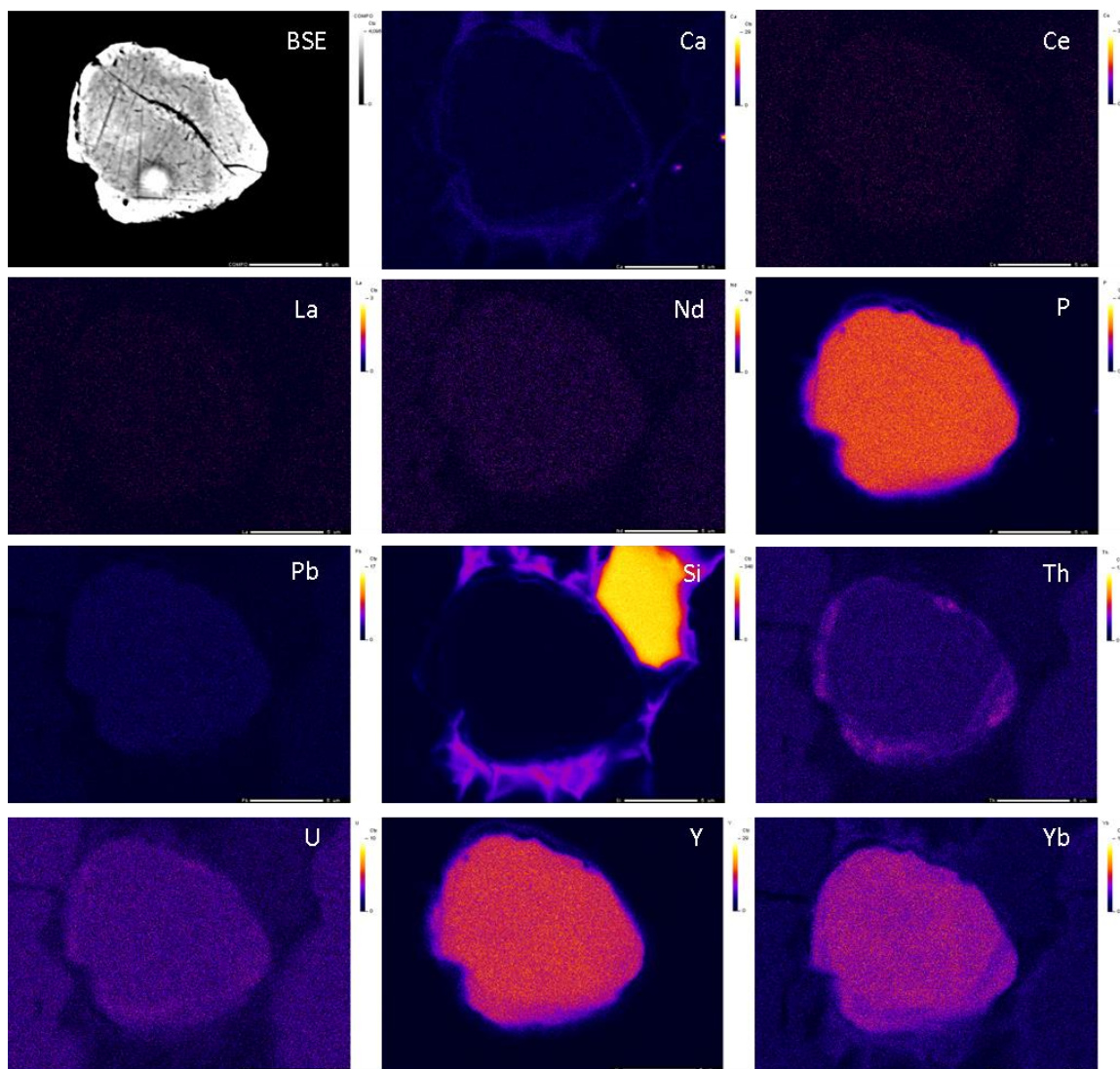


Plate 6-9 Qualitative WDS element maps of xenotime grain 847 from sample 716. Each micrograph represents a spectrum intensity from one of twelve elements analyzed. Micrographs are labeled with the corresponding element and graduated scale of counts per second.

6.5 Sample 709 Description

Sample 709 is an example of magnetite-hematite iron ore from Deposit No.1. The sample was collected from drill hole MR1-08-177 at 22 m. The unit consists of 0.1-1.5 mm cataclastic magnetite with oxidized margins forming a porous poorly sorted matrix. Micro folding is also observed being overprinted by the brecciation. Hematization of magnetite clasts produces a cross-hatch pattern showing increased porosity. Mineral abundances are 40% magnetite 60% hematite. Porosity of the matrix

is estimated at 2.5%. Total iron content is 69% with minor amounts of SiO₂ (0.44%), Al₂O₃ (0.49%) and MgO (0.04%).

6.5.1 709 BSE-EDS Feature Mapping

BSE-EDS feature mapping identified 84 zircon, 214 monazite, 194 xenotime and 7 baddeleyite (Figure 6-21). Zircons were small ranging between 8.81-105.78 μm². Monazite and xenotime are more abundant but fine grained averaging 51.25 μm² and 73.41 μm² respectively. Baddeleyite are the smallest, ranging between 4.2 to 5.99 μm in length and averaging 12.20 μm² in area. Zircon, monazite, xenotime and baddeleyite show no spatial correlation, although the lower portion of the section contains higher abundances.

6.5.2 709 SEM Imaging and Element Mapping of Features

BSE imaging of monazite and xenotime show anhedral crystals with serrated feathery edges of secondary growth (Plate 6-10). Element mapping indicates faint to distinct Ca-Th zoning at feathery monazite margins (Plate 6-9) and Ca-U-Yb zoning at xenotime margins (Plate 6-10). Baddeleyite forms spongy anhedral masses in pits and pore spaces between hematite and altered magnetite. BSE and SE imaging did not identify zoning or irregularities within baddeleyite.

WDS point analyses of zonation in monazite margins indicates a 0.2-0.4% increase in Ca and 0.9-1.3% increase in Th. Thorium values overall in monazites were less than 0.2% except at feathery rims. Analyses of the xenotime rim in grain 3478 show a 0.2% increases in Ca and U while Th increases by 0.5%.

Sample 709 Feature Map

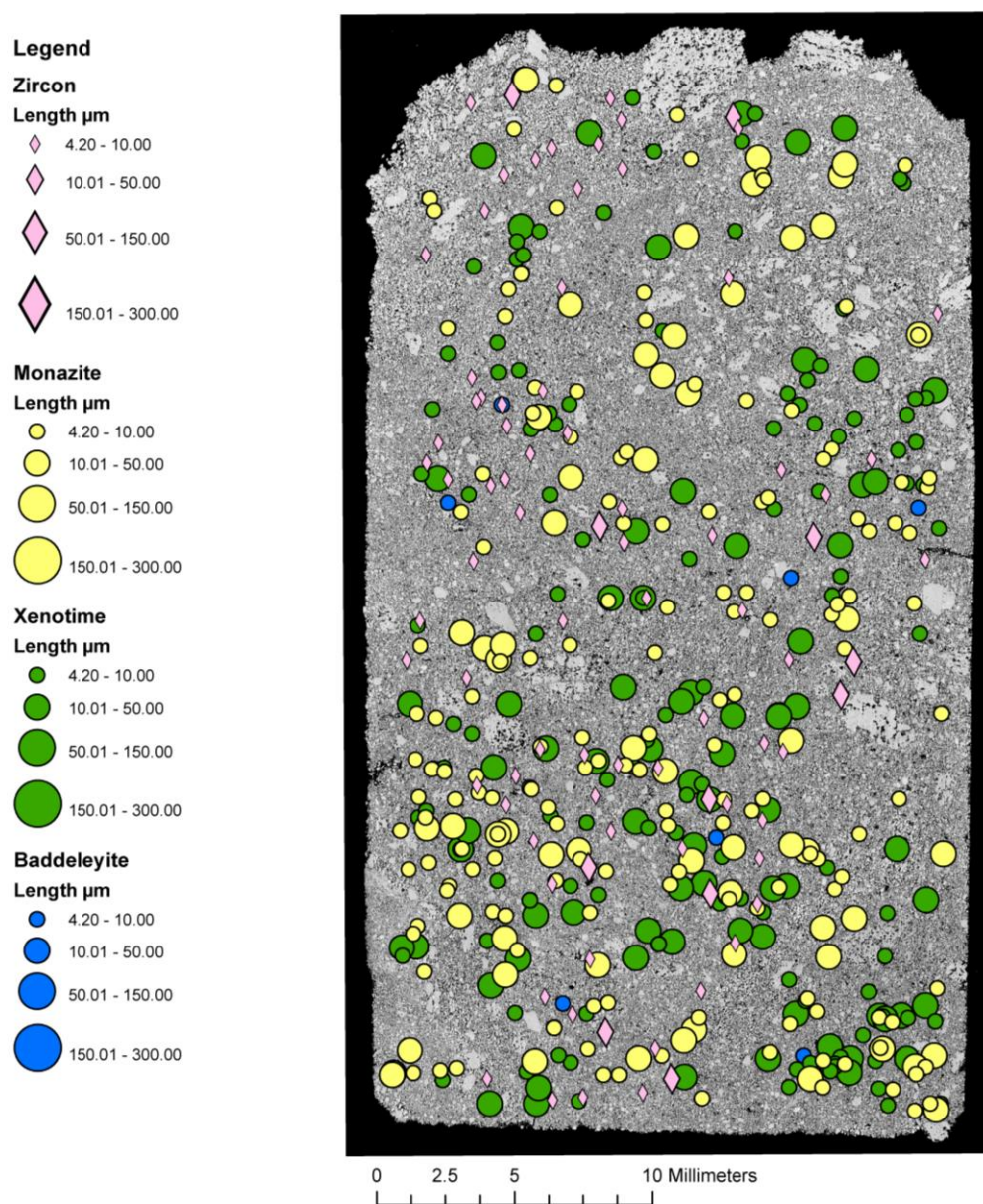


Figure 6-21 BSE-EDS feature map of polished thin section of magnetite-hematite ore sample 709. Zircons, monazite, xenotime and baddeleyite are depicted by graduated circles based on length plotted on BSE montage image of sample 709. The feature scan area is the full width and length of the polished thin section.

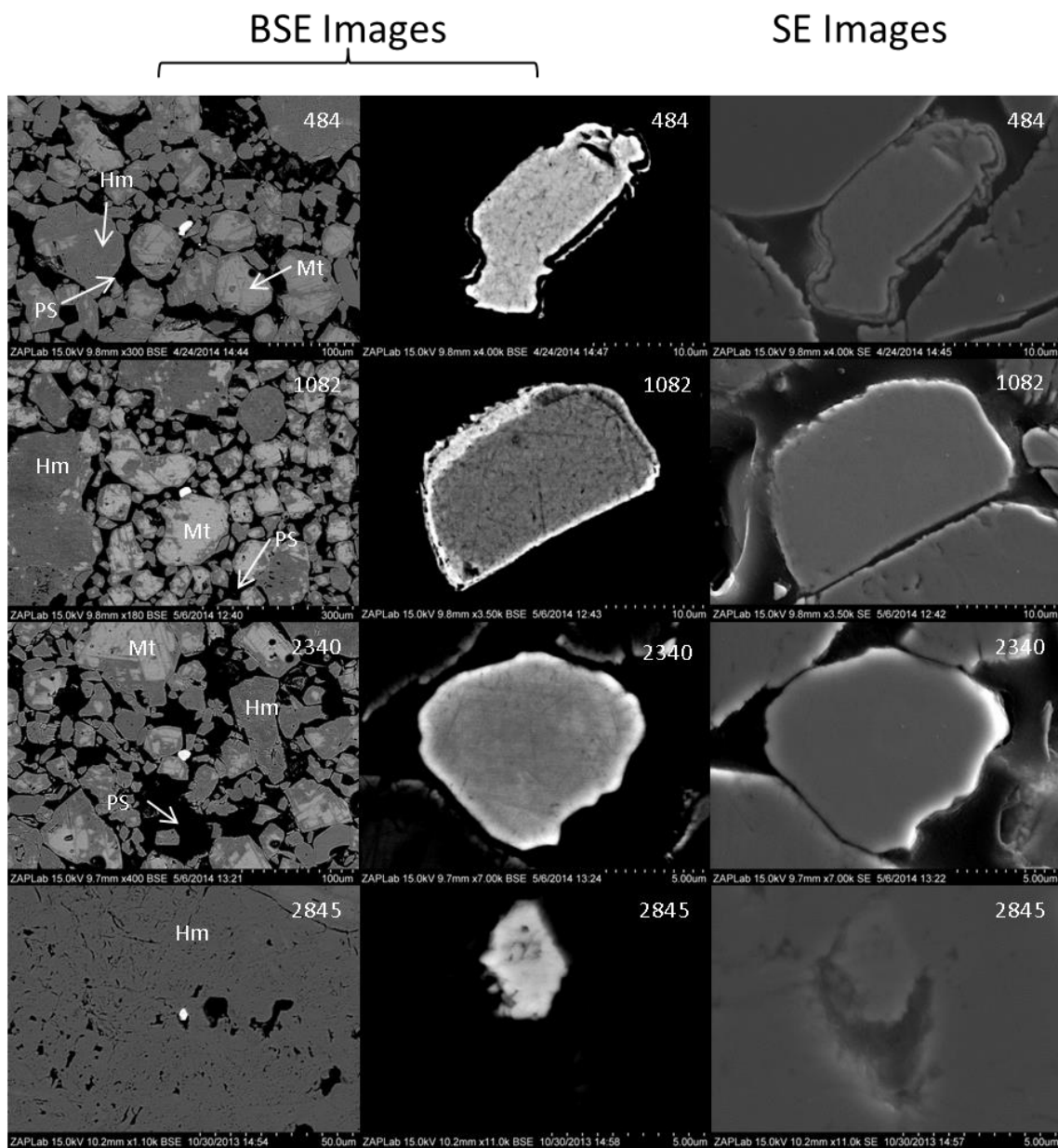


Plate 6-10 Collage of representative datable phase morphologies in sample 709. Micrographs are arranged in columns by backscatter (BSE) and secondary electron (SE) sources with grain numbers. Monazite 484 is irregular monazite grain surrounded by hematized magnetite (Mt) clasts and pore spaces (PS). Blocky xenotime is shown by grain 1082 while grain 2340 is a typical anhedral zircon. Baddeleyite 2845 is located within a pore space of hematite (Hm) clast.

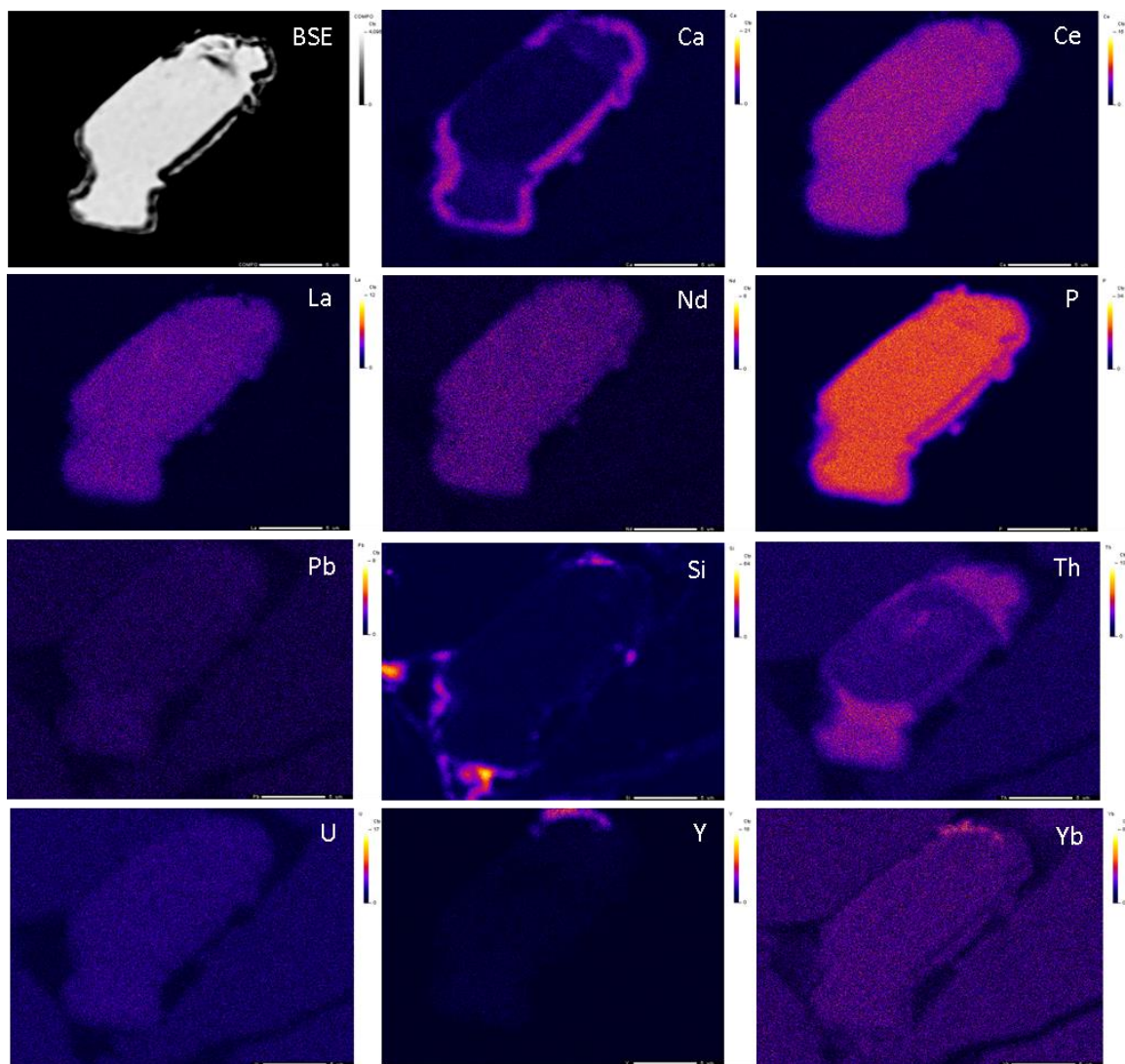


Plate 6-11 Qualitative WDS element maps of monazite grain 484 from sample 709. Each micrograph represents a spectrum intensity from one of twelve elements analyzed. Micrographs are labeled with the corresponding element and graduated scale of counts per second.

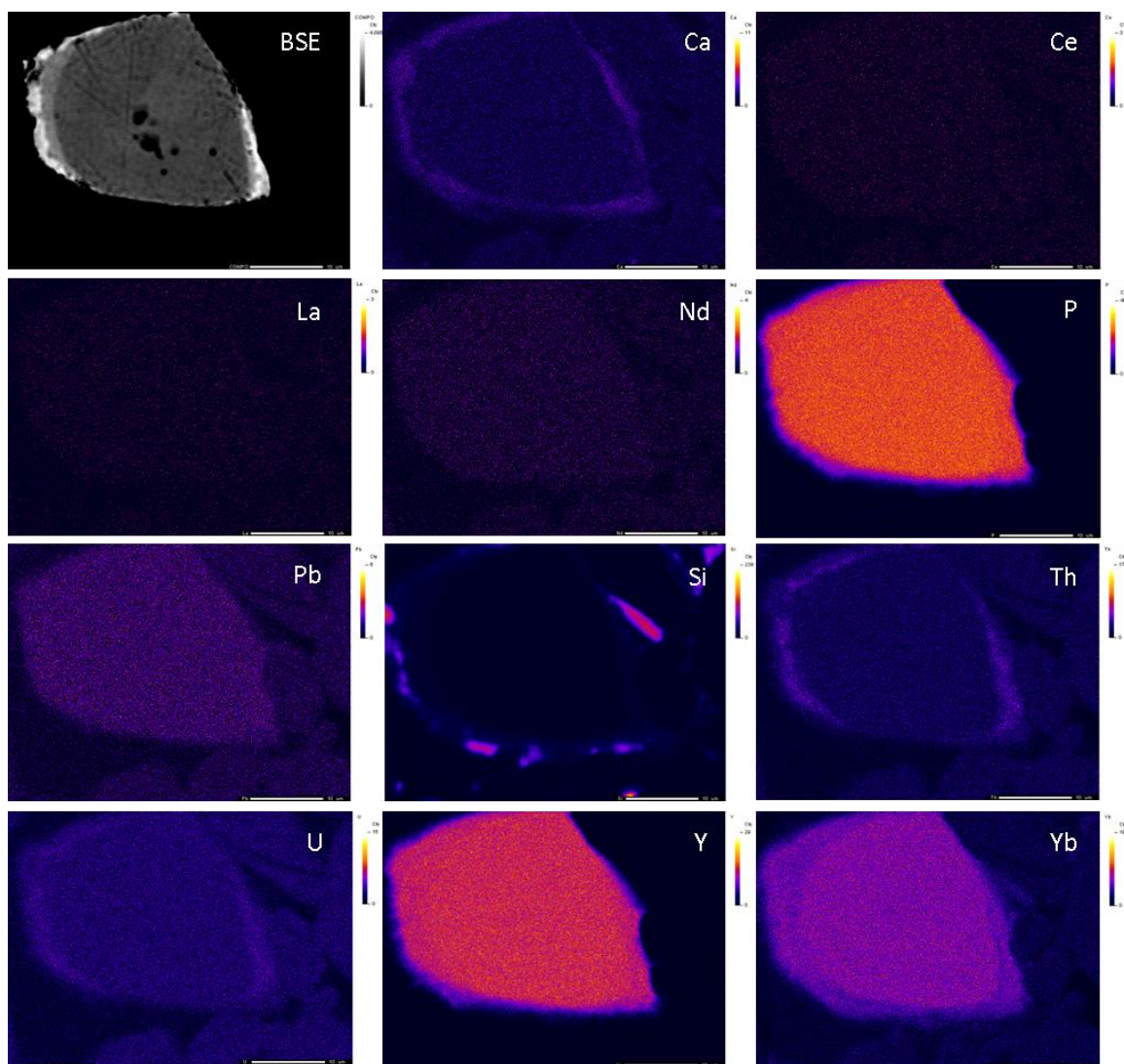


Plate 6-12 Qualitative WDS element maps of xenotime grain 1082 from sample 709. Each micrograph represents a spectrum intensity from one of twelve elements analyzed. Micrographs are labeled with the corresponding element and graduated scale of counts per second.

6.6 Sample 6416 Description

Sample 6416 is a surface grab sample of high grade hematite iron ore collected from the southern limb of Deposit No.1 near the collar of drill hole MR1-226-12. The sample contains martite (25%) microplaty hematite (74%) and minor magnetite (1%). Martite crystals are subhedral octahedra surrounded by 5-25 μm microplaty hematite.

Martite crystals also show cross-hatch plates of hematite forming vugs. Large vugs form where coarse hematite blades overprint finer blades and martite. The porosity is estimated at 2%. Zircon, monazite, xenotime and baddeleyite are trace accounting for only 0.25% of the bulk composition and are not distinguishable by optical petrography.

6.6.1 6416 BSE-EDS Feature Phase Mapping

Feature mapping of sample 6416 identified 670 grains that include zircon, monazite, xenotime and baddeleyite. Zircons are low in abundance accounting for eleven crystals averaging 5.15 microns in length. Monazites and xenotime are much higher in concentrations totalling 84 and 23. The average area of monazite and xenotime is $26.51 \mu\text{m}^2$ and $20.02 \mu\text{m}^2$ respectively. Only four baddeleyites were identified ranging in area between $12.20 \mu\text{m}^2$ to $33.23 \mu\text{m}^2$. Spatial correlations are scattered except the top margin shows a linear horizontal trend of xenotime. Petrographic and SEM imaging have not identified a textural relationship to the trend.

6.6.2 6416 SEM Imaging and Element Mapping of Features

Monazites show a feathery and aggregated cluster textures in pore spaces and at the margins of martite. Xenotime exhibits the same aggregate clustering morphology but are identified within martite and at the boundaries of martite pseudomorphs. Baddeleyite forms at the margins of zircon by BSE and EDS analysis.

Sample 6416 Feature Map

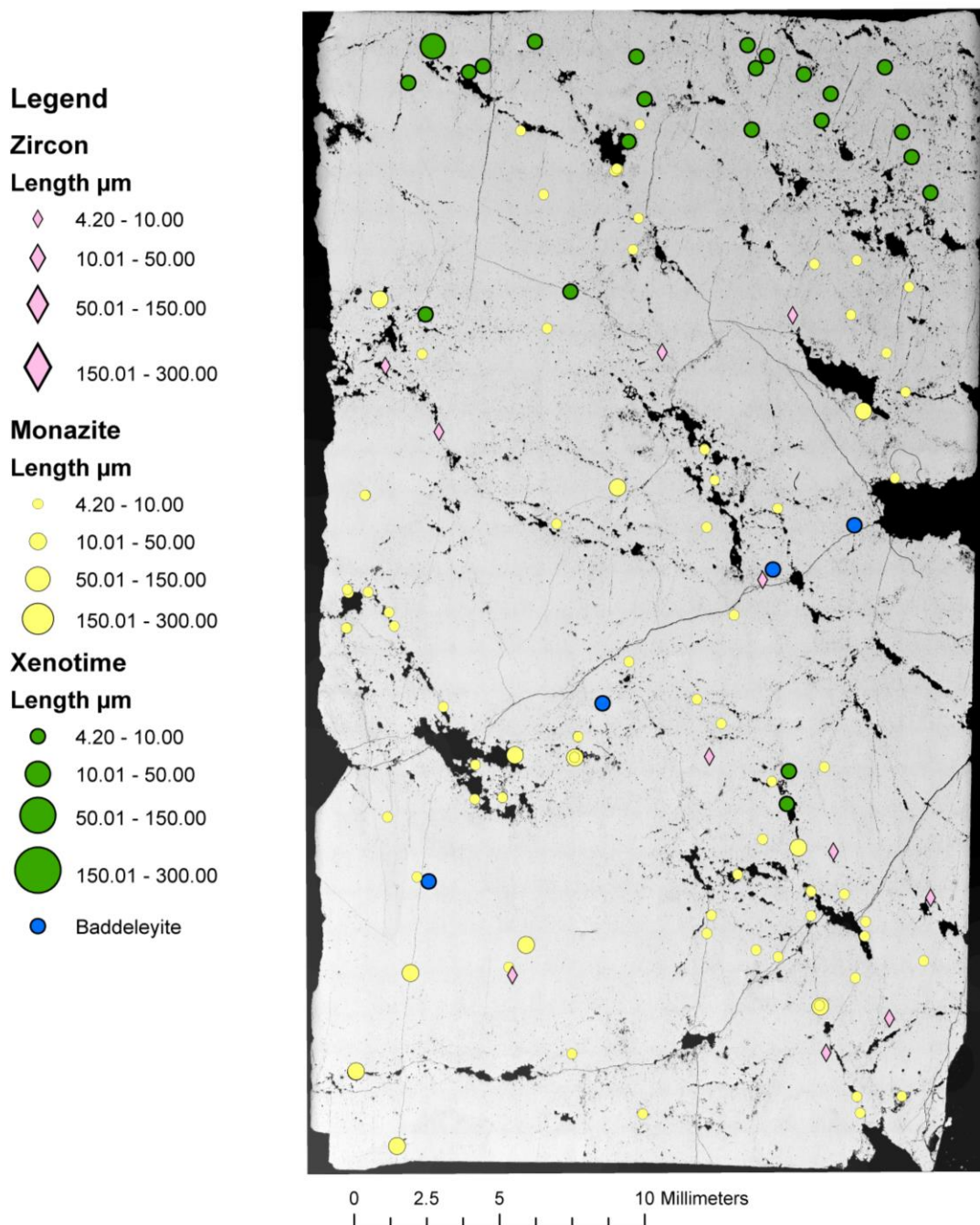


Figure 6-22 BSE-EDS feature map of polished thin section of magnetite-hematite ore sample 6416. Zircons, monazite, and xenotime are depicted by graduated circles based on length plotted on BSE montage image of sample 6416. The feature scan area is the full width and length of the polished thin section.

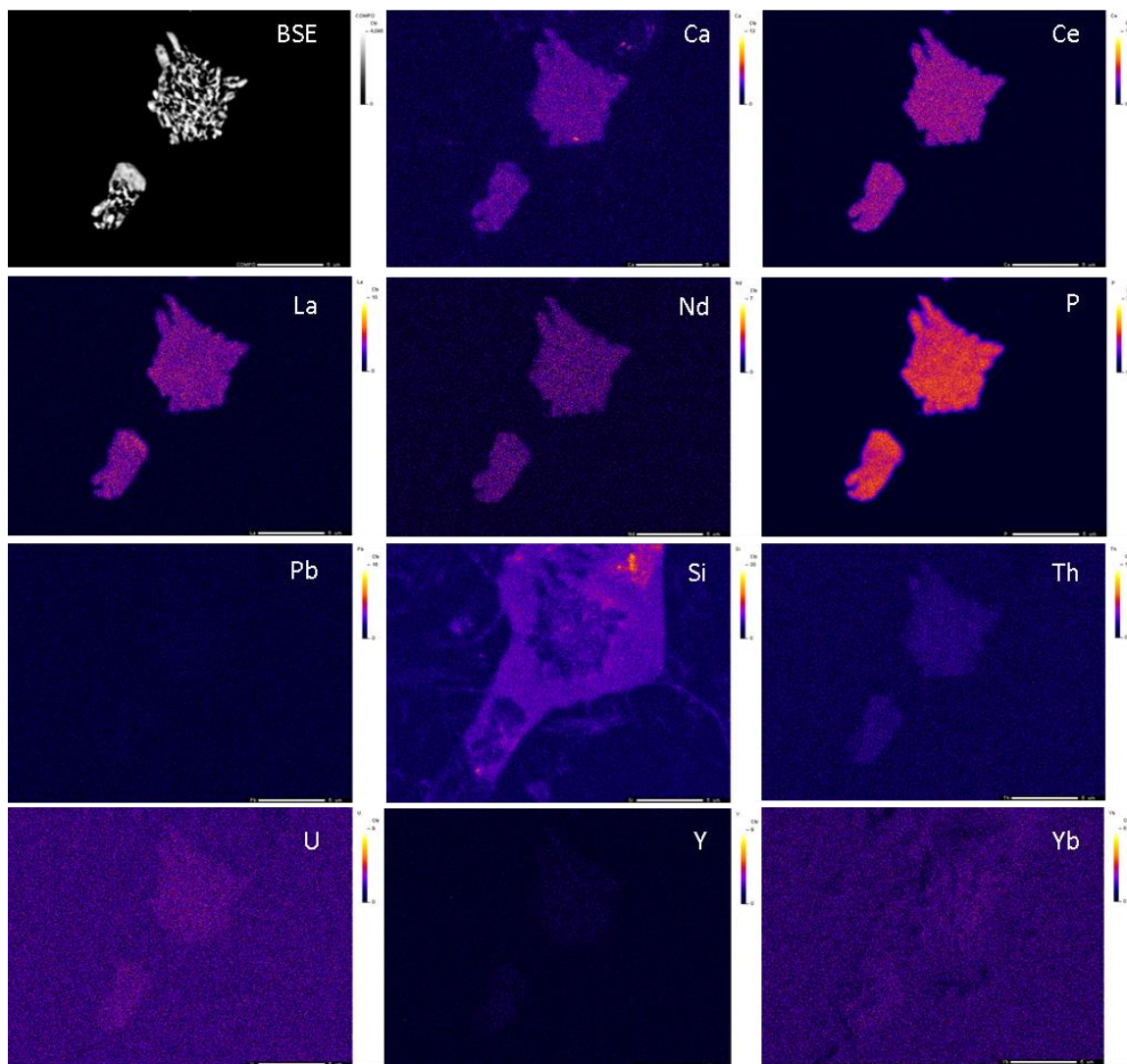


Plate 6-14 Qualitative WDS element mapping of monazite 615 from sample 6416. Each micrograph represents a spectrum intensity from one of twelve elements analyzed. Micrographs are labeled with the corresponding element and graduated scale of counts per second.

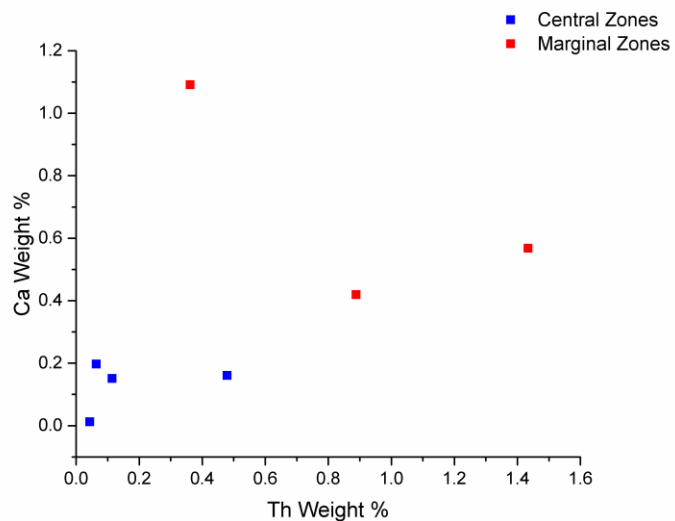


Figure 6-23 Calcium-thorium scatter plot of EMP analyses from monazites in sample 716, 709 and 6416. Marginal zones are in red and central zones in blue.

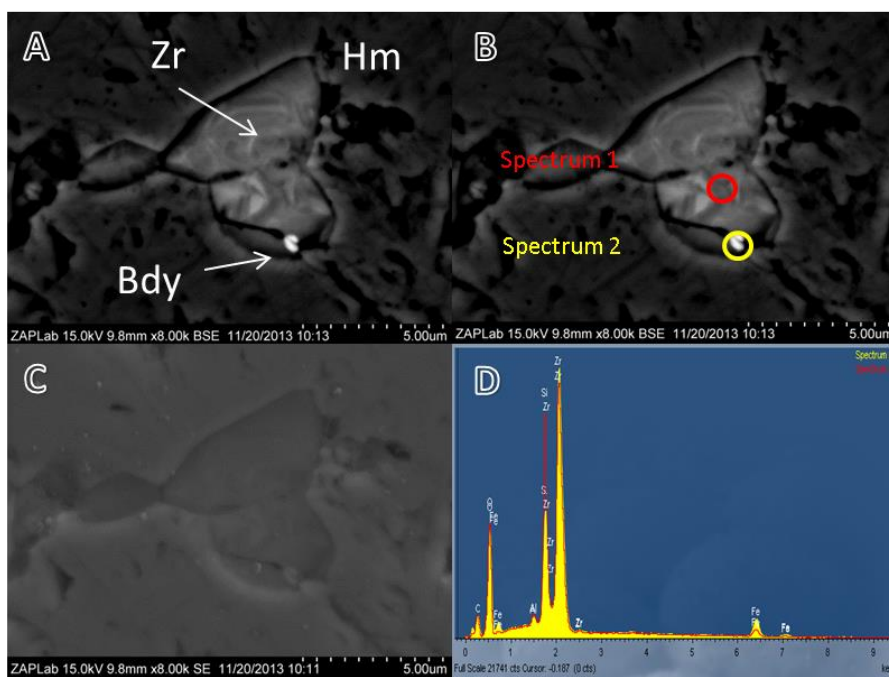


Plate 6-15 BSE and SE images of zircon in hematite ore sample 6416. Zircon has baddeleyite growing from its margin (A). B shows the location of EDS spectrum spot analysis. C is a SE image of the zircon and baddeleyite. D is an EDS spectrum of the two points.

Chapter 7 Discussion

7 Introduction

This chapter discusses and interprets the results presented in chapters 4, 5 and 6. Lithologies are defined in more detail by combining petrographic and geochemical data and are compared to previously mapped units. Geochronological data are interpreted and tied to footwall and ore zone mineral paragenesis. Metamorphic assemblages are presented and linked to their pressure-temperature environment. Collectively, interpretations are used to construct a metallogenic model outlining how hydrothermal alteration and metamorphic processes transform banded iron formation into high grade direct shipping iron ore.

7.1 Litho-Tectonic Stratigraphy

7.1.1 Footwall

Detailed geological mapping of Deposit No.1 has identified major discrepancies with regard to previously identified rock types. Historically recognized mafic-felsic volcanics, greywackes, and conglomerates are not identified in outcrop or drill core logging of the immediate footwall to Deposit No.1. Instead plutonic, metamorphosed and hydrothermally altered rocks are identified; monzogranite, syenogranite, metagabbro, quartz-augen schist, biotite schist and chlorite schist.

Monzogranite and syenogranite are composed of interlocking subhedral to euhedral twinned feldspars, micas and quartz. Their hypidiomorphic textures are plutonic, not metamorphic in nature. Polysynthetic twinned plagioclase and tartan twining of microcline crystals are of magmatic origins and not due to metamorphic recrystallization (Vernon, 1999). Coarse prismatic zircon stems from plutonic origin as well. Previous defined footwall felsic volcanics by Jackson (1966; 2000) and BIMC (2004-present) are not accurate due to the coarse relict hypidiomorphic textures of twined feldspars, biotite and quartz. Numerous inclusions of biotite and quartz in partially twinned albite and orthoclase in the immediate monzogranites and syenogranites to Deposit No.1 may indicate secondary K-feldspar formation post crystallization.

Whole rock geochemistry classifies all three granitoids (monzo-syeno and alkali feldspar granite) as weakly peraluminous. Cesium averages are abnormally high in monzogranite (1113 ppm). Cs bearing minerals (pollucite or avogadrite) are not identified alluding to residence in micas. Trace element discrimination plots modeled after Pearce et al. (1984) designate monzogranite as volcanic arc granites and syenogranites as within plate type. The SIAM classification system, designed by Chappell and White (1974 and 2001), White (1979) and Loiselle and Wones (1979), classifies monzogranite and syeno-alkali feldspar granite as I-type.

With exception of Eu, REE and HSFCE concentrations in granites are mainly concentrated in accessory silicates, oxides and phosphates (70-95%) (Bea, 1996). As the granites are peraluminous, phosphates and zircon hold 95% of REE and HSFCE abundances (Bea, 1996). Differences in REE profiles reflect varying incompatible element partitioning environments or melt sources during crustal and petrogenetic evolution (Hanson, 1978; Watson and Harrison, 1984; Linnen et al., 2014). Contrasting REE profiles support petrographic inspection of the granites, demonstrating monzogranite are petrogenetically different than syeno and alkali-feldspar granite. Normalized chondrite REE patterns display marked Eu depletions and higher REE concentrations in syeno and alkali-feldspar granites compared to monzogranites. HREE depletion is often attributed to hornblende speciation fractionating large concentrations of HREEs. Hornblende forms as an accessory phase in monzogranites and may partially explain its mild HREE variance. Near identical REE profiles of syeno and alkali-feldspar granite illustrate, potentially, the same melt source and tectonic environment of emplacement. Comingling of these two granite phases in outcrop also shows syeno and alkali-feldspar granites are coeval.

Metagabbro exhibits an equigranular texture of interlocking plagioclase, hornblende with minor interstitial quartz. Whole rock and mineral compositions are not indicative of a komatiitic parent as previously mapped by MacLeod (2012) (Nockolds, 1954). Bulk rock geochemistry of the metagabbro identifies tholeiitic basalt composition (Nockolds, 1954; Jensen, 1976). Average normalized chondrite La/Sm (1.16) values define the metagabbro composition to be transitional mid ocean ridge basalt (TMORB)

(Schilling et al., 1983). The gabbro's flat line REE profile is also identical to TMORB in both profile and value (Sun and Nesbitt, 1979). Bulk rock chemistry of the metagabbro also shows much lower Cr (463 ppm) and Ni (97 ppm) values compared to ultramafic serpentinites (Cr 1803 ppm and Ni 2810 ppm). Average Cr values are elevated when compared to average MORB gabbroic and basaltic rocks implying moderate differentiation or a semi-depleted mantle source (Thompson, 1973).

Footwall sedimentary quartzites, mapped and defined by both Jackson (1966, 2000) and MacLeod (2012), are neither sedimentary nor "quartzite" in texture, mineralogy or bulk rock composition. Quartzites are redefined as altered-silicified granitoids composed feldspar, quartz and mica in a hypidiomorphic to allotriomorphic texture. Coarse subhedral to euhedral twined feldspars are altered to patchy quartz clusters and augens. Secondary quartz overprints a primary igneous fabric and gives the siliceous texture at a macroscopic scale. ASG gradationally contacts granitoids and clearly demonstrates no primary lithology change. ASG units are massive with lineated biotite and quartz augens at margins. Previously logged psammities and tuffs by BIMC are the result of misidentified minerals and tectonic fabrics. For example, lineated biotite patches in ASG sample 6066 were first defined as volcanic clasts; however, petrography reveals sample 6066 is composed of medium to coarse subhedral microcline, quartz and twinned plagioclase. Compositionally, "quartzite" contains 90% or more quartz (mineral) or $\geq 90\%$ SiO₂ chemically (Boggs, 2006). Bulk rock compositions of quartzite (ASG) average 77.43% and do not exceed 81.50% SiO₂.

Quartz augen schists units (Figure 4-1) were defined as metavolcanics, metasediment and paragneiss by Jackson (1966, 2000). MacLeod (2012) cited deformed paragneiss for the origin of aluminous schist (QAMBS). The volcanic-sedimentary textures and gneissic banding observed by these authors are not present. Conglomerate lenses recognized by Jackson (1966, 2000) are miss-interpreted tectonic and alteration textures. The conglomerate outcrops at the base of Deposit No.1 are boudinage monzogranite lithons in biotite schist. Chlorite-amphibole patches overprint the biotite matrix and form high relief nodules. The contrast between boundinage monzogranites and chlorite-amphibole nodules create the pseudo-polymictic texture previously

described by Jackson (2000). Gneiss banding is faux banding caused by quartz-augen lineations in relation with secondary muscovite and biotite forming 1-5 mm thick spaced mylonitic shear bands and foliation. Coarse extensional lineations are formed by mylonitized quartz and feldspar. Abrasion and dissolution along shear planes forms the annealed quartz-augens with margins of polygonal quartz. The spaced foliation in combination with lineated quartz-augens gives the appearance of banding in viewing angles parallel to quartz-augen lineation (Plate 4-3).

The protolith of quartz-augen schist is monzogranite. Lineated quartz augens and relict feldspar blocks transition gradationally into ASG units and the quartz-augens schist from monzogranite. Euhedral zircons, feldspars and quartz are enveloped by secondary micas at contacts between ASG and QAMBS units. These euhedral grains span across the contact and are of primary origin. Therefore, the contact is the result of secondary deformation and alteration, not lithological. Symmetrical REE and trace element profiles between monzogranite, ASG and QAMBS units also illustrate a single monzogranite protolith. Biotite and chlorite schists have gradational contacts to QAMBS and contain relict quartz-augens. The seamless transition between the three schist units and the same REE and trace element profiles to QAMBS units demonstrates footwall biotite and chlorite schists originate from QAMBS units and thus a monzogranite protolith.

7.1.2 Ore Zone

The major reclassification of ore zone units is with regards to ore types. Previously MacLeod (2012) and BIMC have classified high grade iron ores on grade. Grade is a reflection of mineralogy and its corresponding abundances. Magnetite ores are the highest grade while magnetite-hematite and hematite ores are lower in total iron content sequentially. Drill core data cannot decipher zonation of ore types within the Deposit No.1 ore body at the current moment. Relict and brecciated BIF in HGIF also cannot be correlated along strike.

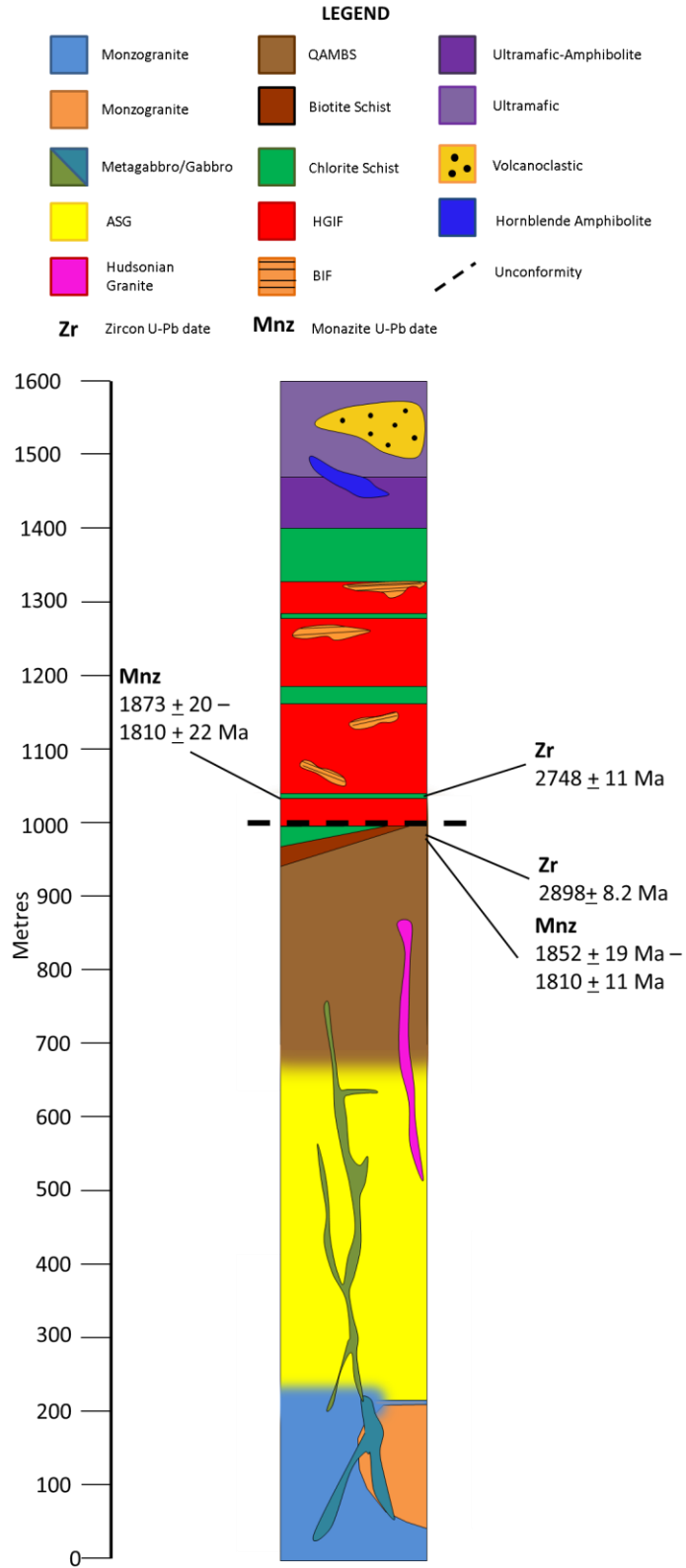


Figure 7-1 Tectonic stratigraphic column of Mary River Group and basement granitoids.

Chlorite schists are interleaved with iron ore are not correlated along strike in drill holes with exception of the thicker central chlorite schist unit. The whole rock chemistry of ore zone chlorite schist shows high Cr, Ni, Zn and V, uncharacteristic of metasediments or volcanics. Ore zone chlorite schist is also higher in Al and Zr compared to studies of other Neoproterozoic ultramafics (komatiites) (Dostal and Mueller, 1997). Euhedral zircons identified by feature mapping and the absence of baddeleyite is inconsistent with an ultramafic-mafic parent (Malich et al., 2007). Chlorite schists are interpreted to have a mixed volcanoclastic and ultramafic parentage.

7.1.3 Hangingwall

Hangingwall units mapped by Jackson (1966) are more in line with drill results than MacLeod (2012). Ultramafic-amphibolite; deemed amphibolitic komatiite by MacLeod (2012), directly contacts chlorite schist and BIF. The unit grades west to east from talc and carbonate veined serpentinites to unaltered serpentinites (drill holes MR1-14-227 & 228). Amphibolitic ultramafics mapped east of the Mary River by MacLeod (2012) are not identified in the new more detailed geological map of Deposit No.1. Furthermore, drill core shows volcanoclastics are interleaved with ultramafics. Gabbros identified by Jackson (1966) are hornblende amphibolites sharply contacting ultramafics, ultramafic-amphibolites and volcanoclastics.

7.1.4 Structure

Lineations and F_3 style folds are the most predominant structural features in footwall, ore and hangingwall zones of Deposit No.1. Isoclinal folds (F_3) defined by deformed relict BIF and magnetite-hematite ore which are overprinted by brecciation. Lineations crosscut and penetrate through F_3 axial planes at a rake of 074° and plunge of 54° . Oriented QAMBS samples contain sigma shaped quartz-augen lineations exhibiting bottom-up top-down sense of shear. Measurements combined with the sense of shear indicate the lineations are extensional not compressional and postdate folding. Lineations measured in all three immediate footwall units exhibit the same $\sim 074^\circ/54^\circ$ rake and plunge, indicating ASG, QAMBS and metagabbro units are deformed by the same

extensional event. Moreover, lineations in QAMBS, metagabbro and ASG units are traced across contacts for more than 50 metres.

Epidote-carbonate-horblende (ECH) veining is identified in granitoids and ASG units. ECH veins are linear in outcrop and drill core and are over printed by quartz-augens, muscovite and biotite. Veining is interpreted to be post-collisional because they are not fold. With this data combined, a new metamorphic-tectonic stratigraphic column is presented in Figure 7-1.

7.2 Geochronology

7.2.1 Zircon

Footwall QAMS and QABS samples contain large 50-300 μm euhedral crystals with oscillatory planar zones 5-25 μm thick. Zircon zoning is identical to magmatic textures categorized by Corfu et al. (2003). Average Th/U concentrations of central and marginal zircon zones are 0.44 and 0.34 respectively. Igneous zircons generally contain a Th/U value greater than 0.5 while metamorphic zircons average a much lower Th/U (~ 0.01) (Hoskin and Schaltegger, 2003). Although average Th/U values of footwall zircons are lower than 0.5, the ratios of QABS zircon still lie within the accepted range of igneous zircon (Hoskin and Schaltegger, 2003). The zircon populations in both samples are interpreted to have crystallized as primary igneous grains that were then deformed.

About 65% of the igneous zircon population is fractured and brecciated, in-filled with matrix minerals and feature anhedral 5-20 μm monazite-xenotime growth at margins. Grain distribution in both samples is random; however, smaller zircons are distributed in curvilinear chains parallel to foliation. Deformation is ascribed to extensional mylonitic deformation forming the host rock based on the textures described above and the distribution of grains along mylonitic fabrics.

Model $^{206}\text{Pb}/^{207}\text{Pb}$ ages from central zircon zones, in sample 6225, plot as a single concordant age of 2896 ± 8.2 Ma. Marginal zircon zones are discordant and have an upper intercept of 2943 ± 27 Ma and a lower intercept of 1656 ± 100 Ma. Brecciated zircons, such as grain 199, are concordant while cracked zircons with monazite-xenotime

margins are discordant (Figure 7-2). Multiple analyses on individual zircon grains show age differences and discordance at cracked and marginal zones. As an example, QABS zircon 4528 has two $^{206}\text{Pb}/^{207}\text{Pb}$ ages (2876 ± 11.7 Ma and 2528 ± 31 Ma) with mild and strong discordance; however, oscillatory zoning is continuous (Figure 7-2). The large age differences and discordance between pristine and cracked zones of uniform crystal zoning indicates lead loss. Hence, the zircon population of QABS sample 6225 is a single disturbed population of 2896 ± 8.2 Ma igneous zircon. Deformation and alteration of the host rock is coeval. Lead loss in zircon is interpreted to be penecontemporaneous with metasomatism related to alteration during the Paleoproterozoic (1656 ± 100 Ma). Lead loss is also demonstrated by mass balance changes. The morphology and single age of zircon crystals bolster petrography and geochemistry results defining the unit's protolith as monzogranite. The previous interpretation of this unit as a mature metasediment by Jackson (1966; 2000) and MacLeod (2012) without the benefit of zircon data, does not account for prismatic zircon textures and single age population, neither of which are characteristic of detrital zircon populations.

Zircons in ore zone chlorite schist (sample 6220A) are similar in morphology to those in footwall quartz-augen and mica schists described above. Fine oscillatory zoning with mild fractures and monazite growths at margins is distinguished by CL and BSE imaging. Zircons in ore zone chlorite schist are, however; significantly smaller, averaging $11.58 \mu\text{m}$ in length. Th/U proportions average 0.26. Model $^{206}\text{Pb}/^{207}\text{Pb}$ values cluster at a single age of 2748 ± 11 Ma and projects to a much lower intercept of 66 ± 44 Ma. Morphology, Th/U content and single model age defines zircons in ore zone chlorite schist as a single igneous Neoproterozoic population. Also, the large discordance of ages is not projected to the same lower discordance intercept as footwall zircons. Multiple younger lead loss events may account for the low intercept. Given their size, morphology and single age, ore zone zircons are remnants of a former altered volcanic parent.

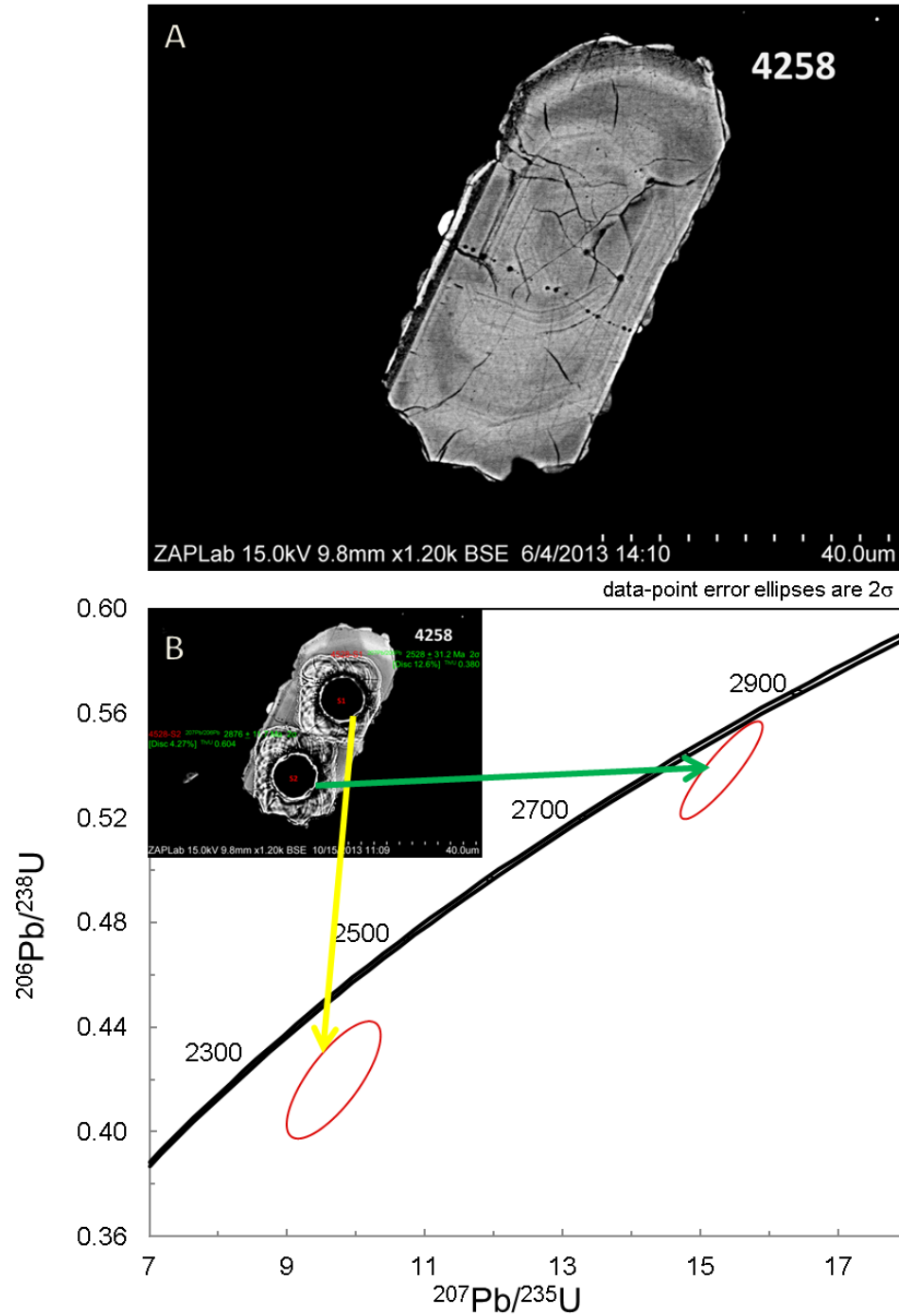


Figure 7-2 Multi-point U-Pb analysis comparison of QABS zircon 4528 from sample 6225. BSE image A shows symmetrical oscillatory zoning with moderate fractures at top of the crystal. B is concordia plot illustrating two laser ablation ages from the same crystal with discordance. The discordance is a result of lead loss.

7.2.2 Monazite

Monazite grains were found to be associated with muscovite, biotite or chlorite within footwall, ore zone and hangingwall schist units but were not identified in granitoids. They are distributed throughout footwall QAMS and QABS samples and in muscovite-biotite assemblages that wrap around quartz-augens (Figure 6-1 and 6-4). Ore zone chlorite schist monazite shows no spatial correlations to rock fabric. Monazite grains hosted in BIF and iron ore are located between magnetite-martite grain boundaries and in pore spaces (Fig. refs).

Monazite grains are cryptocrystalline and anhedral. These anhedral crystals aggregate as clusters (100 μm), patches (100-500 μm) or are disseminated throughout the mica-chlorite matrix of footwall and ore zone schist (Figures 6-1, 6-2). Secondary hydrothermal micas overgrow foliated primary muscovite-biotite, feldspar and quartz. Radiation damage of mica by U-Pb decay in monazite forms pleochroic halos in secondary muscovite and biotite. Pleochroic halos are not present in primary muscovite or biotite. Restriction of pleochroic halos infers monazite was not present at the time of primary muscovite-biotite crystallization. Formation of monazite is interpreted to be coeval with muscovite and biotite alteration that desilicified footwall, ore zone and hangingwall rocks. Monazite grains also have no preferential orientation or incorporation into quartz-augen lineations, primary mica or feldspars and thus did not exist prior to lineation. Cordierite, staurolite and almandine porphyroblasts all overgrow monazite clusters, patches and disseminations. Encapsulation of monazite in porphyroblasts shows it existed before cordierite but did not continue after almandine.

ThO_2 content in all monazites is below 0.5%, the majority below 630 ppm ThO_2 . Igneous monazites contain 3-5% ThO_2 (Schandl and Gorton, 2004) and can reach 14.52% (Kato, 1958). Hydrothermal monazite is <1% ThO_2 and more commonly less than 1000 ppm (Schandl and Gorton, 2004). Monazite textures and morphologies are identical to monazite textures described by Schandl et al. (1991), Poitrasson et al. (1996), Schandl and Gorton (2004) and Kempe et al. (2008) from hydrothermally altered ore deposits and granites which include the Kid Creek Mine, Timmins Canada, the Carnmenellis granite, U.K. and the Llallagua tin porphyry, Bolivia. Fracture infills of monazite in apatite and

growth along zircon margins also support a secondary-hydrothermal origin as well. Monazite is therefore hydrothermal by texture and composition.

BSE imaging and WDS element scanning of monazite identifies, chemically, at least two generations of monazite and xenotime growth in footwall and ore zone units. QABS monazites show faint zoning at margins while ore zone chlorite schist monazite exhibits strong light and dark zoning in BSE images. BSE imaging of xenotime in iron ores also shows zoning at margins. WDS element scanning illustrates that monazites are chemically and texturally zoned with respect to Ca and Th in magnetite-hematite ore. Central zones, representing first generation of monazite, contain very little calcium and are compact cryptocrystalline. Calcium rich monazites are feathery and form rims and overgrowths. Calcium rich feathery rims are mildly enriched with respect to Th. Hematite ores only contain feathery calcium bearing feathery monazites.

Zoning textures are typical of hydrothermal monazite. Experimental monazite and xenotime experiments regarding hydrothermal alteration have produced identically zoned and feathery textures (Hetherington et al., 2010) (Plate 7-1). Elemental Th and Ca enrichment is documented in experiments using hydrothermal fluids NaOH, $\text{Na}_2\text{Si}_2\text{O}_5 + \text{H}_2\text{O}$, $\text{CaF}_2 + \text{H}_2\text{O}$ and HCl (Harlov and Hetherington, 2010; Hetherington et al., 2010). Pseudomorphic textures in experimentation are analogous to hydrothermal alteration (Harlov and Hetherington, 2010). The reaction is considered a coupled dissolution-precipitation reaction (Harlov et al., 2005; Harlov and Hetherington, 2010). Similar coupled dissolution-precipitation in monazite ($2\text{REE}^{3+} = \text{Th}^{4+} + \text{Ca}^{2+}$) is documented by Poitrasson et al. (1996), accompanying chloritization of the Carnmenellis granite, England.

Different generations of monazite are also indicated by U-Pb isotope analysis. Concordant $^{206}\text{Pb}/^{207}\text{Pb}$ age ellipsoids of monazites in quartz-augen biotite schist are separated beyond error and represent a spread of ages. The MSWD value for both specifies the average projected group model age. Monazite feature 2674, is an equivocal example. The feature has two grains separated by a faint boundary. Ages of the two grains are 1855 ± 22 Ma and 1800 ± 12 Ma. These ages do not overlap in

$^{206}\text{Pb}/^{207}\text{Pb}$ value error; though, U-Pb age error ellipsoids do overlap (Figure 7-3). The minor overlap of error ellipsoids is negligible given the resolution of LA-ICP-MS. The gap in age and texture define the two grains as different generations. Zoning observed by BSE imaging in monazite patches in sample 6220A were not isotopically differentiated because of targeting and analytical imprecision.

The monazite U-Pb age systematics in both samples are similar. Model $^{206}\text{Pb}/^{207}\text{Pb}$ ages of QABS monazite ranged between 1855 ± 22 Ma and 1800 ± 12 Ma. (Figure 6-18). Monazite $^{206}\text{Pb}/^{207}\text{Pb}$ model ages in ore zone chlorite schist (sample 6220A) have a similar spread ($1873 \pm 20 - 1810 \pm 22$ Ma) but show a minor discordance. The distribution along concordia is inconsistent with a single age population. Due to their age, origins and paragenesis, monazites are interpreted to be the result of the same hydrothermal processes that occurred in both footwall schists and ore zone schists. U-Pb ages of hydrothermal monazite range between 1873 ± 20 Ma to 1800 ± 12 Ma collectively. The age range represents a protracted 41-105 million year period of hydrothermal activity that chronologically brackets mass desilicification of BIF (Figure 7-4) and the formation of high-grade iron ore.

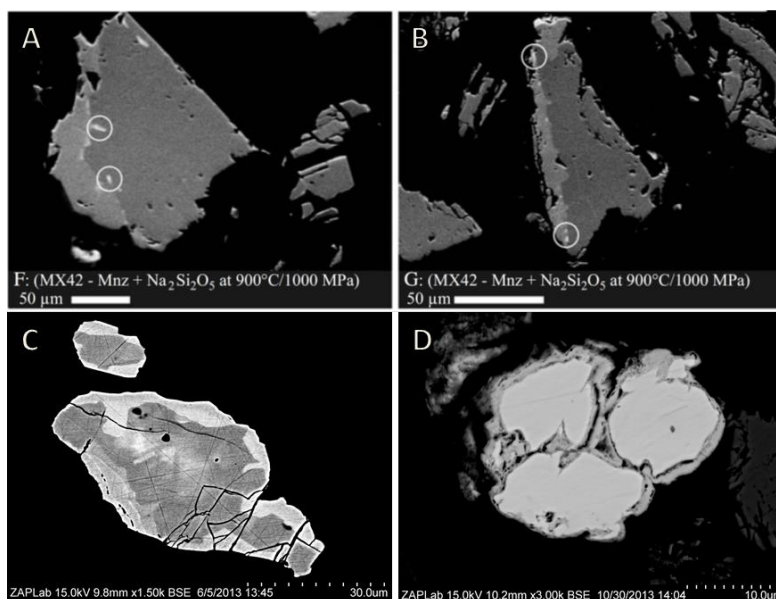


Plate 7-1 Plate comparing hydrothermal monazite textures. Micrographs A and B are BSE images of hydrothermally altered monazites showing secondary zoning from experiments conducted by Hetherington et al. (2010). C and D are monazite grains (11451 and 3180) from chlorite schist and magnetite-hematite ore.

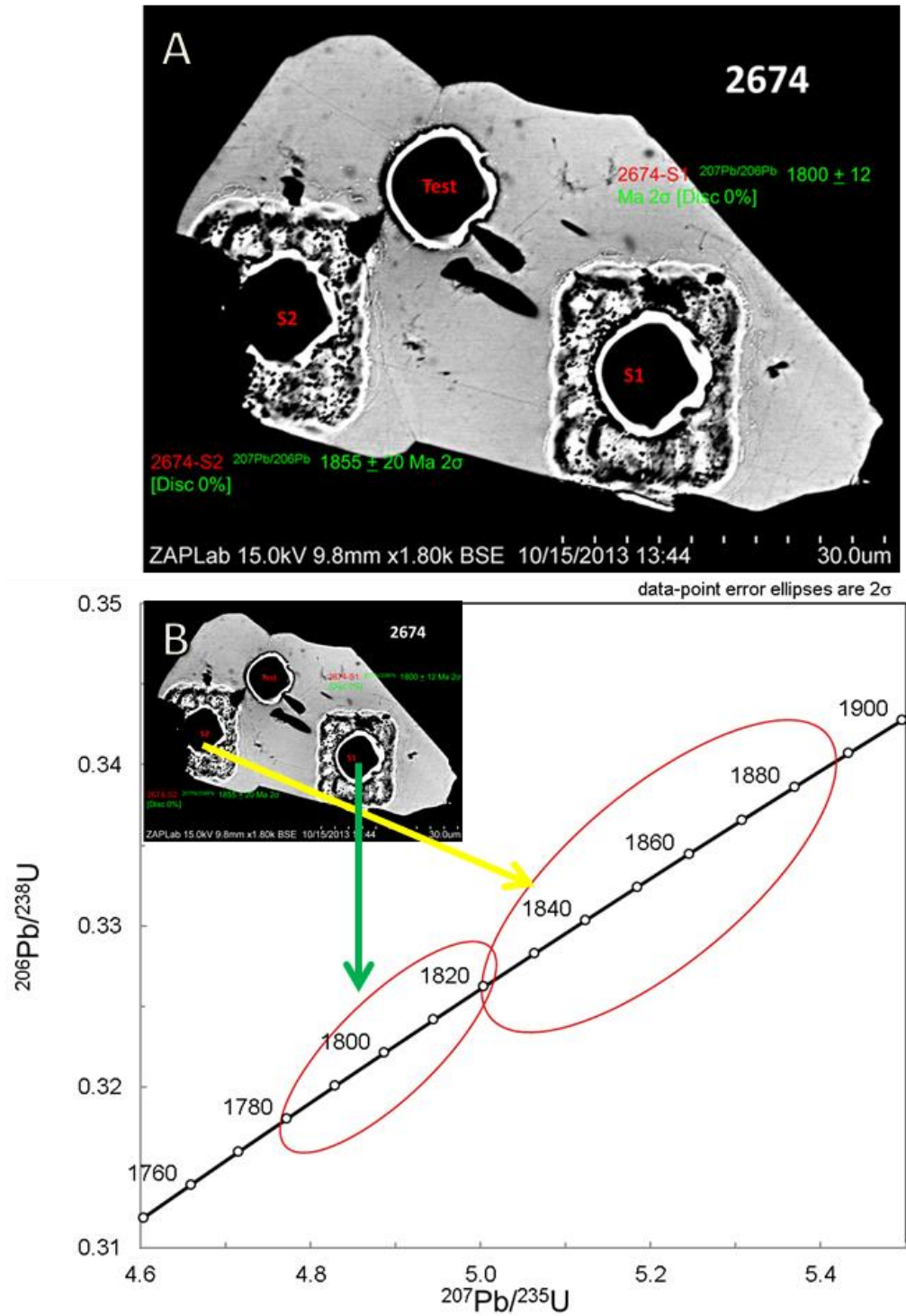


Figure 7-3 Geochronology comparison of multiple point analysis of monazite 2674 from QABS sample 6225. Separation of error ellipses is equivocal to general spread witnessed. BSE image (A) shows monazite grain with ablated spots and ages. B is a concordia plot with the ages identified.

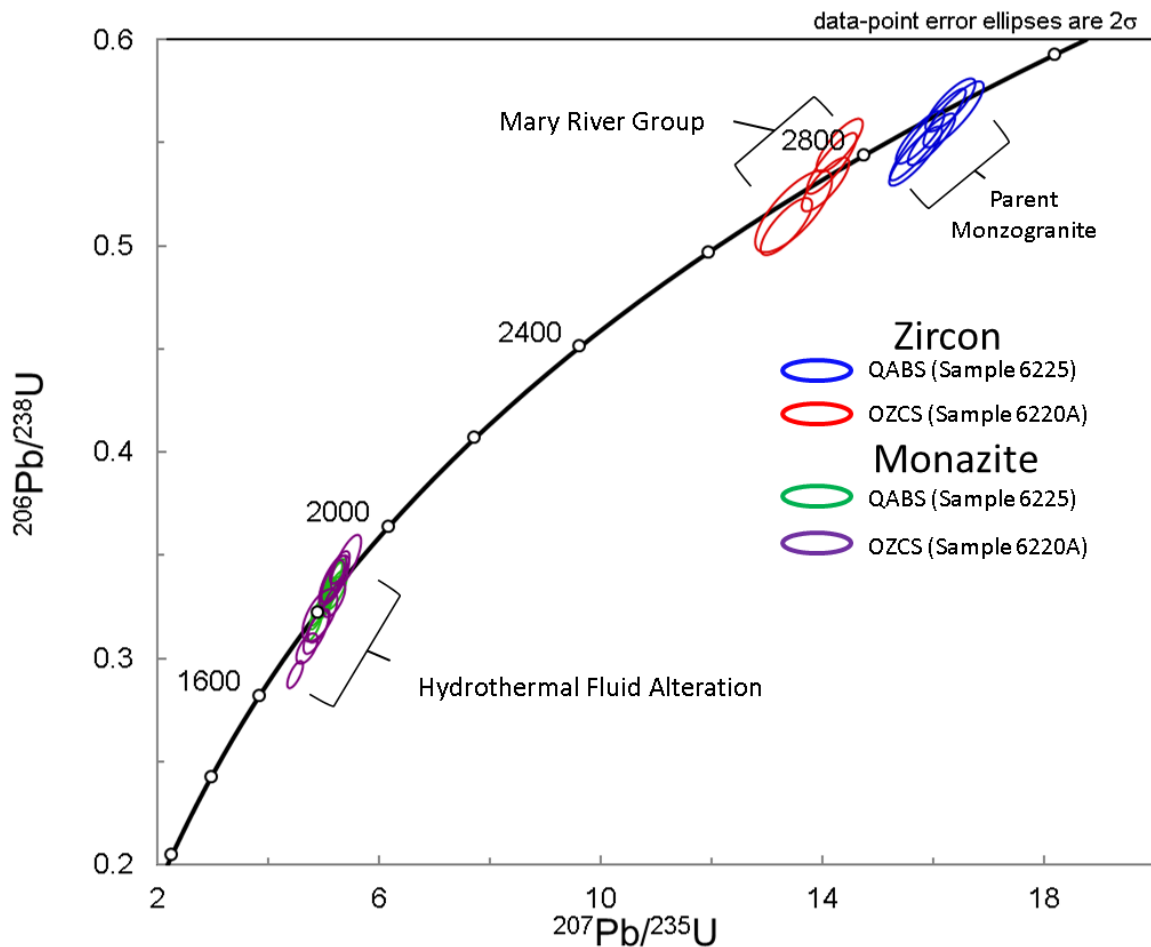


Figure 7-4 Concordia plot illustrating all zircon and monazite ages. Footwall zircon ages indirectly date monzogranite parent while ore zone zircons bracket Mary River Group deposition. Hydrothermal fluid alteration is constrained by monazite ages.

7.3 Paragenesis & Mass Balance

7.3.1 Footwall

The protolith of the immediate footwall schist at Deposit No.1 is monzogranite. Petrographic study has identified mineralogical and textural transitions while geochemical analysis shows identical REE patterns. The monzogranite REE profile through to chlorite schist becomes elevated, but remains symmetrical. Normalized REE profiles of syeno and alkali-feldspar granites differ with lower HREE abundances and marked Eu anomalies. The general enrichment of REEs in footwall schist is from

residual increase due to large bulk rock losses (SiO_2 Na_2O others...) as the majority of REEs are hosted in trace minerals zircon, monazite, xenotime and titanite.

The overall progression from monzogranite to chlorite schist is accompanied by massive silica loss by sequential hydrolysis mineral reactions. Footwall mineral reactions are of two types; hydrothermal alteration and metamorphic. Hydrothermal reactions involve the addition and or release of ions or complexes. Metamorphic reactions form mineral phases as products with exception of water and mainly results in porphyroblastic growth. Mineral reactions are categorized into three paragenetic stages:

Stage 1 is the mobilization of carbonate and magnesium by epidote-carbonate-hornblende veining crosscutting footwall intrusives. Veining textures show secondary influxes and mobilization of CO_3 , MgO and H_2O . The reaction of plagioclase to epidote involves the addition of water and liberates Na, Al, Si from plagioclase. A free OH⁻ is expelled into solution. As the reaction is isolated to veining inferring fluid influx is responsible and not in-situ metamorphic dehydration.

Stage 2 involves the breakdown of feldspar and quartz to muscovite followed by the growth of cordierite porphyroblasts forming QAMS units. The feldspar-quartz reaction to muscovite is the most important reaction as it releases SiO_2 and condenses the rock volumetrically significantly by $\sim 14\text{-}49 \text{ cm}^3$ per mole of altered feldspar (Robie et al., 1979). K-feldspar altering to muscovite requires 2H^+ donated from water (H_2O). The reaction results in 6 SiO_2 moles and 3 K^+ moles going into solution. Plagioclase is similar but releases only 1.5 SiO_2 moles and 1.125 moles Ca and 0.75 moles Na. Quartz is also converted to muscovite but requires 0.5 moles K_2O , 1.5 moles Al_2O_3 and one mole H_2O . The K_2O needed to alter quartz from muscovite is sourced from the liberated 3 K^+ in the K-feldspar reaction. The overall result is that a third to half of SiO_2 in the rock is released by the breakdown of feldspars and quartz during this stage. Such hydrous feldspar-quartz reactions are consistent with experimental work completed on the $\text{K}_2\text{O} / \text{Na}_2\text{O}-\text{Al}_2\text{O}_3-\text{SiO}_2-\text{H}_2\text{O}$ system of feldspar equilibria by Hemley and Jones (1964). Bulk mineralogical changes to muscovite from quartz define silica loss because muscovite compositions are limited between 45.24-48.42% SiO_2 (Deer et al., 1992). The quartz to

muscovite reaction, though stoichiometrically balanced, does not reflect mass balance change. The equation shows the mineral proportions of reactants and products and not total dissolved SiO₂. The dissolved SiO₂ of this reaction remains unknown. Terminal growth of cordierite porphyroblasts after muscovite alteration is a partial devolatilization reaction and produces some metamorphic biotite.

Stage 3 further desilicifies the footwall by the biotization of quartz, cordierite and muscovite to biotite. Biotization forms quartz-augen muscovite-biotite, biotite and chlorite schists. Alteration of cordierite porphyroblasts to biotite relinquishes 2.5 moles of Al₂SiO₅ and an unknown amount of water. The relinquished Al₂SiO₅ combines with quartz, water, iron, magnesium and potassium in a hydrous reaction forming biotite. Muscovite to biotite also requires additional Fe and Mg to complete the reaction. Retrogression of biotite to chlorite incorporates additional water but discharges 2 moles K⁺, 1 mole of Fe-Mg and 3 moles of SiO₂. These chemical reactions indicate alteration after porphyroblastic growth of cordierite. The total amount of SiO₂ dissolved to form biotite from quartz is unknown. The overall bulk rock chemistry increases in Fe (15.88-16.10%) and Mg (7.03-9.95%).

Porphyroblastic growth of andalusite, staurolite, grunerite and almandine follow biotization and chloritization. Porphyroblastic growth of andalusite from biotite frees Fe, Mg, Si, K and H₂O. Staurolites overprinting biotite, ripidolite, cordierite and an unknown Al₂SiO₅ species also free Fe (2.5 moles), Mg (2.5 moles) and H₂O (*n* moles) in a partial dehydration reaction. Garbenschiefer grunerite overgrows ripidolite and again cannot incorporate all Fe and Mg and Al stoichiometrically. The final porphyroblast growth is almandine over biotite and ripidolite. The overgrowth of biotite leaves excess K and Mg in the system. Overgrowth of almandine over ripidolite leaves 2.5 moles of Mg in excess.

Chloritized mica is incorporated and consumed in stage 2 cordierites and in stage 3 andalusite-staurolite-grunerite-almandine. Both alteration phases of stages 2 and 3 were chloritized prior to porphyroblastic growth. Cordierite, andalusite, staurolite, grunerite and almandine overgrow lineated and foliated fabrics hosting oriented ilmenite

and rutile inclusions. All porphyroblastic growth in each of the stages is then post-tectonic. Extensional shearing continued after stage 2. Secondary fluor-apatite which formed during stage 2 exhibits microboundage textures in QAMS sample 6078. Although large porphyroblasts are not rotated or sheared in footwall rocks, lineated zones may have been under constant tension.

ASG units formed during both stage 2 and 3. Crosscutting ECH veining in ASG units altered feldspars prior to silicification (sample 6063). ASG units are affected by secondary muscovite and biotite, but overall show strong silica replacement of feldspars and mica. The paragenetic relationship to quartz-augen schists is coeval as gradational contacts show diffuse silicification-mica alteration. Mass balance changes indicate a 14% SiO₂ increase. The overall calculated SiO₂ gain in footwall ASG units (Equation 7-1) is 221 million tonnes!

$$ASG_{Vol} = (1.658 \times 10^6 m^2)_{Area} \times (350 m)_{Depth}$$

$$SiO_{2Increase} = ASG_{Vol}(m^3) \times \rho \left(\frac{Kg}{m^3} \right) \times \frac{\Delta SiO_2 Kg_{ASG}}{100 Kg_{MGr}}$$

$$221 Mt SiO_{2Increase} = 580300000 m^3 \times \rho \left(2730 \frac{Kg}{m^3} \right) \times \frac{14 SiO_2 Kg_{ASG}}{100 Kg_{MGr}}$$

Equation 7-1 Silica increase in ASG calculation.

The precursor rock to biotite and chlorite schist units was muscovite-cordierite schist. This precursor schist had an estimated mineral abundance of 75-80% muscovite, 10% cordierite and 5-10% quartz resulting in a ~48.5% SiO₂ composition. Mass balance calculations show that SiO₂ accounts for 87% of the loss in elemental mass. We can estimate the precursor muscovite-cordierite schist lost ~31.65% SiO₂ from the parent monzogranites. The SiO₂ loss from muscovite cordierite schist illustrates the masking of large silica loss during stage 2 where muscovite predominated.

Mass balance changes from monzogranite to chlorite schist demonstrate a massive silica loss of 39.32 - 43.77% of the original SiO₂. Influxes of iron and magnesium

attribute 15.87 - 16.10% and 7.0 - 9.95%. Fe and Mg values in altered schists are 5.76-5.84 times the original iron content and 4.34-6.14 times the original magnesium content. Losses of Na are in line with the break down and dissolution of feldspars. Gains of titanium, phosphorus and potassium in biotite schists are congruent with mineral additions of ilmenite, monazite-apatite and mica. Trace elements generally stay within compositional variance with exception of Ni and Cu as a result from the breakdown of sulphides. All units show Pb loss of 18.22 to 32.95 ppm and correlate to the Pb loss in zircons.

The addition of aluminum in biotite and chlorite schists is artificial. Large porphyroblasts of aluminosilicates create heterogeneity and bias sample Al content. As a result, there is 5-6% reduction in abundance in biotite schists that do not have porphyroblastic growth. QABS units that have undergone the same biotitization and contain lesser porphyroblastic growth do not show Al influxes. Zirconium gains of 49.97 to 234.08 ppm above compositional variance are incongruent with thin section interpretation. The mineral zircon is of primary igneous origin and through alteration and volume loss should increase sequentially from QAMS to CS. Zircon influxes do not appear petrographically in footwall schists and may represent bias sample splitting during riffing. Secondary baddeleyite is identified in hematite ore but has not been witnessed in footwall schists.

7.3.2 Ore Zone

The paragenetic sequence of BIF to iron ore is both textural and mineralogical. BIF banding is obliterated by isoclinal folding and brecciation, as exhibited in samples 716 and 709. It is unclear whether brecciation of BIF stems from early transpositional folding or late extensional shearing. Silica leaching occurred after brecciation, leaving carbonates, phosphates and residual silicates in pore spaces. Carbonates, phosphates and silicate in pore spaces are identified as influxed impurities as they cannot be traced back to primary unaltered BIF. Residual carbonate, silicates are overprinted by granoblastic polygonal magnetite illustrating metamorphic recrystallization of magnetite breccia textures. Granoblastic magnetite is later oxidized at margins by hematite veins forming martite and microplaty hematite ores.

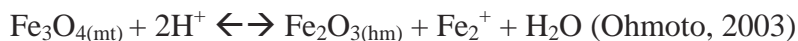
Oxidation of granoblastic magnetite grain boundaries is ubiquitous. Several reactions have been proposed to explain the redox change from magnetite to hematite. The first is the addition of oxygen as a redox agent (Equation 1). Equation 2 is proposed by Webb et al. (2003) invoking oxygenated meteoric water as the oxidizing agent. Another has been proposed by Ohmoto (2003) as a reversible acid-base reaction between magnetite and aqueous H^+ to liberate divalent iron and form water.



Equation 7-2 Magnetite to hematite redox reaction by free oxygen.



Equation 7-3 Magnetite to hematite oxidation by aqueous oxygen.



Equation 7-4 Magnetite to hematite oxidation by acid base reaction.

Textures in massive magnetite-hematite ore demonstrate veining created by fluid migration through granoblastic magnetite. Equation 1 requires vapor state of oxygen which is not identified texturally. Equation 2 is proposed for supergene enriched BIF in the Hammersley Basin. The equation is unlikely given the metamorphic history and reducing conditions. Also pitting textures and inverse vertical grading, characteristics of supergene enrichment are not present. Additionally, equations 1 and 2 culminate in a 2% molar volume (Robie et al., 1979) and contradict the coliform textures of hematite ore. Equation 3 is representative of textural veining as it requires aqueous fluids and the transformation results in volume loss of up to 32% (Ohmoto, 2003). Liberated Fe^{2+} is substantial and when combined with volume loss explains the moderate to strong porosity of hematite ores and stage 3 Fe gains in footwall schists.

Mass balance changes in ore are dominated by SiO_2 loss. Fv values of the BIF-ore transformation by Gressens' and arithmetic methods show more than double the amount of BIF, volumetrically, is needed to produce one volume unit of iron ore (2.17-2.25 cm^3 per 1 cm^3 iron ore). Gressens' method also shows a 21.1-26.1% increase in iron

above compositional variance implying either iron residually increase by silica volume loss or by mobilization during the formation of all magnetite and hematite ore types. Iron mobilization is suspect during the formation of magnetite ore because only hematization shows massive iron oxide mobilization in the form of veining (Plate 4-5). Relict martite veinlets in altered BIF sample 716 do crosscut silica banding but are not of the same magnitude. Also, hematization and martization reactions release iron into solution. The excess or “added” iron to the system during magnetite ore formation is interpreted to have come from excess volume of BIF being desilicified.

The amount of BIF needed to produce the 418 million tonne iron ore reserve is calculated to be 178-184 million cubic metres (Equation 7-5). As the reserves are confined to a 2 km long open pit, original areas can be calculated given static depths. For example, at a thickness of 100 metres, the length of the BIF unit would have been between 890-922 metres. If BIF was 25 metres thick, the length would have been between 3.56 and 3.69 km. Observations of several fold noses within the ore body with interbedded schists suggest BIF must have been closer to 25 metres in thickness. Desilicification of this vast amount of BIF is calculated in Equation 7-6 and results in a total of 247-256 million tonnes SiO₂ removed!

A

$$Ore_{Vol} = (4.18 \times 10^{11} Kg)_{Mass} \times \left(\frac{1 m^3}{5100 Kg} \right)_{Density^{-1}}$$

B

$$BIF_{Vol} = Ore_{Vol}(m^3) \times Fv(2.17 \text{ or } 2.25)$$

$$BIF_{Vol} = 178 - 184 m^3$$

Equation 7-5 Parent BIF volume calculation. Equation A uses the ore body mass and the density inverse to find ore volume (OreVol). Equation B derives the original BIF volume by multiplying the ore volume by the volume factors (Fv).

A

$$BIF_{Mass} = BIF_{Vol} \times \rho_{BIF}$$

$$6.509 - 6.749 \times 10^{11} \text{ Kg} = 178184 \text{ m}^3 \times \frac{3660 \text{ Kg}}{1 \text{ m}^3}$$

B

$$247 - 256 \text{ Mt} = SiO_{2Loss} = BIF_{Mass} \times \left(\frac{1 \text{ Kg BIF}}{.379 \text{ SiO}_2 \text{ Kg}} \right)$$

Equation 7-6 Total silica loss calculation from BIF to iron ore. Equation A shows BIF_{Mass} is equal to its volume (BIF_{Vol}) multiplied by its density ρ_{BIF} . Equation B calculates total silica loss (SiO_{2Loss}) by using the proportion of in Kg of silica in BIF from bulk rock analysis.

Several major and trace elements show enrichments and depletions within iron ores. The enrichment Ca, Mg and Mn in magnetite and hematite ores demonstrate mobilization of these elements during all stages of ore enrichment. Ca mobilization (0.1-0.43 g per 100 g sample) occurs throughout the process as minor constituent. Previous interpretations of carbonate proto-ore are not substantiated by mass balance calculations or texture. Mobilization of Ca is higher in hematite ores and associated with secondary hydrothermal monazite rims and overgrowths. Mn is mobile in its divalent state and precipitates when oxidized (Mn^{3+} and Mn^{4+}) as sulphides, carbonates and hydroxides (Krauskopf, 1957). The valence state and thus solubility is Eh dependent rather than pH (Yang et al., 2014). Small quantities of acid (HCl) can increase solubility of Mn by a magnitude of 5. Mobility and enrichment of Mn in magnetite ore corresponds to reducing conditions. Such Mn enrichment is not passed on to hematite ores. Lower Mn values in hematite iron ore may signify a mobilization environment that changed or sporadic mobility. Phosphorus is enriched in hematite ores by 0.36 % P_2O . The lack of phosphorus in magnetite ores does not correlate to the same paragenesis of sequential footwall increases. Numerous phosphate species mapped in feature scans are secondary but do not sum to substantial amounts suggesting some sampling, analytical or preparation error.

Trace element enrichment in magnetite ores are W, Bi, Mo, Ni, Zn and minor Co. W and Mo enrichment during magnetite ore formation requires a fluid temperature of ~300°C or more (Hedenquist and Lowenstern, 1994). Experimental dissolution of Bi₂O₃ by Tooth et al. (2013) shows mobility is possible through a range of temperatures but significant amounts of transport require >400°C fluids. Ni has low solubility and mildly dissolves in H₂O-HCl fluid experiments by Lin and Popp (1984). Cr is also very immobile in solution. Values of Ni and Cr must be from primary origin. Interleaved volcanics, ultramafics, or random clastic detritus may reflect the source of Ni and Cr.

Hematite ores are enriched above compositional variance in Y, V, Co and Ge. Increases of vanadium (7.37 ppm) and yttrium (2.49-4.95 ppm) differ from normalized values by MacLeod (2012) (V 0.47-1.49 ppm and Y 0.27-2.18 ppm). Hematite ore sample 6416 alone contains 111 ppm V which is 10X the average of BIF. Vanadium occurs in several oxidation states (V³⁺, V⁴⁺ and V⁵⁺) and is redox sensitive (Cornelis et al., 2008). The most common state is the oxidized V⁵⁺ (Sracek et al., 2014). Vanadium is mobile under mild to moderate oxidizing and acidic conditions. Oxidized vanadium species can hydrolyze into H_nVO₄ⁿ⁻³ species within a pH range of 3.6-6.8 (Wanty and Goldhaber, 1992). MacLeod (2012) noted vanadium depletions as an indication that *f*O₂ was buffered. Mass balance calculations clearly show increases. Mobility of vanadium is more likely a result of lower pH conditions related to the acid base reactions of Equation 3.

Geochemistry of ore zone chlorite schist contains high Cr and Ni values indicative of an ultramafic parent. High Al content in chlorite schist is in line with that of a quartzo-feldspathic rock and not consistent with an ultramafic precursor. Geochronology further demonstrates a single igneous zircon age characteristic of a volcanic rock. Hence, ore zone chlorite schists have a mixed ultramafic-volcanic parentage. This conclusion has been reached by Nicpon (2011) as well, though hangingwall stratigraphy was not fully known. Interleaving of volcanoclastics in ultramafics combined with Al, Cr and Ni immobility may account for garnet growth bands observed in ore zone chlorite schist (Figure 7-5).

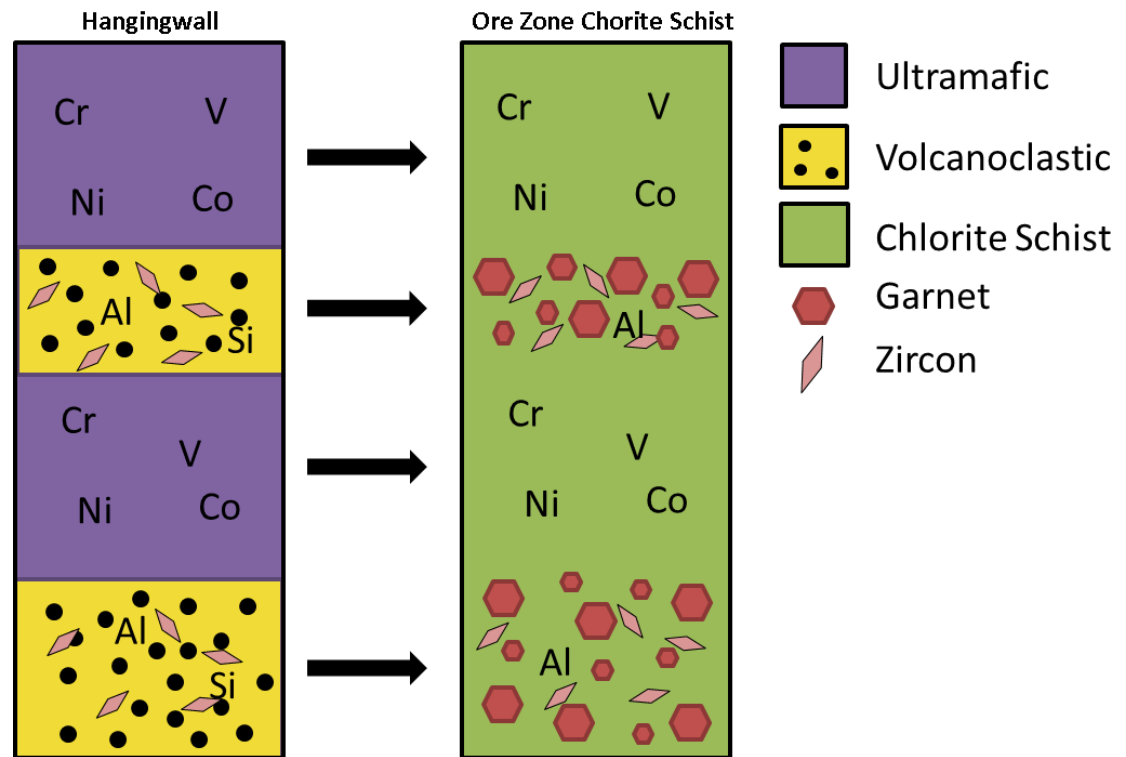


Figure 7-5 Interpretation of hangingwall ultramafics altering to chlorite schist. Interleaved volcanoclastic Al composition residually increases producing almandine during metamorphism.

7.3.3 Hangingwall

Hangingwall units are chlorite schist, biotite schist, ultramafic, ultramafic amphibolite, hornblende-amphibolite and volcanoclastic. Brittle and ductile deformation textures are identified in drill core and include brecciation, veining and lineation. The paragenesis of hangingwall units is almost the same as the footwall. Volcaniclastics and ultramafics are biotitized, chloritized and then overprinted by staurolite, grunerite and garnet. Large cordierites are overprinted by staurolite and biotite. Previous muscovite alteration is not apparent and evident of low feldspar content in hangingwall lithologies. Ultramafics are carbonatized and overprinted by talc. Talc retrogrades forming chlorite and serpentine and is then overgrown by anthophyllite bowties.

Hangingwall chlorite schist and biotite schist contain much higher Cr, V, Ni, Zn and Co than their footwall counterparts. Normalized REE patterns are flat with minor LREE enrichment in volcanoclastics and in hangingwall schists compared to footwall

schists. Hangingwall chlorite and biotite schist are therefore a product of alteration from a volcanic protolith not a granitoid. Small lenses of volcanoclastics and hornblende-amphibolite interbedded with ultramafics and ultramafic-amphibolite make discerning the exact protolith difficult. Nearly identical REE profile further complicates protolith determination via geochemical means.

7.4 Metamorphism

7.4.1 Assemblages and Facies

Metamorphic overprinting is not apparent in western footwall granitoids. Monzo and syenogranites in thin section from western drill holes only contain mild chlorite-actinolite growths from biotite. Footwall granitoids west of ASG units are defined as greenschist facies rocks.

Metamorphic overprinting in the immediate footwall and hangingwall lithologies to iron ore is higher grade and more complex. Hydrothermal alteration phases in footwall and hangingwall schists are terminated by large porphyroblastic growth of aluminosilicates. Both alteration stages have an independent and terminal metamorphic node. Terminal porphyroblastic growth overprints a partially to fully chloritized mica schist. Inclusions of chloritized micas are identified in all porphyroblasts, demonstrating retrogression prior prograde metamorphic recrystallization. Porphyroblastic growth of aluminosilicates incorporates oriented micas, Fe-Ti oxides and quartz-augens. Oriented inclusions are parallel to the external foliation, thus defining post-tectonic porphyroblastic growth. An exception is made for garnets in hangingwall chlorite and biotite schists. Poikiloblastic hangingwall garnets contain rotated aligned inclusions and an outer deformed foliated matrix. The foliated chlorite-biotite-quartz is rotated in porphyroblasts at 30°. Hangingwall garnet growth is therefore syntectonic.

Cordierite porphyroblasts are only stable in QAMS units with muscovite, quartz and minor biotite. Cordierite is altered and overprinted by biotite leaving relicts in QAMBS, QABS and biotite schists. The stable metamorphic mineral assemblage for stage 2 is cordierite-muscovite-quartz and biotite. Paucity and sporadic cordierite growth is demonstrated in the corresponding AFK metamorphic compatibility diagram (Figure 7-

6). QAMS compositions lie closer to the muscovite-biotite tie line than the muscovite-cordierite tie line. A cordierite-muscovite mineral assemblage is typical of low pressure-low temperature amphibolite facies in Buchan-type metamorphism (Winkler, 1979).

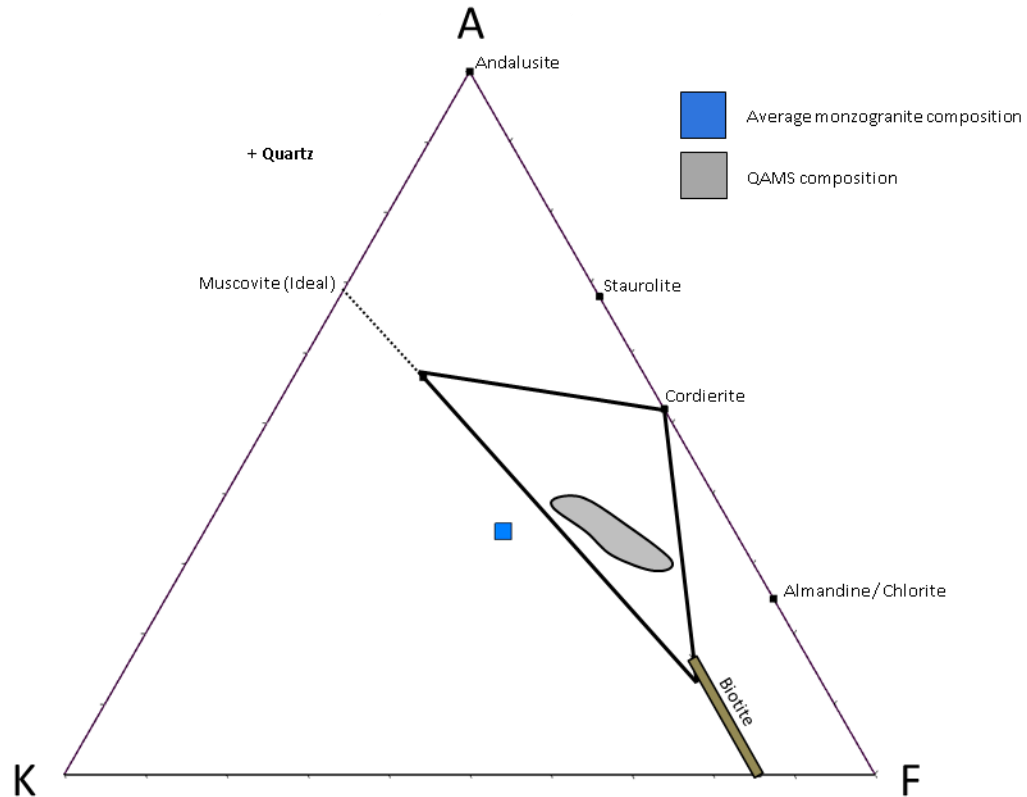


Figure 7-6 AFK diagram of QAMS metamorphic assemblage. Monzogranite composition is also plotted.

Metamorphism of stage 3 altered rocks (QAMBS, QABS, BS and CS) creates several stable prograde porphyroblasts, not all of which are in equilibrium. Andalusite is in equilibrium with staurolite and almandine in QAMBS, QABS and biotite schists. Almandine porphyroblasts incorporate staurolite as inclusions. In contrast, chlorite schists only contain porphyroblasts of grunerite and almandine. Garbenschiefer grunerite overprints chlorite which is then overgrown by large almandine porphyroblasts. Staurolite-garnet and grunerite-almandine are metamorphic prograde assemblages and not separate metamorphic events because the neither staurolite nor grunerite show retrogression textures. Trace element chemistry and textural paragenesis support this. The metamorphic mineral assemblage must be truncated into two assemblages due to bulk rock composition differences and stable metamorphic assemblages. QAMBS,

QABS and BS units have almandine-staurolite-andalusite-biotite-quartz assemblage and chlorite schists have an almandine-grunerite-ripidolite \pm quartz assemblage.

AFK compatibility representation of the two stages shows consistencies regarding mineral abundances (Figures 7-7 and 7-8). Biotite schist compositions plot further away from andalusite. The large separation indicates a higher likelihood of staurolite-garnet growth and the lower probability of andalusite nucleation. Prograde reaction rims in biotite schist sample 6205 show andalusite is coated by an amorphous Al-Si-Fe-H₂O material. Andalusite naturally substitutes Fe³⁺ for Al³⁺ in its six-fold coordinated Al-1 site. In spite of this, andalusite has only shown to contain limited Fe²⁺ in experiments (<1% FeO) (Meisel et al., 1990). EMP analysis of andalusite measured an average total Fe amount of 0.62% or 0.018 cation. Low iron content in andalusite reflects low Fe³⁺ in the biotite matrix. The low Fe content of andalusite with the described prograde reaction rims illustrates andalusite growth instability in a Fe²⁺ rich matrix.

The contrast of metamorphic assemblages between biotitized units and chlorite schist is due to differences in bulk chemical composition. Chlorite schist contains the highest iron-magnesium values and the lowest SiO₂. In order for biotite schist to host grunerite as stable assemblage, the composition must increase in either Fe or Mg because the two mineral assemblages are compositionally exclusive. The result is chlorite schist hosts minerals with higher Fe-Mg components (almandine and grunerite). Minerals with higher a Fe-Mg composition are more compatible with chlorite schists than lower Fe-Mg minerals.

MacLeod (2012) associated porphyroblastic almandine growth to the garnet-staurolite upper amphibolite facies zone of metamorphosed pelitic rocks. Rocks hosting stage 3 metamorphism are not of pelitic bulk composition and hold much higher Fe-Mg content and lower Si values. Figure 7-9 illustrates composition changes of stage 2 and 3 alteration. Higher Fe-Mg values change thermodynamics of metamorphic mineral reactions. Experimental mineral reaction projections by Miyano and Klein (1989) place the formation of grunerite at upper greenschist facies for iron rich rocks. Mel'nik (1982) identifies grunerite growth as low as 350°C for iron rich rock as well. Almandine growth

from chlorite and biotite occurs between 400-500°C in Fe rich rocks (Miyano and Klein, 1989). Moreover, electrum gold identified in the PS2 serpentinites and quartz veins (Herbranson, 2013) would have been mobilized at mid to upper amphibolite temperatures. Peak metamorphic temperatures by MacLeod (2012) were overestimated. This study defines stage 3 metamorphism to be low amphibolite facies.

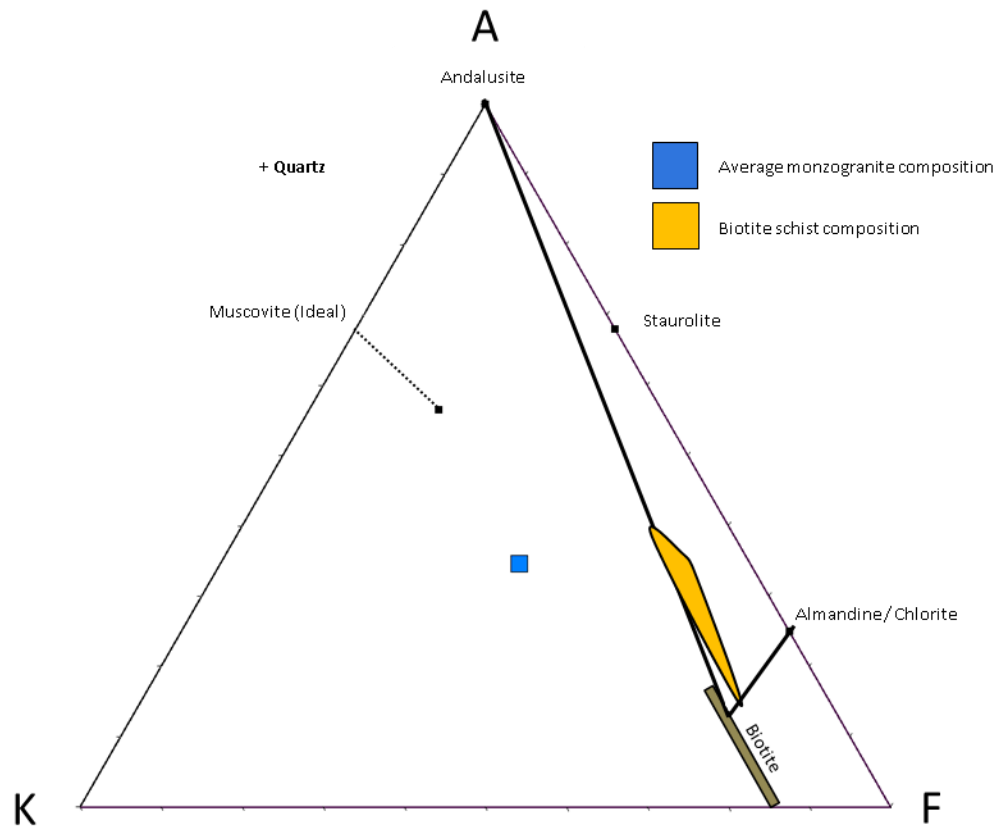


Figure 7-7 AFK diagram of footwall biotite schist assemblage. Average monzogranite composition is plotted as well.

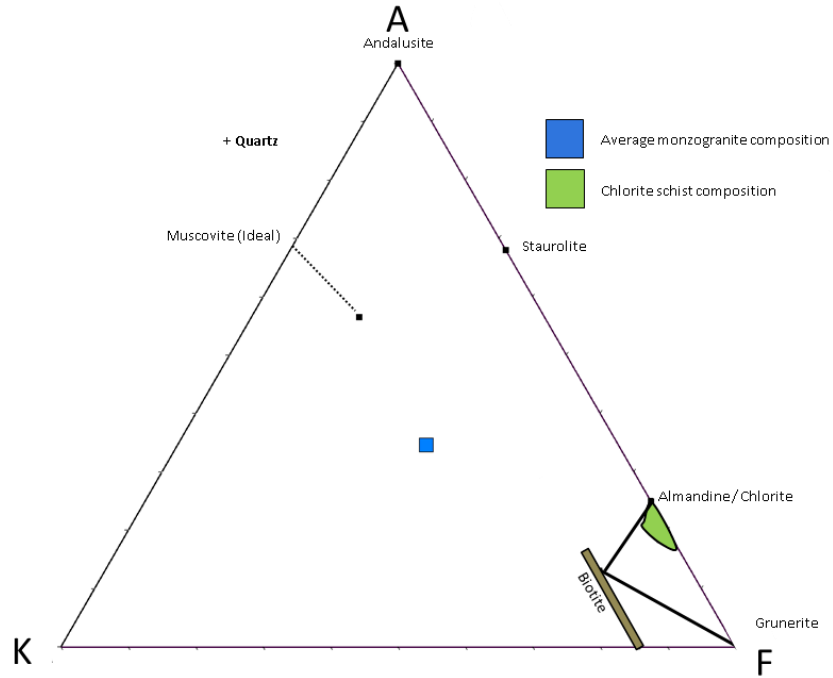


Figure 7-8 AFK diagram of footwall chlorite schist assemblage. Average monzogranite composition is plotted too.

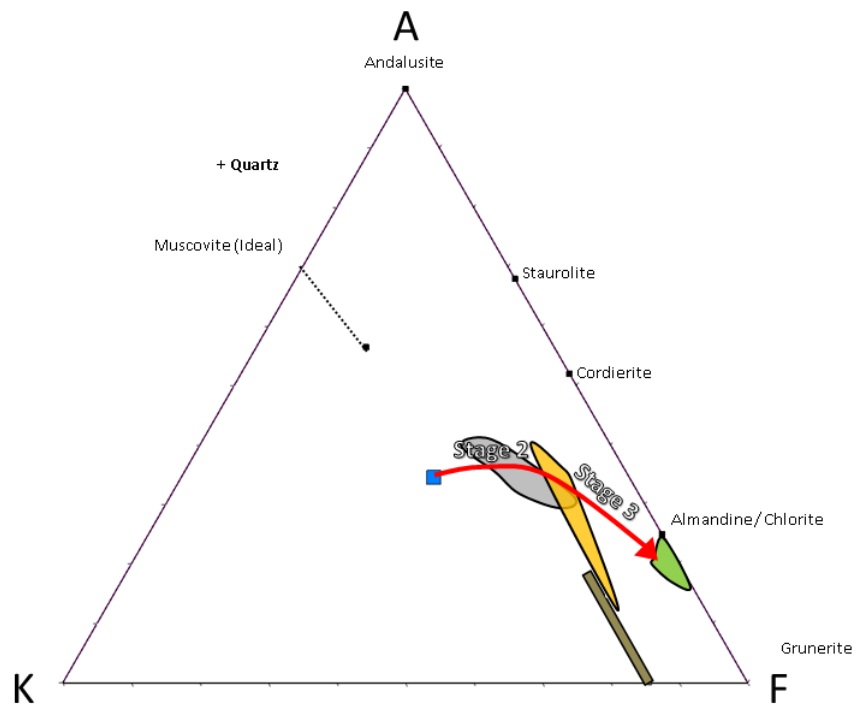


Figure 7-9 Compilation AFK diagram showing progression of footwall schist composition.

Ore zone chlorite schist hosts the same metamorphic assemblage as footwall chlorite schist with the addition of martite (almandine-ripidolite-grunerite-martite). Chlorite compositions are more uniform and reflect homogenization with the large surround Fe-Mg reservoir (BIF-HGIF). Hangingwall chlorite and biotite schists have the same mineral assemblages as the corresponding footwall schists, yet they have different parents. Ore zone and hangingwall chlorite schist are products of the same alteration and metamorphism as footwall rocks therefore are lower amphibolite facies as well.

Ultramafics have two units with independent metamorphic mineral assemblages. Ultramafic-amphibolites are a talc-carbonate or anthophyllite-talc assemblage and ultramafic units comprise serpentinite (antigorite) -chlorite \pm carbonate. Talc and anthophyllite are low to upper amphibolite facies ultramafic minerals indexed between 450° and ~725° (Fyfe, 1962; Greenwood, 1963, 1971; Moody, 1976; Chernosky and Autio, 1979). Serpentine is greenschist, reaching a maximum stability temperature of ~400° (Moody, 1976).

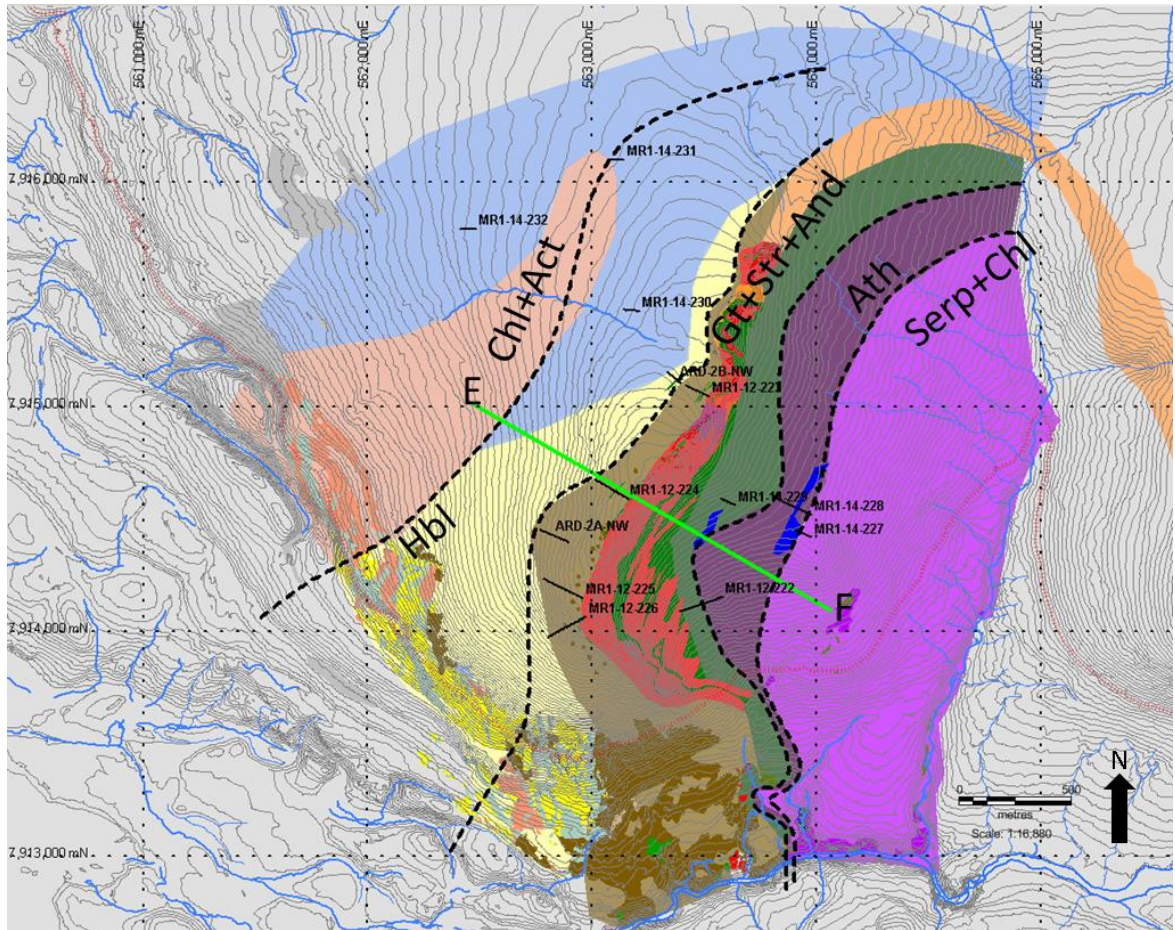
7.4.2 Isograds

Isograds determined from petrographic analysis of outcrop and drill core samples and are plotted in Figure 7-10. Distribution of amphibolite assemblages is limited to footwall schists, ore zone schists and the immediate hangingwall. Footwall, ore and hangingwall zones are lower amphibolite facies. Varying chemical composition of metamorphosed units provides several metamorphic mineral assemblages. The amphibolite facies is divided into several isograds indicating mineral-in boundaries which include: hornblende, garnet-staurolite-andalusite and anthophyllite. Greenschist facies are chlorite-actinolite in footwall granitoids and serpentinite-chlorite in hangingwall ultramafics.

Amphibolite facies begin at the hornblende isograd contact between alter-silicified granitoids and monzo-syenogranite in the most southwestern portion of the map area. The footwall metagabbro assemblage defines the hornblende isograd at this contact. The hornblende isograd extends northeast to hole MR1-14-231. The garnet-staurolite-andalusite isograd is confined to footwall, ore zone and hangingwall schists and is

bounded by the ultramafic-amphibolite contact. Anthophyllite defines the amphibolite facies of ultramafic rocks and sharply ends with emergence of serpentine. All amphibolite facie isograds include hornblende as a stable metamorphic phase.

Amphibolite facies is confined to lineated and altered footwall, ore zone and hangingwall rocks. Porphyroblastic growth is only present in altered footwall, ore zone and hangingwall schists. Distribution of amphibolite facies implies structure (extensional lineation) and alteration controls. Bounding greenschist facies granitoids and serpentinites illustrate a channelized and elevated geothermal gradient.



LEGEND

Overburden	Chlorite Schist	Ultramafic	Projected Chlorite Schist	Section Line
Monzogranite	BIF	Ultramafic-Amphibolite	Projected QAMBS	River
Syenogranite	HGIF	Hbl Amphibolite	Projected BIF	
Meta-Gabbro	Specularite HGIF	Projected MGR	Contour	
Altered Silicified Granitoid	Hudsonian Granite	Projected SGR	UTM Grid	
QAMBS	Mafic Volcanic	Projected ASG	Drill Hole Trace	
			Isograd	

Figure 7-10 Geology map with mineral in isograds. Cross-section E-F transect is also plotted.

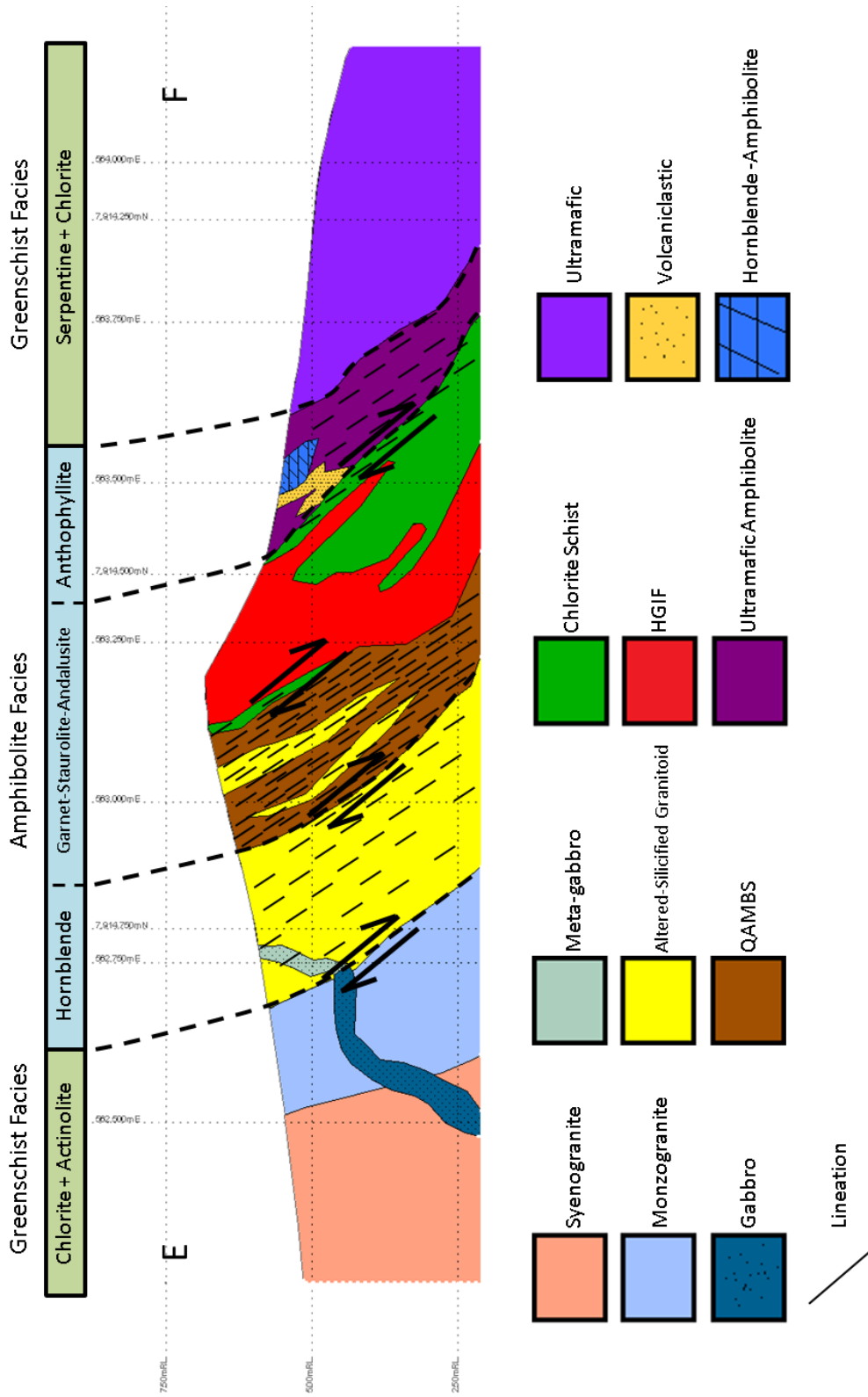


Figure 7-11 Tectono-stratigraphic E-F cross-section of Deposit No.1. Isograds and facies are label according to zone.

7.4.3 Thermometry & P-T Zones

Geothermometry involves the application of the Gibbs free energy equation to mineral systems in the form of Equation 7-7. More importantly it applies experimental solid solutions between minerals to understand the P-T conditions of a metamorphic system. The variables of Equation 7-7 are the change in Gibbs free energy (ΔG^0), the gas constant (R), temperature (T) and the equilibrium constant of the reaction (K). The equilibrium constant K_D in Equation 7-8 is calculated through experimentation. The change in entropy (S_r^0) and enthalpy (ΔH_r^0) is also calculated through experimentation. The system is then represented in a simplified equation where T can be calculated (Equation 7-9).

Garnet-biotite thermometry was completed using the almandine + phlogopite = pyrope + annite reaction completed by Ferry and Spear (1978) (Equation 7-10). Garnet chlorite thermometry used Dickenson and Hewitt (1986) experimentation data modified by Laird (1988) (Equation 7-11). The two thermometers are ion exchange thermometers that substitute Fe^{2+} and Mg^{2+} between minerals. Both are excellent thermometers because they are independent of pressure (Will, 1998).

Biotite and chlorite schist units, with the late porphyroblastic almandine growth, were calculated for thermometry. Two were samples were almandine chlorite schist from the ore zone and one footwall biotite schist. It is important to note that Fe^{3+} was not determined for the minerals species nor was a value approximated. The actual Fe^{2+} ion exchange of may be lower. But given the mineral textures of andalusite and strong mobility of iron, Fe^{3+} should be in low supply within the biotite-chlorite matrix. Calculations were made using Geothermobarometry software (GTB) v2.1 created by Frank Spear and Matthew Kohn (1999).

$$0 = \Delta G^0 + RT \ln K$$

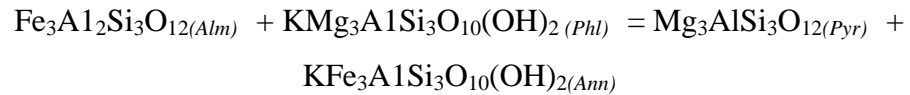
Equation 7-7 Gibbs free energy equation.

$$K_D = \frac{X_{Fe}^{Bt} \times X_{Mg}^{Grt}}{X_{Mg}^{Bt} \times X_{Fe}^{Grt}}$$

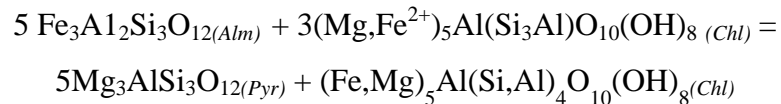
Equation 7-8 Equilibrium constant equation for garnet-biotite reaction. Activity coefficients are labeled X.

$$\left(\ln K_D = \frac{-2109}{T(k)} + 0.782 \right) = \frac{-\Delta H_r^0}{RT} + \frac{\Delta S_r^0}{R}$$

Equation 7-9 Derived thermodynamic equation for garnet-biotite thermometry (Ferry and Spear, 1978).



Equation 7-10 Garnet-biotite reaction.



Equation 7-11 Garnet-chlorite reaction.

The results of garnet-chlorite and garnet biotite are listed in Figures 7-12 and 7-13. Mn zoned almandine garnets from ore zone chlorite schist show an increase in temperature from core to rim. Equilibrated temperatures projected past the andalusite zone are not significant because the metamorphic facies of the stage 3 garnet growth is stable with andalusite. The average core temperature recorded within the andalusite zone was 368.7°C. The max intermediate zone temperature measured 432.3°C and the max rim temperature reached 480.9°C. Garnet biotite temperatures reached 432.2°C at core compositions and 442.10°C at rim compositions. PS2 garnet thermometry of homogenous almandine reached a peak temperature of 550°C.

Temperatures across Fe-Mn zoning increment to peak rim temperatures. Mn zoning in ore zone garnets display a buckshot or diffuse core and sharp margins known as mixed-type zoning (Banno and Chii, 1978). EMP analyses plotted in Figure 4-22 grade from Mn to Fe rich zones without a clear grouping. Iron, magnesium and manganese zoning of garnet porphyroblasts is attributed to disequilibrium with respect to the surrounding matrix (Trzcieski, 1977; Spear and Daniel, 2001). Atherton (1968) showed garnet growth during prograde metamorphism increases Fe and Mg and depletes Mn and

Ca, explaining Mn to Fe transitions in garnet. Diffuse zoning is then related to disequilibrium and depletion of Mn during growth. Mn enriched rims display a minor overall growth. Enriched Mn rims have been proposed by Banno and Chii (1978) to be growth at higher temperatures and equilibrium with the surrounding matrix.

Temperatures derived from individual thermometers show similar temperatures in different footwall and ore zone rocks. Given the previously discussed paragenetic sequence, temperatures from both thermometers are the result of the same late stage metamorphic event. Calculated temperatures of samples are consistent with upper greenschist to lower amphibolite facies metamorphism. Garnet growth at low temperatures is not uncommon. Spessartine garnet growth at greenschist facies is common, identified by Brown (1967;1969), in the Otago schists of New Zealand. Makrygina and Suvorova (2011) depict spessartine garnets form at temperatures as low as 350°C.

Experimental mineral phase reactions of staurolite from chlorite and muscovite intersect peak garnet-chlorite temperatures at 476°C and 900 bars. The garnet-chlorite thermometry intercept with the pelitic almandine-chlorite mineral phase reaction is at a pressure of 200 bars and a temperature of 479°C. The temperature and pressure intercept of PS2 garnet-chlorite thermometry with the chlorite-almandine reaction for metapelites is 550° within the andalusite phase zone. In both examples, garnet remains as the peak temperature index mineral and staurolite the peak pressure index mineral.

Mineral reaction curves of Fe rich rocks by Miyano and Klein (1989) are also plotted in Figure 7-15 and show biotite-chlorite can form almandine and later grunerite at lower temperatures, ideally near the core temperatures of ore zone almandines. Temperature variations are the result of thermodynamic differences related to composition. Mineral reaction systems in SiO₂ rich systems (pelites) are not applicable due to the ultramafic-high Fe - Al composition of footwall and ore zone schists. P-T loops cannot be constructed at this time given the difference in temperature of mineral reaction curves. Also no common geobarometer is present, other than andalusite. The

maximum metamorphic depth is defined to be 3550 bar or 13.5 km (continental crust density).

Localized high heat flux coupled with structurally and chemically controlled porphyroblastic growth is not indicative of regional Barrovian or Buchan metamorphism. Previous metamorphic temperatures were estimated by Jackson (2000) and MacLeod (2012) to be mid-upper amphibolite facies (550°-700°C). Garnet-biotite and garnet-chlorite illustrate lower temperatures. The new P-T zone contrasts the area defined by Jackson (2000) by mineral assemblage, temperature (100°-200°C) and pressure (1000 bars) (Figure 7-14). Locally, P-T conditions may have reached 550°C as seen in at the PS2 site. Differences arise from the interpretations of stable metamorphic assemblages, lack of electron microprobe data and unknown paragenesis. Also, the geobarometry reactions applied by Jackson (2000) are not observed in thin section. MacLeod (2012) identified clinopyroxene in sample 4-8 at Deposit No.4 and attributed its formation to temperatures above 500°C (600-700°C) based on metamorphic assemblages outline by Klein (2005). The sample was of amphibolitic-wacke adjacent to crosscutting pegmatites. The observed clinopyroxene was surrounded by quartz and not in contact with any other minerals, violating metamorphic equilibrium. The sample area may have also been influenced by contact metamorphism by the adjacent crosscutting pegmatite.

Temperature differences of 100-200° exists between footwall-ore zone schists and hangingwall ultramafic amphibolites (Figure 7-15). Anthophyllite assemblages initiate at 600°C at the expense of talc. The works of Trommsdorff and Evans (1972); Evans and Trommsdorff (1974) combined by the experiments of Trommsdorff and Connolly (1990) have strongly shown that CO₂ and Fe strongly affect the anthophyllite stability field. CO₂ and Fe mobility within ultramafics is unknown. Anthophyllite assemblages (ultramafic-amphibolites) are in sharp contact with serpentinites (700° vs 400°C) alluding to a lower P-T condition.

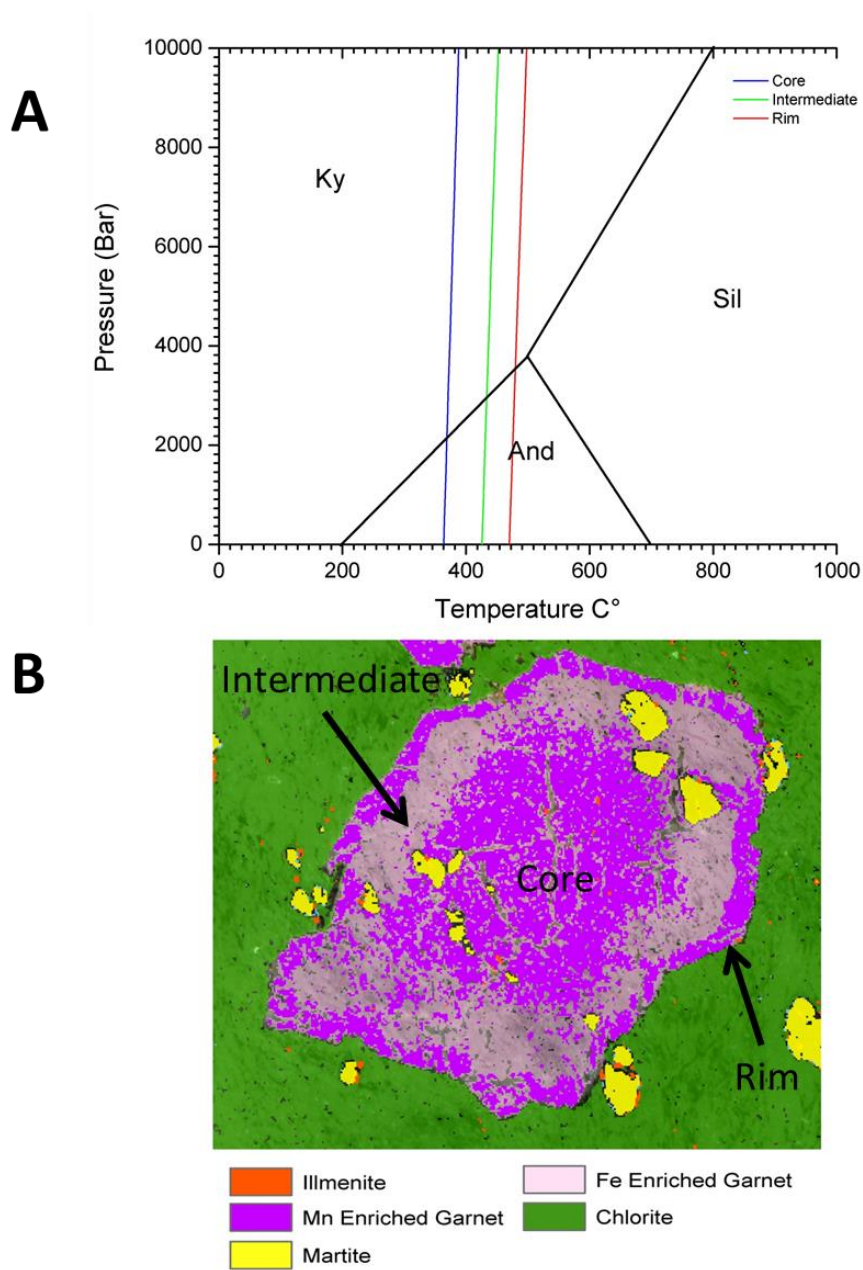


Figure 7-12 Garnet-chlorite P-T diagram (A) and EDS map of Mn zoned ore zone almandine (B). K_D temperature lines from average core, intermediate and rim zones in almandine from sample 6220A. Picture B is a EDS map of Mn zoned almandine.

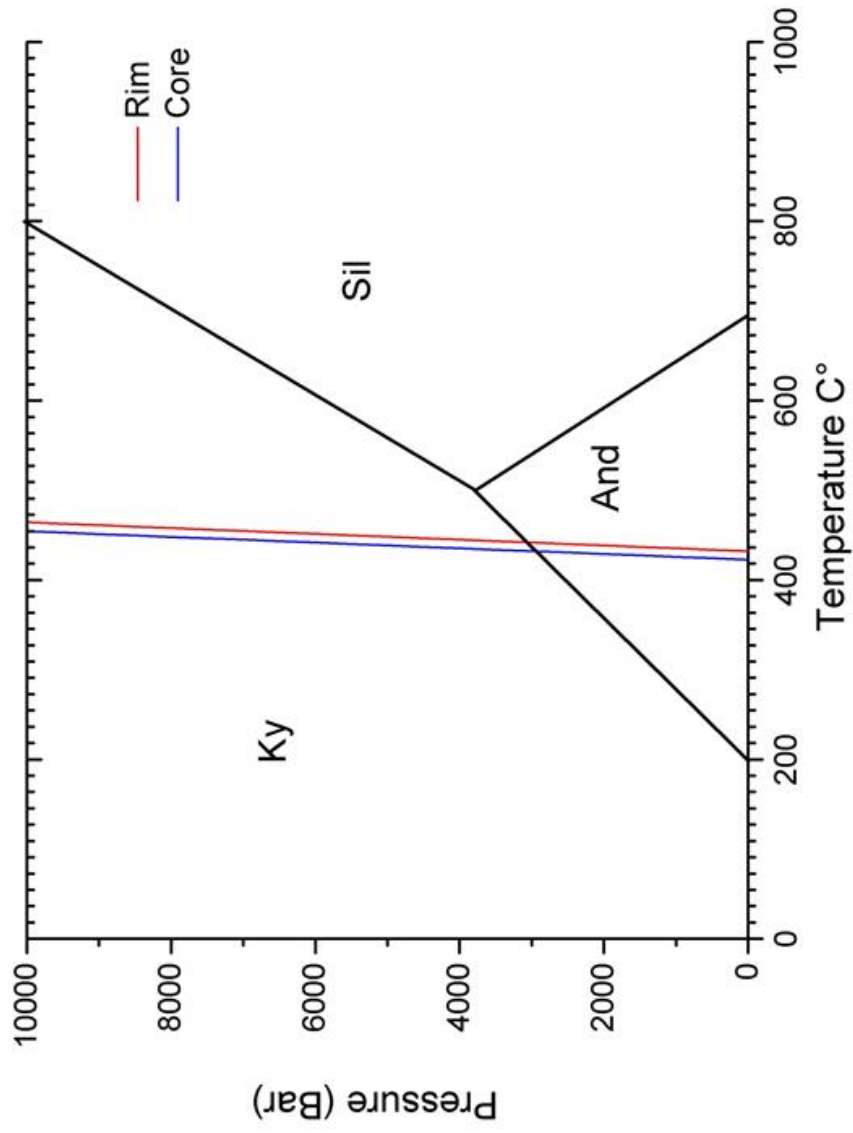


Figure 7-13 K_D temperature lines of garnet biotite thermometry of core and rim zones from sample 6227

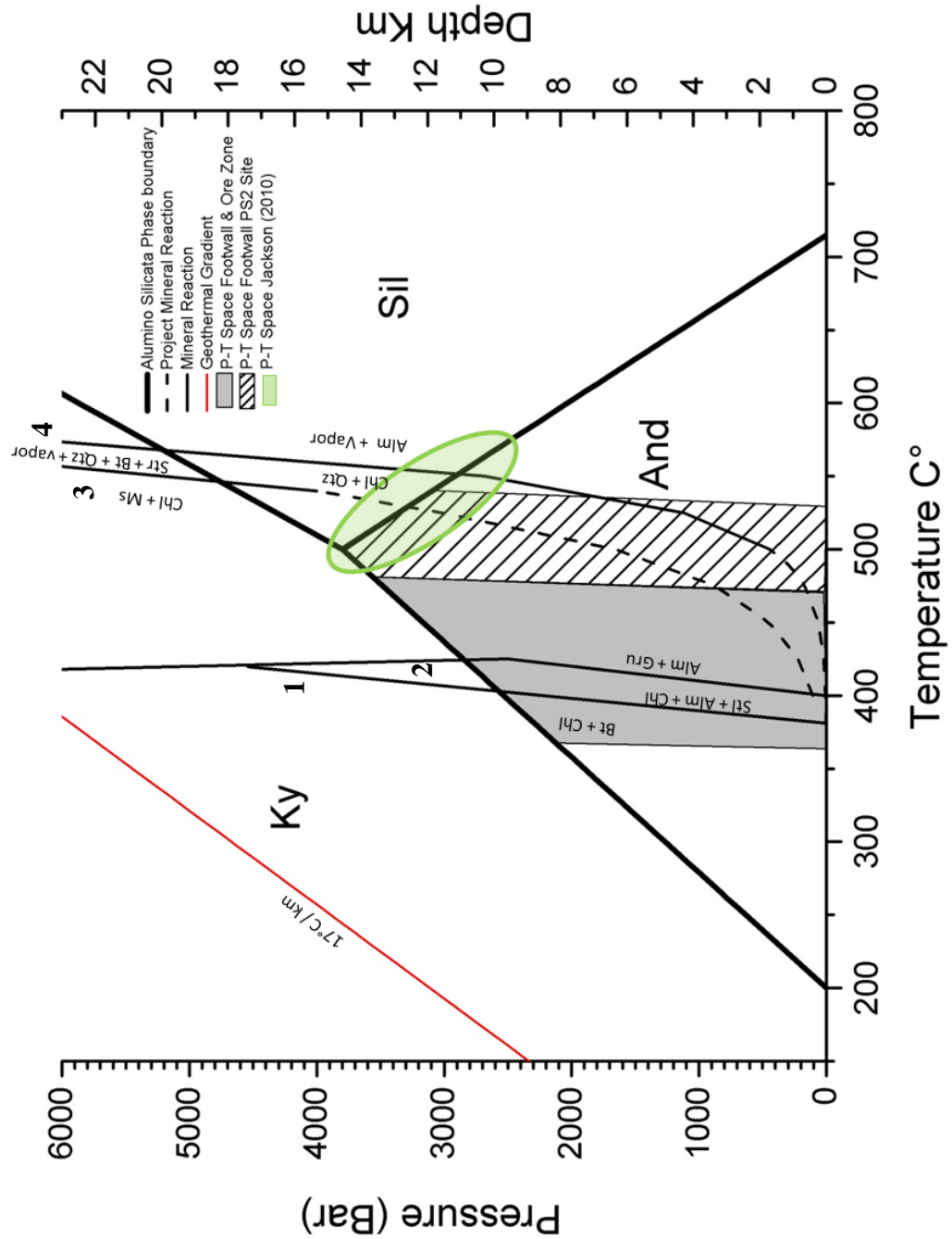


Figure 7-14 P-T diagram of garnet-chlorite thermometry with mineral reaction lines. Equations 1 and 2 are taken from Miyano and Klein (1989) and represent mineral reactions of biotite and chlorite to almandine, chlorite, grunerite and stilpnomelane in Fe rich rocks. Equations 3 and 4 are derived from Hoschek (1969) and Hsu (1968) represent the staurolite and garnet experiments of pelitic rocks.

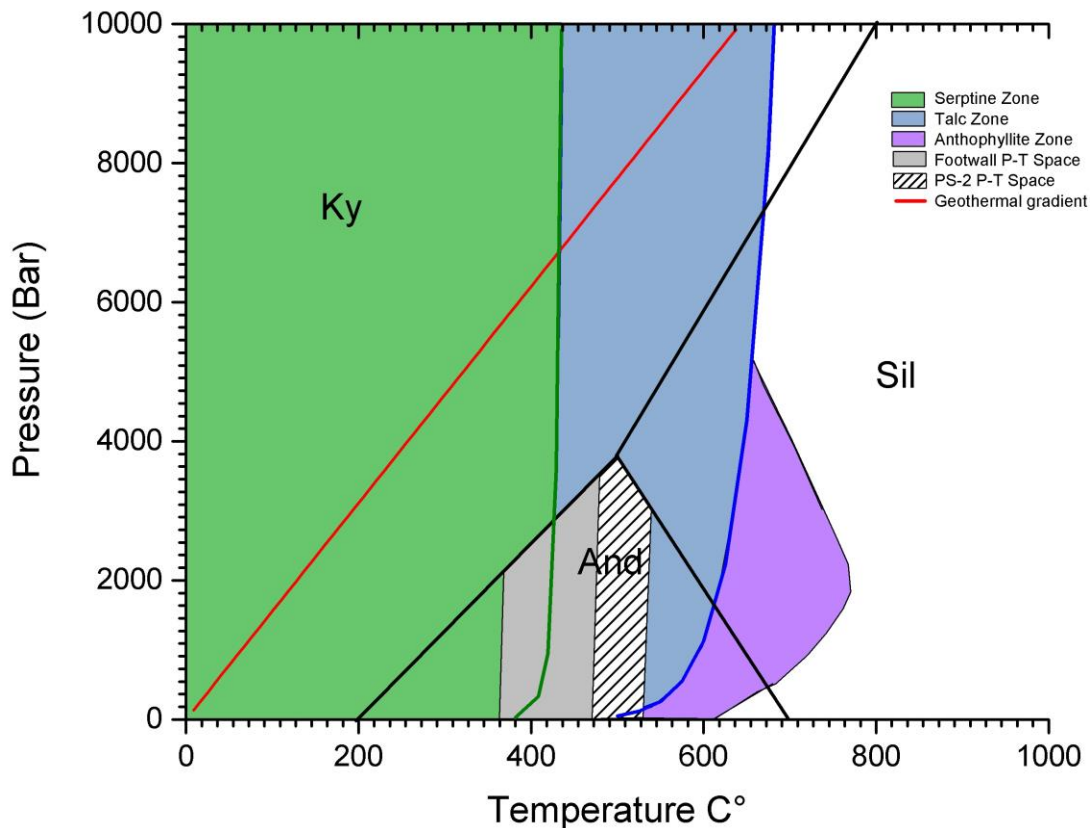


Figure 7-15 P-T diagram displays serpentine, talc and anthophyllite stability fields. Serpentine and anthophyllite stability field is plotted on the experiments by Moody (1976) and Chernosky and Autio (1979). P-T zones of footwall and ore zone schist are outline and filled.

7.5 Tectonic-Paragenetic Model

Revisions to tectonostratigraphic setting, in conjunction with zircon geochronology, reveal a 148 Ma nonconformity between the Mesoarchean granitoid basement and Neoproterozoic supracrustals. Extensional lineated-mylonitic shear zones at the interface between footwall granitoids and supracrustals are identified and measured. Orientation of lineations in mylonitic shear zones average $074^{\circ}/54^{\circ}$. Lamination orientation is nearly perpendicular to the last F_3 axial fold planes and so forth not a consequence thereof.

Paragenesis of mylonitic shear zones (footwall schists) illustrates massive silica loss in the form of two alteration events separated by a cordierite and andalusite-

staurolite-grunerite-almandine growth. Paragenesis of footwall shear zones is congruent with formation of ore zone and hangingwall schists.

Mass balance calculations determine 10-20% volume losses in mylonitized-altered footwall schist units. Contacting footwall biotite and chlorite schists to HGIF may have lost up to 60% volume. High volume losses in mylonitized footwall schists is comparable to tectonic studies of other mylonite shear zones in the Qaudrilátero Ferrifero, Brazil (Hippertt, 1998), granitic mylonites in the Blue Ridge Province, central Appalachians (Bailey et al., 1994) and mylonitized granodiorites within detachment faults in Mojave Desert, California (Glazner and Bartley, 1991). Inputting such volume factors into the Gressens' equation for biotite and chlorite schists results in mass balance changes above or below current compositions or below total component availability from parent monzogranite. The conservation of volume is related to hydrothermal alteration of quartz forming mica in reactions 4-5 and 4-9. Molar volume increases as quartz alters to muscovite and biotite are 72.5 cm^3 and 93.0 cm^3 per mole. Volume gains by quartz-mica reactions are not directly proportional to the system because the original amount of quartz reacting to form muscovite is not known. What can be said is that the reaction involves substantial volume gain. It also must be said that the transition from feldspar to muscovite does account volume loss. K-feldspar to muscovite and plagioclase to muscovite reactions produce 49.3 cm^3 and 14.2 cm^3 per mole volume loss. Volume gains and losses are well known in ductile shear zones. A study conducted by Wibberley (1999) quantified a 51% volume gain from muscovite cemented ultracataclasites and a 49% volume loss in neighboring phyllonites in the Pelvoux Massif.

The formation of mylonitic shear zones is attributed to seven softening processes outlined by White et al. (1980); superplasticity, geometrical softening, continual recrystallization, reaction softening, chemical softening, pore fluid effects and shear heating. All of these processes require internal-environmental changes to differ rheological properties. Foliations of hydrothermal micas are defined and bounded by lineations. Hydrothermal micas form strong foliations oriented parallel to lineations. The mica foliations are interstitial and wrap around lineated quartz and feldspar. Foliation textures are coeval to the extension as lineation did not generate preferentially

on a foliation plane. Hence, hydrothermal alteration is coeval to penecontemporaneous with shearing. The feldspar to mica and the quartz to mica alteration during the formation of footwall mylonites is defined as reaction softening (White and Knipe, 1978).

Reaction-enhanced softening is due to fluid increase producing micas with lowering coefficients of friction (White and Knipe, 1978). Another way is for influxing fluids to directly reducing shear stress. This is known as chemical softening (White and Knipe, 1978) and identified in shear zones of the Lewisian complex (Beach, 1980). Small amounts of water introduced to shearing may drop flow stress rates by 50% in quartz. The coeval origin of hydrothermal micas in extensional mylonitic shear zones provides an explanation as to how brittle-ductile deformation occurred at higher crustal depths.

Studies of shear zones and faults in relation to fluid flow have correspondingly illustrated porosity and permeability that have allowed and further aided metasomatic processes (Dipple and Ferry, 1992; Bruhn et al., 1994; Eichhubl and Boles, 2000). Mylonitic shear zones in the French Massif Central measured porosities of 1% at margins and up to 8% in central zones (Géraud et al., 1995). Permeabilities of the French Massif Central shear zones are 5×10^{-16} and $5 \times 10^{-15} \text{ m}^2$ and are on par with estimated values of Dipple and Ferry (1992) (10^{-17} to 10^{-15} m^2). More importantly mylonitic permeabilities form an anisotropic network of tubes and fractures parallel to shearing that can channelize fluids (Géraud et al., 1995). The channelization of permeabilities in mylonitic shear zones justifies structural controlled alteration in hydrothermally altered footwall units. Granitoids that are not lineated show no sign of alteration. Heavily lineated granitoids show the highest degrees of alteration forming schists composed of hydrothermal micas. Lineated-foliated fabrics also explain channelization of heat flow forming localized porphyroblastic growth.

As a result of the described extensional shear zones and alteration, a new postcollisional-tectonic model is proposed for the paragenesis of BIF to iron ore. First, the Transhudson Orogeny isoclinally folds and displaces the Mary River Group, creating a structural nonconformity. The single igneous zircon age population from footwall schists compared to the single age populations in interbedded ore zone chlorite schist define a 148 Ma gap and support structural juxtaposition.

An extensional brittle environment commenced after folding producing cross-cutting epidote-carbonate-hornblende veining of stage 1 alteration. Extension continued forming quartz-augen lineations aided by inflowing of silica poor fluids breaking down feldspars, in turn producing the muscovite alteration of stage 2 (1873 ± 20 Ma). Elevated temperatures and fluids weakened shear strengths of the footwall monzogranites causing chemical and reaction softening which increased shearing at contact zones to supracrustals. Channelized silica poor fluids altered folded and brecciated BIF and volcanics while at the same time transporting vast amounts of silica out of the deformed supercrustals, enriching footwall schists in Mg, P, Ti, and minor Fe. Silica poor hanging wall lithologies buffered silica-poor fluids while enriching them respect to Mg. Hydrothermal fluids of stage 2 also produced secondary fluor-apatite, ilmenite and phengitic muscovite. Percolated fluids eventually were buffered by siliceous footwall granitoids that enabled expulsion of silica by saturating hydrothermal fluids. Stage 2 hydrothermal alteration partially retrogrades to chlorite and fully terminates by metamorphic recrystallization and porphyroblastic growth of cordierite.

Another extensional event followed cordierite growth supported by microboudinaged stage 2 fluor-apatites and rotated syntectonic hangingwall garnets. Fluid influxes followed, culminating in stage 3 alteration. Stage 3 hydrothermal fluids strongly mobilized Fe^{2+} forming hematite ores and variants thereof through martization of recrystallized granoblastic magnetite. Stage 3 fluid compositions are interpreted to be lower pH because of the mobilization Fe^{2+} and volume loss illustrated in Equation 3. Fe-Mg mobilization in footwall QAMS and cordierite-muscovite schist units resulted in strong pervasive biotization of muscovite and cordierite. Elements Fe, Mg, Ti, P, Cu and Ni are enriched in footwall schists. Hematite ores are enriched in Ca, Mg and P. Hydrothermal biotite alteration retrogrades to ripidolite chlorite. Garbenschiefer grunerite and large almandines overprint the chloritized matrix in a dehydration reaction.

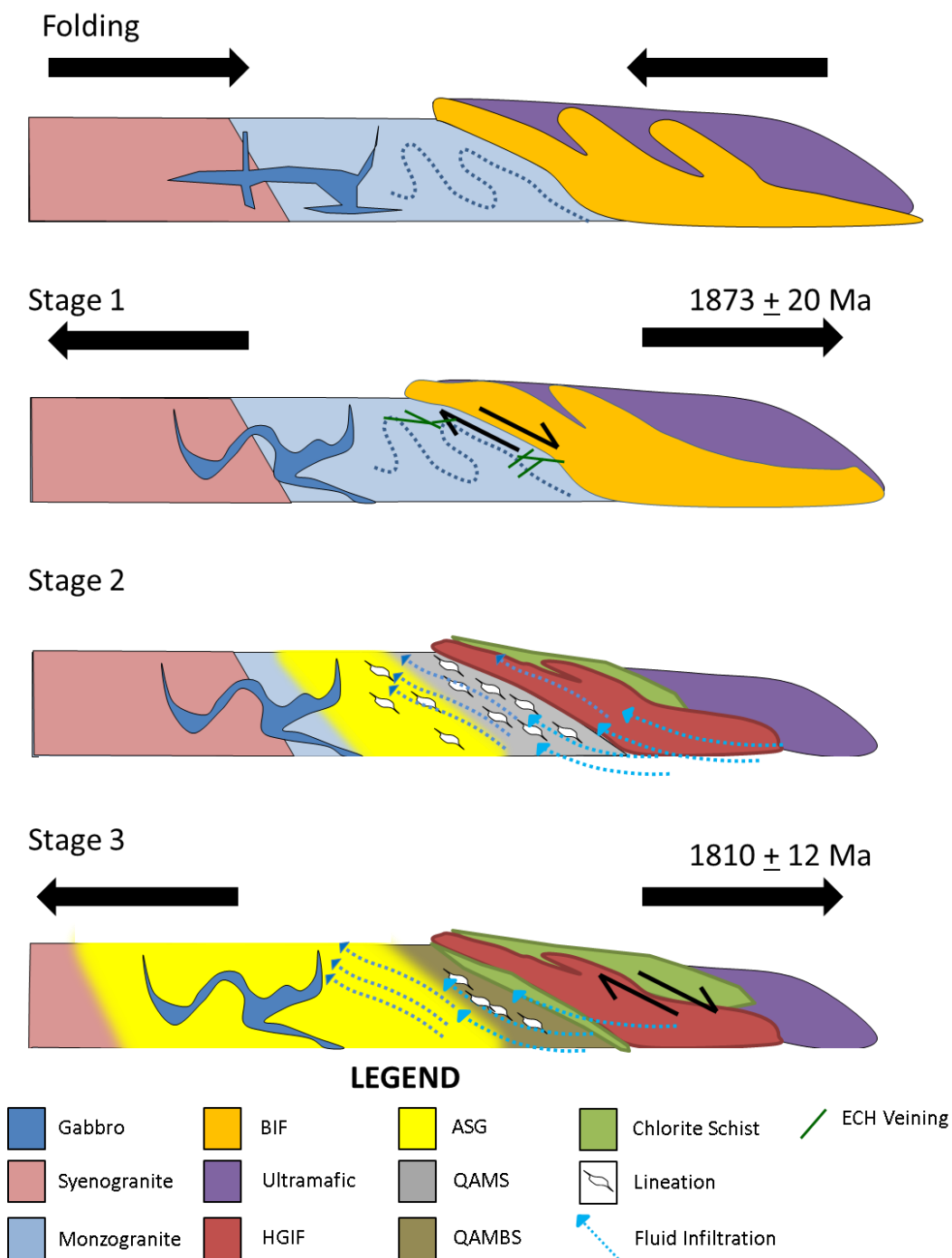


Figure 7-16 Metallogenic model for high grade iron ore in the Mary Group. Three stages of alteration with extension are displayed. Folding and thrusting prior to 1873 Ma emplace the MRG and deformed adjacent basement rocks. Extension followed first, creating the epidote-carbonate-hornblende veining. Hydrothermal fluids ensued after, altering feldspar and quartz to muscovite and silicifying footwall granitoids (stage 2). Stage 3 shows more extension with shearing in the hangingwall accompanied by biotization/chloritization.

Chapter 8 Conclusions

8 Introduction

Investigation of Deposit No.1 lithologies has generated considerable data pertaining to mineral textures, geochemistry and geochronology. Linking this information to the complex paragenetic history allows for several conclusions regarding the Mary River Group's lithology, stratigraphy, metamorphism and relationship of BIF to direct shipping iron ore. These conclusions are presented below. Comparisons are drawn to previous investigations by MacLeod (2012) and Jackson (1966; 2000).

8.1 Lithotectonic Setting

At Deposit No.1, the Mary River Group is defined as a Neoproterozoic (2745 ± 11 Ma) BIF-ultramafic-volcanic package with lesser mafic intrusives juxtaposed structurally against a ~2900 Ma Mesoproterozoic granitoid basement. The Neoproterozoic supracrustals of the Mary River Group are isoclinally folded prior to structural emplacement against basement. Supracrustals are composed of Algoma-type BIF, serpentinite (komatiite?), gabbro (hornblende-amphibolites) and intermediate composition volcanoclastics. Basal quartzites, metasediments and paragneiss previously defined are re-interpreted to be quartz-augen mica schists deformed after tectonized monzogranite. Basement complex lithologies are composed monzogranites, syenogranites and gabbro. Monzogranites transition into quartz-augen, biotite and chlorite schist toward the contact to HGIF. Monzogranites directly contact BIF in the northern limb. Syenogranites exhibit similar alterations but are not in direct contact with HGIF. U-Pb zircon geochronology dates QABS units to be 2898 ± 11 Ma. Therefore, footwall zircon geochronology indirectly dates parent monzogranites to be ~2900 Ma. Syenogranite and gabbro phases are younger than 2900 Ma but older than the Hudsonian structural overprint. The age of late granite and pegmatite crosscutting the MRG and their relation to hydrothermal influx is unknown.

BIF and HGIF form the basal unit of the MRG at Deposit No.1 and separated by 10-500 metre thick quartz-augen schist to footwall granitoids. Bounding schist units are

products of hydrothermal alteration and metamorphism of both Mesoarchean and Neoproterozoic packages. Iron ores form massive tabular bodies hosting lenses of relict-brecciated BIF and interleaved almandine-grunerite-ripidolite schists. Direct shipping iron ores are classified into magnetite, magnetite-hematite and hematite ores.

8.2 Metamorphism & Paragenesis

The metamorphic history of the Mary River Group at Deposit No.1 is complex, from upper greenschist to lower amphibolite facies with localized mid amphibolite facies. Chlorite facies are defined by chlorite-actinolite and serpentine assemblages in footwall granitoids and hangingwall serpentinite and volcanoclastic units. Amphibolite facies is characterized by coarse porphyroblastic growth of cordierite, andalusite, staurolite, grunerite and almandine in footwall, ore zone and hangingwall schists and anthophyllite growth in the immediate ultramafics contacting HGIF. Porphyroblastic growth of Fe-Mg silicates punctuates two retrograded hydrothermal alteration episodes that desilicified the footwall monzogranites, BIF and the immediate hangingwall. The prograde, retrograde and hydrothermal alteration overprints are structurally confined by foot and hangingwall extensional shear zones. The occurrence and equilibrium texture of andalusite after stage 3 alteration places amphibolite facies within a low pressure to moderate temperature environment (368-481°C at 3550 bars max). Index minerals of kyanite and silimanite are not observed at Deposit No.1.

Garnet-biotite and garnet-chlorite thermometric calculations of footwall biotite and ore zone chlorite schist reach maximum temperatures of 481°C with localized zones of 550°C. Thermometry intersections to experimental mineral reactions curves representing prograde mineral sequences cannot be utilized due to the high Fe-Mg-Al content of altered footwall schists. Staurolite porphyroblasts likely represent peak pressure and almandines peak temperature. Metamorphic mineral assemblages in footwall rocks are defined in two stages: a cordierite-muscovite-biotite-quartz stage, and (A) andalusite-staurolite-garnet-biotite stage and (B) almandine-grunerite-ripidolite stage. Ultramafic-amphibolites have an anthophyllite-talc assemblage. High pressure and temperature aluminosilicate polymorphs, kyanite and silimanite, are not observed. The

P-T space defined by andalusite and thermometry are lower than the estimated and calculated zones of Jackson (2000) and MacLeod (2012).

The transition of BIF to direct shipping iron ore involves extensional shearing, an elevated geothermal gradient and influx of hydrothermal fluid to remove massive amounts of silica. The paragenesis is divided into three stages. Stage 1 is the formation of brittle deformation forming ECH veining mobilizing carbonate and Mg. Stage 2 involves extensional mylonitization of footwall with influx of silica poor fluids. These fluids alter feldspars and quartz to muscovite which then retrograde and are overprinted by cordierite porphyroblasts. Stage 2 is the primary loss of silica event forming high grade iron ore. Stage 3 further desilicifies the footwall, ore zone and hangingwall through biotitization mobilizing large amounts of Fe and Mg. Alteration retrogrades again and is overprinted by andalusite, staurolite, grunerite and almandine porphyroblasts. Mass balance changes depict enrichment of P and Ti during these alteration stages as well as. Mylonitized footwall units, interleaved ore zone schists and brecciated BIF provided conduits for fluid migration and interaction. Hydrothermal monazites are identified in footwall, ore zone and hangingwall schists. The same monazites are also documented in altered BIF, magnetite-hematite and hematite ore. Hydrothermal monazites are not present in unaltered granitoids or hangingwall volcanics or ultramafic units. These monazites are texturally and chemically coeval with footwall, ore zone and hangingwall hydrothermal alteration. U-Pb dating of hydrothermal monazites temporally bracket silica loss between 1873 ± 73 to 1810 ± 22 Ma, a 41-105 Ma period.

8.3 Model Validation – Hypothesis Testing

At the beginning of this study, 5 questions were hypothesized to test models proposed by Jackson (2000) and MacLeod (2012). The following provides answers to the questions asked.

The initial metamorphic-deformation model by Jackson (1966, 2000) proposed for the formation of direct shipping iron ore is not applicable. Silica mobilization and mass transfer from intense folding and pressure solution can dissolve minerals at fold

noses. Volume loss associated with folding may exceed 50% as seen in the siliceous marbles of the Corsican schist, France (Caron et al., 1987). However, volume losses are isolated to fold noses (Caron et al., 1987). Other intense folding such as the Helvetic nappe folds, Switzerland, only account for a 1-10% volume loss (Rowan et al., 1991). Adjacent limbs of Helvetic nappe folds show 1-10% volume gains as well (Rowan et al., 1991). Dissolution through deformation cannot not adequately mobilize and account for such massive silica loss.

MacLeod (2012) proposed a dome-keel extensional model related to collapse of the Hudsonian orogen. The model is based on the work of Marshak et al. (1992), Marshak et al. (1997), Marshak (1999) and others. The proposed model states that hot infrastructural buoyant crust ascended creating normal mylonitic shear zones against the Mary River Group. Transient heat advected from the ascending gneiss dome and granites metamorphosed supracrustals to amphibolite facies. Hydrothermal alteration is caused by driving water from H₂O rich supracrustals (komatiites).

By reviewing the data in previous sections, several problems arise from this model. An extensional mylonitic shear zone does exist at the contact between the MRG and basement lithologies. Detailed petrography, lithochemistry and geochronology reveals the adjacent basement to be mylonitized and altered monzogranite. Mylonitic-lineation fabrics dissipate 500 m west of Deposit No.1 into undeformed and unaltered granitoids. These granitoids (monzogranites and syenogranites) are traced kilometres west of Deposit No.1 without intermittent gneiss outcrops. The core of the McBeth gneiss dome is located over 90 km to the northwest and separated by this granitoid terrane (Wanless and Loveridge, 1978). ⁸⁷Sr/⁸⁶Sr ages of core gneisses and quartz monzonites in the McBeth gneiss dome are thermally disturbed reporting errochron ages of 2605 Ma and 1964 Ma (Wanless and Loveridge, 1978). The closest known gneiss-migmatite zone is north of Deposit No.4, more than 40 km northwest of Deposit No.1 (Jackson, 1966, 2000; Jackson et al., 1978). A direct contact and relationship to regional gneiss is not present.

The newly defined mineral paragenesis presented differs in interpretation and sequence from the gneiss-dome model. MacLeod (2012) interpreted alkaline brines mobilized Fe-Mg-Ca forming a carbonate-magnetite proto ore. The presence of carbonates is minimal and isolated to two magnetite ore samples signifying sampling bias. Footwall carbonatization is only exemplified by ECH veining at the initial stages of extension. Ultramafics show mild to moderate carbonate alteration in the immediate hangingwall. Carbonates altering serpentinites are overprinted by talc, then retrograded to chlorite and finally overprinted by anthophyllite. Hangingwall ultramafics therefore have the same prograde-retrograde paragenetic history as footwall units and therefore only show carbonate alteration in the first stage of alteration. Mass balance calculations illustrate minor very Ca mobility (<0.5%) during all stages of ore formation. Comparisons drawn by MacLeod (2012) to the findings of carbonate altered Superior-type BIF hosted iron ores are unwarranted. Proterozoic Krivoy Rog and Mount Tom Price deposits are deposited on carbonates and shales. The carbonate reservoir is orders of magnitude higher than the ultramafic-volcanics in the Deposit No.1 hangingwall and granitoid footwall. Banded carbonate samples and marbles identified by MacLeod (2012) are likely relict carbonate facies BIF because no alteration phase identified is capable systematic layering.

The major paragenetic discrepancy of the gneiss dome model is the difference between metamorphic mineral assemblages and their relation to iron ore formation. Cordierite porphyroblasts that terminate massive muscovite alteration, are considered a prograde mineral assemblage alongside staurolite, grunerite and almandine by MacLeod (2012). Cordierite's instability is well document and cannot coexist given dissolution textures in relation to biotite alteration and pinnite retrogression or by the bulk rock composition of stage 3 metamorphism (see Figure 7-6, 7-7, 7-8).

Second, martization of granoblastic ore is attributed to cooling post almandine growth by a cooler low pH fluid by MacLeod (2012). Ore zone chlorite schist sample 6220A clearly illustrates zoned almandine growth over a chloritized biotite matrix incorporating vuggy martite clasts composed of microplaty hematite. Martite inclusions in garnet indicate hematization prior and in relation with biotization-chloritization.

Other inconsistencies of MacLeod's model are metamorphic facies and their distribution. Low pressure high temperature metamorphism by decompression heating of gneiss and associated migmatite is spread out on a regional gradient scale of ~4km or more (Marshak et al., 1992). Deposit No.1 amphibolite facies are 1-2.3 km wide and bounded by greenschist facies granitoids and ultramafics. Multiple metamorphic retrograde-prograde overprints are not amenable to a single regional heat flow. More importantly isograds follow alteration-deformational boundaries and are parallel to extensional shear planes. Regional metamorphism cannot explain the tight facies distribution, lack of high grade metamorphic facies or absence of metamorphic gradient.

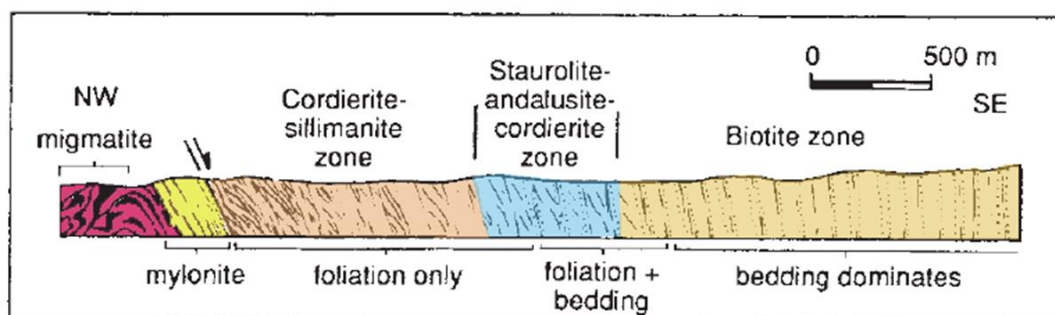


Figure 8-1 Metamorphic cross-section of low pressure-high temperature gneiss dome metamorphism from the Quadrilatero Ferrifero. Modified from Marshak et al. (1992).

Moreover, zircon geochronology does not indicate a prior regional metamorphic overprint. Zircons in ore zone chlorite schist are euhedral with oscillatory zoning. Footwall and ore zone chlorite schist are the most deformed, altered and metamorphosed units yet they retain pristine single age zircon populations. Zircons can form metamorphic rims at prehnite-pumpellyite facies temperatures of 250°C inferring metamorphism was rapid or low grade (Rasmussen, 2005). Furthermore, Jackson (2000) places the Deposits No.1 within a greenschist facie isograd (Figure 1-8). Zircon textures and the distribution of amphibolite facies infer the Deposit No.1 Mary River Group did not undergo regional amphibolite metamorphism. Sporadic and rapid poikiloblastic growth shows amphibolite metamorphic nodes were pulses.

The gneiss dome model and lithotectonic setting was developed using samples of ore zone schist and metasediment from Deposits No.1, 4 and. Iron ores from Deposit

No.4 and 5 differ from those of Deposit No.1. Deposit No.4 iron ores are granoblastic magnetite crosscut by veins of specularite (Fulcher, 2011). Staurolite and cordierite porphyroblasts are not observed in any footwall schist at the deposit either. Also, Fulcher (2011) illustrated several garnet generations (pre, syn and post-tectonic) are present in the Deposit No. 4 ore zone chlorite schist. Deposit No.4-5 chlorite schists also contain crenulated amphiboles overprinted by chlorite. These textures allude to a pre-existing medium grade metamorphic footprint prior to alteration. The compiled gneiss dome model does not take into account these characteristics.

The gneiss dome model is considered inaccurate. Components of the model still stand strong. Those components include extension, crustal uplift and an elevated geothermal gradient. A direct relationship to the formation of a gneiss dome cannot be determined at this time due to lack of mapping, geochronological and structural data of regional gneiss domains. Revisions are required to account for the described paragenetic-metamorphic history. A more general post-collisional model is preferred and summarized below.

- 1) Structurally deformed (folded and or brecciated) supracrustals are juxtaposed against basement rocks.
- 2) Post-collisional buoyancy causes normal shearing by influxed fluids inducing chemical and reaction softening of dome and keel boundary zone. Intense extension ensues causing lineations and mylonitic grain reduction.
- 3) Hydrothermal fluids are channelized by mylonitic-shear fabrics into deformed and brecciated supracrustals at contacts. The fluid leaches silica and mobilizes various elements depending on fluid composition.
- 4) Hydrothermal fluids cause refrigeration of metasomatized zone. Retrograde chlorite forms ubiquitously across footwall, ore zone and hangingwall.
- 5) Metasomatized rocks are overprinted by a pluse of heat forming large porphyroblastic growth of Fe-Mg-Al silicates.

The new model allows for channelized heat flow and different sources of heat (decompression, pegmatite magmatic exct...) to generate an elevated geotherm. The model is coherent with alteration and metamorphic facie types and distribution. Step repetition is permitted to yield different alteration-metamorphic assemblages.

8.4 Regional Implications & Final Remarks

This study has revealed major inconsistencies to lithology, stratigraphy, deformation, metamorphism and geochronology. The works of Jackson (1966, 2000), Gross (1966), Macleod (2012) and others have used Deposit No.1 as an analog for regional stratigraphy, metamorphism and tectonics.

The Mary River Group has been ideally correlated as a BIF-komatiite-quartzite-metasediment-volcanic sequence to the other greenstone belt terranes on the Melville Peninsular on mainland Nunavut. Correlations to the Woodburn Lake Group, Prince Albert Group and Eque Bay (Bethune and Scammell, 2003a, b) area are not cohesive. The quartzite marker commonly used is not sedimentary and footwall volcanics are absent.

Regionally mapped Mary River Group belts have included quartzite and biotite schists as metasediments in 10-65 km long greenstone belts averaging ~5 km in thickness. Newly define lithologies and stratigraphy question regionally mapped Mary River Group supracrustals. The thickness of the belts is greatly reduced using the redefined Deposit No.1 stratigraphy. BIF and HGIF are the only units within altered-deformed zones that can distinguish the Mesoarchean basement from Neoproterozoic supracrustals. Lithologies, stratigraphically lower than BIF or HGIF, need more scrutiny for rock type identification. Previously characterized upper amphibolite facies and thus isograds, may actually be lower grade metamorphic facies if altered prior to metamorphism.

References

- Anseau, M. R., Biloque, J. P., and Fierens, P., 1976, Some studies on the thermal solid state stability of zircon: *Journal of Material Science*, v. 11, p. 578-582.
- Appel, P. W. U., 1980, On the early Archean Isua iron-formation, west Greenland: *Precambrian Research*, v. 11, p. 73-87.
- , 1987, Geochemistry of the early Archean Isua iron-formation, west Greenland, *in* Appel, P. W. U., and LaBerge, G. L., eds., *Precambrian Iron-formations*: Athens, Greece, Theophrastus Publications, S.A., p. 31-67.
- Atherton, M., 1968, The variation in garnet, biotite and chlorite composition in medium grade pelitic rocks from the Dalradian, Scotland, with particular reference to the zonation in garnet: *Contributions to Mineralogy and Petrology*, v. 18, no. 4, p. 347-371.
- Bailey, C. M., Simpson, C., and De Paor, D. G., 1994, Volume loss and tectonic flattening strain in granitic mylonites from the Blue Ridge province, central Appalachians: *Journal of Structural Geology*, v. 16, no. 10, p. 1403-1416.
- Banno, S., and Chii, S., 1978, A model to explain the Mn enrichment in the rim of zoned garnet: *Geochemical Journal*, v. 12, p. 253-257.
- Bea, F., 1996, Residence of REE, Y, and U in granites and crustal protoliths; Implications for the chemistry of crustal melts: *Journal of petrology*, v. 37, no. 5, p. 521-552.
- Beach, A., 1980, Retrogressive metamorphic processes in shear zones with special reference to the Lewisian complex: *Journal of Structural Geology*, v. 2, no. 1-2, p. 257-263.
- Bekker, A., Planavsky, N. J., Krapež, B., Rasmussen, B., Hofmann, A., Slack, J. F., Rouxel, O. J., and Konhauser, K. O., 2014, 9.18 - Iron Formations: Their Origins and Implications for Ancient Seawater Chemistry, *in* Turekian, H. D. H. K., ed., *Treatise on Geochemistry (Second Edition)*: Oxford, Elsevier, p. 561-628.
- Bekker, A., Slack, J. F., Planavsky, N., Krapez, B., Hofman, A., Konhauser, K. O., and Rouxel, O. J., 2010, Iron Formation: The Sedimentary Product of a Complex Interplay among Mantle, Tectonic, Oceanic, and Biospheric Processes: *Economic Geology*, v. 105, p. 467-508.
- Beletsev, Y. N., 1973, Genesis of high-grade iron ores of Krivoyrog type, Genesis of Precambrian Iron and Manganese Deposits; *Proceedings of the Kiev Symposium*, Volume 9: Kiev, UNESCO Earth Sci Ser, p. 167-180.

- Belousova, E. L., Griffin, W. L., O'Reilly, S. Y., and Fisher, N. I., 2002, Igneous zircon: trace element composition as an indicator of source rock type: *Contributions to Mineralogy and Petrology*, v. 143, p. 602-622.
- Bethune, K. M., and Scammell, R. J., 2003, Distinguishing between Archean and Paleoproterozoic tectonism, and evolution of the Isortoq fault zone, Ege Bay area, north-central Baffin Island, Canada: *Canadian Journal of Earth Sciences*, v. 40, no. 8, p. 1111-1135.
- , 2003, Geology, geochronology, and geochemistry of Archean rocks in the Ege Bay area, north-central Baffin Island, Canada: constraints on the depositional and tectonic history of the Mary River Group of northeastern Rae Province: *Canadian Journal of Earth Sciences*, v. 40, no. 8, p. 1137-1167.
- Beukes, N. J., 1984, Sedimentology of the Kuruman and Griquatown Iron-formations, Transvaal Supergroup, Griqualand West, South Africa: *Precambrian Research*, v. 24, no. 1, p. 47-84.
- Beukes, N. J., and Gutzmer, J., 2008, Origin and paleoenvironmental significance of major iron formations at the Archean-Proterozoic boundary: *Reviews in Economic Geology*, v. 15, p. 5-47.
- Beukes, N. J., Gutzmer, J., and Mukhopadhyay, J., 2002, The geology and genesis of high-grade hematite iron ore deposits: *Australasian Institute of Mining and Metallurgy*, v. 7/2002, no. 1, p. 23-29.
- Beukes, N. J., Mukhopadhyay, J., and Gutzmer, J., 2008, Genesis of high-grade iron ores of the Archean iron ore group around Noamundi, India: *Economic Geology*, v. 103, p. 365-386.
- Boatner, L. A., 2002, Synthesis, structure, and properties of monazite, pretulite, and xenotime: *Reviews in Mineralogy and Geochemistry*, v. 48, p. 87-121.
- Boggs, S. J., 2006, *Principles of sedimentology and stratigraphy*, Prentice Hall.
- Bostock, H. S., 1970, Physiographic subdivisions of Canada, *in* Douglas, R. J. W., ed., *Geology and Economic Minerals of Canada*: Ottawa, Ontario, Canada, Geological Survey of Canada, p. 9-30.
- Brown, E. H., 1969, Some zoned garnets from the greenschist facies: *The American Mineralogist*, v. 54, p. 1662-1677.
- Bruhn, R., Parry, W., Yonkee, W., and Thompson, T., 1994, Fracturing and hydrothermal alteration in normal fault zones: pure and applied geophysics, v. 142, no. 3-4, p. 609-644.
- Canada, T. A. o., 2006, *Nunavut*: Natural Resources Canada.

- Canfield, D. E., 2005, The early history of atmospheric oxygen: Homage to Robert M. Garrels Annual Review of Earth and Planetary Sciences, v. 33, p. 1-36.
- Caron, J. M., Potdevin, J. L., and Sicard, E., 1987, Solution-deposit processes and mass transfer in the deformation of a minor fold: Tectonophysics, v. 135, p. 77-86.
- Chappell, B. W., and White, A. J. R., 1974, Two contrasting granite types: Pacific Geology, v. 8, p. 173-174.
- , 2001, Two contrasting granite types: 25 years later: Australian Journal of Earth Sciences, v. 48, p. 489-499.
- Chernosky, J. V., and Autio, L. K., 1979, The stability of anthophyllite in the presence of quartz: American Mineralogist, v. 64, no. 3-4, p. 294-303.
- Cloud, P., 1972, A working model of the primitive Earth: American Journal of Science, v. 272, no. 6, p. 537-548.
- , 1973, Paleocological Significance of the Banded Iron-Formation: Economic Geology, v. 68, no. 7, p. 1135-1143.
- , 1983, Banded iron formation-A gradulist's dilemma, *in* Trendall, A. F., and Morris, R. C., eds., Iron formations: Facts and problems, Volume 6: Amsterdam, Elsevier, p. 401-416.
- Cloud, P. E. J., 1965, Significance of the Gunflint (Precambrian) Microflora: Science, v. 148, no. 3666, p. 27-35.
- Clout, J. M. F., and Simonson, B. M., 2005, Precambrian iron formations and iron formation-hosted iron ore deposits: Economic Geology, v. 100th Anniversary Volume, p. 643-679.
- Corfu, F., Hancher, J. M., Hoskin, P. W. O., and Kinny, P., 2003, Atlas of Zircon Textures: Reviews in Mineralogy and Geochemistry, v. 53, no. 1, p. 469-500.
- Cornelis, G., Johnson, C. A., Gerven, T. V., and Vandecasteele, C., 2008, Leaching mechanisms of oxyanionic metalloids and metal species in alkaline solid wastes: A review: Applied Geochemistry, v. 23, no. 5, p. 955-976.
- Crewe, A. V., Eggenberger, D. N., Wall, J., and Welter, L. M., 1968, Electron gun using a field emission source: The Review of Scientific Instruments, v. 39, no. 4, p. 576-583.

- Dalstra, H., and Flis, M., 2008, High-grade iron ore exploration in an increasingly steel-hungry world: The past, current, and future role of exploration models and technological advances: *Reviews in Economic Geology*, v. Vol 15, p. 393-409.
- Dalstra, H., and Guedes, S., 2004, Giant hydrothermal hematite deposits with Mg-Fe metasomatism: A comparison of the Carjás, Hamersley and other iron ores: *Economic Geology*, v. 99, p. 1793-1800.
- Dalstra, H. J., and Rosière, C. A., 2008, Structural controls on high-grade iron ores hosted by banded iron formation: A global perspective: *Reviews in Economic Geology*, v. 15, p. 73-106.
- Davy, R., 1983, A contribution on the chemical composition of Precambrian iron-formations, *in* Trendall, A. F., and Morris, R. C., eds., *Iron-Formations Facts and Problems*, Volume 6: Amsterdam, Elsevier, p. 325-344.
- De La Rocha, C. L., Brzezinski, M. A., and DeNiro, M. J., 2000, A first look at the distribution of the stable isotopes of silicon in natural waters: *Geochimica et Cosmochimica Acta*, v. 64, no. 14, p. 2467-2477.
- Dean, J. R., 2005, *Practical Inductively Coupled Plasma Spectroscopy*, John Wiley & Sons Ltd., 184 p.:
- Deer, W. A., Howie, R. A., and Zussman, J., 1992, *An introduction to the rock forming minerals*, Prentice Hall, 696 p.:
- Dickenson, M. P., and Hewitt, D. A., 1986, A garnet-chlorite geothermometer: *Geological Society of America Abstracts with Programs*, v. 18, p. 584.
- Dipple, G., and Ferry, J., 1992, Metasomatism and fluid flow in ductile fault zones: *Contributions to Mineralogy and Petrology*, v. 112, no. 2-3, p. 149-164.
- Dorr II, J. N. V., 1964, Supergene iron ores of the Minas Gerais, Brazil: *Economic Geology*, v. 59, no. No.7, p. 1203-1240.
- Dostal, J., and Mueller, W. U., 1997, Komatiite Flooding of a Rifted Archean Rhyolitic Arc Complex: Geochemical Signature and Tectonic Significance of the Stoughton-Roquemaure Group, Abitibi Greenstone Belt, Canada: *The Journal of Geology*, v. 105, no. 5, p. 545-564.
- Edwards, P. R., Martin, R. W., and Lee, M. R., 2007, Combined cathodoluminescence hyperspectral imaging and wavelength dispersive X-ray analysis of minerals: *American Mineralogist*, v. 92, p. 235-242.
- Eichhubl, P., and Boles, J. R., 2000, Rates of fluid flow in fault systems; evidence for episodic rapid fluid flow in the Miocene Monterey Formation, coastal California: *American Journal of Science*, v. 300, no. 7, p. 571-600.

- Evans, B. W., and Trommsdorff, V., 1974, Stability of enstatite + talc, and CO₂ - metasomatism of metaperidotite, Val d'Efra, Lepontine Alps: *American Journal of Science*, v. 274, no. 3, p. 274-296.
- Ewers, W. E., 1983, Chemical factors in the deposition and diagenesis of banded iron-formation, *in* Trendall, A. F., and Morris, R. C., eds., *Iron formation: Facts and problems*: Amsterdam, Elsevier, p. 491-512.
- Faure, G., and Mensing, T. M., 2005, *Isotopes: Principles and applications*, Hoboken, New Jersey, John Wiley & Sons, Inc., 897 p.:
- Ferry, J., and Spear, F., 1978, Experimental calibration of the partitioning of Fe and Mg between biotite and garnet: *Contributions to Mineralogy and Petrology*, v. 66, no. 2, p. 113-117.
- Finch, R. J., and Hanchar, J. M., 2003, Structure and chemistry of zircon and zircon-group minerals: *Reviews in Mineralogy and Geochemistry*, v. 53, p. 1-25.
- Floran, R. J., and Papike, J. J., 1978, Mineralogy and petrology of the Gunflint iron formation, Minnesota-Ontario: Correlation of compositional and assemblage variations at low to moderate grade: *Journal of Petrology*, v. 19, no. Part 2, p. 215-288.
- French, B., 1973, Mineral assemblages in the diagenetic and low-grade metamorphic iron-formation: *Economic Geology*, v. 68, p. 1063-1074.
- French, B. M., 1968, Progressive contact metamorphism of the Biwabik iron-formation, Mesabi Range, Minnesota, *in* Survey, M. G., ed.: *Minnesota*, p. 103.
- Frost, B. R., 1979, Metamorphism of iron-formation: Parageneses in the system Fe-Si-C-O-H: *Economic Geology*, v. 74, p. 775-785.
- Fryer, B. J., 1983, Rare earth elements in iron formation, *in* Trendall, A. F., and Morris, R. C., eds., *Iron formation; Facts and problems, Volume 6*: Amsterdam, Elsevier, p. 345-358.
- Fulcher, S. A., 2011, Geological context and character of the schist unit at Deposit No. 4, Mary River iron ore deposit, Baffin Island, Nunavut [HBSc. Monograph]: University of Ottawa, 72 p.
- Fyfe, W. S., 1962, On the relative stability of talc, anthophyllite, and enstatite: *American Journal of Science*, v. 260, no. 6, p. 460-466.
- Garrels, R. M., Perry, E. A., and Mackenzie, F. T., 1973, Genesis of Precambrian Iron-Formations and the Development of Atmospheric Oxygen: *Economic Geology*, v. 68, no. 7, p. 1173-1179.

- Géraud, Y., Caron, J.-m., and Faure, P., 1995, Porosity network of a ductile shear zone: *Journal of Structural Geology*, v. 17, no. 12, p. 1757-1769.
- Glazner, A. F., and Bartley, J. M., 1991, Volume loss, fluid flow and state of strain in extensional mylonites from the central Mojave Desert, California: *Journal of Structural Geology*, v. 13, no. 5, p. 587-594.
- Goldstein, J., Newbury, D., Joy, D., Lyman, C., Echlin, P., Lifshin, E., Sawyer, L., and Michael, J., 2003, *Scanning Electron Microscopy and X-Ray Microanalysis*, New York, N.Y., Kluwer Academic / Plenum Publishers, New York, 687 p.:
- Gole, M. J., and Klein, C., 1981, Banded iron-formations through much of the Precambrian time: *The Journal of Geology*, v. 89, no. 2, p. 169-183.
- , 1981, High-grade metamorphic Archean banded iron-formations, Western Australia: assemblages with coexisting pyroxenes+/- fayalite: *American Mineralogist*, v. 66, p. 87-99.
- Goodwin, A. M., 1956, Facies relations in the Gunflint iron formation: *Economic Geology*, v. 51, p. 565-595.
- Goodwin, A. M., 1962, Structure, stratigraphy, and origin of iron formations, michipicoten area, Algoma district, Ontario, Canada: *Geological Society of America Bulletin*, v. 73, p. 561-586.
- Greenfield, S., Jones, I. L. L., and Berry, C. T., 1964, High Pressure Plasmas as Spectroscopic Emission Source: *Analyst*, v. 89, p. 713-720.
- Greenwood, H. J., 1963, The Synthesis and Stability of Anthophyllite: *Journal of Petrology*, v. 4, no. 3, p. 317-351.
- , 1971, Anthophyllite; corrections and comments on its stability: *American Journal of Science*, v. 270, no. 2, p. 151-154.
- Gresens, R. L., 1967, Composition-volume relationships of metasomatism: *Chemical Geology*, v. 2, p. 47-65.
- Grohmann, C. H., and Campanha, G. A. C., 2010, OpenStereo: open source, cross-platform software for structural geology analysis, Volume Presented at the AGU 2010 Fall Meeting: San Francisco, CA.
- Gross, G. A., 1965, *Geology of iron deposits in Canada*.
- , 1966, The origin of high grade iron deposits on Baffin Island, N.W.T.: *Geological Survey of Canada*.
- , 1972, Primary features in cherty iron-formations: *Sedimentary Geology*, v. 7, no. 4, p. 241-261.

- , 1980, A Classification Of Iron Formations Based on Depositional Environments: Canadian Mineralogist, v. 18, p. 215-222.
- , 1983, Tectonic systems and the deposition of iron formation: Precambrian Research, v. 20, p. 171-187.
- , 1991, Genetic concepts for iron-formation and associated metalliferous sediments: Economic Geology, v. Monograph 8, p. 51-81.
- , 1995, Stratiform Iron, *in* Eckstrand, O. R., Sinclair, W. D., and Thorpe, R. I., eds., Geology of Canadian Mineral Deposit Types, Volume 8: Canada, Geological Survey of Canada, p. 41-73.
- Grout, F. F., 1919, The nature and origin of the Biwabik iron-bearing formation of the Mesabi range, Minnesota: Economic Geology, v. 14, p. 452-464.
- Gucsik, A., 2009, Cathodoluminescence and its application in the planetary sciences, Berlin, Springer-Verlag Berlin Heidelberg.
- Hamade, T., Konhauser, K. O., Raiswell, R., Goldsmith, S., and Morris, R. C., 2003, Using Ge/Si ratios to decouple iron and silica fluxes in Precambrian banded iron formations: Geology, v. 31, no. 1, p. 35-38.
- Han, T.-M., and Runnegar, B., 1992, Megascopic Eukaryotic Algae from the 2.1-Billion-Year-Old Negaunee Iron-Formation, Michigan: Science, v. 257, no. 5067, p. 232-235.
- Hanson, G. N., 1978, The application of trace elements to the petrogenesis of igneous rocks of granitic composition: Earth and Planetary Science Letters, v. 38, p. 26-43.
- Harlov, D. E., and Hetherington, C. J., 2010, Partial high-grade alteration of monazite using alkali-bearing fluids: Experiment and nature: American Mineralogist, v. 95, p. 1105-1108.
- Harlov, D. E., Wirth, R., and Förster, H.-J., 2005, An experimental study of dissolution–reprecipitation in fluorapatite: fluid infiltration and the formation of monazite: Contributions to Mineralogy and Petrology, v. 150, no. 3, p. 268-286.
- Hedenquist, J. W., and Lowenstern, J. B., 1994, The role of magmas in the formation of hydrothermal ore deposits: Nature, v. 370, no. 6490, p. 519-527.
- Hegner, E., and Jackson, G. D., 1990, Nd isotropic constraints on the Late Archean and Early Proterozoic crust formation in Baffin and Ellesmere islands, northern

Labrador and Ungava Peninsula, eastern Canada, American Geophysical Union fall meeting, Volume 71, p. 1689 (abstract).

- Hemley, J. J., and Jones, W. R., 1964, Chemical aspects of hydrothermal alteration with emphasis on hydrogen metasomatism: *Economic Geology*, v. 59, no. 4, p. 538-569.
- Herbranson, I. D., 2013, Geologic map, petrographic and geochemical analysis of the PS-2 gold showing, Mary River district, Baffin Island, Canada [HBS.c.: University of British Columbia, 67 p.
- Hetherington, C. J., Harlov, D. E., and Budzyń, B., 2010, Experimental metasomatism of monazite and xenotime: mineral stability, REE mobility and fluid composition: *Mineralogy and Petrology*, v. 99, p. 165-184.
- Hikichi, Y., and Nomura, T., 1987, Melting temperatures of monazite and xenotime: *J. Am. Ceram. Soc.*, v. 70, p. C-252-C-253.
- Hill, S. J., 1999, Inductively coupled plasma spectrometry and its applications, *in* Ibbett, R. N., ed.: Sheffield, UK, Sheffield Academic Press Ltd, p. 1-34.
- Hippertt, J. F., 1998, Breakdown of feldspar, volume gain and lateral mass transfer during mylonitization of granitoid in a low metamorphic grade shear zone: *Journal of Structural Geology*, v. 20, no. 2-3, p. 175-193.
- Hoffman, P. F., 1988, United plates of America, the birth of a craton: Early proterozoic assembly and growth of Laurentia *Annual Reviews Earth and Planetary Science*, v. 16, p. 543-603.
- , 1990, Subdivision of the Churchill Province and extent of the Trans-Hudson Orogen: *Geological Association of Canada Special Paper*, v. 37, p. 15-39.
- Hoschek, G., 1969, The stability of staurolite and chloritoid and their significance in metamorphism of pelitic rocks: *Contributions to Mineralogy and Petrology*, v. 22, no. 3, p. 208-232.
- Hoskin, P. W. O., and Schaltegger, U., 2003, The composition of zircon and igneous and metamorphic petrogenesis: *Reviews in Mineralogy and Geochemistry*, v. 53, no. 1, p. 27-62.
- Hsu, L. C., 1968, Selected phase relationships in the system Al-Mn-Fe-Si-O-H: A model for garnet equilibria: *Journal of Petrology*, v. 9, no. 1, p. 40-83.
- Jackson, G. D., 1966, Geology and mineral possibilities of the Mary River Region, northern Baffin Island: *Canadian Journal of Mining*, v. 87, no. 6, p. 57-61.

- , 1969, Reconnaissance of north-central Baffin Island: Geological Survey of Canada.
- , 2000, Geology of the Clyde-Cockburn Land map area, north-central Baffin Island, Nunavut, Geological Survey of Canada.
- Jackson, G. D., and Berman, R. G., 2000, Precambrian metamorphic and tectonic evolution of northern Baffin Island, Nunavut, Canada: *The Canadian Mineralogist*, v. 38, p. 399-421.
- Jackson, G. D., Davidson, A., and Morgan, W. C., 1978, Geology, Icebound Lake, District of Franklin: Geological Survey of Canada, scale 1:250000.
- Jackson, G. D., Hunt, P. A., Loveridge, W. D., and Parrish, R. R., 1990, Reconnaissance geochronology of Baffin Island, N.W.T: Geological Survey of Canada.
- Jackson, G. D., and Morgan, W. C., 1978, Precambrian metamorphism on Baffin and Bylot Islands: *Metamorphism in the Canadian Shield*, v. Paper 78-10, p. 249-267.
- Jackson, G. D., and Taylor, F. C., 1972, Correlation of major Archean rock units in the northeastern Canadian Shield: *Canadian Journal of Earth Sciences*, v. 9, p. 1650-1669.
- Jackson, J. A., and Bates, R. L., 1997, *Glossary of geology*, Alexandria, Va, American Geological Institute, 1-769 p.:
- James, H. L., 1954, Sedimentary facies of iron formation: *Economic Geology*, v. 49, p. 235-294.
- James, H. L., 1983, Distribution of banded iron-formation in space and time, *in* Trendall, A. F., and Morris, R. C., eds., *Iron-formation: Facts and problems*, Volume 6: Amsterdam, Elsevier, p. 471-490.
- Jensen, L. S., 1976, A new cation plot for classifying subalkaline volcanic rocks: Ontario Geological Survey, v. Miscellaneous Paper 66, p. 1-22.
- Johns, S. M., and Young, M. D., 2006, Bedrock geology and economic potential of the Archean Mary River group, northern Baffin Island, Nunavut: *Current Research*, v. C5, p. 1-13.
- Kato, T., 1958, A study of monzaitite from the EBISU mine, Gifu Prefecture: *Mineralogical Journal*, v. No.4, p. 224-235.
- Kempe, U., Lehmann, B., Wolf, D., Rodionov, N., Bombach, K., Schwengfelder, U., and Dietrich, A., 2008, U-Pb SHRIMP geochronology of Th-poor hydrothermal monzaitite: An example from the Llallagua tin-porphyry deposit, Bolivia: *Geochimica et Cosmochimica Acta*, v. 72, p. 4352-4366.

- Klein, C., 1973, Changes in mineral assemblage with metamorphism of some banded Precambrian iron formations *Economic Geology*, v. 68, p. 1075-1088.
- , 1974, Greenalite, stilpnomelane, minnesotaite, crocidolite and carbonates in a very low-grade metamorphic Precambrian iron-formation: *Canadian Mineralogist*, v. 12, p. 475-498.
- , 1978, Regional metamorphism of Proterozoic iron formation, Labrador Trough, Canada: *American Mineralogist*, v. 63, p. 898-912.
- , 1983, Diagenesis and metamorphism of Precambrian banded iron formations, *in* Trendall, A. F., and Morris, R. C., eds., *Iron formations: Facts and problems*, Volume 6: Amsterdam, Elsevier, p. 417-469.
- , 2005, Some Precambrian banded iron-formations (BIFs) from around the world: Their age, geologic setting, mineralogy, metamorphism, geochemistry, and origin: *American Mineralogist*, v. 90, p. 1473-1499.
- Klein, C., and Ladeira, E. A., 2002, Petrography and geochemistry of the least altered banded iron-formation of the Archean Carajás formation, northern Brazil: *Economic Geology*, v. 97, p. 643-651.
- Krauskopf, K. B., 1957, Separation of manganese from iron in sedimentary processes: *Geochimica et Cosmochimica Acta*, v. 12, no. 1-2, p. 61-84.
- Krumbein, W. C., and Garrels, R. M., 1952, Origin and classification of chemical sediments in terms of pH and oxidation-reduction potentials: *The Journal of Geology*, v. 60, no. 1, p. 1-33.
- Kump, L. R., and Holland, H. D., 1992, Iron in Precambrian rocks: Implications for the global oxygen budget of the ancient Earth: *Geochimica et Cosmochimica Acta*, v. 56, no. 8, p. 3217-3223.
- Laajoki, K., and Saikkonen, R., 1977, On the geology and geochemistry of the Precambrian iron formations in Väyrylänkylä, south Puolanka area, Finland: *Geological Survey of Finland, Bulletin 292*, p. 5-130.
- Labrador Iron Mines Holdings Limited, L., 2014, Labrador Iron Mines reports third quarter results: Toronto, Ontario, Labrador Iron Mines Holdings Limited, p. 1-7.
- Laird, J., 1988, Chlorites: metamorphic petrology, *Hydrous Phyllosilicates: Review in Mineralogy*.
- Lan, T.-G., Fan, H.-R., Santosh, M., Hu, F.-F., Yang, K.-F., and Liu, Y., 2014, U-Pb zircon geochronology, geochemistry and isotopes of the Changyi banded iron formation in the eastern Shandong Province: Constraints on BIF Genesis and

implications for Paleoproterozoic tectonic evolution of the north China Craton: *Ore Geology Reviews*, v. 56, p. 472-486.

- Lascelles, D., 2002, A new look at old rocks an alternative model for the origin of in situ iron ore deposits derived from banded iron-formation: *Australasian Institute of Mining and Metallurgy Publication Series*, v. 7/2002, p. 107-126.
- Lascelles, D. F., 2006, The Mount Gibson banded iron formation-hosted magnetite deposit: Two distinct processes for the origin of high-grade iron ore: *Economic Geology*, v. 101, p. 651-666.
- , 2007, Black smokers and density currents: A uniformitarian model for the genesis of banded iron-formations: *Ore Geology Reviews*, v. 32, no. 1-2, p. 381-411.
- Laurila, T. E., Hannington, M. D., Petersen, S., and Garbe-Schoenberg, D., 2014, Early depositional history of metalliferous sediments in the Atlantis II Deep of the Red Sea: Evidence from rare earth element geochemistry: *Geochimica et Cosmochimica Acta*, v. 126, p. 146-168.
- Lepland, A., Arrhenius, G., and Cornell, D., 2002, Apatite in early Archean Isua supracrustal rocks, southern west Greenland: its origin, association with graphite and potential as a biomarker: *Precambrian Research*, v. 118, p. 221-241.
- Lewry, J. F., and Collerson, K. D., 1990, The Trans-hudson orogen: Extent, subdivision and problems: *Geological Association of Canada Special Paper*, v. 37, p. 1-14.
- Lima-de-Faria, J., 1994, *Structural mineralogy: An Introduction*, Dordrecht, Netherlands, Kluwer Academic Publishers, 346 p.:
- Lin, S., and Popp, R. K., 1984, Solubility and complexing of Ni in the system NiO-H₂O-HCl: *Geochimica et Cosmochimica Acta*, v. 48, no. 12, p. 2713-2722.
- Lindberg, P., 2010, Preliminary structural geology observations of the Mary River iron ore deposits & recommendations for applying structural analysis and magnetic correlation p. 1-16.
- , 2011, Structural geology of the northern portion of Mary River deposit No.1, including north limb extension; Baffin Island, Nunavut Canada.
- Linnen, R. L., Samson, I. M., Williams-Jones, A. E., and Chakhmouradian, A. R., 2014, 13.21 - Geochemistry of the rare-earth element, Nb, Ta, Hf, and Zr deposits, *in* Turekian, H. D. H. K., ed., *Treatise on Geochemistry (Second Edition)*: Oxford, Elsevier, p. 543-568.

- Loiselle, M. C., and Wones, D. R., 1979, Characteristics and origin of anorogenic granites: Geological Society of America Abstracts with Programs 11, v. no.7, p. 468.
- M, K., 1935, Static potential and secondary emission of bodies under electron irradiation: Z. Tech. Phys, v. 113, p. 260-280.
- MacLeod, M. E., 2012, Metallogenic setting of high-grade iron ores, Mary River District, north Baffin Island [MSc. Monograph]: University of Western Ontario, 285 p.
- MacLeod, M. E., and Duke, N. A., 2009, Field report: Economic potential of IOL PI-17.
- , 2009, Geology of IOL PI-17: Nunavut Tunngavik Inc., scale 1:50,000 scale.
- MacLeod, W. N., 1966, The Geology and iron deposits of the Hamersley Range area, *in* Australia, G. S. o. W., ed., Bulletin: Australia, p. 170.
- Makrygina, V., and Suvorova, L., 2011, Spessartine in the greenschist facies: Crystallization conditions: *Geochemistry International*, v. 49, no. 3, p. 299-308.
- Malich, K. N., Petrov, O. V., Badanina, I. Y., and Presneyakov, S. L., 2007, Zircon from ultramafic-mafic intrusions at the Noril'sk are (Russia): A compositional and U-Pb study, *Goldschmidt, Volume (Abstract)*: Cologne, Germany, p. A616.
- Marfunin, A. S., 1979, Luminescence, Spectroscopy, luminescence and radiation centers in minerals: New York, Springer-Verlag Berlin Heidelberg, p. 364.
- Marshak, S., 1999, Deformation style way back when: thoughts on the contrasts bewtween Archean/Paleoproterozoic and contemporary orogens: *Journal of Structural Geology*, v. 21, p. 1175-1182.
- Marshak, S., Alkmim, F. F., and Evangelista, H. J., 1992, Proterozoic crustal extension and the generation of dome-and-keel structure in an Archean granite-greenstone terrane: *Nature*, v. 357, p. 491-493.
- Marshak, S., Tinkham, D., Alkmim, F., Brueckner, H., and Bornhorst, T., 1997, Dome-and-keel provinces formed during Paleoproterozoic orogenic collapse—core complexes, diapirs, or neither?: Examples from the Quadrilátero Ferrífero and the Penokean orogen: *Geology*, v. 25, no. 5, p. 415–418.
- Martycak, K., Zeman, J., and Vacek-Vesely, M., 1994, Supergene processes on ore deposits - a source of heavy metals: *Environmental Geology*, v. 23, p. 156-165.
- McCulloch, M. T., and Wasserburg, G. J., 1978, Sm-Nd and Rb-Sr chronology of continental crust formation: *Science*, v. 200, no. 4345, p. 1003-1011.

- McDonough, W. F., and Sun, S. s., 1995, The composition of the Earth: Chemical Geology, v. 120, no. 3–4, p. 223-253.
- Meisel, W., Schnellrath, J., Greisbach, P., and Gutlich, P., 1990, The state of iron in andalusite: Hyperfine Interactions, v. 57, p. 2261-2268.
- Mel'nik, I. P., 1973, Physiochemical conditions of the formation of the Precambrian ferruginous quartzites, Kieve, Akad. Nauk Ukrainskoe SSR Institut geokhimii i fiziki mineralov, 272 p.:
- Mel'nik, Y. P., 1982, Precambrian banded iron-formations, Elseiver, Developments in Precambrian geology, v. 5, 1-310 p.:
- Miller, A. R., Densmore, C. D., Degens, E. T., Hathaway, J. C., Manheim, F. T., McFralin, P. F., Pocklington, R., and Jokela, A., 1966, Hot brines and recent iron deposits in the deeps of the Red Sea: Geochimica et Cosmochimica Acta, v. 30, p. 341-359.
- Miyano, T., and Klein, C., 1989, Phase equilibria in the system $K_2O-FeO-MgO-Al_2O_3-SiO_2-H_2O-CO_2$ and the stability limit of stilpnomelane in metamorphosed Precambrian iron-formations: Contributions to Mineralogy and Petrology, v. 102, no. 4, p. 478-491.
- Mojzsis, S. J., Arrhenius, G., McKeegan, K. D., Harrison, T. M., Nutman, A. P., and Friend, C. R. L., 1996, Evidence for life on Earth before 3,800 million years ago: Nature, v. 384, no. 7, p. 55-59.
- Moody, J. B., 1976, An experimental study on the serpentization of iron-bearing olivines: The Canadian Mineralogist, v. 14, no. 4, p. 462-478.
- Moorbath, S., O'nions, R. K., and Pankhurst, R. J., 1973, Early Archean age for the Isua iron formation, west Greenland: Nature, v. 245, no. 5421, p. 138-139.
- , 1975, The evolution of early Precambrian crustal rocks at Isua, west Greenland- Geochemical and isotopic evidence: Earth and Planetary Science Letters, v. 27, p. 229-239.
- Morgan, W. C., 1982, Geology, Koch Island, District Franklin; Geological Survey of Canada, Map 1535A: Geological Survey of Canada, scale 1:250000.
- Morris, R. C., 1980, A textural and mineralogical study of the relationship of iron ore to banded iron-formation in the Hamersley iron province of Western Australia: Economic Geology, v. 75, p. 184-209.
- Morris, R. C., 1985, Genesis of iron ore in banded iron-formation by supergene and supergene-metamorphic processes - a conceptual model, *in* Wolf, K. H., ed.,

- Handbook of strata-bound and stratiform ore deposits: Amsterdam, Elsevier, p. 73-235.
- , 1998, BIF-hosted iron ore deposits - Hamersley style: *Journal of Australian Geology & Geophysics*, v. 17, no. 4, p. 207-211.
- Morris, R. C., and Kneeshaw, M., 2011, Genesis modelling for the Hamersley BIF-hosted iron ores of Western Australia: a critical review: *Australian Journal of Earth Sciences*, v. 58, no. 5, p. 417-451.
- Ni, Y., Hughes, J. M., and Mariano, A. N., 1995, Crystal chemistry of the monazite and xenotime structures: *American Mineralogist*, v. 80, p. 21-26.
- Nicpon, B. C., 2011, Chlorite Schist in the Footwall of High Grade Iron Ore Hosted within the Mary River Group, Northern Baffin Island [BSc. Monograph]: University of Western Ontario, 52 p.
- Nockolds, S. R., 1954, Average chemical compositions of some igneous rocks: *Geological Society of America Bulletin*, v. 65, no. 10, p. 1007-1032.
- Nourse, J. E., 1879, Narrative of the second Arctic expedition made by Charles F. Hall : his voyage to Repulse Bay, sledge journeys to the Straits of Fury and Hecla and to King William's land, and residence among the Eskimos, during the years 1864-'69 633 p.:
- O'Neil, J., Carlson, R. W., Paquette, J.-L., and Francis, D., 2012, Formation age and metamorphic history of the Nuvvuagittuq Greenstone Belt: *Precambrian Research*, v. 220–221, no. 0, p. 23-44.
- Oatley, C. W., 1972, The scanning electron microscope United Kingdom, Cambridge University Press, Cambridge Monographs on Physics.
- Ohmoto, H., 2003, Nonredox Transformations Of Magnetite-Hematite in Hydrothermal Systems: *Economic Geology*, v. 98, p. 157-161.
- Pagel, M., Barbin, V., Blanc, P., and Ohnenstetter, D., 2000, Cathodoluminescence in geosciences, New York, Springer-Verlag Berlin Heidelberg 514 p.:
- Parrish, R. R., 1990, U-Pb dating of monazite and its application to geologic problems: *Canadian Journal of Earth Sciences*, v. 27, p. 1431-1449.
- Pearce, J. A., Harris, N. B. W., and Tindle, A. G., 1984, Trace element discrimination diagrams for the tectonic interpretation of granitic rocks: *Journal of Petrology*, v. 25, p. 956-983.
- Pecoits, E., Gingras, M. K., Barley, M. E., Kappler, A., Posth, N. R., and Konhauser, K. O., 2009, Petrography and geochemistry of the Dales Gorge banded iron

- formation: Paragenetic sequence, source and implications for paleo-ocean chemistry: *Precambrian Research*, v. 172, p. 163-187.
- Poitrasson, F., Chenery, S., and Bland, D. J., 1996, Contrasted monazite hydrothermal alteration mechanisms and their geochemical implications: *Earth and Planetary Science Letters*, v. 145, no. 1-4, p. 79-96.
- Rasmussen, B., 2005, Zircon growth in very low grade metasedimentary rocks: evidence for zirconium mobility at ~250°C: *Contributions to Mineralogy and Petrology*, v. 150, no. 2, p. 146-155.
- Rasmussen, B., and Buick, R., 1999, Redox state of the Archean atmosphere: Evidence from detrital heavy minerals in ca. 3250–2750 Ma sandstones from the Pilbara Craton, Australia: *Geology*, v. 27, no. 2, p. 115-118.
- Rasmussen, B., Fletcher, I. R., Muhling, J. R., Thorne, W. S., and Broadbent, G. C., 2007, Prolonged history of episodic fluid flow in giant hematite ore bodies: Evidence from in situ U–Pb geochronology of hydrothermal xenotime: *Earth and Planetary Science Letters*, v. 258, no. 1-2, p. 249-259.
- Reed, S. J. B., 2005, *Electron Microprobe Analysis and Scanning Electron Microscopy in Geology*, 232 p.:
- Reed, T. B., 1962, Induction-Coupled Plasma Torch: *Journal of Applied Physics*, v. 32, no. 5, p. 821-824.
- Robie, R. R., Hemingway, B. S., and Fisher, J. R., 1979, Thermodynamic properties of minerals and related Substances at 298.15 K and 1 bar (10^5 Pascals) pressure at higher temperatures: *U.S. Geological Survey Bulletin*, v. 1452, p. 1-456.
- Rosenblum, S., and Fleischer, M., 1995, The distribution of rare-earth elements in minerals of the monazite family: *U.S. Geological Survey Bulletin* 2140, p. 1-62.
- Rosière, C. A., and Rios, F. J., 2004, The origin of the hematite in high-grade iron ores based on infrared microscopy and fluid inclusion studies: The example of the Conceição mine, Quadrilátero Ferrífero, Brazil: *Economic Geology*, v. 99, p. 611-624.
- Rowan, M. G., Kligfield, R., and Erslev, E. A., 1991, Volume flux during folding in the Helvetic nappes, Switzerland: *Geology*, v. 19, no. 10, p. 1001-1004.
- Rutherford, E., and Soddy, F., 1902, LXIV. The cause and nature of radioactivity.—Part II: *Philosophical Magazine Series 6*, v. 4, no. 23, p. 569-585.
- Sandborn-Barrie, M., Davis, W. J., Berman, R. G., Rayner, N., Skulski, T., and Sanderman, H., 2014, Neoproterozoic continental crust formation and

Paleoproterozoic deformation of the central Rae craton, Committee Bay belt, Nunavut: *Canadian Journal of Earth Sciences*, v. 51, p. 635-667.

Schandl, E. S., Davis, D. W., Gorton, M. P., and Wasteneys, H. A., 1991, Geochronology of hydrothermal alteration around volcanic-hosted massive sulphide deposits in the Superior Province: Ontario Geological Survey Miscellaneous Paper 156, p. 105-120.

Schandl, E. S., and Gorton, M. P., 2004, A textural and geochemical guide to identification of hydrothermal monazite: Criteria for selection of samples for dating epigenetic hydrothermal ore deposits: *Economic Geology*, v. 99, p. 1027-1035.

Schilling, J. G., Zajac, M., Evans, R., Johnston, T., White, W., Devine, J. D., and Kingsley, R., 1983, Petrologic and geochemical variations along the Mid-Atlantic Ridge from 29 degrees N to 73 degrees N: *American Journal of Science*, v. 283, no. 6, p. 510-586.

Skipton, D. R., Schneider, D. A., and St-Onge, M. R., 2012, Preliminary observations on Archean and Paleoproterozoic metamorphism and deformation of the southern Hall Peninsula, Baffin Island, Nunavut: Summary of Activities, Canada-Nunavut Geoscience Office, p. 29-42.

Spear, F. S., and Daniel, C. G., 2001, Diffusion control of garnet growth, Harpswell Neck, Maine, USA: *Journal of Metamorphic Geology*, v. 19, no. 2, p. 179-195.

Spear, F. S., and Kohn, M. J., 1999, *Geothermobarometry, Volume 2.1*: Troy New York, Rensselaer Polytechnic Institute.

Speer, J. A., 1982, Zircon: *Reviews in Mineralogy and Geochemistry*, v. 5, p. 67-112.

Spier, C. A., Oliveira, S. M. B., Rosière, C. A., and Ardisson, J. D., 2007, Mineralogy and trace-element geochemistry of the high-grade iron ores of the Águas Claras Mine and comparison with the Capão Xavier and Tamanduá iron ore deposits, Quadrilátero Ferrífero, Brazil: *Mineralium Deposita*, v. 43, no. 2, p. 229-254.

Sracek, O., Mihaljevič, M., Křibek, B., Majer, V., Filip, J., Vaněk, A., Penížek, V., Ettler, V., and Mapani, B., 2014, Geochemistry and mineralogy of vanadium in mine tailings at Berg Aukas, northeastern Namibia: *Journal of African Earth Sciences*, v. 96, no. 0, p. 180-189.

Sun, S.-S., and Nesbitt, R. W., 1979, Geochemical characteristics of mid-ocean ridge basalts: *Earth and Planetary Science Letters*, v. 44, no. 1, p. 119-138.

- Taylor, D., Dalstra, H. J., Harding, A. E., Broadbent, G. C., and Barley, M. E., 2001, Genesis of high-grade hematite orebodies of the Hamersley Province, Western Australia: *Economic Geology*, v. 96, p. 837-873.
- Thompson, G., 1973, Trace-element distributions in fractionated oceanic rocks, 2. Gabbros and related rocks: *Chemical Geology*, v. 12, no. 2, p. 99-111.
- Thorne, W. S., Hagemann, S. G., and Barley, M., 2004, Petrographic and geochemical evidence for the evolution of the North Deposit, Mt Tom Price, Western Australia: *Mineral Deposita*, v. 39, p. 766-783.
- Tooth, B., Etschmann, B., Pokrovski, G. S., Testemale, D., Hazemann, J.-L., Grundler, P. V., and Brugger, J., 2013, Bismuth speciation in hydrothermal fluids: An X-rayabsorption spectroscopy and solubility study: *Geochimica et Cosmochimica Acta*, v. 101, p. 156-172.
- Trendall, A. F., 1968, Three great basins of Precambrian banded Iron formation deposition: A systematic comparison: *Geological Society of America Bulletin*, v. 79, p. 1527-1544.
- , 1983, The Hamersley Basin, *in* Trendall, A. F., and Morris, R. C., eds., *Iron Formations Facts and Problems*, Volume 6: Amsterdam, Elsevier Publishing Inc., p. 69-129.
- Trendall, A. F., and Blockley, J. G., 1970, The iron formations of the Precambrian Hamersley Group Western Australia.
- Trommsdorff, V., and Connolly, J. A. D., 1990, Constraints on phase-diagram topology for the system CaO-MgO-SiO₂-CO₂-H₂O: *Contributions to Mineralogy and Petrology*, v. 104, no. 1, p. 1-7.
- Trommsdorff, V., and Evans, B. W., 1972, Progressive metamorphism of antigorite schist in the Bergell tonalite aureole (Italy): *American Journal of Science*, v. 272, no. 5, p. 423-437.
- Trzcieski, W. E., 1977, Garnet zoning; product of a continuous reaction: *The Canadian Mineralogist*, v. 15, no. 2, p. 250-256.
- Utting, D. J., Little, E. C., Coulthard, R. D., Brown, O. H., Hartman, G. M. D., Huscroft, C. A., and Smith, J. S., 2006, Glacial history and drift prospecting Conn Lake and Buchan Gulf, northern Baffin Island, Nunavut: *Current Research 2006* v. C3.
- van den Boorn, S. H. J. M., van Bergen, M. J., Nijman, W., and Vroon, P. Z., 2007, Dual role of seawater and hydrothermal fluids in early Archean chert formation; evidence from silicon isotopes: *Geology*, v. 35, no. 10, p. 939-942.
- van den Boorn, S. H. J. M., van Bergen, M. J., Vroon, P. Z., de Vries, S. T., and Nijman, W., 2010, Silicon isotope and trace element constraints on the origin of

- ~3.5 Ga cherts: Implications for Early Archaean marine environments: *Geochimica et Cosmochimica Acta*, v. 74, no. 3, p. 1077-1103.
- Van Hise, C. R., and Leith, C. K., 1911, *Geology of the Lake Superior region, U.S. Geological Survey Monograph*, U.S. Geological Survey, p. 641.
- Van Kranendonk, M. J., Philippot, P., Lepot, K., Bodorkos, S., and Pirajno, F., 2008, Geological setting of Earth's oldest fossils in the ca. 3.5 Ga Dresser Formation, Pilbara Craton, Western Australia: *Precambrian Research*, v. 167, no. 1-2, p. 93-124.
- Vernon, R. H., 1999, Quartz and feldspar microstructures in metamorphic rocks: *The Canadian Mineralogist*, v. 37, p. 513-524.
- von Ardenne, M., 1938, The scanning electron microscope: Theoretical fundamentals: *Z. Tech. Phys.*, v. 109, p. 553-572.
- Wanless, R. K., and Loveridge, W. D., 1978, Rubidium-strontium isotopic age studies: Paper 77-14, v. Report 2, p. 70.
- Wanty, R. B., and Goldhaber, M. B., 1992, Thermodynamics and kinetics of reactions involving vanadium in natural systems: Accumulation of vanadium in sedimentary rocks: *Geochimica et Cosmochimica Acta*, v. 56, no. 4, p. 1471-1483.
- Watson, E. B., and Harrison, T. M., 1984, Accessory minerals and the geochemical evolution of crustal magmatic systems: a summary and prospectus of experimental approaches: *Physics of earth and planetary interiors*, v. 35, p. 19-30.
- Webb, A. D., Dickens, G. R., and Oliver, N. H. S., 2003, From banded iron-formation to iron ore: geochemical and mineralogical constraints from across the Hamersley Province, Western Australia: *Chemical Geology*, v. 197, no. 1-4, p. 215-251.
- White, A. J. R., 1979, Sources of granite magmas: *Geological Society of America Abstracts with Programs* 11, v. no.7, p. 539.
- White, S. H., Burrows, S. E., Carreras, J., Shaw, N. D., and Humphreys, F. J., 1980, On mylonites in ductile shear zones: *Journal of Structural Geology*, v. 2, no. 1-2, p. 175-187.
- White, S. H., and Knipe, R. J., 1978, Transformation- and reaction-enhanced ductility in rocks: *Journal of the Geological Society*, v. 135, no. 5, p. 513-516.
- Wibberley, C., 1999, Are feldspar-to-mica reactions necessarily reaction-softening processes in fault zones?: *Journal of Structural Geology*, v. 21, no. 8-9, p. 1219-1227.

- Will, T. M., 1998, Phase equilibria in metamorphic rocks: Thermodynamic background and petrological applications Berlin, Springer, Lecture notes in earth sciences, 315 p.:
- Williams, M. L., Jercinovic, M. J., and Hetherington, C. J., 2007, Microprobe monazite geochronology: Understanding geologic processes by intergrating composition and chronology: Annual Review of Earth and Planetary Sciences, v. 35, p. 135-175.
- Winkler, H. G. F., 1979, Petrogenesis of metamorphic rocks, Springer-Verlag.
- Wodicka, N., Corrigan, D., Nadeau, L., and Erdmann, S., New U-Pb geochronological results from Melville Peninsula: unravelling the Archean and early Plaeoproterzoic magmatic history of the north-central Rae craton, *in* Proceedings Geological Association of Canada - Mineralogical Association of Canada - Society of Economic Geologists for Geology Applied to Mineral Deposits Joint Annual Meeting, Ottawa, ON, 2011, Volume 34, p. 236.
- Yang, B., Zeng, Z., Wang, X., Yin, X., and Chen, S., 2014, Pourbaix diagrams to decipher precipitation conditions of Si-Fe-Mn-oxyhydroxides at the PACMANUS hydrothermal field: Acta Oceanologica Sinica, v. 33, no. 12, p. 58-66.
- Young, M. D., Sanderman, H., Berniolles, F., and Gertzbein, P. M., 2004, A preliminary stratigraphic and structural geology framework for the Archean Mary River Group, northern Baffin Island, Nunavut: Current Research, v. C1, p. 1-14.
- Zhu, X.-Q., Tang, H.-S., and Sun, X.-H., 2014, Genesis of banded iron formation: A series of experimental simulations: Ore Geology Reviews, v. 63, p. 465-469.
- Zworykin, V. K., Hiller, J., and R.L., S., 1942, A scanning electron microscope: ASTM Bulletin, v. 117, p. 15-23.

Appendix 1 Samples

Appendix 1 Samples

SAMPLE	Lithology	Zone	Deposit	Easting	Northing	Drill Hole	From	To
709	Magnetite-hemite Ore	OZ	No.1			MR1-08-177	22	22.1
716	BIF	OZ	No.1			MR1-08-177	37	37.1
6057	CS	OZ	No.1	563560	7915367			
6062	ASG	FW	No.1			ARD-2A-SE	22.3	22.45
6063	ASG	FW	No.1			ARD-2A-SE	22.85	23
6065	ASG	FW	No.1			ARD-2A-SE	29.75	29.9
6066	ASG	FW	No.1			ARD-2A-SE	37.85	38
6068	ASG	FW	No.1			ARD-2A-SE	54.5	54.65
6072	ASG	FW	No.1			ARD-2A-SE	87.6	87.75
6073	MGr	FW	No.1			ARD-2A-SE	99.3	99.45
6075	QAMS	FW	No.1			MR1-12-223	27.1	27.25
6076	QAMS	FW	No.1			MR1-12-223	29.05	29.2
6077	CS	FW	No.1			MR1-12-223	31.75	31.9
6078	QAMS	FW	No.1			MR1-12-223	35.56	35.71
6079	CS	FW	No.1			MR1-12-223	42.85	43
6080	QAMS	FW	No.1			MR1-12-223	51.75	51.9
6201	CS	FW	No.1			MR1-12-223	55.43	55.58
6202	BS	FW	No.1			MR1-12-223	60.58	60.73
6203	BS	FW	No.1			MR1-12-223	61.42	61.57
6204	BS	FW	No.1			MR1-12-223	62.2	62.35
6205	BS	FW	No.1			MR1-12-223	64.35	64.5
6206	CS	FW	No.1			MR1-12-223	71.36	71.51
6207	ASG	FW	No.1			MR1-12-223	80.23	80.38
6208	QAMS	FW	No.1			MR1-12-223	82.03	82.18
6209	QAMS	FW	No.1			MR1-12-223	87.85	88
6210	QAMS	FW	No.1			MR1-12-223	88.68	88.83
6211	QAMS	FW	No.1			MR1-12-223	97.75	97.9
6212	ASG	FW	No.1			MR1-12-223	113.2	113.35
6213	QAMBS	FW	No.1			MR1-12-223	117.9	118.05
6214	BS	FW	No.1			MR1-12-223	132.6	132.75
6215	BS	FW	No.1			MR1-12-223	134.45	134.6
6216	CS	FW	No.1			MR1-12-223	137.52	137.67
6217	BS	FW	No.1			MR1-12-223	166.4	166.55
6218	BS	FW	No.1			MR1-12-223	172.85	173
6219	CS	FW	No.1			MR1-12-223	174.27	174.42
6220	CS	OZ	No.1			MR1-12-226	75.55	75.7
6221	CS	OZ	No.1			MR1-12-226	102.05	102.2
6222	CS	FW	No.1			MR1-12-226	118.26	118.41
6223	BS	FW	No.1			MR1-12-226	120.93	121.08

SAMPLE	Lithology	Zone	Deposit	Easting	Northing	Drill Hole	From	To
6224	QABS	FW	No.1			MR1-12-226	122.55	122.7
6225	QABS	FW	No.1			MR1-12-226	134.11	134.26
6226	CS	FW	No.1			MR1-12-226	126.1	126.25
6227	BS	FW	No.1			MR1-12-226	130.46	130.61
6228	QAMBS	FW	No.1			MR1-12-226	138.92	139.07
6230	QAMS	FW	No.1			MR1-12-226	171.65	171.8
6231	QAMBS	FW	No.1			MR1-12-226	187.85	188
6232	QAMBS	FW	No.1			MR1-12-226	221.45	221.6
6243	CS	FW	No.1			MR1-12-226	136.65	136.8
6244	QAMBS	FW	No.1			MR1-12-226	236	236.15
6245	BS	FW	No.1			MR1-12-226	251.5	251.65
6246	QAMBS	FW	No.1			MR1-12-225	81.74	81.89
6247	QAMS	FW	No.1			MR1-12-225	221.65	221.8
6248	QAMBS	FW	No.1			MR1-12-225	271.17	271.32
6249	QAMBS	FW	No.1			MR1-12-225	276.2	276.35
6250	ASG	FW	No.1			MR1-12-225	279.5	279.65
6251	QAMBS	FW	No.1			ARD-2A-NW	14	14.15
6253	ASG	FW	No.1			ARD-2A-NW	32.74	32.89
6255	QAMBS	FW	No.1			ARD-2A-NW	64.6	64.75
6257	ASG	FW	No.1			ARD-2A-NW	79.19	79.34
6257	ASG	FW	No.1			ARD-2A-NW	79.19	79.34
6258	ASG	FW	No.1			ARD-2A-NW	87.64	87.79
6260	QAMBS	FW	No.1			ARD-2A-NW	106.44	106.59
6401	BIF	OZ	No.1	540974	7929568			
6402	ASG	FW	No.1	563746	7915662			
6403	ASGr	FW	No.1	563543	7915246			
6405	ASGr	FW	No.1	562878	7913451			
6406	Mgb	FW	No.1	562638	7913085			
6407	Mgb	FW	No.1	562638	7913085			
6416	HO	OZ	No.1	562714	7912796			
6501	CS	HW	No.1			MR1-14-229	7.73	7.88
6502	CS	HW	No.1			MR1-14-229	20.1	20.25
6503	BS	HW	No.1			MR1-14-229	24.15	24.28
6504	BS	HW	No.1			MR1-14-229	42.76	43.04
6506	BS	HW	No.1			MR1-14-229	54	54.19
6507	BS	HW	No.1			MR1-14-229	59.95	60.05
6509	MGr?	HW	No.1			MR1-14-229	50.5	50.65
6510	Mgb	HW	No.1			MR1-14-232	54.9	55
6511	BS	FW	No.1			MR1-14-232	87	87.15
6512	MGr	FW	No.1			MR1-14-232	97.8	97.95

SAMPLE	Lithology	Zone	Deposit	Easting	Northing	Drill Hole	From	To
6513	MGr	FW	No.1			MR1-14-232	101.4	101.5
6514	Mgb	FW	No.1			MR1-14-231	42.37	42.5
6515	Mgb	FW	No.1			MR1-14-231	58.1	58.2
6516	SGr	FW	No.1			MR1-14-231	84.3	84.45
6517	SGr	FW	No.1			MR1-14-231	98.75	98.95
6518	MGr	FW	No.1			MR1-14-230	40.4	40.6
6519	MGr	FW	No.1			MR1-14-230	62.1	62.25
6520	BS	FW	No.1			MR1-14-230	89.75	89.9
6521	UM	HW	No.1			MR1-14-228	20.4	20.55
6522	UM	HW	No.1			MR1-14-228	23.4	23.5
6523	UMA	HW	No.1			MR1-14-228	45	45.15
6524	UMA	HW	No.1			MR1-14-228	53.2	53.35
6525	UM	HW	No.1			MR1-14-228	89.5	89.65
6526	UMA	HW	No.1			MR1-14-228	105.85	106
6527	VCCx	HW	No.1			MR1-14-228	181.73	181.28
6528	CS	HW	No.1			MR1-14-228	236.7	236.85
6529	Hbl-Amp	HW	No.1			MR1-14-227	18.75	19
6530	VCPC	HW	No.1			MR1-14-227	24.9	25.1
6531	VCPC	HW	No.1			MR1-14-227	29.65	29.85
6532	VCPC	HW	No.1			MR1-14-227	39.75	40
6533	UMA	HW	No.1			MR1-14-227	103.55	103.65
6534	QAMBS	FW	No.1	563007	7914439			
6535	QAMBS	FW	No.1	563043	7913515			
6536	BIF	OZ	No.5					
15918	MGr(A)	FW	No.1	563626	7913143			
15919	QAMBS	FW	No.1	563319	7913015			
15920	MGr	FW	No.1	563013	7913525			
15921	Mgb	FW	No.1	562972	7912960			
15922	Mgb	FW	No.1	562972	7912960			
15923	QAMS	FW	No.1	562993	7913034			
15924	Mgb	FW	No.1	562956	7913025			
15925	Mgb	FW	No.1	562962	7912983			
15926	Mgb	FW	No.1	562888	7913403			
15927	ASGr	FW	No.1	562882	7913419			
15928	CS	FW	No.1	562881	7914024			
15929	Mgb	FW	No.1	562754	7913619			
15930	ASG	FW	No.1	562762	7913496			
15931	Mgb	FW	No.1	562790	7913452			
15932	Mgb	FW	No.1	562754	7913619			
15933	BSSgr	FW	No.1	562761	7913371			

SAMPLE	Lithology	Zone	Deposit	Easting	Northing	Drill Hole	From	To
15934	Mgb	FW	No.1	562737	7913206			
15935	AFGr	FW	No.1	562419	7913797			
15936	QAMBS	FW	No.1	562445	7913838			
15937	SGr	FW	No.1	562533	7913720			
15938	SGr	FW	No.1	562502	7913738			
15939	ASGr	FW	No.1	562429	7913755			
15940	AFGr	FW	No.1	562429	7913755			
15941	Mgb	FW	No.1	562431	7913706			
15942	SGr	FW	No.1	561815	7914833			
15943	ASGr	FW	No.1	561971	7914342			
6066A	ASG	FW	No.1			ARD-2A-SE	37.85	38
6218A	BS	FW	No.1			MR1-12-223	172.85	173
6220A	CS	OZ	No.1			MR1-12-225	75.55	75.7
6229A	QAMS	FW	No.1			MR1-12-226	150.3	150.45
6229B	QAMBS	FW	No.1			MR1-12-226	150.3	150.45
6404A	ASGr	FW	No.1	562867	7913561			

Appendix 2 EMPA

Appendix 2 EMPA

Point	Comment	MgO(Mass%)	Al2O3(Mass%)	FeO(Mass%)	Cr2O3(Mass%)	ZnO(Mass%)	V2O3(Mass%)	MnO(Mass%)	TiO2(Mass%)	CaO(Mass%)	Total(Mass%)			
1	6078_Rutile_01	0.002	0.058	0.852	0.015	-0.006	0.055	0	99.032	0.039	100.047			
2	6078_Rutile_02	0.014	0.054	0.89	0.008	-0.002	0.055	-0.005	99.099	0.01	100.123			
3	6225_Rutile_01	0.012	0.229	3.459	-0.007	-0.005	0.034	0.007	96.505	0.017	100.251			
4	6225_Rutile_02	0.014	0.335	2.326	0.012	0	0.069	0.006	97.898	0.084	100.744			
5	6220A_Hematite_01	0.013	0.478	84.138	-0.006	-0.02	0.153	0.016	0.327	0.017	85.116			
6	6220A_Rutile_01	0.006	0.045	0.76	-0.016	-0.001	0.057	0.005	100.778	0.022	101.656			
Point	Comment	F(Mass%)	CaO(Mass%)	Cl(Mass%)	P2O5(Mass%)	Total(Mass%)								
1	6078_apatite_01	2.886	54.376	0.111	41.385	98.758								
2	6078_apatite_02	3.061	54.162	0.112	41.443	98.778								
3	6078_apatite_03	3.15	54.709	0.107	42.075	100.041								
4	6225_apatite_01	2.639	55.109	0.138	43.395	101.281								
5	6225_apatite_02	2.634	54.778	0.137	43.063	100.612								
6	6225_apatite_03	2.397	54.634	0.155	42.743	99.929								
Point	Comment	MgO(Mass%)	Al2O3(Mass%)	FeO(Mass%)	Cr2O3(Mass%)	ZnO(Mass%)	V2O3(Mass%)	MnO(Mass%)	TiO2(Mass%)	CaO(Mass%)	Total(Mass%)			
1	6225_limenite_01	0.212	47.674	-0.002	-0.002	0.029	0.623	51.076	0.01	99.729	0.76			
2	6225_limenite_02	0.234	0.109	47.61	-0.008	-0.006	0.018	0.628	51.115	0.006	99.706			
4	6220A_limenite_01	0.031	0.086	33.436	-0.008	-0.002	0.016	0.047	56.117	0.021	89.744			
Point	Comment	F(Mass%)	MgO(Mass%)	SiO2(Mass%)	Na2O(Mass%)	Al2O3(Mass%)	FeO(Mass%)	Cr2O3(Mass%)	MnO(Mass%)	P2O5(Mass%)	CaO(Mass%)	K2O(Mass%)	TiO2(Mass%)	Total(Mass%)
1	6078_Muscovite_01	0.343	1.034	46.268	0.413	34.577	2.227	0.006	0.099	-0.001	0.063	9.764	1.034	95.737
2	6078_Muscovite_02	0.009	1.291	45.008	0.439	33.835	2.253	0.011	0.015	-0.001	0.04	10.234	0.76	93.975
3	6078_Muscovite_03	0.203	1.969	44.417	0.385	33.618	3.112	0.027	0.019	0.002	0.061	9.586	0.816	94.215
4	6078_Muscovite_04	0.289	1.05	45.121	0.403	34.041	2.135	0.013	0.016	0	0.025	10.026	0.865	93.984
5	6078_Muscovite_05	0.178	1.034	45.341	0.402	34.023	2.123	-0.005	0.003	-0.004	0.023	10.165	0.88	94.163
6	6078_Muscovite_06	0.147	1.255	46.009	0.407	33.422	2.255	-0.006	-0.001	-0.007	0.032	10.103	0.805	94.421
7	6078_Muscovite_07	0.226	1.294	45.672	0.422	34.081	2.139	0.013	0.01	-0.001	0.051	9.934	0.911	94.752
8	6078_Muscovite_08	0.501	0.973	45.453	0.537	34.14	2.058	-0.027	0.01	0.006	0.223	10.051	1.019	95.016
9	6078_Muscovite_09	0.136	1.63	45.706	0.38	32.661	2.238	-0.008	0.006	0	0.03	9.838	0.828	93.445
10	6078_Muscovite_10	0.138	0.914	45.581	0.424	34.629	2.036	0.019	-0.014	0.007	0.024	9.95	0.983	94.601
11	6078_Biotite_01	0.376	11.853	35.607	0.106	18.739	15.986	-0.038	0.185	-0.005	0.028	9.592	1.954	94.383
12	6078_Biotite_02	0.384	12.495	35.322	0.087	18.665	15.605	0.039	0.204	-0.009	0.026	9.588	1.93	94.336
13	6078_Biotite_03	0.256	12.478	35.44	0.087	18.721	15.685	0.038	0.199	-0.004	0.022	9.531	1.851	94.304
14	6078_Biotite_04	0.401	12.411	35.109	0.096	18.666	15.796	0.02	0.157	0.01	0.05	9.378	1.926	93.82
15	6078_Biotite_05	0.334	12.523	34.999	0.078	18.598	16.426	0.03	0.174	-0.003	0.026	8.934	1.975	94.004
16	6078_Chlorite_01	0.104	1.01	45.343	0.374	34.21	2.422	-0.002	0.027	0.008	0.023	10.233	1.017	94.769
17	6078_Biotite_06	0.329	12.127	35.35	0.098	18.744	16.209	-0.003	0.152	0.001	0.02	9.389	1.944	94.36
18	6078_Biotite_07	0.562	12.419	35.524	0.108	18.634	15.401	-0.011	0.149	0.008	0.124	9.353	1.913	94.184
19	6078_Biotite_08	0.462	12.028	35.682	0.085	18.793	15.473	0.05	0.144	0.023	0.123	9.578	1.903	94.196
20	6078_Biotite_09	0.643	12.277	35.762	0.102	18.679	15.502	-0.018	0.162	-0.003	0.078	9.75	1.96	94.804
21	6078_Biotite_10	0.489	11.39	34.822	0.073	18.378	18.291	-0.01	0.13	0.006	0.021	9.246	1.952	94.788
22	6078_Chlorite_02	0.312	20.174	28.178	0.014	20.488	17.443	0.027	0.049	-0.001	0.034	0.056	0.079	86.853
23	6078_Chlorite_03	0.296	18.371	29.224	0.015	19.908	17.47	0.006	0.059	0.001	0.035	0.088	0.665	86.948
24	6078_Chlorite_04	0.333	19.566	27.656	0.018	20.366	18.335	0.015	0.065	-0.001	0.037	0.043	0.092	86.525
25	6078_Chlorite_05	0.273	19.326	28.457	0.035	20.652	17.352	0.019	0.03	-0.001	0.084	0.169	0.256	86.652
26	6078_Chlorite_06	0.228	17.824	29.597	0.032	19.113	17.446	-0.001	0.054	0.007	0.043	1.555	1.632	87.53
27	6078_Chlorite_07	0.17	17.882	28.501	0.071	19.627	17.439	-0.007	0.073	0	0.088	0.782	1.328	85.954
28	6078_Chlorite_08	0.417	17.652	29.034	0.013	19.691	17.524	-0.013	0.09	-0.01	0.045	1.359	1.977	87.779
29	6078_Chlorite_09	0.674	19.38	28.005	0.034	19.975	17.809	0.003	0.111	-0.006	0.079	0.11	0.201	86.275
30	6078_Chlorite_10	0.197	19.325	28.411	0.029	20.012	17.164	0	0.035	0.002	0.031	0.307	0.703	86.216
31	6225_Biotite_01	0.57	9.99	34.933	0.198	19.565	18.752	-0.007	0.019	0.01	0.084	3.085	1.195	94.494
32	6225_Biotite_02	0.309	9.947	35.268	0.284	19.383	18.654	-0.007	0.045	0.008	0.079	8.956	1.432	94.558
33	6225_Biotite_03	0.206	9.515	34.804	0.242	19.536	18.93	0.03	0.056	-0.002	0.019	8.886	1.398	93.62
34	6225_Biotite_04	0.208	9.769	34.745	0.264	19.234	18.561	0.015	0.043	0.002	0.019	8.972	1.414	93.246
35	6225_Biotite_05	0.153	9.969	35.475	0.293	19.621	19.156	-0.019	0.06	0	0.012	8.945	1.293	94.958
36	6225_Biotite_06	0.422	10.444	35.258	0.249	19.227	19.04	-0.025	0.051	0.007	0.091	8.966	1.245	94.975
37	6225_Biotite_07	0.068	10	35.148	0.31	19.174	18.823	-0.001	0.042	0.01	0.067	8.779	1.342	93.762
38	6225_Biotite_08	0.296	10.274	35.298	0.244	19.094	18.553	-0.013	0.037	0.004	0.041	8.757	1.514	94.099
39	6225_Biotite_09	0.216	9.83	34.844	0.298	19.514	19.109	-0.025	0.02	0.001	0.105	9.107	1.414	94.433
40	6225_Biotite_10	0.254	10.149	34.873	0.285	19.477	19.227	-0.003	0.058	0	0.033	9.105	1.292	94.75
41	6225_Chlorite_01	0.004	15.079	24.12	0.019	23.565	23.856	-0.014	0.079	0.005	0.026	0.018	0.062	86.819
42	6225_Chlorite_02	0.293	14.785	23.995	0.031	23.142	23.568	0.027	0.092	0.006	0.051	0.059	0.075	86.124
43	6225_Chlorite_03	0.184	15.305	24.669	0.036	23.608	23.967	0.009	0.11	0.011	0.042	0.043	0.073	88.057
44	6225_Chlorite_04	0.008	14.913	24.312	0.027	23.123	23.914	0.001	0.088	-0.01	0.032	0.044	0.08	86.532
45	6225_Chlorite_05	0.247	14.874	24.191	0.029	23.226	23.567	0.009	0.102	0.004	0.039	0.05	0.074	86.412
46	6225_Pinite_01	0.065	4.237	46.757	0.237	32.114	5.233	-0.022	0.083	0.007	0.113	5.83	0.005	94.659
47	6225_Pinite_02	0.018	4.613	47.203	0.275	32.311	5.39	0.025	0.089	-0.005	0.155	5.526	-0.004	95.596
48	6225_Pinite_03	0.102	3.514	46.756	0.155	32.312	4.841	0.019	0.059	0.014	0.107	6.171	0.016	94.068
49	6225_Pinite_04	0.112	3.921	46.814	0.216	32.139	4.937	-0.008	0.055	-0.01	0.12	6.841	0.012	95.149
50	6225_Pinite_05	0.146	3.772	46.489	0.147	32.467	5.051	0.062	0.067	0	0.131	5.849	0.014	94.105
51	6220A_Chlorite_01	0.227	14.89	26.736	0.011	24.256	20.393	0.035	0.188	0.011	0.05	0.017	0.031	86.845
52	6220A_Chlorite_02	0.277	15.441	25.39	0.054	23.16	20.422	0	0.218	0.02	0.055	0.05	0.05	85.137
53	6220A_Chlorite_03	0.193	16.025	25.182	0.03	22.457	21.333	-0.015	0.286	0.004	0.044	0.067	0.039	85.645
54	6220A_Chlorite_04	0.195	16.58	24.682	0.018	22.468	22.113	0.031	0.23	-0.001	0.027	0.01	0.051	86.414
55	6220A_Chlorite_05	0.231	16.413	25.883	0.036	22.349	20.796	-0.009	0.269	0.013	0.078	0.036	0.051	86.146
56	6220A_Chlorite_06	0.316	16.652	25.158	0.034	22.415	21.383	-0.015	0.202	0.014	0.039	0.028	0.032	86.258
57	6220A_Chlorite_07	0.166	16.156	25.597	0.019	22.736	21.085	0.009	0.204	-0.003	0.032	0.027	0.036	86.064
58	6220A_Chlorite_08	0.487	15.902	25.386	0.038	22.422	21.123	-0.041	0.249	0.025	0.051	0.04	0.056	85.738
59	6220A_Chlorite_09	0.069	16.676	25.553	0.023	22.411	21.229	-0.04	0.195	-0.015	0.031	0.011	0.045	86.288
60	6220A_Chlorite_10	0.248	16.636	25.088	0.018	22.565	21.63	-0.02	0.234	0.012	0.041	0.015	0.065	85.532

Point	Comment	F(Mass%)	MgO(Mass%)	SiO2(Mass%)	Na2O(Mass%)	Al2O3(Mass%)	FeO(Mass%)	Cr2O3(Mass%)	MnO(Mass%)	P2O5(Mass%)	CaO(Mass%)	K2O(Mass%)	TiO2(Mass%)	Total(Mass%)
1	6225_Garnet_01	0.221	2.804	36.182	0.059	21.392	34.749	-0.001	3.015	0.093	0.583	0.034	0.022	99.153
2	6225_Garnet_02	0.104	2.54	36.416	0.041	21.602	35.173	-0.008	3.215	0.029	0.695	0.005	0.041	99.853
3	6225_Garnet_03	0.211	2.48	36.501	0.017	21.298	35.084	0.01	3.015	0.078	0.576	0.015	0.053	99.538
4	6225_Garnet_04	0.184	3.066	36.128	0.037	21.266	34.916	0.021	2.552	0.041	0.571	0.018	0.023	98.823
5	6225_Garnet_05	0.004	2.657	36.532	0.05	21.286	35.016	-0.017	3.1	0.04	0.807	0.021	0.029	99.525
6	6220A_Garnet_rim01	0.151	2.77	36.847	0.045	21.671	31.304	0	6.824	0.01	0.614	0.006	0.024	100.266
7	6220A_Garnet_inner02	0.11	2.449	36.293	0.038	21.258	35.825	0.038	2.567	0.041	0.357	0.014	0.004	98.994
8	6220A_Garnet_inner03	0.064	1.945	36.292	0.015	21.197	34.029	-0.001	5.064	0.015	0.709	-0.001	0.018	99.346
9	6220A_Garnet_core04	0.227	2.087	36.07	0.023	21.164	34.03	0.014	4.703	0.012	0.54	0.012	0.036	98.518
10	6220A_Garnet_inner05	0.054	2.736	36.262	0.042	21.415	36.508	-0.001	1.193	0.051	0.374	0.033	0.006	98.673
11	6220A_Garnet_rim06	0.074	2.77	36.086	0.03	21.368	31.535	0.004	6.793	0.005	0.602	-0.001	0.015	99.281
12	6220A_Garnet_rim07	0.058	2.599	36.333	0.023	21.357	31.325	0.013	6.921	0.019	0.592	0.002	0.015	99.257
13	6220A_Garnet_inner08	0.22	2.11	35.909	0.015	20.746	30.963	-0.015	8.616	0.186	0.344	0.002	0.08	99.176
14	6220A_Garnet_inner09	0.128	1.445	35.862	0.037	20.719	29.026	-0.003	10.911	0.087	0.565	0.002	0.068	98.847
15	6220A_Garnet_inner10	0.039	1.785	35.766	0.023	21.007	32.39	-0.006	7.863	0.2	0.334	0.008	0.031	99.44
16	6220A_Garnet_rim11	0.067	2.722	36.468	0.034	21.216	31.108	0.013	6.751	0.015	0.6	0.01	0.027	99.031
17	6220A_Garnet_rim12	0.002	2.868	36.666	0.056	21.227	30.904	0.038	6.482	-0.002	0.622	0.027	0.017	98.907
18	6220A_Garnet2_core1	0.146	2.925	36.302	0.017	21.282	37.133	0.014	0.939	0.057	0.382	0.017	0.026	99.24
19	6220A_Garnet2_core2	0.067	2.772	36.248	0.041	21.259	37.075	0	0.975	0.036	0.371	0.015	0.012	98.871
20	6220A_Garnet2_core3	0.114	3.081	36.197	0.051	21.309	36.853	-0.006	0.559	0.073	0.411	0.038	0.024	98.714
21	6220A_Garnet2_core4	0.071	2.851	36.295	0.018	21.386	37.043	0.021	0.985	0.029	0.354	0.014	0.019	99.086
22	6220A_Garnet2_rim1	0.083	2.751	36.516	0.011	21.363	30.693	-0.014	7.478	0.005	0.646	0.012	0.007	99.551
23	6220A_Garnet2_rim2	0.14	2.751	36.098	0.012	21.282	31.496	-0.02	6.649	0.025	0.694	0.004	0.022	99.153
24	6220A_Garnet2_rim3	0.206	2.792	36.029	0.035	21.288	31.721	0.018	6.792	0.035	0.497	0.01	0.026	99.449
25	6220A_Garnet2_rim4	0.067	2.767	36.253	0.052	21.434	30.807	-0.007	7.1	0.036	0.613	0.015	0.029	99.166
Point	Comment	F(Mass%)	MgO(Mass%)	SiO2(Mass%)	Na2O(Mass%)	Al2O3(Mass%)	FeO(Mass%)	Cr2O3(Mass%)	MnO(Mass%)	P2O5(Mass%)	CaO(Mass%)	K2O(Mass%)	TiO2(Mass%)	Total(Mass%)
1	6225_Stauroilite_01	0.173	1.815	26.912	0.003	51.648	14.136	0.026	0.165	0.001	0.024	0.01	0.52	95.433
2	6225_Stauroilite_02	0.066	1.827	26.902	-0.012	51.686	13.921	-0.003	0.182	0.007	0.016	0.002	0.571	95.165
3	6225_Stauroilite_03	-0.052	1.796	26.939	0.011	51.499	14.086	-0.027	0.168	0.002	0.024	0.031	0.473	94.95
4	6225_Stauroilite_04	0.118	1.87	27.622	0.021	51.649	14.113	0.014	0.116	0.008	0.027	0.03	0.314	95.902
5	6225_Stauroilite_05	0.099	1.841	27.257	0.017	51.874	14.017	-0.021	0.15	-0.002	0.011	0.011	0.578	95.332
6	6225_Stauroilite_06	0.079	1.697	27.095	0.005	51.649	13.975	-0.002	0.168	0.005	0.03	0.022	0.76	95.483
7	6220A_unknown_garnet_rim_01	0.184	0.233	48.382	0.026	34.611	1.053	0.019	0.131	0.101	0.159	0.289	0.036	85.224
8	6220A_unknown_garnet_rim_02	0.251	0.075	48.092	0.022	37.745	0.594	-0.005	0.059	0.034	0.063	0.047	0.019	86.996
Point	Comment	F(Mass%)	MgO(Mass%)	SiO2(Mass%)	Na2O(Mass%)	Al2O3(Mass%)	FeO(Mass%)	Cr2O3(Mass%)	MnO(Mass%)	P2O5(Mass%)	CaO(Mass%)	K2O(Mass%)	TiO2(Mass%)	Total(Mass%)
1	6225_Cordierite_01	0.117	8.202	47.516	0.139	32.313	8.219	0.003	0.18	0.005	0.038	0.028	0.006	96.766
2	6225_Cordierite_02	0.192	8.129	47.694	0.134	32.403	8.105	-0.012	0.161	-0.01	0.022	0.011	0.006	96.835
3	6225_Cordierite_03	0.07	8.259	47.679	0.142	32.538	8.016	0.006	0.185	-0.001	0.022	0.007	0.008	96.931
4	6225_Cordierite_04	0.136	8.247	47.941	0.107	32.554	8.172	0.018	0.161	0.01	0.025	0.015	0.01	97.396
5	6225_Unknown next to pinite_05	0.251	4.533	40.462	0.069	30.592	7.938	-0.037	0.051	-0.004	0.285	3.453	0.008	87.601
Point	Comment	F(Mass%)	MgO(Mass%)	SiO2(Mass%)	Na2O(Mass%)	Al2O3(Mass%)	FeO(Mass%)	Cr2O3(Mass%)	MnO(Mass%)	P2O5(Mass%)	CaO(Mass%)	K2O(Mass%)	TiO2(Mass%)	Total(Mass%)
1	6227_Stauroilite_01	-0.132	1.635	27.361	0.01	51.828	14.867	0.021	0.013	0	0.019	0.008	0.481	96.111
2	6227_Stauroilite_02	0.097	1.584	26.696	0.013	52.749	15.034	0.004	0.003	0.012	0.013	0.013	0.32	96.538
3	6227_Stauroilite_03	0.07	1.67	26.585	0.02	52.612	15.402	0.007	0.01	0.005	0.007	0.007	0.499	96.894
4	6205_Andalusite_01	-0.126	0.052	36.468	0.047	60.288	0.778	-0.011	0.02	0.003	0.043	0.007	0.023	97.592
5	6205_Andalusite_02	-0.054	0.042	36.884	0.027	60.552	0.812	0.006	0.02	0.01	0.02	0.017	0.021	98.357
6	6205_Andalusite_03	0.027	0.021	37.321	0.028	61.069	0.653	0.002	-0.015	-0.001	0.006	0.006	0.02	99.137
7	6205_Andalusite_2_01	-0.028	0.072	36.847	0.013	61.068	0.924	-0.003	-0.01	0.015	0.008	0.009	0.014	98.929
8	6205_Andalusite_2_02	0.018	0.056	37.077	0.013	60.868	0.806	-0.014	-0.02	-0.001	0.004	0.005	0.031	98.843
9	6205_Andalusite_2_03	-0.113	0.036	37.161	0.02	61.243	0.799	0.025	-0.012	0	0.007	0.009	0.031	99.206
Point	Comment	F(Mass%)	MgO(Mass%)	SiO2(Mass%)	Na2O(Mass%)	Al2O3(Mass%)	FeO(Mass%)	Cr2O3(Mass%)	MnO(Mass%)	P2O5(Mass%)	CaO(Mass%)	K2O(Mass%)	TiO2(Mass%)	Total(Mass%)
1	6227_Garnet_core01	0.016	2.566	36.607	0.047	21.244	37.816	0.029	1.346	0.11	0.551	0.028	0.077	100.437
2	6227_Garnet_core02	-0.12	2.623	36.532	0.028	21.171	37.995	0.006	1.198	0.078	0.428	0.011	0.08	100.003
3	6227_Garnet_core03	-0.139	2.651	36.184	0.043	21.131	37.739	0.018	1.148	0.113	0.427	0.025	0.069	99.409
4	6227_Garnet_rim01	-0.105	2.137	36.748	0.03	21.362	39.898	-0.021	0.204	0.076	0.169	0.02	0.02	100.538
5	6227_Garnet_rim02	0.075	2.253	36.636	0.012	21.411	39.334	-0.001	0.141	0.095	0.212	0.008	0.002	100.178
6	6227_Garnet_rim03	0.035	2.408	36.712	0.034	21.458	39.401	0.019	0.144	0.065	0.23	0.011	-0.002	100.515
Point	Comment	MgO(Mass%)	Al2O3(Mass%)	FeO(Mass%)	Cr2O3(Mass%)	ZnO(Mass%)	V2O3(Mass%)	MnO(Mass%)	TiO2(Mass%)	CaO(Mass%)	Total(Mass%)			
1	6526_Chromite_01	0.817	1.116	58.625	30.55	0.503	0.354	0.425	1.818	0.013	94.221			
2	6526_Magnetite_01	0.36	0.269	78.633	11.245	0.107	0.33	0.148	0.982	0.008	92.088			
3	6526_Magnetite_02	0.259	0.143	82.146	7.829	0.075	0.311	0.081	0.461	0.011	91.316			
4	6526_Magnetite_03	0.217	0.157	82.306	7.431	0.044	0.281	0.083	0.486	0.012	91.017			
5	6526_Magnetite_04	0.314	0.183	80.667	8.86	0.055	0.303	0.098	0.657	0.01	91.147			
6	6533_Magnetite_01	2.264	0.232	71.088	17.488	0.234	0.196	0.634	0.261	0.003	92.4			
7	6533_Magnetite_02	2.069	0.158	76.186	12.417	0.106	0.171	0.33	0.128	0.01	91.575			
8	6533_Magnetite_03	1.969	0.153	76.733	12.021	0.088	0.169	0.324	0.144	0.012	91.613			
9	6533_Magnetite_04	1.311	0.013	83.278	5.767	0.005	0.128	0.089	0.029	0.006	90.626			
10	6533_Magnetite_05	0.844	-0.024	87.084	1.525	-0.001	0.035	0.042	0.015	0.01	89.53			

Point	Comment	F(Mass%)	MgO(Mass%)	SiO2(Mass%)	Na2O(Mass%)	Al2O3(Mass%)	FeO(Mass%)	Cr2O3(Mass%)	MnO(Mass%)	P2O5(Mass%)	CaO(Mass%)	K2O(Mass%)	TiO2(Mass%)	Total(Mass%)
1	6526_Amphibole_01	-0.002	27.5	58.148	0.043	0.094	9.518	0.051	0.232	0.005	0.291	0.02	0.021	95.921
2	6526_Amphibole_02	0.018	27.271	58.02	0.046	0.054	10.069	0.037	0.303	0.007	0.286	0.018	0.007	96.146
3	6526_Amphibole_03	-0.006	27.173	57.963	0.043	0.082	10.010	0.015	0.278	0.004	0.339	0.007	0.027	95.926
4	6526_Amphibole_04	0.062	27.379	58.142	0.052	0.105	8.83	0.017	0.268	-0.004	0.531	0.02	0.016	95.418
5	6526_Amphibole_05	0.048	27.128	57.286	0.055	0.104	11.163	0.054	0.293	-0.002	0.346	0.013	0.061	96.549
6	6526_Amphibole_06	-0.035	27.61	57.986	0.056	0.073	9.607	0.023	0.218	0.003	0.263	0.008	0.012	95.824
7	6526_Amphibole_07	-0.015	27.149	57.219	0.032	0.049	10.784	0.028	0.342	0.01	0.272	0.016	0.012	95.898
8	6526_Amphibole_08	-0.012	26.423	57.081	0.047	0.118	10.405	0.032	0.287	0.007	0.375	0.004	0.009	96.342
9	6526_Amphibole_09	0.002	27.657	58.245	0.036	0.05	9.165	0	0.221	0.005	0.261	0.016	0.005	95.663
10	6526_Amphibole_10	-0.053	27.037	57.097	0.042	0.069	11.095	0.023	0.299	0.007	0.383	0.004	0.01	96.013
11	6519_Amphibole_01	0.137	13.015	46.37	0.843	8.631	13.923	0.017	0.928	0.008	11.962	0.611	0.077	96.522
12	6519_Amphibole_02	0.099	12.222	45.227	0.967	9.921	14.619	0.015	0.91	0.002	11.859	0.703	0.159	96.703
13	6519_Amphibole_03	0.213	14.314	49.01	0.691	6.494	12.445	-0.009	0.888	-0.005	12.011	0.363	0.086	96.501
14	6519_Amphibole_04	0.071	14.317	48.234	0.598	6.135	12.623	-0.014	0.909	0.008	12.11	0.318	0.206	96.515
15	6519_Amphibole_05	0.081	12.466	45.922	0.891	9.186	14.02	-0.005	0.885	0.005	11.899	0.612	0.114	96.076
16	6519_Amphibole_06	0.021	13.174	47.264	0.783	8.078	13.508	0.003	0.893	0.003	11.999	0.584	0.095	96.405
17	6519_Amphibole_07	0.161	12.082	45.186	0.97	9.51	14.886	-0.014	0.896	0.007	11.824	0.789	0.312	96.709
18	6519_Amphibole_08	0.086	13.79	47.999	0.722	7.026	13.218	0.017	0.825	0.01	12.037	0.453	0.185	96.368
19	6519_Amphibole_09	0.116	13.718	48.024	0.744	7.118	12.894	0.003	0.898	-0.003	11.961	0.478	0.112	96.063
20	6519_Amphibole_10	0.093	15.454	50.544	0.497	4.938	11.389	0.003	0.918	-0.003	12.128	0.259	0.063	96.283
21	6519_Biotite_01	0.198	12.478	36.653	0.066	17.017	15.927	0.027	0.552	-0.005	0.047	8.886	1.701	94.547
22	6519_Biotite_02	0.141	12.598	36.438	0.055	16.735	15.885	0.021	0.572	0.01	0.032	8.836	1.766	94.089
23	6519_Biotite_03	0.109	12.71	36.547	0.051	17.183	15.349	0.006	0.54	0.003	0.054	9.989	1.458	93.999
24	6519_Biotite_04	0.259	12.798	36.513	0.049	16.962	15.109	0.026	0.528	0.006	0.065	9.779	1.49	94.634
25	6519_Biotite_05	0.206	12.467	36.229	0.048	16.761	15.803	0.003	0.574	-0.002	0.032	9.742	1.871	93.734
26	6519_Biotite_06	0.222	12.085	36.133	0.037	16.636	16.559	-0.023	0.533	-0.003	0.036	9.38	1.803	93.988
27	6519_Biotite_07	0.114	12.154	36.085	0.061	16.591	16.542	0.035	0.571	-0.005	0.059	9.852	1.934	93.993
28	6519_Biotite_08	0.051	11.34	35.694	0.049	16.843	17.734	-0.009	0.577	-0.018	0.049	9.663	1.886	93.959
29	6519_Biotite_09	0.35	12.889	36.385	0.045	17.036	15.855	0.027	0.559	-0.004	0.045	9.855	1.327	94.369
30	6519_Biotite_10	0.299	13.268	36.587	0.053	16.756	15.291	0.002	0.483	-0.003	0.056	9.977	1.135	93.904
31	15940_Biotite_01	0.261	10.996	29.91	0.047	17.517	24.781	-0.007	0.654	0.005	0.113	2.845	0.808	87.391
32	15940_Biotite_02	0.14	10.818	28.276	0.046	19.705	29.299	-0.029	0.234	-0.011	0.075	0.099	0.079	85.741
33	15940_Biotite_03	0.098	9.833	24.259	0.091	20.186	30.497	-0.004	0.26	0.003	0.097	0.235	0.044	85.599
34	15940_Biotite_04	-0.017	8.005	24.482	0.046	19.482	32.843	0.023	0.313	0.003	0.094	0.108	0.145	85.527
35	15940_Biotite_05	0.331	11.943	27.37	0.023	18.336	27.316	-0.003	0.796	0.005	0.068	0.512	0.275	86.972
36	6533_Talc_01	-0.002	30.398	61.027	0.144	0.424	1.125	0.109	0.008	0.007	0.027	0.029	0.079	93.375
37	6533_Talc_02	-0.009	30.515	61.274	0.122	0.296	1.031	0.077	-0.008	0.008	0.017	0.034	0.074	93.431
38	6533_Talc_03	-0.033	30.403	61.341	0.175	0.432	1.095	0.063	-0.009	0.003	0.012	0.019	0.083	93.584
39	6533_Serpentine_01	-0.081	33.879	32.6	0.055	14.233	3.05	1.057	0.017	-0.003	0.058	0.067	0.061	84.993
40	6533_Serpentine_02	0.021	37.282	41.523	0.042	0.248	3.283	0.022	0.07	0.015	0.062	0.056	0.064	82.688
41	6533_Talc_04	-0.007	38.981	41.72	0.037	0.016	3.21	-0.023	0.045	0.013	0.046	0.042	0.03	84.11
42	6533_Talc_05	0.027	39.152	41.578	0.029	0.008	3.294	0.047	0.045	0.002	0.027	0.025	0.031	84.265
43	6533_Serpentine_03	0.023	38.869	41.793	0.056	0.099	2.807	0.053	0.024	0.007	0.09	0.076	0.048	83.945
44	6533_Serpentine_04	0.075	37.719	42.968	0.052	0.149	3.103	0.092	0.051	0.007	0.05	0.064	0.043	84.373
45	6533_Serpentine_05	0.054	40.25	44.583	0.031	0.041	1.057	-0.011	0.013	0.008	0.007	0.018	0.016	86.067
Point	Comment	F(Mass%)	MgO(Mass%)	SiO2(Mass%)	Na2O(Mass%)	Al2O3(Mass%)	FeO(Mass%)	Cr2O3(Mass%)	MnO(Mass%)	P2O5(Mass%)	CaO(Mass%)	K2O(Mass%)	TiO2(Mass%)	Total(Mass%)
1	15940_Albite_01	0.028	-0.008	62.546	9.783	22.589	0.007	-0.006	-0.01	0.003	2.938	0.11	-0.007	97.973
2	15940_Albite_02	-0.028	-0.013	65.013	9.926	22.274	0.062	0.036	0.012	0.008	2.795	0.244	-0.012	100.317
3	15940_Albite_03	-0.072	-0.008	65.137	10	22.335	0.02	-0.023	-0.007	0.014	2.787	0.17	0.007	100.36
4	15940_Albite_04	-0.062	0.001	64.483	9.619	22.589	0.062	0.002	-0.025	-0.004	3.154	0.137	0.005	99.961
5	15940_Albite_05	-0.01	0.003	64.953	10.01	22.316	0.001	0.041	-0.011	0.002	2.802	0.127	0.004	100.238
6	15940_K-Spar_01	0.034	-0.007	64.448	0.499	18.823	-0.015	-0.003	0.012	0.001	0.035	16.209	-0.014	100.022
7	15940_K-Spar_02	0.092	0.008	64.136	0.55	18.574	0.018	0.029	0.016	0.003	0.073	16.223	0	99.722
8	15940_K-Spar_03	-0.032	-0.009	64.523	0.588	18.81	0.017	-0.005	0.028	-0.007	0.029	16.131	0.011	100.084
9	15940_K-Spar_04	-0.05	-0.012	64.407	0.508	18.702	0.029	0.013	0.022	-0.004	0.036	16.364	-0.001	100.014
10	15940_K-Spar_05	0.009	0.01	64.545	0.512	18.779	0.007	-0.026	0.016	-0.004	0.039	16.095	0.001	99.983

Trace Elements (ppm)

SAMPLE	Lithology	Zone	Deposit	Li	Ba	Cs	Sr	Rb	La	Ce	Pr	Nd	Sm	Eu	Gd	Tb	Dy	Ho	Er	Tm	Yb	Lu
6057	CS	OZ	No.1	0	0.09	49.1	27.1	1.4	40.4	82.6	9.97	39.4	7.52	2.88	6.35	0.79	3.71	0.75	1.8	0.28	1.63	0.26
6073	MGr	FW	No.1	10	2.31	1165	384	55.6	52	97.3	10.5	36.7	6.13	1.07	5.8	0.89	5.21	1.08	2.84	0.48	3.03	0.46
6077	CS	FW	No.1	30	0.56	792	12.5	40.2	16	32.5	3.53	14.1	3.13	0.65	2.49	0.48	2.77	0.51	1.51	0.2	1.45	0.19
6078	QAMS	FW	No.1	10	1.71	3250	26	127	34.4	75.9	8.75	33.8	6.45	1.06	5.07	0.7	4.06	0.78	2.32	0.34	2.13	0.34
6080	QAMS	FW	No.1	20	0.53	600	11.5	72.9	18.9	40.9	4.4	15.2	2.57	0.63	2.7	0.42	2.6	0.54	1.73	0.29	2.01	0.33
6202	BS	FW	No.1	30	5.56	1485	22.8	215	68.1	133.5	15	55.3	10.6	2.22	9.79	1.43	6.96	1.34	3.72	0.5	3.2	0.48
6203	BS	FW	No.1	40	5.83	926	8	194	93.5	189.5	21.6	76.7	14.1	2.67	11.9	1.49	7.51	1.46	3.47	0.54	3.37	0.52
6206	CS	FW	No.1	20	0.52	922	16.5	46.2	14.4	31.6	4	16.5	3.73	0.73	3.02	0.46	2.6	0.54	1.34	0.2	1.31	0.21
6209	QAMS	FW	No.1	100	3.09	1625	23.1	163	10.6	24.5	2.94	11.7	2.23	0.54	1.95	0.27	1.3	0.2	0.63	0.11	0.6	0.09
6210	QAMS	FW	No.1	20	2.26	2550	24	162	29.1	63.4	7.5	28.2	5.09	1.08	3.78	0.5	2.31	0.36	0.87	0.1	0.99	0.15
6211	QAMS	FW	No.1	10	1.4	2260	14.4	113	28	56.4	6.33	24.5	4.69	1.3	3.75	0.48	2.65	0.57	1.43	0.22	1.21	0.21
6212	ASG	FW	No.1	0	0.6	1840	19.3	77.7	6.8	13.1	1.4	5	1.12	0.4	1.32	0.2	1.09	0.26	0.72	0.13	0.8	0.13
6213	QAMS	FW	No.1	10	1.23	2220	19.6	126	42.7	88.2	10.05	36	6.67	1.34	5.86	0.86	4.6	0.9	2.71	0.39	2.36	0.36
6216	BS	FW	No.1	50	6.97	722	11.6	312	39.8	82.2	10	39.5	9.45	1.4	7.78	1.04	5.52	1.02	2.53	0.34	2.4	0.36
6220	CS	OZ	No.1	10	0.67	49.5	5.5	7.1	44	97.5	12.1	47.5	9.64	2.98	8.42	1.34	8.37	1.82	5.22	0.77	4.94	0.73
6221	CS	OZ	No.1	0	0.16	6.1	2.1	1.8	54.1	107	12.4	47.1	7.31	2.15	5.66	0.67	3.35	0.61	1.85	0.24	1.81	0.28
6224	QABS	FW	No.1	110	4.22	1325	14	150	62.1	118.5	13.1	48.6	8.57	2.02	7.09	0.99	5.08	1.04	2.65	0.34	2.25	0.4
6225	QABS	FW	No.1	80	4.17	1090	12.1	132.5	36.9	75	8.19	30.2	5.36	1.36	4.47	0.64	4.12	0.85	2.19	0.3	2.01	0.35
6227	BS	FW	No.1	20	6.41	2050	21.7	208	68.2	135	15.1	54.2	9.22	2.31	7.53	1.1	5.77	1.27	3.03	0.44	2.71	0.43
6229A	QAMS	FW	No.1	20	2.18	1240	23.2	117.5	19.8	38.4	4.33	14.7	2.83	0.85	2.81	0.47	2.88	0.62	1.68	0.28	1.96	0.31
6229B	QAMBS	FW	No.1	10	3.33	1470	24.1	159.5	51.6	96.5	10.45	37.3	6.59	1.55	5.19	0.7	3.72	0.74	2.14	0.25	1.73	0.26
6230	QAMS	FW	No.1	30	2.54	1640	87.7	153	41.3	84.6	9.57	34.2	6.11	1.82	4.81	0.68	3.74	0.77	2.05	0.31	1.96	0.34
6231	QAMBS	FW	No.1	20	1.17	1620	108	83.9	29.2	57.9	6.22	20.8	3.86	1.29	3.65	0.5	3.01	0.6	1.75	0.26	1.67	0.28
6251	QAMBS	FW	No.1	50	4.74	392	154.5	141	43.5	84.5	8.98	29.4	5.71	1.73	4.97	0.74	4.57	1.08	3.06	0.47	3.58	0.64
6253	ASG	FW	No.1	10	2.71	787	170.5	74.7	57.1	106.5	11.35	39	7.22	1.15	5.48	0.9	4.98	1.14	3.13	0.54	3.42	0.5
6257	ASG	FW	No.1	10	1.2	724	116	56.9	18.3	34.7	3.78	12.9	2.54	0.65	2.4	0.41	2.73	0.62	1.64	0.26	1.66	0.29
6401	BIF	OZ	No.1	0	0	4.1	3.1	0.7	5.4	10.9	1.31	5.2	0.97	0.6	0.71	0.1	0.71	0.21	0.6	0.08	0.56	0.1
6402	ASG	FW	No.1	10	0.41	1475	21.5	146.5	21.2	44	4.7	16.3	3.28	0.61	2.78	0.44	2.67	0.5	1.51	0.28	1.77	0.3
6403	ASGr	FW	No.1	10	1.19	107	47	379	14.5	42.6	5.9	21.7	7.62	0.13	8.56	1.91	14.3	3.29	11.15	2.21	17.2	2.82
6404A	ASGr	FW	No.1	10	0.95	79.2	18.4	269	2.5	7.1	0.94	3.4	1.73	0	1.8	0.52	3.8	0.9	3.17	0.68	5.05	0.85
6405	ASGr	FW	No.1	10	0.5	247	36.4	210	10	30.5	4.37	17.3	6.51	0.06	7.16	1.66	11.8	2.62	8.91	1.74	11.75	1.97
6406	Mgb	FW	No.1	80	6	673	72.8	498	7.6	16.9	2.17	8.5	2.55	0.53	2.56	0.52	3.44	0.72	2.22	0.38	2.16	0.3
6407	Mgb	FW	No.1	40	0.94	54.9	90.8	132	2.3	6.1	0.95	5	1.72	1.44	2.4	0.39	2.73	0.61	1.62	0.27	1.74	0.24
6416	HO	OZ	No.1	0	0.03	9.1	6.6	2	2.2	4.6	0.56	2.2	0.49	0.36	0.77	0.14	0.71	0.21	0.67	0.1	0.72	0.1
6501	CS	HW	No.1	30	0.17	10.5	2.4	2	5.3	12.9	1.97	10.2	3.01	0.92	3.7	0.63	4.34	1.1	3.17	0.49	2.89	0.49
6502	CS	HW	No.1	50	1.51	182.7	7	54.3	3.2	8.2	1.23	6.4	2.36	0.95	3.25	0.61	4.03	0.84	2.54	0.4	2.59	0.37
6503	BS	HW	No.1	90	1.75	405	24	79	5	12.5	1.97	10.9	3.25	1.42	3.93	0.72	4.57	0.89	2.79	0.37	2.39	0.39
6509	MGr	FW	No.1	0	0.27	406	24.3	110.5	29.6	58.8	6.8	24.5	5.38	0.35	4.45	0.8	4.85	1	3.16	0.5	3.53	0.58
LDL				10	0.5	0.01	0.1	0.2	0.5	0.5	0.03	0.1	0.03	0.03	0.05	0.01	0.5	0.01	0.5	0.01	0.03	0.01

SAMPLE	Lithology	Zone	Deposit	Th	U	Y	Zr	Hf	Nb	Ta	Ga	Cr	V	Sn	Ti	W	As	Bi	Hg	Sb	Se	Te	Ag	Cd	Co	Cu	Mo	Ni	Pb	Sc	Zn	LOI	Total
6057	CS	OZ	No.1	10.6	2.69	20.1	155	3.6	5.5	0.5	15.4	2330	120	1	0	0	1.2	0.35	0.006	0.19	0.2	0.01	0	2.3	88	14	1	1080	28	17	131	2.85	101.03
6073	MGr	FW	No.1	27.7	10.4	32.2	197	5.4	10.7	0.9	15.2	20	17	3	0	1	0.3	6.38	0.005	0.05	0.7	0.05	1.2	0.5	3	30	0	9	74	4	33	0.94	99.38
6077	CS	FW	No.1	10.5	6.11	13.3	137	3.7	6.9	1	20.9	10	52	2	0	3	2.2	1.67	0.008	0.1	0.5	0.02	0	0	39	3	0	101	16	5	62	9.5	98.06
6078	QAMS	FW	No.1	12.3	3.88	19.9	521	12.3	16.9	1.1	19.2	10	59	3	0.7	5	2.8	0.36	0.005	0.1	0.6	0.01	0	0	15	53	0	11	21	12	32	3.27	100.59
6080	QAMS	FW	No.1	37	9.02	16.2	121	4	8.9	1.3	15.1	10	11	1	0	3	0	0.07	0.005	0	0.2	0	0	0	15	2	0	13	13	3	17	3.35	101.39
6202	BS	FW	No.1	23.1	13.95	34.2	419	10.7	16.6	1.3	37.2	10	93	4	1.6	3	0	0.08	0.007	0	0.7	0	0	0	23	1	0	10	21	21	36	3.13	101.17
6203	BS	FW	No.1	20.8	15.55	35.4	343	8.5	15.7	1.3	32.6	0	84	3	1	1	0.1	0.25	0.008	0	0.7	0.04	0	0	25	1	3	12	20	11	55	4.47	99.3
6206	CS	FW	No.1	5.84	3.59	12	147	3.5	9.1	0.5	25.2	10	123	4	0	4	0	0.03	0.006	0	0.2	0	0	0	23	0	0	65	4	6	43	8.93	99.01
6209	QAMS	FW	No.1	3.08	3.22	5.4	81	2.2	4.6	0.3	19.2	50	120	3	1.2	5	0	0.05	0.005	0	0.2	0	0	0	22	3	0	61	9	13	53	4.38	98.63
6210	QAMS	FW	No.1	5.84	6.14	8.2	100	2.8	5.2	0.5	22.2	40	142	3	1.1	5	0	0.04	0	0.3	0	0	0	22	3	0	57	16	14	36	3.88	100.26	
6211	QAMS	FW	No.1	9.07	6.22	13.7	409	9.6	7.8	0.6	16.1	40	18	2	0.6	3	0.1	0.08	0	0.3	0.01	0	0	8	13	2	6	16	6	36	2.52	100.9	
6212	ASG	FW	No.1	29.5	7.81	8.4	71	3	1.7	0.3	13.3	10	0	1	0	5	0	0.02	0	0	0	0	0	0	1	5	0	2	20	1	7	2.2	101.2
6213	QAMS	FW	No.1	18.75	5.52	24.4	328	8.3	9.9	0.9	20.1	10	40	3	0.5	4	0	0.11	0	0.3	0	0	0	0	12	0	0	3	30	12	55	3.23	99.52
6216	BS	FW	No.1	11.65	4.14	28.9	135	3.6	10.6	0.5	22.1	760	193	4	1.5	1	2.5	0.02	0	0.5	0.01	0	0.5	47	0	0	179	33	20	143	3.98	100.45	
6220	CS	OZ	No.1	16	4.86	45	350	9.4	17.3	1.6	24.7	20	107	1	0	2	106.5	0.03	0	0.06	2.3	0.28	0	1.5	15	55	2	72	4	10	350	7.99	98.05
6221	CS	OZ	No.1	17.65	2.94	19.6	191	4.9	8.1	0.6	23.5	1160	204	1	0	4	1.2	0.02	0.007	0	0.2	0.02	0	0	46	1	0	296	0	12	95	8.07	100.07
6224	QABS	FW	No.1	18.5	7.77	26.5	411	9.5	12	0.8	18.5	40	77	3	0.6	1	0.8	0.09	0	0.4	0.01	0	0	13	1	0	16	8	13	67	3.73	100.16	
6225	QABS	FW	No.1	12.4	3.24	22.2	483	11	12	0.8	18.5	20	68	2	0.7	1	0	0.18	0	0.3	0	0	0	12	2	0	11	7	12	43	2.67	100.05	
6227	BS	FW	No.1	16	5.14	30.2	638	14.7	17.9	1.2	31.9	20	105	3	0.9	9	0	0.06	0	0.5	0	0	0	0	12	8	0	23	15	16	18	0.9	100.28
6229A	QAMS	FW	No.1	15.6	4.5	17.4	110	3.6	7	0.7	20	10	17	2	0	6	0.2	0.07	0	0.2	0	0	0	0	4	2	0	5	11	3	38	2.24	100.9
6229B	QAMBS	FW	No.1	13.35	3.3	18.5	491	11.3	12.5	0.7	22.6	20	58	3	0.6	4	0.3	0.09	0	0.4	0	0	0	10	2	0	12	13	10	56	2.45	101.06	
6230	QAMS	FW	No.1	12.2	2.59	19.3	426	9.5	11.4	0.7	17	20	64	2	0.7	2	0	0.61	0	0.4	0	0	0	10	12	0	8	10	12	50	1.89	101.87	
6231	QAMBS	FW	No.1	11.45	2.66	16.7	445	10.4	11.1	1	19.9	20	63	2	0	2	0.1	0.07	0	0.4	0.01	0	0	9	38	0	7	5	12	49	2.13	101.95	
6251	QAMBS	FW	No.1	19.3	7.45	30.4	746	15.5	20.2	2.9	22	10	36	4	0.6	1	0	0.11	0	0.05	0.9	0.01	0	0	14	67	2	4	65	16	109	0.98	99.97
6253	ASG	FW	No.1	27.5	8.02	30.3	231	6.3	8.8	1.2	15.2	10	14	2	0	0	0.2	0.07	0	0.8	0	0	0	3	50	0	2	49	5	27	0.61	99.39	
6257	ASG	FW	No.1	11.7	8.05	18.5	89	2.8	5.6	1.2	13.8	10	10	2	0	2	0	0.09	0	0.2	0.01	0	0	2	10	2	0	39	2	41	0.63	100.12	
6401	BIF	OZ	No.1	0.34	0.3	5.5	3	0	0.5	0	0.8	20	10	0	0	1	0	0.03	0.005	0.12	0	0.02	0	0	0	0	0	2	0	1	0	-1.49	100.03
6402	ASG	FW	No.1	19.95	6.44	15.4	94	3.3	6.4	0.9	13.3	10	5	2	0.5	4	0.1	0.03	0	0	0	0	0	2	9	0	7	37	2	23	1.67	100.47	
6403	ASGr	FW	No.1	35	14.65	108	150	13.1	63	13.7	25.2	20	0	18	1.3	2	0.4	0.22	0.005	0.06	1.6	0	0	0	14	0	4	40	4	18	1.59	101.97	
6404A	ASGr	FW	No.1	31.3	11.05	28.8	142	12	56.6	16.6	26.2	10	0	15	0.8	1	0.3	0.37	0	0.4	0.01	0	0	1	6	0	1	49	4	18	0.61	101.69	
6405	ASGr	FW	No.1	35.9	9.93	66.3	153	10.1	59.3	9	25.4	10	0	13	0.7	2	0.3	0.11	0	0.13	0	0	0	2	9	0	3	61	4	51	0.67	101.58	
6406	Mgb	FW	No.1	3.35	1.26	23.6	86	2.5	6.6	0.3	21.7	210	201	2	2.9	2	0	0.12	0	0.6	0.01	0	0	59	283	0	93	5	29	158	2.07	98.74	
6407	Mgb	FW	No.1	0.42	0.11	14.7	43	1.4	1.9	0	14.3	280	270	3	0	0	0	0.15	0	0.5	0.01	0	0	56	252	0	132	0	28	99	2.26	99.07	
6416	HO	OZ	No.1	0.21	0.56	7.3	3	0	0	0	1.4	10	0	0	0	2	1.5	0.05	0.006	0.34	0	0.01	0.6	0	0	1	3	22	0	0	0.32	95.34	
6501	CS	HW	No.1	0.28	0.11	26.7	61	1.9	2.7	0.1	26	660	438	1	0	4	0.1	0.03	0.005	0	0.3	0.01	0	0	88	140	0	266	0	34	189	8.07	100.22
6502	CS	HW	No.1	0.42	0.15	21.7	64	2	2.7	0.2	19.7	710	360	1	0	3	0.4	0.03	0	0.3	0.02	0	0	78	39	0	185	0	41	74	7.58	98.59	
6503	BS	HW	No.1	0.3	0.09	22.9	69	1.8	2.8	0.2	22.9	1000	548	1	0	1	0.2	0.02	0	0.4	0.03	0	0	59	251	0	173	0	50	45	7.43	100.19	
6509	MGr	FW	No.1	38	11.5	31.1	124	4.6	13.3	1.6	18.1	20	8	4	0.5	3	0.2	0.04	0	0.6	0.01	0	0	2	27	0	2	30	2	14	0.89	99.45	
LDL				0.05	0.05	0.5	2	0.2	0.2	0.1	0.1	10	5	1	0.5	1	0.1	0.01	0.005	0.05	0.2	0.01	0.5	0.5	1	1	1	1	2	1	1	2	

SAMPLE	Lithology	Zone	Deposit	Li	Ba	Cs	Sr	Rb	La	Ce	Pr	Nd	Sm	Eu	Gd	Tb	Dy	Ho	Er	Tm	Yb	Lu
6513	MGr	FW	No.1	30	0.95	766	30.2	116.5	18.5	38.1	4.73	17.7	4.03	0.44	4.06	0.77	5.29	1.04	3.52	0.55	4	0.65
6514	Mgb	FW	No.1	10	0.64	156.8	359.5	24.5	2.6	6.6	1.06	5.6	1.89	0.81	3.08	0.46	3.35	0.71	2.3	0.31	2.19	0.32
6516	SGr	FW	No.1	0	1.17	170.5	21.3	131	16.9	43.2	5.95	24.8	7.91	0.08	9.61	1.75	11.55	2.5	7.51	1.17	8.1	1.19
6517	SGr	FW	No.1	10	4.77	171.2	28	134	14.5	37.6	5.43	22	7.3	0.13	9.51	1.99	13.35	2.9	9.35	1.34	10.45	1.49
6518	MGr	FW	No.1	10	6.12	1696	422	65.5	19.8	33.9	3.8	13.6	2.36	0.55	2.1	0.4	2.66	0.51	1.59	0.25	1.74	0.25
6521	UM	HW	No.1	0	0.18	9.5	13	0.2	3.7	4.9	0.39	1.2	0.16	0	0.15	0.02	0.14	0.02	0.04	0	0.08	0.01
6522	UM	HW	No.1	0	0.14	7.4	9.3	0.3	0	0.7	0.08	0.4	0.05	0	0.06	0.01	0.08	0.01	0.1	0	0.11	0.01
6527	VCCx	HW	No.1	40	1.7	347	191.1	38.5	6.1	14.9	2.34	11.6	3.7	1.92	4.72	0.82	5.35	1.19	3.95	0.49	3.45	0.55
6528	CS	HW	No.1	40	0.79	19.8	8	24.6	2.2	5.1	0.83	4.3	2.52	1.11	4.97	1.03	6.25	1.24	3.89	0.56	3.93	0.56
6529	Hbl-Amp	HW	No.1	20	2.4	173.7	370.5	18.6	2.8	6.8	0.95	5.2	1.66	0.56	2.59	0.43	2.96	0.64	1.75	0.21	1.68	0.25
6530	VCPc	HW	No.1	10	0.26	19.1	189.3	3.2	13.7	27.2	3.36	13.5	3.31	0.83	3.79	0.65	4.03	0.83	2.54	0.36	2.31	0.35
6531	VCPc	HW	No.1	20	3.34	192.6	151.3	9.9	13.1	25.5	3.2	12.2	3.19	0.8	3.46	0.56	3.77	0.76	2.42	0.29	2.26	0.3
6532	VCPc	HW	No.1	50	39.1	559	167.7	96.1	14.6	27.7	3.4	14	3.1	0.8	3.74	0.65	3.91	0.83	2.41	0.3	2.25	0.35
6533	UM	HW	No.1	0	0.2	2.2	7.9	0.3	0	0	0.03	0.2	0.08	0.03	0.11	0.03	0.11	0.02	0.07	0	0.12	0.02
6536	BIF	OZ	No.5	0	0.08	3.5	1.3	0.3	2.9	4.8	0.58	2.4	0.48	0.26	0.79	0.14	0.89	0.23	0.83	0.05	0.68	0.14
15918	MGr(A)	FW	No.1	60	1.89	1327	337	148.5	65.8	106.5	10.6	33.7	4.62	1.4	3.67	0.51	3.22	0.64	2.03	0.28	1.58	0.27
15919	QAMBS	FW	No.1	10	3.14	4340	208	106	89	154.5	16.7	61.4	11.2	2.09	9.02	1.34	7.75	1.5	3.94	0.43	2.85	0.38
15920	MGr	FW	No.1	80	5.24	1535	147.6	382	25.6	46	5.4	20.2	4.03	0.79	3.46	0.56	3.56	0.71	2.34	0.31	2.16	0.3
15921	Mgb	FW	No.1	10	0.39	172.9	196.9	12.8	5.6	13.6	2.03	10.2	2.98	1.18	4.4	0.72	4.84	1.08	3.47	0.39	2.96	0.39
15922	Mgb	FW	No.1	20	0.7	744	149.7	70.2	5.1	11.3	1.64	8.3	2.66	1.08	3.57	0.58	4.13	0.85	2.93	0.35	2.56	0.38
15923	QAMS	FW	No.1	30	1.5	2870	143.1	135.5	59.5	103.5	11.05	39.2	6.3	1.24	5.27	0.77	4.34	0.84	2.43	0.3	2.19	0.39
15924	Mgb	FW	No.1	20	0.32	34.2	373.5	7	4	9.1	1.38	6.2	2.03	0.82	2.66	0.47	3.18	0.66	1.99	0.27	2.01	0.31
15925	Mgb	FW	No.1	30	1.63	338	339.5	42.2	5.8	12.3	1.74	8.1	2.65	0.82	3.31	0.63	4.18	0.92	2.95	0.39	2.94	0.43
15926	Mgb	FW	No.1	70	5.86	215	162.7	535	2.2	5.3	0.72	3.7	1.37	0.6	2.1	0.48	3.25	0.82	2.62	0.33	2.59	0.41
15927	ASGr	FW	No.1	30	1.19	560	35.6	261	19	45.3	6.72	25.9	7.78	0.08	8.62	1.7	11.5	2.77	10.4	2.02	16.05	2.47
15928	CS	FW	No.1	30	5.03	3745	11.1	191.5	54.1	101.5	12.15	49.1	9.04	2.49	8.25	1.15	6.53	1.17	3.46	0.45	3.21	0.45
15929	Mgb	FW	No.1	30	1.39	216.5	335	69.3	4.4	10.2	1.47	7.5	2.36	0.74	3.18	0.58	3.75	0.89	2.48	0.34	2.52	0.39
15930	ASG	FW	No.1	20	0.31	754	22.1	89.1	26.1	50.8	5.73	20.4	3.62	0.41	3.76	0.63	3.89	0.82	2.92	0.4	3.16	0.44
15931	Mgb	FW	No.1	20	0.41	205	330	47.2	5.5	12.2	1.72	8.7	2.7	0.95	3.59	0.66	4.19	0.91	2.79	0.38	2.67	0.41
15932	Mgb	FW	No.1	140	8.55	1127	13.4	455	2.1	5.8	0.84	3.7	1.63	0.45	2.6	0.69	5.16	1.18	3.98	0.55	4.12	0.55
15933	BSSgr	FW	No.1	130	7.24	566	9.9	493	6.6	14.7	2.09	10.9	3.39	0.6	4.81	0.87	6.03	1.34	4.09	0.6	4.18	0.62
15934	Mgb	FW	No.1	50	0.95	575	335	105	3.7	8.3	1.3	6	1.93	0.75	2.77	0.5	3.12	0.63	1.85	0.27	2.02	0.29
15935	AFGr	FW	No.1	10	0.33	348.5	22.6	125	10.3	33.4	4.09	17.4	6.59	0.11	7.64	1.68	12.2	2.78	9.16	1.46	11.1	1.54
15936	QAMBS	FW	No.1	40	2.94	1312	37.7	339	24.5	54.4	5.53	21.8	4.24	1.36	3.47	0.49	3.16	0.72	1.73	0.26	2.03	0.36
15937	SGr	FW	No.1	20	1.06	559	35.3	307	15.5	36.3	4.98	20.6	6.05	0.23	7.41	1.52	10.9	2.7	8.26	1.5	10.75	1.7
15938	SGr	FW	No.1	50	3.39	1165	168.2	328	27.1	54.9	6.3	23.4	5.32	0.44	5.72	1.21	8.88	2.21	6.58	1.33	8.61	1.37
15939	ASGr	FW	No.1	10	0.33	955	37.8	106	5.5	21	2.34	10.4	3.54	0.16	3.99	0.97	7.17	1.68	5.44	1.02	8.24	1.23
15940	AFGr	FW	No.1	10	0.61	180	17.9	230	12.1	41.1	5.21	21.5	7.09	0.11	8.25	1.67	11.3	2.74	8.39	1.51	10.95	1.71
15941	Mgb	FW	No.1	30	1.84	152.2	194.4	124.5	2.5	7.4	1.16	6.2	2.19	0.8	2.94	0.53	3.39	0.82	2.26	0.35	2.33	0.31
15942	SGr	FW	No.1	20	1.38	380.5	18.7	243	30.1	66.5	7.75	29.1	6.17	0.21	5.65	0.96	5.44	1.18	3.55	0.59	4.13	0.54
15943	ASGr	FW	No.1	10	1.25	209.5	27.6	81.9	13.7	34.7	4.33	17.6	3.98	0.22	4.78	0.88	5.46	1.18	3.39	0.63	4.49	0.71
LDL				10	0.5	0.01	0.1	0.2	0.5	0.5	0.03	0.1	0.03	0.03	0.05	0.01	0.5	0.01	0.5	0.01	0.03	0.01

Appendix 4 Density

Appendix 4 Density

SAMPLE	Deposit	Mass Cup (g)	Sample Mass with cup (g)	Sample Mass (g)	Volume 1 (cm ³)	Volume 2 (cm ³)	Volume 3 (cm ³)	Volume Average (cm ³)	Volume Average Calc.	Volume Stdev	Density 1 (g/cm ³)	Density 2 (g/cm ³)	Density 3 (g/cm ³)	Density Average
709	No.1	2.1276	24.3833	22.2572	4.27	4.28	4.28	4.27	4.27	0.003	5.21	5.20	5.21	5.21
716	No.1	2.1274	19.0621	16.93471	4.55	4.54	4.55	4.55	4.55	0.003	3.73	3.73	3.73	3.72
6057	No.1	2.1316	9.0978	6.96613	2.08	2.08	2.08	2.08	2.08	0.001	3.35	3.34	3.34	3.34
6073	No.1	2.1315	8.5312	6.39969	2.33	2.33	2.33	2.33	2.33	0.001	2.75	2.75	2.75	2.75
6077	No.1	2.1312	7.1483	5.01705	1.75	1.75	1.75	1.75	1.75	0.001	2.87	2.87	2.87	2.87
6078	No.1	2.1311	8.3370	6.20595	2.20	2.21	2.21	2.21	2.21	0.002	2.81	2.81	2.81	2.81
6080	No.1	2.1313	7.5551	5.42385	1.95	1.95	1.95	1.95	1.95	0.001	2.78	2.78	2.78	2.78
6202	No.1	2.1312	9.1515	7.02035	2.28	2.28	2.28	2.28	2.28	0.001	3.08	3.08	3.08	3.08
6203	No.1	2.1310	9.0976	6.96659	2.25	2.25	2.25	2.25	2.25	0.002	3.09	3.09	3.09	3.09
6206	No.1	2.1309	8.3423	6.21149	2.14	2.14	2.14	2.14	2.14	0.002	2.91	2.91	2.91	2.91
6209	No.1	2.1312	10.4060	8.2748	2.97	2.97	2.97	2.97	2.97	0.001	2.79	2.79	2.79	2.79
6210	No.1	2.1306	9.8717	7.74108	2.73	2.73	2.73	2.73	2.73	0.002	2.83	2.84	2.83	2.83
6211	No.1	2.1312	9.9777	7.84656	2.82	2.82	2.82	2.82	2.82	0.001	2.78	2.78	2.78	2.78
6212	No.1	2.1311	9.4700	7.33892	2.67	2.67	2.67	2.67	2.67	0.002	2.75	2.75	2.75	2.75
6213	No.1	2.1311	8.8598	6.72868	2.41	2.41	2.41	2.41	2.41	0.000	2.80	2.80	2.80	2.80
6216	No.1	2.1310	9.0796	6.94855	2.33	2.33	2.33	2.33	2.33	0.001	2.98	2.98	2.98	2.98
6220	No.1	2.1311	9.8142	7.68315	2.18	2.19	2.19	2.18	2.18	0.002	3.52	3.52	3.51	3.52
6221	No.1	2.1308	8.2966	6.16585	2.03	2.03	2.03	2.03	2.03	0.002	3.04	3.03	3.03	3.03
6224	No.1	2.1311	9.9819	7.85086	2.79	2.79	2.79	2.79	2.79	0.001	2.82	2.82	2.82	2.82
6225	No.1	2.1308	9.4012	7.27044	2.55	2.55	2.55	2.55	2.55	0.000	2.85	2.85	2.85	2.85
6227	No.1	2.1306	9.0277	6.89708	2.09	2.09	2.09	2.09	2.09	0.001	3.30	3.30	3.30	3.30
6230	No.1	2.1305	8.9939	6.86337	2.46	2.46	2.46	2.46	2.46	0.001	2.79	2.79	2.79	2.79
6231	No.1	2.1310	10.1020	7.97096	2.92	2.92	2.92	2.92	2.92	0.001	2.73	2.73	2.73	2.73
6251	No.1	2.1303	10.4809	8.35056	3.00	3.00	3.00	3.00	3.00	0.000	2.78	2.78	2.78	2.78
6253	No.1	2.1310	10.4143	8.28331	3.07	3.07	3.07	3.07	3.07	0.001	2.70	2.70	2.70	2.70
6257	No.1	2.1301	10.5988	8.46871	3.15	3.15	3.15	3.15	3.15	0.001	2.69	2.69	2.69	2.69
6401	No.1	2.1277	17.2754	15.10273	4.20	4.20	4.20	4.20	4.20	0.001	3.60	3.60	3.60	3.60
6402	No.1	2.1294	10.6221	8.4927	3.16	3.16	3.16	3.16	3.16	0.001	2.69	2.69	2.69	2.69
6403	No.1	2.1291	9.5476	7.41853	2.77	2.77	2.77	2.77	2.77	0.001	2.68	2.68	2.68	2.68
6405	No.1	2.1287	9.8140	7.68523	2.89	2.89	2.89	2.89	2.89	0.001	2.66	2.66	2.66	2.66
6406	No.1	2.1285	9.5122	7.38367	2.54	2.54	2.54	2.54	2.54	0.001	2.91	2.91	2.90	2.90
6407	No.1	2.1285	9.2726	7.14406	2.35	2.35	2.35	2.35	2.35	0.001	3.04	3.04	3.04	3.04
6416	No.1	2.1295	23.6279	21.49842	4.19	4.20	4.20	4.20	4.20	0.004	5.13	5.12	5.12	5.12
6516	No.1	2.1280	9.5508	7.42281	2.80	2.80	2.80	2.80	2.80	0.000	2.65	2.65	2.65	2.65
6517	No.1	2.1275	10.9330	8.80954	3.28	3.29	3.28	3.28	3.28	0.001	2.68	2.68	2.68	2.68
6518	No.1	2.1274	10.7667	8.63936	3.17	3.18	3.18	3.17	3.17	0.001	2.72	2.72	2.72	2.72
15935	No.1	2.1271	10.4358	8.30869	3.14	3.14	3.14	3.14	3.14	0.001	2.65	2.65	2.65	2.65
15939	No.1	2.1269	10.9873	8.86046	3.34	3.34	3.34	3.34	3.34	0.001	2.66	2.66	2.66	2.66
6229A	No.1	2.1282	9.5773	7.44906	2.69	2.69	2.69	2.69	2.69	0.001	2.77	2.77	2.77	2.77
6229B	No.1	2.1280	9.6820	7.55396	2.68	2.68	2.68	2.68	2.68	0.001	2.82	2.82	2.82	2.82
6404A	No.1	2.1279	10.8251	8.69725	3.29	3.30	3.30	3.29	3.29	0.001	2.64	2.64	2.64	2.64
6404B	No.1	2.1278	10.9217	8.79388	2.86	2.86	2.86	2.86	2.86	0.001	3.07	3.07	3.07	3.07
GCS-016	No.1	2.1282	10.6485	8.52029	2.64	2.64	2.64	2.64	2.64	0.002	3.23	3.23	3.23	3.23

Appendix 5 U-Pb Isotope Data

Appendix 5 U-Pb Isotope Data

Measurements: Analysis	207Pb/206Pb		206Pb/238U		207Pb/235U		Standardized Concordia:		86Sr Kcs	U ppm	Pb206 ppm	Th/U	Age, Ma	206Pb/238U		207Pb/235U		%Disc	Sigma				
	207Pb/206Pb	Sigma	206Pb/238U	Sigma	207Pb/235U	Sigma	206Pb/238U	Sigma						207Pb/235U	Sigma								
1888-S2	0.19004	0.00170	0.39979	0.00570	288.31082	0.28353	9.322326	0.13682	0.40752	0.00446	0.73017	4.6	434	177	0.50	2517	17	2370	14	2204	20	15	1
4258-S1	0.20742	0.00173	0.55176	0.00954	118.03469	0.44491	9.674291	0.27880	0.41985	0.00916	0.75709	1.4	366	154	0.38	2529	31	2404	26	2260	42	13	2
1014-S2	0.16751	0.00174	0.47014	0.00543	143.36075	0.05151	10.35773	0.20648	0.43344	0.00712	0.82404	0.6	329	142	0.12	2580	19	2467	16	2321	32	12	2
1888-S1	0.20126	0.00105	0.46175	0.00364	286.89771	0.17576	12.99476	0.16685	0.48196	0.00522	0.84915	2.1	255	123	0.24	2789	11	2679	12	2536	23	11	1
4388-S1	0.20227	0.00091	0.51863	0.00361	238.20732	0.30747	14.29837	0.14577	0.52787	0.00455	0.84451	0.3	403	213	0.42	2797	9	2770	10	2733	19	3	1
4363-S1	0.20512	0.00140	0.50003	0.00693	84.91639	0.21970	14.05124	0.23562	0.51224	0.00765	0.89077	0.7	145	74	0.30	2818	12	2753	16	2666	33	7	1
1328-S3	0.20387	0.00185	0.60015	0.00772	79.96458	0.32067	14.56813	0.26541	0.52221	0.00807	0.84872	0.5	224	117	0.44	2845	16	2787	17	2709	34	6	2
1958-S4	0.20526	0.01189	0.27366	0.01564	17.23863	0.52315	7.90953	0.93677	0.28049	0.01405	0.65989	0.9	17	5	0.73	2961	90	2220	67	1694	70	50	3
4258-S2	0.21081	0.00136	0.62032	0.00709	121.85893	0.44885	15.30457	0.24359	0.53826	0.00763	0.89082	1.3	283	152	0.60	2876	12	2834	15	2776	32	4	1
3598-S2	0.21284	0.00087	0.53593	0.00428	117.80253	0.42068	15.49052	0.16845	0.54348	0.00512	0.86068	0.2	197	107	0.59	2880	9	2846	10	2798	21	4	1
3446-S1	0.21321	0.00101	0.54657	0.00377	212.68779	0.66322	15.75606	0.16187	0.55245	0.00470	0.82799	1.7	357	197	0.96	2881	9	2862	10	2835	20	2	1
4388-S2	0.2172	0.00145	0.52179	0.00668	130.38088	0.35385	15.76664	0.17809	0.05624	0.06524	0.83349	2.7	194	107	0.47	2881	10	2863	11	2837	22	2	1
3446-S2	0.21482	0.00112	0.56226	0.00412	120.76810	0.45047	16.31246	0.18388	0.56631	0.00526	0.82058	0.4	203	116	0.64	2891	10	2895	11	2901	22	0	1
3690-S1	0.21388	0.00112	0.63880	0.00673	84.30494	0.42918	15.90618	0.27975	0.55404	0.00910	0.93367	0.1	183	101	0.58	2892	10	2871	17	2842	38	2	2
1328-S2	0.21148	0.00239	0.59559	0.00755	54.15335	0.29418	14.74504	0.29720	0.51314	0.00833	0.80558	0.4	149	76	0.40	2893	19	2799	19	2670	35	9	2
1958-S1	0.21519	0.00085	0.52602	0.00419	145.07019	0.52408	15.68413	0.19479	0.54357	0.00686	0.86763	0.6	140	76	0.73	2900	12	2858	12	2798	24	4	1
1014-S1	0.21378	0.00137	0.70278	0.00633	62.32371	0.40598	17.60604	0.30041	0.60941	0.00697	0.90602	0.2	178	109	0.56	2902	12	2868	17	3088	38	7	2
3598-S1	0.21593	0.00099	0.54315	0.00396	153.34826	0.44286	15.97147	0.17485	0.55170	0.00511	0.84659	0.2	256	141	0.61	2905	9	2875	10	2832	21	3	1
1108-S2	0.21881	0.00116	0.54061	0.00470	135.20186	0.49330	16.36925	0.21986	0.56378	0.00654	0.85498	0.4	130	73	0.61	2910	11	2899	13	2882	27	1	1
5590-s1	0.19053	0.002146	0.140233	0.003485	435.1625977	0.123545	3.6783003	0.104044	0.145894	0.003715	0.900179	1.6	2038	297	0	2679	20	1567	22	678	21	72	1
4431-s2	0.19275	0.000909	0.517339	0.005218	185.5450287	0.309001	14.17144	0.183433	0.540017	0.006033	0.863051	0.5	924	498	0	2745	11	2761	12	2784	25	-2	1
4431-s1	0.19576	0.000686	0.528931	0.004241	203.199509	0.30969	14.31449	0.170777	0.548762	0.005272	0.86172	0.5	1079	582	0	2735	12	2771	11	2820	22	-4	1
3165-s1	0.202143	0.004087	0.462842	0.010183	143.5208588	0.272881	13.82119	0.41706	0.509115	0.01106	0.719849	0.5	787	401	0	2601	34	2738	28	2653	47	6	2
2626-s1	0.19429	0.002528	0.488537	0.007599	128.0704193	0.234351	13.48116	0.282248	0.516609	0.008123	0.748642	0.6	678	350	0	2735	23	2714	20	2686	34	2	2
3275-s1	0.19474	0.001359	0.004565	0.004565	130.4841309	0.262928	13.35062	0.189475	0.509422	0.005642	0.78643	0.4	667	340	0	2743	15	2705	13	2654	24	4	1
7778-s1	0.19642	0.001	0.498593	0.00419	124.2432175	0.331885	14.05669	0.174861	0.005324	0.004661	0.807584	0.4	666	353	0	2763	12	2754	12	2741	22	1	1
2059-s1	0.197071	0.002025	0.403185	0.005457	99.83261871	0.275543	11.34301	0.213796	0.42582	0.006287	0.783348	0.5	585	249	0	2770	19	2552	18	2287	28	21	1

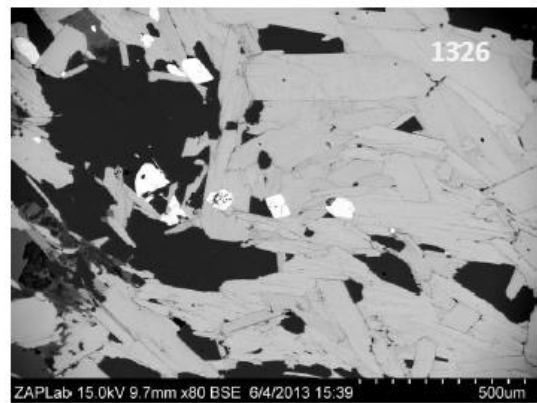
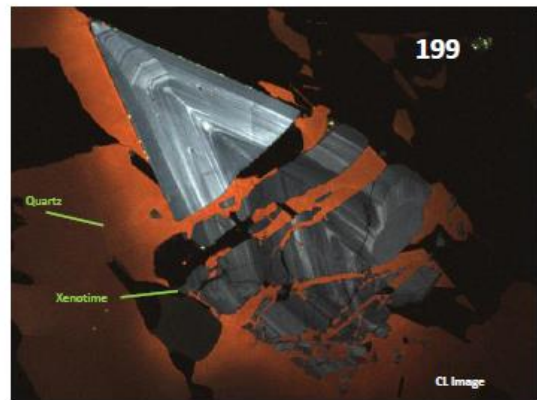
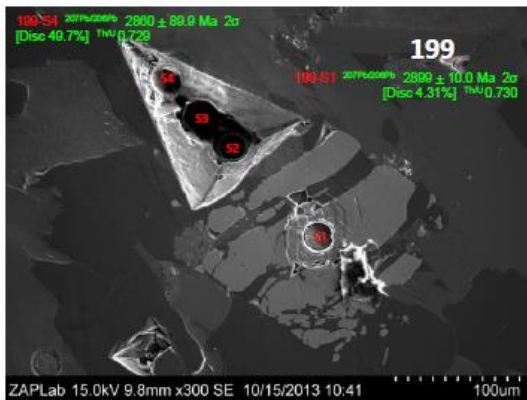
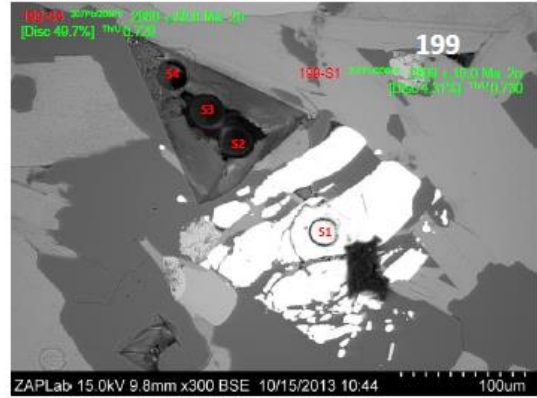
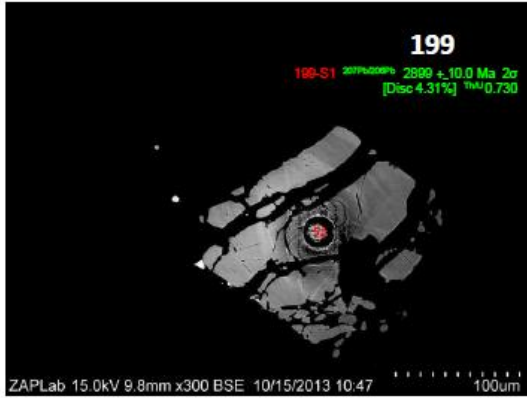
6225
Zircon

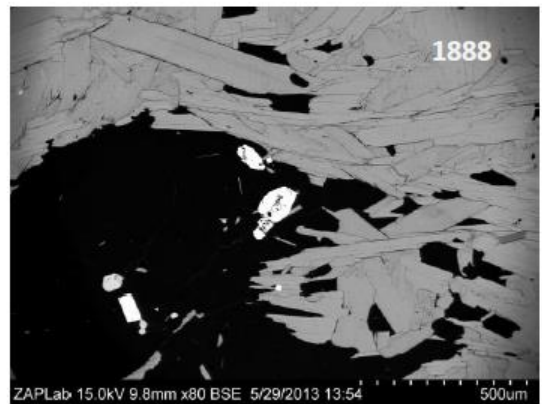
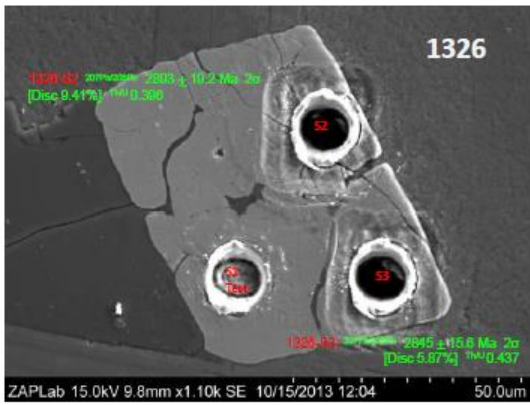
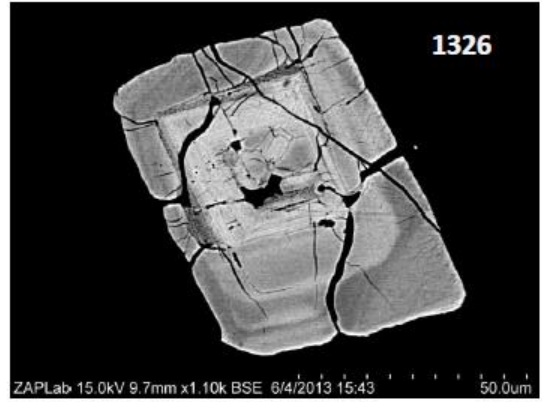
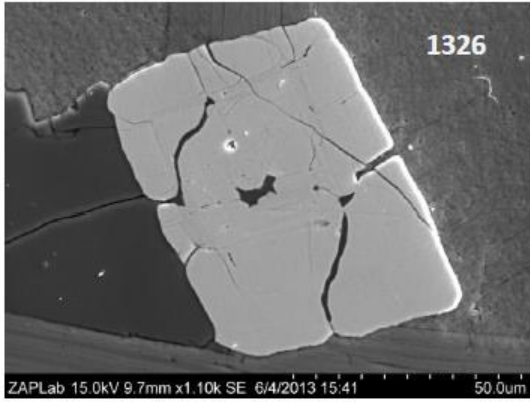
6220A
Zircon

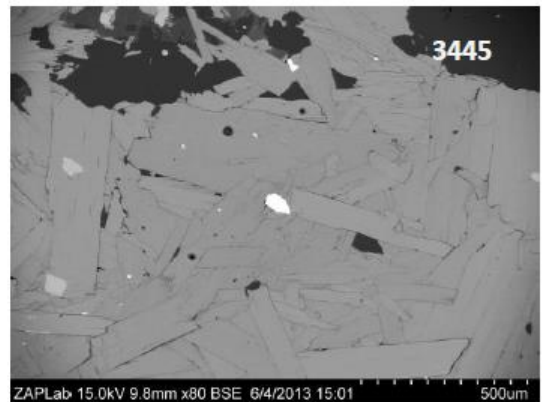
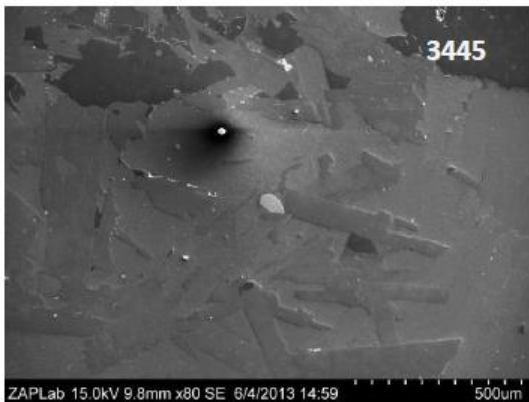
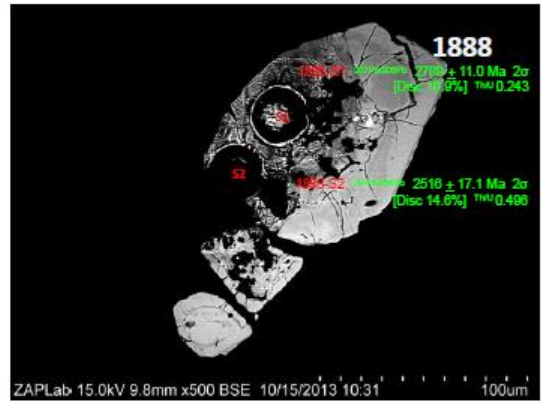
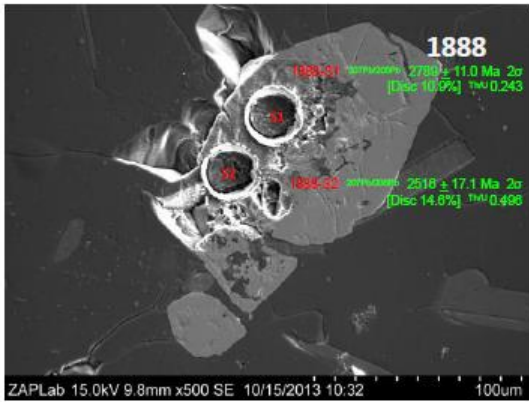
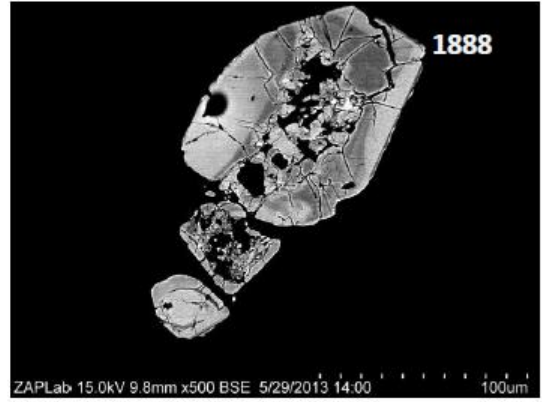
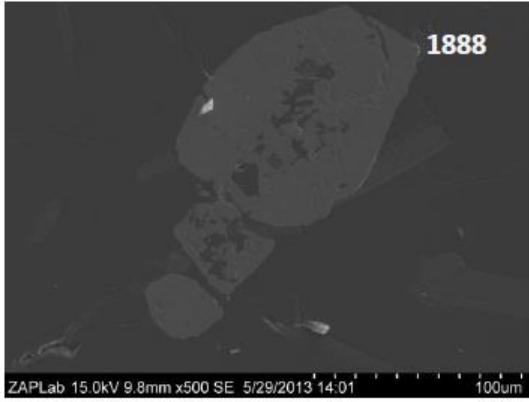
Measurements		Standardized Concordia										Ages Ma		Th/U		Pb206		U		86Sr		206Pb/235SiAlm		206Pb/238SiAlm		%Disc		SiAlm	
Analysis	207Pb/206SiAlm	206Pb/235SiAlm	206Pb/238SiAlm	Th/U	207Pb/235SiAlm	206Pb/235SiAlm	206Pb/238SiAlm	RhoXy	Kcgs	U	Pb206	Th/U	207Pb/206SiAlm	206Pb/235SiAlm	206Pb/238SiAlm	207Pb/235SiAlm	206Pb/238SiAlm	206Pb/235SiAlm	206Pb/238SiAlm	%Disc	SiAlm	%Disc	SiAlm	%Disc	SiAlm	%Disc	SiAlm	%Disc	SiAlm
3420-S2	0.111689	0.000828	0.290602	0.002733	1.209	450684	0.079212	5.043585	0.06899	0.003472	0.774989	0.1827	16	1827	12	1826	17	0	1										
3420-S1	0.111333	0.000721	0.292928	0.002397	548	9248047	0.092007	5.071869	0.061242	0.003094	0.773995	0.1817	14	1831	10	1844	15	-2	1										
3420-S3	0.111154	0.000665	0.292153	0.002538	900	4052124	0.082938	5.069544	0.060637	0.003213	0.810915	0.1816	13	1831	10	1845	16	-2	1										
2674-S1	0.110376	0.000586	0.28273	0.001961	931	7335205	0.154277	4.891434	0.05196	0.00288	0.782233	0.1800	12	1801	9	1802	13	0	1										
2674-S2	0.113914	0.001182	0.29118	0.003143	312	4043884	0.189991	5.209661	0.085197	0.003988	0.727302	0.1855	20	1854	14	1853	19	0	2										
2162-S1	0.111503	0.000612	0.275012	0.001947	881	5661011	0.117389	4.826074	0.055824	0.002843	0.778865	0.1815	13	1789	10	1768	14	3	1										
2162-S2	0.115096	0.001757	0.322875	0.007018	165	0059814	0.246335	5.858587	0.162841	0.009403	0.813884	0.1870	29	1955	24	2037	39	-10	3										
1531-S1	0.112098	0.001052	0.287184	0.003293	437	1368408	0.386256	5.186912	0.066419	0.004347	0.773129	0.1824	19	1850	14	1875	21	-3	2										
1531-S2	0.110844	0.000688	0.286838	0.002278	487	8742065	0.367935	5.22462	0.062915	0.003242	0.794284	0.1806	14	1857	10	1903	16	-6	1										
1081-S1	0.111164	0.000608	0.283433	0.002134	557	43927	0.379246	5.304887	0.059904	0.003127	0.801084	0.1821	12	1870	10	1914	15	-6	1										
1081-S2	0.112545	0.000756	0.289004	0.002409	643	0604248	0.376433	5.566101	0.071883	0.003624	0.781111	0.1838	15	1911	11	1979	17	-9	1										
3781-S1	0.111144	0.000725	0.28652	0.002569	691	8021851	0.145809	5.388358	0.069999	0.003652	0.801464	0.1819	14	1883	11	1942	17	-8	1										
4406-S1	0.110564	0.000617	0.290701	0.001949	836	3961792	0.169889	5.27302	0.052459	0.002773	0.800653	0.1827	12	1866	8	1914	13	-7	1										
4406-S2	0.111534	0.000617	0.284133	0.001983	562	1802368	0.116277	5.045525	0.054249	0.002733	0.775643	0.1832	12	1824	9	1817	13	1	1										
4401-S1	0.111798	0.000614	0.289443	0.001883	461	972229	0.176059	5.028673	0.052873	0.002601	0.759722	0.1842	12	1848	9	1852	13	-1	1										
4401-S2	0.112378	0.000638	0.294567	0.002116	610	8671875	0.26986	5.072014	0.055384	0.0032916	0.802858	0.1842	12	1848	9	1852	13	-1	1										
4550-S1	0.111108	0.000587	0.290625	0.002131	746	6964111	0.119806	5.067184	0.054395	0.003014	0.802858	0.1822	12	1831	9	1838	14	-1	1										
4550-S2	0.110746	0.000627	0.295944	0.002784	804	8637085	0.228512	5.170151	0.066746	0.003659	0.83929	0.1817	13	1848	11	1875	18	-4	1										
3596-S1	0.11336	0.00109	0.311837	0.004801	472	6986694	0.242191	5.565902	0.107637	0.005604	0.84208	0.1852	19	1911	17	1985	28	-7	2										
3596-S2	0.117218	0.002146	0.336362	0.009138	257	6333618	0.199125	6.165423	0.205743	0.010596	0.828299	0.1906	33	2000	29	2082	49	-11	4										
1087-S1	0.111345	0.000601	0.282303	0.001718	589	2318115	0.320355	4.881711	0.054019	0.002079	0.002747	0.1806	13	1799	9	1794	13	1	1										
14952-S1	0.112166	0.001481	0.313784	0.004179	40	74725342	0.520616	0.102038	0.338408	0.004719	0.711477	0.1825	213	24	80164	1853	601	16	161449	1879	008	22	69707	-3	39838	2	14986		
14952-S2	0.112642	0.001449	0.292754	0.00256	42	3494998	0.469547	0.07805	0.304813	0.003016	0.595296	0.1827	67	24	0448	1766	446	13	85897	1715	131	14	89062	0	10194	1	1666034		
14952-S3	0.112642	0.002257	0.314972	0.004783	24	65179062	0.4928395	0.128566	0.320891	0.005195	0.620596	0.1822	219	36	68853	1807	132	21	86957	1794	08	25	31439	1	768883	2	737764		
14952-S4	0.113853	0.001427	0.311661	0.003864	37	94313812	0.4858305	0.092074	0.312643	0.004255	0.718069	0.1843	451	23	71228	1795	055	15	89188	1753	699	20	87136	5	559185	1	1887254		
11451-S1	0.111949	0.000934	0.28954	0.002243	73	07901001	0.481733	0.057818	0.292155	0.002678	0.710632	0.1820	068	16	40627	1727	594	10	68538	1652	288	13	35544	10	44429	1	123455		
4506-S1	0.110889	0.001259	0.332454	0.003728	55	17188644	0.5147789	0.088864	0.337434	0.004189	0.719224	0.1810	027	21	6637	184	03	14	62189	1874	315	20	17211	-4	09407	1	1916429		
3396-S1	0.114487	0.00123	0.313533	0.002835	83	94529724	0.5189395	0.080617	0.328502	0.003461	0.678118	0.1873	158	20	475	1850	878	13	18465	1831	118	16	78118	2	577729	1	1591573		
13284-S1	0.112821	0.001352	0.293488	0.002739	52	2793579	0.4910538	0.080167	0.315771	0.003312	0.642424	0.1844	785	22	49023	1804	068	13	72047	1769	044	16	2125	4	693499	1	165749		
13284-S2	0.116763	0.003185	0.305536	0.006383	13	50295553	0.5431242	0.190144	0.33782	0.007278	0.615412	0.1904	801	48	78791	1889	798	29	72266	1676	173	34	86615	1	732046	3	539788		
13284-S3	0.112332	0.001056	0.302506	0.002281	49	957901	0.528657	0.073267	0.344161	0.003191	0.669084	0.1822	481	18	6058	1866	692	11	8007	1906	656	15	29884	-5	33712	1	1567405		
13284-S4	0.110541	0.001882	0.324861	0.004352	33	48925018	0.557237	0.125285	0.369792	0.005281	0.634083	0.1782	659	31	4945	1909	498	19	28458	2028	421	24	81598	-16	0848	2	8481314		
2409-S1	0.11237	0.001169	0.355488	0.005616	54	41252136	0.6139024	0.124091	0.404189	0.006792	0.851333	0.1802	005	20	32957	1995	813	17	59988	2188	298	31	12096	-25	3236	2	64916		
2409-S2	0.113428	0.001421	0.297169	0.004024	77	4599762	0.6450397	0.101027	0.337668	0.004948	0.742193	0.1813	215	23	87463	1846	11	16	71618	1875	439	23	81098	-3	95598	1	2175702		
2409-S3	0.114154	0.00179	0.369418	0.006736	51	93951797	0.6454239	0.160207	0.418569	0.007887	0.759085	0.1829	443	29	03463	2039	684	21	67993	2253	981	35	75081	-27	5515	3	321146		
2409-S4	0.115574	0.001343	0.333025	0.005066	72	26475525	0.5889234	0.119592	0.376265	0.006293	0.78963	0.1856	476	22	34492	1959	649	17	50783	2058	814	28	16182	-12	7426	2	237731		
2409-S5	0.124605	0.002255	0.31737	0.008993	37	45799874	0.988481	0.43312	0.353645	0.01017	0.397453	0.1997	050	113	5185	1974	172	61	40068	1951	982	48	2615	2	640781	6	701281		
2409-S6	0.114576	0.001405	0.314471	0.00472	84	28025055	0.5401867	0.110801	0.346617	0.00544	0.765218	0.1848	693	23	71895	1885	15	17	48161	1918	422	25	99009	-4	362	2	236979		
2409-S7	0.115719	0.001816	0.321856	0.006851	54	05160522	0.5433367	0.148995	0.350951	0.007679	0.797904	0.1836	726	29	6742	1890	134	17	34										

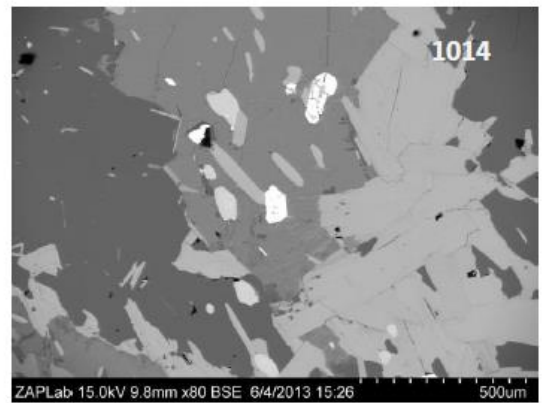
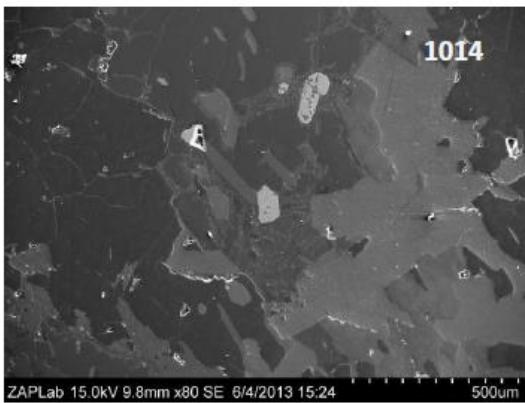
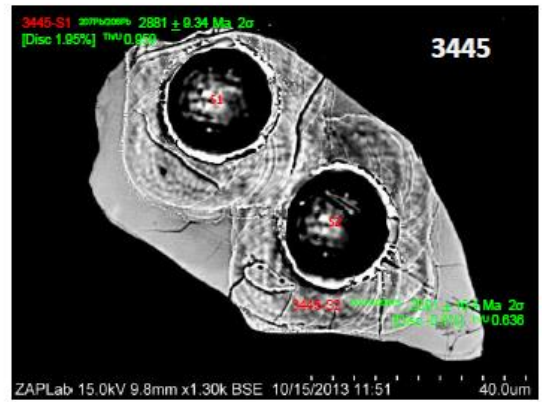
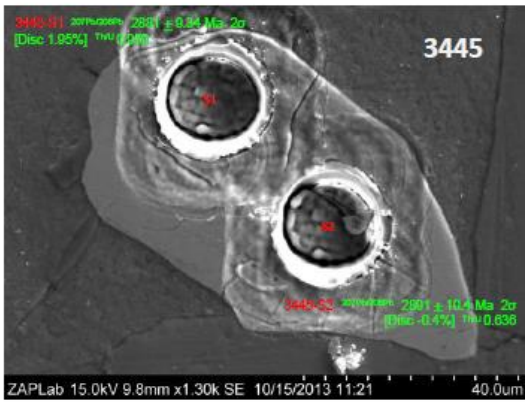
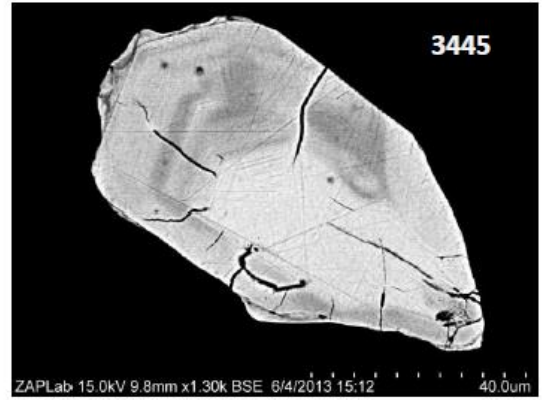
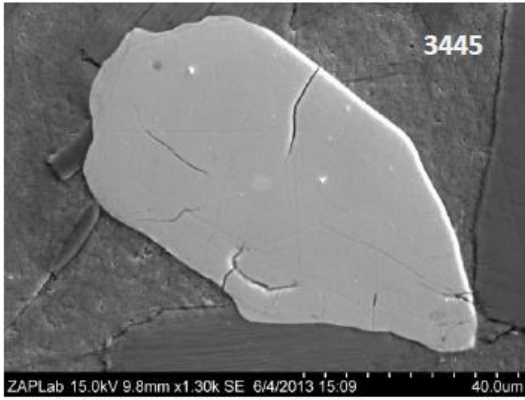
Appendix 6 Zircon & Monazite Images

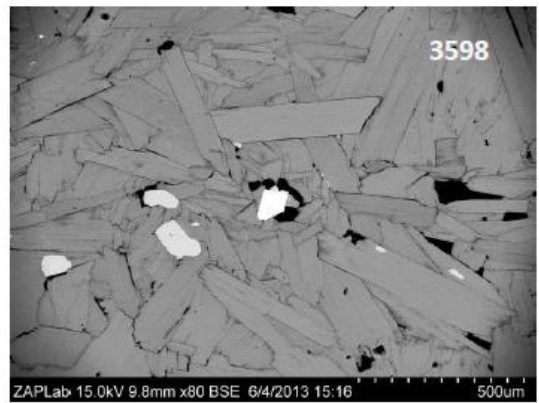
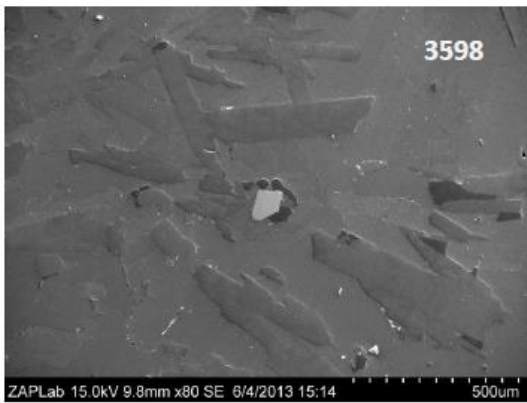
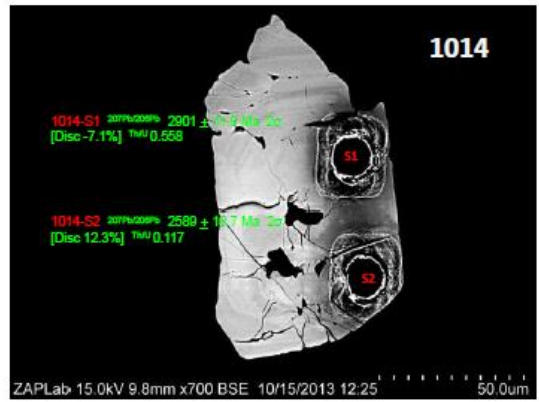
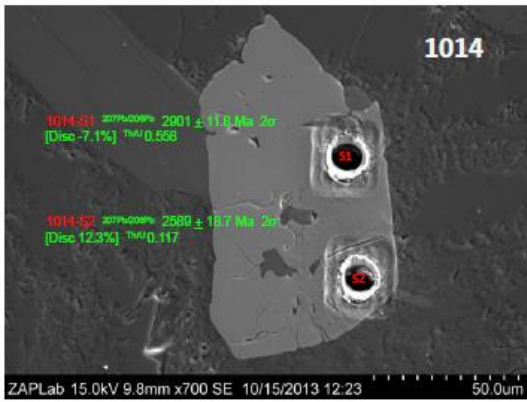
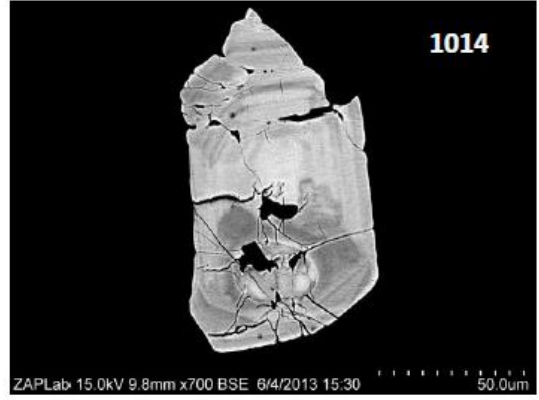
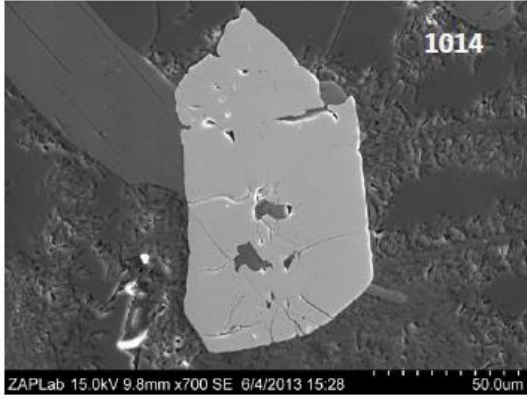
Appendix 6 Zircon & Monazite Images

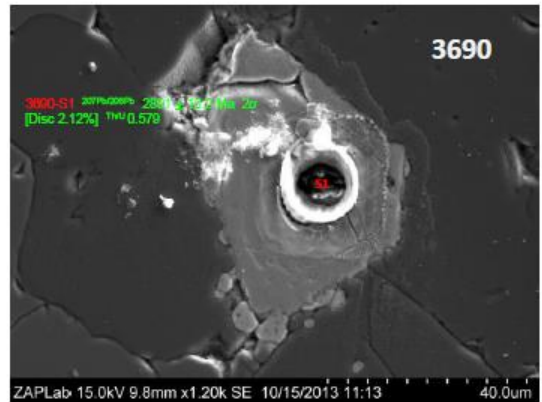
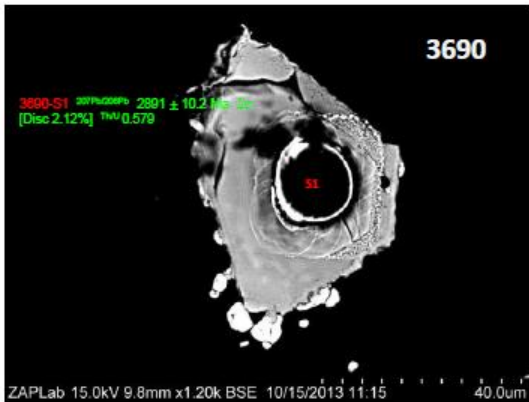
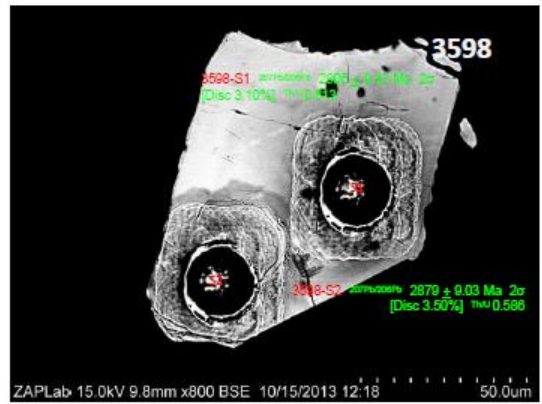
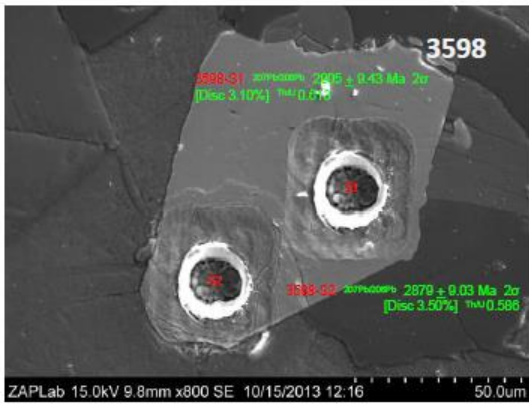
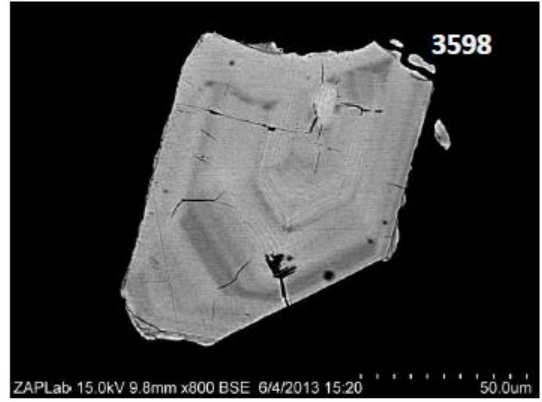
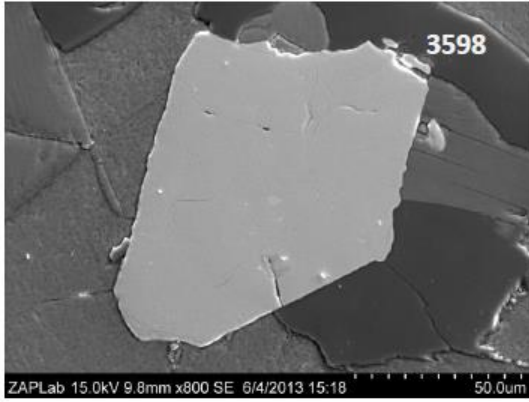


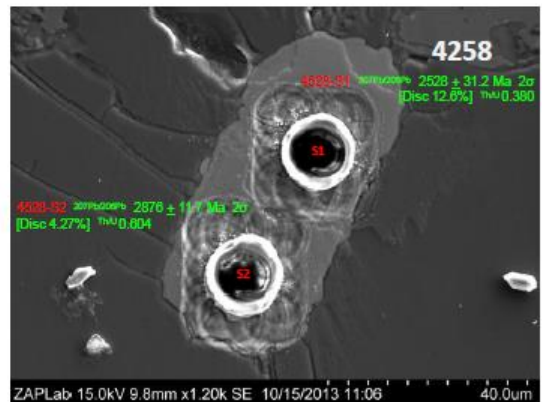
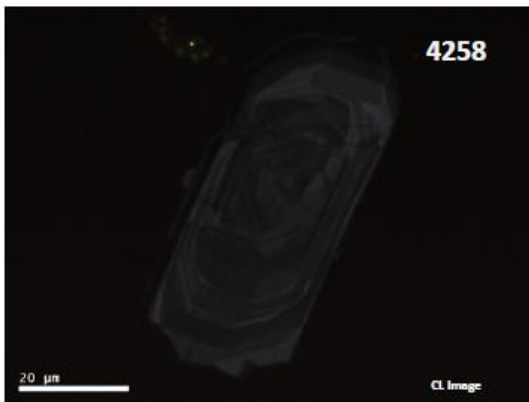
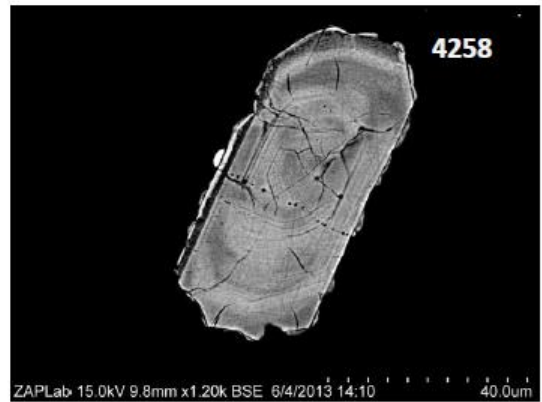
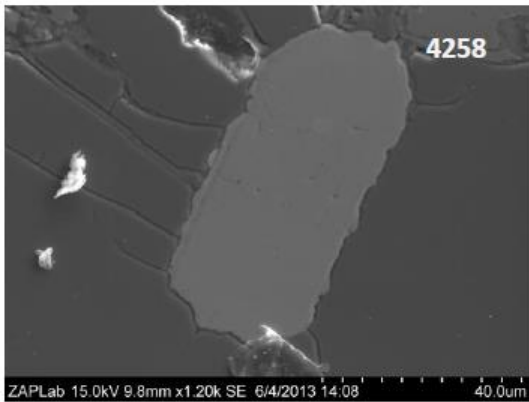
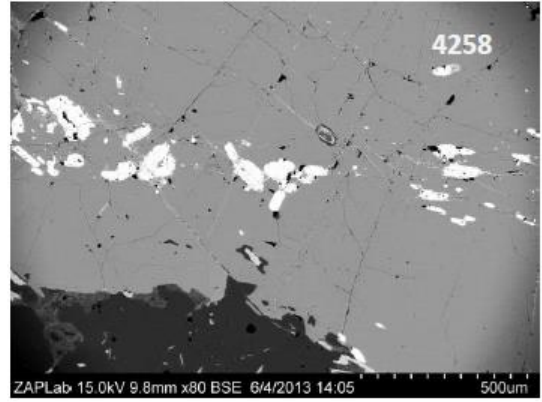
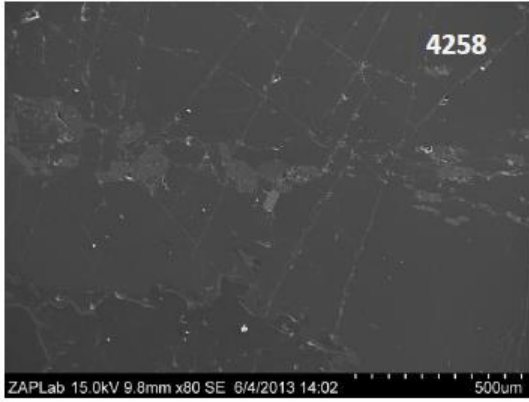


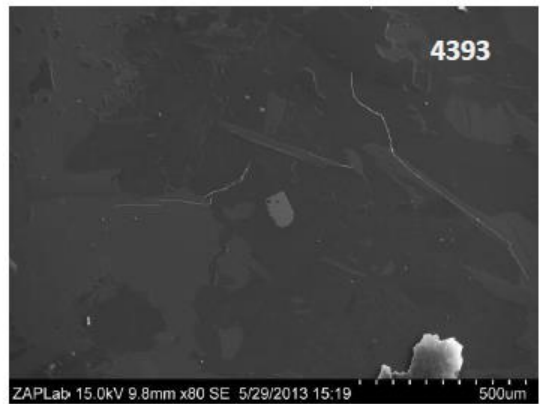
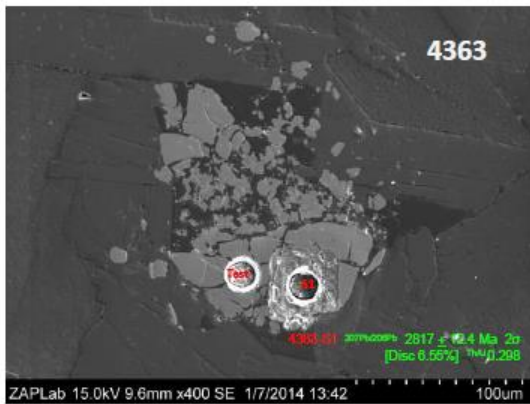
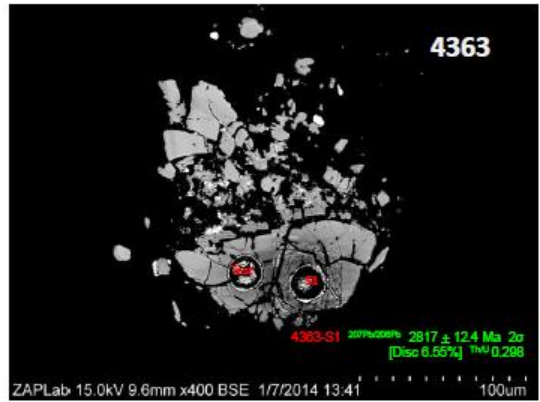
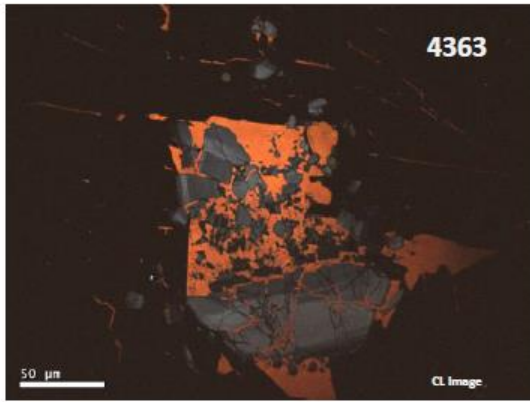
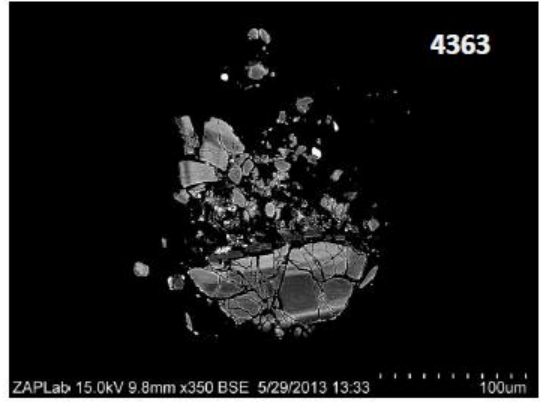
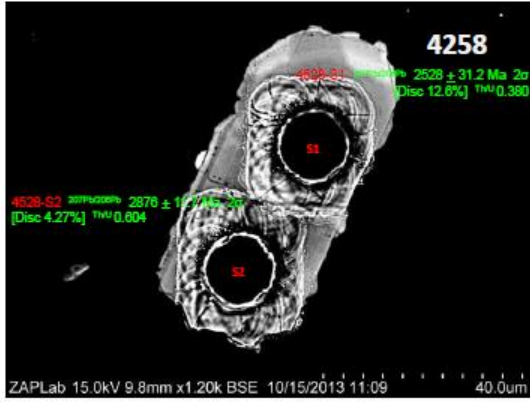


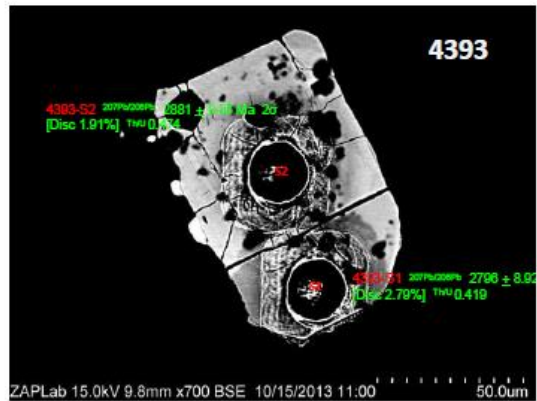
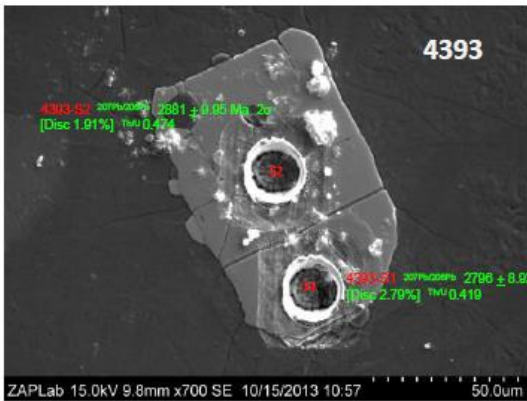
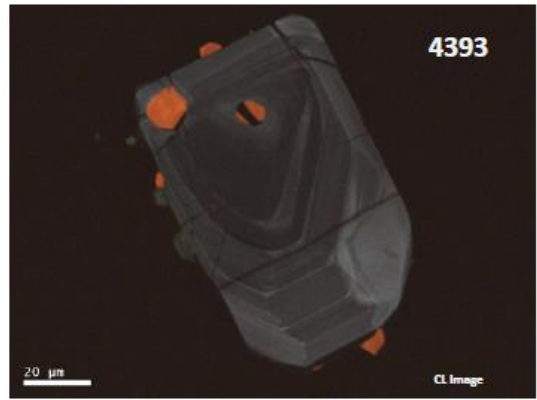
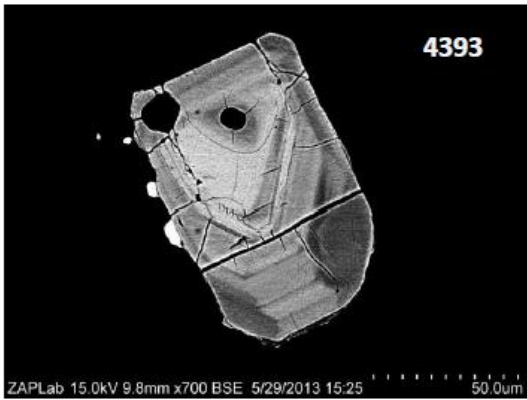
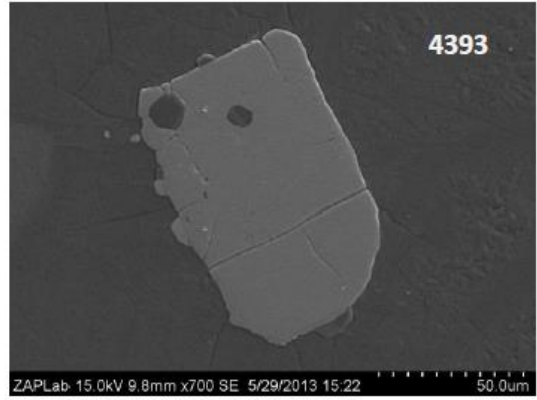
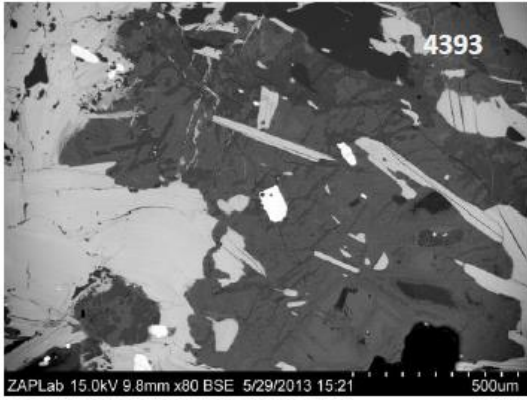


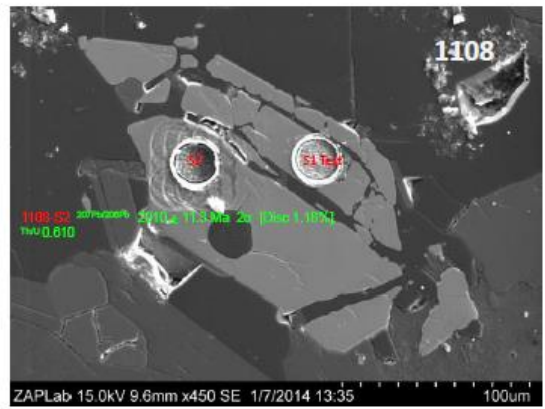
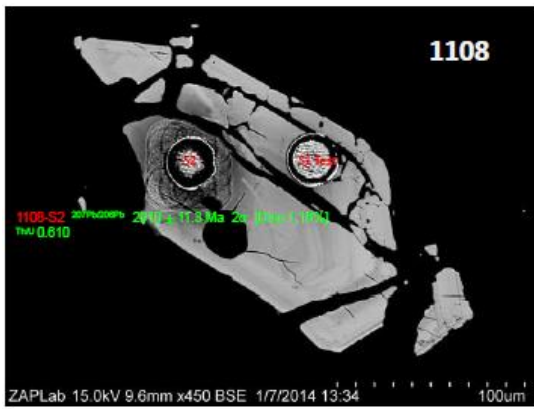
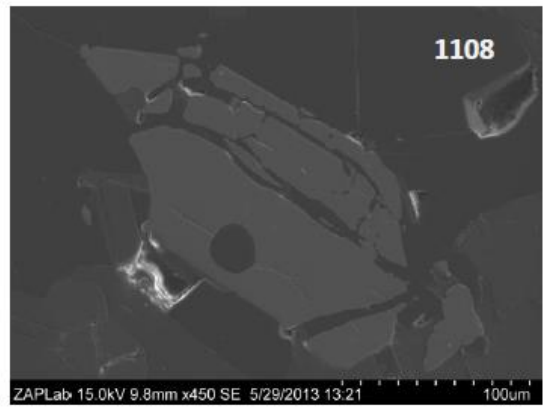
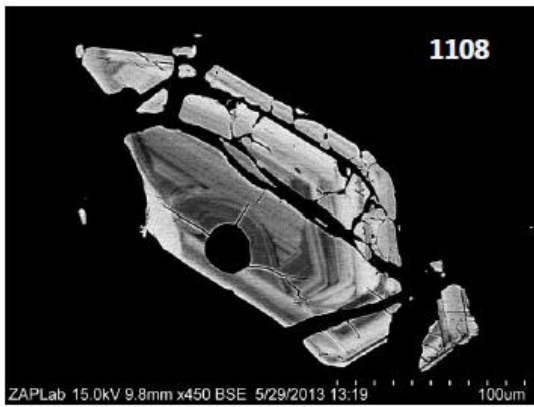
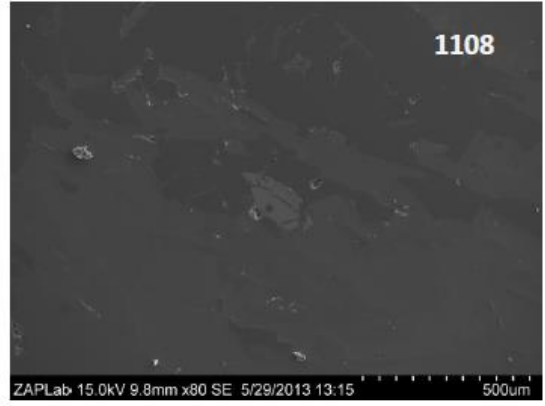
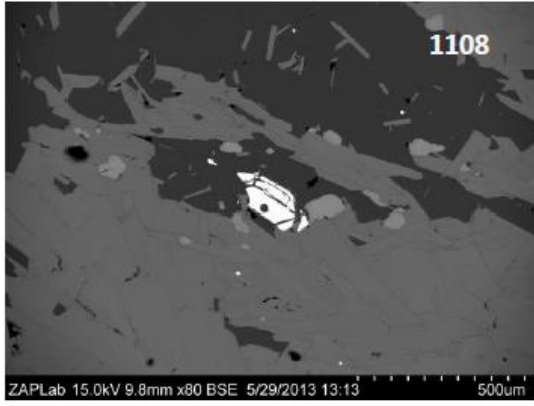




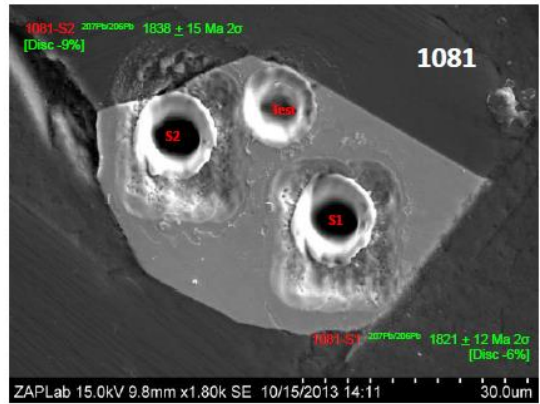
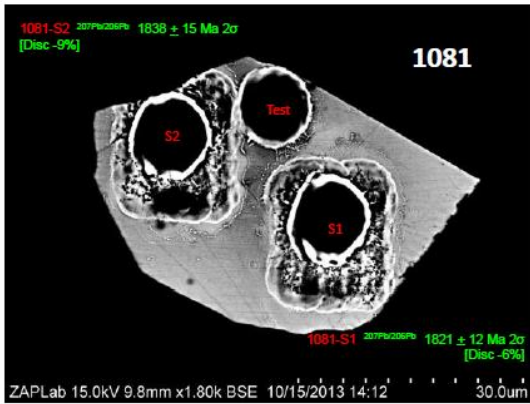
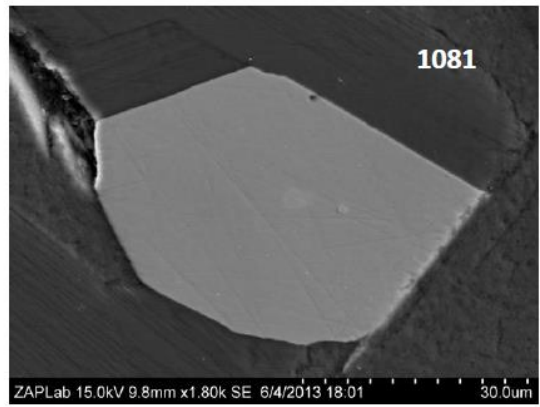
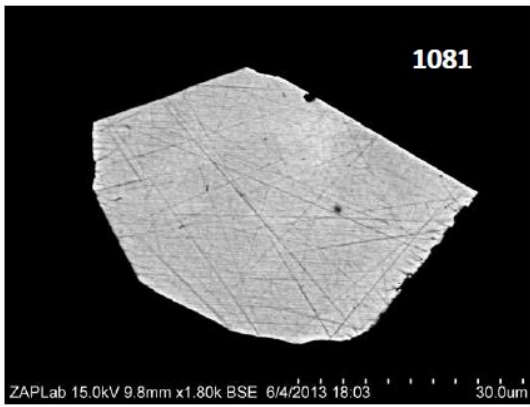
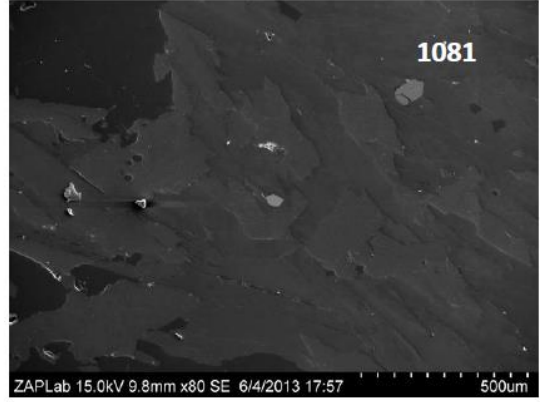
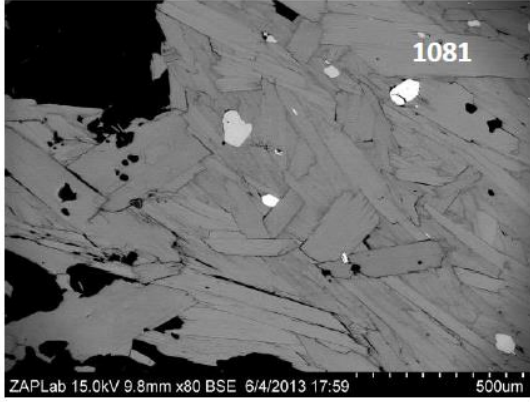


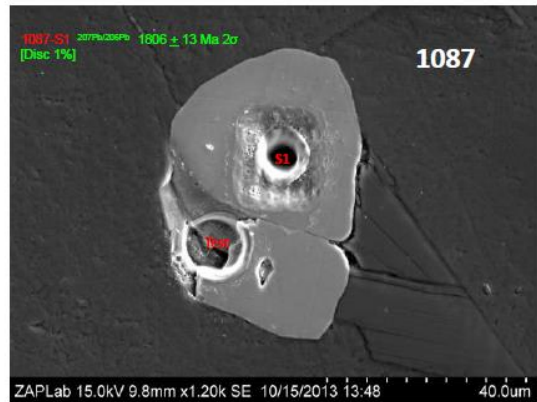
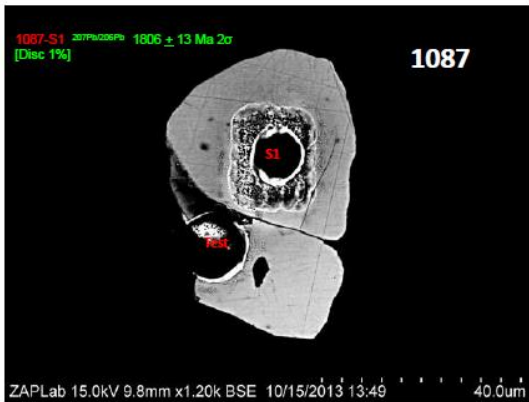
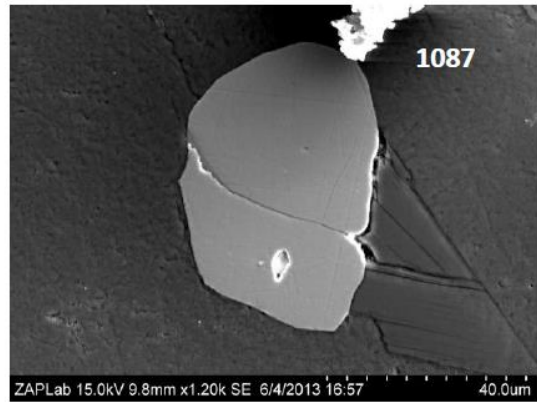
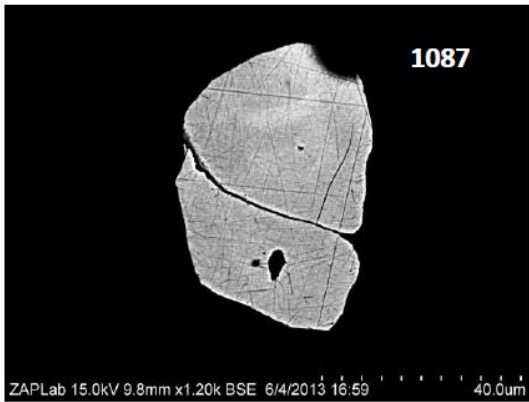
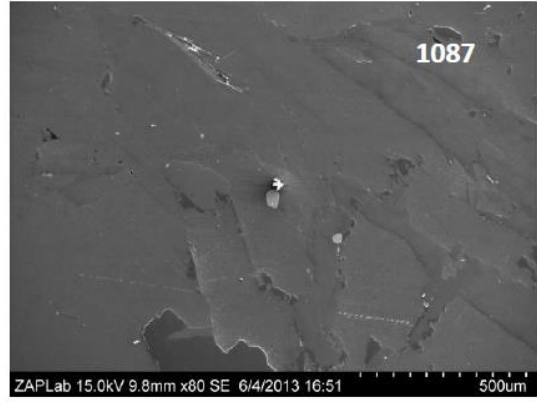
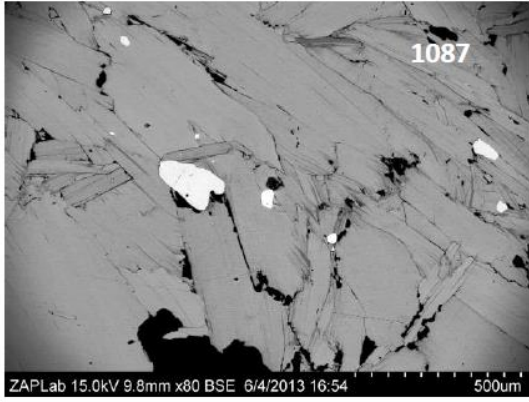


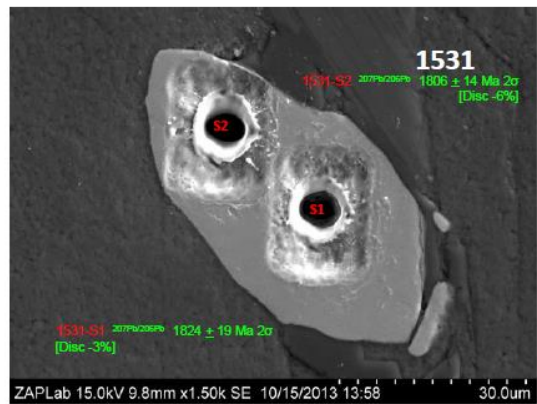
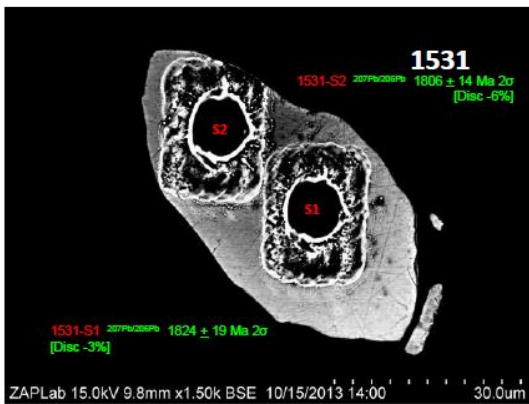
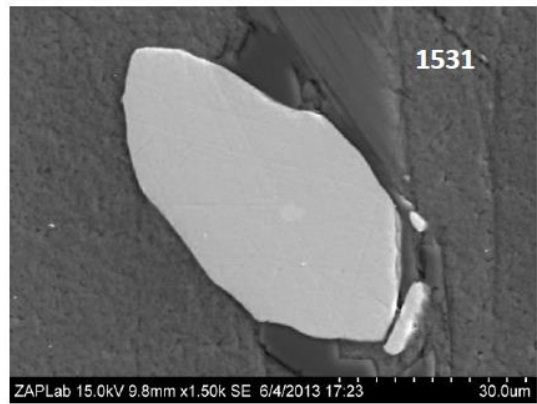
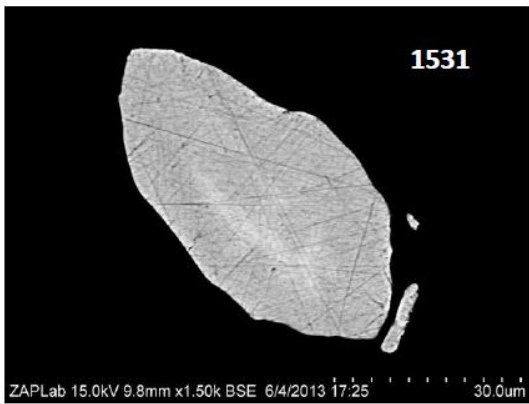
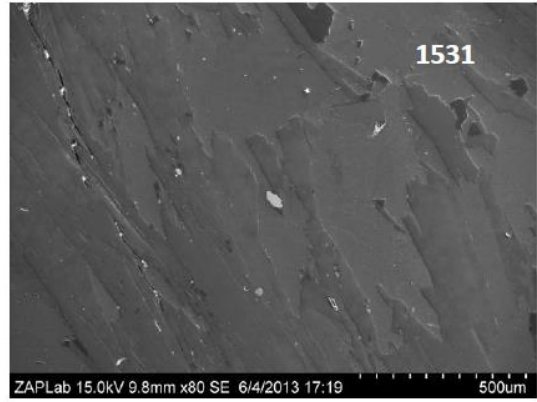
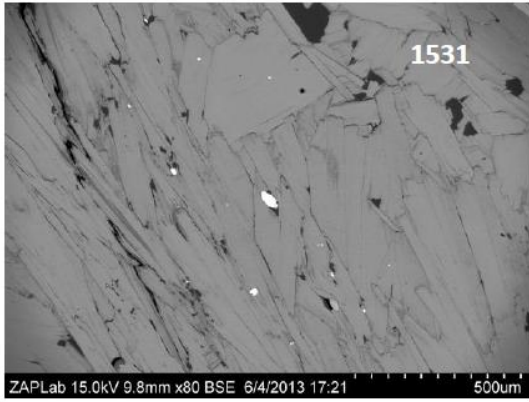


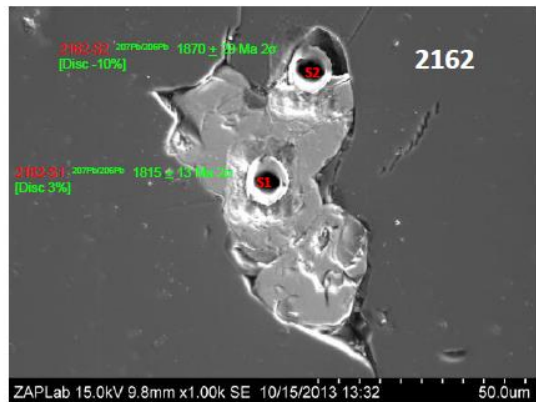
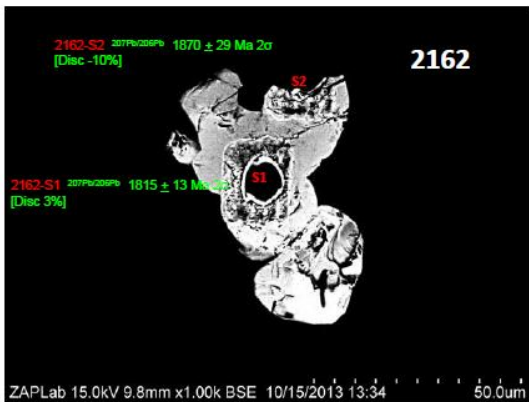
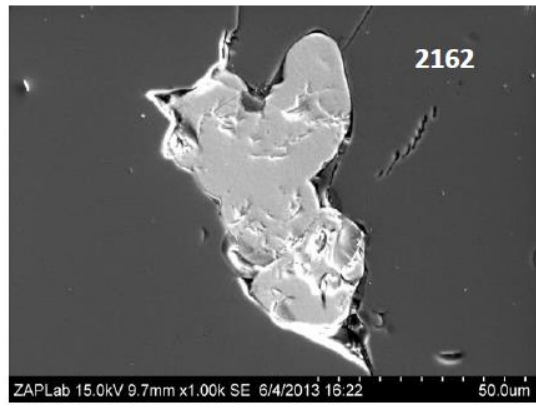
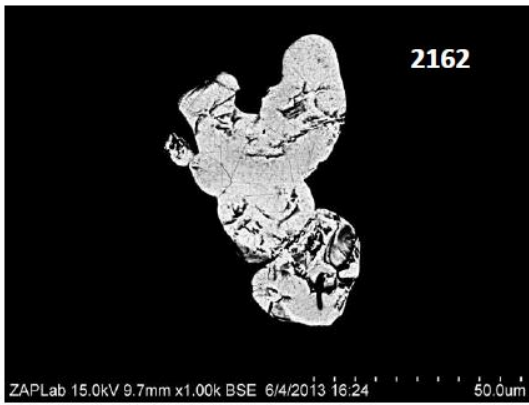
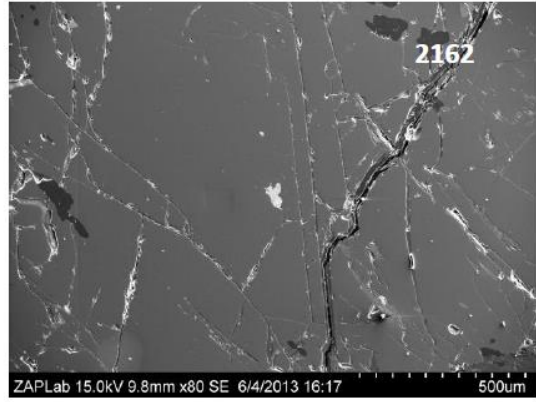
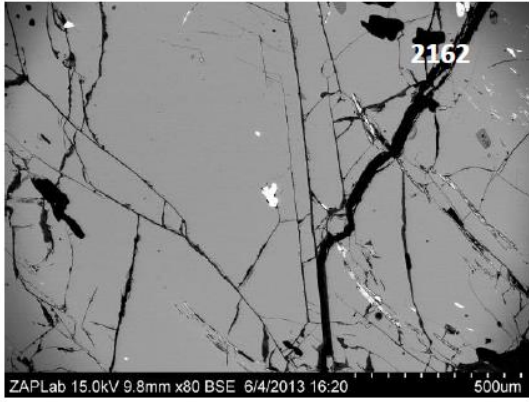


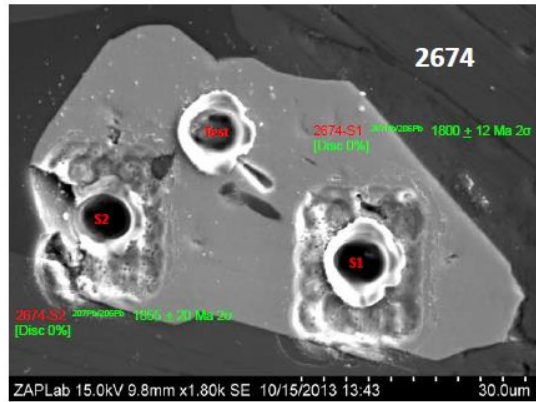
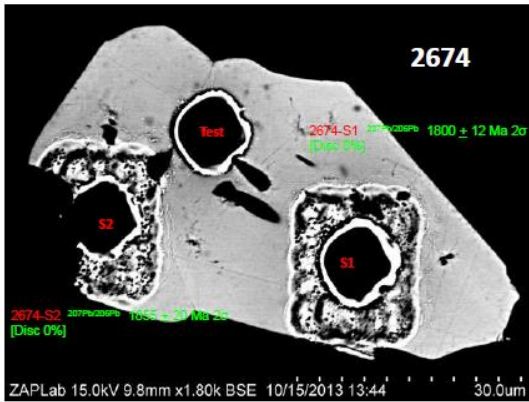
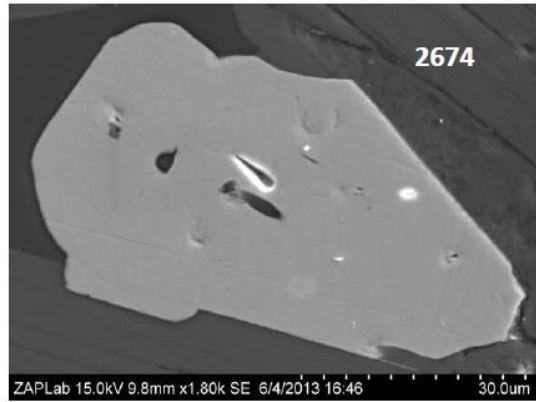
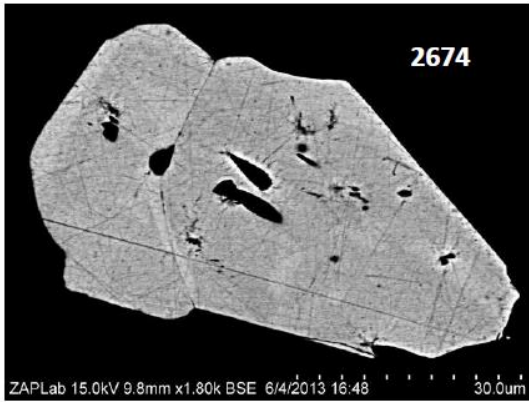
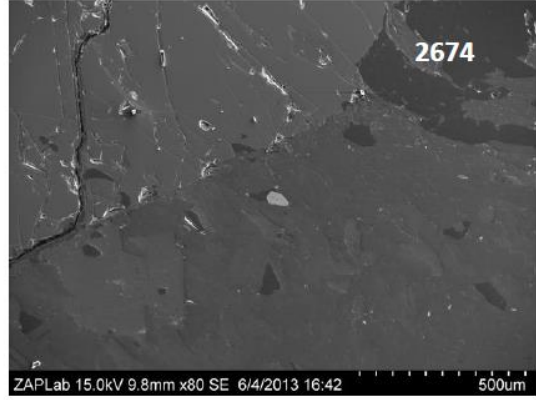
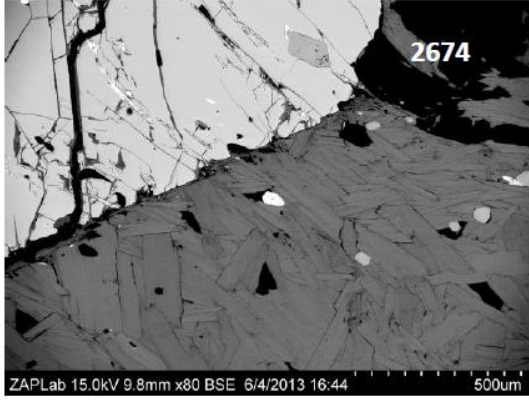
6225 Monazite

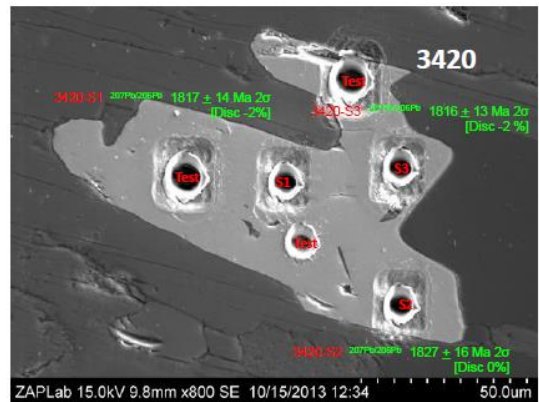
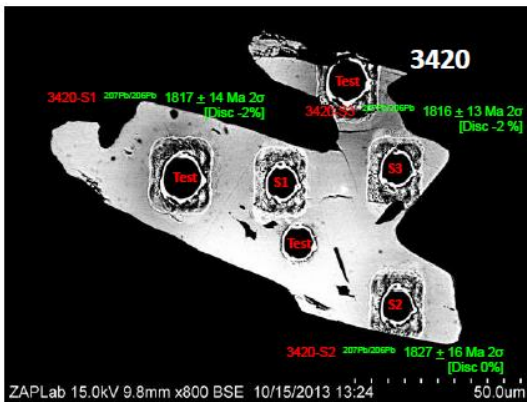
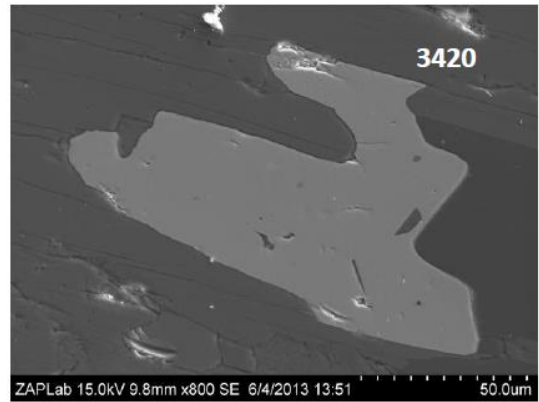
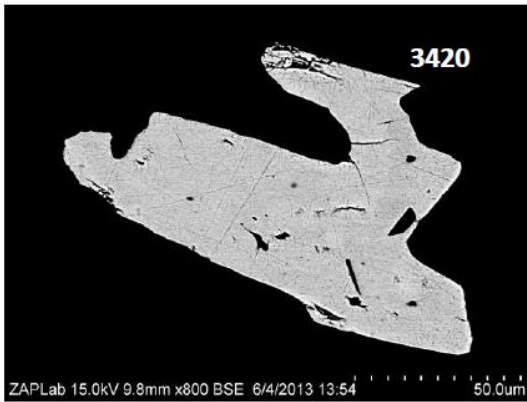
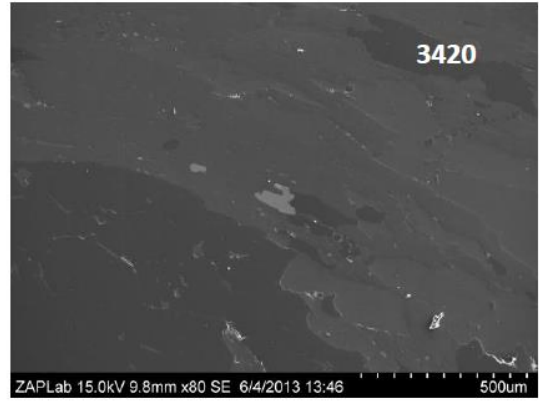
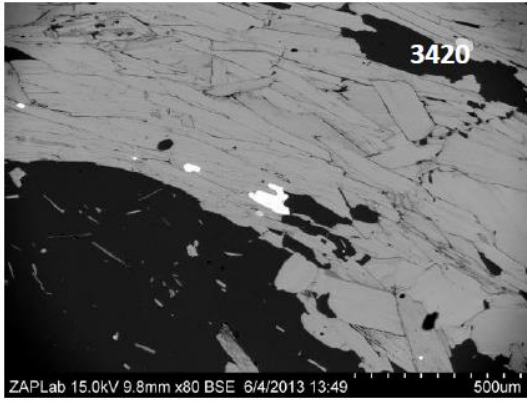


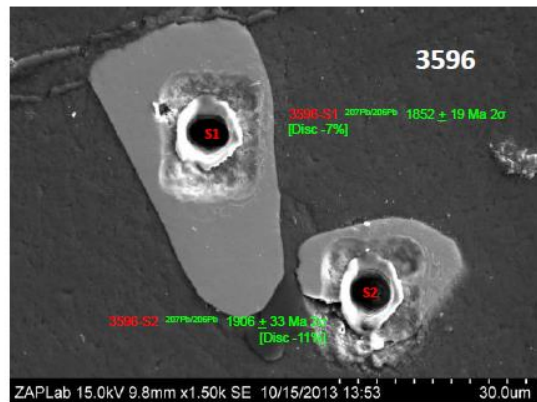
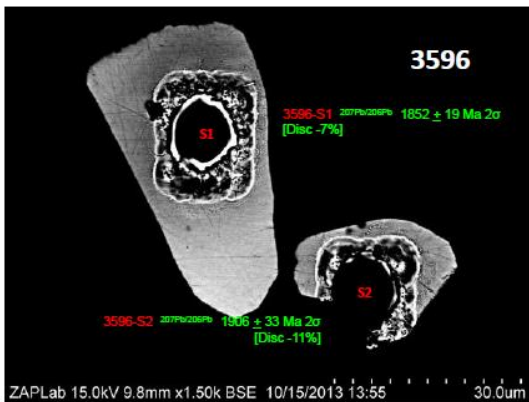
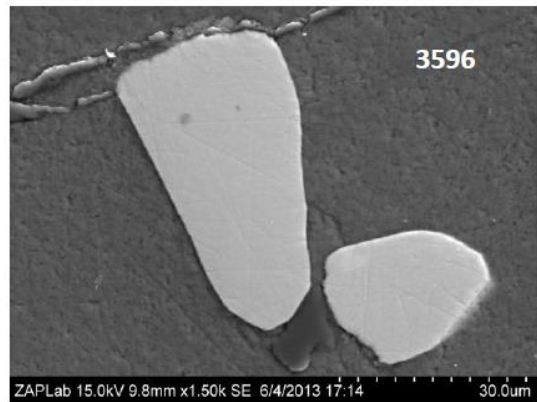
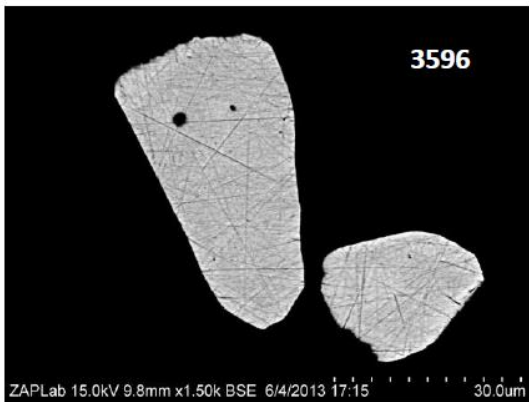
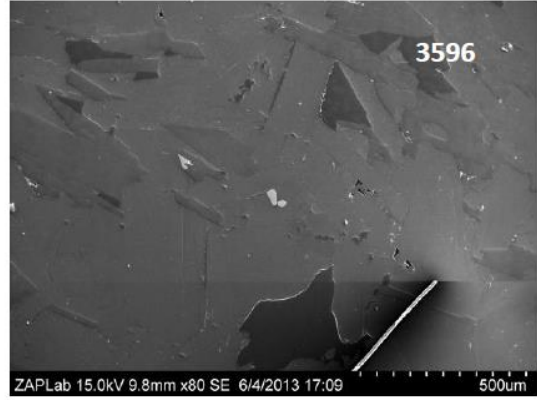
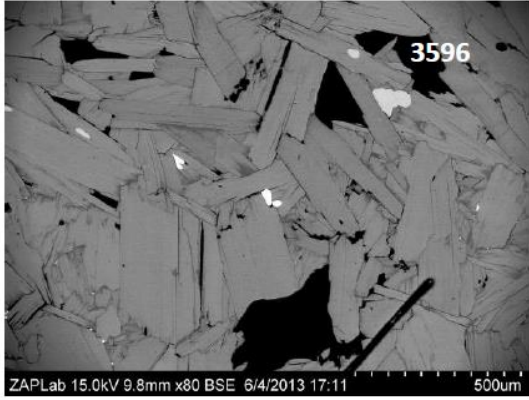


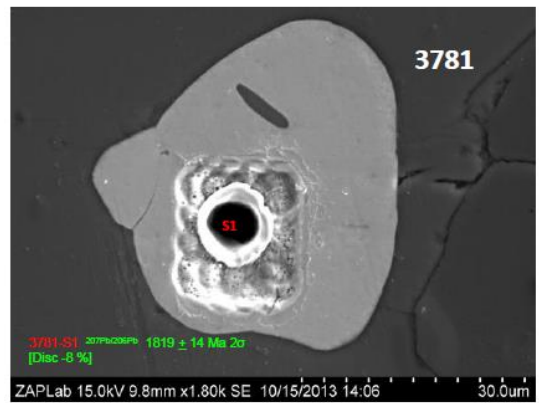
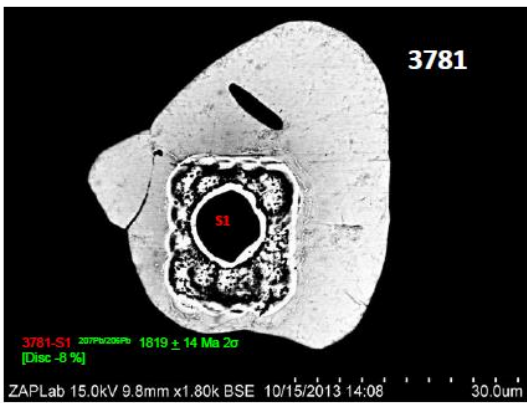
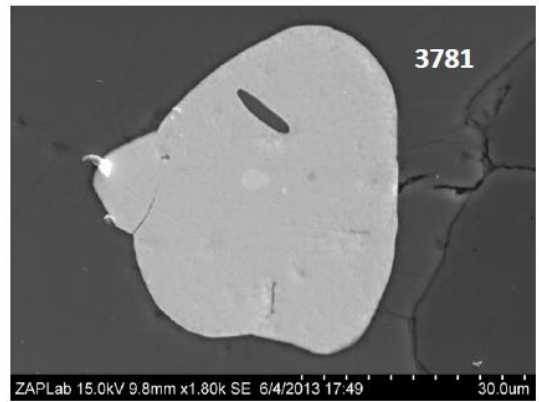
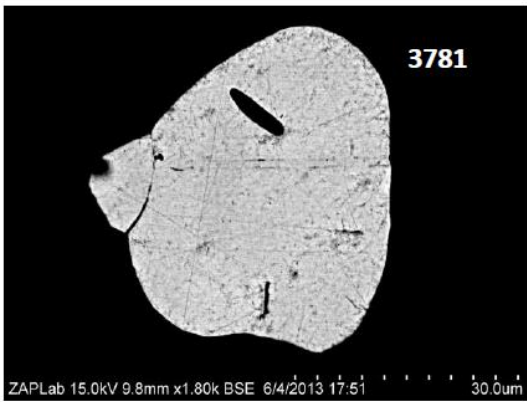
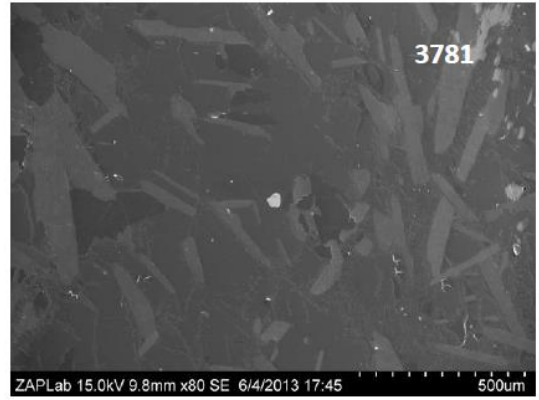
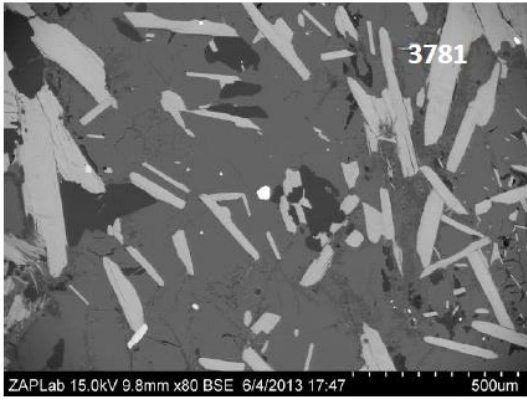


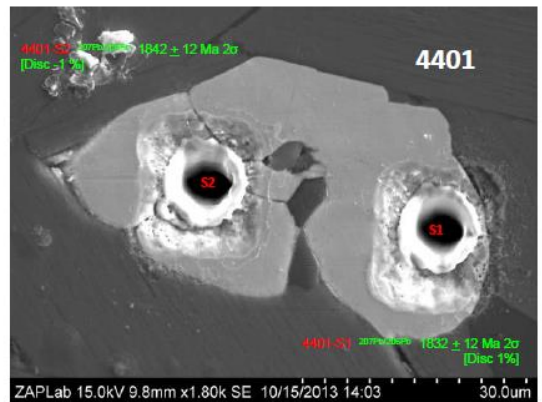
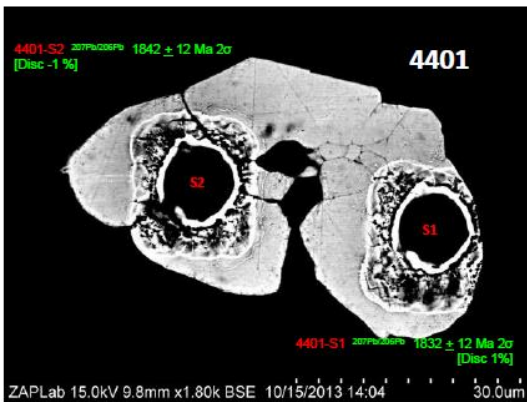
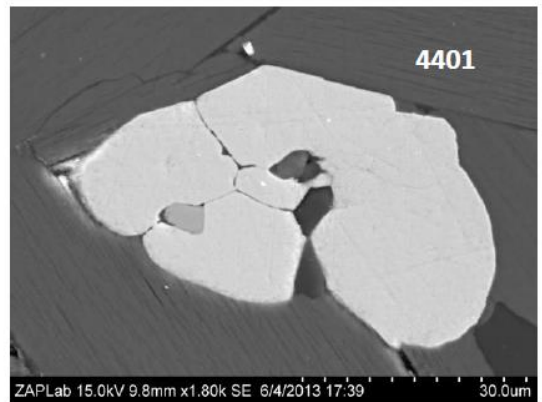
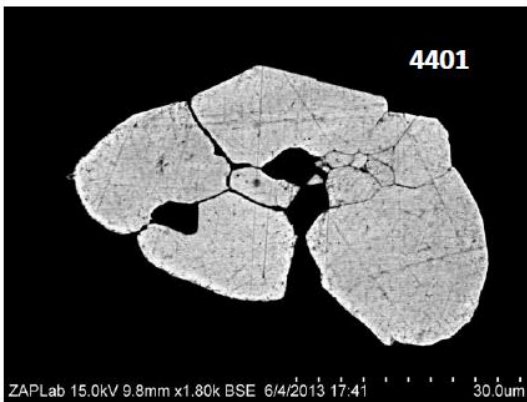
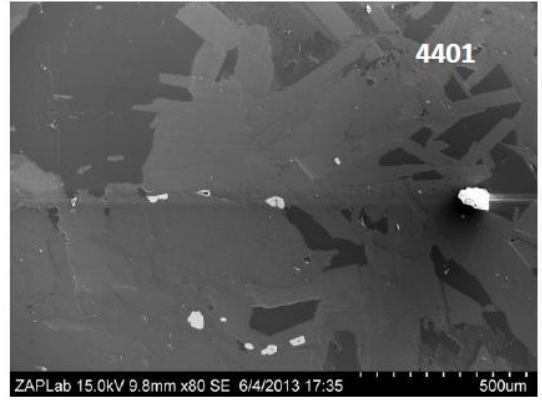


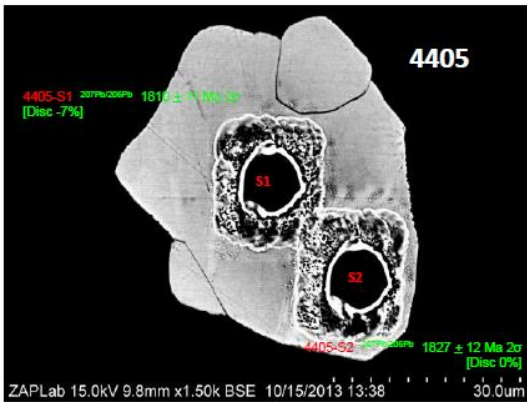
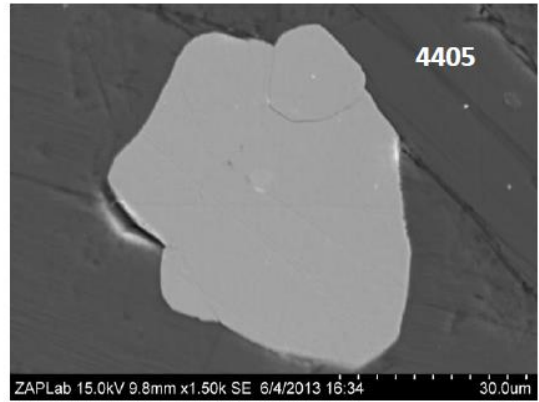
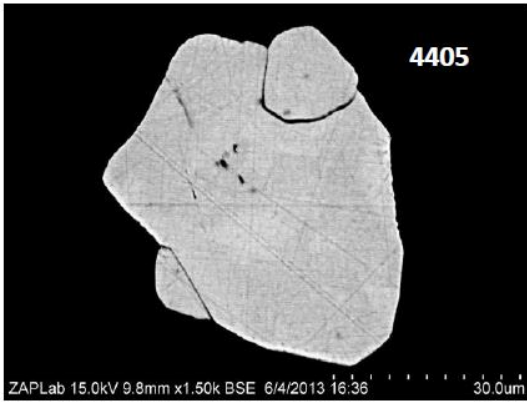
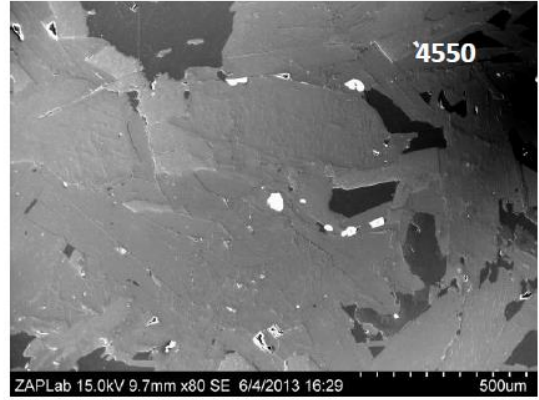
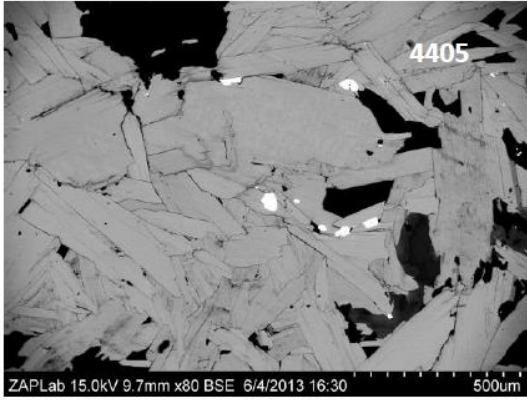


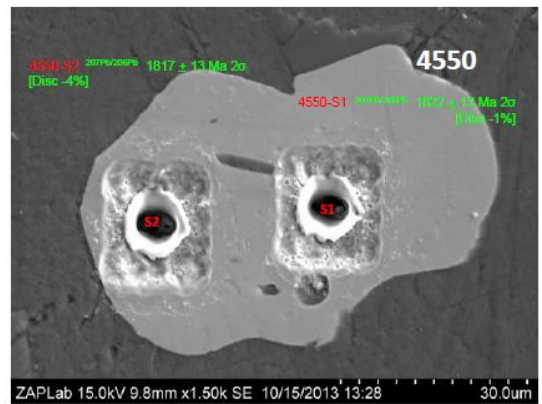
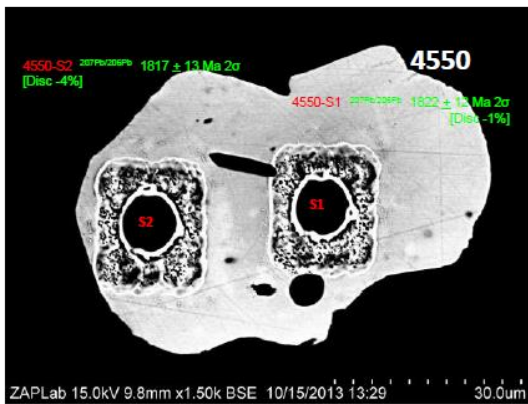
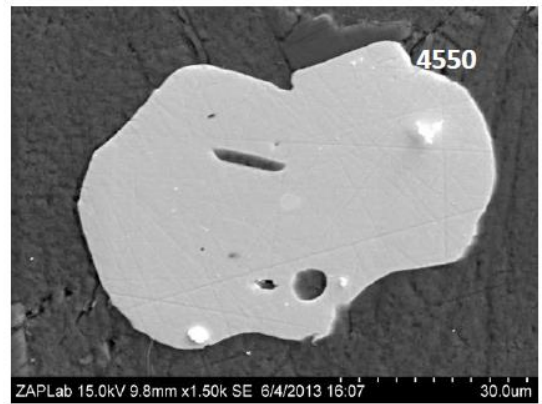
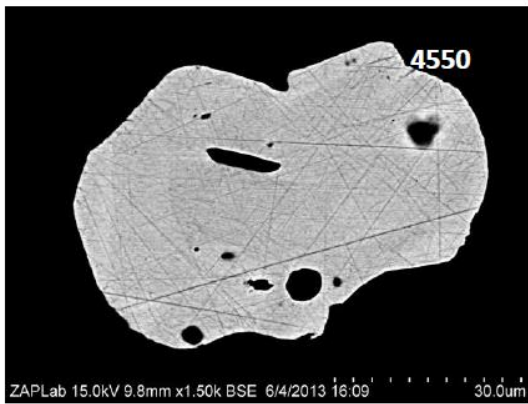
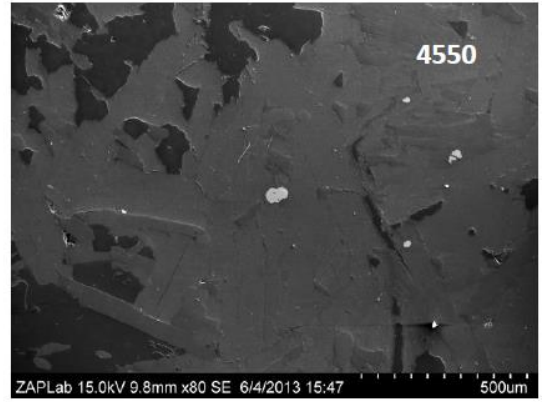
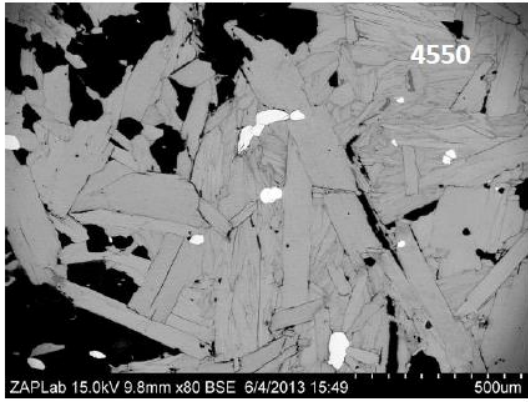




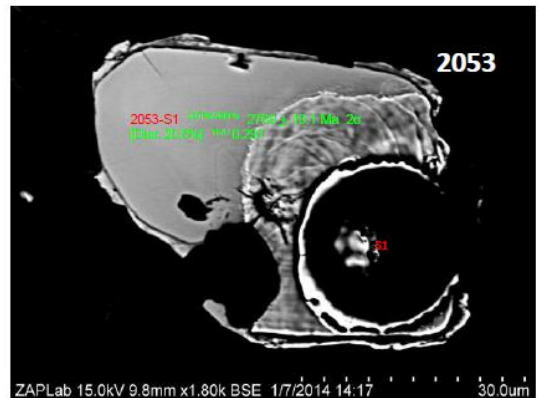
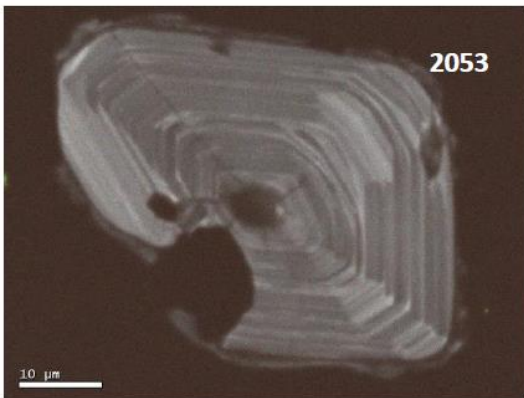
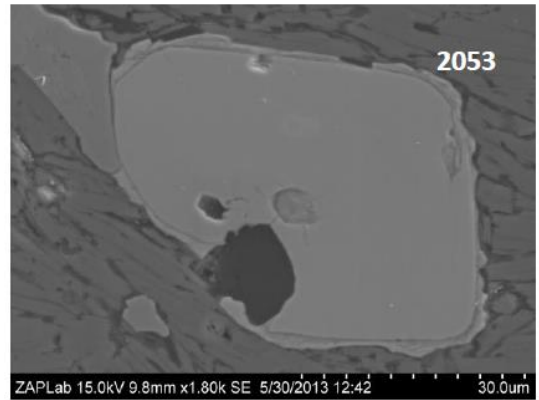
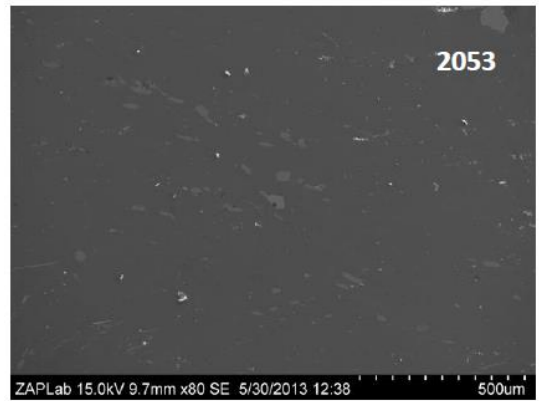
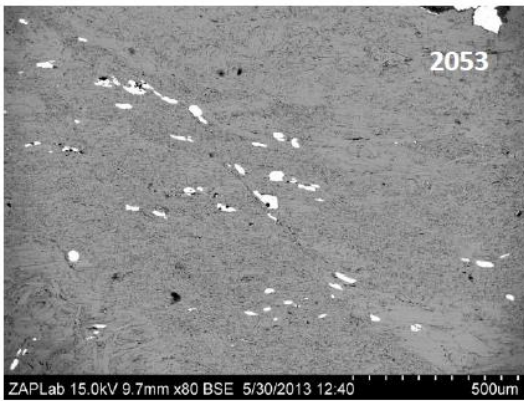


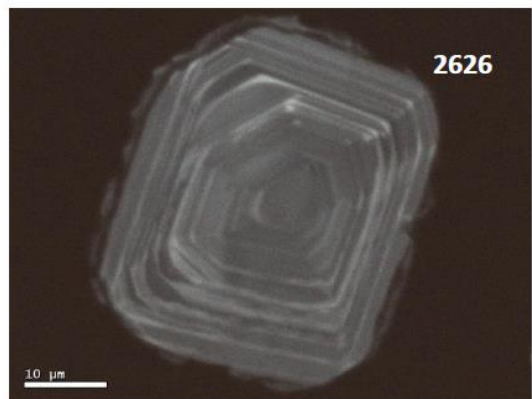
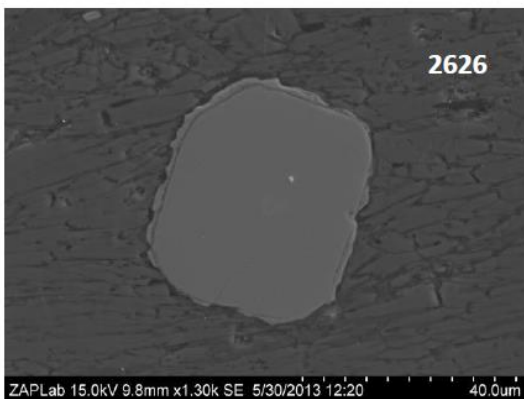
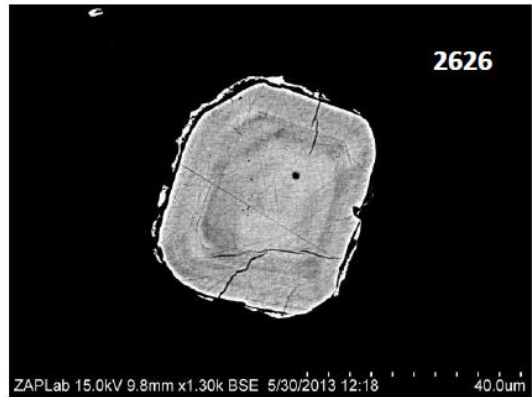
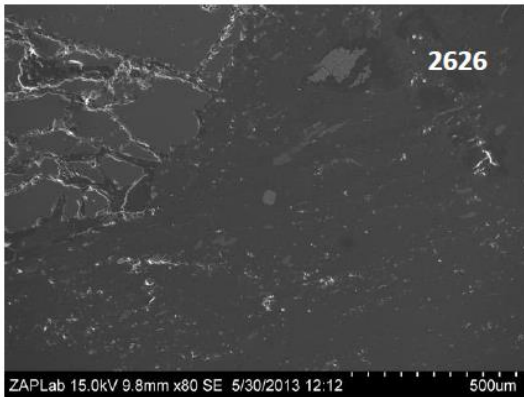
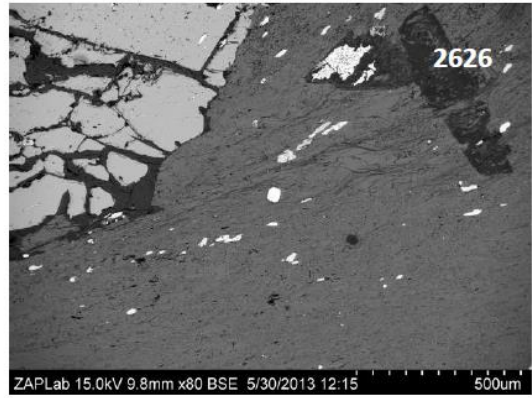
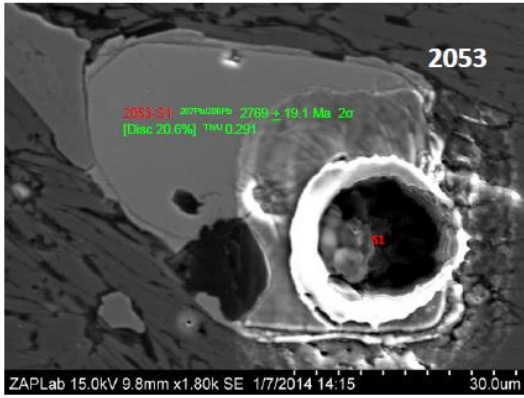


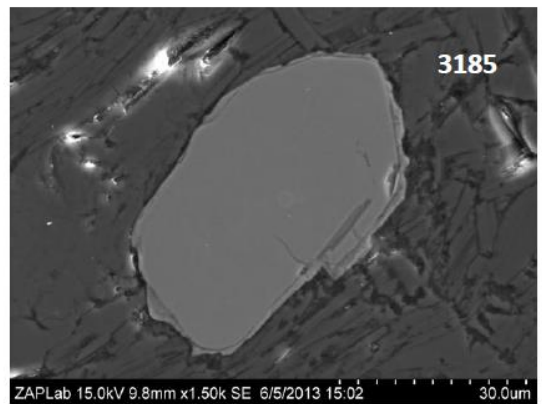
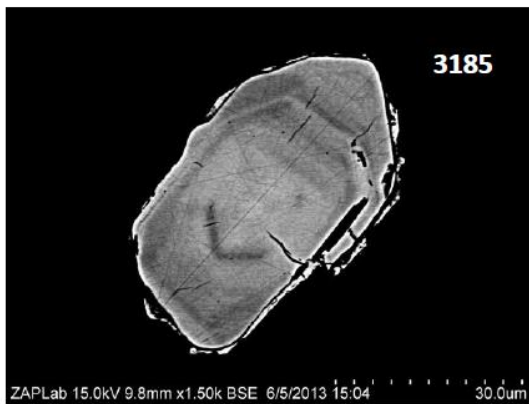
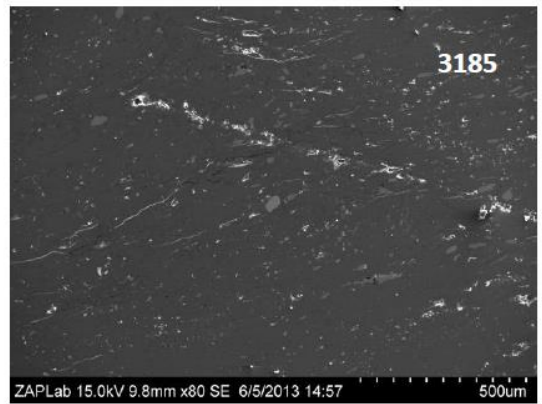
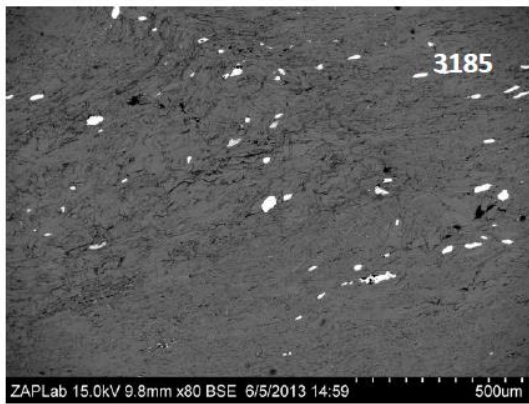
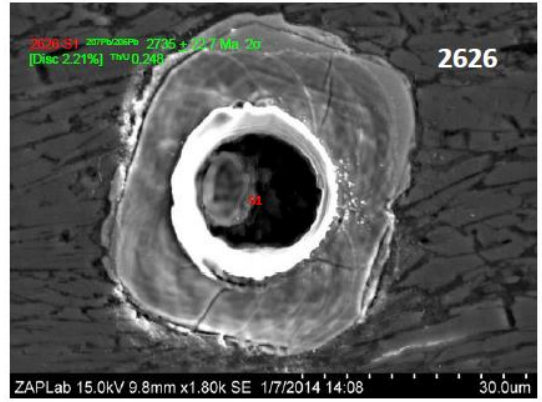
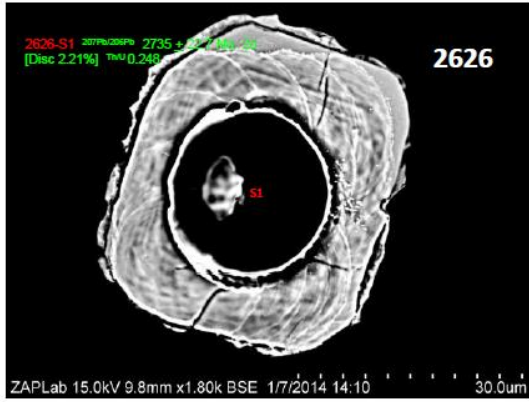


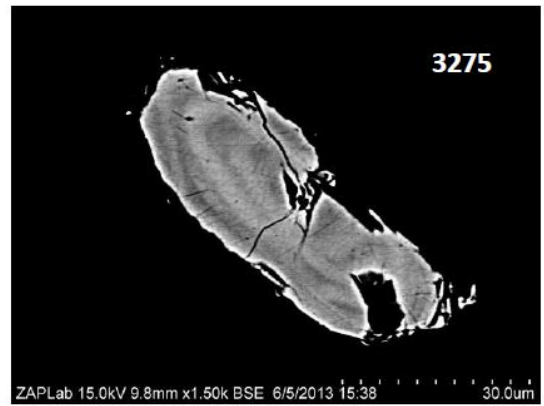
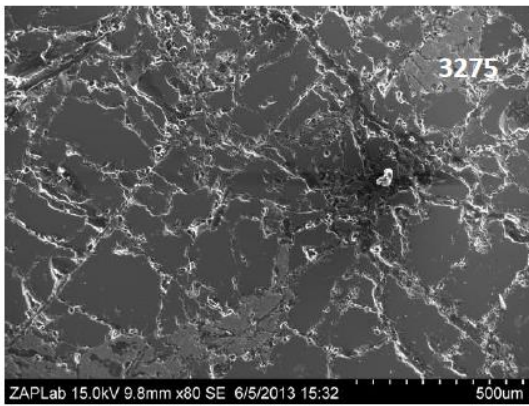
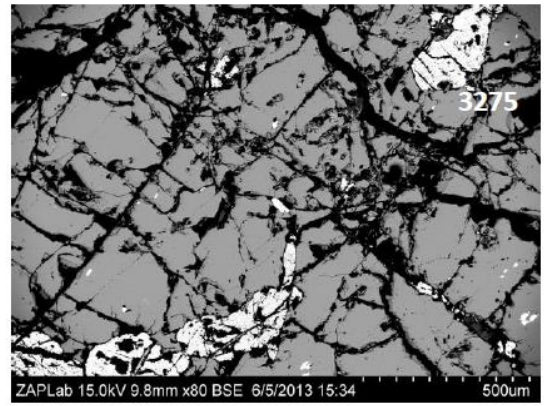
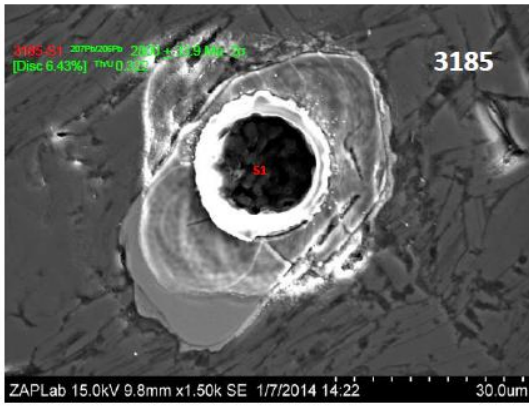
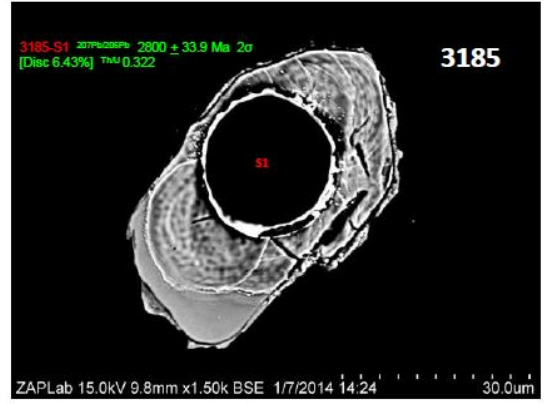
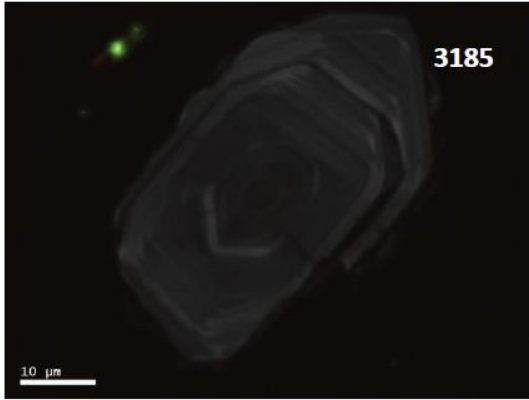


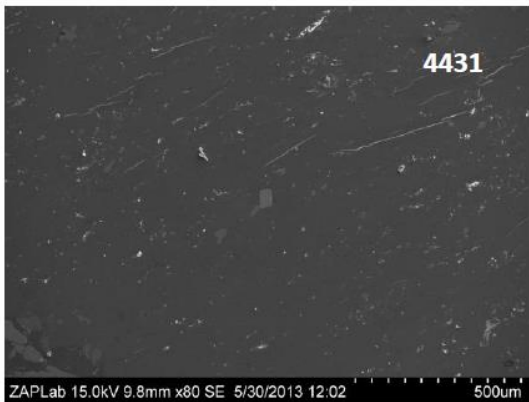
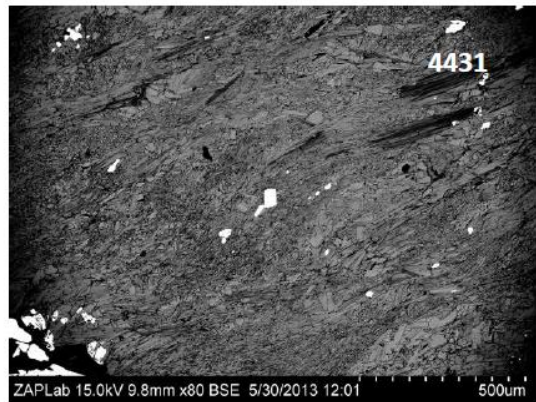
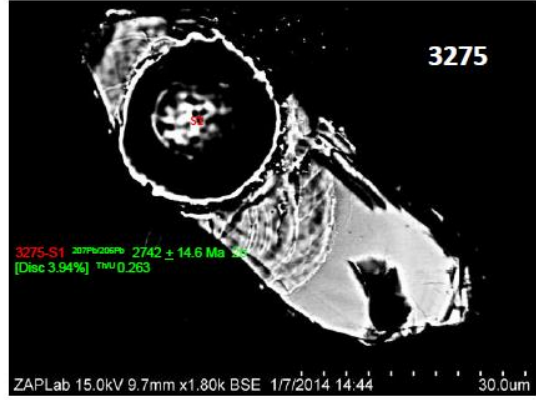
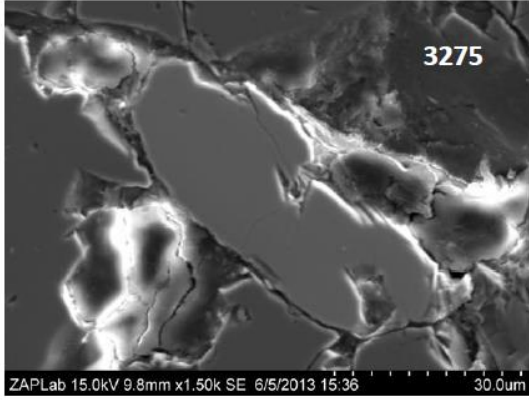
6220A Zircon

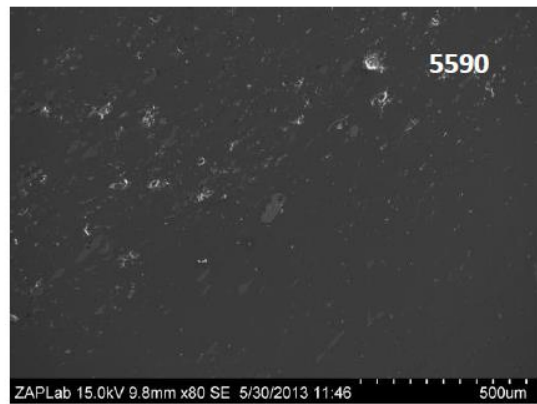
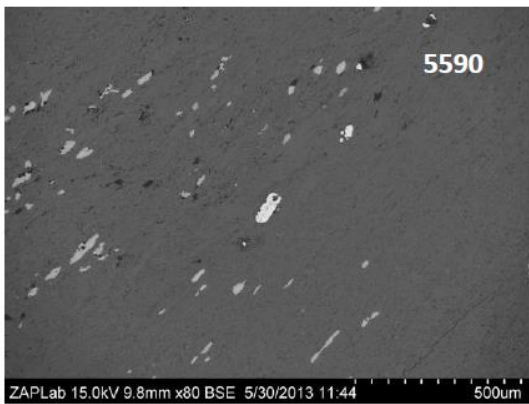
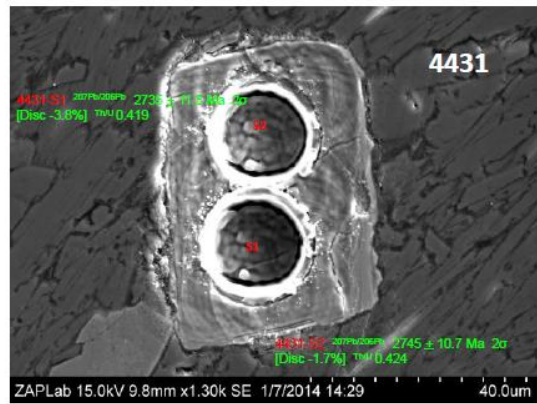
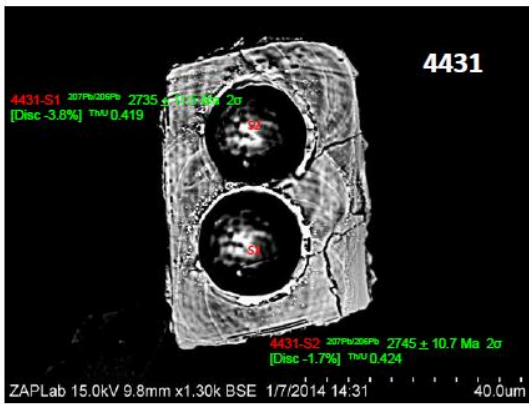
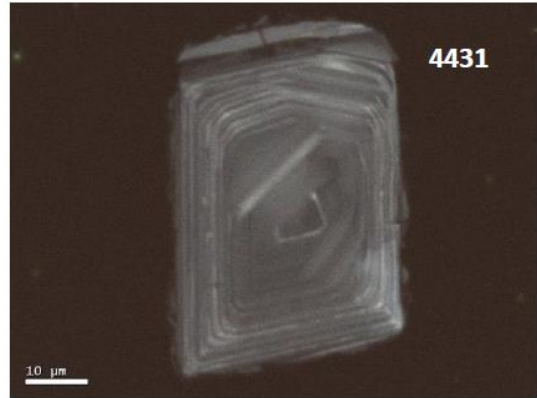
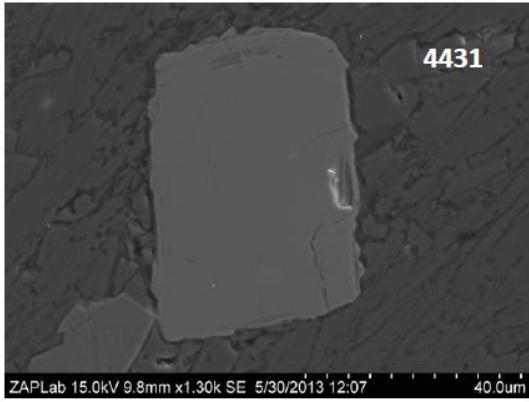


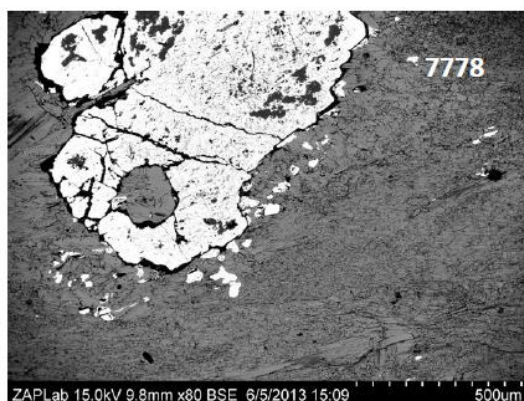
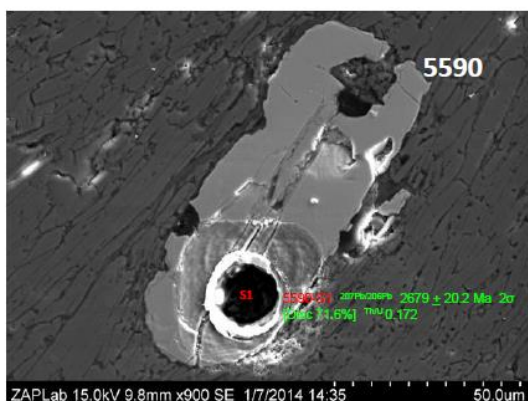
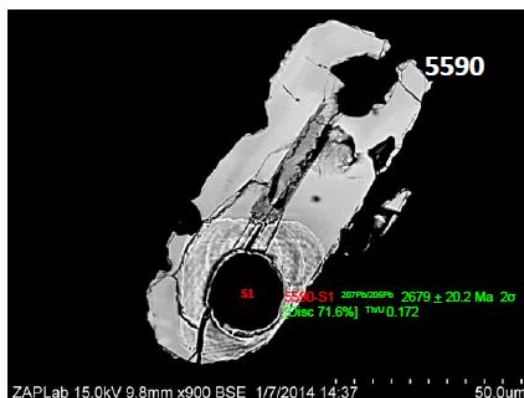
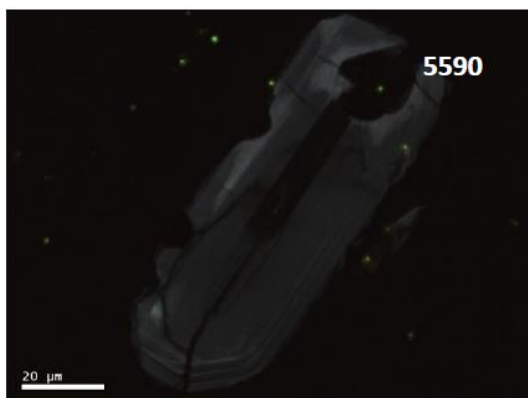
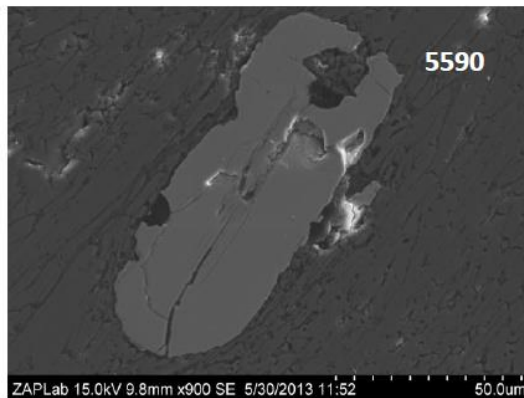


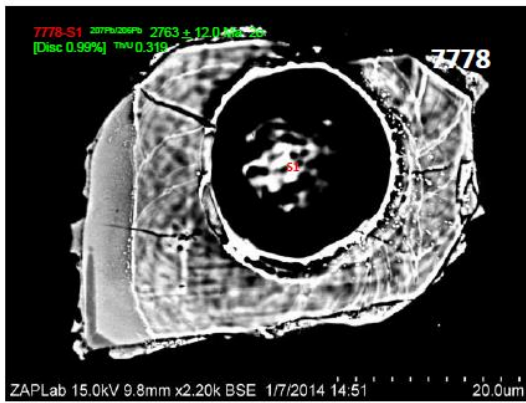
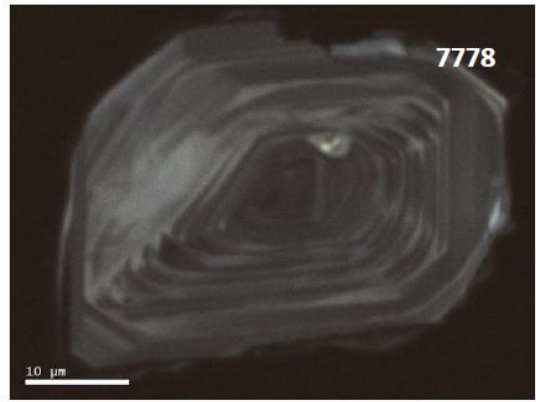
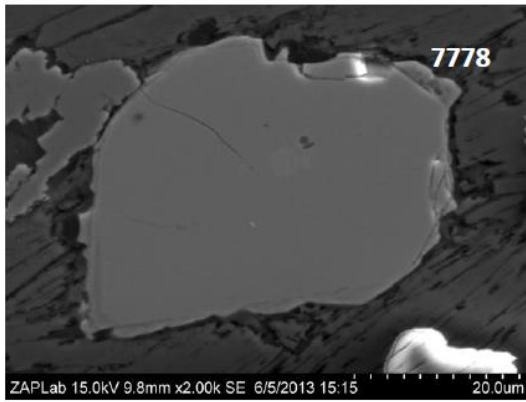
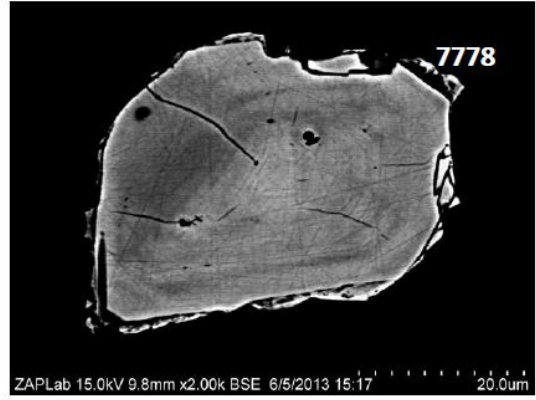
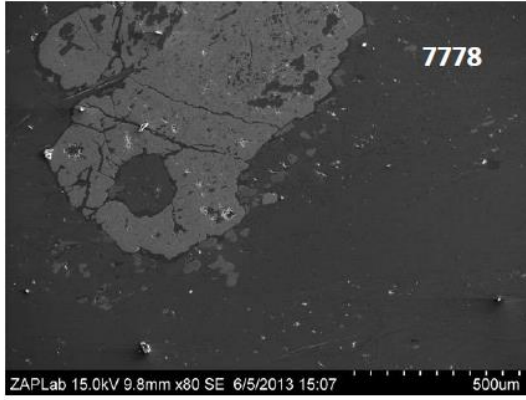




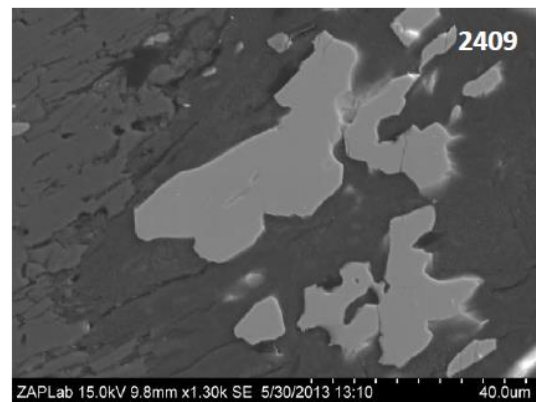
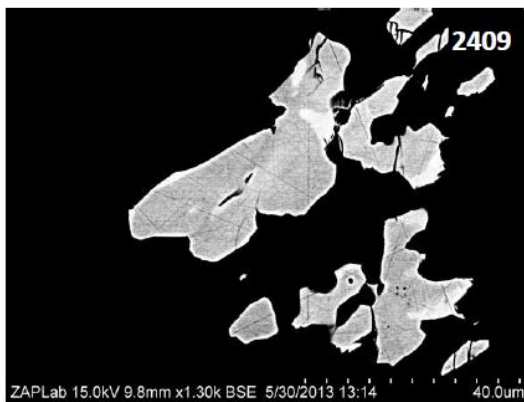
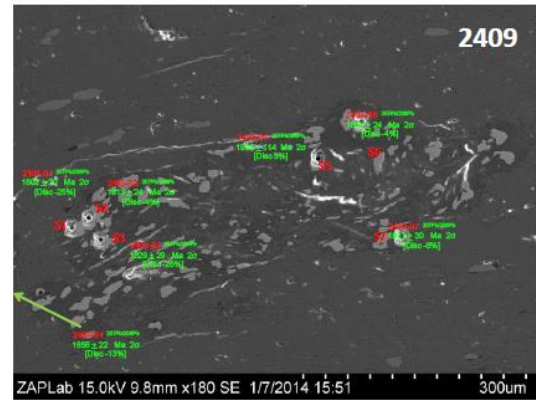
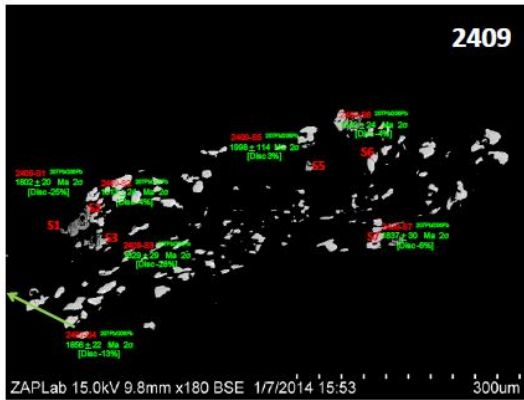
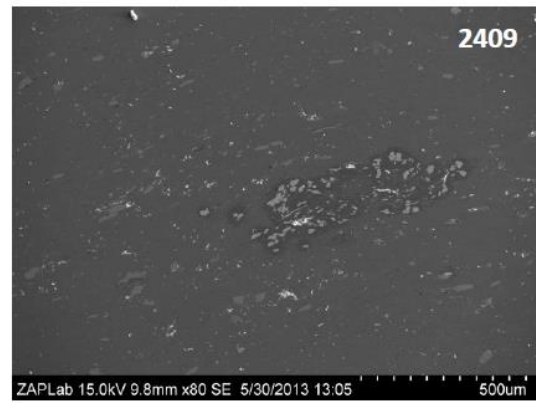
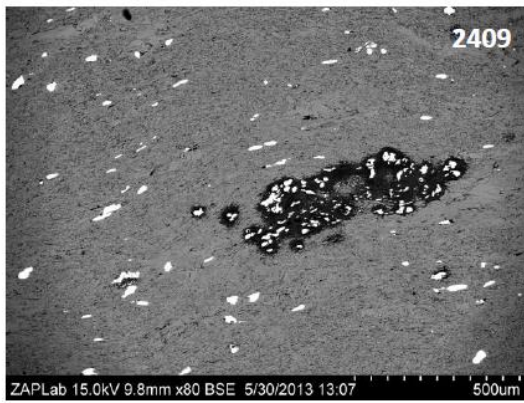


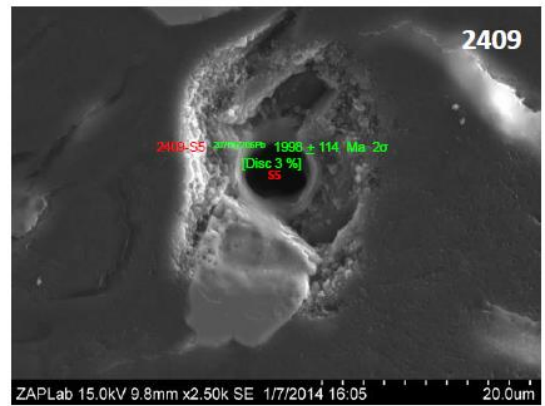
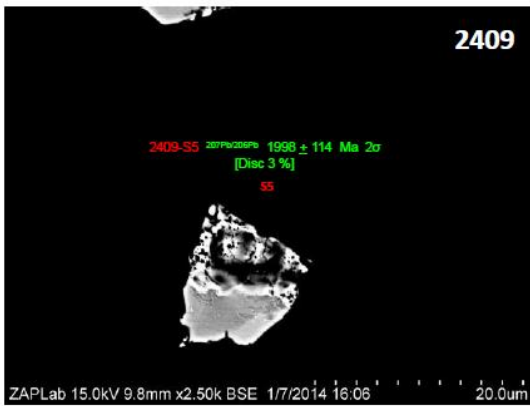
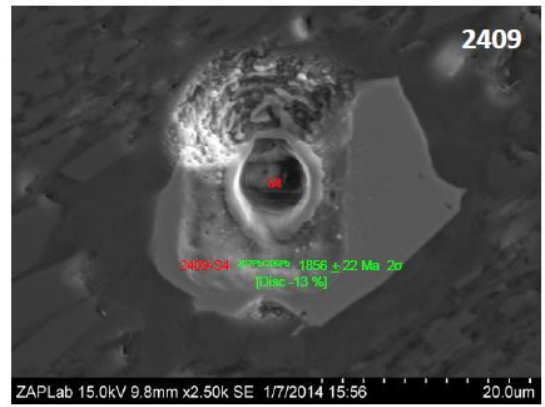
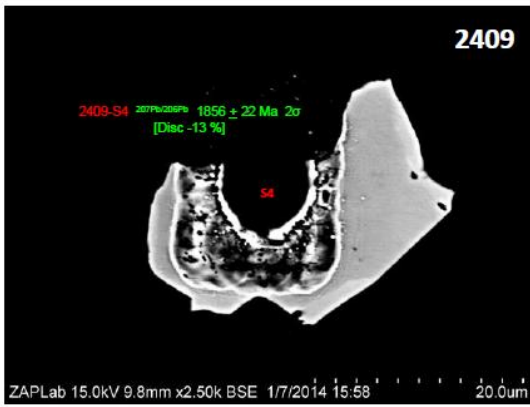
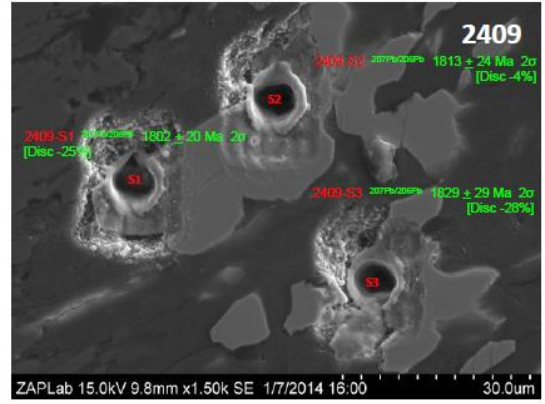
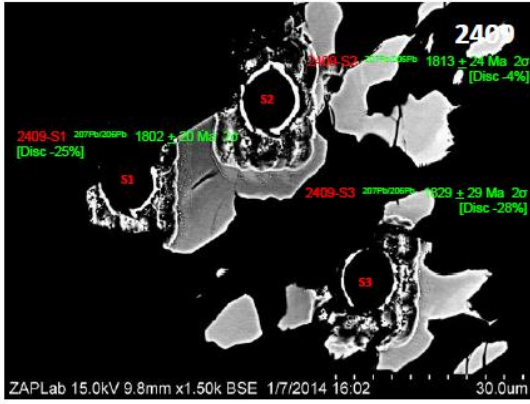


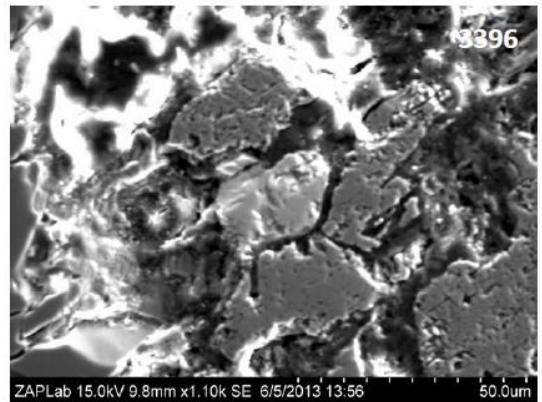
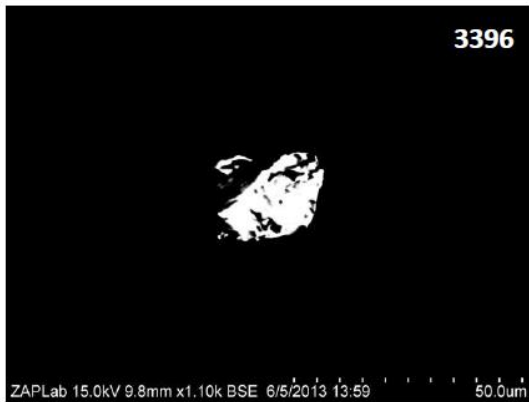
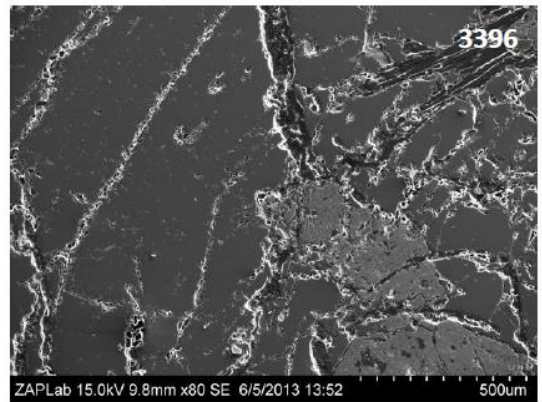
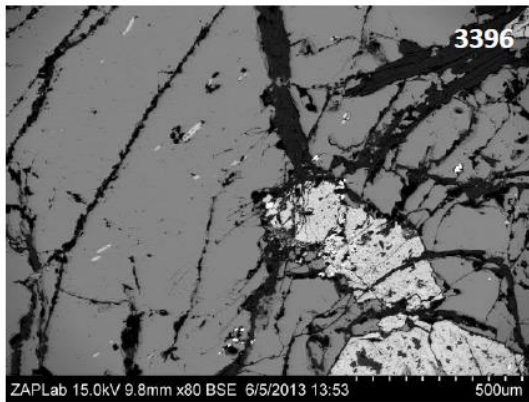
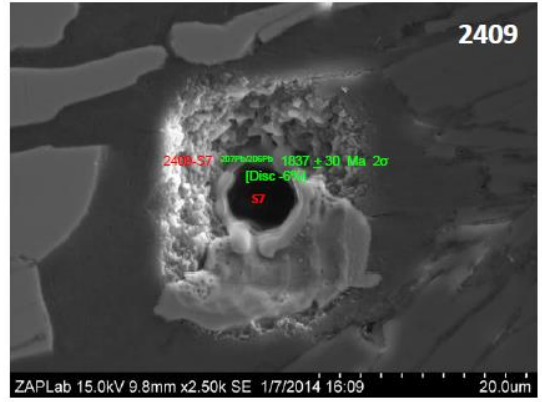
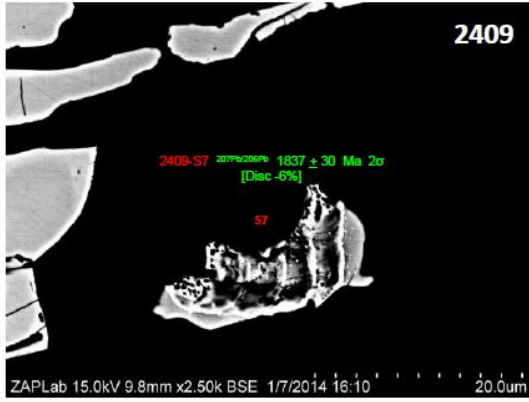


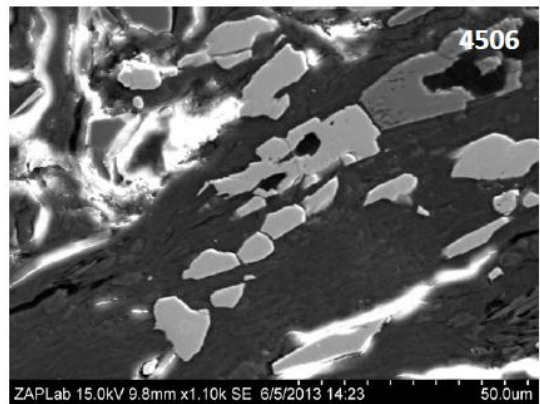
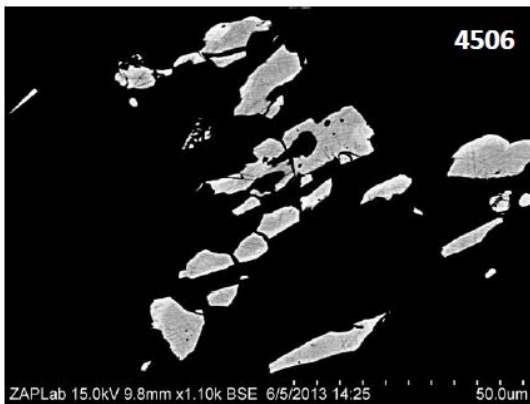
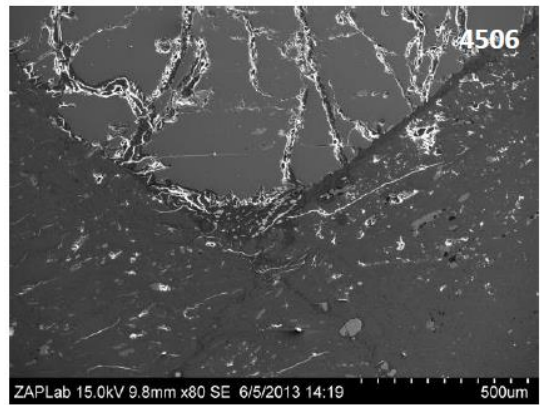
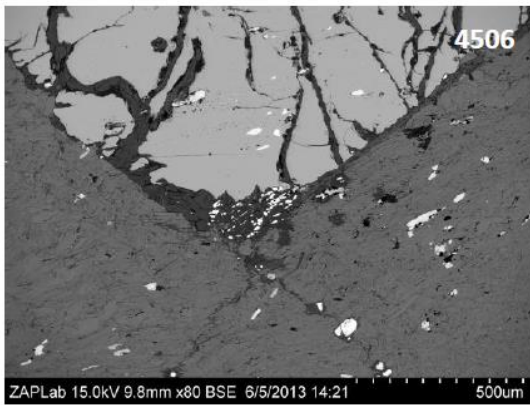
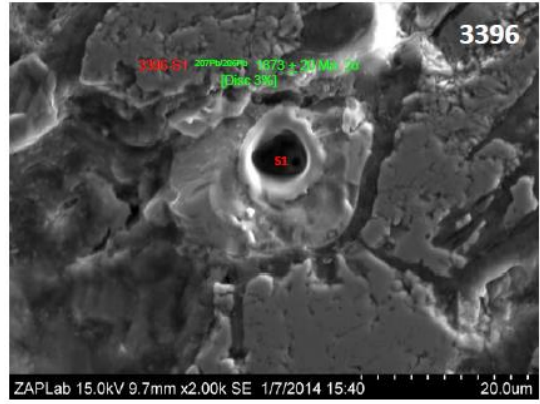
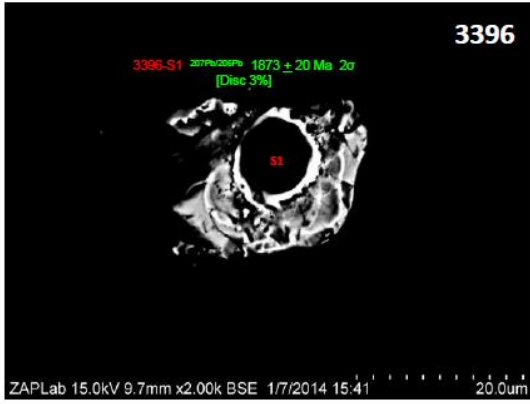


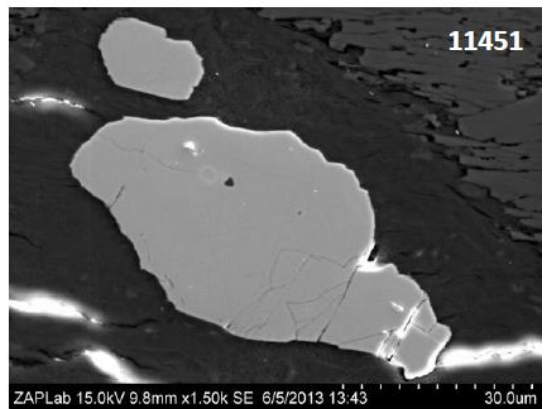
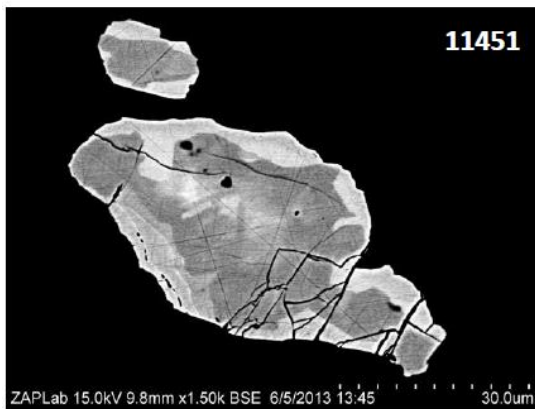
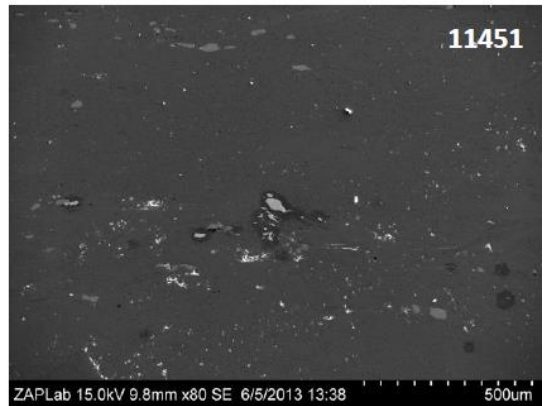
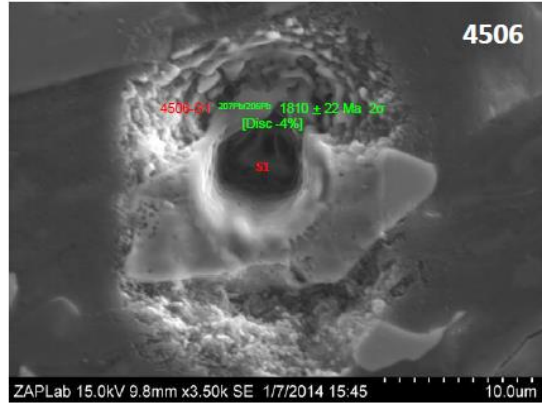
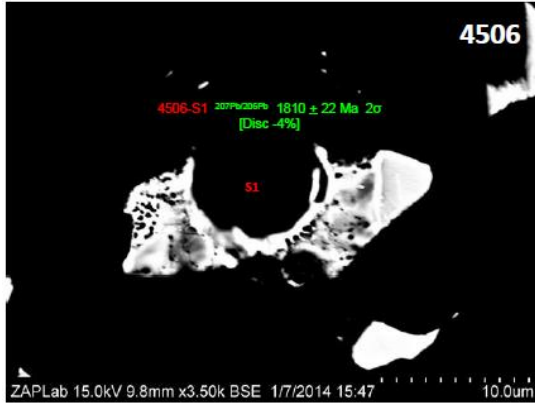
6220A Monazite

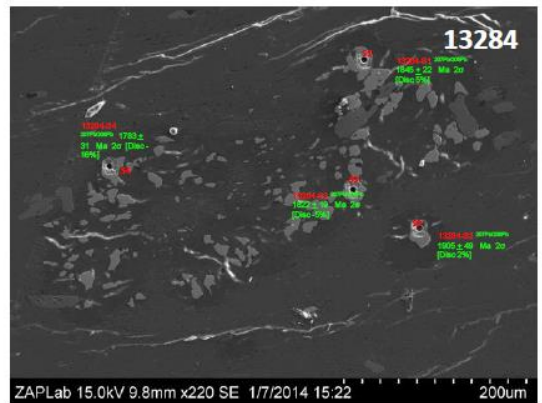
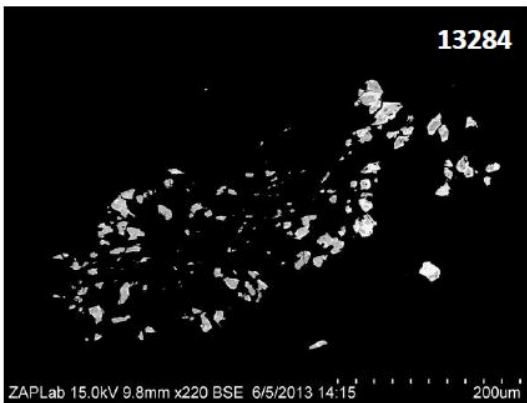
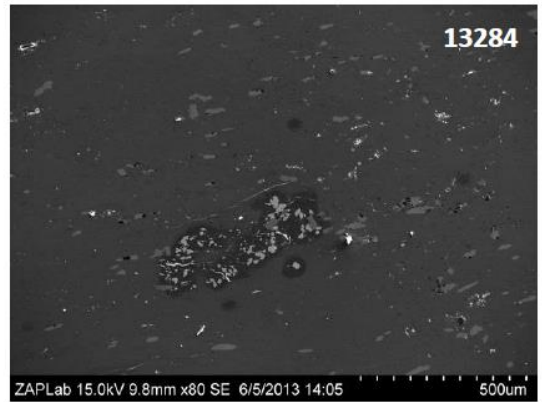
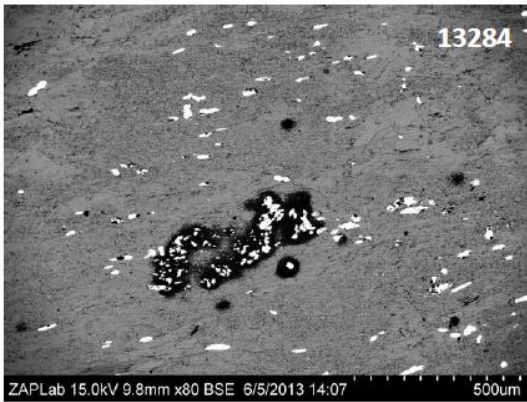
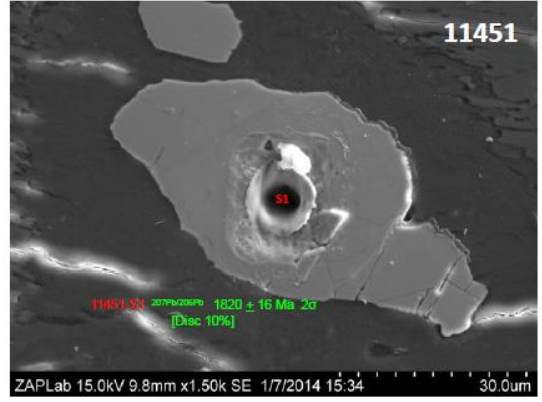
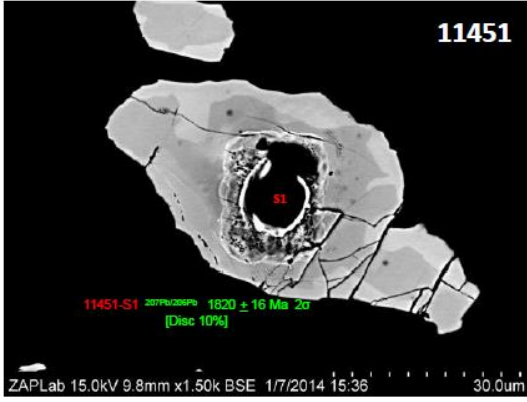


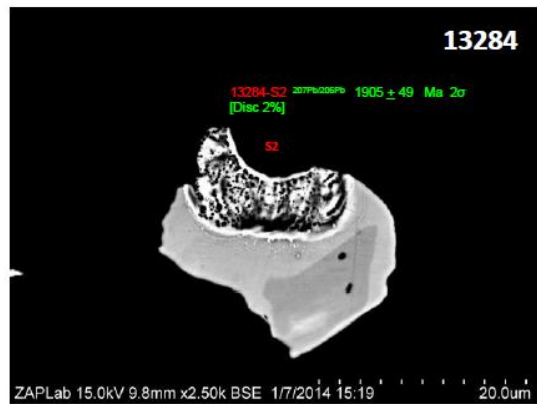
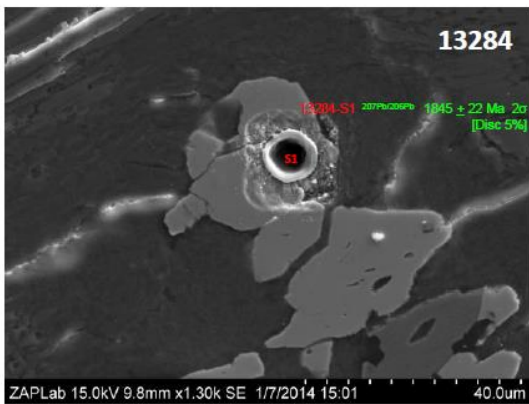
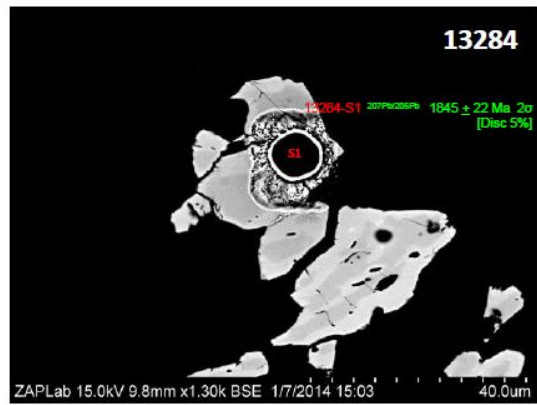
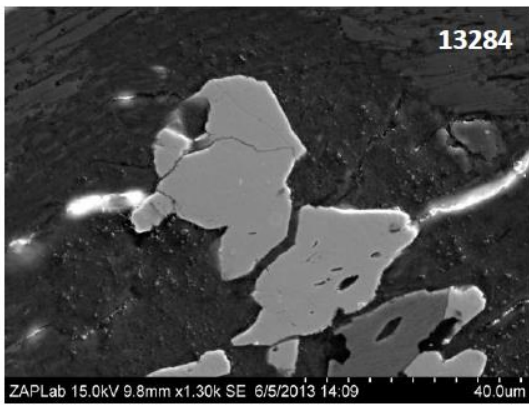
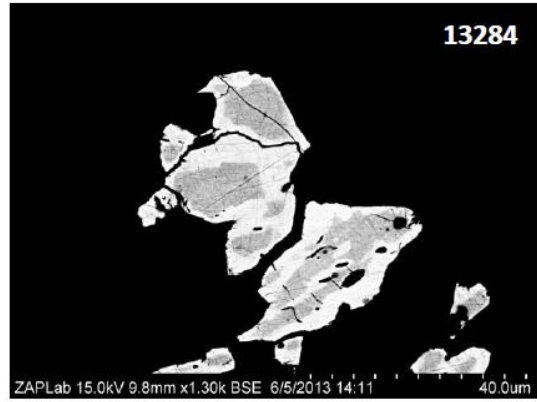
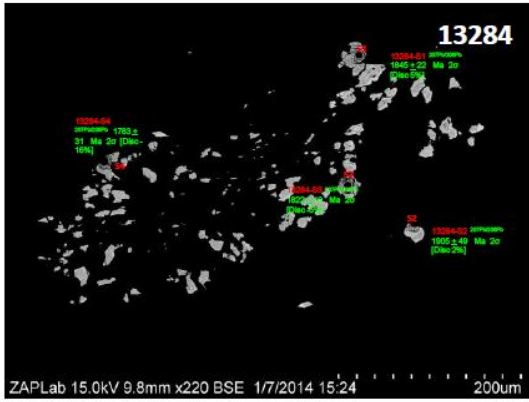


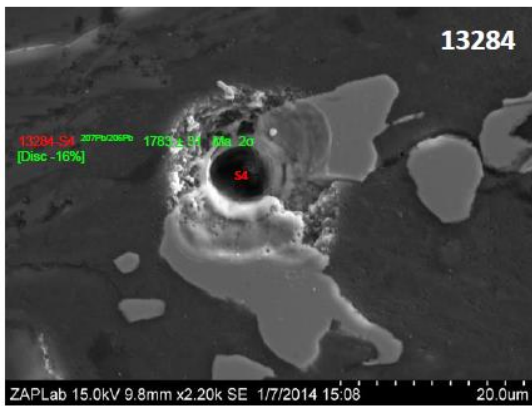
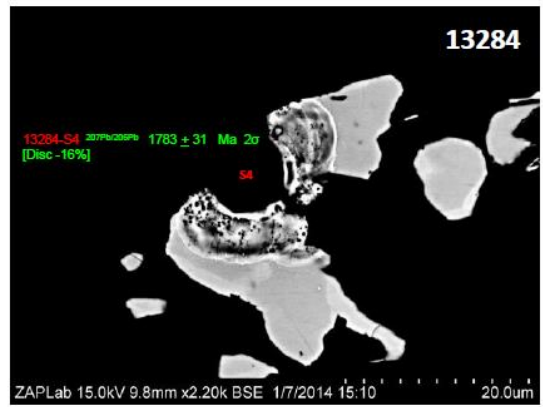
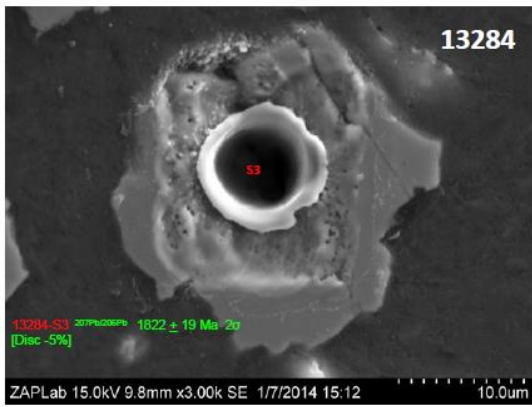
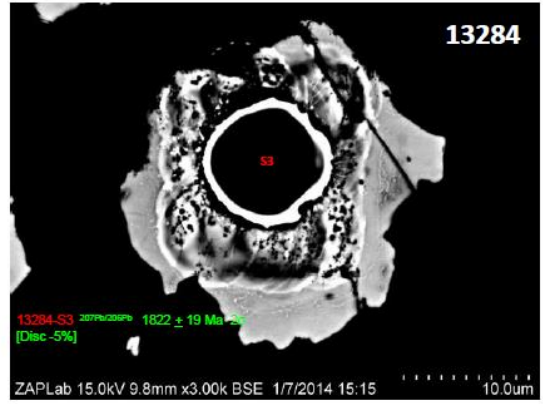
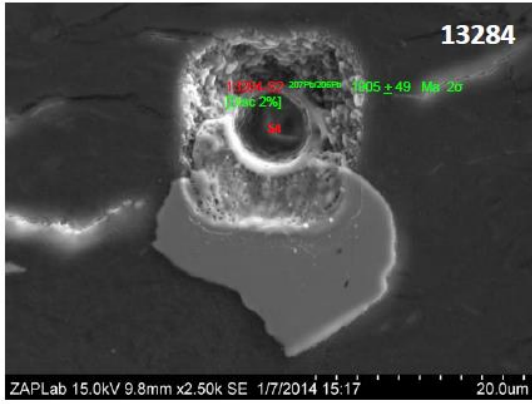


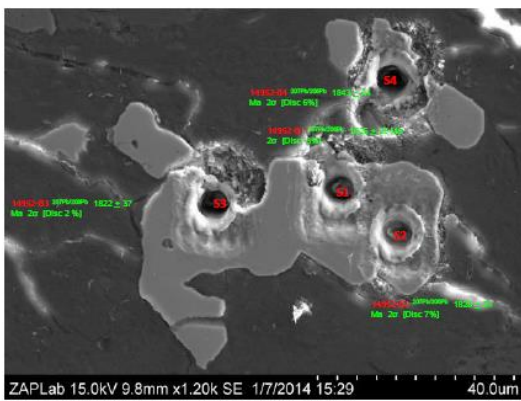
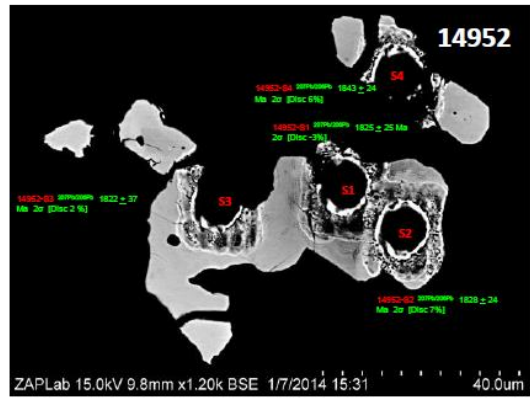
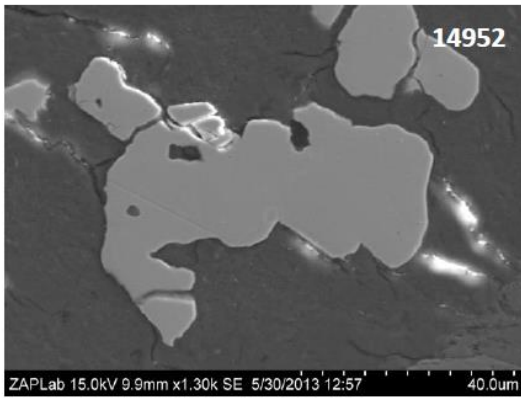
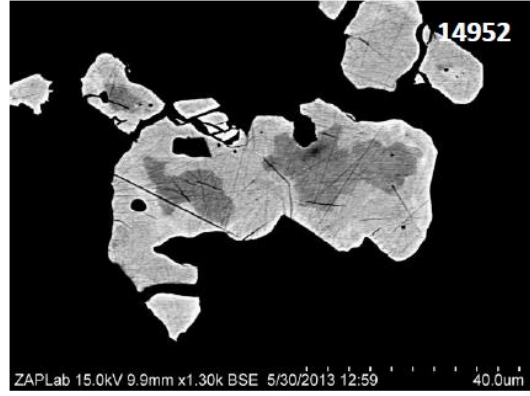
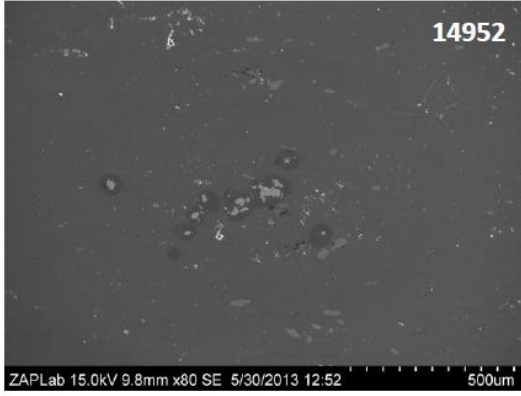












Curriculum Vitae

Name: Sean Fulcher

Post-secondary Education and Degrees: University of Ottawa
Ottawa, Ontario, Canada
2006-2011 HBSc.

Honours and Awards: NSERC IPS-1 Scholarship
2013-2014

Nortel Admission Scholarship
2006-2007

Related Work Experience

Teaching Assistant
The University of Western Ontario
2012-2014

Geologist
Baffinland Iron Mines Corporation
2010, 2012-2014

Exploration Geologist
Detour Gold Corporation
2011-2012

Geologist
Taseko Mines Limited – Hunter Dickinson Inc.
2011